THIS WEEK

EDITORIALS

PHYSICS If supersymmetry theory is wrong, then what is right? **p.6**

WORLD VIEW Give postdoc researchers a proper career not false hope **p.7**



The generation game

Birth-cohort studies offer invaluable data on the links between childhood development and later life, but today's efforts could learn something from a pioneering project that turns 65 this week.

ow and then, Britain creates something it can really be proud of. The Beatles, fish and chips, cream teas and pubs tend to rank high in polls, as can the Royal Family, particularly with wedding bells in the air. But ask epidemiologists, and they will probably praise a lesser-known British achievement: birth-cohort studies, the observation of groups of people from birth onwards.

This week, members of the oldest British birth cohort, all born in one week in March 1946, will celebrate their 65th birthdays (see page 20). They are part of the longest-running human experiment of its type, an endeavour that — along with later generations, including cohorts born in 1958, 1970 and at the turn of the millennium — is the envy of researchers around the world. The cohorts offer important lessons for scientists who want to launch similar efforts today, as well as for politicians who question the merits of funding such work. The 1946 cohort shows, in stunning detail, how long-term studies can pay off. It has provided a treasure-trove of data linking early socioeconomic status, health and development to later events, such as disease, educational attainment and well-being. And it is already starting to show how genetics and a lifetime of experiences influence the ageing process. Sometimes, the only way to understand human life is to study it. This week, the United Kingdom announced that it will spend some £33.5 million (US\$54.5 million) over five years on cohort research, including a new study of about 90,000 children.

Not all cohort studies receive universal praise. The National Children's Study in the United States, which is recruiting participants and aims to track around 100,000 children from birth to age 21, has been more than a decade in the planning, cost US\$194 million in 2010, and to its critics is a vast and overambitious data-gathering exercise without clear goals. Plans for a British birth cohort in the 1980s were vetoed by the Conservative government.

It is not just about money — the 1946 cohort, after all, has survived on a hand-to-mouth basis for most of its existence. The study was triggered by concerns about falling fertility rates in post-war Britain. Its gung-ho leader, James Douglas, was able to contact and question some 13,000 mothers who gave birth soon after the end of the Second World War — and to publish influential results within two years that prompted legislation leading to improved access to pain-relief during childbirth. Such rapid data collection and response would be impossible today, given the (often necessary) legal, ethical and bureaucratic framework erected around research in the intervening decades. Participants are now harder to recruit, and more likely to move away or drop out. And as science has developed, so the hypotheses and factors examined in modern cohort studies have proliferated. Gadgets measure every pollutant breathed, calorie consumed or step walked in pregnancy, and are accompanied by intelligence tests, studies of behaviour and parenting style, and countless clinical tests and biomolecular studies. The US National Children's Study has suffered from spiralling complexity and cost, partly attributable to investigators wanting to measure every possible variable.

One way to avoid this kind of scientific paralysis is to follow new cohorts every ten years or so. Questions not asked of one group can then be held over for the next. The need to initiate cohort studies is particularly pressing at the moment, with the deep budget cuts taking place in the United Kingdom and elsewhere threatening to increase

"Studies of today's children are just as valuable as studies of those born in 1946."

financial, health and educational inequalities. How, except by following those born during and immediately after the financial storm, can society learn about the longterm social impacts of these changes over a lifetime? Such questions are particularly urgent in the United States, and much will be learned from the National Children's Study,

but it ought to articulate a clear, science-based vision and prove that it can provide value for money. Does the study need the dozens of data-collection centres that it has scattered across the country, or can it be streamlined? Such questions must be carefully considered by politicians and scientists vying for a piece of the action.

In return, those who run cohorts must share their rich data with suitable collaborators — while adhering to appropriate confidentiality standards — and ensure that results are disseminated widely, particularly to policy-makers. Lifestyles and science are both more complex in 2011, but studies of today's children are just as valuable as studies of those born in 1946. Happy birthday to the Douglas babies — and here's to the next generation. ■

Invest to diversify

Despite many federal initiatives, the number of US scientists from minority groups remains low.

inorities and other marginalized groups have not always enjoyed the best relationship with science. In the 1930s, researchers from the US government started a series of experiments that recruited hundreds of African American men infected with syphilis, then left their disease untreated to study its natural progression. (The government did, however, provide free burial insurance.) More recently, American Indians from the Havasupai tribe sued Arizona State University in Tempe over claims that geneticists had collected and analysed blood samples from tribe members without obtaining proper consent. The two parties settled that suit last year. Indigenous peoples in other countries such as Australia also have historical reasons to be suspicious of mainstream scientists.

For more than a decade, US leaders have been trying to move beyond that troubled past and recruit minorities into science and engineering. There are strong moral arguments for doing so. But in times of massive budgetary shortfalls, morals do not guarantee funds. Congress and the public should recognize the powerful practical reasons to support programmes that aim to raise the numbers of minorities in science.

A key issue is that of numbers. There is concern in the United States about the shrinking proportion of home-grown scientists. Foreign-born students, particularly from China and India, account for almost all of the growth in the number of science doctoral degrees granted in America. And many then take their skills back home. Minorities make up a growing share of the US population and represent a relatively untapped pool from which to draw the next generation of scientists.

They also bring fresh ideas to research. This sometimes results in the pursual of topics that can help specific communities but have not managed to capture the attention of mainstream researchers. An example of which is Katie McDonald, who embarked on a research project as an American Indian student at a tribal college in Montana. She found higher-than-expected levels of mercury in local fish and has helped her own tribe to avoid health problems (see page 25).

Bringing more diversity into the ranks of researchers will help to overcome the lingering suspicion of science that persists in some minority communities. In doing so, it will encourage members of the public to accept the products of research, whether they are government health recommendations or reports about the changing climate. Without that kind of trust, researchers could see their work ignored by segments of the population.

For these and other reasons, the US government has poured

substantial funds into pulling more underrepresented minorities into science. The National Science Foundation spent more than \$110 million on this in 2010, and other agencies, such as the National Institutes of Health, NASA and the US Department of Education, also have programmes to boost minority participation in science.

These initiatives still have a long way to go. The National Research Council (NRC) reported last year that underrepresented minori-

"Minorities represent a relatively untapped pool from which to draw the next generation of scientists."

ties made up 28% of the US population in 2006 but accounted for only 9% of college-educated Americans in the science and engineering workforce.

And in some cases, the numbers are proving hard to move. In 2008, American Indians comprised just 0.7% of the bachelor's degrees awarded in science and engineering — a proportion that is unchanged since 2000. Science bachelor's degrees earned by black students has also stayed constant at 8.3%. For doctoral

degrees, the figures are even starker. American Indians, who represent 1% of the population, earn only 0.3% of the PhDs in science and engineering. Black people make up 13% of the US population but accounted for just 3% of the doctoral degrees awarded in 2008 in these fields.

The problem creates a vicious cycle. Similar proportions of minority and white students enter university intending to study science. However, the completion rate for minorities is lower. Many factors contribute to this gap, according to the NRC, but one remains the poor diversity of university faculty members and the scarcity of role models in science for students from minority groups.

Dark rumblings

The Large Hadron Collider is stirring up trouble, and that's good news for science.

In the 1860s, physics looked beautiful. The Scottish physicist James Clerk Maxwell had just published a series of papers that unified electricity, magnetism and light into a theory that could be expressed in a few equations. In doing so, he settled a long-running debate over whether light was a continuous wave of energy or a spray of tiny particles. It was, to anyone who understood Maxwell's work, quite obviously a wave. That raised a question, although it seemed to be more of a niggling detail to Maxwell's devotees: like water waves or sound, the new, electromagnetic light waves should need a medium through which to travel. If Maxwell was right, what did it look like?

So began the search for the notorious ether. In one spectacular experiment in 1887, Albert Michelson and Edward Morley designed and built a prototype interferometer to measure the speed of light at different points in Earth's orbit and showed that the speed was constant — impossible if light and Earth were flowing through an unseen liquid. Contrary to all their expectations, the ether wasn't there.

There are some parallels between physics then and physics now. Like the 1860s, the 1960s saw an incredible unification of modern physical theories. This time, the standard model of particle physics took Maxwell's electromagnetic force and wove it with the strong and weak nuclear forces. According to the theory, at sufficiently high energies the weak and electromagnetic forces merge into a single, electroweak force.

Like Maxwell's theory, the standard model is powerful, but there are some details that it can't quite explain. One is dark matter, a so-far undetected entity that makes up most of the matter in the cosmos. Another is dark energy, a force that seems to be pushing the Universe apart. There are some other unexplained odds and ends too, but

nothing formidable enough to push the standard model from its perch.

To deal with some of the problems, the best theorists of the day have proposed an extension of the model, known as supersymmetry. This modification unifies the electroweak force with the strong nuclear force, and suggests some elementary particles that might explain dark matter.

Now, an experiment has come along to challenge the standard model and its offspring. The Large Hadron Collider (LHC), a 27-kilometre proton–proton collider on the French–Swiss border near Geneva, Switzerland, is delivering a torrent of data that can be used to probe the boundaries of the standard model. But the collider has yet to find evidence of the particles suggested by supersymmetry theory (see page 13). If it finds nothing in the next year, the theory will look like it is in serious trouble. If it finds nothing in two years, then many theorists will probably abandon it, just as theorists eventually had to abandon extensions of Maxwell's work that explained away the missing ether.

The parallels with history shouldn't be taken too seriously. The LHC is a much more elaborate experiment than the one done by Michelson and Morley. It uses proton collisions to probe unknown energies for all sorts of things, not just the supersymmetrical particles some hope it will find. Nor is the LHC likely to deliver a clear refutation of supersymmetry — the theory, the data and the analysis are all much more complicated than they were 125 years ago.

But comparison can remind us of something that is easily overlooked: the negative results now coming out of the LHC should be just as stimulating as any positive findings. Michelson and Morley's experiment, and others like it, eventually led Albert Einstein to axiomatically accept that light travelled at a constant speed and could be both a wave and a particle. Those revelations never really disproved Maxwell's theories, but they did help to develop special relativity and quantum mechanics — the two greatest theories of the twentieth

NATURE.COM
To comment online, click on Editorials at:
go.nature.com/xhunqv

century. In the same way, the LHC's results — whatever they may be — could force scientists to think differently. If one beautiful theory can't explain the data, then there must be another out there somewhere that can. ■

WORLD VIEW A personal take on events



Give postdocs a career, not empty promises

To avoid throwing talent on the scrap heap and to boost prospects, a new type of scientific post for researchers is needed, says **Jennifer Rohn**.

The career structure for scientific research in universities is broken, particularly in the life sciences, my own overcrowded field. In coffee rooms across the world, postdocs commiserate with each other amid rising anxiety about biology's dirty little secret: dwindling opportunity. Fellowships are few, every advertised academic post draws a flood of candidates, and grants fund only a tiny fraction of applicants.

The scientific job market has been tight for decades, but the recent global recession and accompanying austerity measures have brought it into sudden focus for young — and some not so young — researchers, who face a widening chasm between their cycles of contract work and a coveted lab-head position.

This is a familiar lament, but I also propose a solution: we should professionalize the postdoc role and turn it into a career rather than a scientific stepping stone.

Consider the scientific community as an ecosystem, and it is easy to see why postdocs need another path. The system needs only one replacement per lab-head position, but over the course of a 30-40-year career, a typical biologist will train dozens of suitable candidates for the position. The academic opportunities for a mature postdoc some ten years after completing his or her PhD are few and far between.

Most fellowships are earmarked for youth and not applicable to experienced postdocs. Landing a lab-head position requires a strong publication record, which can be as much about luck as skill and hard work. Rare ancillary research positions, such as technicians and scientific officers, are frequently junior — or also on short-term contracts linked to a grant. Competition for senior positions in industry is just as fierce.

Beyond research, there are science-related jobs, such as in publishing, grants administration and public engagement. But these positions seldom require more than a doctorate, if that. And to force a highly trained postdoc from research is a terrible waste of time and public expense. The ageing postdoc may well struggle to make up for those lost ten years when starting again in a different career. Meanwhile, after many years of relatively low pay, they can be years behind in terms of savings and pensions.

The scientific enterprise is run on what economists call the 'tournament' model, with practitioners pitted against one another in bitter pursuit of a very rare prize. Given that cheap and disposable trainees -

PhD students and postdocs — fuel the entire scientific research enterprise, it is not surprising that few inside the system seem interested in change. A system complicit in this sort of exploitation is at best indifferent and at worst cruel. I have no doubt

◆ NATURE.COM Discuss this article online at: go.nature.com/vflfb8

that most lab heads want the best for their many apprentices, but at the system level, the practice continues. Few academics could afford to warn trainees against entering the ring — if they frightened away their labour force, research would grind to a halt.

An alternative career structure within science that professionalizes mature postdocs would be better. Permanent research staff positions could be generated and filled with talented and experienced postdocs who do not want to, or cannot, lead a research team — a job that, after all, requires a different skill set. Every academic lab could employ a few of these staff along with a reduced number of trainees. Although the permanent staff would cost more, there would be fewer needed: a researcher with 10-20 years experience is probably at least twice as efficient as a green trainee. Academic labs could thus become smaller, streamlined and more efficient. The slightly fewer trainees in the pool

> would work in the knowledge that their career prospects are brighter, and that the system that trains them wants to nurture them, not suck them dry and spit them out.

> An added benefit would be that instead of labs completely turning over every 4–5 years, with precious lore and knowledge lost along the way, they would have continuity. Fresh blood in a lab is useful, but so too are experienced people who can train others more efficiently, who are in touch with the latest techniques and who have firsthand knowledge of the lab's carefully amassed treasure-trove of materials.

Where should the cut-off be made to allow for the smaller number of trainees admitted? People with PhDs are useful to society, and are eminently employable in non-research fields. I would not necessarily advocate restricting their numbers, but every candidate should be given

a realistic assessment of their chances of becoming a lab head. The model I propose would reduce the number of trainee postdocs infused into the system, and then apply market forces — much as medical schools in many countries regulate the number of trainees by using the principles of supply and demand.

It won't be easy. Staff positions are typically attached to a lab head's temporary grant, not to the institutes that house them. Finance and numbers will need to be carefully balanced. Universities would have to create new permanent positions, and be willing to fund them long term. But the first step is to admit we have a problem, and that the problem is worth tackling.

Jennifer Rohn is a cell biologist at University College London and editor of http://LabLit.com. Her most recent book is The Honest Look (Cold Spring Harbor Laboratory Press). e-mail: jenny@lablit.com

T0

A HIGHLY TRAINED

POSTDOC

FROM RESEARCH

IS A TERRIBLE

M. OEGGERLI/SPL

A mammalian change of heart

Many fish can replace lost cardiac tissue throughout their lives, but adult mammals cannot. Researchers have now discovered a stage very early in life at which mammals can mend their own hearts through the replication of cells called cardiomyocytes.

Hesham Sadek and Eric Olson at the University of Texas Southwestern Medical Center in Dallas and their team surgically removed about 15% of muscle tissue from the ventricle walls of 1-day-old mice. One week later, they found evidence of cardiomyocyte proliferation in the heart. The animals fully recovered their muscle tissue and organ function within two months. The same procedure performed on 7-day-old mice did not lead to cardiomyocyte proliferation or recovery.

This work may lead to new strategies for reawakening regeneration in the adult mammalian heart after injury. Science 331, 1078-1080 (2011) For a longer story on this research, see: go.nature.com/ io3ccw

CONSERVATION

Identifying reef fish at risk

More than one-third of coral-reef fish species in the Indian Ocean, such as the butterflyfish Chaetodon trifascialis (pictured), could become extinct in their local environment as a result of climate change.

Nicholas Graham at James Cook University in



CLIMATE-CHANGE IMPACTS

More sneezing in a warmer world

Climate change is bad news for people with allergies: a warmer climate means a longer pollen season. In just 15 years, the pollen season of one common allergen has lengthened by as much as 27 days in some parts of North America.

The prevalence of allergies is increasing in the United States, but linking this increase with climate change has been a stretch. A team led by Lewis Ziska at the US Department of Agriculture in Beltsville, Maryland, compared readings

of ragweed pollen (pictured) since 1995 at 10 stations across North America with changes in temperature and first frost. They found a clear link between recent warming and the length of the pollen season. What's more, the farther north they looked, the greater the extension to the season — so allergy-prone Canadians should consider buying tissues in bulk.

Proc. Natl Acad. Sci. USA doi:10.1073/ pnas.1014107108 (2011)

Townsville, Australia, and his colleagues developed a method for predicting how vulnerable species are to local extinction, taking into

> account variables such as how picky the fish are about their food or habitat.

> > The researchers found that 56 of the 134 fish species studied were at risk of losing their habitat, shelter or food sources as a

result of climate change. Interestingly, those fish at greatest risk from climate change were not the same as those at greatest risk from

overfishing. The predictions could be used to better manage animal populations and habitats, helping to ensure survival under climate change and other pressures. Ecol. Lett. doi:10.1111/j.1461-0248.2011.01592.x (2011)

NEUROSCIENCE

Think of yourself when quitting

In smoking-cessation programmes, cognitive therapy is more successful if it is tailored to individuals than if it is applied generically. The difference may lie in the recruitment of brain areas

activated by thinking about oneself, scientists have found.

Hannah Faye Chua and her colleagues at the University of Michigan in Ann Arbor presented would-be quitters with messages relevant to their lives and the obstacles they perceived to changing their smoking behaviour, while scanning their brains with functional magnetic resonance imaging.

Activation of the dorsomedial prefrontal cortex, an area that is activated when people think about themselves, was correlated with how likely participants were to have stopped smoking four months after the scanning.

This correlation was not seen when the patients were given non-tailored messages about smoking during scanning. Nature Neurosci. doi:10.1038/ nn/2761 (2011)

BIOLOGY

Predators trigger plankton stealth

Tiny water-dwelling organisms called phytoplankton can adopt a 'stealth' mode to avoid the attentions of predators.

Many types of plankton group together into chains, and some respond to grazers by increasing their group size until the chains are too large to eat. Erik Selander of the Technical University of Denmark in Charlottenlund and his colleagues show that predators can trigger the opposite response in Alexandrium tamarense.

When exposed to small plankton-eating crustaceans called copepods, chains of Alexandrium adopt stealth behaviour, splitting into single cells or very short chains and swimming more slowly. The phytoplankton drastically reduces its encounters with grazers through this mechanism, the authors report.

Proc. Natl Acad. Sci. USA doi:10.1073/pnas.1011870108 (2011)

EPIDEMIOLOGY

Farm kids benefit from microbes

Exposure to diverse microbes could explain why children who grow up on farms are less likely to develop asthma than their suburban counterparts.

Previous work showed that children raised on farms are protected from childhood asthma and a class of allergic reactions called 'atopy'. Now, Markus Ege of the University Children's Hospital Munich in Germany and his colleagues have analysed the microbial populations in dust collected from 933 children's rooms. They found that bacteria and

fungi were more numerous and widespread in samples collected for children who live on farms. They also found that the risk of asthma and atopy decreased as the number of microbial taxa increased. In particular, fungi from two genera, Eurotium and Penicillium, were tightly associated with reduced asthma risk.

N. Engl. J. Med. 364, 701-709

CLIMATE CHANGE

Sea-ice models don't measure up

Climate models do a poor job when it comes to simulating sea-ice change in the Arctic.

Michael Winton of the Geophysical Fluid Dynamics Laboratory in Princeton, New Jersey, compared data from the era of satellite observations and five state-of-the-art climate models of Northern Hemisphere sea-ice cover. All of the model simulations considerably underestimated the observed sea-ice decline.

Substantial natural variability in the annual sea ice would be necessary to explain the discrepancy between observations and even the best-performing model. It is more likely that current climate models are not nearly sensitive enough to accurately gauge the behaviour of sea ice in response to warming, the authors say.

J. Clim. doi:10.1175/ 2011JCLI4146.1 (2011)

GENETICS

Clues from big-hearted mice

Mice bearing the mutations underlying two human heart syndromes have pointed the way to possible treatments. Noonan and LEOPARD syndromes both cause short stature, facial deformities and abnormally thick hearts that cannot pump properly.

Benjamin Neel and Toshiyuki Araki of the Ontario Cancer Institute in Toronto,

COMMUNITY CHOICE

ANIMAL BEHAVIOUR

Dogs keep an eye on their owners

A HIGHLY READ on elsevier com up to 21 February

Dogs are famously good at reading human body language, following human gaze and stealing human food. But not all humans are equal in the eyes of Canis familiaris.

Paolo Mongillo and his colleagues at the University of Padua in Italy investigated the attention dogs paid to their owners and to strangers. Each dog watched as its owner and a stranger walked back and forth across a test room in opposite directions, popping in and out of two doors.

Not surprisingly, the dogs kept their eyes on their owners most of the time, and stared at the doors they had gone through. At least, young dogs did. Dogs over the age of seven didn't stare at the door their owners had gone through with the same frequency, perhaps indicating some cognitive decline, or that they have learned over the years that their owners always come back in the end.

Anim. Behav. 80, 1057-1063 (2010)

Canada, and their co-workers, engineered mice to have the mutation in the Raf1 gene that underlies Noonan disease. In addition to features of the human syndrome, the mice had increased activity of the Mek protein. Pups given a Mek inhibitor started small but they grew faster and caught up with normal mice by a couple of weeks after birth.

Meanwhile, Neel and Maria Kontaridis of Harvard Medical School in Boston and their colleagues inserted into mice the mutation in the Ptpn11 gene that causes LEOPARD syndrome. The activity of a protein called mTor was abnormally high in these mice, and giving them the mTor inhibitor rapamycin repaired heart defects.

J. Clin. Invest. doi:10.1172/ JCI44929 (2011) J. Clin. Invest. doi:10.1172/ JCI44972 (2011)

NANOTECHNOLOGY

Slip and slide pores for sensors

Taking their inspiration from nature, researchers have coated nanopores with fluid bilayers to sense single proteins. The



creation, which mimics the pores in the olfactory system of a silk moth (**pictured**), was developed by Michael Mayer at the University of Michigan in Ann Arbor, Jerry Yang at the University of California Collino and the University of Californ creation, which mimics the University of California, San Diego, and their team.

By modifying the lipid with specific ligands, the researchers can control which proteins move through the pore, and how long their journey takes. The system can also be tweaked to slow down proteins that would otherwise translocate too fast to be analysed accurately. Nature Nanotechnol. doi:10.1038/

NNANO.2011.12 (2011)

◇ NATURE.COM

For the latest research published by Nature visit:

www.nature.com/latestresearch

SEVEN DAYS The news in brief

POLICY

Irish election

Scientists in the Republic of Ireland hope that support for science will continue after the Fine Gael party came to power in elections held on 25 February, ousting the long-standing incumbents, Fianna Fáil. Fine Gael, which must form a coalition government, will have to deal with the country's economic crisis by cutting some public spending. The party is opposed to research using human embryonic stem cells, which has never benefited from clear regulation in Ireland. See go.nature.com/ftx2hu for more.

Forest mission

India will spend 460 billion rupees (US\$10 billion) over a decade planting new forests and improving the quality of tree cover in existing forests, according to a plan approved by the Prime Minister's Council on Climate Change on 23 February. Subject to expected parliamentary approval, this 'National Mission for a Green India' one of eight missions under a national action plan on climate change — will start from 2012.

Push for carbon tax

Australia's prime minister Julia Gillard has proposed placing a fixed tax on carbon dioxide from July 2012, calling the move "an essential economic reform". It is the third time that Australia's government has vowed to tax carbon emissions to tackle climate change; Gillard's predecessor Kevin Rudd twice failed to get a carbon-cutting bill past his Senate. Speaking on 24 February, Gillard said she hoped to move to a marketbased emissions trading scheme three to five years after the fixed price comes in. Its value has not yet been decided.



Dire threats to coral reefs

More than 60% of the world's coral reefs are directly threatened by local human activities such as coastal pollution and destructive fishing. When global pressures, including rising ocean temperatures or ocean acidification, are taken into account, about 75% are threatened, with the proportion expected to rise to 90%

by 2030. The World Resources Institute in Washington DC published the statistics on 23 February in Reefs at Risk, a report updating a 1998 study. The latest report emphasized that reefs affect society, providing food and coastline protection, and said that they can rebound if communities stop unsustainable practices.

Egypt reshuffle

As protests continue across the Arab world, Egypt's interim cabinet was reshuffled last week and included new appointees to oversee education and science. Amr Salama, a professor of civil engineering, is minister of scientific research, replacing Hani Helal. Ahmed Gamal Moussa replaces Ahmed Zaki Badr as education minister. Both appointees are respected by scientists and had held similar positions in 2004, only to be sacked a year later. They may have little chance to make an impact, with the interim government in place for six months at most. See go.nature. com/ghqimz for more.

India's budget

Indian scientists were disappointed by increases in funding for research

agencies in the country's 2011-12 budget, presented on 28 February. The Indian ministry for science and technology saw a 17% increase on last year's budget to some 75.5 billion rupees (US\$1.67 billion), while atomic energy and space also saw doubledigit percentage increases. But with the economy booming and inflation running above 8%, "if we want to catch up with China we must make big investments in science", C. N. R. Rao, chairman of the prime minister's scientific advisory council, told Nature. "These lollipops will not do."

Shuttle swansong

NASA's space shuttle *Discovery* launched for its 39th and final flight on 24 February, taking six astronauts as well as

supplies and additional science capabilities to the International Space Station on an 11-day mission. NASA's other two shuttles are each due to fly once more this year before the agency's shuttle fleet retires.

M. CONLIN/OSF/PHOTOLIBRARY.COM

Unethical studies

A meeting of the US presidential bioethics commission in Washington DC this week triggered reporting of past unethical human experiments by US researchers, mostly from the 1940s to the 1960s. The commission met in part to discuss last year's revelations that US government researchers secretly gave syphilis to hundreds of Guatemalan prison inmates in the 1940s (see Nature 467, 645; 2010). But the Associated Press, trawling medical journals and old newspaper

10 | NATURE | VOL 471 | 3 MARCH 2011

articles, dug up more than 40 instances of similarly dubious tests. All had been publicly disclosed, unlike the syphilis experiments, but did not draw the condemnation at the time that they would today.

Oil-spill health study

A study claiming to be the largest ever to follow up the long-term effects of an oil spill on human health was launched on 28 February (see nihgulfstudy.org). The National Institutes of Health says it has committed US\$19 million to the project so far; its National Institute of Environmental Health Sciences hopes to spend a decade following 55,000 of the workers and volunteers who supported the clean-up effort after the Deepwater Horizon disaster in the Gulf of Mexico.

Booking a rocket

The first contracts have been signed to send researchers into suborbit using commercial spacecraft. The Southwest Research Institute, in San Antonio, Texas, said last week it had paid for six scientists to fly with XCOR Aerospace, based in Mojave, California, and had paid deposits for two scientists to fly with Virgin Galactic, whose spacecraft will take off from Spaceport America in New Mexico. The institute may opt to purchase a total of 17 seats

with the two companies, each costing US\$100,000–200,000. Scientists would conduct experiments including biomedical monitoring and atmospheric imaging.

Viral response plan

Medical virologists from around the world gathered in Washington DC on 1-3 March to work out the details of a Global Virus Response Network. Meeting attendees, invited by virologist Robert Gallo of the University of Maryland School of Medicine in Baltimore, hope to form an organization that would act as a global first-responder to identify, investigate and eradicate viral outbreaks. The network would also inform governments, health organizations and the public about existing viruses and attract scientists to the field.

Wheat killer

A research programme tackling a devastating wheat fungus has been granted US\$40 million over five years as part of a partnership between the Bill & Melinda Gates Foundation in Seattle, Washington, and the UK Department of International Development. The Durable Rust Resistance in Wheat project, involving more than a dozen institutes and coordinated by Cornell University in Ithaca, New

York, aims to create plants that can withstand strains of the evolving stem-rust pathogen Ug99. See go.nature. com/4wm8te for more.

PEOPLE



German plagiarism

Germany's defence minister, Karl-Theodor zu Guttenberg (pictured), has resigned after a row over plagiarism in his PhD thesis. The University of Bayreuth withdrew Guttenberg's doctoral thesis in law last week, confirming that large parts of the document, written in 2006, were plagiarised. German chancellor Angela Merkel initially argued that academic wrongdoings didn't diminish Guttenberg's political merits, but public pressure forced his resignation on 1 March. Thousands of German academics and doctoral students had joined the outcry, signing an online letter complaining that Merkel was trivializing academic plagiarism.

COMING UP

3-6 MARCH

The American
Association for
Cancer Research
hosts a conference in
Vancouver, Canada,
exploring links between
stem cells and cancer.
go.nature.com/5lwqim

7-11 MARCH

Preliminary analysis of dust picked up from a distant asteroid last year by the Hayabusa spacecraft will be among highlights of the 42nd Lunar and Planetary Science Conference in The Woodlands, near Houston, Texas.

go.nature.com/eugq9g

9-13 MARCH

The 10th International Conference on Alzheimer's & Parkinson's Diseases will take place in Barcelona, Spain, and focus on new possibilities for treating the conditions.

go.nature.com/jcgygu

Climate inquiry

An inquiry has exonerated climate scientists with the National Oceanic and Atmospheric Administration in Washington DC of data manipulation or unethical behaviour. Requested by Senator James Inhofe (Republican, Oklahoma), it is the latest of many investigations to clear researchers of implications of scientific misconduct in e-mails from the Climatic Research Unit at the University of East Anglia, UK, leaked in November 2009. In a report released on 24 February, the inspector general of the US commerce department, who headed the inquiry, found no evidence of wrongdoing in the e-mails.

⇒ NATURE.COM

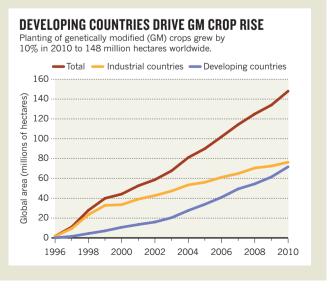
For daily news updates see: www.nature.com/news

inde a total of 17 oear

TREND WATCH

C. JAMES/ISAAA

Developing countries look poised to overtake industrialized countries in planting genetically modified (GM) crops (see chart). Brazil, Argentina, India, China and South Africa together accounted for 43% of the global total of biotech crops planted commercially last year. In 2010, Pakistan and Myanmar grew GM crops commercially for the first time, opting for biotech cotton. Sweden also made its first foray into commercial GM crops, planting the 'Amflora' highstarch potato.



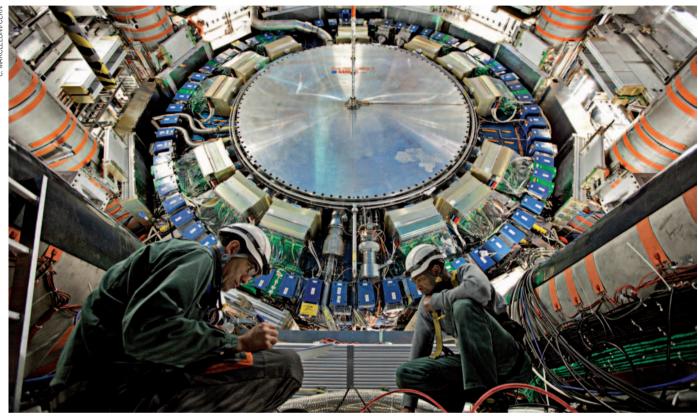
NEWSINFOCUS

POLICY Unease over rapid revamp of National Institutes of Health **p.15**

BIOMEDICINE Precise gene editing makes the move into the clinic **p.16**

ENVIRONMENT China counts the cost of fast development **p.19**





"Any squarks in here?" The ATLAS detector (above) at the Large Hadron Collider has failed to find predicted 'super partners' of fundamental particles.

PHYSICS

Beautiful theory collides with smashing particle data

Latest results from the LHC are casting doubt on the theory of supersymmetry.

BY GEOFF BRUMFIEL

onderful, beautiful and unique" is how Gordon Kane describes supersymmetry theory. Kane, a theoretical physicist at the University of Michigan in Ann Arbor, has spent about 30 years working on supersymmetry, a theory that he and many others believe solves a host of problems with our understanding of the subatomic world.

Yet there is growing anxiety that the theory, however elegant it might be, is wrong. Data from the Large Hadron Collider (LHC), a 27-kilometre proton smasher that straddles the French–Swiss border near Geneva, Switzerland,

have shown no sign of the 'super particles' that the theory predicts¹⁻³. "We're painting supersymmetry into a corner," says Chris Lester, a particle physicist

NATURE.COM
Read more at
Nature's LHC
special:
www.nature.com/lhc

at the University of Cambridge, UK, who works with the LHC's ATLAS detector. Along with the LHC's Compact Muon Solenoid experiment, ATLAS has spent the past year hunting for super particles, and is now set to gather more data when the LHC begins a high-power run in the next few weeks. If the detectors fail to find any super particles by the end of the year, the theory could be in serious trouble.

Supersymmetry (known as SUSY and pronounced 'Susie') emerged in the 1970s as

▶ a way to solve a major shortcoming of the standard model of particle physics, which describes the behaviour of the fundamental particles that make up normal matter (see 'The bestiary'). Researchers have now found every particle predicted by the model, save one: the Higgs boson, theorized to help endow other particles with mass.

The Higgs is crucial to the theory, but its predicted mass is subject to wild fluctuations caused by quantum effects from other fundamental particles. Those fluctuations can increase the Higgs' expected mass to a point at which other fundamental particles should be much more massive than they actually are, effectively breaking the standard model. Theorists can eliminate the fluctuations from their equations, but only by setting the Higgs mass to a very precise value — a fraction heavier or lighter and the whole theoretical edifice collapses. Many physicists are uncomfortable with any theory that requires such delicate fine-tuning to work.

SUSY offers an alternative to this 'fine-tuning' problem. The theory postulates that each regular particle has a heavier supersymmetrical partner, many of which are unstable and rarely interact with normal matter. The quantum fluctuations of the supersymmetrical particles perfectly cancel out those of the regular particles, returning the Higgs boson to an acceptable mass range.

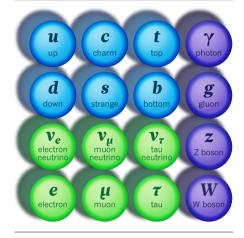
Theorists have also discovered that SUSY can solve other problems. Some of the lightest supersymmetrical particles could be the elusive dark matter that cosmologists have been hunting for since the 1930s. Although it has never been seen, dark matter makes up about 83% of the matter in the Universe, according to observations of how galaxies move. SUSY can also be used to bring together all the forces except gravity into a single force at high energies, a big step towards a 'theory of everything' that unifies and explains all known physics — one of the ultimate goals of science. Perhaps most important for some theorists, "SUSY is very beautiful mathematically", says Ben Allanach, a theorist at the University of Cambridge.

SUSY's utility and mathematical grace have instilled a "religious devotion" among its followers, says Adam Falkowski, a theorist at the University of Paris-South in France. But colliders have failed to turn up direct evidence of the super particles predicted by the theory.

THE BESTIARY

Could shadowy super particles be lurking behind the standard model's observed fundamental particles and forces?





SUSY'S MID-LIFE CRISIS

1970-74	Several theorists independently develop SUSY
1981	Supersymmetric version of the standard model proposed
1983	SUSY used to explain dark matter
1990	SUSY suggested as a way to unify electroweak and strong forces
2000	Large Electron Positron collider (the LHC's predecessor) fails to find evidence of SUSY particles called sleptons
2008	Tevatron sets mass limits on supersymmetric quarks (squarks)

The Tevatron at the Fermi National Accelerator Laboratory in Batavia, Illinois, for example, has found no evidence of supersymmetrical quarks ('squarks') at masses of up to 379 gigaelectronvolts (energy and mass are used interchangeably in the world of particle physics).

LHC tightens limits on SUSY masses

The LHC is now rapidly accumulating data at higher energies, ruling out heavier territory

for the super particles. This creates a serious problem for SUSY (see 'SUSY's mid-life crisis'). As the super particles increase in mass, they no longer perfectly cancel out the troubling quantum fluctuations that they were meant to correct. Theorists can still make SUSY work, but only by assuming very specific masses for the super particles — the kind of fine-tuning exercise that the theory was invented to avoid. As the LHC collects more data, SUSY will require increasingly intrusive tweaks to the masses of the particles.

So far the LHC has doubled the mass limit set by the Tevatron, showing no evidence of squarks at energies up to about 700 gigaelectronvolts. By the end of the year, it will reach 1,000 gigaelectronvolts — potentially ruling out some of the most favoured variations of supersymmetry theory.

"I'm wouldn't say I'm concerned," says John Ellis, a theorist at CERN, Europe's particle-physics lab near Geneva, who has worked on supersymmetry for decades. He says that he will wait until the end of 2012 — once more runs at high energy have been completed — before abandoning SUSY. Falkowski, a long-time critic of the theory, thinks that the lack of detections already suggest that SUSY is dead.

"Privately, a lot of people think that the situation is not good for SUSY," says Alessandro Strumia, a theorist at the University of Pisa in Italy, who recently produced a paper about the impact of the LHC's latest results on the fine-tuning problem⁴. "This is a big political issue in our field," he adds. "For some great physicists, it is the difference between getting a Nobel prize and admitting they spent their lives on the wrong track." Ellis agrees: "I've been working on it for almost 30 years now, and I can imagine that some people might get a little bit nervous."

"Plenty of things will change if we fail to discover SUSY," says Lester. Theoretical physicists will have to go back to the drawing board and find an alternative way to solve the problems with the standard model. That's not necessarily a bad thing, he adds: "For particle physics as a whole it will be really exciting." SEEEDITORIAL P.6

- ATLAS Collaboration. Preprint at http://arxiv.org/ abs/1102.2357 (2011).
- CMS Collaboration. Preprint at http://arxiv.org/ abs/1101.1628 (2011).
- 3. ATLAS Collaboration. Preprint at http://arxiv.org/abs/1102.5290 (2011).
- Strumia, A. Preprint at http://arxiv.org/ abs/1101.2195 (2011).



S. ALLEN/NFL/GETTY IMAGES

LATEST NEWS



Sports are beginning to address brain damage in participants go.nature.com/ssgflq

MORE NEWS

- Meat-growing researcher suspended go.nature.com/wrfhqz
- Radioactivity presents a challenge for XENON100 dark-matter detector go.nature.com/l6xiyu
- Rare sulphur dominates the deep go.nature.com/148oew





Metaphors used by scientists can mislead the public go.nature. com/lytdhl

PHOTOS 12/ALAMY

POLICY

NIH revamp rushes ahead

Translational-science centre remains on the fast track, despite concerns about upheaval.

BY MEREDITH WADMAN

Teremy Berg was fighting rush-hour traffic on his way home from the US National Institutes of Health (NIH) in Bethesda, Maryland, on 8 February when he took an unexpected call. On the line was a senior NIH official who was helping to plan the dismantling of the agency's National Center for Research Resources (NCRR) to make way for a translational-medicine centre strongly backed by Francis Collins, director of the NIH.

The caller asked Berg, who is head of the US\$2-billion National Institute of General Medical Sciences (NIGMS) at the NIH, to consider whether his institute could absorb the Institutional Development Award (IDeA), an NCRR programme that builds research infrastucture in states with historically limited success at winning NIH grants. He wanted an answer by the following day.

"I was given approximately 24 hours to decide whether NIGMS should take on a large (>\$200M), complicated program not closely related to our core mission," Berg wrote on 22 February in an open letter to the Scientific Management Review Board, which advises Collins on structural changes at the NIH. Berg agreed to absorb the programme, but "with very little comfort that this was a sound decision". He went on to urge the board to fight the hasty dissolution of the NCRR.

Berg's complaint is one of a deluge facing Collins and his staff as they rush to launch the National Center for Advancing Translational Sciences (NCATS) by the start of the US government's 2012 budget year on 1 October. Most critics do not disagree with the reasoning for the proposed centre — Collins wants the NIH to become more strategically engaged in turning promising compounds into clinically approved drugs, a process that often stalls for lack of resources and know-how. Rather, many are challenging the speed at which NCATS is being established — and the even greater speed with which Collins decided in December to dissolve the NCRR, transfer a significant por-

Critics fear that the changes will put at risk programmes that they say are working extremely well. tion of it to the new centre and scatter the rest across the NIH (see graphic). It will be the first such break-up in the NIH's 81 years.

Sixteen US senators wrote to Collins on 14 February,

supporting IDeA and urging him to slow the pace of the reorganization to gauge its impact. Other critics fear that the changes will put at risk NCRR programmes that they say are working extremely well. "Why are we fixing what isn't broken?" asks Brad Bolon, director of GEMpath, a biopharmaceutical consultancy in Longmont, Colorado. (see page 36).

Collins, who has made translational research one of five priorities for his tenure at the NIH, sees NCATS as removing the risk

from early-stage therapeutic compounds by bringing them through the first phases of drug development, to the point at which companies are willing to license them. The centre would consolidate several existing NIH projects most prominently the Clinical and Translational Science Awards, which at \$490 million in 2010, is the largest NCRR programme. And if congressional spending committees agree to a White House request for a 10% budget boost for the NIH Office of the Director, which is responsible for organizing programmes across the agency, Collins plans to channel \$100 million of that money to NCATS to fund the Cures Acceleration Network, a grant programme supporting 'high need' drug-development projects.

Collins' decision to push ahead quickly with NCATS means that the rest of the \$1.3-billion NCRR — which supports a diverse collection of infrastructure and training programmes, from primate-research centres to high-end instrumentation grants — cannot simply be left intact. This is because of a 2006 law that caps the number of NIH institutes and centres at 27; the dissolution of the NCRR creates the needed opening for NCATS. Lawrence Tabak, principal deputy director of the NIH and cochairman of the NCRR Task Force, a working group deciding what to do with the remaining pieces of the centre, says that, "given the opportunity to think this through", the group had decided that the remaining NCRR programmes would thrive better if strategically

CHANGE AT THE US NATIONAL INSTITUTES OF HEALTH

The proposed dissolution of the National Center for Research Resources and creation of the National Center for Advancing Translational Sciences will lead to some programme relocations (figures are for fiscal year 2010).

AS OF MARCH 2011

National Center for Research Resouces

Clinical and Translational Science Awards (US\$490 million)
Shared and High-End Instrumentation (\$65 million)
Division of Comparative Medicine (\$197 million)
Extramural Construction (\$1 billion, 2009–10)
Institutional Development Award (\$229 million)
Research Centers in Minority Institutions (\$59 million)
Biomedical Technology Research Resources (\$150 million)

Office of the Director

Rapid Access to Intervention Development (\$5.8 million) Molecular Libraries Program (\$113 million)

National Human Genome Reseach Institute

Therapeutics for Rare and Neglected Diseases (\$24 million)

* Proposed by President Barack Obama for fiscal year 2012

BY OCTOBER 2011

National Center for Advancing Translational Sciences

Clinical and Translational Science Awards
Therapeutics for Rare and Neglected Diseases
Cures Acceleration Network (\$100 million)*
Rapid Access to Intervention Development
Molecular Libraries Program

Office of the Director: Infrastructure Entity

Shared and High-End Instrumentation
Division of Comparative Medicine
Extramural Construction

National Institute of Biomedical Imaging and Bioengineering

Imaging and Point-of-Care Biomedical Technology Research Centers grants
Imaging and Point-of-Care research grants for Technology Research and Development

National Institute of General Medical Sciences

Institutional Development Award
All other Biomedical Technology Research Centers grants
All other research grants for Technology Research and Development

National Institute on Minority Health and Health Disparities

Research Centers in Minority Institution

EMORY UNIV.

placed in other NIH institutes and in the Office of the Director.

Many constituents of the NCRR fear for the futures of their programmes in institutes that didn't sign up for them and may not share the NCRR's commitment. "Dr Tabak and Francis Collins say this is going to be budget neutral," says one member of the NCRR's external advisory council. "But when you take a programme from one institute and hand it to another, perhaps without their agreement, you know that within five years or so that orphan programme could be budgeted out of existence."

That concern was especially evident in mid-January, when Tabak's group proposed a 'straw' model — designed to generate discussion — for the dissolution of the NCRR that showed much of its portfolio in an 'interim infrastructure unit'. Some critics were mollified when Tabak issued a revised plan last week,

calling the infrastructure entity permanent and placing it in the Office of the Director. The latest plan includes other adjustments: for

→ NATURE.COM

For more on Francis Collins's plans for the NIH, visit:

go.nature.com/guzqcy

example, the straw model had divided the NCRR's primate and non-primate animal-model resources, but the revised model keeps them together under the director's office.



Stuart Zola's research centre is slated to become the responsibility of the NIH Office of the Director.

Stuart Zola, director of the Yerkes National Primate Research Center in Atlanta, Georgia, which is currently funded by the NCRR, is one of those whose fears were soothed by the adjustments. "Given that we were going to be moved, it makes sense to be moved into another broad-based environment" rather than a disease-specific institute, he says.

"The willingness to listen to the stakeholders is very clearly evident in the new document," says William Talman, president of the Federation of American Societies for Experimental Biology in Bethesda, Maryland, who praises Collins for making a "bold stroke" in launching NCATS. Still, he says: "I don't think I will be comfortable until the test of time determines exactly what the outcome is."

Those seeking to challenge the dismantling of the NCRR will have another opportunity to voice concern at a meeting for stakeholders on 14 March. However, the window of opportunity to stop the process is narrowing. Collins plans to deliver a detailed budget for the new centre to Congress in the coming weeks, and last week he told reporters that he is preparing to search for the future director of NCATS.

GENE THERAPY

Targeted gene editing enters clinic

Patients with HIV first to receive experimental gene therapy.

BY HEIDI LEDFORD

disrupts a single gene may have had its first success in the clinic, potentially boosting immune-cell counts in a small number of patients with HIV. The results, presented on 28 February at the Conference on Retroviruses and Opportunistic Infections in Boston, Massachusetts, mark an important therapeutic test for enzymes known as zinc finger nucleases — small proteins that can be designed to bind to and edit specific DNA sequences by virtue of their zinc-bearing structures.

The study, a phase I safety trial, tested a zinc finger enzyme developed by Sangamo Bio-Sciences in Richmond, California. It included six men with HIV who were already taking the standard regimen of antiretroviral drugs. The drugs had kept the virus at bay, but their immune-cell counts remained abnormally low. Researchers removed a sample of CD4⁺ T cells, the type of immune cells affected by HIV, from each man and used Sangamo's

enzyme to disrupt the CCR5 gene, which encodes a protein that HIV uses to enter $CD4^+$ cells. The engineered cells were then infused back into the patients. Immune-cell counts subsequently rose for five of the six patients who received the therapy.

"It's very exciting," says John Rossi, a molecular biologist at the City of Hope's Beckman Research Institute in Duarte, California. "If they did this several times in a given patient, you could establish a high percentage of resistant cells."

The inspiration for targeting the *CCR5* gene comes from the small percentage of people who, thanks to a natural mutation in the gene, are resistant to most types of HIV infection. At the meeting on Monday, Jacob Lalezari of Quest Clinical Research in San Francisco, California, reported that the engineered cells migrated throughout the body and thrived in the gut mucosa — a key reservoir of HIV. No serious side effects were seen.

The zinc finger nuclease technique is promising for the treatment of many diseases beyond HIV, says Patrick Aubourg, who studies gene therapy at France's national biomedical agency INSERM in Paris. The method could replace the more common technique of inserting modified genes into the genome, in which researchers have less control over the gene in question. But he cautions that the technique still has a relatively low efficiency and might have off-target effects.

Meanwhile, Rossi, who is himself embarking on an HIV study that will use Sangamo's

"If they did this several times in a given patient, you could establish a high percentage of resistant cells." zinc finger nucleases, says that it is not yet clear whether the patients' CD4⁺ cell count rose because of the *CCR5* disruption or because the extracted cells were activated as part of the proto-

col for growing them outside the body. And because levels of HIV were already below the threshold of detection in these patients, it is too early to say what effect the therapy could have on patients that have more of the virus. Researchers do not yet know what fraction of a person's CD4+ cells would need to be HIV-resistant to significantly rein in the virus's spread and liberate patients from a lifetime of antiretroviral drugs.

"It's going to take a while to put all of those pieces together," says Carl June, who studies T cells at the University of Pennsylvania in Philadelphia, and is an investigator on another HIV trial involving Sangamo's nuclease. "But it's at least conceivable now." ■

PHARMACEUTICALS

Traditional drug-discovery model ripe for reform

Academic researchers set to play much greater role in pharmaceutical development.

BY DANIEL CRESSEY

a slew of blockbuster medicines about to lose patent protection, the voices arguing that the traditional drugdevelopment process is too expensive and inefficient to survive are getting louder.

Employing thousands of in-house scientists to develop drug candidates from scratch has turned into a billion-dollar gamble that simply isn't delivering enough profitable products to market. Bernard Munos, founder of the Inno-Think pharmaceutical policy research group in Indianapolis, Indiana, is not alone in believing that the next three years "will probably see an implosion of the old model" of drug discovery.

So what comes next? Cutbacks, certainly: witness Pfizer's dramatic announcement early last month that it will soon close its research site at Sandwich, UK, and slice roughly US\$1.5 billion from its proposed 2012 research and development spend (see *Nature* **470**, 154; 2011). But beyond that, perhaps, a rethink of the old divisions of labour is needed.

Canny drug-makers are listening to those who propose that they should increasingly outsource early-stage drug development, including phase I safety trials, to academia or to small, specialist companies. This would leave pharmaceutical companies to focus on their strengths: running large clinical trials and marketing medicines.

One such model was the focus of a meeting in Toronto, Canada, on 16 February, involving some 40 leading lights from industry, academia and funding agen-

"Heavy investment is required, and it has to be carried by somebody's money."

cies. The meeting was co-convened by Chas Bountra, head of the Structural Genomics Consortium at the University of Oxford, UK, who argues that a key problem with the current system is that companies tend to work in parallel, identifying similar or identical target molecules while remaining unaware that the compounds may have already been tested and discarded by rivals. "What we're trying to do is reduce that duplication," he says.

His scheme adopts the highly collaborative



The kit may have improved, but the in-house drug discovery model has changed relatively little.

approach pioneered by those working on cures for neglected diseases, in which intellectual property (IP) restrictions are lifted. Companies would begin to compete only after early clinical trials had shown a drug to be safe and potentially effective. Up to that point, all data on prospective drug candidates would be published openly. This would allow targets to be validated much more quickly, says Bountra, potentially giving enormous savings in cost. It would also prevent companies "exposing patients to molecules that other organizations already know are going to be ineffective".

The model would rely heavily on academic scientists supported by a global initiative costing about \$325 million a year, with half coming from the pharmaceutical industry and half from public and charitable sources. Successful drug candidates would be made available for the initiative's commercial sponsors to buy and bring to market.

Industry already believes that this is a fine solution for programmes in areas without major commercial interest, such as neglected

diseases, says Stephen Friend, an organizer of the meeting and president of non-profit research organization Sage Bionetworks, based

NATURE.COM
For a longer
interview with
Patrick Vallance, see
go.nature.com/be99zf

in Seattle, Washington. The key difference in the Toronto proposal is that it may also be a "viable way to improve return on investment in commercially important areas", he says.

Bountra is confident that within the next two months he will complete negotiations to sign up two industry partners, two public funding partners and two academic partners. The response at the meeting, to which all the large drug companies sent representatives, was very positive from all involved, say attendees. "The more we discussed it, the more convinced we were that this is the only way forward," says Bountra. A follow-up meeting in San Francisco in April will flesh out the plans.

Meanwhile, government funders of research are trying out similar initiatives. The UK Medical Research Council has established the Developmental Pathway Funding Scheme to support the development of basic science into drugs and medical devices. And Francis Collins, head of the US National Institutes of Health, is proposing a National Center for Advancing Translational Sciences to push more basic science towards the medical market (see page 15).

Ted Bianco, director of technology transfer for the Wellcome Trust, a UK biomedical research funder, agrees that shifting early-stage drug discovery work to academia could fix

some of pharma's problems. The trust's Seeding Drug Discovery initiative already funds researchers to optimize drug candidates and take them through to clinical trials. But Bianco points out that commercial partners in Bountra's initiative would expect to see a financial return: "The dilemma is that heavy investment is required, and it has to be carried by somebody's money."

Bountra's IP-free model could also deprive collaborating universities of the opportunity to profit from spin-out companies, says Melanie Lee, chief executive of Syntaxin, a biotech company based in Oxford, UK, who attended the Toronto meeting. Bountra says he doubts that will discourage academics, who get into drug discovery to develop medicines, not to acquire intellectual property.

But Patrick Vallance, senior vice-president for medicines development and discovery at London-based drug-makers GlaxoSmithKline (GSK), also believes that IP will be the most contentious part of Bountra's model. "I'm completely on board with the idea you don't really know if you're on track until you've done an experiment in the clinic, and that you should publish that early," he says. But "it's much more complex to determine where you need to secure the IP along that chain, and I think it will differ from molecule to molecule".

Nevertheless, his company is experimenting with open innovation, having last year put more than 13,000 potential antimalarial drug structures into the public domain to encourage academics to identify promising leads. "One of the reasons I want to push that model very hard is that if it works in malaria — and we've yet to see what the uptake from academics and others is — I don't see how you could do anything but pursue it in other areas," says Vallance.

Vallance notes that industry is also developing new models of academic collaboration. GSK announced this month that it will collaborate with Mark Pepys, head of medicine at the Royal Free and University College Medical School in London, to develop a candidate drug for amyloidosis, a protein disorder. The idea, says Vallance, is not just to buy up promising molecules, but to form long-term partnerships that last all the way through drug development.

All these models put academic researchers at the heart of drug discovery. But they will fail unless more money flows from governments, charities and industry into academic labs, says Cathy Tralau-Stewart, who heads Imperial College London's drug discovery research unit. "Academic drug discovery is growing and is becoming much more important," she says, "but if we don't solve the funding issues, then the pharma companies will not have a pipeline of innovative drugs in ten years' time."

Budget woes sink marine archive

Oceanographic library could be a casualty of California's \$25-billion deficit.

BY ERIKA CHECK HAYDEN

The fiscal crisis at the University of California looks set to engulf the world's largest collection of research materials focused on marine sciences.

On 11 February, Brian Schottlaender, librarian at the University of California, San Diego (UCSD), proposed closing the Scripps Institution of Oceanography Library, along with four other libraries affiliated with UCSD, including the Medical Center Library and the Science & Engineering Library.

Schottlaender had been asked to cut US\$6 million out of his \$25-million budget as part of a \$500-million reduction for the entire

University of California system. Newly elected state governor Jerry Brown, who faces a \$25-billion state deficit. announced the reduction in January. The Scripps library closure is the highest-profile casualty of the cuts so far, but it is unlikely to be the last.

The library includes some 227,000 books and 700 print periodicals along with an extensive archive that charts the history of oceanography, including documents from the 1872-76 voyage of HMS Challenger - a

landmark global oceanographic expedition. News of the planned closure has elicited a storm of protest. "Closing the Scripps library is almost unthinkable," says Walter Munk, a pioneering oceanographer who spent his entire professional career at the Scripps institution. "The Scripps library is a unique asset to the community of oceanographers everywhere." A group of Scripps graduate students has organized a petition opposing the closure.

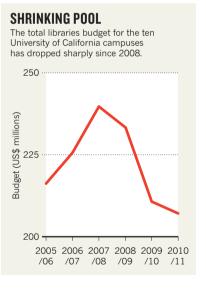
Select collections and services from the library could be moved to a larger library on UCSD's main campus as early as this summer, according to Schottlaender. And

Peter Brueggeman, director of the Scripps library, notes that about half of the library's collection has been digitized through a partnership with Google. But, he says, "the reality is that many research-oriented library resources are not yet digitized, are not freely available or are not affordable at this time".

Schottlaender points out that, before this year's proposed cut, his budget had already been reduced by 16% since 2008 and that the Scripps library, with 34,000 visitors last year, is not as heavily used as other libraries on campus. "My hands are more are less tied. Everything is getting cut everywhere," Schottlaender says.

Other libraries are feeling the pinch too (see 'Shrinking pool'). At the University of Cali-

fornia, San Francisco, librarian Karen Butter says that she doesn't have the budget to subscribe to some databases that researchers want, such as BIOBASE, which contains products such as the Human 🗒 Gene Mutation Database, an archive of mutations associated with disease. She adds that the university is negotiating with publishers to lower the cost of online access to individual journals, because packages of journals are no longer affordable. On 1 January, the University of California



library system cancelled its site licence to the Informa Healthcare journals — the first time the university has cancelled a subscription to a 'bundle' of journals.

At the University of California, Santa Cruz, hundreds of undergraduate and graduate students occupied its science and engineering library in 2009 and 2010 to protest over cuts in library hours. In May, the students voted to institute a \$6.50 library fee per student per quarter to pay to keep the library open. But the fee ends in 2013. At that point, says university librarian Virginia Steele, "we're facing a really difficult dilemma". ■

China faces up to 'terrible' state of its ecosystems

Wetlands hardest hit by land reclamation and pollution.

BY JANE QIU IN BEIJING

ounting the cost of decades of breakneck development, Chinese scientists and policy-makers last week outlined the daunting challenges they face in trying to halt the country's environmental degradation.

Government officials at the Symposium on Ecosystem Monitoring and Evaluation in Beijing promised to step up investment in ecological conservation and restoration over the next five years, although no precise details were given. Other delegates warned that the lack of a national long-term strategic plan for the environment, compounded by insufficient coordination among government sectors, could jeopardize such efforts.

"The ecological situation is terrible," admits Xu Jun of the Ministry of Science and Technology. More than a quarter of China's grasslands, for instance, have been lost to farming and mining activities in the past decade, and 90% of the country's remaining 4 million square kilometres of grassland is in poor health. The grassland loss contributes to problems such as water shortages and sandstorms.

Coastal areas are under even greater pressure — from pollution, drainage and development. "Of all ecosystems, wetlands are the worst hit," says Yu Xiubo, an ecologist at the

Beijing-based Institute of Geographic Sciences and Natural Resources Research, part of the Chinese Academy of Sciences (CAS).

A recent report by the China Council for International Cooperation on Environment and Development (CCICED), a joint Chinese and international advisory board to the government, shows that 57% of the country's coastal wetlands have disappeared since the 1950s, largely due to land reclamation (see 'Wetland threats'). Over the same period, the area covered by mangrove forests and coral reefs fell by 73% and 80%, respectively.

On the basis of development projects approved by the government, the authors of the CCICED report estimate that another 5,800 square kilometres of coastal area will be lost by 2020, eating away at the total 385,000 square kilometres of remaining wetlands.

RECOVERY EFFORTS

China has not ignored the problem. The forestry ministry has been mapping wetlands nationwide, and 2,538 nature reserves have been established covering about 15% of the country's total area, including half of the natural wetland ecosystems, according to Cui Lijuan, director of the Institute of Wetland Research in Beijing. However, nature reserves are often poorly protected from development.

Over the past five years, the science ministry has spent 500 million renminbi (US\$76 million) on the monitoring, evaluation and restoration of key ecosystems, says Xu. He says that funding will increase significantly, and will include a new focus on assessing the impact of pollution on public health. In collaboration with the CAS, the environment ministry will spend the next two years conducting a national ecological survey, following up on a survey done in 2000. Among the survey's goals are an assessment of the services provided by key ecosystems, and the impact of major engineering projects, including the Three Gorges Dam in central China.

According to Zhong Xianghao, an ecologist at the CAS Institute of Mountain Hazards and Environment in Chengdu, monitor-

ing and restoring the fragile ecosystems of western China will be a priority. The government has earmarked

NATURE.COM
For more, read
Nature China:
www.nature.com/nchina



Goodbye mangroves, hello rice fields — but at what cost to China's ecological health?

15.5 billion renminbi between 2008 and 2015 for conservation projects and to create a monitoring network of ten ecological stations in the region. An additional 13.4 billion renminbi per year will be paid to farmers and nomadic peoples to conserve grassland in parts of western China, says Yang Zhi of the agriculture ministry.

Yet China will struggle to preserve its remaining intact ecosystems (see 'China's resources') in the face of the growing demand for land. This is being driven by population growth and by the government's plan to quadruple the country's gross domestic product between 2000 and 2020.

And some delegates at the symposium used the Chinese saying *jiulong zhishui*, meaning 'taming the water with nine dragons', to describe the overlapping monitoring efforts of various government ministries. These efforts are all too often short term and uncoordinated, says Cui, when "it takes decades to get a good idea of the baseline and changes of ecosystems".

WETLAND THREATS China's most endangered ecosystems are being degraded by factors linked to economic development. Unwise use of water resources 6.6% Soil and water loss and Land siltation 8% reclamation 30.3% Exploitation of biologica resources 24.2% Pollution 26.1% CHINA'S RESOURCES Percentage of world total Arable land Wetland Grassland Population

In 1946, scientists started tracking thousands of British children born during one cold March week. On their 65th birthday, the study members find themselves more scientifically valuable then ever before.

BY HELEN PEARSON

n Tuesday 5 March 1946, Patricia Malvern was born in a small flat in Cheltenham, UK, near the boilers that her dad stoked to warm the building above. She weighed in at 9 pounds, 2 ounces (4 kilograms).

The next day, David Ward was "one of the few Catholics born in a Jewish hospital" opposite Hampton Court, near London. Ward doesn't know exactly what he weighed, although his dad said later that he looked "like a skinned rabbit".

Throughout the rest of that week, just months after the end of the Second World War, 16,695 babies were born in England, Scotland and Wales. Health visitors carefully recorded the weights of the vast majority on a four-page questionnaire, along with countless other details including the father's occupation, the number of rooms and occupants (including domestics) in the baby's home and whether the baby was legitimate or illegitimate. Over subsequent years, the information files on more than 5,000 of these children thickened, then bulged. Throughout their school years and young adulthood and on into middle age, researchers weighed, measured, prodded, scanned and quizzed the group's bodies and minds in almost every way imaginable.

This week, the group has much to celebrate. They are turning 65, the age at which many in the United Kingdom retire and, as such, a milestone in British life. They will also celebrate being part of the longest-running birth-cohort study in the world. These ordinary men and women are now some of the best-studied people on the planet. And this makes them some of the most scientifically valuable, because it has allowed researchers to track their health and wealth throughout their lives, and to search for factors that could explain their trajectories.

The exercise has revealed some surprises. It has shown that the heaviest babies were most at risk of breast cancer decades later; that children born into lower social classes were more likely to gain weight as adults;

that women with higher IQ reached menopause later in life; and that young children who spent more than a week in hospital were more likely to suffer behaviour and education problems later on.

A generation under study

All told, the results from the 1946 birth cohort — now known as the National Survey of Health and Development and run by the Medical Research Council (MRC) — have filled 8 books and some 600 papers so far. Perhaps more than anything else, the survey has shown that early life matters — a lot. "Ultimately, where you get to in early adulthood is strongly influenced by where you come from," says Michael Wadsworth, who led the study for nearly 30 years, until 2007.

Children who were born into better socioeconomic circumstances were most likely to do well in school and university, escape heart disease, stay slim, fit and mentally sharp and, so far at least, to survive. (Ward, whose father worked his way up in a Walthamstow-based drycleaning business, went on to university and built a career in journalism. Malvern, whose father left home when she was five and who wore third-hand clothes, left school at 16 and "bitterly regrets" the fact that her mother couldn't afford to pay tuition for her to train as a teacher.)

⇒ NATURE.COM

Listen to a podcast about the 1946 birthcohort study at: go.nature.com/7rhmk3 Those lessons are arguably more urgent today than they were in 1946 when, caught up in postwar optimism, Britain was introducing major educational reforms and a National Health Service (NHS) to ensure that good schooling and health were available to all. The contrast with the



Diana Kuh leads the UK National Survey of Health and Development, which has compiled thick files on more than 5,000 people since their birth in 1946.

country's mood this winter couldn't be starker. Students have been rioting to protest against the government's plan to introduce £9,000 (US\$14,600) annual fees for universities; plans are afoot to drastically reform the NHS (eviscerate it, critics say); and sweeping budget cuts are threatening public services — including early childhood support centres, for which the cohort's data once helped provide impetus. "I find these changes very worrying," says Diana Kuh, who now directs the survey and says she is saving up for her grandchildren to attend university.

"It's unique and groundbreaking in the history of epidemiology. It's the only study to have chased an entire cohort across its life course — and it's not yet finished," says Ezra Susser, an epidemiologist who works with cohort studies at Columbia University in New York. He says that cohort research has been vital in seeding the idea that disease evolves as a result of events throughout life. "You gain enormous depth of understanding in how that disease came to be by following someone over their life course."

Now, as the cohort members enter old age, the study offers a precious opportunity to understand how a lifetime of experiences might hasten or slow their decline — an urgent question for countries such as the United Kingdom and United States, whose populations are rapidly ageing and sickening. In the latest round of data collection, running from 2006 to 2010 and costing £2.7 million, study members underwent almost every modern biomedical test, including echocardiograms, measures of blood-vessel function, whole-body bone, muscle and fat scans, and tests of blood, memory and how quickly they could get up from a chair.

The data will provide a detailed starting point from which to measure the cohort members' inevitable decline, and the opportunity to analyse the information is already swelling an extensive network of collaborators. Some are testing how genes interact with a lifetime of experiences to lead to obesity or disease; others plan to scan participants' genomes for 'epigenetic' marks — molecular traces left, perhaps, by early birth

weight or by life's inequalities — that alter gene expression and might provide a molecular explanation for effects in later life. Greg Duncan, an economist at the University of California, Irvine, who studies the impact of child poverty, hopes that follow-up studies could help to answer a question arising from the earlier findings on socioeconomic status and health: "What are the active ingredients in social class?"

It is this ability to draw associations between biological data, from blood pressure right down to genes, and life as it is actually lived that makes the cohort study so unusual, say its leaders. "These are real people," says Kuh. "This is what it is to be human and normal."

Next Steps in Making Motherhood Easier

The first few decades of the twentieth century found Britain acutely concerned about its falling birth rate and stagnant infant mortality. (The thought at the time, as Kuh puts it, was "how are we going to maintain Britain and its empire?") A Population Investigation Committee recommended a maternity survey to explore whether the social and economic costs of childbearing were discouraging prospective parents. James Douglas was appointed to head it.

Douglas, a physician, had spent part of the war conducting vast studies of air-raid casualties. He set about launching an investigation that today would be ethically difficult, logistically nightmarish and financially prohibitive: sending health visitors to interview the mothers of every child born in that March week. He reached 13,687 of them. "It was crazily ambitious," says Wadsworth, who inherited the study leadership from Douglas more than three decades later. Yet "he pulled it off".

NEWS FEATURE

In 1948, when Douglas's book about the study's results appeared, the baby boom was in full swing and concerns about birth rate had mostly dissipated. But the volume, *Maternity in Great Britain*, made a stir by revealing shocking disparities between rich and poor in infant survival and women's care. One widely reported result showing that only 20% of women who gave birth at home were offered pain relief, and that the poor suffered most, spurred a parliamentary bill allowing more midwives to deliver gas and air.

Douglas decided to turn the study into a tool for documenting social

inequality and gauging the impact of newly minted welfare reforms such as the NHS. In particular, he realized that he had the perfect weapon for testing the success of the 1944 Education Act, which had introduced a nationwide system of exams for 11-yearolds — the 11+ — intended to channel the brightest, regardless of background, into elite 'grammar' schools. He selected a sample of the original 13,687 children spanning geography and social class, ending up with 5,362, whose health, growth and other data were regularly recorded and then transferred onto punch cards. Douglas also tested the children's cognition as they reached 8, 11 and 15, and tracked their course through school.



BRITAIN'S SQUANDERED

TREASURY OF TALENT

To the architects of the welfare state, the results were discouraging. Bright children from the middle classes were more likely to pass the 11+ and do well at school than were equally bright working-class children, although supportive parents and good teachers could better a child's odds. The attrition of smart but poor boys (girls counted for less) became known as the 'waste of talent', turning Douglas's next two books — *The Home and the School* (1964) and *All Our Future* (1968) — into must-read educational references and contributing to the introduction of non-selective 'comprehensive' schools in the 1960s.

While Douglas was studying the group's diverging paths, the children were walking them. Malvern, who was cripplingly embarrassed by taking free school meals, failed her 11+. She blames a class teacher so violent that Malvern would sleep without covers in order to catch a cold and avoid school, and who "walloped me across the head" on the day of the exam. After she left school, Malvern went to learn typing at Government Communications Headquarters in Cheltenham. Ward's

father, meanwhile, was planning to buy a house, and his mother tested him on Latin vocabulary over the ironing. He was one of 4 children out of 66 in his school's top two classes who passed the 11+ exam, and he and his sister were the first in their family to attend university.

As the 1970s rolled on and the participants entered their thirties, Douglas was losing steam. Most of his questions about the cohort members' education, occupations and social mobility had been answered, and Douglas was heading towards retirement. Medical epidemiologists thought that the cohort should be mothballed until its members got

interesting again, when they started to sicken and die. The MRC, which had been funding the project since 1962, dithered about what to do with it; even Douglas thought the project was finished.

LIFE'S PATTERN DECIDED-

AT THE AGE OF SEVEN

For Wadsworth, a social epidemiologist who had joined Douglas's team in 1968, it was just getting going. "I thought the changing pattern of health of these people would be interesting over life," he says.

After he took the helm in 1979, Wadsworth convinced the MRC to fund a new round of data collection as the cohort reached 36, then again at 43 and 53. He started assessing the group's physical capabilities and health, including blood pressure, heart and lung function, diet and exercise. He wanted to see how these indicators had been influenced by earlier life — and then chart them into the future.

Correlations tumbled out of the data. In 1985, Wadsworth and his team reported that cohort members whose birth weight had been low had higher blood pressure as adults¹. It was an early hint that fetal and infant growth shape adult health, a link that became known as the Barker hypothesis after David Barker, an epidemiologist at the University of Southampton, UK, who published a 1989 analysis of birth weight and health in a different cohort². He found that babies with the lowest birth weights had the highest risk of heart disease as adults.

Study after study from the 1946 cohort supported the link, showing a tangle of connections between infant and child growth or development and adult traits from cognitive ability to frailty, diabetes, obesity, cancer and schizophrenia risk. "It isn't the same story every time, but we find an endless stream of long-term associations in quite 'noisy' data," says Kuh. "Big babies were more likely to get breast cancer. Small babies were more likely to have poor grip strength. Those who grew fast postnatally have more cardiovascular risk." (Says Ward: "I find that quite extraordinary, almost in a poetic way, that there is something that spans all those years, that something was set down, determined at that stage.")

A major question for scientists today is how to explain these connections: which biological systems in infants are so important, and how

are lasting scars laid down on them? One possible answer lies in epigenetics: the chemical footprints, such as methyl groups, stamped on DNA by early life events that alter gene-expression patterns and might contribute to later disease. Martin Widschwendter, an oncologist at University College London (UCL), for example, is planning to analyse tens of thousands of possible methylation sites in the cohort's DNA, looking for changes that could explain the link between birth weight and breast-cancer risk. The detailed life-course information that can be combined with the DNA "is really only available via these cohorts", says Widschwendter.



David Ward as a baby in 1947 with his mother and sister; and in 1976 with his son and daughter.

The doctor's son does better than a dustman's

Yet Kuh and others emphasize that fates are not fixed by early life. "I don't ever want the findings to be interpreted as purely deterministic," says Kuh; she prefers the more optimistic idea that disease risks result from an accumulation of experiences throughout life, and that

education, diet or other factors can shift poor trajectories to better ones. Marcus Richards, an epidemiologist who is leading the cognition studies on the group, points to evidence from the 1946 cohort — and supported by many other studies — that regular physical exercise in a person's thirties and forties can slow their cognitive decline with age. "We can take that research and say, here is very clear-cut evidence of something you can do to protect your cognitive health as you get older, and this is how you should do it," says Richards.

The 1980s brought a vivid lesson in the power of environment. Hardly any of the Douglas babies, nourished on post-war rations, were fat as children — a sharp contrast to those of today — and they had maintained a healthy weight throughout young adulthood. But now incomes were climbing, eating out was more affordable, and cars were the way to get around. As the cohort approached their thirties, the line plotting the proportion who were obese edged upwards; in their late thirties it soared³. And although those in lower socioeconomic brackets did get fatter faster, no social class was immune.

Somewhere on one of those curves is Malvern, who found her own weight creeping up when she moved to Luxembourg in 1992 and stopped work as a school bursar. She weighed 11 ½ stone (73 kilograms) when she moved. "When I came back in 2000 I was horrified: I was 15 stone. It was the pâté and the baguettes and the cheese and having visitors," she thinks—on top of the menopause. Malvern has since lost weight, and Ward has kept himself trim, he says, by living in the Peak District, where "you can't get anywhere without going up and down a hill".

Cleverness 'delays

the menopause'

As women in the study reached their fifties, a more mysterious pattern emerged: those who had performed well on childhood intelligence tests tended to reach menopause several years

later than those who had performed poorly⁴. "We tested almost to destruction every social and behavioural pathway; we threw almost everything we had at that to see if we could make that association go away and it didn't," says Richards. But once the researchers considered the association, it began to make sense. Their theory now is that child-hood cognition provides a readout of brain development, including that of some areas that respond to hormones or are responsible for hormone production. In short, high IQ scores could indicate a brain that was well-developed all round, and so was able to sustain reproduction

for longer. Kuh says that she has been testing whether genes are responsible, "so far without success".

In 2005, as the cohort neared 60 and Wadsworth neared the end of his scientific career, the project's future was again in jeopardy. The MRC was pondering whether to keep paying for it and, if it did, who should lead it. "We didn't know if the study would be closed down—and Mike was retiring. It was a very unstable period," says Kuh.

Kuh — who had trained in economics — wanted to build up the biomedical data that Wadsworth had been collecting. Until that time, all the

examinations had been performed at the study members' homes, but by this stage the nurses were staggering under all the equipment. To really understand the participants' physiology and biology, Kuh argued, the study needed to get them to a clinic. "People appreciate a free bone scan," she says. By 2008 she had convinced the MRC to pay for every willing cohort member to visit one of a number of clinics around the country and had established a dedicated research unit, now housed in a Georgian terrace in central London.

Ward went to a clinic in Manchester for his exam. He learned that he has signs of osteoporosis in his spine, and that he can no longer stand on one leg for long with his eyes closed. "You wobble rather more and I ended up hopping about the place." He recalls the food diary he had to prepare as a "serious challenge". "You don't want to admit that you had that extra glass of plonk or another slice of cake, but you say, hang on, this is science, I've got to tell the truth".

Kuh and her colleagues — the study now has about 25 full-time researchers and support staff and 100 collaborators — are still compiling such truths about their thousands of participants. "Now the cohort is one of the most phenotyped in the world," says Kuh. Once her paper summarizing the latest data goes public⁵, Kuh is expecting the queue of epidemiologists, geneticists and other scientists who want to collaborate to lengthen, and last November she hired someone for three years especially to cope with the increased data sharing. As the cohort ages and falls ill, the study will continue monitoring participants' health and trying to tease out the influence of early experience. "One big question we can ask is, are these life effects we see in mid life going to wane?" says Kuh. Or will they, as some epidemiologists expect, get more dramatic with age?

Kuh is also thinking about how best to exploit genomic and other biomedical analyses. At least one study has hinted at the power of the cohort's life-course data combined with genetics. Last year, Rebecca Hardy, a statistician with the survey, published a study of two hot genes called *FTO* and *MC4R*, variants

of which have been identified as risk factors for obesity⁶. When she analysed DNA collected from the cohort in 1999, she found that the association of those variants with body mass index increased in early adult life, then weakened as the cohort grew older. Perhaps, Hardy speculates, any effects of the genes on appetite or fat storage were overwhelmed by that onslaught of fat-promoting influences in the 1980s, a possibility that might become clearer when she tests a further panel of obesity-linked genes.

Ever protective of her study members and the limited DNA samples





Patricia Malvern aged 16; and aged 51, holding one of her grandchildren.







The research team never forgets to send birthday cards to the cohort.

CARDS & CALLS

How to keep a cohort together – for 65 years

After tracking its subjects' health and well-being for longer than any other study, the 1946 British birth-cohort study has lessons to offer its younger siblings. British birth cohorts were started in 1958, 1970 and 2000, and another is provisionally planned. In the United States, children are being enrolled in the National Children's Study, which aims to follow some 100,000 children from before birth to age 21. Yet other cohort studies have been felled by bureaucratic infighting, spiralling costs or a lack of sustained funding. Diana Kuh, director of the 1946 survey, attributes its survival to having fairly autonomous, dedicated leaders and a relatively low budget. "We've always had to offer good value for money."

The 1946 study also shows that building a strong relationship with the participants is vital. Every year, the members receive a birthday card, signed by the research team and telling them about the latest results. One participant, Patricia Malvern, says that the card means a lot to her. "Somehow, over the years I began to feel I knew the team members, although I had never met any." One year the

card showed a sunset, and some recipients complained about the suggestion that they were entering the evening of life. Kuh and her colleagues responded to those complaints, like every other enquiry from the participants, with personal letters or calls. Kuh says that this relationship has been crucial to keeping an average of 80% of the original cohort in the study. When leaders of other studies hear that figure, she says, "people are amazed".

But some factors in its success can't be duplicated today. In 1946, recruitment and consent issues were a lot simpler: "If someone was willing to see you, that was consent," says Kuh, "and the response rates were over 90% probably because people didn't think they could choose not to participate." Those simpler days also brought constraints. In the early years of the study, questions about money and sex were "off the table", illegitimate children were turfed out of the study, and mothers were not asked whether they smoked in pregnancy because "the minister for health was telling the soldiers to smoke," says Kuh. "But that's part of being the history of science, really." H.P.

she has, Kuh says that she views the latest molecular biology techniques with caution. "I feel a huge responsibility to deliver," she says. Quite often, she says, outside researchers have an attitude of "give us all the cohort data and we'll rush this through and find millions of associations. I say, well, that sounds very interesting; can you come back with a hypothesis?" Even so, when Kuh compiles a plan for the MRC's fiveyearly review of the survey in 2012, she knows that working out how to incorporate these technologies "is going to be key". The falling cost of DNA sequencing means that ploughing through participants' entire genomes is an almost inevitable step, she acknowledges. "The questions are, when is the best time — and what would we learn from it?"

A survey taking on

a life of its own

For now, Kuh has more immediate planning concerns: five 65th-birthday parties, at which the study members will meet each other for the first time. The parties are causing her some anxiety. Wadsworth had considered and rejected the idea of a 50th- or 60th-birthday bash, in case the get-together ended up influencing the participants' life course in some way. "Basically, we thought people might leave their partners and get off with someone in the study," he says. But Kuh decided that recognizing and rewarding the members was worth the risk. (She even wrote to Buckingham Palace to request a garden-party invitation for the study members. "I wrote such a nice letter. I learned all about how to address the Queen, and I'm still hoping to get a reply.")

Ward and Malvern are pleased to have been part of the study. "It gives me a fair old bit of pride in a way," says Ward. "Just things like bed-wetting. What did I contribute to the nation's store of knowledge on bed-wetting?" Neither is perturbed by the idea of the researchers watching them until they crumble and die. "I suppose," says Ward, "it helps you accept that you're mortal, you're not going to last forever."

Some 13% of subjects have died so far — and the study already has something to say about the fate of the rest. Kuh flips open some graphs of survival rates that she has calculated. They show the proportion of the survey members surviving up to age 60, separated by father's social class. And they reveal yet another curious correlation for Kuh and her colleagues to dig into. Kuh points out a blue line representing a group of women from better-off backgrounds, whose death rate is about half that of everyone else⁷. Kuh has not been able to attribute the effect to less smoking or other obvious factors, and she suspects that these women took advantage of the educational and health opportunities afforded by post-war Britain to improve themselves. "They really changed their lives with education. The girls, if they got through, they did really well."

Yet the study is lending a touch of immortality to all its participants, whether men and women, born into comfort or poverty. Traces of them will live on in preserved DNA, cell lines frozen in liquid nitrogen — and in their records, now all transferred from punch cards to computers. "You're very aware that your memory is going," says Ward. "But you also know that in the archive is a version of you."

"I often call it an alternative biography in there," he adds, "and that I'd quite like to get my hands on." ■ SEE EDITORIAL P.5

Helen Pearson is Nature's chief features editor.

- 1. Wadsworth, M. E. J., Cripps, H. A., Midwinter, R. E. & Colley, J. R. T. Br. Med. J. 291, 1534-1538 (1985).
- Barker, D. J. P., Osmond, C., Winter, P. D., Margetts, B. & Simmonds, S. J. Lancet **334,** 577–580 (1989)
- Li, L., Hardy, R., Kuh, D., Lo Conte, R. & Power, C. Am. J. Epidemiol. 168, 1008-1015 (2008).
- 4. Kuh, D. et al. Menopause 12, 475-482 (2005).
- Kuh, D. et al. Int. J. Epidemiol. **40**, e1–9 (2011). Hardy, R. et al. Hum. Mol. Genet. **19**, 545–552 (2010). Kuh, D. et al. Soc. Sci. Med. **68**, 1565–1573 (2009).



Research on the reservation

American Indians have had some unhappy interactions with scientists in the past. Now, America's tribal colleges are rapidly expanding their own research.

By Zoë Corbyn

atie McDonald had never given much thought to the trout in Flathead Lake except when fishing with her family. She didn't wonder about heavy-metal

family. She didn't wonder about heavy-metal pollution or how that might affect people eating the fish. But that was before the then-19-year-old student started a bachelor's degree in environmental science at Salish Kootenai College in northwest Montana and had to choose a research project. She saw that trout consumption was going up on the Flathead Indian Reservation, where she lived. Poor people, in particular, had begun to receive donated fish. So McDonald set out to see whether there was cause for concern.

Her institution is a tribal college, one of 36 scattered around the United States (see 'US tribal colleges') and serving some of the least-developed communities in the country. But thanks to several federal programmes seeking to boost science within tribal colleges, McDonald had access to equipment such as

a state-of-the-art mercury analyser. She ran samples of the lake trout (*Salvelinus namay-cush*) and found surprisingly high levels of the toxic metal¹.

The results were compelling enough for the tribal government to advise women of child-bearing age to avoid eating older, larger fish from the lake altogether — a more stringent recommendation than state guidelines that suggest eating no more than one a month, says Barry Hansen, the tribes' fisheries biologist.

Douglas Stevens, head of life sciences at Salish Kootenai, says that McDonald's work shows students how their scientific research can serve the local community.

That message is big change for American Indians, who have typically been research subjects rather than investigators in studies ranging from anthropology to genetics. And like indigenous peoples around the world, American Indians have sometimes been treated poorly by the scientific establishment. In a high-profile case last year, Arizona's

Native American researchers found raised levels of mercury in fish from Flathead Lake, Montana, which borders the Flathead Indian Researvation.

Havasupai Indian tribe settled a lawsuit it had filed against Arizona State University in Tempe for conducting genetic analyses that the tribe says were done without express permission.

That case and others have fostered a climate of suspicion among some American Indians towards mainstream researchers. But tribal colleges are now trying to harness science for their communities' own purposes by building up their capacity for both training and research. With an influx of funding from several federal agencies over the past decade, these institutions have started to hire more faculty members with research credentials, develop better facilities and establish science degree programmes.

Although there are difficulties, particularly in research quality and publication rates, supporters say that the increasing focus on scientific research at tribal colleges is helping both students and their communities.

It can be seen "as an act of resistance" says Luana Ross, the president of Salish Kootenai. "We are taking control of the research process."

DEMAND FOR DOCTORATES

The emphasis on research is part of a broader set of changes at tribal colleges, most of which operate in self-governed nations. Unlike mainstream US universities, where undergraduates typically pursue four-year bachelor's degrees, tribal colleges have traditionally offered only two-year degrees and vocational training. Because many of them serve relatively poor communities with struggling primary and secondary schools, tribal colleges must provide remedial education to make up for gaps in students' basic skills and knowledge.

But several tribal colleges are also seeking

to raise the level of their instruction by hiring teachers with more training. The percentage of staff with doctorates at tribal colleges rose by nearly 40% from 2003 to 2009, going from about 8% to 11% of the total, according to figures from the American Indian Higher Education Consortium, based in Alexandria, Virginia.

The focus on science seems to be having an effect. Although enrolment at tribal colleges has been decreasing, the number of students pursuing degrees in science rose by more than 70% between 2003 and 2009, to about 1,200 students altogether. And eight tribal colleges now offer full four-year bachelor's degrees, with about 70 applied-science bachelor's programmes available.

The initiatives at tribal colleges are aided by a collection of programmes totalling about US\$20 million annually, from federal agencies such as the National Science Foundation (NSF).

"One of the reasons for the phenomenal growth in science enrolment at the tribal colleges is because they are able to provide undergraduate research opportunities," says Jody

Chase, who manages the NSF's Tribal Colleges and Universities Program. Since 2001, that programme has provided \$13.5 million a year in funding to strengthen science courses at tribal colleges and other institutions serving Native Americans in Alaska and Hawaii.

Many of the research projects at tribal colleges focus on the local community. Researchers at Diné College in the Navajo Nation of Arizona, for example, worked with scientists from the US Geological Survey in Reston, Virginia, to investigate

why residents in the Shiprock area of the reservation have roughly five times the rate of respiratory illness seen in nearby communities, despite a relatively low incidence of smoking. The area is home to some of the largest coalmining and electricity-generating operations in the United States.

By examining hospital records and monitoring indoor air quality in more than 130 homes, the researchers linked respiratory problems to high concentrations of particulate matter from the burning of coal in stoves not designed for that purpose². The coal is provided at low or no cost to Navajo living near coal mines, as part of reservation lease agreements. The study has led to a large community-education campaign emphasizing, for example, the importance of leaving a window open. The college has also recommended that the tribe support a

stove-replacement programme.

Scientists working outside the tribal colleges say that the focus on research is raising standards at these institutions. "They have had some really good successes," says David Burgess, a Native American cell biologist at Boston College in Massachusetts, who is involved with the Society for the Advancement of Chicanos and Native Americans in Science. Burgess says that the presentations given by many tribal-college students at the society's annual conference are getting stronger.

GLOBAL PHENOMENON

The research expansion has parallels in other countries such as Norway, New Zealand and Canada, where universities serving indigenous peoples are conducting studies on topics of local interest that would not otherwise be explored. "It is a global phenomenon," says Boni Robertson, a professor of indigenous policy at Australia's Griffith University in Queensland, and co-chair of the World Indigenous Nations Higher Education Consortium.

But along with their successes, America's

SALISH KOOTENAL COLLEGE

LITTLE BIG HORN COLLEGE

HASKELL INDIAN NATIONS UNIVERSITY

WATER COLLEGE Setween 2003 and 2009, science enrolment at America's 36 tribal colleges climbed by 70%.

tribal colleges have run into some hurdles in their scientific efforts. Enrolment in science programmes has climbed, but the number of students completing two-year or four-year science degrees remained essentially flat from 2004 to 2009.

There are also concerns about the research at these institutions. Barbara Howard, a senior scientist at the non-profit MedStar Health Research Institute in Hyattsville, Maryland, has worked in Indian country since the late 1980s directing the Strong Heart Study, the largest epidemiological study of Native Americans. Howard welcomes the rise in undergraduate research at the tribal colleges, and says it is the best way to encourage students to go on to graduate school. But, she says, the tribal colleges need to improve in terms of their "research quantity and complexity".

A major obstacle is that many faculty

members don't have the necessary experience to undertake research — a problem that the American Indian College Fund (AICF), based in Denver, Colorado, is trying to rectify. It awards fellowships to faculty members at tribal colleges to start and finish PhDs and do their own research. Yet although the organization recruits intensively, each programme receives only a handful of applications.

Doing a PhD on a local Indian issue can be a tough slog, says Valerie (Pretty Paint) Small, a faculty member at Little Big Horn College on the Crow reservation in southern Montana. She has an AICF science fellowship to finish her PhD at Colorado State University in Fort Collins, where she is studying the invasion of a non-native tree species on Crow tribal lands. "So many people know so little about our contemporary issues," she says. "University professors don't make much of an effort to see where you might be coming from if you are on the reservation."

Faculty members at tribal colleges also struggle to publish their work, in part because of large teaching loads. To improve publica-

tion rates, colleges such as Salish Kootenai are forming writing groups for faculty members, and administrators are exploring ways to give staff time off for research. And the AICF hopes to start a peerreviewed, interdisciplinary journal this year that would publish research undertaken at tribal colleges.

Some scientists wonder whether tribal colleges would be better off expanding their partnerships with research-intensive universities rather than trying to do research on their own. "Why recreate those resources when they can

partner with other institutions and develop new kinds of synergy?" asks Spero Manson, a Native American medical anthropologist who directs the Centers for American Indian and Alaska Native Health at the University of Colorado in Denver.

But Daniel Wildcat, acting dean of natural and social sciences at Haskell Indian Nations University in Kansas, says that doing research within tribal colleges allows Native Americans to "design their own research agendas", in which tribal values rather than those of outsiders determine what gets studied.

SEEEDITORIAL P.5

Zoë Corbyn is a freelance journalist based in San Francisco.

- Stevens, D. K., McDonald, K. & Bishop, N. Environ. Bioindicators 4, 303–317 (2009).
- Bunnell, J. E. et al. J. Environ. Public Health 2010, 260525 (2010).

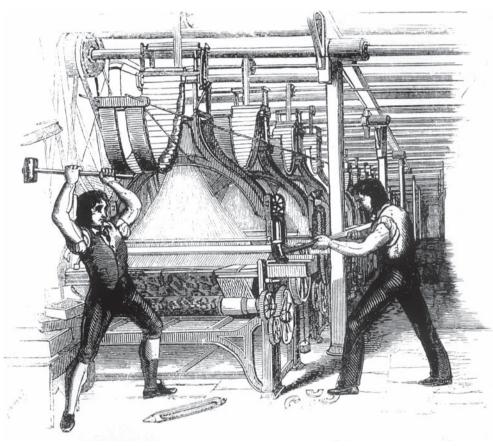
MARY EVANS PICTURE LIBRARY

COMMENT

DEVELOPMENT Calestous Juma's optimistic prescription for food in Africa **p.31**

years after discovery, Ötzi goes on show **p.34** **ENVIRONMENT** A call to halt deep-sea vent mining before it starts **p.36**

POLICY Unrealistic NIH restructure will inhibit translational research **p.36**



A nineteenth-century engraving of machine-breakers attacking machinery in a textile factory.

In praise of Luddism

Two centuries on from the Luddite insurrection, **David Edgerton** celebrates today's most important opponents to new ideas, inventions and innovations: scientists.

In March 1811, machine-breakers struck in the centre of England. They were not the first or the last, but they started what became known as the Luddite outrages or insurrection. The targets were employers and their machines — stocking-makers and their knitting frames at first, later other textile manufacturers and machines. The breakers were hand-knitters whose livelihood was threatened. The name came from General or King Ludd, the leader the Luddites invented as a signatory to proclamations.

Since then, especially in the late twentieth century, a Luddite has been someone opposed to progress, especially to science and technology. Nowadays, it is a generalized term of unthinking abuse designed to crush any criticism.

In fact, opposition to most new ideas, inventions and innovations is essential for progress. Most grant applications and scientific papers are

rejected; most inventions have to be rejected if there is to be enough time and money to develop any at all. Scientists have had a crucial role in this opposition — they led the charge against new gadget mania during the Second World War, and afterwards.

If by 'Luddism' we mean, as was the case in 1811, opposition to specific novelties for particular reasons, as opposed to novelty in general, then Luddism is indispensable and scientists should cultivate their important, and venerable, role as its most rigorous practitioners.

It is not sufficiently recognized that creation, scientific or otherwise, is a tragic business. Most inventions meet nothing but indifference, even from experts. Patents are little more than a melancholy archive of failure. Most ideas of every sort are rejected, as would be clear if there was a repository for abandoned drafts, rejected manuscripts, unperformed plays and unfilmed treatments. The reason is not hostility to novelty.

▶ On the contrary, most new ideas and products must be rejected because there are so many of them. In the rich world, some institutions and individuals have been so fecund with inventions that not even all the good ones could be used: there have been many processes to make, say, synthetic ammonia, or take colour photographs, but only a few are used. The point is not whether we reject, but how we do it, and why.

Scientific Luddism, however, doesn't even acknowledge its own existence. How could it, in a world in which science is held to be about creativity, innovation, the future, ideas, inventions and spin-outs? Party poopers are not welcome.

WAR ON WASTE

Science has a long and distinguished history of Luddism. In the early eighteenth century, some natural philosophers — such as the Royal Society's Jean Desaguliers — worked to discredit many projects and doubtless saved fortunes from being invested in perpetual motion machines. For example, with the rise of science-based industry in the late nineteenth century, chemicals companies employed scientists not just to control processes, or to create, but also to assess, and thus usually reject, inventions. Within government, scientists were used to sift through the thousands of ideas for potentially war-winning gadgets that were received from patriotic inventors in both great wars of the twentieth century.

In the Second World War, British scientists were actively involved in opposing new ideas for weapons. Surely there were enough Luddites in government and the armed forces in Britain that no help was needed from scientists? That certainly was the public view of many scientists

who railed against administrators and politicians educated in the classics and history. The reality was very different: the British political and military elite (supported by many scientists of course) was addicted to new machines, to machines that would transform war and allow a great scientific nation to triumph over hordes of continental conscripts. Neville

"In the Second World War, British scientists were actively involved in opposing new ideas for weapons."

Chamberlain, prime minister between May 1937 and May 1940, who had a university education in science, was one such neophile, but in this as in so much else, he was overshadowed by his successor Winston Churchill.

Churchill was a noted enthusiast for machines and an inventor himself. His close personal adviser on matters scientific, technical and economic, was an Oxford professor, the physicist Frederick Lindemann, easily the most influential academic or scientist to have served in government. Their response to the crisis of 1940 — the fall of Norway, the evacuation of Denmark and the fall of France — involved a call for more radical weapons. Between them they encouraged all sorts of new gadgets: aerial mines to bring down bombers, jet engines, the atomic bomb, anti-aircraft rockets, anti-tank devices of many kinds. Their enthusiasm was boundless, their progress-chasing relentless.

Among the Luddites were the physiologist Archibald V. Hill, the chemist Henry Tizard and the physicist Patrick Blackett, all experienced scientific advisers. Hill was elected by the graduates of the University of Cambridge to one of their two Parliamentary seats (a system abolished in the late 1940s) and was the only scientific Nobel laureate ever to sit in the Commons. He was a conservative, but one of Churchill's strongest opponents. Blackett was a socialist, who won his Nobel prize after the war. Tizard was the dean of scientific advisers, and associated with the most technically progressive part of government since the First World War — the air force.

All three men turned against the inventors and the prime minister who so actively supported them. As Hill complained to Parliament in February 1942: "There have been far too many ill-considered inventions, devices, and ideas put across, by persons with influence in high places, against the best technical advice ... They have cost the country vast sums of money and a corresponding effort in development and

production, to the detriment of profitable expenditure of labour and materials elsewhere."

We know from Hill's papers that he thought the greatest waste of money was the anti-aircraft rocket programme dating from the 1930s. He estimated that this giant effort cost the equivalent of between 3 and 16 battleships, or the same number of very large factories, and consumed three or four times more cordite than used to fire the same number of conventional anti-aircraft shells. He called it a "most infernal waste of time, effort, manpower and material". By June 1941, the government was demanding production of 9 million rockets a year, despite the fact that they barely worked. They are now all but forgotten. In fact, production never exceeded 2.5 million, and was saved by an unexpected new use for the rockets as ship- and tank-busters.

Blackett, who headed operational research for the navy, engaged in a general critique of the pursuit of novelty. Writing in December 1941, in a paper setting out the principles of operational research, he criticized the call for 'New weapons for old', as a form of "escapism". Too little effort was going into "the proper use of what we have got", he wrote. Changing tactics could be more effective than changing weapons¹. He and Tizard wanted to redeploy scientists from research and development to "improve the operational efficiency of equipment and methods now in use". Both men also opposed Britain building an atomic bomb, on the grounds that it was likely to take longer and cost more than promised. In this they were proved correct — there was no bomb until the US one of 1945, and far from being cheaper than conventional explosive, it was the most expensive ever made. The US bomb took at least 2 years longer, and cost 50 times more, than the British bomb was meant to.

Being a scientific Luddite was not easy. Charles Goodeve, who had been the Admiralty's senior scientist during the Second World War, recalled that "the voices of reason" who opposed, on the grounds of cost, the extraordinary wartime scheme to build a gigantic aircraft carrier out of ice (codename Habakkuk) were "shouted down by cries of 'obstruction" in the internal deliberations of government. Goodeve estimated (although this is certainly an exaggeration) that Habakkuk was the most serious misallocation of Allied effort of any wartime invention². It was supported by scientists of distinction, most notably the socialist crystallographer J. D. Bernal, but fortunately was not pursued beyond the experimental stage.

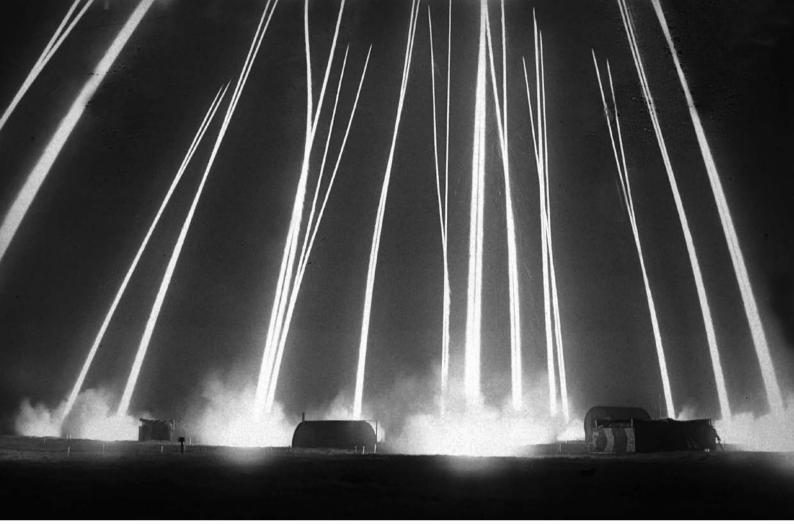
The Second World War has been treated as a moment of triumph for British science, and this is associated with a small range of well-known devices — radar, jet engines, penicillin, the Mulberry artificial harbour, the Pipe Line Under The Ocean (PLUTO) and sometimes the Habakkuk. Of these, only radar made a definite positive contribution to the war. Most of the rest were either irrelevant to it, or of marginal importance. British jet engines made no impact, nor did the atomic bomb, which marked rather than caused the end of the war. The two Mulberry harbours towed to the Normandy beaches, although much celebrated, contributed less than propaganda implies then and since. The Americans managed perfectly well after the Mulberry built for them was destroyed in a storm before it was even finished. The PLUTO, which took petrol across the English Channel, although built at great expense, was, as US Luddites had suggested, quite unnecessary and, furthermore, worked very badly.







Churchill's Luddites: Archibald V. Hill, Patrick Blackett and Henry Tizard.



A 'Z' battery of anti-aircraft rockets in action in 1944. Physiologist Archibald V. Hill declared them an "infernal waste of time, effort, manpower and material".

The reality is that the British war effort would have been more effective had none of these projects gone ahead and the vast cost of development and deployment been spent elsewhere. The lesson is this: not every famous technology is important.

LUDDITES NEEDED

After the Second World War, Britain could have done with more scientific Luddites. Successful opposition to British nuclear power stations in the 1950s and 1960s would have saved the nation billions of pounds, because they generated electricity more expensively than need have been the case. A stronger opposition to Concorde (the dissenters included the future Nobel laureate, physicist Nevill Mott) would have deprived some rich people of time spent in the air, and the British and French taxpayers could have spent more on developing other modes of transport, perhaps speeding up the development of trains.

Today publicly funded researchers are under pressure to identify the probable 'impact' of their work. Instead of making fun of scientists for pooh-poohing the economic prospects of their own discoveries — Ernest Rutherford describing atomic energy as "moonshine" is the much-repeated example — we should celebrate the unseen work that rightly stops the great majority of ideas and inventions from getting anywhere. That great British innovation, the National Institute for Health and Clinical Excellence (NICE), which brings evidence to bear on medical procedures and drugs, is under huge pressure from interested pharmaceutical firms and sponsored patients' groups to endorse products of doubtful utility. We need much more serious opposition to the gigantic waste of innovative resources that goes into 'me too' drugs. We also need to reject the fake technical fixes that are everywhere on offer — often the problem is not lack of technical means, but something else entirely. Feeding the world might benefit from genetic modification technology, but it will not be achieved if the only change is more genetically modified crops.

Above all, we should reject the idea that even the original Luddites were opposed to progress, or the machine. In response to a government bill to make machine-breaking a capital offence, the poet Lord Byron explained to the House of Lords that the Luddites imagined that "the maintenance and well-doing of the industrious poor were objects of greater consequence that the enrichment of a few by any improvement in the implements of trade". Yet, said this great defender of the Luddites, "the adoption of the enlarged machinery... might have been beneficial to the master without being detrimental to the servant", but the state of the economy at the time meant that this was not the case³. Similarly most people said to be Luddites today are not against progress or science and technology in general, but against particular manifestations in particular contexts, just as scientists are.

Scientists should embrace and refine their Luddite sides — as a public service, and as a service to knowledge and invention. Using their authority, they should insist on the difference between science as whole and a particular part, and of the necessity of nay-saying. That would in itself help to raise the level of elite (let alone public) discussion above its current, depressingly low level.

David Edgerton is at the Centre for the History of Science, Technology and Medicine at Imperial College London, London SW7 2AZ, UK. His book Britain's War Machine: Weapons, Resources and Experts in the Second World War will be published in the United Kingdom on 31 March by Allen Lane and in the United States in August by Oxford University Press. e-mail: d.edgerton@imperial.ac.uk

- 1. Blackett, P. M. S. A Note on Certain Aspects of the Methodology of Operational Research (1943).
- 2. Goodeve, C. The ice island fiasco The Times, 19 April 1951.
- Lord Byron, House of Lords Debates, 27 February 1812; available at go.nature.com/yugddy.



Training for Africa's women farmers is vital if the continent is to shift to more sustainable agriculture.

AGRICULTURE

A bowl half full

Calestous Juma's vision for African farming is refreshingly optimistic, finds Camilla Toulmin.

nnovation, entrepreneurship and investment lie at the heart of Calestous L Juma's upbeat assessment of the future of African agriculture. In The New Harvest, Juma, an expert in international development, shows how agricultural science, the business of development and the institutions that shape food markets are transforming the opportunities of farmers and traders across the continent.

His optimism is refreshing — a welcome antidote to the pessimistic view of African development of previous decades. Forecasts predict annual economic growth of 5-8% for many African countries over the next few years. But important questions remain over how the power and benefits that will come from this growth will be distributed.

Juma's book is timely. The renewed volatility in food and fuel prices is prompting worries about food security and the associated risks of political turmoil, as seen in North African countries. Agriculture is firmly back on the international agenda. Rising food prices are bad for poor people, but bring extra revenue for those producing a surplus. Agricultural land is now an asset, prompting a 'land grab' by companies and foreign governments who have taken advantage of cheap land and poorly governed



The New Harvest: Agricultural Innovation in **Africa** CALESTOUS JUMA Oxford University

Press: 2011. 296 pp. \$19.95

Africa (COMESA), as essential in promoting innovation. By aggregating markets and pooling research resources, benefits

natural-resource rights

economic organi-

zations, such as the

Common Market for

Eastern and Southern

Juma sees regional

in parts of Africa.

can be spread among countries, giving small African nations the economies of scale

needed to compete and diversify. Although many regional bodies have been criticized for the gap between their aspirations and achievements, and for their overlapping and competing mandates, Juma is positive about their future role, citing cross-border planning and investment in electricity and gas distribution as an example of good practice.

The book is filled with examples of improvements in food and farming systems, where governments have energized local groups. For instance, the University of Agriculture in Abeokuta, Nigeria, and the food

company Nestlé are working together on soya beans and cassava to improve varieties and productivity, thus increasing incomes for Nigerian farmers. Similar projects have enhanced the take-up of improved rice varieties with higher yield and greater stress resistance in Benin, Ghana and Ethiopia.

Philosophically, Juma takes an eclectic approach: he draws on three strands of argument. First, he embraces the opportunities of an outward-looking, market-oriented farming system in which productivity grows through new science-based breeds and seeds. Second, he accepts the need for food security and the strengthening of local knowledge networks, indigenous systems and varieties. Third, he acknowledges that a combination of population growth and lack of innovation has led to stagnant conditions and African reliance on food imports.

Juma recognizes that past governments have drained the agriculture industry of revenues in favour of building up other sectors. Long-term neglect has meant that irrigation covers only 4% of Africa's cropped area, and fertilizer use in the continent is one-tenth of the world average. But, he argues, the latest generation of African leaders offers a greater commitment to invest in agriculture.

Juma is keen on applying technology to agriculture. He looks to advances in tissue culture and breeding, such as using a genetic or morphological marker to select for desirable traits, and to cheaper genetic mapping of Africa's crops for improved productivity. He brushes aside sceptics' reservations about genetically modified crops and sees instead the promise of lower pesticide use and higher yields that companies such as Monsanto have brought to smallholder farmers growing cotton in Burkina Faso and South Africa. But he does not address the main concern about genetically modified crops, namely the concentration of economic power held by a few major agrochemical companies.

He lauds the now-ubiquitous mobile telephone for addressing old problems in new ways, and for transforming people's access to market information and financial services. But Juma reminds us that fundamental investments are still needed in basic infrastructure, such as road networks, to get supplies to farmers and harvests to market. Reducing transport costs would greatly increase farmers' ability to respond to market demand.

To foster innovation, Juma champions a "cluster approach", in which groups from government, the private sector, civil society and researchers come together in a variety of partnerships to work on common prob-

◇ NATURE.COM

Call for a global network for farming practices:

go.nature.com/mbgka9

lems, building trust through proximity. In the past, he explains, the state was too dominant: public-sectorled approaches to

agricultural research assumed a pipeline of technology from lab to farm. In future, the farmer should be seen as a co-producer of research, not a recipient of handeddown technology. China is fostering this approach. Juma gives a good illustration of the boom in vegetable production in China's Shandong province, where local government has encouraged a range of businesses and market development.

With its climate changing and population growing, Africa will have to produce food under greater environmental pressure. He argues that agriculture needs to shift towards more sustainable farming patterns, which are also more knowledgeintensive. This will require governments and societies to address the deficit in training and access to education, particularly for women, who are the backbone of food production in many African farming communities. For example, the non-governmental Uganda Rural Development and Training programme teaches farming methods using a curriculum that focuses on building strong female agricultural leaders.

Weak infrastructure and scarce land and water may be harder to overcome than Juma suggests. A few African governments recognize the potential of agriculture to drive economic growth and reduce poverty, but there is still a long way to go. Climate-change impacts could be hugely damaging unless urgent work is done to construct resilient local and national systems. A focus on the benefits of global markets, inward investment and modern technology needs to be balanced by consideration for who gains and who loses.

Concerns are already being raised by farmers' associations about large-scale investment in agricultural land, in 'landgrab' deals negotiated by few people. In Mali, farmers want a moratorium on large land allocations, and have issued a call to remind the government that land, water, forests and natural resources constitute national assets for all citizens. Other investment models, such as contract farming or joint ventures with local farmers, should be considered. Transparency is also needed to ensure that investors undertake their contractual obligations and do not engage in speculation.

Like Juma, I see the glass as half full, but there are many challenges ahead. Nevertheless, The New Harvest reminds us that by working with farmers, nongovernmental organizations, government and business, science has the potential to transform Africa's food security.

Camilla Toulmin is director of the International Institute for Environment and Development, London, UK. e-mail: camilla.toulmin@iied.org



Greenland gives an alarming assessment of climate change in a production as complex as the topic itself.

Poles apart on climate

Two contrasting plays highlight the difficulties of putting global warming on stage, finds Kerri Smith.

Terocious debate has polarized the issue **d** of climate change — and two plays currently running in London reveal many facets of those arguments. Greenland is a rational but disjointed assessment of how urgent and alarming our predicament is, whereas *The Heretic* is an entertaining family drama with a climate sceptic as the protagonist.

Greenland, at the National Theatre, is a production almost as complex and unwieldy as climate change itself. It weaves together several narratives: a student-teacher becomes a green activist; a birdwatcher witnesses habitat change in the Arctic; a couple argue over their individual contributions to global warming. These unfolding tales share the stage with falling rain and a remarkably life-like model of a polar bear.

The most engaging scenes involve the play's climate modeller, Ray, and a government official, Phoebe, sent to gather data ahead of the December 2009 climate negotiations in Copenhagen. She arrives at the lab after he has worked all night on his model; he is reticent to let her see his work before it has been peer reviewed. When they get to Copenhagen, we are given a sense of the convoluted processes involved in drafting an international policy agreement when a dozen weighty volumes fall

Greenland

MOIRA BUFFINI, MATT CHARMAN, PENELOPE SKINNER AND JACK THORNE National Theatre, London. Until 2 April 2011.

The Heretic

Royal Court Theatre, London. Until 19 March 2011.

from the ceiling and land with a thud.

But the multitude of characters and jumbled storylines make this play difficult to follow. Laced with statistics and quotes, it feels at times like a lecture. Greenland's four writers — Moira Buffini, Matt Charman, Penelope Skinner and Jack Thorne — spent months researching the topic by interviewing experts, activists and journalists. The team hoped to convey the complexity of the issue, says the play's artistic director, Ben Power. "We're trying to explore the feeling of powerlessness," he adds. What they actually depict, in shoehorning all their research onto the stage, is confusion.

Richard Bean's The Heretic is easier to watch, with its linear storyline, entertaining

characters and laughout-loud dialogue. But its factual errors will infuriate some scientists.

The play centres on

◇ NATURE.COM Brian Wynne's review of Merchants of Doubt:

go.nature.com/tcsjbk

fictitious professor Diane Cassell, who studies sea-level change in the Maldives. Her data suggest that there is no rise — putting her at odds with her department and making her a target for death threats from an environmental activist group. She infuriates her colleagues even further when she defends her views on a television show hosted by BBC Newsnight presenter Jeremy Paxman — playing himself in a pre-recorded video cameo — leading to a dramatic turn of events.

Cassell also tutors a student with strong environmentalist leanings and helps her own daughter, a Greenpeace member, to battle anorexia. One section draws on the e-mail hacking controversy of November 2009 at the University of East Anglia, UK. Cassell's student hacks into another university's mainframe and discovers e-mails in which the author was keen to 'bury the downturn' — a reference to "hide the decline", a phrase in the real hacked e-mails that was seized upon by climate sceptics.

The problem with The Heretic is that although the 'science' presented is sloppy in places, its mouthpiece, Cassell, is likeable, witty and compelling - perhaps enough to convince the audience that the science is sound. Cassell argues, for instance, that the research on sea levels that went into reports from the Intergovernmental Panel on Climate Change "used a single tide gauge", rather than the many records that climate scientists actually collected. Interviewed after the play, environmental economist Dimitri Zenghelis of the London School of Economics, who consulted on Greenland, voiced concerns about the misinformation that Cassell's character helps to propagate.

Both plays do a good job of portraying their scientific protagonists as people. In *Greenland*, climate scientist Ray worries whether it is irresponsible to start a family given future climate risks. Cassell in *The Heretic* grapples with family and romantic dramas as well as her scientific dilemma. Zenghelis says one helpful aspect of *The Heretic* is that Cassell's character identifies "the problem of objective scientists without an agenda struggling to be heard". But in the real world, it is not the sceptics who have trouble getting their message out: "[*The Heretic*] got things the wrong way around," he says.

On the evidence of these two plays, climate science and theatre do not seem to be natural bedfellows. But like the Iraq War or the Enron financial scandal (both subjects of recent plays), complex topics that affect everyone should be dramatized. They just need to be accurate as well as entertaining. "People said to us, 'For God's sake make it an interesting play! Don't lecture us," Power admits of *Greenland*. In the end, *The Heretic* meets this target. *Greenland* falls short.

Kerri Smith edits Nature's podcasts.

Books in brief



The New Cool: A Visionary Teacher, His *FIRST* Robotics Team, and the Ultimate Battle of Smarts

Neal Bascomb CROWN 352 pp. \$25 (2011)

Robot-building competitions are 'the new cool' in high schools across the United States. Writer Neal Bascomb follows a team of California teenagers and their inspirational physics teacher as they try to win the coveted FIRST (For Inspiration and Recognition of Science and Technology) contest, a nationwide annual project instigated 22 years ago by inventor Dean Kamen. In relating the team's travails, Bascomb shows how children are enthused by hands-on approaches to science and technology.



Moby-Duck: The True Story of 28,800 Bath Toys Lost at Sea and of the Beachcombers, Oceanographers, Environmentalists, and Fools, Including the Author, Who Went in Search of Them

Donovan Hohn VIKING 416 pp. \$27.95 (2011)

After hearing about thousands of plastic toys washed up on Alaskan shores after the loss of a container from a Chinese ship, journalist Donovan Hohn set out to learn about ocean currents. Retracing the journey of the plastic ducks, frogs and turtles across the Pacific, he reveals how floating markers have been used to map the circulation of the seas. And he questions the globalized economic system that sends cheap novelty products on such odysseys in the first place.



Driven to Extinction: The Impact of Climate Change on Biodiversity

Richard Pearson STERLING 264 pp. \$22.95 (2011)
Global warming will result in winners and losers among species, explains Richard Pearson, a biogeographer at the American Museum of Natural History in New York. Offering a balanced assessment of case studies of animals and ecosystems that are already affected by environmental degradation — such as Madagascan geckos, coral reefs and polar bears — he relates how climate change will sever links between organisms. This will lead to inevitable extinctions, he admits. But new niches will emerge in



The Beautiful Invisible: Creativity, Imagination, and Theoretical Physics

which other species might flourish.

Giovanni Vignale OXFORD UNIVERSITY PRESS 320 pp. \$34.95 (2011) Physics is much more than just dry mathematics, argues physicist Giovanni Vignale. Its abstract concepts, such as energy and atoms, are products of the imagination that call for a creative approach, and are best viewed as cultural hand-me-downs that have developed from philosophical ideas throughout the ages. In his thoughtful and wide-ranging book, Vignale explores the esoteric side of the discipline, which he sees as "the military academy of liberal arts" owing to its mix of rigour and creativity.



The Kaguya Lunar Atlas: The Moon in High Resolution

Motomaro Shirao and Charles A. Wood SPRINGER 174 pp. \$39.95 (2011)

Lunar landscapes take on a new realism in this atlas of photographs taken by the high-definition television camera aboard the Kaguya (SELENE) spacecraft, operated by the Japanese space agency JAXA. The oblique views, snapped by the low-flying probe from just 100 kilometres above the Moon's surface, show the terrain as it would be seen by astronauts descending to its surface, rather than the vertical views presented by other satellites.







Ötzi the Iceman has been 'reincarnated' by palaeontological artists Alfons and Adrie Kennis using forensic findings as well as artistic inspiration.

ANTHROPOLOGY

The Iceman defrosted

Marta Paterlini reports on an exhibition marking 20 years since Ötzi, one of the world's oldest natural mummies, was discovered under the Alpine ice.

s dead celebrities go, Ötzi the Iceman must be one of the most Lclosely studied — he has been measured, X-rayed and dated. But the 5,300-yearold mummified corpse, found part-buried in ice on the Tisenjoch Pass in the Alps spanning the Italian–Austrian border in 1991, still holds surprises. Many of his secrets are revealed in Ötzi²⁰, a major exhibition that opened this week at the South Tyrol Museum of Archaeology in Bolzano, Italy, to mark the 20th anniversary of his discovery.

Wounded by an arrowhead in his left shoulder, Ötzi is thought to have frozen to death while fleeing attackers. Much of the analysis so far has concentrated on the belongings found with him, but this has shifted. "So far the attention has been on Ötzi's clothes and tools. Now, the physical body becomes the focus," explains museum director Angelika Fleckinger.

Central to the exhibition is a new reconstruction of his body by twin brothers Alfons and Adrie Kennis, Dutch palaeontological artists who previously put a face to Ötzi20: Life. Science, Fiction,

South Tyrol Museum of Archaeology, Bolzano,

Until 15 January 2012.

today. They sculpted muscles from modelling clay, attaching them to an appropriately sized skeleton. Using a polyurethane mould, they crafted a silicone torso, adding legs in resin and plastic. The model is finished with five thin layers of silicone 'skin', each painted individually.

Neanderthal man. The

artists reconstructed

Ötzi's body by compar-

ing his bone measure-

ments, such as femur

length, to those of men

The skull was made using accurate threedimensional computerized tomography scans of Ötzi's head as a guide. Ultrasound measurements of skull morphology and average skin and flesh thickness were used as the basis for modelling his facial tissues — a technique used in forensic medicine to reveal injuries. Together with traces of some mummified characteristics, "all these data gave us an estimate of his portrait, complete with wrinkles, hair and eyelashes," explains Adrie Kennis.

"What I found peculiar was the small nasal cavities," says Adrie. This trait, along with his fine bones, means that Ötzi would have looked fragile, he adds. The artists also think that he would have appeared older than someone in their mid-forties today, because his features would have been ravaged by greater exposure to the harsher,

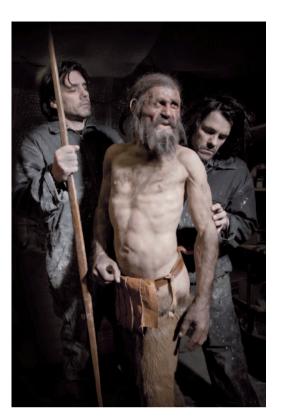
hotter climate of the time.

The reconstruction team had many discussions about the precise moment at which to depict him. "We agreed to stage it a day before his death, when he is wandering up to the mountains, a spark of stress on his face," Adrie explains. Ötzi would have been uncomfortable - he was wounded and on his own, perhaps being followed. This sombre picture contrasts with his smiling face in the museum's earlier model.

Even more striking is the colour of Ötzi's

◇ NATURE.COM King Tutankhamun's death explained? go.nature.com/x7evh9

eyes: not blue, as in the previous portrayal, but brown. This derives from the first analysis of the mummy's DNA,



extracted from a sample of pelvis bone.

When the mummy was defrosted in November 2010 for the first time since its discovery, researchers found that the stomach was filled with matter (previous analyses had been limited to the intestine). Using histological, morphological, DNA and botanical analysis, they aim to determine which bacteria Ötzi was carrying at the time of his death — information they hope will improve their conservation strategy and hint at his dietary habits.

Aside from his recent thaw, Ötzi is usually kept at -6 °C and 98% air humidity, and is misted with water once a month. The droplets freeze on the surface of the body, preserving it in a thin shell of ice. The crystals on his skin are visualized in an installation by British artist Marilène Oliver, also on display in the exhibition. In Ötzi: Frozen, Scanned and Plotted (2007), Oliver converted a computerized tomography scan of the frozen body into an image by drilling some 50,000 holes into 80 acrylic sheets that were then stacked into a translucent three-dimensional block. The result is a ghostly impression of

Ötzi²⁰ embraces the full spectrum of the Iceman's discovery, his life and the media circus and scientific sleuthing that has followed. With plans to update exhibits throughout the year, the show provides a focus for the new scientific findings that are contributing to the emerging picture of Ötzi.

Marta Paterlini is a writer based in Stockholm. e-mail: martapaterlini@gmail.com

Q&A Manolis Papagrigorakis

Facing the past

The Athens-based orthodontist explains the art and science of reconstructing the heads of long-dead people from their skulls alone, including that of Myrtis — a young girl from more than 2,000 years ago, whose recreated face is our first glimpse of an ordinary ancient Greek.



Why did you decide to reconstruct an ancient Greek face?

For 30 years I have been combining my science, which deals in the bone structure of the lower face, with my hobbies of history and art, by studying the craniofacial complex of ancient Greeks. When Myrtis's unusually intact skull was discovered, I saw it as a great opportunity to reveal what an ancient Greek layperson looked like for the

How did you feel when you first saw the finished picture of Myrtis?

It was very emotional to come face to face with someone who could have been your 80 times great-grandmother and at the same time your granddaughter, because

she really resembles today's children. Our detailed reconstruction was published in the January 2011 issue of The Angle Orthodontist.

Where were Myrtis's bones found?

The building of the Athens Metro in 1994-95 brought to light a mass grave in what was once the public cemetery of ancient Athens. Archaeologists found at least 150 skeletons, apparently hastily buried. The site was dated to 430-426 BC,

when Athens was besieged by the Spartans during the Peloponnesian War and an unknown epidemic struck the city.

How did you become involved in the reconstruction?

The archaeologists asked me to examine various bones, which we knew came from victims of the mysterious disease. Within the tooth pulp of three different skulls, we found genes that matched those from a bacterium called Salmonella enterica serovar Typhi, suggesting that the victims died of typhoid fever.

What drew you to Myrtis's remains?

One skull was small, belonging to a child,

and I saw something I hadn't seen in the other skulls unearthed from the mass grave — its jaw bore both permanent teeth and part of its deciduous (baby) dentition. The morphology of the front part of the lower jaw and brow ridge, as well as the size of the lower canine teeth, told us the sex. We deduced her age using X-rays to look at how complete the roots of her teeth were. This suggested that the skull belonged to an 11-year-old girl, to whom we gave the old Greek name Myrtis, meaning myrtle.

How did you reconstruct her face?

We placed numerous markers on her skull to reflect the average tissue depth across the face, according to data tabulated for people of various ages and of each gender.

The Swedish sculptor Oscar Nilsson formed 20 anatomically correct muscles using clay, and worked from the skull outwards until the tissue depth reached the markers. He gave her brown eyes, taking her Greek 🕏 origin into account. The hairstyle and expression were decided after studying sculptures and depictions of children living at the same time as Myrtis.



Myrtis was rebuilt from a skull.

Which features are the hardest to recreate?

The weak points are the ears, the tip of the nose and lips, where there is no bone — only soft tissues and cartilage that have disappeared. I used her dental arch to define the shape and position of her lips, and here my speciality helps. The coexistence of her adult and baby teeth create the look of an overjet, where the top teeth project forwards.

What would her life have been like?

We only know that she lived around 430 BC, when many of the values that sustain contemporary civilization were established. She probably witnessed the building of the Parthenon on the Acropolis in Athens.

INTERVIEW BY ALISON MCCOOK

CORRESPONDENCE

Curb deep-sea mining now

Cindy Lee Van Dover in her review of the Bismarck Sea mining project (*Nature* **470**, 31–33; 2011) accepts the inevitability of interest in excavating the sediments of hydrothermal vents for minerals such as copper, zinc, gold and silver. Many of the hundreds of these sites are accessible, and the issue is widely seen as not whether mining should proceed, but how it can be done profitably and safely.

I approach the issue with a strong bias, based on efforts over decades to figure out how to keep the world working as a biophysical system capable of serving indefinitely as a human habitat. On the overall issue I am not optimistic. On one topic, however, I am certain: the integrity of the oceanic biophysical system is being lost now and the human cost is overwhelming.

The fact is that intrusions into the global environment have passed a limit of acceptability and this one must be seen for the twofold attack on the global commons that it is.

Hydrothermal vents are one of the wonders of Earth: communities of autotrophic organisms that survive on Earth's energy as opposed to photosynthetic energy from the Sun, the source of energy of almost all other life. Each vent site may have its own high degree of endemism, essentially unique life. The mere fact that the sites are commercially attractive as ore is not an adequate reason to exploit them, any more than the existence of the giant redwoods of the Sierra Nevada justifies harvesting them for shingles. The vents are a window onto the history of life. By what right do we destroy them for corporate profit?



Worse, mining of marine sediments mobilizes the noxious minerals they contain, including those that are toxic to other marine life. Suddenly, we have another contribution to the chemical disruption of the ocean. We are well aware of the process and its effects. Do we need more research to confirm our experience?

Global problems all have local origins. Here we have the beginning of another process we shall never be able to stop, once started. Another mountain-top mining. Another Tar Sands of Alberta. Another North Slope oil development. Scientists who join the programme are offering tacit approval of it, no matter what their perspectives. The world is too small for this further destructive intrusion it should be stopped now before it becomes another corporate atrocity, too big and too valuable to stop.

George M. Woodwell Woods Hole Research Center, USA. gmwoodwell@whrc.org

NIH plan will hinder translational studies

The proposal by the US National Institutes of Health (NIH) to dismantle the National Center for Research Resources (NCRR) (see go.nature.com/yw3cq3) is more likely to inhibit than enhance translational research.

Through its Division of Comparative Medicine (DCM), the NCRR has long promoted translational research by supporting facilities and by providing resources and training to identify and target disease mechanisms. The proposed replacement for the NCRR, the National Center for Advancing Translational Sciences (NCATS), acknowledges the value of an integrated DCM by retaining its core functions as a cohesive programme within an 'Infrastructure Entity'.

However, in our view, the vision of NCATS as an incubator for innovative medicines is unrealistic. A major obstacle to developing new treatments through translational science is an inadequate understanding of basic biological pathways and mechanisms — not anaemic efforts by industry to test potential drug candidates. Using the NCRR's existing research resources as a means of enhancing the NIH's traditional strength in mechanistic research is a more certain route to translational success than focusing on chemical screening and intramural bioassays, as proposed for NCATS.

As veteran comparative biologists, we feel that the decision to slash the NCRR to initiate NCATS was undertaken without due diligence or sufficient opportunity for public debate. The rush to establish NCATS without a settled organizational plan and against the advice of numerous translational science researchers bodes ill for the new centre's ability to perform meaningful translational research in the foreseeable future.

The preservation of the DCM in the Infrastructure Entity will maintain core NIH translational science functions. The sprint to form NCATS by dismembering the NCRR might be good politics, but it is bad public policy.

Brad Bolon on behalf of 25 co-authors*, GEMpath, Colorado, USA. brad@gempath.net *See http://dx.doi.org/10.1038/ 471036b for a full list of signatories. SEE NEWS P.15

Neuroscience cuts will hurt key areas

We call on the UK Biotechnology and Biological Sciences Research Council (BBSRC) to reconsider its intention to cut funding for neuroscience by around 20% (see go.nature.com/u4mgyq and go.nature.com/8ig9oy).

The neuroscience currently funded by the BBSRC must survive a rigorous committee selection process. According to the research council, the cut is being imposed not because the neuroscience funded is less than excellent, but because it does not address BBSRC priority areas.

Yet neuroscience research is crucial in every BBSRC priority area. In public health, it can improve the understanding of mental illness, age-related cognitive decline, and diet and exercise factors (through the neural basis of food selection and motivation, respectively). It can improve animal welfare by giving insight into the mental state of farm animals, and is relevant to food security — for example, by controlling crop predation through knowledge of the neural basis of insect behaviour.

The BBSRC funds so much of this research because of the high quality of British neuroscience and because its researchers have consistently proved that they can compete for funding.

So far, the BBSRC has been admirably responsive to research excellence on the ground, and open to going where scientists lead. This imposition of funding priorities from the top is a regrettable change.

Peter A. McNaughton, Trevor W. Robbins University of Cambridge, UK. pam42@cam.ac.uk

Easier citizen science is better

Non-scientists are now participating in research in ways that were previously impossible, thanks to more web-based projects to collect and analyse data. Here we suggest a way to encourage broader participation while increasing the quality of data.

Participation may be passive, as when someone donates their computer's 'downtime' to projects such as SETI@home, or active, as when someone uses eBird to log birds they have spotted. Unfortunately,

the prevailing data-collection and storage practices for active projects inhibit participation by non-experts.

Many projects rely on positive identification, whether explicitly (as for eBird) or by soliciting photographs and descriptions that others can use to classify the observation (as for the UK website iSpot). Because nonexperts often lack the knowledge to identify species, they may opt not to participate or may provide inaccurate data by accidentally misidentifying something. The result is a trade-off between participation and data quality.

This trade-off can be avoided simply by changing the way information is collected and stored. Participants should be given the option to report a sighting in terms of observed attributes, eliminating the need to force a (possibly incorrect) classification. For example, allowing someone to report a bird as oil-covered may be more valuable than asking them to guess what the species is. For such data to be used effectively, they need to be stored in a way that supports attributes rather than fixed, predetermined classes.

Jeffrey Parsons, Roman Lukyanenko and Yolanda Wiersma Memorial University of Newfoundland, Canada. jeffreyp@mun.ca

Include Israel when comparing metrics

Your readers deserve to see research metrics from the Arab world (Nature 469, 453 and 470, 147; 2011) compared with those of its nearest neighbour, Israel.

You compare the number of publications, researchers per million of population and the percentage of gross domestic product (GDP) expended on research and development (R&D). But all of your graphics omit Israel, even though the GDP graphic includes the European Union and Turkey.

The picture would be different had Israel's metrics been included. Israel published 14,943 papers in 2008 (Science

Citation Index). In 2007, there were 7,841 researchers per million population, and civilian expenditure on R&D totalled 4.3% of GDP in 2009 — the highest percentage in the world (Central Bureau of Statistics, State of Israel).

From 1948, Israel and its Arab neighbours started on a roughly equal footing. Israel has achieved much, despite arguably being the poorer nation in terms of traditional measures such as land area, natural resources and freedom from conflict. Its strong investment in human capital, fostered by a free and open society, has produced six decades of spectacular growth. Those achievements stand in contrast to six decades of regrettably slow (and relatively static) progress in the Arab world. Your analysis would have been more accurately portrayed in this context.

David W. Borhani Hartsdale, New York, USA.

david.borhani@alum.mit.edu

Lay aside the ladder of descent

Your argument that the curious Xenoturbella flatworm represents a "crucial intermediate stage of animal evolution" (Nature 470, 161-162; 2011) perpetuates a popular misconception, stemming from a presumption that the features of such ancient living relics are intermediate between those of other extant creatures.

Today's organisms are all at the twig tips of one large tree of life, with no knowable connections between primitive and higher forms. Reproductively isolated populations of species, such as chimpanzees and humans, are not modifications on a 'ladder' of descent — thus living chimpanzees are not our ancestors, but a sister species adapted to a different habitat (tropical forests versus savannah).

Xenoturbella has largely maintained its internal structure and body shape over millions of years of evolution, during which stabilizing selection removed

descendants that were less-well adapted to their environment than their parents.

Such 'living fossils' have always occupied a narrow ecological niche, apparently without ever experiencing much competition from more complex organisms, and so may serve as models for reconstructing crucial steps in animal evolution. But they do not represent 'intermediate' evolutionary forms in the way that some of the famous fossils from the Mesozoic, such as the feathered dinosaurs or ancient snakes with hind legs, are viewed as earlier, extinct connecting links in the tree of life. U. Kutschera Institute of Biology, University of Kassel, Germany.

India needs more plant taxonomists

kut@uni-kassel.de

India, with its wide range of geographical and climatic conditions, has a rich and varied flora of some 45,000 species — almost 7% of the world's flowering plants. But their documentation is seriously compromised by the country's dearth of plant taxonomists.

Although DNA sequence data and barcoding are well on the way to being accepted as the global standard for species identification, India's plant taxonomists are struggling to keep up. A lack of proper training and infrastructure hampers molecular-systematics studies, so the evolutionary lineages of most of the country's plants remain poorly understood.

India's many outstanding botanists, familiar with regional flora, must help plant taxonomists to advance molecular-systematics studies and improve the evolutionary understanding of the country's rich biodiversity.

M. Ajmal Ali King Saud University, Saudi Arabia. majmalali@rediffmail.com R. K. Choudhary Korea Research Institute of Bioscience and Biotechnology, South Korea.

NEWS & VIEWS



Figure 1 | Many eyes — a shoal of blue-striped snapper.

COLLECTIVE BEHAVIOUR

When it pays to share decisions

Theory suggests that the accuracy of a decision often increases with the number of decision makers, a phenomenon exploited by betting agents, Internet search engines and stock markets. Fish also use this 'wisdom of the crowd' effect.

LARISSA CONRADT

aving trouble making a decision? The reason is that you're probably not sure which is the best option. You seldom have perfect information, so might make a bad choice. Sharing decisions with others can help, because several decision makers can pool their information, and also eliminate individual errors¹. Consequently, the risk of making a mistake and settling on a bad option often decreases with the number of decision makers. For example, in court cases, juries consisting of several people are supposed to make correct decisions more often than can a single judge². In humans, there are numerous examples of this phenomenon. In social animals, the same principle should apply, but empirical demonstrations are rare.

Writing in *Proceedings of the National Academy of Sciences*, Ward *et al.*³ now show that larger shoals of fish not only make more-accurate decisions than do smaller shoals or single fish, but also make these decisions faster. In an elegantly designed experiment, combined

with theoretical modelling, the authors gave mosquitofish, Gambusia holbrooki, a choice between a predator-free route and one that led past a predator model. A fish was more likely to make a correct choice (to avoid the predator model) the larger the shoal in which it swam. The size of this increase in accuracy was in close agreement with theoretical predictions. The effect did not arise because large shoals were more likely to contain one particularly clever 'expert' fish, which guided the others. In fact, individual fish did not differ much in their ability to make correct decisions and, moreover, were not even good at it. Thus, the authors have demonstrated a genuine 'wisdom of the crowd' (or, in biological terms, 'many eyes') effect4 (Fig. 1).

The increase in decision speed with shoal size is especially noteworthy, for two reasons. First, we typically expect a trade-off between decision accuracy and speed, so that decision speed decreases with increasing accuracy and vice versa⁵. This is because more-accurate decisions usually require more information, and information gathering takes time (but see

also ref. 6). Second, we expect decision speed to decrease with the number of decision makers, because sharing decisions requires communication between decision makers and it seems plausible that this will also take time. Nevertheless, Ward and colleagues³ found that both decision speed and decision accuracy increased with the number of decision makers (that is, the number of fish in the shoal).

The reason that larger shoals managed to make not only more accurate but also faster decisions probably lies in the way information is communicated. Fish in shoals often move in a self-organized manner, whereby individuals react rapidly to the movements of close neighbours⁷. Indeed, Ward *et al.* present convincing evidence that such a reaction to spatially close companions has a crucial role in the mosquitofish choice of route — pairs of fish within less than 6 centimetres of each other reacted very fast to each other's movement changes; and a fish's choice of route depended significantly on the average choice of close companions.

This simultaneous, self-organized system of

'communication' has two important features. One is that the speed with which information is exchanged is high and hardly decreases with the number of fish in the shoal. The other is that communication is decentralized: that is, information transfer can start from any shoal member⁷. This means that overall decision speed depends crucially on the fastest decision maker(s) within the shoal. For stochastic reasons, a large shoal is more likely than a small one to contain a fish that, by chance, detects a predator relatively quickly, even if the fish do not differ in 'expertise'.

In short, the higher likelihood of a shoal containing a fast decision maker, coupled with swift, decentralized information transfer, could explain the increase in decision speed with shoal size. However, such fast decision making usually also involves a cost, namely that of an increased risk of false positives². That is, if the fastest decision maker made a mistake (and 'detected' a predator that did not exist), this mistake could also be amplified¹, and the group might stage a costly 'escape' when none was necessary. The experiments of Ward and colleagues³ did not allow for such a situation — there was always one predator model present, and fish could either avoid it (true positive) or not (false negative). It remains to be seen whether accuracy and speed of decision making still increase together if fish are faced with a situation in which false positives are possible.

Fast and accurate decision making is highly desirable in many walks of life, for humans as well as animals. Ward and colleagues' study shows that it can be achieved by sharing decisions widely and using a self-organized system of communication. This is, of course, exactly the strategy that has long been exploited by Internet search engines, and in this sense the mosquitofish of Ward and co-workers' experiments are not that dissimilar from Google.

However, there are three caveats about the benefits of decision sharing. First, if the abilities of potential decision makers vary widely, it might still be better to listen to one 'expert'2. Second, there is the danger of information cascades, whereby decision makers no longer contribute independent information but instead amplify shared misconceptions1. Finally, in many decisions, the goals of individual decision makers differ: that is, different members of the decision-making group favour different outcomes. In such a context, the sharing of decisions can have disadvantages as well as advantages⁸. Although sharing might still increase the available information, it can also hand influence on the outcome to decision makers whose goals differ from your own. To date, surprisingly little is known about good decision-making strategies in these kinds of conflict situations. ■

Larissa Conradt is in the Department of Biology, School of Life Sciences, University of

Sussex, Falmer, Brighton BN1 9QG, UK. e-mail: l.conradt@sussex.ac.uk

- Sumpter, D. J. T. & Pratt, S. C. Phil. Trans. R. Soc. B 364, 743–753 (2009).
- List, C. *Trends Ecol. Evol.* 19, 168–169 (2004).
 Ward, A. J. W., Herbert-Read, J. E., Sumpter, D. J. T.
- Ward, A. J. W., Herbert-Read, J. E., Sumpter, D. J. & Krause, J. Proc. Natl Acad. Sci. USA 108, 2312–2315 (2011).
- 4. Surowiecki, J. The Wisdom of Crowds

- (Doubleday, 2004).
- Franks, N. R., Dechaume-Moncharmont, F.-X., Hanmore, E. & Reynolds, J. K. *Phil. Trans. R. Soc. B* 364, 845–852 (2009).
- Gigerenzer, G. & Goldstein, D. G. Psychol. Rev. 103, 650–669 (1996).
- Couzin, I. D., Krause, J., Franks, N. R. & Levin, S. A. Nature 433, 513–516 (2005).
- 8. Conradt, L. & Roper, T. J. Nature **421**, 155–158 (2003).

ATOMIC PHYSICS

Atoms playing dress-up

The idea of using ultracold atoms to simulate the behaviour of electrons in new kinds of quantum systems — from topological insulators to exotic superfluids and superconductors — is a step closer to becoming a reality. SEE LETTER P.83

MICHAEL CHAPMAN & CARLOS SÁ DE MELO

uring the past decade or so, physicists have been trying to implement one of the last of Richard Feynman's ingenious ideas. This was to build a 'quantum scale model', using controllable quantum particles, to simulate the workings of otherwise intractable quantum systems and to investigate thorny problems in condensed-matter physics. On page 83 of this issue, Lin and colleagues' inch closer to building a new kind of quantum simulator using cold gases of atoms.

At less than one-millionth of a degree above absolute zero, cold atomic gases are extremely versatile and can be controlled with great precision. They can be composed of bosons (particles with integer spin) or fermions (particles with half-integer spin). And, just like electron gases, they can be confined in a variety of environments, including crystalline lattices and disordered media. Furthermore, the mutual interactions between the atoms of a gas can be controlled, by modifying atomic collisions, to mimic real, solid-state systems. Using these tools, researchers have been able to reproduce the essential quantum physics of several canonical condensed-matter systems, including superfluids, in which particles (electrons or atoms) move without resistance, and insulators, in which particles are pinned to an underlying lattice structure.

However, exploring some of the remaining uncharted territory in condensed-matter physics using cold atomic gases will require additional tools. One of the things missing from the toolbox had been the ability to mimic the effects of magnetic fields on the electron's charge — a challenge because atoms are neutral. These effects are central to many exotic phenomena, including the quantum Hall effect and superconductivity. In an earlier study, Lin and colleagues demonstrated^{3,4} a solution: they generated a fictitious magnetic field in an atomic system, using tailored beams of light.

Now, the same group² adds a new tool to the toolbox by creating artificial 'spin-orbit coupling' in a neutral atomic system. But in order to understand the significance of this experimental achievement, let us take a step back and understand the concept of spin-orbit coupling.

In addition to their electronic charge, electrons (like all fundamental particles) have an intrinsic spin. Loosely, we can think of the electron as spinning about an axis through its centre, with the spinning giving it a magnetic character similar to that of a tiny bar magnet. Atoms, being composed of fundamental particles, also have an intrinsic spin. But how does the spin of particles interact with their orbital motion?

The interaction of an object's spin with its orbit (spin-orbit coupling) is ubiquitous in both the microscopic and macroscopic worlds. One example is the synchronization of the rotation (spinning) of the Moon and its orbit around Earth, which means that we can only see one face of the Moon. Another example is the motion of electrons orbiting an atom's nucleus: the motion is altered by the spin of the electrons owing to the electric field of the nucleus, and this gives rise to the atom's fine structure (small shifts in its energy levels). Similar effects occur in free electrons moving through electric fields in solids, for example the fields generated by the underlying crystalline lattice.

It is hoped that quantum simulators based on atomic gases will illuminate the physics of electron systems. But it is first necessary to devise a technique to make neutral atoms mimic the interaction of the spin of moving electrons with electric fields, and so engineer spin–orbit coupling (Fig. 1). Building on a recent theoretical suggestion⁵ of how this might be accomplished, Lin *et al.*² were able to create experimentally an artificial coupling between the spin of rubidium (⁸⁷Rb) gas atoms (bosons of spin 1) and their centre-of-mass motion. To achieve the coupling, the authors

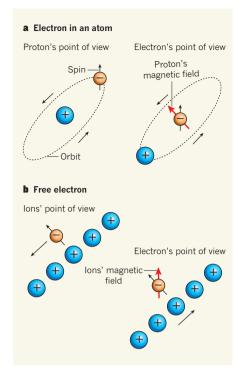


Figure 1 | Spin–orbit coupling. a, In an atom, an electron (orange) orbits the nucleus (blue; here composed of a single proton). From the electron's point of view, the proton orbits the electron and produces a magnetic field that couples with the electron's spin and alters its orbit. b, If the electron is roaming freely through a group of ions, from the electron's point of view it is the ions that move. The ions' motion generates a magnetic field that couples to the electron's spin. In real solids, this coupling between the electron's spin and its motion (spin–orbit coupling) is more complex, but the essence of the interaction is the same as that depicted here. Lin and colleagues² engineer spin–orbit coupling in a neutral atomic system.

used a pair of lasers to transfer linear momentum to the atoms' centre-of-mass and create mixed atomic spin states, which are composed of two different spin orientations. The mixed-spin states couple directly with the momentum transferred to the atoms' centre-of-mass (orbital) motion, creating a 'dressed state', thus leading to an artificial spin-orbit coupling. (For a review of related ideas, see ref. 6.)

A great advantage of the authors' experiment² lies in the possibility of controlling spin-orbit coupling — from no coupling at all to strong coupling — through optical means. If the lasers are turned off, spin-orbit coupling disappears: the spin and the centre-of-mass motion are independent. If the lasers are turned on, spin-orbit coupling occurs and scales with the lasers' intensity. This type of control is not typically available in condensed-matter systems such as in semiconductors or superconductors.

What's more, Lin and colleagues² have shown that the artificial spin-orbit coupling can be used to change the interaction between atoms that are in different spin states. The ability to change the interactions between a pair of atoms allows the researchers to study transitions between a phase in which atoms with different spin states repel weakly, and are mixed in the same spatial region (lasers off), to a phase in which atoms with different spin states repel strongly and are spatially separated (above a threshold of laser intensity).

The authors' creation and control of artificial spin–orbit coupling in atoms has implications beyond atomic-gas physics, in particular because there is no fundamental reason why their experiments should not be performed with fermions. In condensed-matter systems, the spin–orbit coupling of the constituent electrons (fermions of spin ½) can have important consequences for semiconductors, superconductors and magnetic materials. In mercury telluride (HgTe) semiconductors, for example, strong spin–orbit coupling can produce topological insulators⁷. These unconventional semiconductors insulate electric current in their bulk but conduct electricity on their

surface, a rather unusual and peculiar effect that may be useful for electronic applications. The creation of adjustable artificial spin—orbit coupling in atoms opens up exciting possibilities for realizing quantum simulators of topological insulators and exotic forms of superfluidity and superconductivity.

Michael Chapman and Carlos Sá de Melo are in the School of Physics, Georgia Institute of Technology, Atlanta, Georgia 30332, USA. e-mails: mchapman@gatech.edu; carlos.sademelo@physics.gatech.edu

- Feynman, R. P. Int. J. Theor. Phys. 21, 467–488 (1982).
- Lin, Y.-J., Jiménez-García, K. & Spielman, I. B. Nature 471, 83–86 (2011).
- 3. Lin, Y.-J., Compton, R. L., Jiménez-García, K., Porto, J. V. & Spielman, I. B. *Nature* **462**, 628–632 (2009).
- 4. Zwierlein, M. Nature 462, 584-585 (2009).
- Liu, X.-J., Borunda, M. F., Liu, X. & Sinova, J. Phys. Rev. Lett. 102, 046402 (2009).
- Dalibard, J., Gerbier, F., Juzeliúnas, G. & Öhberg, P. Preprint at http://arxiv.org/abs/1008.5378v1 (2010).
- 7. Qi, X. L. & Zhang, S. C. *Physics Today* **63**(1), 33–38 (2010).

PROTEIN FOLDING

Protection from the outside

Protein folding is a high-stakes process, with cell dysfunction and death being the unforgiving penalties for failure. Work in bacteria hints that organisms manage this process beyond the boundaries of the cytoplasm — and even the cell.

EVAN T. POWERS & WILLIAM E. BALCH

rotein misfolding can instigate disease one way or another¹: it can cause both loss of function by leading to an insufficient amount of functional proteins, and gain of toxic function through the aggregation of misfolded proteins. Suppressing misfolding and aggregation is the job of the proteostasis network^{2,3}, particularly the various classes of chaperones — evolutionarily conserved proteins that help other proteins to fold productively. Folding protection must operate in many environments, both inside and outside the cell. Writing in Nature Structural and Molecular Biology, Quan et al.4 identify in bacteria a new structural class of chaperone called Spy that, unusually, functions outside the typical cellular remit for chaperone activity.

For their analysis, Quan and colleagues created two 'sandwich fusion proteins' by inserting L53A I54A Im7 — an unstable version of the protein Im7, which is often used in protein-folding studies⁵ — into two other proteins: β-lactamase and DsbA. When folded, β-lactamase and DsbA confer resistance to

the antibiotic penicillin and to cadmium ions (Cd^{2+}) , respectively. However, the insertion of a foreign protein into their sequences makes their folding dependent on the folding of the inserted protein. Thus, in the sandwich fusion proteins, L53A I54A Im7 folding leads to two independent selectable markers: penicillin resistance and Cd^{2+} resistance.

The authors⁴ induced expression of their fusion proteins in the periplasm of the bacterium *Escherichia coli*; the periplasm is the space between the inner and outer membranes in Gram-negative bacteria. In most cases, they observed no resistance to either penicillin or Cd^{2+} , presumably because the inability of L53A I54A Im7 to fold prevented β -lactamase and DsbA from folding. A number of strains, however, did gain both penicillin and Cd^{2+} resistance.

The resistant strains also produced a massive amount of Spy, suggesting that this little-known periplasmic protein had a hitherto unrecognized chaperone activity. The researchers corroborate this result *in vitro*, showing that Spy can inhibit both aggregation and promote folding, even at

sub-stoichiometric concentrations.

Quan *et al.* also show that Spy activity is independent of the cellular energy molecule ATP. This is not surprising, given that the protein functions outside the cytoplasm. However, operation of Spy at sub-stoichiometric concentrations is surprising, because chaperones that work in this way generally use ATP⁶. According to conventional wisdom, it is difficult — if not impossible — to imagine a mechanism for how a chaperone actively remodels the protein-folding energy landscape without an energy input. It is equally difficult to reconcile Spy's effects on protein folding and aggregation with a simple holdase mechanism, in which a chaperone passively binds to unfolded proteins.

There could be several explanations. To protect nascent peptides emerging through the inner membrane, Spy could work during protein translation, binding transiently to nascent proteins to stabilize them. Spy could be an efficient protective osmolyte, and thus thermodynamically stabilize proteins' native states by promoting the formation of hydrogen-bonded secondary structures⁷, which would be consistent with its high levels in the periplasm. Or Spy could be a steric foldase — a type of chaperone that stabilizes the folded state of proteins by binding to them⁸. Clearly, Spy's mechanism of action merits further investigation.

The discovery of Spy adds to the current repertoire of chaperones functioning in the periplasmic space of Gram-negative bacteria and raises questions about the existence of extra-cytoplasmic, or outer, proteostasis networks (the outPN) in complex eukaryotes (plants and animals). Whereas the bacterial inner membrane rigorously protects the cytoplasm and the intracellular proteostasis networks (inPN), the outer membrane is permeable to small molecules (those with a molecular mass of less than roughly 600). It functions as a filter to retain periplasmic proteins close to the surface of E. coli, thus preventing their dilution in the environment. It is perhaps only a modest stretch to compare the bacterial periplasmic space to the interstitial spaces in vertebrates (Box 1).

Unfortunately, our knowledge of the composition and function of the outPN in complex eukaryotes is limited. Although small amounts of the classic chaperones Hsp70 and Hsp90 can be found outside the cell under stress conditions¹⁰, their roles remain controversial, and the lack of extracellular ATP makes them ill-suited to a chaperoning role outside the cell. In addition, abundant plasma proteins such as albumin and globulins can bind to other proteins, but their potential role as outPN components remains to be carefully explored. Nonetheless, there is evidence for potential outPN players that chaperone defective proteins — including α1-acid glycoprotein¹¹, α-1-antitrypsin^{12,13}, asialoglycoproteins¹⁴, plasma gelsolin¹⁵, clusterins 16, α2-macroglobulins 17 and transthyretin,

BOX 1

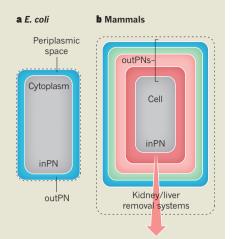
Chaperone networks

In addition to the intracellular proteostasis network (inPN) in its cytoplasm,

Escherichia coli produces many chaperones⁸ — including Spy, identified by Quan et al.⁴ — that protect protein folding in the periplasm in an ATP-independent manner (a).

Mammals have a number of distinct interstitial spaces filled with bodily fluids that could also operate independently of ATP to protect the major organ systems (b). However, unlike the periplasmic space of *E. coli*, which is open to the environment, the interstitial systems are closed. Interstitial fluids ultimately communicate with the environment through the kidney filtration system, or through uptake and metabolism by the liver.

Plasma (red) provides components of the extracellular chaperone network (outPN) to the peritoneal (abdomen), pericardial (heart), pleural (lungs), synovial (joints) and amniotic fluids (for simplicity, all grouped in pink). Each might form an interstitial system protecting a separate organ system, and all have a rich protein content, reflecting their passive coupling



to plasma. Both the lymphatic system (green), which houses a key arm of the immune system, and the central nervous system's cerebrospinal fluid (CFS; blue) seem to be separate from the plasma outPN-related fluids. CFS is largely devoid of protein, but is possibly protected by the blood–brain barrier through the plasma outPN. E.T.P. & W.E.B.

which is thought to be protective against Alzheimer's disease¹⁸.

Is there an equivalent of stress-related Spy induction in humans? At least one possibility is the proteins whose levels increase during the acute-phase response to inflammation 17 (such as $\alpha 1$ -acid glycoprotein and haptoglobulin) and that have protein-folding protective functions. Even the innate and adaptive immune responses could be seen as highly evolved out PN systems (Box 1).

Undoubtedly, the intracellular proteostasis network is conserved and universal^{2,3}. But the observations^{4,9} that the seemingly lowly *E. coli* can protect itself from a periplasmic folding problem by the production of Spy and other non-ATP-dependent chaperones could shift our view of the role of the interstitial space towards it being a home for a comparable extracellular proteostasis network in vertebrates^{2,3}. Indeed, the outPN in vertebrates could report on and manage extracellular protein-folding stress, working in parallel with inflammatory and immune responses (Box 1). After all, like *E. coli*, vertebrates experience stressful situations every day. ■

Evan T. Powers is in the Department of Chemistry and William E. Balch is in the Department of Cell Biology, The Skaggs Institute for Chemical Biology, Department of Chemical Physiology and Institute for Childhood and Neglected Diseases, The Scripps Research Institute, La Jolla, California 92037, USA. e-mails: epowers@scripps.edu; webalch@scripps.edu

- Powers, E. T., Morimoto, R. I., Dillin, A., Kelly, J. W. & Balch, W. E. *Annu. Rev. Biochem.* 78, 959–991 (2009)
- Balch, W. E., Morimoto, R. I., Dillin, A. & Kelly, J. W. Science 319, 916–919 (2008).
- Roth, D. M. & Balch, W. E. Curr. Opin. Cell Biol. doi:10.1016/j.ceb.2010.11.001 (2010).
- Quan, S. et al. Nature Struct. Mol. Biol. doi:10.1038/ nsmb.2016 (2011).
- 5. Capaldi, A. P., Kleanthous, C. & Radford, S. E. *Nature Struct. Biol.* **9**, 209–216 (2002).
- Saibil, H. R. Curr. Opin. Struct. Biol. 18, 35–42 (2008).
- Street, T. O., Bolen, D. W. & Rose, G. D. Proc. Natl Acad. Sci. USA 103, 13997–14002 (2006).
- 8. Pauwels, K., Van Molle, I., Tommassen, J. & Van Gelder, P. *Mol. Microbiol.* **64**, 917–922 (2007).
- Allen, W. J., Phan, G. & Waksman, G. Adv. Protein Chem. Struct. Biol. 78, 51–97 (2009).
- Horváth, I., Multhoff, G., Sonnleitner, A. & Vigh, L. Biochim. Biophys. Acta 1778, 1653–1664 (2008).
- 11.Zsila, F. Bioorg. Med. Chem. Lett. **20**, 1205–1209 (2010).
- 12.Zsila, F. Biochem. Biophys. Res. Commun. **393**, 242–247 (2010).
- 13.Bouchecareilh, M., Conkright, J. J. & Balch, W. E. Proc. Am. Thorac. Soc. 7, 415–422 (2010).
- Stockert, R. J. *Physiol. Rev.* **75**, 591–609 (1995).
 Page, L. J. *et al. Proc. Natl Acad. Sci. USA* **106**, 11125–11130 (2009).
- 16.Wyatt, A., Yerbury, J., Poon, S., Dabbs, R. & Wilson, M. Adv. Cancer Res. **104**, 89–114 (2009).
- 17.Cray, C., Zaias, J. & Altman, N. H. Comp. Med. **59**, 517–526 (2009).
- 18.Buxbaum, J. N. & Reixach, N. Cell. Mol. Life Sci. **66**, 3095–3101 (2009).

Annelid who's who

The origin of the annelids is buried in distant evolutionary time. A molecular phylogeny resolves their deep family interrelationships and provides a picture of their 'urannelid' ancestor. SEE LETTER P.95

DETLEV ARENDT

ome animals are so familiar that we can scarcely believe we know little about their origins. Take earthworms, for example, common to everyone's garden, which belong to a large phylum of invertebrates — the annelids (ringed worms). The hitherto shrouded evolutionary history of annelids is now illuminated by Struck *et al.* on page 95 of this issue¹.

Annelids are global players in terrestrial and freshwater environments, and in marine ecosystems, where they live in and on the sea floor. But the identity of their nearest relatives (maybe molluscs, maybe flatworms), and even their affinities within the phylum, has remained a puzzle. This lack of understand-

ing has another edge, given that various annelid species serve as model organisms for the investigation of basic biological processes. Embryologists and neuroscientists have studied leeches for decades. And the ragworm *Platynereis* has recently emerged as a valuable model for studying development, evolution and neurobiology², along with *Capitella*, *Hydroides* and other marine species³. Just imagine working on vertebrate models such as fish, mice and frogs without knowing their evolutionary interrelationships.

Struck et al. have made a significant advance in the reconstruction of annelid phylogeny, having resolved their internal affinities. Using molecular techniques, they have studied the relationships between various annelid families and orders, and have obtained a surprisingly clear result. It turns out that annelids are deeply subdivided into two main groups, the Errantia (to which the ragworm belongs) and the Sedentaria (to which the leech, earthworm, *Capitella* and *Hydroides* belong).

As the names suggest, the subdivision of annelids into the Errantia and Sedentaria matches their overall lifestyles (Fig. 1). Members of the Errantia are free to move about, and crawl, swim or burrow. Many are predators or feed on macroalgae. By contrast, representatives of the Sedentaria are hemi-sessile burrowers or tube dwellers (apart from the highly specialized, parasitic leeches). They eat sediment or surface deposits, or filter the surrounding water with their tentacle crowns.

In 1865, a similar grouping, but excluding the earthworms and leeches, was put forward by Jean Louis Armand de Quatrefages de Bréau. However, it was dismissed by later authors, who considered the similarities in lifestyle to be convergent adaptations due to similar ecological constraints. Ironically, Struck and colleagues' study¹ reveals that the older classification was closer to the truth, thus 'revising the revision'. The authors' phylogeny demonstrates that broad features of lifestyle and morphology, even if sometimes challenging to quantify, can be at least as informative as ultrastructural or fine morphological characteristics, and are not necessarily much more prone to



Figure 1 | An illustration of the Errantia and Sedentaria by Ernst Häckel, dated 1904. To take just two examples, top right is Eunice magnifica (Grube, 1866), Eunicidae, an errantian; top left is Sabellastarte spectabilis (Grube, 1878), Sabellidae, a sedentarian. Errantians often have especially prominent lateral appendages with bristles, for undulatory crawling. Many sedentarians exhibit beautiful tentacle crowns for filtering plankton and other food particles from the water.

the complication of convergent evolution.

The work is another success story in the young discipline of phylogenomics — which attempts to resolve evolutionary history by genomic comparisons — and is one of the first aimed at probing deep within a phylum. Struck and co-workers have sequenced about a thousand expressed-sequence tags (complementary DNA library clones) from 17 members of annelid families and complemented these collections with existing data, yielding a total representation of 34 annelid species. They selected 231 genes common to at least one-third of the total taxa, and aligned and concatenated them into a supermatrix of 47,953 amino acids.

Next, they reconstructed a phylogenetic tree using refined methods capable of handling the diversity of amino-acid substitution processes in such a supermatrix. Many of the nodes in their tree, especially that separating the Errantia from the Sedentaria, had remarkably high support values (contrasting with those of previous annelid phylogenies based on single genes⁴), making it highly likely that this grouping is definitive.

The case of the annelids exemplifies both the beauty and the pitfalls of phylogeny reconstruction when applying the principle of parsimony,

which settles on the tree minimizing gain or loss of particular characteristics. At the molecular level, this approach has proved very powerful, and it has been further enhanced by the advent of phylogenomics. But it is becoming increasingly obvious that, on the basis of morphological characteristics alone, there is a serious problem: the apparent ease with which such characteristics are lost.

This point is illustrated by a morphological parsimony analysis of annelid phylogeny⁵ that established a group, the Palpata, whose members were defined by the presence of specific head appendages (palpae) — the implication being that other groups without palpae had never had them. The new annelid phylogeny instead indicates independent loss of palpae in errantian and sedentarian groups, as was previously suggested^{6,7} by two of the co-authors of the current paper¹. This example corroborates the general idea of frequent and independent loss of traits during animal evolution.

Finally, the new work¹ nicely illustrates how, once the (molecular) phylogeny has been solved, matrices of morphological characteristics can be used to reconstruct the common ancestors of the respective groups. If a given characteristic is found in both branches resulting from a node, it must have been present in the common ancestor. In this way, we can infer a lot about the 'urannelid', the last common ancestor of all annelids. Most significantly, it was an animal richly equipped

ARIXVERLAG

with sensory organs. It had chemosensory nuchal organs and palpae; a pair of two-celled larval eyes for phototaxis²; and possibly a pair of more elaborate, multicellular adult eyes with an alternating arrangement of rhabdomeric photoreceptors and shading pigment cells. The latter combination is found in extant errantians⁸ and in the sipunculans⁹, which represent an outgroup to both errantians and sedentarians (see Fig. 1 of the paper¹).

The urannelid was segmented, a detail that is clear from the nested position of two unsegmented taxa, the echiurans and sipunculans, within segmented groups¹⁰. This ancestor probably lived on the sea floor, using its relatively complex lateral appendages for undulatory crawling (as seen in today's Errantia and for example in the Spionidae, which lie in the basal part of the Sedentaria branch of the tree). Given the power of phylogenomics, we might

soon know what the urannelid mollusc- or flatworm-like relatives looked like in the ancient oceans

Detlev Arendt is in the Developmental Biology Unit, European Molecular Biology Laboratory, 69012 Heidelberg, Germany. e-mail: arendt@embl.de

- 1. Struck, T. H. et al. Nature **471**, 95–98 (2011).
- 2. Jékely, G. *et al. Nature* **456,** 395–399 (2008).
- McDougall, C. et al. Parasite 15, 321–328 (2008).
 Struck, T. H. et al. BMC Evol. Biol. 7, 57 (2007).
- Rouse, G. W. & Fauchald, K. Zoologica Scripta 26, 139–204 (1997).
- Purschke, G., Hessling, R. & Westheide, W. J. Zool. Syst. Evol. Res. 38, 165–173 (2000).
- 7. Bleidorn, C. J. Zool. Syst. Evol. Res. **45**, 299–307 (2007). 8. Purschke, G., Arendt, D., Hausen, H. & Müller, M. C. M.
- Arthropod Struct. Dev. **35**, 211–230 (2006).

 9. Hermans, C. O. & Eakin, R. M. Z. Zellforsch. Mikrosk. Anat. **100**, 325–339 (1969).
- Kristof, A., Wollesen, T. & Wanninger, A. Curr. Biol. 18, 1129–1132 (2008).

CLIMATE CHANGE

Another Antarctic rhythm

A novel explanation for the long-term temperature record in Antarctic ice cores invokes local solar radiation as the driving agent. This proposal will prompt palaeoclimate scientists to pause and to go back to basics. SEE LETTER P.91

KOJI FUJITA

Antarctic and Greenland ice sheets is one of the main sources of our understanding of past climate. A component of that understanding is that, on timescales of 20,000 years and more, climate change in Antarctica is determined by the amount of solar radiation (insolation) reaching high northern latitudes in summer. On page 91 of this issue, Laepple *et al.*¹ call into question some of the evidence for that view.

Precisely dated polar ice cores have allowed examination of the 'bipolar see-saw' relationship of air temperatures between the hemispheres on millennial timescales², as well as of longer-term, glacial–interglacial climate change paced by variations in Earth's orbit — the Milankovitch forcing of ice ages³. In these studies, the use of isotopes that are stable in water, in the form of the ratios of oxygen and deuterium isotopes, is well established. These ratios constitute the fundamental proxy measurements for estimating past temperatures from ice cores at both poles²⁻⁴.

Because ice cores consist of ice, the stableisotope ratios in the ice stem from those contained in precipitation (snow, which becomes compacted to ice). In other words, if there is no precipitation, no isotopic signal remains in the ice core. This simple principle has been acknowledged in interpreting the Greenland ice-core record⁵. Subsequent studies^{6,7} have described how changes in the seasonal pattern of precipitation during glacial–interglacial cycles have significantly biased the isotopic temperature record in Greenland. But it was thought that the effect in Antarctica was probably minor because of its comparatively stable precipitation seasonality.

Laepple and co-authors¹ apply this idea of precipitation seasonality to the Antarctic icecore record. However, they do not deal with changes in seasonal patterns, as the previous studies did, but instead consider the situation in which seasonality is itself unchanging and in which snow accumulation over inland Antarctica is maximal in winter and minimal in summer. This seasonality in snowfall has various causes, such as the strong radiative cooling that induces clear-sky precipitation and increased moisture transport in winter, and sublimation of ice into water vapour in summer.

By assuming that this seasonal pattern of snow accumulation has persisted throughout glacial-interglacial cycles, and that the local air temperature has fluctuated according to the present-day relationship between temperature and insolation, the authors¹ produce an accumulation-weighted insolation signal as a record of temperatures in Antarctic ice cores. They find that it has the opposite phase to the orbital-precession component (determined by long-term changes in the orientation of Earth's rotational axis) of the local summerinsolation signal — and so, surprisingly, that it is in phase with summer-insolation intensity in the Northern Hemisphere.

If the Antarctic local temperature is determined by local insolation, the precession component in the ice-core temperature signal should be out of phase with Northern Hemisphere insolation, because the precession component is out of phase between the two hemispheres. However, the precession component filtered from the isotopic temperature record in the Antarctic ice cores is coherent and in phase with the Northern Hemisphere insolation intensity³ — seemingly supporting the Milankovitch theory, according to which southern climate is driven by insolation changes at high northern latitudes.

But does the close phasing necessarily support a causal relationship? Perhaps not. Laepple and co-authors1 have rethought how the signals of temperature change are produced. Their accumulation-weighted insolation record suggests that a precession rhythm synchronized with — but not caused by — the Northern Hemisphere could be generated if the local temperature fluctuated in line with local insolation conditions in the Southern Hemisphere. The unveiling of this 'pseudorhythm' strikes at the foundation of temperature estimates gleaned by analysing isotope ratios in ice cores. Does it mean, as Laepple et al. suggest, that the evidence from Antarctic ice cores cannot be used to support or refute the Milankovitch theory?

This theory is supported not just by temperatures inferred from Antarctic ice cores, but also by sea surface temperatures recorded in sediment cores from the Southern Ocean. In these cores, the orbital-precession rhythm is often found to be in phase with summer insolation in the Northern Hemisphere and therefore opposing the local summer insolation⁸. The seasonality of snow accumulation does not affect sediment processes in the ocean. Furthermore, the existence of shorter (millennial timescale) but strong bipolar see-saw connections between the two hemispheres implies that there are indeed mechanisms for the interhemispheric propagation of climate signals through the ocean and/or atmosphere². There is no reason to believe that such mechanisms have not operated over longer timescales.

A caveat regarding the results themselves is that Laepple and colleagues' insolation-based air-temperature estimate shows a rather small amplitude (around 0.7 °C peak to peak) compared with that derived from ice cores (3 °C peak to peak). This is probably because the authors' use of local insolation as the temperature proxy means that they

assume zero insolation during winter (polar night) throughout glacial–interglacial cycles. They themselves acknowledge this point, and suggest that other factors not accounted for in their approach may explain the discrepancy.

Nevertheless, we must now consider that the orbital-precession rhythm in Antarctic ice cores can partly be attributed to local conditions. In the same way that an ill-fitting piece of a jigsaw puzzle can be disconcerting, this pseudo-rhythm will be discomfiting to those who study palaeoclimate and climate dynamics. 'Is the signal I see really created by climate change?', is a question they will have

to ask themselves. And they will need to take a hard look at the principles on which their data are founded. The relationship between the isotopes in water and air temperature, for instance, is based on geographical (spatial) observations only. But its temporal variability has not been confirmed at any ice-core drilling sites in inland Antarctica, even by observations on an annual timescale. Sometimes, in science as in life, it is necessary to pause in order to make progress.

Koji Fujita *is in the Graduate School of Environmental Studies, Nagoya University,*

Chikusa-ku, Nagoya 464-8601, Japan. e-mail: cozy@nagoya-u.jp

- Laepple, T., Werner, M. & Lohmann, G. Nature 471, 91–94 (2011).
- EPICA Community Members. Nature 444, 195–198 (2006).
- 3. Kawamura, K. et al. Nature **448**, 912–916 (2007).
- North Greenland Ice Core Project Members. Nature 431, 147–151 (2004).
- Steig, E. J., Grootes, P. M. & Stuiver, M. Science 266, 1885–1886 (1994).
- Werner, M., Mikolajewicz, U., Heimann, M. & Hoffmann, G. Geophys. Res. Lett. 27, 723–726, doi:10.1029/1999GL006075 (2000).
- Jouzel, J. et al. J. Geophys. Res. 108, 4361, doi:10.1029/2002JD002677 (2003).
- 8. Pahnke, K. et al. Science 301, 948-952 (2003).

STEM CELLS

The dark side of induced pluripotency

Induced pluripotent stem cells have great therapeutic potential. But genomic and epigenomic analyses of these cells generated using current technology reveal abnormalities that may affect their safe use. SEE ARTICLES P.58, P.63 & P.68

MARTIN F. PERA

'nduced pluripotent stem cells (iPSCs) are generated through the reprogramming of differentiated adult cells and can be coaxed to develop into a wide range of cell types. They therefore have far-reaching potential for use in research and in regenerative medicine. But the ultimate value of these cells as disease models or as sources for transplantation therapy will depend on the fidelity of their reprogramming to the pluripotent state, and on their maintenance of a normal genetic and epigenetic (involving aspects other than DNA sequence) status. Five recent surveys^{1–5}, including three in this issue¹⁻³, show that the reprogramming process and subsequent culture of iPSCs in vitro can induce genetic and epigenetic abnormalities in these cells. The studies raise concerns over the implications of such aberrations for future applications of iPSCs.

It has long been known⁶ that, during cultivation *in vitro*, human embryonic stem cells (ESCs) can become aneuploid; that is, they acquire an abnormal number of chromosomes. The new papers have applied various state-of-the-art genomic technologies to assess in detail the occurrence and frequency of genetic and epigenetic defects in both human iPSCs and ESCs.

Hussein *et al.*¹ (page 58) studied copy number variation (CNV) across the genome during iPSC generation, whereas Gore and colleagues² (page 63) looked for point mutations in iPSCs using genome-wide sequencing of protein-coding regions. Lister *et al.*³ (page 68)

examined DNA methylation — an epigenetic mark — across the genomes of ESCs and iPSCs at the single-base level. These studies, along with other investigations into changes in chromosome numbers⁴ and CNV⁵ in the two kinds of stem cell, lead to the conclusion that reprogramming and subsequent expansion of iPSCs in culture can lead to the accumulation of diverse abnormalities at the chromosomal, subchromosomal and singlebase levels. Specifically, three common themes, regarding the genetic and epigenetic stability of ESCs and iPSCs, emerge.

First, by several measures, iPSCs display more genetic and epigenetic abnormalities than do ESCs or fibroblasts — the cells from which they originated. Chromosomal abnormalities appear early during the culturing of iPSCs⁵, a phenomenon not generally observed in ESCs. Also, the frequency of mutations in iPSCs is estimated to be ten times higher than in fibroblasts². And there are greater numbers of novel CNVs (CNVs not found in the cell of origin or in human genomes of comparable background) in iPSCs than in ESCs^{1,5}. Similarly, the epigenome of iPSCs features incomplete reprogramming (with cells retaining epigenetic marks of the cell of origin), aberrant methylation of CG dinucleotides, and abnormalities in non-CG methylation — an epigenetic feature seen only in pluripotent cells³.

Second, the studies show that genetic abnormalities can arise at different stages of iPSC generation. Some lesions are inherited from the cell used for reprogramming. Gore *et al.*² employ a particularly sensitive approach to

demonstrate that a subset of point mutations found in iPSC lines pre-existed in a small minority of fibroblasts used for reprogramming. Other lesions seem to arise early on in reprogramming, as mentioned previously. For example, Hussein et al. found large numbers of new CNVs during early passages (subcultures) following reprogramming, but noted that subsequent growth in vitro seemingly selected against most of the changes, which implies that they are deleterious for the cells that bear them. The studies also report changes that apparently relate to long-term adaptation to cell culture. These include over-representation either of the short arm of chromosome 12 (12p) or of this entire chromosome^{4,5}, and of a subregion in the long arm of chromosome 20 (ref. 5). Both of these changes have been observed⁶ in ESC lines, with an increased number of 12p being a hallmark of testicular germ-cell tumours — the malignant prototype of human pluripotent stem cells.

Third, several of the groups^{2,4,5} report clues to the potential function of the genetic lesions that arise in ESCs and iPSCs. For example, regions prone to amplification, deletion or point mutation seem to be enriched in genes involved in cell-cycle regulation and cancer. Although the changes observed do not strongly implicate any particular gene functionally as a target for change during the amplification of iPSCs or during their adaptation to culture conditions, the frequent association of the affected genes with cancer gives cause for concern.

This highly significant body of data¹⁻⁵ provides a revealing, in-depth portrait of the status of the genome and the epigenome during cellular reprogramming. But it also leaves open some fairly challenging questions.

The studies provide little insight into the crucial question of what aspects of the reprogramming methods might predispose the cells to the accumulation of recurrent genetic or epigenetic lesions. Although recurrence of change in specific genomic regions across a number of cell lines strongly implies a selective process, in several studies the researchers noted that there was no obvious correlation between the extent of genetic damage in a

given population of reprogrammed cells and the methods used for their reprogramming or propagation. Hussein *et al.*¹ provide some evidence that CNV occurred more frequently at sites prone to replication stress. It is not clear, however, whether this stress is unique to the reprogramming process, or whether it would be common to any experimental situation in which a cultured cell is subjected to strong selection and replication pressures in witre

Despite extensive evaluation of recurrent genetic change in a vast number of cell lines, we are only slightly closer to identifying which particular genes within the larger chromosomal regions that are commonly subject to duplication in iPSCs and ESCs might be under selection. Years of cytogenetic studies of germcell tumours have also identified large genomic regions that are commonly over-represented in these cancers, but the identification of the specific genes involved in the transformation of these pluripotent cells has remained elusive. A possible interpretation of the data

on the genetics of germ-cell tumours is that multiple genetic regions, or large regulatory regions, are crucial to the process of oncogenesis *in vivo*. Perhaps a similar mechanism is in play during *in vitro* adaptation of ESCs or iPSCs.

With regard to evaluating the safety of ESCs and iPSCs, a key issue is the biological significance of the changes that these studies¹⁻⁵ report. Clearly, aneuploid cell lines would not be used in therapy (although they might be useful for research into the basis of genetic disorders associated with anomalies in chromosome number or other genetic abnormalities). Cell lines bearing mutations of established functional consequence in oncogenes or tumour suppressors, or in genes associated with Mendelian disorders (those usually due to a single gene), could equally not be used therapeutically. However, the many subchromosomal changes, CNVs or point mutations that are not obviously associated with known disease-related genetic abnormalities pose challenges to interpretation. This is

because it is unclear how best to assess the effects of new genetic lesions on the growth, differentiation, tumorigenicity and functionality of pluripotent stem cells or their differentiated progeny. High-throughput functional genomics will probably be required to answer these questions. Pluripotent cells themselves will provide the most promising platform for such studies.

Martin F. Pera is at the Eli and Edythe Broad Center for Regenerative Medicine and Stem Cell Research, Keck School of Medicine, University of Southern California, Los Angeles, California 90033, USA. e-mail: pera@usc.edu

- 1. Hussein, S. M. et al. Nature 471, 58-62 (2011).
- 2. Gore, A. et al. Nature 471, 63-67 (2011).
- 3. Lister, R. et al. Nature 471, 68-73 (2011).
- 4. Mayshar, Y. et al. Cell Stem Cell **7**, 521–531 (2010)
- . Laurent, L. C. et al. Cell Stem Cell 8, 106–118 (2011).
- Baker, D. E. C. et al. Nature Biotechnol. 25, 207–215 (2007).

CLIMATE CHANGE

Rethinking the sea-ice tipping point

Summer sea-ice extent in the Arctic has decreased greatly during recent decades. Simulations of twenty-first-century climate suggest that the ice can recover from artificially imposed ice-free summer conditions within a couple of years.

MARK C. SERREZE

ill the Arctic's floating cover of sea ice pass a critical threshold, or tipping point, beyond which a rapid, irreversible slide occurs to a seasonally ice-free Arctic Ocean? The question is a pertinent one bearing on the adaptability of Arctic marine life¹, how ice loss influences atmospheric circulation and precipitation patterns within and beyond the Arctic², and prospects for resource extraction and marine shipping³. According to a new study by Tietsche and colleagues⁴, and other recent work⁵, concerns over a tipping point may be unfounded.

That the Arctic is moving towards a seasonally ice-free state is clear. Over the period of satellite observations (1979 onwards), linear trends in the decline of sea-ice extent have been recorded for all months. The trends are smallest in winter and largest in September, the end of the melt season. When referenced to a 1979–2000 mean, the rate of decline in sea-ice extent for September is about 12% per decade; Fig. 1). A key driver of this seasonal asymmetry in trends is that spring ice cover is

increasingly dominated by relatively thin ice that formed during the previous autumn and winter, with less of the generally thicker ice that has survived at least one summer-melt period⁶. Because less energy is required to melt out thin ice, with other factors equal, the thinner the ice in spring, the lower the ice extent at the end of summer. Thin spring ice also strengthens the seasonal albedo feedback, whereby dark (low albedo) open-water areas are exposed to the Sun earlier in the melt season, leading to stronger seasonal heating of the upper ocean that, in turn, helps to melt more ice, exposing even more of the dark ocean.

Concern over a tipping point stemmed from a modelling study⁷ by Holland and colleagues published in 2006. They found that, as the climate warmed and the spring sea-ice cover thinned in response to rising greenhouse-gas levels, a strong kick from natural climate variability could more easily induce a reduction in sea-ice extent sufficiently large to set the albedo feedback process into high gear. As a result, the path of a general downward trend in summer ice cover would be interrupted by sudden plunges spanning a decade or

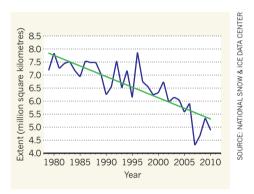


Figure 1 | September sea-ice extent in the Arctic for 1979–2010. Satellite data (blue) show that September sea-ice extent is decreasing in the Arctic, and that, relative to the 1979–2000 mean, the rate of decline is about 12% per decade; green line represents the best fit to the satellite data. Tietsche and colleagues' simulations⁴ indicate that the extent can recover from artificially imposed ice-free summer conditions within two years.

more, hastening the slide to a seasonally icefree ocean. The concern was fuelled in 2007 by a record September minimum in sea-ice extent — 23% below the previous record set in 2005 — driven by a combination of several decades of sea-ice thinning and a highly unusual summer weather pattern.

Specifically, a combination of especially high atmospheric pressure over the Beaufort Sea, north of Alaska, in conjunction with low pressure over Siberia, drew warm air into the Arctic, hastening melt, while at the same time helping to transport some of the remaining thick ice out of the Arctic into the North Atlantic Ocean⁶. Was this the kick initiating a rapid, irreversible decline in ice extent? Although there was widespread speculation over this



50 Years Ago

The Birds of Borneo. By Bertram E. Smythies — This is a very unusual bird book. The main body of the work (about 460 pages) consists of a detailed systematic account of all the 549 species of birds that have been found in Borneo ... But it is the hundred pages that precede this excellent treatise that put this book in a class apart ... Lord Medway's chapter gives a fascinating account of the cave swiftlets, the saliva-built nests of which are the edible birds' nests of commerce, and which echo-navigate in the darkness of the caves where millions congregate to breed. [Mr. Tom] Harrison remarks that Governments "by some complicated zoo-geology, claim the guano as a mineral and allow extraction (for fertilizer) under licence. Thus what comes out of the swiftlets' mouth as spit is succinctly dissociated from what comes out of the other end".

From Nature 4 March 1961

100 Years Ago

In the Prussian Diet of February 18, Prof. Kirchner ... is reported to have said that, during the last few weeks, three cases of plague had occurred in London, the infection being conveyed by ship-rats. This statement has been officially denied ... With regard to rat infection, three rats which had probably escaped from a ship were examined at the London Docks in November last, and two of them were found to be suffering from plague, but at present there is no evidence of the existence of a plague epizootic among rats in the London Docks area. The destruction of rats ... is still carried out at the London Docks, and careful precautions are being taken to prevent rats in ships from infected ports from escaping ashore, and possibly initiating an epizootic among the shore rats. From Nature 2 March 1911

possibility, the Septembers of 2008 and 2009 instead saw successively higher sea-ice extent.

One interpretation of this apparent shortterm recovery is that the spring ice cover needs further thinning for a tipping point to occur⁸. An alternative is that there is no true tipping point. Tietsche et al.4 do not argue against the mainstream view that a seasonally ice-free Arctic Ocean is inevitable if greenhouse-gas concentrations continue to rise. The issue is how we get there - with or without a tipping point.

Tietsche and colleagues performed a series of reference simulation runs with a global climate model driven by the middle-of-the-road Intergovernmental Panel on Climate Change A1B greenhouse-gas emissions scenario for the twenty-first century. In these simulations, the September ice cover typically disappears by the year 2070 and beyond. The authors then performed perturbation runs, whereby every 20 years they artificially removed the entire sea-ice cover on 1 July. Instead of maintaining ice-free conditions, ice extent in September recovered to values typical of the reference runs within a couple of years, even in the later parts of the century.

The crux is winter. Initially, with ice-free summers, the ocean picks up a great deal of extra heat, delaying autumn ice growth. If there was a tipping point, this summer heat gain would lead to ice cover the following spring being thin enough to completely melt out over the following summer. Instead, so much ocean heat is lost during the darkness of the polar winter that enough ice grows to survive the next summer's melt.

Although the paper by Tietsche and colleagues4 brings a more optimistic view of the Arctic's future, the troubling interpretation from other recent modelling studies is that periods of rapid twenty-first-century sea-ice loss, hastening the evolution to ice-free summers, don't need to be preceded by a critical threshold of sea-ice thickness, greenhouse-gas concentration or combination of factors that lie at the heart of the tipping-point argument⁵. As we move through the coming decades and the climate warms, the ice cover will simply become more vulnerable to triggers that cause rapid loss events. So although the tippingpoint argument can perhaps be laid to rest, we may nevertheless be looking at ice-free summers only a few decades from now.

Mark C. Serreze is at the Cooperative Institute for Research in Environmental Sciences, National Snow and Ice Data Center, University of Colorado at Boulder, Boulder, Colorado 80309-0449, USA. e-mail: serreze@nsidc.org

- 1. Durner, G. M. et al. Ecol. Monogr. 79, 25-58 (2009).
- Budikova, D. Glob. Planet. Change 68, 149-163 (2009).
- www.pame.is/amsa/amsa-2009-report
- 4. Tietsche, S., Notz, D., Jungclaus, J. H. & Marotzke, J. Geophys. Res. Lett. doi:10.1029/2010GL045698
- Holland, M. M., Bitz, C. M., Tremblay, L.-B. & Bailey D. A. Am. Geophys. Union Geophys. Monogr. Ser. 180, 133-150 (2008).
- 6. Stroeve, J. et al. EOS Trans. Am. Geophys. Union doi:10.1029/2008E0020001 (2008).
- Holland, M. M., Bitz, C. M. & Tremblay, B. Geophys. Res. Lett. doi:10.1029/2006GL028024 (2006).
- Serreze, M. C. & Stroeve, J. C. Nature Rep. Clim. Change 2, 142-143 (2008).

MOLECULAR BIOLOGY

The expanding arena of DNA repair

The protein Sae2 mediates the repair of double-strand breaks in DNA. It emerges that Sae2 activity is controlled by both its modification with acetyl groups and its degradation by the process of autophagy. SEE ARTICLE P.74

CATHERINE J. POTENSKI & HANNAH L. KLEIN

ells use myriad ways to regulate the complex processes involved in their I function. To control protein activity and stability, for example, an oft-used mechanism is post-translational modification of the protein. On page 74 of this issue, Robert et al. report one such modification that links the seemingly unrelated processes of DNA-damage repair and autophagy. Their observations simultaneously highlight the depth of cellular ingenuity and the immense interconnectedness of biological pathways.

The authors began by examining the effect of a specific post-translational modification — protein acetylation, in which an acetyl group is added to a protein. They used the drug valproic acid (VPA) to inhibit histone deacetylase (HDAC) enzymes, thereby causing hyperacetylation of histone proteins and reduced HDAC activity². This treatment had no effect on cells, but after exposure to various DNA-damaging agents, the apparently normal VPA-treated cells were unable to activate the typical response to DNA damage.

Robert *et al.* present several lines of evidence to explain the failure of the DNA-damage response, including breakdown of the cell-cycle checkpoint mechanism. Although malfunction of cell-cycle checkpoints could be due to mishaps at any step in DNA repair, it is a strong indicator of a failure to properly process DNA double-strand breaks (DSBs). Indeed, the authors show that VPA-treated cells could not correctly repair such breaks.

Several proteins are responsible for repairing DSBs³, among them Sae2, Exo1, the MRX/N complex, Sgs1 (BLM) and Dna2. Robert *et al.* report a significant reduction in the association of Sae2 and Exo1 with broken DNA ends in VPA-treated cells. More intriguingly, the cellular levels of the two proteins were severely reduced in these cells, which would explain the failure of DSB repair. But why would VPA treatment affect Sae2 and Exo1 levels?

An analysis⁴ of all cellular proteins modified by acetylation of their lysine amino-acid residues identified some that mediate DNA repair, including Exo1. Although Sae2 was not among the acetylated proteins identified⁴, the study did point to the possibility that Sae2 is acetylated, and that its acetylated version is unstable. Deacetylation by HDACs would convert Sae2 to a stable form, but VPA treatment inhibits this.

Indeed, Robert and co-workers¹ also find that Sae2 can be acetylated and that two HDACs — Hda1 and Rpd3, which have similar functions — promote its deacetylation. What's more, depletion of these two HDACs had similar effects to VPA treatment, leading to negligible Sae2 levels, heightened DNA-damage sensitivity and failure to activate cell-cycle checkpoints. Consistent with these observations, a recent study⁵ showed that the lysine deacetylase enzyme SIRT6 positively regulates the repair of DSBs through deacetylation of CtIP, the mammalian form of Sae2.

But this is only half the story. Why would inhibition of deacetylation (in other words, acetylation) destabilize Sae2? Considering the consequences of treating mammalian cells with VPA and other HDAC inhibitors^{2,6,7}, Robert and colleagues propose — and provide evidence in yeast — that VPA stimulates autophagy, a degradation process that is normally linked to the cellular response to starvation and to organelle turnover. The authors further show that mutant cells defective in autophagy could overcome the inability of HDAC mutants to repair DSBs, presumably by stabilizing Sae2. They also saw the same spectrum of traits in a histone acetyltransferase mutant, which could not acetylate Sae2.

These findings are particularly noteworthy because they bring autophagy into the DNA-repair network. Autophagy can be triggered by inhibition of the enzyme TOR1 kinase⁸. Indeed, Robert *et al.* find that inhibiting this enzyme with the drug rapamycin induces

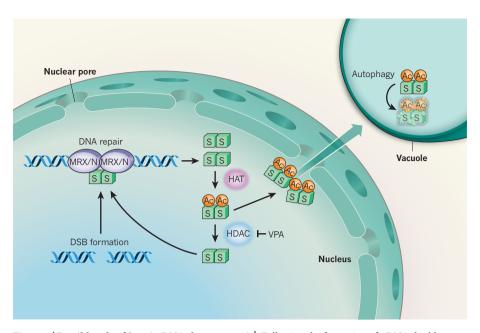


Figure 1 | Possible role of Sae2 in DNA-damage repair¹. Following the formation of a DNA double-strand break (DSB), the damaged DNA is moved to the nuclear pore to protect the bulk undamaged DNA from unnecessary processing by the DNA-repair machinery. In its deacetylated form, one such mediator, Sae2 (S), together with the MRX/N complex, binds to the DNA ends to aid the initiation of the end-resection step of repair. Subsequently, Sae2 might be released as a macromolecular complex and acetylated by histone acetylases (HATs), which promote its expulsion through the nuclear pore and ultimately its degradation by the process of autophagy. Valproic acid (VPA) inhibits Sae2 deacetylation by blocking the activity of histone deacetylase (HDAC) enzymes.

autophagy and results in destabilization of Sae2.

From their results, the authors propose the following model (Fig. 1). Severely damaged DNA — such as DSBs that are difficult to repair — might become sequestered at the nuclear pores⁹, possibly to keep the cell's repair enzymes away from the bulk DNA that, although undamaged, could contain structures such as DNA nicks and gaps as a normal consequence of DNA replication. If the repair enzymes were close by, they could mistake these structures for damage and 'repair' them, leading to mutations and rearrangements.

In the case of Sae2, for example, although HDACs maintain it in an active state for repairing damaged DNA, at some point it will become acetylated and be expelled through the nuclear pore to the vacuole — the cellular site of autophagic degradation in yeast. Thus, a potentially dangerous enzyme is eliminated, preventing it from unnecessarily repairing replication-associated structures such as stalled replication forks. It remains unclear whether Sae2 is targeted for degradation after the completion of DNA repair and whether a checkpoint signal is involved.

Many further questions remain. Do other post-translational modifications, such as ubiquitination, phosphorylation and SUMOylation, regulate Sae2? Because of its association with autophagy, ubiquitination is most likely to play a part. But how does this relate to acetylation?

Also, several proteins that mediate the

DNA-damage response — including Cdk1, Ku, MRN, Blm and Rfa1 — are acetylated^{1,4}. Which of these are controlled through acetylation and autophagic degradation? Are nuclear pores an essential component of acetylation-promoted autophagy of DNA-repair complexes? Does a similar regulatory process occur during meiotic cell division, when DSBs abound and their repair is carefully choreographed? Is there an intranuclear cycle of acetylation—deacetylation, or is all acetylated Sae2 targeted for degradation?

These questions must be tackled before researchers can embark on exploring how this newly identified layer of DNA-damage regulation can be exploited to find targets for cancer therapy — a setting in which cells experience more DNA damage than usual.

Catherine J. Potenski and **Hannah L. Klein** are in the Department of Biochemistry, New York University School of Medicine, New York, New York 10016, USA.

e-mail: hannah.klein@nyumc.org

- 1. Robert, T. et al. Nature 471, 74-79 (2011).
- Göttlicher, M. et al. EMBO J. 20, 6969–6978 (2001).
- Mimitou, E. P. & Symington, L. S. DNA Repair doi:10.1016/j.dnarep.2010.12.004 (2011)
- 4. Choudhary, C. et al. Science 325, 834–840 (2009).
- Kaidi, A., Weinert, B. T., Choudhary, C. & Jackson, S. P. Science 329, 1348–1353 (2010).
- Shao, Y., Gao, Z., Marks, P. A. & Jiang, X. Proc. Natl Acad. Sci. USA 101, 18030–18035 (2004).
- Fu, J., Shao, C.-J., Chen, F.-R., Ng, H.-K. & Chen, Z.-P. Neuro-Oncology 12, 328–340 (2010).
- 8. Degenhardt, K. et al. Cancer Cell 10, 51–64 (2006).
- 9. Nagai, S. et al. Science 322, 597-602 (2008).



Has the Earth's sixth mass extinction already arrived?

Anthony D. Barnosky^{1,2,3}, Nicholas Matzke¹, Susumu Tomiya^{1,2,3}, Guinevere O. U. Wogan^{1,3}, Brian Swartz^{1,2}, Tiago B. Quental^{1,2}†, Charles Marshall^{1,2}, Jenny L. McGuire^{1,2,3}†, Emily L. Lindsey^{1,2}, Kaitlin C. Maguire^{1,2}, Ben Mersey^{1,4} & Elizabeth A. Ferrer^{1,2}

Palaeontologists characterize mass extinctions as times when the Earth loses more than three-quarters of its species in a geologically short interval, as has happened only five times in the past 540 million years or so. Biologists now suggest that a sixth mass extinction may be under way, given the known species losses over the past few centuries and millennia. Here we review how differences between fossil and modern data and the addition of recently available palaeontological information influence our understanding of the current extinction crisis. Our results confirm that current extinction rates are higher than would be expected from the fossil record, highlighting the need for effective conservation measures.

f the four billion species estimated to have evolved on the Earth over the last 3.5 billion years, some 99% are gone¹. That shows how very common extinction is, but normally it is balanced by speciation. The balance wavers such that at several times in life's history extinction rates appear somewhat elevated, but only five times qualify for 'mass extinction' status: near the end of the Ordovician, Devonian, Permian, Triassic and Cretaceous Periods².³. These are the 'Big Five' mass extinctions (two are technically 'mass depletions')⁴. Different causes are thought to have precipitated the extinctions (Table 1), and the extent of each extinction above the background level varies depending on analytical technique⁴.⁵, but they all stand out in having extinction rates spiking higher than in any other geological interval of the last \sim 540 million years³ and exhibiting a loss of over 75% of estimated species².

Increasingly, scientists are recognizing modern extinctions of species^{6,7} and populations^{8,9}. Documented numbers are likely to be serious underestimates, because most species have not yet been formally described^{10,11}. Such observations suggest that humans are now causing the sixth mass extinction^{10,12–17}, through co-opting resources, fragmenting habitats,

introducing non-native species, spreading pathogens, killing species directly, and changing global climate^{10,12–20}. If so, recovery of biodiversity will not occur on any timeframe meaningful to people: evolution of new species typically takes at least hundreds of thousands of years^{21,22}, and recovery from mass extinction episodes probably occurs on timescales encompassing millions of years^{5,23}.

Although there are many definitions of mass extinction and gradations of extinction intensity^{4,5}, here we take a conservative approach to assessing the seriousness of the ongoing extinction crisis, by setting a high bar for recognizing mass extinction, that is, the extreme diversity loss that characterized the very unusual Big Five (Table 1). We find that the Earth could reach that extreme within just a few centuries if current threats to many species are not alleviated.

Data disparities

Only certain kinds of taxa (primarily those with fossilizable hard parts) and a restricted subset of the Earth's biomes (generally in temperate latitudes) have data sufficient for direct fossil-to-modern comparisons

Table 1 | The 'Big Five' mass extinction events

The Ordovician event⁶⁴⁻⁶⁶ ended ~443 Myr ago; within 3.3 to
1.9 Myr 57% of genera were lost, an estimated 86% of species.

The Devonian event⁶⁴⁻⁶⁶ ended ~443 Myr ago; within 3.3 to
1.9 Myr 57% of genera were lost, an estimated 86% of species.

The Devonian event^{4,64,67-70} ended ~359 Myr ago; within 29 to
2 Myr 35% of genera were lost, an estimated 75% of species.

Global cooling (followed by global warming), possibly tied to the diversification of land plants, with associated weathering, paedogenesis, and the drawdown of global CO₂. Evidence for widespread deep-water anoxia and the spread of anoxic waters by transgressions. Timing and importance of

bolide impacts still debated.

The Permian event $^{54,71-73}$ ended $\sim\!251$ Myr ago; within 2.8 Myr to 160 Kyr 56% of genera were lost, an estimated

The Triassic event^{74,75} ended \sim 200 Myr ago; within 8.3 Myr to 600 Kyr 47% of genera were lost, an estimated 80% of species.

The Cretaceous event $^{58-60.76-79}$ ended $\sim\!65$ Myr ago; within 2.5 Myr to less than a year 40% of genera were lost, an estimated 76% of species.

Siberian volcanism. Global warming. Spread of deep marine anoxic waters. Elevated $\rm H_2S$ and $\rm CO_2$ concentrations in both marine and terrestrial realms. Ocean acidification. Evidence for a bolide impact still debated.

Activity in the Central Atlantic Magmatic Province (CAMP) thought to have elevated atmospheric CO_2 levels, which increased global temperatures and led to a calcification crisis in the world oceans.

A bolide impact in the Yucatán is thought to have led to a global cataclysm and caused rapid cooling. Preceding the impact, biota may have been declining owing to a variety of causes: Deccan volcanism contemporaneous with global warming; tectonic uplift altering biogeography and accelerating erosion, potentially contributing to ocean eutrophication and anoxic episodes. CO₂ spike just before extinction, drop during extinction.

Myr, million years. Kyr, thousand years.

96% of species.

¹Department of Integrative Biology, University of California, Berkeley, California 94720, USA. ²University of California Museum of Paleontology, California, USA. ³University of California Museum of Vertebrate Zoology, California, USA. ⁴Human Evolution Research Center, California, USA. †Present addresses: Departamento de Ecologia, Universidade de São Paulo (USP), São Paulo, Brazil (T.B.Q.); National Evolutionary Synthesis Center, 2024 W. Main Street, Suite A200, Durham, North Carolina 27705, USA (J.L.M.).

BOX 1

Severe data comparison problems

Geography

The fossil record is very patchy, sparsest in upland environments and tropics, but modern global distributions are known for many species.

A possible comparative technique could be to examine regions or biomes where both fossil and modern data exist—such as the near-shore marine realm including coral reefs and terrestrial depositional lowlands (river valleys, coastlines, and lake basins). Currently available databases⁶ could be used to identify modern taxa with geographic ranges indicating low fossilization potential and then extract them from the current-extinction equation.

Taxa available for study

The fossil record usually includes only species that possess identifiable anatomical hard parts that fossilize well. Theoretically all living species could be studied, but in practice extinction analyses often rely on the small subset of species evaluated by the IUCN. Evaluation following IUCN procedures³⁴ places species in one of the following categories: extinct (EX), extinct in the wild (EW), critically endangered (CR), endangered (EN), vulnerable (VU), near threatened (NT), least concern (LC), or data deficient (DD, information insufficient to reliably determine extinction risk). Species in the EX and EW categories are typically counted as functionally extinct. Those in the CR plus EN plus VU categories are counted as 'threatened'. Assignment to CR, EN or VU is based on how high the risk of extinction is determined to be using five criteria³⁴ (roughly, CR probability of extinction exceeds 0.50 in ten years or three generations; EN probability of extinction exceeds 0.20 in 20 years or five generations; VU probability of extinction exceeds 0.10 over a century²⁴).

A possible comparative technique could be to use taxa best known in both fossil and modern records: near-shore marine species with shells, lowland terrestrial vertebrates (especially mammals), and some plants. This would require improved assessments of modern bivalves and gastropods. Statistical techniques could be used to clarify how a subsample of well-assessed taxa extrapolates to undersampled and/or poorly assessed taxa²⁵.

Taxonomy

Analyses of fossils are often done at the level of genus rather than species. When species are identified they are usually based on a morphological species concept. This can result in lumping species together that are distinct, or, if incomplete fossil material is used, over-splitting species. For modern taxa, analyses are usually done at the level of species, often using a phylogenetic species concept, which probably increases species counts relative to morphospecies.

A possible comparative technique would be to aggregate modern phylogenetic species into morphospecies or genera before comparing with the fossil record.

Assessing extinction

Fossil extinction is recorded when a taxon permanently disappears from the fossil record and underestimates the actual number of extinctions (and number of species) because most taxa have no fossil record. The actual time of extinction almost always postdates the last fossil occurrence. Modern extinction is recorded when no further individuals of a species are sighted after appropriate efforts. In the past few decades designation as 'extinct' usually follows IUCN criteria, which are conservative and likely to underestimate functionally extinct species³⁴. Modern extinction is also underestimated because many species are unevaluated or undescribed.

A possible comparative technique could be to standardize extinction counts by number of species known per time interval of interest (proportional extinction). However, fossil data demonstrate that background rates can vary widely from one taxon to the next^{35,86,87}, so fossil-to-modern extinction rate comparisons are most reliably done on a taxon-by-taxon basis, using well-known extant clades that also have a good fossil record.

Time

In the fossil record sparse samples of species are discontinuously distributed through vast time spans, from 10^3 to 10^8 years. In modern times we have relatively dense samples of species over very short time spans of years, decades and centuries. Holocene fossils are becoming increasingly available and valuable in linking the present with the past^{48,90}.

A possible comparative technique would be to scale proportional extinction relative to the time interval over which extinction is measured.

(Box 1). Fossils are widely acknowledged to be a biased and incomplete sample of past species, but modern data also have important biases that, if not accounted for, can influence global extinction estimates. Only a tiny fraction (<2.7%) of the approximately 1.9 million named, extant species have been formally evaluated for extinction status by the International Union for Conservation of Nature (IUCN). These IUCN compilations are the best available, but evaluated species represent just a few twigs plucked from the enormous number of branches that compose the tree of life. Even for clades recorded as 100% evaluated, many species still fall into the Data Deficient (DD) category²⁴. Also relevant is that not all of the partially evaluated clades have had their species sampled in the same way: some are randomly subsampled²⁵, and others are evaluated as opportunity arises or because threats seem apparent. Despite the limitations of both the fossil and modern records, by working around the diverse data biases it is possible to avoid errors in extrapolating from what we do know to inferring global patterns. Our goal here is to highlight some promising approaches (Table 2).

Defining mass extinctions relative to the Big Five

Extinction involves both rate and magnitude, which are distinct but intimately linked metrics²⁶. Rate is essentially the number of extinctions divided by the time over which the extinctions occurred. One can also

derive from this a proportional rate—the fraction of species that have gone extinct per unit time. Magnitude is the percentage of species that have gone extinct. Mass extinctions were originally diagnosed by rate: the pace of extinction appeared to become significantly faster than background extinction³. Recent studies suggest that the Devonian and Triassic events resulted more from a decrease in origination rates than an increase in extinction rates^{4,5}. Either way, the standing crop of the Earth's species fell by an estimated 75% or more². Thus, mass extinction, in the conservative palaeontological sense, is when extinction rates accelerate relative to origination rates such that over 75% of species disappear within a geologically short interval—typically less than 2 million years, in some cases much less (see Table 1). Therefore, to document where the current extinction episode lies on the mass extinction scale defined by the Big Five requires us to know both whether current extinction rates are above background rates (and if so, how far above) and how closely historic and projected biodiversity losses approach 75% of the Earth's species.

Background rate comparisons

Landmark studies^{12,14-17} that highlighted a modern extinction crisis estimated current rates of extinction to be orders of magnitude higher than the background rate (Table 2). A useful and widely applied metric

Table 2 | Methods of comparing present and past extinctions

General method	Variations and representative studies	References
Compare currently measured extinction rates to background rates assessed from fossil record	E/MSY*‡ Comparative species duration (estimates species durations to derive an estimate of extinction rate)*‡ Fuzzy Math*‡	7, 10, 15, 27, 62 14 44, 80
	Interval-rate standardization (empirical derivation of relationship between rate and interval length over which extinction is measured provides context for interpreting short-term rates);	This paper
Use various modelling techniques, including species-area relationships, to assess loss of species	Compare rate of expected near-term future losses to estimated background extinction rates*†‡	
	Assess magnitude of past species losses†‡ Predict magnitude of future losses. Ref. 7 explores several models and provides a range of possible outcomes using different impact storylines†‡	42, 45 7, 14, 15, 27, 36, 62, 81–84
Compare currently measured extinction rates to mass-extinction rates	Use geological data and hypothetical scenarios to bracket the range of rates that could have produced past mass extinctions, and compare with current extinction rates (assumes Big Five mass extinctions were sudden, occurring within 500 years, producing a 'worst-case scenario' for high rates, but with the possible exception of the Cretaceous event, it is unlikely that any of the Big Five were this fast):	This paper
Assess extinction in context of long-term clade dynamics	Map projected extinction trajectories onto long-term diversification/ extinction trends in well-studied clades‡	This paper
Assess percentage loss of species	Use IUCN lists to assess magnitude or rate of actual and potential species losses in well-studied taxa‡	This paper and refs 6, 7, 10, 14, 15, 20, 36 and 62
Use molecular phylogenies to estimate extinction rate	Calculate background extinction rates from time-corrected molecular phylogenies of extant species, and compare to modern rates	85

Fuzzy Math attempts to account for different biases in fossil and modern samples and uses empirically based fossil background extinction rates as a standard for comparison: 0.25 species per million years for marine invertebrates, determined from the 'kill-curve' method's, and 0.21 species's to 0.46 species' per million years for North American mammals, determined from applying maximum-likelihood techniques. The molecular phylogenies method assumes that diversification rates are constant through time and can be partitioned into originations and extinctions without evidence from the fossil record. Recent work has demonstrated that disentanglement of diversification from extinction rates by this method is difficult, particularly in the absence of a fossil record, and that extinction rates estimated from molecular phylogenies of extant organisms are highly unreliable when diversification rates vary among lineages through time^{46,88}.

has been E/MSY (extinctions per million species-years, as defined in refs 15 and 27). In this approach, background rates are estimated from fossil extinctions that took place in million-year-or-more time bins. For current rates, the proportion of species extinct in a comparatively very short time (one to a few centuries) is extrapolated to predict what the rate would be over a million years. However, both theory and empirical data indicate that extinction rates vary markedly depending on the length of time over which they are measured^{28,29}. Extrapolating a rate computed over a short time, therefore, will probably yield a rate that is either much faster or much slower than the average million-year rate, so current rates that seem to be elevated need to be interpreted in this light.

Only recently has it become possible to do this by using palaeontology databases^{30,31} combined with lists of recently extinct species. The most complete data set of this kind is for mammals, which verifies the efficacy of E/MSY by setting short-interval and long-interval rates in a comparative context (Fig. 1). A data gap remains between about one million and about 50 thousand years because it is not yet possible to date extinctions in that time range with adequate precision. Nevertheless, the overall pattern is as expected: the maximum E/MSY and its variance increase as measurement intervals become shorter. The highest rates are rare but low rates are common; in fact, at time intervals of less than a thousand years, the most common E/MSY is 0. Three conclusions emerge. (1) The maximum observed rates since a thousand years ago (E/MSY \approx 24 in 1,000-year bins to E/MSY \approx 693 in 1-year bins) are clearly far above the average fossil rate (about E/MSY \approx 1.8), and even above those of the widely recognized late-Pleistocene megafaunal diversity crash^{32,33} (maximum E/MSY ≈ 9, red data points in Fig. 1). (2) Recent average rates are also too high compared to pre-anthropogenic averages: E/MSY increases to over 5 (and rises to 23) in less-than-50-year time bins. (3) In the scenario where currently 'threatened' species³⁴ would ultimately go extinct even in as much as a thousand years, the resulting rates would far exceed any reasonable estimation of the upper boundary for variation related to interval length. The same applies if the extinction scenario is restricted to only 'critically endangered' species³⁴. This does not imply that we consider all species in these categories to be inevitably destined for extinction—simply that in a worst-case scenario where that occurred, the extinction rate for mammals would far exceed normal background rates. Because our computational method maximizes the fossil background rates and minimizes the current rates (see Fig. 1 caption), our observation that modern rates are elevated is likely to be particularly robust. Moreover, for reasons argued by others²⁷, the modern rates we computed probably seriously underestimate current E/MSY values.

Another approach is simply to ask whether it is likely that extinction rates could have been as high in many past 500-year intervals as they have been in the most recent 500 years. Where adequate data exist, as is the case for our mammal example, the answer is clearly no. The mean per-million-year fossil rate for mammals we determined (Fig. 1) is about 1.8 E/MSY. To maintain that million-year average, there could be no more than 6.3% of 500-year bins per million years (126 out of a possible 2,000) with an extinction rate as high as that observed over the past 500 years (80 extinct of 5,570 species living in 500 years). Million-year extinction rates calculated by others, using different techniques, are slower: 0.4 extinctions per lineage per million years (a lineage in this context is roughly equivalent to a species)35. To maintain that slower million-year average, there could be no more than 1.4% (28 intervals) of the 500-year intervals per million years having an extinction rate as high as the current 500-year rate. Rates computed for shorter time intervals would be even less likely to fall within background levels, for reasons noted by ref. 27.

Magnitude

Comparisons of percentage loss of species in historical times^{6,36} to the percentage loss that characterized each of the Big Five (Fig. 2) need to be refined by compensating for many differences between the modern and the fossil records^{2,37–39}. Seldom taken into account is the effect of using different species concepts (Box 1), which potentially inflates the numbers of modern species relative to fossil species^{39,40}. A second, related caveat is that most assessments of fossil diversity are at the level of genus, not species^{2,3,37,38,41}. Fossil species estimates are frequently obtained by calculating the species-to-genus ratio determined for well-known groups, then extrapolating that ratio to groups for which only genus-level counts exist. The over-75% benchmark for mass extinction is obtained in this way².

^{*}Comparison of modern short-term rates with fossil long-term rates indicate highly elevated modern rates, but does not take into account interval-rate effect.

[†] Assumes that the relationship between number and kind of species lost in study area can be scaled up to make global projections

[‡] Assumes that conclusions from well-studied taxa illustrate general principles

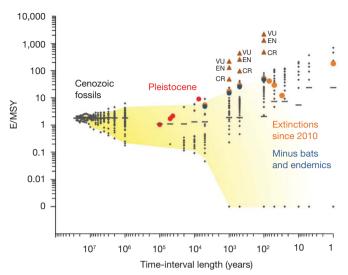


Figure 1 | Relationship between extinction rates and the time interval over which the rates were calculated, for mammals. Each small grey datum point represents the E/MSY (extinction per million species-years) calculated from taxon durations recorded in the Paleobiology Database³⁰ (million-year-ormore time bins) or from lists of extant, recently extinct, and Pleistocene species compiled from the literature (100,000-year-and-less time bins)^{6,32,33,89–97}. More than 4,600 data points are plotted and cluster on top of each other. Yellow shading encompasses the 'normal' (non-anthropogenic) range of variance in extinction rate that would be expected given different measurement intervals: for more than 100,000 years, it is the same as the 95% confidence interval, but the fading to the right indicates that the upper boundary of 'normal' variance becomes uncertain at short time intervals. The short horizontal lines indicate the empirically determined mean E/MSY for each time bin. Large coloured dots represent the calculated extinction rates since 2010. Red, the end-Pleistocene extinction event. Orange, documented historical extinctions averaged (from right to left) over the last 1, 30, 50, 70, 100, 500, 1,000 and 5,000 years. Blue, attempts to enhance comparability of modern with fossil data by adjusting for extinctions of species with very low fossilization potential (such as those with very small geographic ranges and bats). For these calculations, 'extinct' and 'extinct in the wild' species that had geographic ranges less than 500 km² as recorded by the IUCN⁶, all species restricted to islands of less than 105 km², and bats were excluded from the counts (under-representation of bats as fossils is indicated by their composing only about 2.5% of the fossil species count, versus around 20% of the modern species count³⁰). Brown triangles represent the projections of rates that would result if 'threatened' mammals go extinct within 100, 500 or 1,000 years. The lowest triangle (of each vertical set) indicates the rate if only 'critically endangered' species were to go extinct (CR), the middle triangle indicates the rate if 'critically endangered' + 'endangered' species were to go extinct (EN), and the highest triangle indicates the rate if 'critically endangered' + 'endangered' + 'vulnerable' species were to go extinct (VU). To produce Fig. 1 we first determined the last-occurrence records of Cenozoic mammals from the Paleobiology Database³⁰, and the last occurrences of Pleistocene and Holocene mammals from refs 6, 32, 33 and 89-97. We then used R-scripts (written by N.M.) to compute total diversity, number of extinctions, proportional extinction, and E/MSY (and its mean) for time-bins of varying duration. Cenozoic time bins ranged from 25 million to a million years. Pleistocene time bins ranged from 100,000 to 5,000 years, and Holocene time bins from 5,000 years to a year. For Cenozoic data, the mean E/MSY was computed using the average within-bin standing diversity, which was calculated by counting all taxa that cross each 100,000-year boundary within a million-year bin, then averaging those boundary-crossing counts to compute standing diversity for the entire million-year-and-over bin. For modern data, the mean was computed using the total standing diversity in each bin (extinct plus surviving taxa). This method may overestimate the fossil mean extinction rate and underestimate the modern means, so it is a conservative comparison in terms of assessing whether modern means are higher. The Cenozoic data are for North America and the Pleistocene and Holocene data are for global extinction; adequate global Cenozoic data are unavailable. There is no apparent reason to suspect that the North American average would differ from the global average at the million-year timescale.

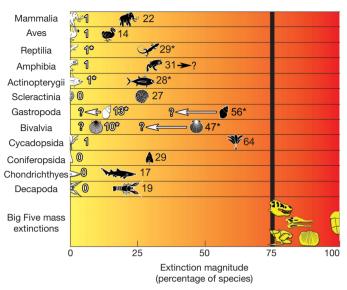


Figure 2 | Extinction magnitudes of IUCN-assessed taxa⁶ in comparison to the 75% mass-extinction benchmark. Numbers next to each icon indicate percentage of species. White icons indicate species 'extinct' and 'extinct in the wild' over the past 500 years. Black icons add currently 'threatened' species to those already 'extinct' or 'extinct in the wild'; the amphibian percentage may be as high as 43% (ref. 19). Yellow icons indicate the Big Five species losses: Cretaceous + Devonian, Triassic, Ordovician and Permian (from left to right). Asterisks indicate taxa for which very few species (less than 3% for gastropods and bivalves) have been assessed; white arrows show where extinction percentages are probably inflated (because species perceived to be in peril are often assessed first). The number of species known or assessed for each of the groups listed is: Mammalia 5,490/5,490; Aves (birds) 10,027/10,027; Reptilia 8,855/1,677; Amphibia 6,285/6,285, Actinopterygii 24,000/5,826, Scleractinia (corals) 837/837; Gastropoda 85,000/2,319; Bivalvia 30,000/310, Cycadopsida 307/307; Coniferopsida 618/618; Chondrichthyes 1,044/1,044; and Decapoda 1,867/1,867.

Potentially valuable comparisons of extinction magnitude could come from assessing modern taxonomic groups that are also known from exceptionally good fossil records. The best fossil records are for near-shore marine invertebrates like gastropods, bivalves and corals, and temperate terrestrial mammals, with good information also available for Holocene Pacific Island birds^{2,33,35,42–44}. However, better knowledge of understudied modern taxa is critically important for developing common metrics for modern and fossil groups. For example, some 49% of bivalves went extinct during the end-Cretaceous event⁴³, but only 1% of today's species have even been assessed⁶, making meaningful comparison difficult. A similar problem prevails for gastropods, exacerbated because most modern assessments are on terrestrial species, and most fossil data come from marine species. Given the daunting challenge of assessing extinction risk in every living species, statistical approaches aimed at understanding what well sampled taxa tell us about extinction risks in poorly sampled taxa are critically important²⁵.

For a very few groups, modern assessments are close to adequate. Scleractinian corals, amphibians, birds and mammals have all known species assessed⁶ (Fig. 2), although species counts remain a moving target²⁷. In these groups, even though the percentage of species extinct in historic time is low (zero to 1%), 20–43% of their species and many more of their populations are threatened (Fig. 2). Those numbers suggest that we have not yet seen the sixth mass extinction, but that we would jump from one-quarter to halfway towards it if 'threatened' species disappear.

Given that many clades are undersampled or unevenly sampled, magnitude estimates that rely on theoretical predictions rather than empirical data become important. Often species-area relationships or allied modelling techniques are used to relate species losses to habitatarea losses (Table 2). These techniques suggest that future species extinctions will be around 21–52%, similar to the magnitudes expressed

in Fig. 2, although derived quite differently. Such models may be sensitive to the particular geographic area, taxa and species-area relationship that is employed, and have usually used only modern data. However, fossil-to-modern comparisons using species-area methods are now becoming possible as online palaeontological databases grow^{30,31,45}. An additional, new approach models how much extinction can be expected under varying scenarios of human impact⁷. It suggests a broader range of possible future extinction magnitudes than previous studies, although all scenarios result in additional biodiversity decline in the twenty-first century.

Combined rate-magnitude comparisons

Because rate and magnitude are so intimately linked, a critical question is whether current rates would produce Big-Five-magnitude mass extinctions in the same amount of geological time that we think most Big Five extinctions spanned (Table 1). The answer is yes (Fig. 3). Current extinction rates for mammals, amphibians, birds, and reptiles (Fig. 3, light yellow dots on the left), if calculated over the last 500 years (a conservatively slow rate²⁷) are faster than (birds, mammals, amphibians, which have 100% of species assessed) or as fast as (reptiles, uncertain because only 19% of species are assessed) all rates that would have produced the Big Five extinctions over hundreds of thousands or millions of years (Fig. 3, vertical lines).

Would rates calculated for historical and near-time prehistoric extinctions result in Big-Five-magnitude extinction in the foreseeable future—less than a few centuries? Again, taking the 500-year rate as a useful basis of comparison, two different hypothetical approaches are possible. The first assumes that the Big Five extinctions took place suddenly and asks what rates would have produced their estimated species losses within 500 years (Fig. 3, coloured dots on the right).

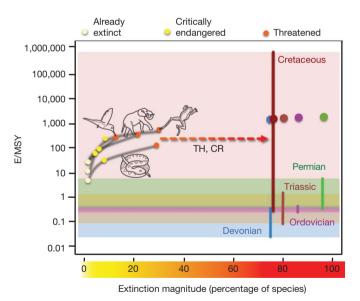


Figure 3 | Extinction rate versus extinction magnitude. Vertical lines on the right illustrate the range of mass extinction rates (E/MSY) that would produce the Big Five extinction magnitudes, as bracketed by the best available data from the geological record. The correspondingly coloured dots indicate what the extinction rate would have been if the extinctions had happened (hypothetically) over only 500 years. On the left, dots connected by lines indicate the rate as computed for the past 500 years for vertebrates: light yellow, species already extinct; dark yellow, hypothetical extinction of 'critically endangered' species; orange, hypothetical extinction of all 'threatened' species. TH: if all 'threatened' species became extinct in 100 years, and that rate of extinction remained constant, the time to 75% species loss—that is, the sixth mass extinction—would be ∼240 to 540 years for those vertebrates shown here that have been fully assessed (all but reptiles). CR: similarly, if all 'critically endangered' species became extinct in 100 years, the time to 75% species loss would be ∼890 to 2,270 years for these fully assessed terrestrial vertebrates.

(We emphasize that this is a hypothetical scenario and that we are not arguing that all mass extinctions were sudden.) In that scenario, the rates for contemporary extinctions (Fig. 3, light yellow dots on the left) are slower than the rates that would have produced each of the Big Five extinctions in 500 years. However, rates that consider 'threatened' species as inevitably extinct (Fig. 3, orange dots on the left) are almost as fast as the 500-year Big Five rates. Therefore, at least as judged using these vertebrate taxa, losing threatened species would signal a mass extinction nearly on par with the Big Five.

A second hypothetical approach asks how many more years it would take for current extinction rates to produce species losses equivalent to Big Five magnitudes. The answer is that if all 'threatened' species became extinct within a century, and that rate then continued unabated, terrestrial amphibian, bird and mammal extinction would reach Big Five magnitudes in ~240 to 540 years (241.7 years for amphibians, 536.6 years for birds, 334.4 years for mammals). Reptiles have so few of their species assessed that they are not included in this calculation. If extinction were limited to 'critically endangered' species over the next century and those extinction rates continued, the time until 75% of species were lost per group would be 890 years for amphibians, 2,265 years for birds and 1,519 years for mammals. For scenarios that project extinction of 'threatened' or 'critically endangered' species over 500 years instead of a century, mass extinction magnitudes would be reached in about 1,200 to 2,690 years for the 'threatened' scenario (1,209 years for amphibians, 2,683 years for birds and 1,672 years for mammals) or \sim 4,450 to 11,330 years for the 'critically endangered' scenario (4,452 years for amphibians, 11,326 years for birds and 7,593 years for mammals).

This emphasizes that current extinction rates are higher than those that caused Big Five extinctions in geological time; they could be severe enough to carry extinction magnitudes to the Big Five benchmark in as little as three centuries. It also highlights areas for much-needed future research. Among major unknowns are (1) whether 'critically endangered', 'endangered' and 'vulnerable' species will go extinct, (2) whether the current rates we used in our calculations will continue, increase or decrease; and (3) how reliably extinction rates in well-studied taxa can be extrapolated to other kinds of species in other places^{7,20,25,34}.

The backdrop of diversity dynamics

Little explored is whether current extinction rates within a clade fall outside expectations when considered in the context of long-term diversity dynamics. For example, analyses of cetacean (whales and dolphins) extinction and origination rates illustrate that within-clade diversity has been declining for the last 5.3 million years, and that that decline is nested within an even longer-term decline that began some 14 million years ago. Yet, within that context, even if 'threatened' genera lasted as long as 100,000 years before going extinct, the clade would still experience an extinction rate that is an order of magnitude higher than anything it has experienced during its evolutionary history⁴⁶.

The fossil record is also enabling us to interpret better the significance of currently observed population distributions and declines. The use of ancient DNA, phylochronology and simulations demonstrate that the population structure considered 'normal' on the current landscape has in fact already suffered diversity declines relative to conditions a few thousand years ago^{47,48}. Likewise, the fossil record shows that species richness and evenness taken as 'normal' today are low compared to preanthropogenic conditions^{10,27,32,33,42,45,49}.

Selectivity

During times of normal background extinction, the taxa that suffer extinction most frequently are characterized by small geographic ranges and low population abundance³⁸. However, during times of mass extinction, the rules of extinction selectivity can change markedly, so that widespread, abundant taxa also go extinct^{37,38}. Large-bodied animals and those in certain phylogenetic groups can be particularly hard hit^{33,50-52}. In that context, the reduction of formerly widespread ranges⁸ and disproportionate culling of certain kinds of species⁵⁰⁻⁵³ may be

particularly informative in indicating that extinction-selectivity is changing into a state characterizing mass extinctions.

Perfect storms?

Hypotheses to explain the general phenomenon of mass extinctions have emphasized synergies between unusual events^{54–57}. Common features of the Big Five (Table 1) suggest that key synergies may involve unusual climate dynamics, atmospheric composition and abnormally high-intensity ecological stressors that negatively affect many different lineages. This does not imply that random accidents like a Cretaceous asteroid impact^{58,59} would not cause devastating extinction on their own, only that extinction magnitude would be lower if synergistic stressors had not already 'primed the pump' of extinction ⁶⁰.

More rigorously formulating and testing synergy hypotheses may be especially important in assessing sixth mass extinction potential, because once again the global stage is set for unusual interactions. Existing ecosystems are the legacy of a biotic turnover initiated by the onset of glacial–interglacial cycles that began $\sim\!2.6$ million years ago, and evolved primarily in the absence of *Homo sapiens*. Today, rapidly changing atmospheric conditions and warming above typical interglacial temperatures as $\rm CO_2$ levels continue to rise, habitat fragmentation, pollution, overfishing and overhunting, invasive species and pathogens (like chytrid fungus), and expanding human biomass 6,7,18,20 are all more extreme ecological stressors than most living species have previously experienced. Without concerted mitigation efforts, such stressors will accelerate in the future and thus intensify extinction 7,20 , especially given the feedbacks between individual stressors 56 .

View to the future

There is considerably more to be learned by applying new methods that appropriately adjust for the different kinds of data and timescales inherent in the fossil records versus modern records. Future work needs to: (1) standardize rate comparisons to adjust for rate measurements over widely disparate timescales; (2) standardize magnitude comparisons by using the same species (or other taxonomic rank) concepts for modern and fossil organisms; (3) standardize taxonomic and geographic comparisons by using modern and fossil taxa that have equal fossilization potential; (4) assess the extinction risk of modern taxa such as bivalves and gastropods that are extremely common in the fossil record but are at present poorly assessed; (5) set current extinction observations in the context of longterm clade, species-richness, and population dynamics using the fossil record and phylogenetic techniques; (6) further explore the relationship between extinction selectivity and extinction intensity; and (7) develop and test models that posit general conditions required for mass extinction, and how those compare with the current state of the Earth.

Our examination of existing data in these contexts raises two important points. First, the recent loss of species is dramatic and serious but does not yet qualify as a mass extinction in the palaeontological sense of the Big Five. In historic times we have actually lost only a few per cent of assessed species (though we have no way of knowing how many species we have lost that had never been described). It is encouraging that there is still much of the world's biodiversity left to save, but daunting that doing so will require the reversal of many dire and escalating threats 7.20,61–63.

The second point is particularly important. Even taking into account the difficulties of comparing the fossil and modern records, and applying conservative comparative methods that favour minimizing the differences between fossil and modern extinction metrics, there are clear indications that losing species now in the 'critically endangered' category would propel the world to a state of mass extinction that has previously been seen only five times in about 540 million years. Additional losses of species in the 'endangered' and 'vulnerable' categories could accomplish the sixth mass extinction in just a few centuries. It may be of particular concern that this extinction trajectory would play out under conditions that resemble the 'perfect storm' that coincided with past mass extinctions: multiple, atypical high-intensity ecological stressors, including rapid, unusual climate change and highly elevated atmospheric CO₂.

The huge difference between where we are now, and where we could easily be within a few generations, reveals the urgency of relieving the pressures that are pushing today's species towards extinction.

- Novacek, M. J. (ed.) The Biodiversity Crisis: Losing What Counts (The New Press, 2001).
- Jablonski, D. Extinctions in the fossil record. Phil. Trans. R. Soc. Lond. B 344, 11–17 (1994).

This paper summarizes, from a palaeontological perspective, the difficulties of comparing the past and present extinctions.

- Raup, D. M. & Sepkoski, J. J. Mass extinctions in the marine fossil record. Science 215, 1501–1503 (1982).
 - This is a statistical assessment of the Big Five extinction rates relative to background rates.
- Bambach, R. K. Phanerozoic biodiversity mass extinctions. Annu. Rev. Earth Planet. Sci. 34, 127–155 (2006).
 - This paper discusses the definition of mass extinctions and mass depletions, and the relative role of origination versus extinction rates in causing the diversity reductions that characterize the Big Five.
- Alroy, J. Dynamics of origination and extinction in the marine fossil record. Proc. Natl Acad. Sci. USA 105, 11536–11542 (2008).
- IUCN. International Union for Conservation of Nature Red List (http://www.iucn.org/about/work/programmes/species/red_list/) (2010).
- Pereira, H. M. et al. Scenarios for global biodiversity in the 21st century. Science 330, 1496–1501 (2010).
- Ceballos, G. & Ehrlich, P. R. Mammal population losses and the extinction crisis. Science 296, 904–907 (2002).
- Hughes, J. B., Daily, G. C. & Ehrlich, P. R. Population diversity: its extent and extinction. Science 278, 689–692 (1997).
- Dirzo, R. & Raven, P. H. Global state of biodiversity and loss. Annu. Rev. Environ. Resour. 28, 137–167 (2003).
- This paper is an overview of the taxonomic and spatiotemporal patterns of biodiversity and the magnitude of the current biodiversity crisis.
- Joppa, L. N., Roberts, D. L. & Pimm, S. L. How many species of flowering plants are there? Proc. R. Soc. Lond. B. doi:10.1098/rspb.2010.1004 (2010).
- Leakey, R. & Lewin, R. The Sixth Extinction: Patterns of Life and the Future of Humankind (Doubleday, 1992).
- Wake, D. B. & Vredenburg, V. T. Are we in the midst of the sixth mass extinction? A view from the world of amphibians. Proc. Natl Acad. Sci. USA 105, 11466–11473 (2008)
- May, R. M., Lawton, J. H. & Stork, N. E. in Extinction Rates (eds Lawton, J. H. & May, R. M.) Ch. 1, 1–24 (Oxford University Press, 1995).

This paper compares fossil-background and recent extinction rates and explains the numerous assumptions that are required for the comparison.

- Pimm, S. L., Russell, G. J., Gittleman, J. L. & Brooks, T. M. The future of biodiversity. Science 269, 347–350 (1995).
- This paper explains and uses the E/MSY metric to compare the fossilbackground, current, and predicted future extinction rates.
- Myers, N. Mass extinctions: what can the past tell us about the present and future? Palaeogeogr. Palaeoclimatol. Palaeoecol. 82, 175–185 (1990).
- Pimm, S. L. & Brooks, T. M. in Nature and Human Society: The Quest for a Sustainable World (eds Raven, P. H. & Williams, T.) 46–62 (National Academy Press, 1997).
- Barnosky, A. D. Heatstroke: Nature in an Age of Global Warming 1–269 (Island Press, 2009).
- Vredenburg, V. T., Knapp, R. A., Tunstall, T. S. & Briggs, C. J. Dynamics of an emerging disease drive large-scale amphibian population extinctions. *Proc. Natl Acad. Sci. USA* 107, 9689–9694 (2010).
- Hoffmann, M. et al. The impact of conservation on the status of the world's vertebrates. Science 330, 1503–1509 (2010).
- Avise, J. C., Walker, D. & Johns, G. C. Speciation durations and Pleistocene effects on vertebrate phylogeography. Proc. R. Soc. Lond. B 265, 1707–1712 (1998).
- 22. Weir, J. T. & Schluter, D. The latitudinal gradient in recent speciation and extinction rates of birds and mammals. *Science* **315**, 1574–1576 (2007).
- Lu, P. J., Yogo, M. & Marshall, C. R. Phanerozoic marine biodiversity dynamics in light of the incompleteness of the fossil record. *Proc. Natl Acad. Sci. USA* 103, 2736–2739 (2006).
- Vié, J.-C., Hilton-Taylor, C. & Stuart, S. N. (eds) Wildlife in a Changing World—An Analysis of the 2008 IUCN Red List of Threatened Species 180 (IUCN, 2009).
- Baillie, J. E. M. et al. Toward monitoring global biodiversity. Conserv. Lett. 1, 18–26 (2008).
- Şengör, A. M. C., Atayman, S. & Özeren, S. A scale of greatness and causal classification of mass extinctions: implications for mechanisms. *Proc. Natl Acad.* Sci. USA 105, 13736–13740 (2008).
- Pimm, S., Raven, P., Peterson, A., Sekercioglu, Ç. H. & Ehrlich, P. R. Human impacts on the rates of recent, present, and future bird extinctions. *Proc. Natl Acad. Sci. USA* 103, 10941–10946 (2006).
- Foote, M. Temporal variation in extinction risk and temporal scaling of extinction metrics. Paleobiology 20, 424–444 (1994).
- This paper addresses the effect of interval length on extinction metrics using simulations.
- Foote, M. & Raup, D. M. Fossil preservation and the stratigraphic ranges of taxa. Paleobiology 22, 121–140 (1996).
- 30. PBDB. The Paleobiology Database (http://paleodb.org/cgi-bin/bridge.pl) (2010).
- NEOMAP. The Neogene Mammal Mapping Portal (http://www.ucmp.berkeley.edu/neomap/) (2010).

- 32. Barnosky, A. D. Megafauna biomass tradeoff as a driver of Quaternary and future extinctions. *Proc. Natl Acad. Sci. USA* **105**, 11543–11548 (2008).
- Koch, P. L. & Barnosky, A. D. Late Quaternary extinctions: state of the debate. Annu. Rev. Ecol. Evol. Syst. 37, 215–250 (2006).
- Mace, G. M. et al. Quantification of extinction risk: IUCN's system for classifying threatened species. Conserv. Biol. 22, 1424–1442 (2008).
 - This paper explains the methodology used by the IUCN to assess the extinction risks of extant species.
- Alroy, J. Constant extinction, constrained diversification, and uncoordinated stasis in North American mammals. *Palaeogeogr. Palaeoclimatol. Palaeoecol.* 127, 285–311 (1996)
- Stork, N. E. Re-assessing current extinction rates. Biodivers. Conserv. 19, 357–371 (2010).
- Jablonski, D. Lessons from the past: evolutionary impacts of mass extinctions. Proc. Natl Acad. Sci. USA 98, 5393–5398 (2001).
- Jablonski, D. Extinction and the spatial dynamics of biodiversity. Proc. Natl Acad. Sci. USA 105, 11528–11535 (2008).
- 39. Purvis, A., Jones, K. E. & Mace, G. M. Extinction. Bioessays 22, 1123-1133 (2000).
- Agapow, P.-M. et al. The impact of the species concept on biodiversity studies. Q. Rev. Biol. 79, 161–179 (2004).
- Alroy, J. et al. Phanerozoic trends in the global diversity of marine invertebrates. Science 321, 97–100 (2008).
- 42. Steadman, D. W. Extinction and Biogeography of Tropical Pacific Birds (University of Chicago Press, 2006).
- Raup, D. M. & Jablonski, D. Geography of end-Cretaceous marine bivalve extinctions. Science 260, 971–973 (1993).
- Regan, H. M., Lupia, R., Drinnan, A. N. & Burgman, M. A. The currency and tempo of extinction. Am. Nat. 157, 1–10 (2001).
- Carrasco, M. A., Barnosky, A. D. & Graham, R. W. Quantifying the extent of North American mammal extinction relative to the pre-anthropogenic baseline. PLoS ONE 4, e8331 (2009).
 - This paper uses species-area relationships based on fossil data to demonstrate that the recent biodiversity baseline for mammals is substantially depressed with respect to its normal condition.
- Quental, T. B. & Marshall, C. R. Diversity dynamics: molecular phylogenies need the fossil record. *Trends Ecol. Evol.* 25, 434–441 (2010).
- Anderson, C. N. K., Ramakrishnan, U., Chan, Y. L. & Hadly, E. A. Serial SimCoal: a population genetics model for data from multiple populations and points in time. *Bioinformatics* 21, 1733–1734 (2005).
- Ramakrishnan, U. & Hadly, E. A. Using phylochronology to reveal cryptic population histories: review and synthesis of four ancient DNA studies. *Mol. Ecol.* 18, 1310–1330 (2009).
 - This paper uses a hypothesis-testing framework to reveal population histories and compare past populations to present ones.
- Blois, J. L., McGuire, J. L. & Hadly, E. A. Small mammal diversity loss in response to late-Pleistocene climatic change. *Nature* 465, 771–774 (2010).
- Cardillo, M. et al. Multiple causes of high extinction risk in large mammal species. Science 309, 1239–1241 (2005).
- Davies, T. J. et al. Phylogenetic trees and the future of mammalian biodiversity. Proc. Natl Acad. Sci. USA 105, 11556–11563 (2008).
- Isaac, N. J. B., Turvey, S. T., Collen, B., Waterman, C. & Baillie, J. E. M. Mammals on the EDGE: conservation priorities based on threat and phylogeny. *PLoS ONE* 2, e296 (2007).
- Russell, G. J., Brooks, T. M., McKinney, M. M. & Anderson, C. G. Present and future taxonomic selectivity in bird and mammal extinctions. *Conserv. Biol.* 12, 1365–1376 (1998).
- 54. Erwin, D. H. The Permo-Triassic extinction. *Nature* **367**, 231–236 (1994).
- Arens, N. C. & West, I. D. Press-pulse: a general theory of mass extinction? Paleobiology 34, 456–471 (2008).
- Brook, B. W., Sodhi, N. S. & Bradshaw, C. J. A. Synergies among extinction drivers under global change. *Trends Ecol. Evol.* 23, 453–460 (2008).
- 7. Jablonski, D. in *Dynamics of Extinction* (ed. Elliott, D. K.) 183–229 (Wiley, 1986).
- Alvarez, L. W., Alvarez, W., Asaro, F. & Michel, H. V. Extraterrestrial cause for the Cretaceous-Tertiary extinction. Science 208, 1095–1108 (1980).
- Schulte, P. et al. The Chicxulub asteroid impact and mass extinction at the Cretaceous-Paleogene boundary. Science 327, 1214–1218 (2010).
- Prauss, M. L. The K/Pg boundary at Brazos-River, Texas, USA—an approach by marine palynology. *Palaeogeogr. Palaeoclimatol. Palaeoecol.* 283, 195–215 (2009).
- GB03. Global Biodiversity Outlook 3 94 (Secretariat of the Convention on Biological Diversity, 2010).
- Mace, G. et al. in Millenium Ecosystem Assessment, Ecosystems and Human Wellbeing: Biodiversity Synthesis (eds Ceballos, S. L. G., Orians, G. & Pacala, S.) Ch. 4, 77–122 (World Resources Institute, 2005).
- Cardillo, M., Mace, G. M., Gittleman, J. L. & Purvis, A. Latent extinction risk and the future battlegrounds of mammal conservation. *Proc. Natl Acad. Sci. USA* 103, 4157–4161 (2006).
- Sepkoski, J. J. in Global Events and Event Stratigraphy in the Phanerozoic (ed. Walliser, O. H.) 35–51 (Springer, 1996).
- Sheehan, P. M. The Late Ordovician mass extinction. Annu. Rev. Earth Planet. Sci. 29, 331–364 (2001).
- Sutcliffe, O. E., Dowdeswell, J. A., Whittington, R. J., Theron, J. N. & Craig, J. Calibrating the Late Ordovician glaciation and mass extinction by the eccentricity cycles of Earth's orbit. Geology 28, 967–970 (2000).
- Sandberg, C. A., Morrow, J. R. & Zlegler, W. in Catastrophic Events and Mass Extinctions: Impacts and Beyond (eds Koeberl, C. & MacLeod, K. G.) 473–387 (Geological Society of America Special Paper 356, GSA, 2002).

- McGhee, G. R. The Late Devonian Mass Extinction 1–302 (Columbia University Press, 1996).
- 69. Murphy, A. E., Sageman, B. B. & Hollander, D. J. Eutrophication by decoupling of the marine biogeochemical cycles of C, N, and P: a mechanism for the Late Devonian mass extinction. *Geology* **28**, 427–430 (2000).
- Algeo, T. J., Scheckler, S. E. & Maynard, J. B. in *Plants Invade the Land: Evolutionary and Environmental Approaches* (eds Gensel, P. G. & Edwards, D.) 213–236 (Columbia University Press, 2000).
- Berner, R. A. Examination of hypotheses for the Permo-Triassic boundary extinction by carbon cycle modeling. Proc. Natl Acad. Sci. USA 99, 4172–4177 (2002).
- Payne, J. L. et al. Calcium isotope constraints on the end-Permian mass extinction. Proc. Natl Acad. Sci. USA 107, 8543–8548 (2010).
- Knoll, A. H., Bambach, R. K., Payne, J. L., Pruss, S. & Fischer, W. W. Paleophysiology and end-Permian mass extinction. *Earth Planet Sci. Lett.* 256, 295–313 (2007).
- Hesselbo, S. P., McRoberts, C. A. & Palfy, J. Triassic-Jurassic boundary events: problems, progress, possibilities. *Palaeogeogr. Palaeoclimatol. Palaeoecol.* 244, 1–10 (2007).
- Ward, P. D. et al. Sudden productivity collapse associated with the Triassic-Jurassic boundary mass extinction. Science 292, 1148–1151 (2001).
- Archibald, J. D. et al. Cretaceous extinctions: multiple causes. Science 328, 973 (2010).
- 77. Keller, G. Cretaceous climate, volcanism, impacts, and biotic effects. *Cretac. Res.* **29.** 754–771 (2008).
- Mukhopadhyay, S., Farley, K. A. & Montanari, A. A short duration of the Cretaceous-Tertiary boundary event: evidence from extraterrestrial helium-3. *Science* 291, 1952–1955 (2010).
- Royer, D. L. CO₂-forced climate thresholds during the Phanerozoic. Geochim. Cosmochim. Acta 70, 5665–5675 (2006).
- McCallum, M. L. Amphibian decline or extinction? Current declines dwarf background extinction rate. J. Herpetol. 41, 483–491 (2007).
- 81. Rosenzweig, M. L. Loss of speciation rate will impoverish future diversity. *Proc. Natl Acad. Sci. USA* **98**, 5404–5410 (2001).
- 82. Thomas, C. D. et al. Extinction risk from climate change. *Nature* **427**, 145–148 (2004)
- 83. Pimm, S. L. & Raven, P. H. Extinction by numbers. Nature 403, 843-845 (2000).
- 84. Sinervo, B. et al. Erosion of lizard diversity by climate change and altered thermal niches. Science **328**, 894–899 (2010).
- Roelants, K. et al. Global patterns of diversification in the history of modern amphibians. Proc. Natl Acad. Sci. USA 104, 887–892 (2007).
- Raup, D. M. A kill curve for Phanerozoic marine species. Paleobiology 17, 37–48 (1991).
- Foote, M. Estimating taxonomic durations and preservation probability. Paleobiology 23, 278–300 (1997).
- Rabosky, D. L. Extinction rates should not be estimated from molecular phylogenies. *Evolution* 64, 1816–1824 (2010).
- Barnosky, A. D. & Lindsey, E. L. Timing of Quaternary megafaunal extinction in South America in relation to human arrival and climate change. Quat. Int. 217, 10–29 (2010).
- 90. Turvey, S. T. Holocene Extinctions (Oxford University Press, 2009).
- 91. Faith, J. T. & Surovell, T. A. Synchronous extinction of North America's Pleistocene mammals. *Proc. Natl Acad. Sci. USA* **106**, 20641–20645 (2009).
- Surovell, T., Waguespack, N. & Brantingham, P. J. Global archaeological evidence for proboscidean overkill. *Proc. Natl Acad. Sci. USA* 102, 6231–6236 (2005).
- 93. Finlayson, C. et al. Late survival of Neanderthals at the southernmost extreme of Europe. Nature **443**, 850–853 (2006).
- 94. Morwood, M. J. *et al.* Archaeology and age of a new hominin from Flores in eastern Indonesia. *Nature* **431**, 1087–1091 (2004).
- 95. Orlova, L. A., Vasil'ev, S. K., Kuz'min, Y. V. & Kosintsev, P. A. New data on the time and place of extinction of the woolly rhinoceros *Coelodonta antiquitatis* Blumenbach, 1799. *Dokl. Akad. Nauk* **423**, 133–135 (2008).
- Reumer, J. W. F. et al. Late Pleistocene survival of the saber-toothed cat Homotherium in Northwestern Europe. J. Vertebr. Paleontol. 23, 260–262 (2003).
- 97. MacPhee, R. D. E. Extinctions in Near Time: Causes, Contexts, and Consequences (Kluwer Academic/Plenum Publishers, 1999).

Acknowledgements S. Beissinger, P. Ehrlich, E. Hadly, A. Hubbe, D. Jablonski, S. Pimm and D. Wake provided constructive comments. Paleobiology Database data were contributed by M. Carrano, J. Alroy, M. Uhen, R. Butter, J. Mueller, L. van den Hoek Ostende, J. Head, E. Fara, D. Croft, W. Clyde, K. Behrensmeyer, J. Hunter, R. Whatley and W. Kiessling. The work was funded in part by NSF grants EAR-0720387 (to A.D.B.) and DEB-0919451 (supporting N.M.). This is University of California Museum of Paleontology Contribution 2024.

Author Contributions All authors participated in literature review and contributed to discussions that resulted in this paper. A.D.B. planned the project, analysed and interpreted data, and wrote the paper. N.M. and S.T. performed key data analyses and interpretation relating to rate comparisons. G.O.U.W., B.S. and E.L.L. assembled critical data. T.B.Q. and C.M. provided data, analyses and ideas relating to diversity dynamics and rate-magnitude comparisons. J.L.M. helped produce figures and with N.M., S.T., G.O.U.W., B.S., T.B.Q., C.M., K.C.M., B.M. and E.A.F. contributed to finalizing the text.

Author Information Reprints and permissions information is available at www.nature.com/reprints. The authors declare no competing financial interests. Readers are welcome to comment on the online version of this article at www.nature.com/nature. Correspondence should be addressed to A.D.B. (barnosky@berkeley.edu).

ARTICLE

Copy number variation and selection during reprogramming to pluripotency

Samer M. Hussein^{1,2*}, Nizar N. Batada^{3*}, Sanna Vuoristo², Reagan W. Ching⁴, Reija Autio^{5,6}, Elisa Närvä⁵, Siemon Ng³, Michel Sourour¹, Riikka Hämäläinen^{1,2}, Cia Olsson², Karolina Lundin², Milla Mikkola², Ras Trokovic², Michael Peitz⁷, Oliver Brüstle⁷, David P. Bazett-Jones⁴, Kari Alitalo⁸, Riitta Lahesmaa⁵, Andras Nagy^{1,9} & Timo Otonkoski^{2,10}

The mechanisms underlying the low efficiency of reprogramming somatic cells into induced pluripotent stem (iPS) cells are poorly understood. There is a clear need to study whether the reprogramming process itself compromises genomic integrity and, through this, the efficiency of iPS cell establishment. Using a high-resolution single nucleotide polymorphism array, we compared copy number variations (CNVs) of different passages of human iPS cells with their fibroblast cell origins and with human embryonic stem (ES) cells. Here we show that significantly more CNVs are present in early-passage human iPS cells than intermediate passage human iPS cells, fibroblasts or human ES cells. Most CNVs are formed *de novo* and generate genetic mosaicism in early-passage human iPS cells. Most of these novel CNVs rendered the affected cells at a selective disadvantage. Remarkably, expansion of human iPS cells in culture selects rapidly against mutated cells, driving the lines towards a genetic state resembling human ES cells.

Reprogramming somatic cells to pluripotency can be achieved by forced expression of a defined set of factors^{1,2}. Several methods have been developed for generating human iPS cells, such as retroviral transduction¹, DNA-transposition-based systems^{3,4}, transient plasmid delivery⁵ and integration/plasmid-free systems^{6,7}. To improve efficiency and in an effort to understand the process of reprogramming, several groups have demonstrated that modulating key components of the cell cycle, such as repression of the *Ink4a/Arf* locus or downregulation of the p53–p21 pathway, have marked positive effects on reprogramming efficiency⁸⁻¹². However, p53 suppression can lead to increased levels of DNA damage and genomic instability. These findings suggest that the reprogramming process places a heavy burden on cellular integrity and highlight the importance of further exploring the nature of the DNA damage that is associated with the reprogramming process.

High CNV levels in early-passage human iPS cells

To determine whether reprogramming is associated with *de novo*generated CNVs, we used the Affymetrix SNP array 6.0 to characterize 22 human iPS cell lines along with 17 human ES cell lines¹³, as well as three parental and one unrelated fibroblast lines as controls (Supplementary Table 1). The human iPS cell lines were established either by retroviral² or *piggyBac*^{3,4} gene delivery methods and confirmed as human iPS cells using established criteria¹⁴ (Supplementary Figs 1–3 and Supplementary Table 2). Nine of the 22 human iPS cell lines were characterized at more than one passage to track CNVs during propagation.

The median number of CNVs in human iPS cell lines (109) was about twofold higher than in human ES cell lines (55) and fibroblasts (53) (Supplementary Fig. 4a and Supplementary Tables 3 and 4). We found that the majority of CNVs (52.4%) in human iPS cells were not

present in either human ES cells or fibroblasts (Supplementary Fig. 4b). Interestingly, the number of CNVs negatively correlated with the passage number. This was surprising because fibroblasts and human ES cells showed no significant changes during intermediate length passaging (Supplementary Fig. 4c, d). Both the number and the total size of CNVs in human iPS cell lines decreased during propagation (Fig. 1a and Supplementary Fig. 4e). Neither the reprogramming factor delivery method, fibroblast source or viral integration sites nor the presence or absence of Myc during reprogramming (Fig. 1b, c and Supplementary Fig. 5) influenced these results. This trend was verified in an independent data set on human iPS cell lines derived from four adult skin fibroblasts (Supplementary Table 5), as well as within individual human iPS cell lines analysed at early and later passages (Fig. 1b–d). Our findings indicate that CNVs are generated during the reprogramming process.

Genetic mosaicism in human iPS cells

The decrease in CNVs during passaging could be explained either by DNA repair mechanisms or by mosaicism followed by selection. We propose that DNA repair may not be efficient enough to explain the rapid decrease in CNVs but, instead, that *de novo*-generated CNVs create mosaicism, which is followed by selection favouring less damaged cells during propagation. To obtain direct proof for mosaicism, we established new human iPS cell lines and tested these at very early passages (passage 2 and 3) for CNVs by using fluorescence *in situ* hybridization (FISH). We chose a probe that maps to a locus on chromosome 1 that, according to our single nucleotide polymorphism (SNP) array data, is frequently affected in human iPS cell lines (Fig. 2a). A control probe was selected from a chromosome 1 location that showed normal copy number (2) across all human iPS cell lines that were tested. During early passages, the test probe demonstrated a

¹Samuel Lunenfeld Research Institute, Toronto, Ontario M5T 3H7, Canada. ²Research Program Unit, Molecular Neurology, Biomedicum Stem Cell Center, University of Helsinki, Helsinki FI-00014, Finland. ³Ontario Institute for Cancer Research, Toronto, Ontario M5G 0A3, Canada. ⁴Department of Genetics and Genome Biology, The Hospital for Sick Children, Toronto, Ontario M5G 1L7, Canada. ⁵Turku Centre for Biotechnology, University of Turku and Åbo Akademi University, Turku 20520, Finland. ⁶Department of Signal Processing, Tampere University of Technology, Tampere 33101, Finland. ⁷Institute of Reconstructive Neurobiology, Life and Brain Center, University of Bonn and Hertie Foundation, D-53127 Bonn, Germany. ⁸Molecular Cancer Biology Laboratory, University of Helsinki and Helsinki University Central Hospital, Helsinki FI-00014, Finland. ⁹Department of Molecular Genetics, University of Toronto, Ontario M5S 1A8, Canada. ¹⁰Children's Hospital, University of Helsinki, Helsinki FI-00029. Finland.

^{*}These authors contributed equally to this work.

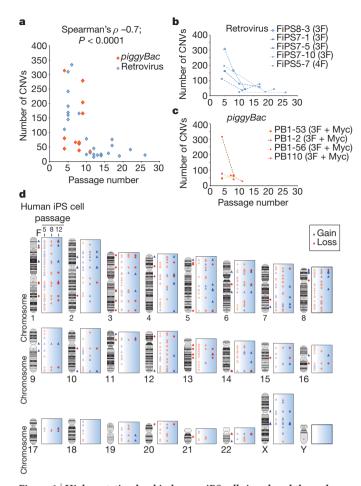


Figure 1 | **High mutation level in human iPS cells is reduced through moderate culture.** a, Number of CNVs in human iPS cell lines with respect to passage number. Each data point represents a sample: blue, retrovirus-derived human iPS cell lines; orange, *piggyBac* lines. Spearman's rank correlation coefficient (*ρ*) and Student's *t*-distribution were used for statistical analysis and *P*-value calculations. **b, c**, With passaging, both retrovirus-derived (**b**) and *piggyBac*-transposon-derived (**c**) human iPS cell lines (listed) show a constant and sharp decrease in the number of CNVs. Numbers in parentheses indicate the number of factors used for generating the corresponding human iPS cell lines: 3F, OCT4, SOX2 and KLF4; 4F, OCT4, SOX2, NANOG and LIN28. **d,** Genomic representation demonstrating the sharp decline in the number of CNVs from early passage (passage 5) to intermediate passage (8) and intermediate–late passage (12) of the human iPS cell line FiPS7-5 relative to the CNVs in the parental fibroblast (F). Blue triangles represent amplifications, and red diamonds represent deletions, with colour intensity varying with passage number.

significantly higher fraction of cells with aberrant copy number state than the control probe (Fig. 2a). The fraction of aberrant cells was also significantly higher in early-passage human iPS cells (18%) than in fibroblasts (3%) or in later-passage human iPS cells (9%) (Fig. 2b, Supplementary Fig. 6 and Supplementary Table 6).

To provide evidence for selection, we focused on regions containing homozygous deletions, which DNA repair mechanisms cannot correct. Although we could detect only a small number of such deletions, our detection rate for homozygous deletions was very reproducible, detecting 98% of the deletions in three to four replicates (Supplementary Table 7). Our false discovery rate was 9.7% for detecting other types of CNV (Supplementary Table 7 and Supplementary Fig. 7), suggesting low error in calling CNVs and robust detection of homozygous deletions. We focused on homozygous deletions found only in human iPS cell lines and not their parental fibroblasts, and we categorized these into three groups: type 'A' homozygous deletions, which are present only in early passages; type 'B' homozygous deletions, which are detected only in later passages; and type 'C' homozygous deletions,

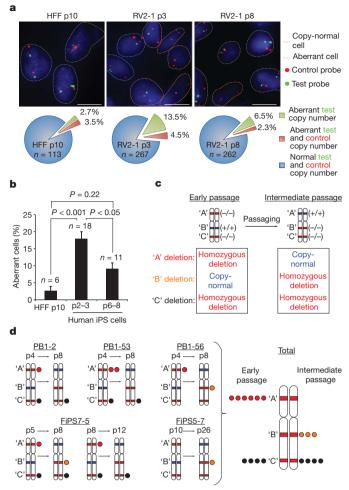


Figure 2 | Increased mosaicism in early-passage human iPS cells. a, Merged FISH field images of human foreskin fibroblast (HFF) cells at passage 10 (p10) and the human iPS cell line RV2-1 at p3 and p8. Test (green) and control (red) probes are located on chromosome 1. The pie charts below the images show the percentage of cells that have only aberrant test probe (but not control probe) foci counts or copy number (green), cells that have aberrant test and control probe foci counts (red), and normal cells (blue). Five different field images were counted per sample; n = the total number of cells counted. Dashed grey lines indicate normal cells, and orange lines indicate aberrant cells. Scale bar, 10 µm. b, Histogram demonstrates the mean fraction of aberrant cells in fibroblasts (HFF p10) and early-passage (p2-3) and intermediate-passage (p6-8) human iPS cells. Each field contained approximately 20–100 cells; n = total number offields counted. Error bars, s.e.m. One-way analysis of variance and the Tukey-Kramer post-hoc test were used for statistical analysis and *P*-value calculations. c, Three categories of homozygous deletions: type 'A', detected only during early passages; type 'B', appearing in later passages; and type 'C', seen in both early and intermediate passages. -/-, homozygous deletion (red band); +/+, normal copy number (blue band). d, Left, non-parental homozygous deletions present in five cell lines passaged from an early passage to an intermediate passage. Each circle represents a homozygous deletion: 'A', red circles; 'B', orange circles; and 'C', black circles. Right, combined total count of homozygous deletions.

which remain during passaging (Fig. 2c). Five of the cell lines presented with non-parental homozygous deletions at an early or intermediate passage (Fig. 2d). In four of the lines, we identified homozygous deletions that were selected against during passaging (type A). We also found type B and type C deletions, suggesting that selection pressure is bidirectional, selecting both for and against CNVs (Fig. 2d).

Novel CNVs in early-passage human iPS cells

We obtained a list of 6,596 non-overlapping common CNVs identified in 270 healthy individuals from two combined studies in the HapMap Project^{15,16}. These common CNVs could be considered to be

functionally the most neutral^{17,18}. We designated the set of CNVs that were identified in our study and that do not belong to common CNVs as novel CNVs. They accounted for 15% of the total CNVs in fibroblasts and 25% in human ES cells but 37% in human iPS cells (Supplementary Fig. 8a). The novel CNV fraction was significantly higher in early-passage human iPS cell lines than in later passages, in which it decreased to levels similar to those found in human ES cells and in fibroblasts (Supplementary Fig. 8b). Only a minority of non-parental human iPS cell CNVs that overlapped human ES cell CNVs were novel (Supplementary Fig. 8c).

Selection against highly damaged human iPS cells

In a mosaic population, CNVs can be identified with SNP arrays only if they are present above the detection threshold level, which depends on the type and the size of CNVs. For example, with the Affymetrix SNP array 6.0 and Genotyping Console 3.0 software algorithm, a trisomy might not be fully detectable if the mutant cell contribution is less than 40% (refs 13, 19). Owing to the multiple probe-based and threshold-based nature of CNV identification, a single large CNV found within a subpopulation of the cells (for example, type L cells in Fig. 3a) could be misrepresented as multiple small, consecutive CNVs, providing a false representation of the data. If the CNV is selected for during maintenance, these type L cells will become more prevalent in the population. Consequently, the detection of this large CNV would be more accurate in intermediate passages (that is, a relatively larger size and number of overlapping CNVs within the intermediate-passage cells would be shared with early-passage cells), and the number of 'false' consecutive CNVs would decrease. In the case of selection against a mutation, the CNV number would still show a decrease with passaging, but this mechanism would not affect the size of overlapping CNVs between early and intermediate passages. The overlap in CNVs between early and intermediate passages would be minimal. We therefore investigated whether this putative error component could account for the observed high number of novel CNVs in early-passage lines (Fig. 3a).

Focusing on novel CNVs present only in human iPS cells, we found that the overlapping CNV size was equivalent among different passages and clones (Fig. 3b), but the number of overlapping (shared) novel CNVs in human iPS cells was relatively small (Fig. 3c), indicating that most CNVs in early-passage lines are not the product of type L cell subpopulations and are indeed 'true' CNVs. Moreover, the rate of selection against novel CNVs in a passage interval (change in novel CNV number divided by number of passages) was significantly higher between the relatively early passages and the intermediate passages than it was between the intermediate and late passages. The latter rate was comparable to the selection rate of human ES cells (Fig. 3d), suggesting that early-passage human iPS cells endure strong selection pressure and lose the majority of their *de novo* mutations. These results demonstrate that most of the novel CNVs in human iPS cells are generated during the reprogramming process.

Novel CNVs recur within fragile regions

To investigate possible sources of negative selection, we asked whether the high level of *de novo* mutations led to functional consequences, such as an increase in senescence or apoptosis or a decrease in self-renewal. We assessed mutations within genes that may affect differentiation, proliferation or maintenance of pluripotency. In early passages but not in later passages, several deletions were found in genes and regions essential for maintaining an undifferentiated state (Supplementary Table 8). Such mutations included deletions in the genes

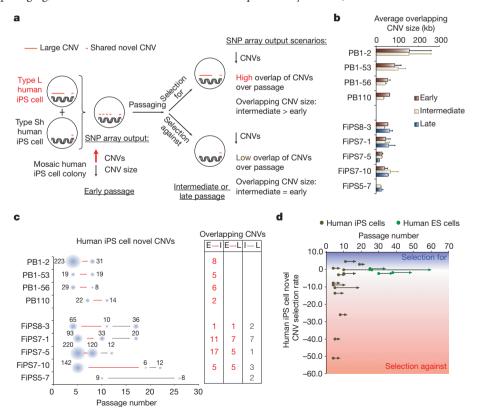


Figure 3 | High selection pressure against *de novo* mutations suggests reprogramming as the source of novel CNVs. a, Possible error in SNP array output from a mosaic human iPS cell colony containing type L cells (cells with a large CNV) and type Sh cells (cells with shared novel CNVs). b, Average overlapping novel CNV size (kilobases, kb) in human iPS cell lines at early, intermediate and late passage. Error bars, s.e.m. c, Left, plot showing the change in the number of novel CNVs in human iPS cells with passaging. Blue circle size

corresponds to the number of CNVs observed at the passage tested, with the number listed next to the circle. Right, the number of overlapping CNVs. Values for early (E) compared with intermediate (I) or late (L) passage are shown in red, and for I compared with L are shown in grey. **d**, Selection rate of human iPS cells. The rate is calculated as change in novel CNV number divided by change in passage number. Four human ES cell lines were used as controls. Arrows indicate the start and the end of the passage range tested for each sample.

encoding the epidermal growth factor receptor, fibroblast growth factor receptor 2, β -catenin (also known as CTNNB1) and polycomb-bound regions, all of which have been implicated in human ES cell maintenance^{20–23}. We also found that six early-passage human iPS cell lines had deletions in the regions encoding the microRNAs let-7c and miR-125b, which affect the expression of genes known to be involved in human ES cell differentiation and maintenance, such as those encoding Myc, Ras, p53 and ERBB3 (refs 24–27).

To explore possible mechanisms behind reprogramming-induced CNVs, we investigated mutations reminiscent of those induced by replication stress, such as DNA replication fork stalling and collapse, and we assessed CNVs found in regions of genomic fragility, such as common fragile sites (CFSs) and subtelomeric regions^{28–30}. CFSs contain late-replicating sequences and are a major target for genomic rearrangements in oncogene-expressing and pre-neoplastic cells³¹⁻³⁴. We compiled a list of CFSs from published reports (Supplementary Table 9) and measured the fraction of recurring deletions within CFS regions compared with the whole genome. Deletions recurred more frequently in CFSs than in the generic part of the genome, and more specifically they recurred more frequently in human iPS cells than in human ES cells and fibroblasts (Fig. 4a and Supplementary Table 9). Furthermore, this recurring CNV fraction consisted mainly of novel CNVs in human iPS cells (Fig. 4a), suggesting that a higher level of novel CNVs may result in part from replication stress^{28,29}. This observation was consistent with previous reports demonstrating increases in the level of reactive oxygen species during reprogramming. Reactive oxygen species are prevalent in cells undergoing replication stress and may contribute to the incidence of mutations in other parts of the genome as well³⁵.

To examine mutations that correlate with senescent or apoptotic cells, we focused on deletions incurred in subtelomeric regions

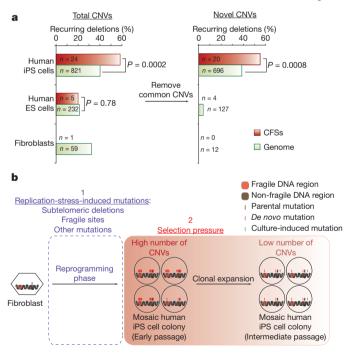


Figure 4 | Frequent mutations in fragile genomic regions influence selection during the expansion of human iPS cells. a, Recurring deletions as a proportion of total CNV deletions and novel CNV deletions, within either CFSs or the whole genome. Deletions are considered to be recurring if they are found in more than one sample (n = the total number of deletions observed). For human iPS cells, only non-parental deletions are considered. The chi-squared test was used for statistical analysis and P-value calculations. b, Summary model illustrating the increase in the number of CNVs that results from replication stress during reprogramming, followed by a selection phase that occurs after reprogramming and eliminates unstable human iPS cells containing high numbers of CNVs.

because these areas have been shown to be highly sensitive to DNA double strand breaks^{36,37} and because deletions within these regions are a major cause of chromosomal instability³⁷. We compared the average deletion size with those seen in CFSs and the whole genome. The average deletion size within subtelomeric regions was significantly larger in early-passage lines than in later passages, while remaining unchanged in the generic part of the genome and in CFSs (Supplementary Fig. 9a). We also found that several early-passage human iPS cell lines had deletions in the subtelomeric region nearest to the telomeres (25 kilobases away) (Supplementary Fig. 9b). The increased selection against large subtelomeric deletions is consistent with the idea that CNVs in these areas probably lead to a higher level of phenotypic change because these areas are gene rich and prone to genomic instability^{38,39}.

Discussion

Two recent studies 40,41 report on the observation of specific genomic aberrations associated with the pluripotent state in human ES cells and human iPS cells. One group carried out a meta-analysis of large numbers of gene expression profiles that had been determined for pluripotent stem cells by different laboratories⁴⁰. They showed that human iPS cells are subject to the type of culture adaptations that have been shown to affect the karyotypic integrity of human ES cells⁴². Their data also suggest that a distinct category of genomic aberrations may be associated with the early phase of human iPS cell establishment. Their conclusion is in line with the second recent report, in which SNP arrays were used to compare CNVs in a large number of normal somatic cell lines, human ES cell lines and human iPS cell lines⁴¹. Interestingly, human ES cells were found to contain more gains, and human iPS cells more deletions, than somatic cell samples. This finding further substantiates the differences between these two types of pluripotent cell. It also underscores the differences in the selection forces that affect human ES cells and human iPS cells (at least during the establishment period) and that could affect the quality of the final products. Data from the second study⁴¹ suggest that the reprogramming process is associated with selection for deletions that affect tumour-suppressor genes, whereas maintenance of the cell lines selects for duplications in oncogenic genes.

From our study, we conclude that the reprogramming process is associated with high mutation rates, causing increased levels of CNVs and genetic mosaicism in the resultant early-passage human iPS cell lines. Our data also suggest that de novo CNVs are the consequence of replication stress (Fig. 4b). Using our approach, we failed to find evidence suggesting that other mechanisms operate. Of the 116 DNA-repair-related and/or checkpoint-related genes that we investigated, we found only four cell lines in which a CNV might have affected a single gene (Supplementary Table 10). However, because our study was limited to CNVs, we could not exclude the possibility of other types of mutation that lead to perturbations of checkpoints or repair of DNA double strand breaks. Such mutations could lead to non-allelic homologous recombination (NAHR)-based rearrangements and/or non-homologous end-joining (NHEJ)-based rearrangements. Both NAHR and NHEJ have been reported to be involved in CNV formation⁴³.

In summary, because most *de novo* mutations confer a growth or survival disadvantage to the cells, they are selected against, eventually leading to a CNV load similar to that found in human ES cells. This negative selection, however, does not exclude the possibility that certain hazardous aberrations give the cell a selective advantage over cells with an intact genome. Our results highlight the importance of understanding the molecular mechanisms underlying the reprogramming of somatic cells to a pluripotent state, with particular emphasis on forces that negatively affect the integrity of the genome. With a better understanding of the reprogramming process, we will increase the likelihood of finding ways to counteract the pitfalls and create human iPS cells that can safely be used for cell-based therapies in the future.

METHODS SUMMARY

Human fibroblast lines were reprogrammed by retroviral transduction¹ and piggyBac transposition as previously described³. Human iPS cell lines were expanded and characterized as previously described¹⁴. In vitro differentiation of human iPS cells was carried out using embryoid body, neuronal and endodermal differentiation protocols as described in the Methods. Teratomas were generated as described elsewhere⁴⁴. Supplementary Table 2 lists the details of the characterization of each human iPS cell clone and the factors used for reprogramming. Bisulphite sequencing of NANOG and OCT4 promoters was performed as previously described⁴⁵. Splinkerette PCR was used to identify viral integration sites in three human iPS cell lines as previously described⁴⁶. FISH protocols are provided in the Supplementary Information. Samples were run on Affymetrix SNP array 6.0, and Genotyping Console 3.0.2 was used to analyse and determine CNV levels, genotype calls and loss of heterozygosity detection as detailed in the Methods.

Full Methods and any associated references are available in the online version of the paper at www.nature.com/nature.

Received 30 March 2010; accepted 27 January 2011.

- Takahashi, K. et al. Induction of pluripotent stem cells from adult human fibroblasts by defined factors. Cell 131, 861–872 (2007).
- Takahashi, K. & Yamanaka, S. Induction of pluripotent stem cells from mouse embryonic and adult fibroblast cultures by defined factors. Cell 126, 663–676 (2006).
- Woltjen, K. et al. piggyBac transposition reprograms fibroblasts to induced pluripotent stem cells. Nature 458, 766–770 (2009).
- Kaji, K. et al. Virus-free induction of pluripotency and subsequent excision of reprogramming factors. Nature 458, 771–775 (2009).
- Yu, J. et al. Human induced pluripotent stem cells free of vector and transgene sequences. Science 324, 797–801 (2009).
- Warren, L. et al. Highly efficient reprogramming to pluripotency and directed differentiation of human cells with synthetic modified mRNA. Cell Stem Cell 7, 618–630 (2010).
- Kim, D. et al. Generation of human induced pluripotent stem cells by direct delivery of reprogramming proteins. Cell Stem Cell 4, 472–476 (2009).
- Utikal, J. et al. Immortalization eliminates a roadblock during cellular reprogramming into iPS cells. Nature 460, 1145–1148 (2009).
- Marión, R. M. et al. A p53-mediated DNA damage response limits reprogramming to ensure iPS cell genomic integrity. Nature 460, 1149–1153 (2009).
- Li, H. et al. The Ink4/Arf locus is a barrier for iPS cell reprogramming. Nature 460, 1136–1139 (2009).
- 11. Kawamura, T. et al. Linking the p53 tumour suppressor pathway to somatic cell reprogramming. *Nature* **460**, 1140–1144 (2009).
- Hong, H. et al. Suppression of induced pluripotent stem cell generation by the p53–p21 pathway. Nature 460, 1132–1135 (2009).
- Närvä, E. et al. High-resolution DNA analysis of human embryonic stem cell lines reveals culture-induced copy number changes and loss of heterozygosity. Nature Biotechnol. 28, 371–377 (2010).
- Chan, E. M. et al. Live cell imaging distinguishes bona fide human iPS cells from partially reprogrammed cells. *Nature Biotechnol.* 27, 1033–1037 (2009).
- McCarroll, S. A. et al. Integrated detection and population-genetic analysis of SNPs and copy number variation. Nature Genet. 40, 1166–1174 (2008).
- Conrad, D. F. et al. Origins and functional impact of copy number variation in the human genome. Nature 464, 704–712 (2010).
- Sebat, J. et al. Large-scale copy number polymorphism in the human genome. Science 305, 525–528 (2004).
- Iafrate, A. J. et al. Detection of large-scale variation in the human genome. Nature Genet. 36, 949–951 (2004).
- Hagenkord, J. M. et al. Array-based karyotyping for prognostic assessment in chronic lymphocytic leukemia: performance comparison of Affymetrix 10K2.0,
- 250K Nsp, and SNP6.0 arrays. *J. Mol. Diagn.* 12, 184–196 (2010).
 20. Eiselleova, L. *et al.* A complex role for FGF-2 in self-renewal, survival, and adhesion of human embryonic stem cells. *Stem Cells* 27, 1847–1857 (2009).
- Brill, L. M. et al. Phosphoproteomic analysis of human embryonic stem cells. Cell Stem Cell 5, 204–213 (2009).
- Wang, L. et al. Self-renewal of human embryonic stem cells requires insulin-like growth factor-1 receptor and ERBB2 receptor signaling. Blood 110, 4111–4119 (2007).
- Boyer, L. A. et al. Polycomb complexes repress developmental regulators in murine embryonic stem cells. Nature 441, 349–353 (2006).
- Melton, C., Judson, R. L. & Blelloch, R. Opposing microRNA families regulate selfrenewal in mouse embryonic stem cells. *Nature* 463, 621–626 (2010).
- Scott, G. K. et al. Coordinate suppression of ERBB2 and ERBB3 by enforced expression of micro-RNA miR-125a or miR-125b. J. Biol. Chem. 282, 1479–1486 (2007).
- Maimets, T., Neganova, I., Armstrong, L. & Lako, M. Activation of p53 by nutlin leads to rapid differentiation of human embryonic stem cells. *Oncogene* 27, 5277–5287 (2008)
- Johnson, S. M. et al. RAS is regulated by the let-7 microRNA family. Cell 120, 635–647 (2005).

- Arlt, M. F. et al. Replication stress induces genome-wide copy number changes in human cells that resemble polymorphic and pathogenic variants. Am. J. Hum. Genet. 84, 339–350 (2009).
- Durkin, S. G. et al. Replication stress induces tumor-like microdeletions in FHIT/ FRA3B. Proc. Natl Acad. Sci. USA 105, 246–251 (2008).
- Sfeir, A. et al. Mammalian telomeres resemble fragile sites and require TRF1 for efficient replication. Cell 138, 90–103 (2009).
- Gorgoulis, V. G. et al. Activation of the DNA damage checkpoint and genomic instability in human precancerous lesions. *Nature* 434, 907–913 (2005).
- 32. Bartkova, J. et al. DNA damage response as a candidate anti-cancer barrier in early human tumorigenesis. *Nature* **434**, 864–870 (2005).
- Casper, A. M., Nghiem, P., Arlt, M. F. & Glover, T. W. ATR regulates fragile site stability. Cell 111, 779–789 (2002).
- 34. Arlt, M. F., Durkin, S. G., Ragland, R. L. & Glover, T. W. Common fragile sites as targets for chromosome rearrangements. *DNA Repair (Amst.)* **5**, 1126–1135 (2006).
- 35. Esteban, M. A. et al. Vitamin C enhances the generation of mouse and human induced pluripotent stem cells. *Cell Stem Cell* **6**, 71–79 (2010).
- Kulkarni, A., Zschenker, O., Reynolds, G., Miller, D. & Murnane, J. P. Effect of telomere proximity on telomere position effect, chromosome healing, and sensitivity to DNA double-strand breaks in a human tumor cell line. *Mol. Cell. Biol.* 30, 578–589 (2010).
- Zschenker, O. et al. Increased sensitivity of subtelomeric regions to DNA doublestrand breaks in a human cancer cell line. DNA Repair (Amst.) 8, 886–900 (2009).
- Linardopoulou, E. V. et al. Human subtelomeres are hot spots of interchromosomal recombination and segmental duplication. Nature 437, 94–100 (2005).
- Riethman, H., Ambrosini, A. & Paul, S. Human subtelomere structure and variation. Chromosome Res. 13, 505–515 (2005).
- 40. Mayshar, Y. et al. Identification and classification of chromosomal aberrations in human induced pluripotent stem cells. Cell Stem Cell 7, 521–531 (2010).
- 41. Laurent, L. C. *et al.* Dynamic changes in the copy number of pluripotency and cell proliferation genes in human ESCs and iPSCs during reprogramming and time in culture. *Cell Stem Cell* **8**, 106–118 (2011).
- Baker, D. E. et al. Adaptation to culture of human embryonic stem cells and oncogenesis in vivo. Nature Biotechnol. 25, 207–215 (2007).
- Hastings, P. J., Lupski, J. R., Rosenberg, S. M. & Ira, G. Mechanisms of change in gene copy number. *Nature Rev. Genet.* 10, 551–564 (2009).
- 44. Mikkola, M. et al. Distinct differentiation characteristics of individual human embryonic stem cell lines. *BMC Dev. Biol.* **6**, 40 (2006).
- Deb-Řinker, P., Ly, D., Jezierski, A., Sikorska, M. & Walker, P. R. Sequential DNA methylation of the Nanog and Oct-4 upstream regions in human NT2 cells during neuronal differentiation. J. Biol. Chem. 280, 6257–6260 (2005).
- Horn, C. et al. Splinkerette PCR for more efficient characterization of gene trap events. Nature Genet. 39, 933–934 (2007).

 $\begin{tabular}{ll} \textbf{Supplementary Information} is linked to the online version of the paper at www.nature.com/nature. \end{tabular}$

Acknowledgements This work was supported by funding for the ESTOOLS consortium under the Sixth RFP of the EU (S.M.H., T.O., R.L. and O.B.), the Academy of Finland (T.O. and R.A.), the Finnish Cancer Organizations (R.L.), the Research Funds of the Helsinki University Hospital (T.O.), the Sigrid Jusélius Foundation (T.O.), the Stem Cell Network Canada, GL2 and ClHR (A.N.). S.M.H. is a recipient of a McEwen Post-doctoral Fellowship from the McEwen Centre for Regenerative Medicine. N.N.B. is the recipient of a New Investigator Award from the Ontario Institute for Cancer Research, through the Ontario Ministry of Research and Innovation. A.N. is Tier 1 Canada Research Chair in Stem Cells and Regeneration. We are grateful to I. Rogers, M. Faiz and K. Nagy for critically reading and editing the manuscript, and J. Ustinov, H. Sariola and J. Palgi for skilled assistance in the characterization of human iPS cells. We thank N. Rahkonen for sample processing, as well as the Finnish Microarray and Sequencing Centre (http://www.btk.fi/), and the Institute of Human Genetics, University of Bonn, for array processing

Author Contributions S.M.H. coordinated and performed most of the experiments in this project, analysed and interpreted the data, and prepared the manuscript. N.N.B. analysed and interpreted the data and prepared an early version of the manuscript. S.V. provided essential experimental assistance and performed some experiments in this study. R.W.C. performed, and advised on the planning of, FISH experiments. R.A. and E.N. analysed and interpreted the data and coordinated the sample processing of the arrays. O.B. and M.P. provided analysed data and samples from Illumina arrays for validation. M.S., S.N., R.H., R.T., M.M., C.O. and K.L. contributed experimentally. D.P.B-J. and K.A. provided essential experimental material and support. R.L. directed the SNP array data generation and analysis. T.O. directed, coordinated and supervised the first stage of the project and contributed to the preparation of the manuscript. A.N. prepared the manuscript, supervised the second stage of the project and helped to interpret the data. K.A. and R.L. contributed equally as co-authors. A.N. and T.O. contributed equally as senior authors.

Author Information Affymetrix SNP array 6.0 data from each individual sample have been deposited with the NCBI Gene Expression Omnibus (http://www.ncbi.nlm.nih.gov/geo/) under accession number GSE26173. Reprints and permissions information is available at www.nature.com/reprints. The authors declare no competing financial interests. Readers are welcome to comment on the online version of this article at www.nature.com/nature. Correspondence and requests for materials should be addressed to T.O. (timo.otonkoski@helsinki.fi) or A.N. (nagy@lunenfeld.ca).

METHODS

SNP array 6.0 analysis. Sample handling and hybridization were performed as previously described¹³. All human ES cell line analysis files, with the exception of CA1 and CA2, were obtained from a previous study¹³. For detecting CNVs and genotype calls, the Affymetrix Genotyping Console 3.0.2 and the Birdseed (v2) algorithm were used, respectively. CNV locations are based on the human genome assembly of March 2006 (NCBI36/hg18). Samples were normalized to 40 International HapMap samples hybridized on the same platform to decrease technical variation (refer to Supplementary Table 11 for HapMap sample codes and SNP profiles)13. For CNV calls, regional GC correction, 10-kilobase (kb) size cut-off value, and a minimum of ten markers were used as analysis configurations. All of the array samples passed quality control requirements, having contrast QC (quality control) and MAPD (median absolute pairwise difference) values within the boundaries (Supplementary Table 12). All identified CNVs were included, except for CNVs spanning centromeric regions (the average marker distribution within these regions is too large (>40kb)) and the Y chromosome in female samples, which was considered as false positive and excluded from the analysis. R (v2.9.2) software and the program Microsoft Excel 2008 (v12.2.3) were used for in silico data analysis and CNV data parsing. R and StatPlus for Microsoft Excel (v5.8.3.8) were used for statistical analysis and P-value calculations.

Cell culture. Human fibroblast lines were cultured in 10% FBS (PromoCell) and GlutaMAX in DMEM (Gibco). Human iPS cells were cultured on mitotically inactivated mouse embryonic fibroblasts (MEFs) in KnockOut DMEM supplemented with 20% KnockOut Serum Replacement (Gibco), 0.1 mM 2-mercaptoethanol (Gibco), 1× GlutaMAX (Gibco), 1× non-essential amino acids (Gibco), 1× ITS liquid media supplement (Sigma) and 6 ng ml⁻¹ FGF2 (Sigma). Human iPS cells were passaged using 20 U ml⁻¹ type IV collagenase (Gibco), approximately every 5 days. Human ES cells were cultured and maintained as previously described 13,44. Bisulphite sequencing. Bisulphite conversion was carried out on each DNA sample (1 µg) using the EpiTect Bisulfite Kit (QIAGEN). OCT4 and NANOG promoters were amplified using previously published⁴⁵ bisulphite-specific primers (Supplementary Table 13) and a PCR protocol consisting of an initial 1-min denaturation step followed by 35 cycles of 95 °C for 15 s, 54 °C for 30 s and 72 °C for 45 s. The resultant PCR product was sequenced using either the appropriate forward primer or the reverse primer at the Centre for Applied Genomics (Toronto). At CG dinucleotides, cytidine-guanine was scored as methylated CG, whereas thymidine-guanine was considered to be an unmethylated CG. Ambiguous CGs were scored using control fibroblasts as a methylated reference. Splinkerette PCR and quantitative PCR. Genomic DNA was extracted using the GenElute Mammalian Genomic DNA Miniprep kit (Sigma). Splinkerette PCR was performed as described previously⁴⁶. Splinkerette primers are listed in Supplementary Table 13, and the start position and location of viral integration sites are listed in Supplementary Table 14. Total RNA was extracted using a NucleoSpin RNA II kit (Macherey-Nagel), with on-column DNase treatment. The amount of RNA was quantified using a Nanodrop (NanoDrop Technologies), and RNA was separated on 1% agarose gels to check its quality. Highly pure RNAs were reverse transcribed using the QuantiTect Reverse Transcription Kit (QIAGEN) as per the manufacturer's protocol. Supplementary Table 13 lists all PCR-amplified genes and CNVs and their corresponding primers. Annealing temperatures of 55-58 °C were used for most primers. For quantitative PCR (Q-PCR), we used LuminoCt SYBR Green qPCR ReadyMix (Sigma), a JANUS automated liquid handling robot (PerkinElmer) and the CFX384 real-time PCR detection system (Bio-Rad).

False discovery estimation and CNV validation. The false positive estimate for the samples was studied by hybridizing three HapMap samples in four replicates (Supplementary Table 7). By using analysis settings identical to those for the main data, we found that, on average, 76.2% of total CNV size was detected in all four replicates, 15.4% in three, 4.8% in two and 3.6% only in one of the replicates. By contrast, for homozygous deletions, no CNVs were detected in only one replicate, indicating very low or negligible false positive detection for homozygous deletions. These values are analogous to those from an earlier study⁴⁷. For further validation of CNVs, CNVs from three ES cell lines were also confirmed by running the same samples on an Illumina Human 610-Quad Chip platform. The CNVs from the Illumina data matched 75% (on average) of the CNVs observed in the Affymetrix data (Supplementary Table 5). The Illumina Data were analysed for log Bayes factors greater than 10 using QuantiSNP software (http://www.well.ox.ac.uk/QuantiSNP). Q-PCR was also used to validate some of the discovered CNVs and to estimate the false discovery rate (see Supplementary Fig. 7 for details).

Human iPS cell generation. Human foreskin fibroblasts (HFFs; CRL-2429, ATCC) and human lung embryonic fibroblasts (IMR90; CCL-186, ATCC) were reprogrammed to human iPS cells as previously described¹. Briefly, retroviral constructs—pMXs-OCT4, pMXs-SOX2, pMXs-KLF4, pMXs-NANOG and

pMXs-LIN28-were obtained by cloning the human cDNA encoding each of the factors into the pMXs retroviral vector. pMXs constructs were transfected separately into the 293-GPG packaging cell line 48 (10^6 cells per 100-mm-diameter culture dish) to produce retroviral supernatant. Fibroblast lines, seeded overnight, were infected twice with different, but equally mixed, combinations of viral supernatants (0.5 ml each supernatant, 4×10^5 cells per 60-mm-diameter dish), over the course of 2 days (see Supplementary Table 2 for the different combinations). The following day, the medium was changed to fibroblast medium. On day 4, infected cells were collected and reseeded on mitotically inactivated MEFs. The next day, the medium was changed to human ES cell medium containing FGF2 as described elsewhere44. Medium was replenished every 2 days. At 20-30 days post transduction, depending on colony size, colonies with human ES-cell-like morphology were picked and expanded for further analysis. For the new piggyBac-transposon-generated human iPS cell lines, HFF cells were seeded in 60-mm-diameter plates at a density of 4×10^5 cells per plate. After 24 h culturing, cells were trypsinized, and they were then electroporated using a 100-µl tip and program number 20 in the Neon Transfection System (Invitrogen) with 250 ng each transposon construct³, 500 ng PB-rtTA construct⁴ and 500 ng pCyL43 PB transposase plasmid³. After 24 h, the medium was supplemented with doxycycline (day 0) and was then changed to human ES cell medium at 48 h after transfection. Cells were fed every 2 days with doxycycline-containing medium (1.5 μg ml⁻¹) for 20–30 days. Doxycycline was removed one passage after picking human iPS cell clones. Human iPS cell colonies were picked and cultured as described above for retrovirus-derived human iPS cells. For sample collection and genomic DNA extraction, cells were scraped in collagenase or dispase (1 mg ml⁻¹) and centrifuged twice at low speed to pellet the cells as small colonies and remove the majority of MEFs, which remain as single cells in suspension and are aspirated with the medium.

Pluripotent stem cell differentiation. For embryoid body formation, the cells were detached by collagenase IV treatment and plated onto ultra-low attachment dishes (Corning) in human ES cell medium without FGF2. The culture medium was changed every 3 days. After 10 days, the embryoid bodies were collected for further analysis. Teratomas were generated as described elsewhere⁴⁴.

For endodermal differentiation, cells were differentiated as described elsewhere 49. In brief, 80-90% confluent cells were cultured on a mitotically inactivated MEF layer for 24 h in RPMI 1640 medium (Gibco) supplemented with GlutaMAX, 100 ng ml⁻¹ recombinant human activin A (provided by M. Hyvönen) and 10% (v/v) WNT3A-conditioned medium (DMEM supplemented with 10% (v/v) KnockOut Serum Replacement and GlutaMAX, conditioned for 7 days on L Wnt-3A cells (ATCC)). The cells were cultured for another 2 days in RPMI 1640 with GlutaMAX, $100\,\mathrm{ng\,ml}^{-1}$ activin A and 0.2% (v/v) FBS to the definitive endoderm (DE) stage. DE-stage cells were then cultured for 3 days in RPMI 1640 supplemented with GlutaMAX, 2% (v/v) FBS and 50 ng ml⁻¹ KGF (R&D Systems) to the primitive gut tube (PG) stage. The cells were cultured for another 3 days with DMEM supplemented with GlutaMAX, 1% (v/v) B-27 supplement (Gibco), 2 µM all-trans retinoic acid (Sigma), 0.25 µM KAAD-cyclopamine (Toronto Research Chemicals) and 50 ng ml⁻¹ noggin (R&D Systems) to the posterior foregut (PF) stage. Finally, the cells were cultured for another 3 days in DMEM supplemented with GlutaMAX and 1% (v/v) B-27 supplement to the pancreatic endoderm (PE) stage. The medium was changed every day, and RNA samples were collected at the end of every stage for Q-PCR and immunocytochemistry.

For neuronal differentiation, cultured cells were detached with type IV collagenase and transferred as small colonies in a 1/1 ratio to ultra-low binding six-well plates (Costar) in NSE medium (Euromed medium supplemented with sodium pyruvate (Gibco), GlutaMAX, N-2 supplement (Gibco), B-27 supplement, 25 μg ml $^{-1}$ human insulin (Sigma), non-essential amino acids, 0.1 mM 2-mercaptoethanol and 0.05% (v/v) BSA (Gibco)). After 6 days in suspension culture, the spheres were transferred onto plates coated with 1/100-diluted growth-factor-reduced Matrigel (BD Biosciences) in a 1/1 ratio of NSE and NB medium. NB medium consists of neurobasal medium (Gibco) supplemented with GlutaMAX, non-essential amino acids, 2% (v/v) B-27 supplement, 2 μg ml $^{-1}$ heparin (Sigma), 0.1 mM 2-mercaptoethanol and 0.05% (v/v) BSA. The cells were cultured for another 10 days, and the medium was changed every other day. The cells were then immunostained for β III-tubulin and nestin.

Immunocytochemistry. Samples were washed with PBS and fixed in 4% paraformaldehyde (Electron Microscopy Sciences) for 15 min at room temperature. After three washes in PBS, cells were permeabilized in 0.2% Triton X-100 in PBS for 12 min and were subsequently washed three times with PBS. Samples were then blocked with Protein Block for 10 min, washed three times with PBS and incubated with primary antibodies overnight at 4 °C. The next day, cells were washed twice with Tween-20-PBS and twice with PBS. Secondary antibodies—Alexa Fluor 594 anti-goat IgG or Alexa Fluor 488 anti-rabbit IgG (both from Invitrogen)—were diluted 1/500 in 0.2% Triton X-100 in PBS, and cells were

RESEARCH ARTICLE

incubated with antibodies for 30 min at 4 $^{\circ}$ C. Primary antibodies were anti-NANOG (Santa Cruz Biotechnology), anti-OCT4 (Santa Cruz Biotechnology), anti-FOXA2 (Santa Cruz Biotechnology), anti-FOXA2 (Santa Cruz Biotechnology), anti-FOXA2 (Santa Cruz Biotechnology), anti-TRA-1-60 (Millipore), anti- $^{\circ}$ BIII-tubulin (R&D Systems), anti-PDX1 (Beta Cell Biology Consortium), anti-NKX6.1 (Beta Cell Biology Consortium) and anti-nestin (Chemicon) antibodies.

Three-dimensional FISH. Human iPS cells were cultured on glass slides seeded with MEF feeder cells. Samples were fixed in 2% paraformaldehyde in PBS for 5 min, washed three times with PBS, permeabilized with 0.5% Triton X-100 in PBS for 20 min, and washed three more times with PBS. The slides were then placed in a solution of 20% glycerol in PBS overnight at 4 $^{\circ}$ C. Slides were frozen in liquid nitrogen, allowed to partly thaw and then placed back into the 20% glycerol solution. This process was repeated five times. After the freeze-thaw procedure, the slides were washed three times in PBS and then placed in a solution of 0.1 M HCl for 5 min. Slides were then washed with 2× SSC and left overnight at 4 °C in a solution of 50% formamide in 2× SSC. Before hybridization, the slides were denatured in a solution of 70% formamide in $2\times$ SSC at 75 °C for 3 min and then immediately placed in a separate container containing the same denaturation solution that had been kept on ice. Control (Bac clone RP11-788E9) and test (Bac clone RP11-58E1) probes were obtained from the Centre for Applied Genomics (Toronto). Test and control probe region coordinates were chr1: 146,828,351-147,150,258 and chr1: 104,629,600-104,808,778, respectively, based on the human genome assembly of March 2006 (NCBI36/hg18). The test probe was selected based on a cluster of CNVs consisting of mainly deletions within a

frequently affected region in chromosome 1 (coordinates Chr1: 145,797,568-147,958,358). The probes were directly labelled with either spectrum green or orange fluorophore-conjugated nucleotides. A hybridization mixture consisting of labelled probe and human Cot-1 DNA in a 2/1 ratio in hybridization buffer (50% formamide, 10% dextran sulphate, 50 nM sodium phosphate buffer, pH 7.0, in $2\times$ SSC) was prepared and denatured at 80 °C for 5 min and then allowed to partially reanneal at 37 $^{\circ}$ C for 20 min. This mixture was then applied to the slides that had been kept on ice during the previous step and left to hybridize overnight at 37 °C. After hybridization, the slides were washed in 50% formamide in $2 \times$ SSC three times at 42 $^{\circ}$ C, then once in a solution of 0.5× SSC at 60 $^{\circ}$ C, and finally in a solution of 2× SSC at room temperature. Slides were mounted with VECTASHIELD containing DAPI (Vector Laboratories) before fluorescence imaging. Images were collected using an IX81 inverted brightfield microscope (Olympus) equipped with a Cascade 512 camera (Photometrics) using a ×60, 1.32 NA, oil-immersion objective and Immersion Oil Type DF (Cargille Labs) imaging medium. Images were collected using MetaMorph Premier 7.7 (Molecular Devices) and analysed with ImageJ (National Institutes of Health).

- Redon, R. et al. Global variation in copy number in the human genome. Nature 444, 444–454 (2006).
- Ory, D. S., Neugeboren, B. A. & Mulligan, R. C. A stable human-derived packaging cell line for production of high titer retrovirus/vesicular stomatitis virus G pseudotypes. *Proc. Natl Acad. Sci. USA* 93, 11400–11406 (1996).
- Kroon, E. et al. Pancreatic endoderm derived from human embryonic stem cells generates glucose-responsive insulin-secreting cells in vivo. Nature Biotechnol. 26, 443–452 (2008).



Somatic coding mutations in human induced pluripotent stem cells

Athurva Gore^{1*}, Zhe Li^{1*}, Ho-Lim Fung¹, Jessica E. Young², Suneet Agarwal³, Jessica Antosiewicz-Bourget⁴, Isabel Canto², Alessandra Giorgetti⁵, Mason A. Israel², Evangelos Kiskinis⁶, Je-Hyuk Lee⁷, Yuin-Han Loh³, Philip D. Manos³, Nuria Montserrat⁵, Athanasia D. Panopoulos⁸, Sergio Ruiz⁸, Melissa L. Wilbert², Junying Yu⁴, Ewen F. Kirkness⁹, Juan Carlos Izpisua Belmonte^{5,8}, Derrick J. Rossi¹⁰, James A. Thomson⁴, Kevin Eggan⁶, George Q. Daley³, Lawrence S. B. Goldstein² & Kun Zhang¹

Defined transcription factors can induce epigenetic reprogramming of adult mammalian cells into induced pluripotent stem cells. Although DNA factors are integrated during some reprogramming methods, it is unknown whether the genome remains unchanged at the single nucleotide level. Here we show that 22 human induced pluripotent stem (hiPS) cell lines reprogrammed using five different methods each contained an average of five protein-coding point mutations in the regions sampled (an estimated six protein-coding point mutations per exome). The majority of these mutations were non-synonymous, nonsense or splice variants, and were enriched in genes mutated or having causative effects in cancers. At least half of these reprogramming-associated mutations pre-existed in fibroblast progenitors at low frequencies, whereas the rest occurred during or after reprogramming. Thus, hiPS cells acquire genetic modifications in addition to epigenetic modifications. Extensive genetic screening should become a standard procedure to ensure hiPS cell safety before clinical use.

Human induced pluripotent stem cells have the potential to revolutionize personalized medicine by allowing immunocompatible stem cell therapies to be developed^{1,2}. However, questions remain about hiPS cell safety. For clinical use, hiPS cell lines must be reprogrammed from cultured adult cells, and could carry a mutational load due to normal *in vivo* somatic mutation. Furthermore, many hiPS cell reprogramming methods use oncogenes that may increase the mutation rate. Additionally, some hiPS cell lines have been observed to contain large-scale genomic rearrangements and abnormal karyotypes after reprogramming³. Recent studies also revealed that tumour suppressor genes, including those involved in DNA damage response, have an inhibitory effect on nuclear reprogramming⁴⁻⁹. These findings suggest that the process of reprogramming could lead to an elevated mutational load in hiPS cells.

To probe this issue, we sequenced the majority of the protein-coding exons (exomes) of 22 hiPS cell lines and the nine matched fibroblast lines from which they came (Table 1). These lines were reprogrammed in seven laboratories using three integrating methods (four-factor retroviral, four-factor lentiviral and three-factor retroviral) and two non-integrating methods (episomal vector and messenger RNA delivery into fibroblasts). All hiPS cell lines were extensively characterized for pluripotency and had normal karyotypes before DNA extraction (Supplementary Methods). Protein-coding regions in the genome were captured and sequenced from the genomic DNA of hiPS cell lines and their matched progenitor fibroblast lines using either padlock probes 10,11 or in-solution DNA or RNA baits 12,13. We searched for single base changes, small insertions/deletions and alternative splicing variants, and identified 12,000–18,000 known and novel variants for each cell line that had sufficient coverage and consensus quality (Table 1).

hiPS cell lines contain a high level of mutational load

We identified sites that showed the gain of a new allele in each hiPS cell line relative to their corresponding matched progenitor fibroblast genome. A total of 124 mutations were validated with capillary sequencing (Fig. 1, Table 2 and Supplementary Fig. 1), which revealed that each mutation was fixed in heterozygous condition in the hiPS cell lines. No small insertions/deletions were detected. For three hiPS cell lines (CV-hiPS-B, CV-hiPS-F and PGP1-iPS), the donor's complete genome sequence obtained from whole blood is publicly available^{14,15}; we used this information to further confirm that all 27 mutations in these lines were bona fide somatic mutations. Because 84% of the expected exomic variants16 were captured at high depth and quality, the predicted load is approximately six coding mutations per hiPS cell genome (see Table 1 for details). The majority of mutations were missense (83 of 124), nonsense (5 of 124) or splice variants (4 of 124). Fifty-three mis-sense mutations were predicted to alter protein function¹⁷ (Supplementary Table 1). Fifty mutated genes were previously found to be mutated in some cancers^{18,19}. For example, *ATM* is a wellcharacterized tumour suppressor gene found mutated in one hiPS cell line, and NTRK1 and NTRK3 (tyrosine kinase receptors) can cause cancers when mutated²⁰ and contained damaging mutations in three hiPS cell lines (CV-hiPS-F, iPS29e and FiPS4F-shpRB4.5) that were reprogrammed in three labs and came from different donors. Two kinase genes from the NEK family, which is related to cell division, were mutated in two independent hiPS cell lines. In addition to cancerrelated genes, 14 of the 22 lines contained mutations in genes with known roles in human Mendelian disorders²¹. Three pairs of hiPS cell lines (iPS17a and iPS17b, dH1F-iPS8 and dH1F-iPS9, and CF-RiPS1.4 and CF-RiPS1.9) shared three, two and one mutation, respectively;

¹Department of Bioengineering, Institute for Genomic Medicine and Institute of Engineering in Medicine, University of California at San Diego, 9500 Gilman Drive, La Jolla, California 92093, USA. ²Department of Cellular and Molecular Medicine and Howard Hughes Medical Institute, University of California at San Diego, 9500 Gilman Drive, La Jolla, California 92093, USA. ³Division of Pediatric Hematology/Oncology, Children's Hospital Boston and Dana Farber Cancer Institute, Boston, Massachusetts 02115, USA. ⁴Department of Anatomy, University of Wisconsin-Madison, Misconsin 53705, USA. ⁵Center of Regenerative Medicine, 08003 Barcelona, Spain. ⁶Howard Hughes Medical Institute, Harvard Stem Cell Institute, Department of Stem Cell and Regenerative Biology, Harvard University, Cambridge, Massachusetts 02138, USA. ⁷Department of Genetics, Harvard Medical School, Boston, Massachusetts 02135, USA. ⁸Salk Institute for Biological Studies, La Jolla, California 92037, USA. ⁹The J. Craig Venter Institute, Rockville, Maryland 20850, USA. ¹⁰Immune Disease Institute, Children's Hospital Boston, Boston, Massachusetts 02115, USA. ⁸These authors contributed equally to this work.

Table 1 | Sequencing statistics for mutation discovery

Cell line	Exome capture method	Quality-filtered sequence (bp)	No. of high-quality coding variants	dbSNP percentage	Shared high-quality coding region (bp)	No. of coding mutations observed/projected
CV-hiPS-F	Padlock + SegCap EZ	9,928,014,640	15,595	98%	16,374,878	14/15
CV-hiPS-B	SegCap EZ	7,977,894,480	14,876	98%	21,891,518	10/12
CV fibroblast	Padlock + SegCap EZ	7,586,731,600	15,442	98%	, <u> </u>	_
DF-6-9-9	Padlock + SegCap EZ*	9,289,593,520	14,366	95%	17,806,151	6/7
DF-19-11	SegCap EZ	3,212,662,880	13,792	95%	21,342,017	7/9
iPS4.7	SegCap EZ	3,132,462,400	14,154	95%	21,729,562	4/5
Foreskin fibroblast	Padlock + SegCap EZ*	8,430,654,720	14,819	95%	_	_
PGP1-iPS	SegCap EZ	4,599,556,400	14,105	95%	19,681,915	3/4
PGP1 fibroblast	SureSelect	3,504,437,120	14,781	95%	_	_
dH1F-iPS8	SegCap EZ	3,950,994,160	13,552	96%	16,874,057	8/10
dH1F-iPS9	SegCap EZ	3,945,196,800	14,191	95%	21,536,158	3/4
dH1F fibroblast	SegCap EZ	3,373,535,920	13,838	95%	_	_
iPS11a	SureSelect	1,836,303,440	13,845	95%	18,557,098	4/5
iPS11b	SureSelect	3,378,603,200	15,152	95%	17,206,934	7/8
Hib11 fibroblast	SureSelect	5,660,864,960	13,579	95%		_
iPS17a	SureSelect	4,805,756,800	15,039	95%	17,888,773	4/5
iPS17b	SureSelect	7,129,037,520	15,400	95%	19,902,076	5/6
Hib17 fibroblast	SureSelect	3,962,506,880	13,365	96%	_	_
iPS29A	SureSelect	4,112,237,360	13,464	94%	17,328,182	2/3
iPS29e	SureSelect	1,669,916,080	13,800	94%	18,985,791	7/9
Hib29 fibroblast	SureSelect	4,388,388,320	14,445	95%	_	_
dH1cF16-iPS1	SeqCap EZ	4,321,661,440	15,061	95%	19,601,528	2/2
dH1cF16-iPS4	SeqCap EZ	4,668,085,920	14,958	95%	23,956,732	6/7
dH1cF16 fibroblast	SeqCap EZ	4,178,664,160	14,879	95%	_	_
CF-RiPS1.4	SeqCap EZ	4,733,743,840	11,344	96%	21,272,233	2/3
CF-RiPS1.9	SeqCap EZ	3,143,591,760	13,674	95%	21,165,013	5/6
CF fibroblast	SeqCap EZ	3,204,874,880	11,855	96%	_	_
FiPS3F1	SeqCap EZ	3,397,397,360	13,333	94%	20,723,620	4/5
FiPS4F7	SeqCap EZ	3,346,801,280	14,584	94%	21,608,258	2/3
HFFXF fibroblast	SeqCap EZ	3,331,494,880	13,040	94%	_	_
FiPS4F2p9	SeqCap EZ	4,725,258,400	18,033	92%	25,188,054	7/7
FiPS4F2p40	SeqCap EZ	4,848,006,000	18,376	92%	25,411,595	11/11
FiPS4F-shpRB4.5	SeqCap EZ	4,911,008,400	19,491	92%	25,240,944	8/8
IMR90 fibroblast	SeqCap EZ	5,019,916,240	18,220	92%	_	_

Quality-filtered sequence represents the total amount of sequence data generated that passed the Illumina GA Ilx quality filter (bp, base pair). The number of high-quality coding variants is the number of variants found with a sequencing depth of at least eight and a consensus quality score of at least 30. The dbSNP percentage represents the percentage of identified variants present in the Single Nucleotide Polymorphism Database. The shared coding region is the portion of the genome, in base pairs, that was sequenced at high depth and quality in both the iPS cell line and its progenitor fibroblast. The number of coding mutations lists both the number of identified coding mutations and a projection of the total number of identified mutations based on the fraction of Consensus Coding Sequence variants 16 (out of \sim 17,000 expected variants) successfully identified in both hiPS cells and fibroblasts.

^{*}For these cell lines, mutation calling was performed individually using both padlock probe data and hybridization-capture data. Each method found five mutations, four of which were shared, leading to a total of six mutations. Padlock probe and hybridization capture have separate strengths (specificity versus unbiased coverage); it seems that these factors directly affect the ability to find separate mutations.

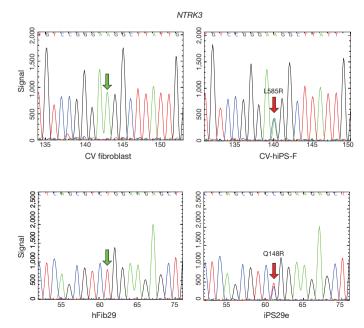


Figure 1 \mid hiPS cells acquired protein-coding somatic mutations. Somatic mutations in the gene *NTRK3* were found in two independent hiPS cell lines but were not present in their fibroblast progenitors. Detailed information for all mutations is in the Supplementary Information.

these most probably arose in shared common progenitor cells before reprogramming. However, most hiPS cell lines derived from the same fibroblast line did not share common mutations (Table 2 and Supplementary Table 1).

These data raise the possibility that a significant number of mutations occur during or shortly after reprogramming and then become fixed during colony picking and expansion. An alternative hypothesis is that the mutations we found are simply the result of age-accrued biopsy heterogeneity or normal somatic mutation during in vitro fibroblast cell culture. The skin biopsies were collected from donors of ages varying from newborn to 82 years; biopsy heterogeneity therefore does not seem to have a primary role, as the mutational load is not correlated (squared linear correlation coefficient, $R^2 = 0.046$) with donor age (Supplementary Fig. 2). We attempted to grow clonal fibroblasts to obtain a control for single-cell mutational load, but a direct assessment was not possible owing to technical difficulties in mimicking the exact culture conditions (Supplementary Methods). Assuming that the skin biopsy is mutation free, we were able to use previously published values for the typical mutation rate in culture to obtain an expectation of ten times fewer mutations per genome than we observed ($P < 1.27 \times 10^{-53}$; Supplementary Methods), indicating that hiPS cell mutational load is higher than normal-culture mutational load. We define the term 'reprogramming-associated mutations' to describe somatic mutations observed in these hiPS cell lines. Reprogramming-associated mutations could pre-exist at low frequencies in the fibroblast population, could occur during the reprogramming process or could occur after reprogramming. All reprogrammingassociated mutations have become fixed in the hiPS cell population.

Table 2 | Genes found to be mutated in coding regions in hiPS cells

Cell line	Mutated genes	No. of non-silent mutations	No. detectable at low frequency in fibroblasts (present/tested)
CF-RiPS1.4	OR52E8, TEAD4	1	NA
CF-RiPS1.9	OR52E8, FAM171A1, TMED9, TEAD4, RASEF	3	NA
CV-hiPS-B	MMP26, DYNC1H1, VMO1, DSC3, CELSR1, FLT4, UBE2CBP, ARHGEF5, IGF2BP3, DLG3	7	7/8
CV-hiPS-F	IQGAP3, SPEN, TNR, PBLD, OR6Q1, INTS4, GSG1, NTRK3, DNAH3, GOLGA4, FAT2, C6orf25, UBR5, SDR16C5	12	4/7
DF19.11	SPATA21, RGS8, LPPR4, KCNJ8, SETBP1, ZNF471, TMEM40	5	NA
DF6-9-9	ZZZ3, AKR1C4, NEK5, DAPL1, ITCH, PPP1R2	5	0/5
dH1CF16-iPS1	IRGQ, TM9SF4	1	NA
dH1CF16-iPS4	PKP1, MYOG, ABCA3, PTPRM, RANBP3L, CALN1	4	NA
dH1F-iPS8	CABC1 (ADCK3), C1orf100, OR5AN1, CACNG3, MYRIP, SLC1A3, DSP, KLRG2	6	NA
dH1F-iPS9	SEMA6C, MYRIP, SLC1A3	3	NA
FiPS3F1	SORCS3, GLRA3, CARM1, EPB41L1	2	NA
FiPS4F7	GDF3, ZER1	2	NA
iPS11a	GTF3C1, SALL1, SLC26A3, ZNF16	3	1/1
iPS11b	MARCKSL1, PRDM16, ATM, LRP4, TCF12, SH3PX3 (SNX33), OSBPL3	5	0/1
iPS17a	HK1, ANKRD12, SCN1A, IFNGR1	4	NA
iPS17b	HK1, CCKBR, ANKRD12, SCN1A, IFT122	5	1/1
iPS29A	PRICKLE1, RFX6	2	2/2
iPS29e	C14orf174 (SAMD15), NTRK3, VAC14, ASB3, STX7, POLR1C, LINGO2	6	1/4
iPS4.7	POLE, UBA2, L3MBTL2, C4orf41	2	NA
PGP1-iPS	C11orf67, OSBPL8, NEK11	1	1/3
FiPS4F2	TMEM57, RANBP6, CTSL1, SAV1, KRT25, BCL2L12, LGALS1, TTYH2*, COPA*, ARSB*, MT1B*	7	NA
FiPS4F-shpRB4.5	NTRK1, CD1B, LRCH3, SH3TC1, GPC2, CDK5RAP2, MYH4, TRMU	5	NA

The full details of each mutation are in Supplementary Table 1.

Reprogramming-associated mutations arise through multiple mechanisms

To test whether some observed mutations were present in the starting fibroblasts at low frequency before reprogramming, we developed a new digital quantification assay (DigiQ) to quantify the frequencies of 32 mutations in six fibroblast lines using ultradeep sequencing (Supplementary Figs 3 and 4). We amplified each mutated region from the genomic DNA of 100,000 cells with a high-fidelity DNA polymerase and sequenced the pooled amplicons with an Illumina Genome Analyser at an average coverage of 10⁶. Although the raw sequencing error is roughly 0.1–1% with the Illumina sequencing platform, detection of rare mutations at a lower frequency is possible with proper filtering and careful selection of controls²². For each fibroblast line, we included the mutation-carrying hiPS cell DNA as the positive control and a 'mutation-free' DNA sample as the negative control for sequencing errors (Supplementary Methods). Comparison of the allelic counts at the mutation positions between the fibroblast lines and the negative controls allowed us to distinguish rare mutations from sequencing errors and estimate the detection limit of the assay. Seventeen of the 32 mutations were found in fibroblasts in the range of 0.3-1,000 in 10,000, and 15 mutations were not detectable (Supplementary Tables 2 and 3). In each fibroblast line with more than one detectable rare mutation, the frequencies of the mutations were very similar, which suggests that a small subpopulation of each fibroblast line contains all pre-existing hiPS cell mutations and that the rest of the cells lacked any of them.

We extended this analysis by asking whether all of the hiPS cell mutations could have pre-existed in the fibroblast populations. For the 15 mutations not detected with the DigiQ assay, the detection limits can be estimated (Supplementary Methods). At seven of the 15 sites, the sequencing quality was high enough that rare mutations at frequencies of 0.6–5 in 100,000 should be detectable with our assay (Supplementary Table 3). Because 30,000–100,000 fibroblast cells were used in the reprogramming experiments, we can rule out the presence of two mutated genes (NTRK3 and POLR1C) in more than one cell of the starting fibroblast population, and five others were present in no more than one or two cells.

As another test of the hypothesis that all of the mutations preexisted in fibroblasts before reprogramming, we examined the exomes of two hiPS cell lines derived from fibroblast line dH1cf16, which was clonally derived from the dH1F fibroblast line and passaged the minimum amount to generate enough cells for reprogramming. The two hiPS cell lines derived from the non-clonal dH1F fibroblast line contained eight and, respectively, three new mutations not found in the fibroblasts; we observed a very similar independent mutational load in the clonal lines (six new mutations in the hiPS cell line dH1cf16-iPS1 and two new mutations in the hiPS cell line dH1cf16-iPS4). Together, these experiments establish that although some of the reprogramming-associated mutations were likely to pre-exist in the starting fibroblast cultures, the others occurred during reprogramming and subsequent culturing. Specific distributions tend to vary across hiPS cell lines (Supplementary Table 3).

Mutations that occur during reprogramming could be due in part to a significantly elevated mutation rate during reprogramming. It is also possible that selection could have an important role. We tested the possibility that an elevated mutation rate might occur because the reprogramming process might be inducing transient repression of p53 (also known as TP53), RB1 and other tumour suppressor genes, which are known to inhibit reprogramming and are required for normal DNA damage responses. Simian virus 40 large-T antigen, which inactivates tumour suppressor and DNA damage response genes²³ (including p53 and RB1), was expressed during reprogramming of three analysed hiPS cell lines (DF6-9-9, DF19-11 and iPS4.7)²⁴. Another hiPS cell line (FiPS4F-shpRB4.5) was generated while directly knocking down RB1 (Supplementary Fig. 5). However, the observed mutational load was very similar in these lines in comparison with the others, indicating that reprogramming-associated mutations cannot be explained by an elevated mutation rate caused by p53 or RB1 repression.

We also probed whether additional mutations could become fixed during extended passaging by extending our analysis of one hiPS cell line. Although most of our hiPS cell lines were sequenced at fairly low passage number (less than 20), to measure the effect of post-reprogramming culturing directly we also sequenced one hiPS cell line (FiPS4F2) at two passages (9 and 40). We discovered that all seven mutations identified in the passage-9 line remained fixed in the passage-40 line, but that four additional mutations were found to be fixed in the passage-40 cell line.

To test the possibility that selection operates during hiPS cell generation, we performed an enrichment analysis to determine whether reprogramming-associated mutated genes were more likely to be

^{*} Mutation was observed at passage 40 but not at passage 9. FiPS4F2 was sequenced at both passage 9 and passage 40. Seven mutations were present after reprogramming (FiPS4F2P9), and four more became fixed after extended culturing (FiPS4F2P40). All seven mutations found after reprogramming were also present after extended culturing.

observed than random somatic mutation in cancer cells. We used the COSMIC database as a source of genes commonly mutated in cancer 18 . We discovered that the reprogramming-associated mutated genes were significantly enriched for genes found mutated in cancer (P = 0.0019; Supplementary Information), which implies that some mutations were selected during reprogramming.

As an alternative test of the selection hypothesis, we asked whether mutations associated with reprogramming could be functional, on the basis of the non-synonymous/synonymous (NS/S) ratio. Traditionally, the analysis of the NS/S ratio is applied to germline mutations that have evolved over a long period of evolutionary time, and is not directly applicable to somatic mutations. However, functional mutations are known to be positively selected in cancers, allowing us to make a direct comparison with mutation characteristics found in cancer genomes. Strikingly, the NS/S ratio is very similar between mutations identified in three recent cancer genome sequencing projects^{25–27} and the reprogramming-associated mutations we found (2.4/1 and 2.6/1, respectively), indicating that a similar degree of selection pressure may be present.

We also checked whether reprogramming-associated mutations could provide a common functional advantage, through a pathway enrichment analysis using Gene Ontology terms²⁸. No statistically significant similarity was identified, indicating that mutated genes have varied cellular functions. Again, identical results were found when performing the same analysis on mutations identified during the genome sequencing of melanoma, breast cancer and lung cancer samples^{25–27}. This lack of enrichment in cancer genomes is generally thought to be due to the presence of many passenger mutations in cancer cells, which could also be the cause for reprogramming-associated mutations. Nonetheless, these analyses suggest that selection of potentially functional mutations could have a role in amplifying rare-mutation-carrying cells and, when coupled with the single-cell bottleneck in hiPS cell colony picking, could contribute to the fixation of initially low-frequency mutations throughout the entire hiPS cell population.

Discussion

Taken together, our results demonstrate that pre-existing and new mutations that occur during and after reprogramming all contribute to the high mutational load we discovered in hiPS cell lines. Although we cannot completely rule out the possibility that reprogramming itself is 'mutagenic', our data argue that selection during hiPS cell reprogramming, colony picking and subsequent culturing may be contributing factors. A corollary is that if reprogramming efficiency is improved to a level such that no colony picking and clonal expansion is necessary, the resulting hiPS cells could potentially be free of mutations.

Despite the power of our experimental approach to identify and characterize reprogramming-associated mutations accurately, their functional significance remains to be shown. This issue parallels a general problem facing the genomics community: high-throughput sequencing technologies have allowed data generation rates to greatly outpace functional interpretation. Additionally, when considering the biological significance of reprogramming-associated mutations, there are two separate functional aspects to consider: whether some of these mutations contributed functionally to the reprogramming of cell fate, and whether some of these mutations could increase disease risk when hiPS-cellderived cells/tissues are used in the clinic. These two aspects are not necessarily connected. Although the functional effects of the 124 mutations remain to be characterized experimentally, it is nonetheless striking that the observed reprogramming-associated mutational load shares many similarities with that observed in cancer. Furthermore, the observation of mutated genes involved in human Mendelian disorders suggests that the risk of diseases other than cancer needs to be evaluated for hiPS-cell-based therapeutic methods. Future long-term studies must focus on functional characterization of reprogramming-associated mutations to aid further the creation of clinical safety standards.

Safe hiPS cells are critical for clinical application. Therefore, just as previous findings of large-scale genome rearrangements in hiPS

cell lines led to the introduction of karyotyping as a standard postreprogramming protocol, routine genetic screening of hiPS cell lines to ensure that no obviously deleterious point mutations are present must become a standard procedure. Complete exome or genome sequencing of hiPS cell lines might be an efficient way to screen out hiPS cell lines that have a high mutational load or have mutations in genes implicated in development, disease or tumorigenesis. Further rigorous work on mutation rates and distributions during *in vitro* culturing and reprogramming of hiPS cells, and perhaps human embryonic stem cells, will be essential to help establish clinical safety standards for genomic integrity.

METHODS SUMMARY

CV-hiPS-F and CV-hiPS-B were reprogrammed from CV fibroblasts using fourfactor retroviral vectors. PGP1-iPS cells were reprogrammed by Cellular Dynamics using the same four factors in a lentiviral vector from PGP1F fibroblasts²⁹. We obtained dH1F-iPS8, dH1F-iPS9, dH1cF16-iPS1, dH1cF16-iPS4, dH1cF16 and dH1F cells from previous cultures30 reprogrammed with retroviral vectors containing the same factors³¹. We obtained DF-6-9-9, DF-19-11, iPS4.7 and FS cells from previously existing cultures; the reprogramming process and characterization of lines has been described previously²⁴. We obtained iPS11a, iPS11b, iPS17a, iPS17b, iPS29A, iPS29e, Hib11, Hib17 and Hib29 cells from previous cultures reprogrammed using retroviral vectors encoding three or four factors³². FiPS3F1 and FiPS4F7 were reprogrammed from HFFxF fibroblasts using similar protocols^{33–35}. FiPS4F2 and FiPS4F-shpRB4.5 were reprogrammed using the same four-factor protocol from IMR90 fibroblasts. We obtained the mRNA-derived lines (CF-RiPS1.4, CF-RiPS1.9 and CF fibroblasts) from previous cultures³⁶. All hiPS cell lines were extensively characterized for pluripotency. Fourteen lines were tested for teratoma formation and shown to express all embryonic germ layers in vivo. DNA was extracted from each cell type using Qiagen's DNeasy kit.

Exome capture was performed with either a library of padlock probes, commercial hybridization-capture DNA baits (NimbleGen SeqCap EZ) or RNA baits (Agilent SureSelect), and the resulting libraries were sequenced on an Illumina GA IIx sequencer. We rejected putative mutations if they were known polymorphisms or contained any minor allele presence in the fibroblast. All candidate mutations were confirmed using capillary Sanger sequencing.

For digital quantification, mutations were PCR-amplified and sequenced using an Illumina GA IIx. These libraries were sequenced to obtain on average 1,000,000 independent base calls for each location. A binomial test was then used to determine whether the observed minor allele frequency could be separated from error and to estimate the frequency of each mutation.

Full Methods and any associated references are available in the online version of the paper at www.nature.com/nature.

Received 29 April 2010; accepted 12 January 2011.

- Takahashi, K. & Yamanaka, S. Induction of pluripotent stem cells from mouse embryonic and adult fibroblast cultures by defined factors. Cell 126, 663–676 (2006).
- Yu, J. et al. Induced pluripotent stem cell lines derived from human somatic cells. Science 318, 1917–1920 (2007).
- Mayshar, Y. et al. Identification and classification of chromosomal aberrations in human induced pluripotent stem cells. Cell Stem Cell 7, 521–531 (2010).
- Hong, H. et al. Suppression of induced pluripotent stem cell generation by the p53-p21 pathway. Nature 460, 1132-1135 (2009).
- Li, H. et al. The Ink4/Arf locus is a barrier for iPS cell reprogramming. Nature 460, 1136–1139 (2009).
- Kawamura, T. et al. Linking the p53 tumour suppressor pathway to somatic cell reprogramming. Nature 460, 1140–1144 (2009).
- Utikal, J. et al. Immortalization eliminates a roadblock during cellular reprogramming into iPS cells. Nature 460, 1145–1148 (2009).
- Marión, R. M. et al. A p53-mediated DNA damage response limits reprogramming to ensure iPS cell genomic integrity. Nature 460, 1149–1153 (2009).
- Ruiz, S. et al. A high proliferation rate is required for somatic cell reprogramming and maintenance of human embryonic stem cell identity. Curr. Biol. 21, 45–52 (2011).
- Porreca, G. J. et al. Multiplex amplification of large sets of human exons. Nature Methods 4, 931–936 (2007).
- Deng, J. et al. Targeted bisulfite sequencing reveals changes in DNA methylation associated with nuclear reprogramming. Nature Biotechnol. 27, 353–360 (2009)
- 12. Bashiardes, S. et al. Direct genomic selection. Nature Methods 2, 63–69 (2005).
- Gnirke, A. et al. Solution hybrid selection with ultra-long oligonucleotides for massively parallel targeted sequencing. Nature Biotechnol. 27, 182–189 (2009).

- Levy, S. et al. The diploid genome sequence of an individual human. PLoS Biol. 5, e254 (2007).
- 15. Drmanac, R. et al. Human genome sequencing using unchained base reads on self-assembling DNA nanoarrays. Science **327**, 78–81 (2009).
- Ng, S. B. et al. Targeted capture and massively parallel sequencing of 12 human exomes. Nature 461, 272–276 (2009).
- Kumar, P., Henikoff, S. & Ng, P. C. Predicting the effects of coding non-synonymous variants on protein function using the SIFT algorithm. *Nature Protocols* 4, 1073–1081 (2009).
- Forbes, S. A. et al. The Catalogue of Somatic Mutations in Cancer (COSMIC). Curr. Protocols Hum. Genet. 10, 10.11 (2008).
- 19. Shah, S. P. et al. Mutational evolution in a lobular breast turnour profiled at single nucleotide resolution. *Nature* **461**, 809–813 (2009).
- Futreal, P. A. et al. A census of human cancer genes. Nature Rev. Cancer 4, 177–183 (2004).
- Hamosh, A., Scott, A. F., Amberger, J. S., Bocchini, C. A. & McKusick, V. A. Online Mendelian Inheritance in Man (OMIM), a knowledgebase of human genes and genetic disorders. *Nucleic Acids Res.* 33, D514–D517 (2005).
- Druley, T. E. et al. Quantification of rare allelic variants from pooled genomic DNA. Nature Methods 6, 263–265 (2009).
- Ahuja, D., Saenz-Robles, M. T. & Pipas, J. M. SV40 large T antigen targets multiple cellular pathways to elicit cellular transformation. *Oncogene* 24, 7729–7745 (2005).
- 24. Yu, J. et al. Human induced pluripotent stem cells free of vector and transgene sequences. Science **324**, 797–801 (2009).
- Pleasance, E. D. et al. A comprehensive catalogue of somatic mutations from a human cancer genome. Nature 463, 191–196 (2010).
- 26. Lee, W. et al. The mutation spectrum revealed by paired genome sequences from a lung cancer patient. *Nature* **465**, 473–477 (2010).
- Ding, L. et al. Genome remodelling in a basal-like breast cancer metastasis and xenograft. Nature 464, 999–1005 (2010).
- 28. Dennis, G. Jr et al. DAVID: Database for Annotation, Visualization, and Integrated Discovery. *Genome Biol.* **4**, P3 (2003).
- Lee, J. H. et al. A robust approach to identifying tissue-specific gene expression regulatory variants using personalized human induced pluripotent stem cells. PLoS Genet. 5, e1000718 (2009).
- Park, I. H. et al. Reprogramming of human somatic cells to pluripotency with defined factors. Nature 451, 141–146 (2008).
- Chan, E. M. et al. Live cell imaging distinguishes bona fide human iPS cells from partially reprogrammed cells. *Nature Biotechnol.* 27, 1033–1037 (2009).
- 32. Dimos, J. T. et al. Induced pluripotent stem cells generated from patients with ALS can be differentiated into motor neurons. Science 321, 1218–1221 (2008).
- 33. Rodriguez-Piza, I. et al. Reprogramming of human fibroblasts to induced pluripotent stem cells under xeno-free conditions. Stem Cells 28, 36–44 (2010).

- Aasen, T. et al. Efficient and rapid generation of induced pluripotent stem cells from human keratinocytes. Nature Biotechnol. 26, 1276–1284 (2008).
- Stewart, S. A. et al. Lentivirus-delivered stable gene silencing by RNAi in primary cells. RNA 9, 493–501 (2003).
- Warren, L. et al. Highly efficient reprogramming to pluripotency and directed differentiation of human cells with synthetic modified mRNA. Cell Stem Cell 7, 618–630 (2010).

Supplementary Information is linked to the online version of the paper at www.nature.com/nature.

Acknowledgements We thank J. M. Akey, G. M. Church, S. Ding, J. B. Li and J. Shendure for discussions and suggestions, S. Vassallo for assistance with DNA shearing, and G. L. Boulting and S. Ratansirintrawoot for assistance with hiPS cell culture. This study is supported by NIH R01 HL094963 and a UCSD new faculty start-up fund (to K.Z.), a training grant from the California Institute for Regenerative Medicine (TG2-01154) and a CIRM grant (RC1-00116) (to L.S.B.G.). L.S.B.G. is an Investigator of the Howard Hughes Medical Institute. A. Gore is supported by the Focht-Powell Fellowship and a CIRM predoctoral fellowship. M.L.W. is supported by an institutional training grant from the National Institute of General Medical Sciences (T32 GM008666). Y.-H.L. is supported by the A*Star Institute of Medical Biology and the Singapore Stem Cell Consortium. Work in the laboratory of J.C.I.B. was supported by grants from MICINN, Sanofi-Aventis, the G. Harold and Leila Y. Mathers Foundation and the Cellex Foundation. G.Q.D. is an investigator of the Howard Hughes Medical Institute and supported by grants from the NIH.

Author Contributions L.S.B.G. and K.Z. co-directed the study. A. Gore, Z.L., L.S.B.G. and K.Z. designed the experiments. J.E.Y., S.A., J.A.-B., I.C., A. Giorgetti, M.A.I., E.K., J.-H.L., Y.-H.L., P.D.M., N.M., A.D.P., S.R., M.L.W., J. Yu, J.C.I.B., D.J.R., J.A.T., K.E., G.Q.D. and L.S.B.G. biopsied, cultured and derived hiPS cell lines. Z.L. performed DNA extraction. A. Gore, Z.L. and K.Z. performed exome library construction, DigiQ library construction and validation Sanger sequencing. H.-L.F. performed Illumina sequencing. A. Gore and K.Z. performed bioinformatic and statistical analysis with contributions from E.F.K. A. Gore, Z.L., L.S.B.G., G.Q.D. and K.Z. wrote the manuscript with contributions from all other authors

Author Information Sequencing results for the mutations reported here are included in Supplementary Figure 1. Raw Illumina sequencing reads are available from the NCBI Short Read Archive, accession SRP005709, except for lines derived from Hib11, Hib17, Hib29, CF, HFFxF, dH1F fibroblasts as the original donors were not consulted about public release of their genome data. Reprints and permissions information is available at www.nature.com/reprints. The authors declare no competing financial interests. Readers are welcome to comment on the online version of this article at www.nature.com/nature. Correspondence and requests for materials should be addressed to L.S.B.G. (Igoldstein@ucsd.edu) or K.Z. (kzhang@bioeng.ucsd.edu).

METHODS

CV fibroblast derivation. Primary fibroblasts were established from a 4-mm dermal punch biopsy of a 63-year-old male using a protocol based on Takashima's method³⁷. The biopsy and subsequent reprogramming protocols and the informed-consent documents were reviewed and approved by the UCSD institutional ESCRO and IRB. Briefly, collagenase type 1A (Sigma) was used to dissociate the biopsy and cells were cultured in fibroblast media (DMEM containing 15% FBS, penicillin/streptomycin, sodium pyruvate, non-essential amino acids and L-glutamine). Fibroblasts were reprogrammed at passage 5. DNA was isolated for sequencing from 3,000,000 fibroblasts at passage 9.

CV-hiPS-B and CV-hiPS-F derivation. For reprogramming, $\sim 100,000$ fibroblasts per well were transduced with pCX4 retroviral vectors encoding OCT4 (POU5F1), SOX2, KLF4, c-MYC (MYC) and \pm EGFP. CV-hiPS-B and CV-hiPS-F were derived from the \pm EGFP and \pm EGFP transductions, respectively. Transduced fibroblasts were trypsinized and seeded onto irradiated mouse embryonic fibroblasts (MEFs) and cultured in HUES media³⁸. Cultures were treated with 2 mM valproic acid for the first seven days post-transduction and 10 nM Y-27632 for the first three weeks (both from EMD Chemicals). After about three weeks post-transduction, individual colonies that morphologically resembled hES were isolated and expanded. Established hiPS cell lines were maintained in HUES media and dissociated cultures for subculturing using 0.05% trypsin/EDTA. DNA for sequencing was isolated from CV-hiPS-B and CV-hiPS-F at passages 13 and 9, respectively.

CV-hiPS characterization. For PCR analysis with reverse transcription, hiPS cells were purified away from MEFs by passage onto Matrigel. Cells were collected and total RNA was isolated with the Ambion PaRIS kit following manufacturer's protocols. First-strand complementary DNA was generated with Superscript II (Invitrogen) following manufacturer's protocols. cDNA was amplified with primers specific for endogenous SOX2, NANOG and OCT4 for 30 cycles. For immunofluorescence experiments, cells were passaged onto Matrigel-coated coverslips and samples were processed using standard methods. Antibodies were used at the following dilutions: NANOG (Santa-Cruz Biotechnology, 1:200), Tra-1-81 (BD Biosciences, 1:500), SOX2 (Chemicon, 1:2,000). Cell Line Genetics performed karyotype analysis of CV hiPS cell lines. For embryoid body generation, hiPS cells were passaged with dispase and plated in suspension culture in embryoid body media (DMEM, 20% FBS, L-glutamine and NEAA) for eight days. On day eight, embryoid bodies were plated onto either Matrigel- or polyornithine/laminincoated coverslips and cultured in either embryoid body media (for endoderm/ mesoderm) or neural differentiation media (DMEM-F12, glutamax, N2 and B27) supplemented with dbcAMP, BDNF and GDNF (for neuroectoderm) for eight days. On day nine, cells were fixed and processed for immunofluorescence as described above. Cell Line Genetics performed karyotype analysis of CV-hiPS cell

CV-hiPS-B was purified away from MEFs by culturing on Matrigel (BD Biosciences) for two passages. CV-hiPS-F was purified by dissociation with Accutase (Innovative Cell Technologies), staining with TRA-1-81 antibody (BD Biosciences) and purifying 5,000,000 TRA-1-81⁺ cells using a BD Biosciences FACSAria II flow cytometer.

dH1F-iPS8 and dH1F-iPS9 derivation. The dH1F fibroblast line was derived from the H1-OGN line previously30. dH1F-iPS8 and dH1F-iPS9 were reprogrammed³¹ with human OCT4, SOX2, KLF4 and c-MYC retroviral vectors from dH1F at passage 5. Briefly, 293T cells in 15-cm plates were transfected with $6.25\,\mu g$ of retroviral vector, 0.75 µg of VSVG vector and 5.625 µg of Gag-Pol vector using FUGENE 6 reagents. Three days after transfection, supernatants were filtered through a 0.45-µm cellulose acetate filter, concentrated by centrifugation at 23,000 r.p.m. for 90 min and stored at $-80\,^{\circ}$ C until use. Transductions were carried out on dH1F fibroblast cells in six-well plates (100,000 cells per well). Viruses were added at a multiplicity of infection of five. Three days after infection, cells were split into plates pre-seeded with MEFs. The medium was changed to human ES culture medium five days after infection. hiPS cell clones stared to emerge about two to three weeks later and were picked and expanded in standard human ES cell culture medium (DMEM/F12 containing 20% KOSR, 10 ng ml⁻¹ human recombinant basic fibroblast growth factor, $\times 1$ NEAA, 5.5 mM 2-ME, 50 units ml $^{-1}$ penicillin and 50 μg ml⁻¹ streptomycin). During cell collection, MEFs were removed by suction pump and collagenase (Gibco) was used to lift the cells. For dH1F, cells were cultured in 10% FBS DMEM. Trypsin-EDTA was used to lift the cells from the plate for collection. DNA was extracted using a Qiagen DNeasy kit at the following passage numbers: 12 (dH1F), 19 (dH1F-iPS8), 17 (dH1F-iPS9).

hiPS 11a, 11b, 17a, 17b, 29A and 29e derivation. Human fibroblasts were generated from 3-mm forearm dermal biopsies following informed consent under an IRB approved by Harvard University. The murine leukaemia retroviral vector pMXs containing the human cDNAs for *KLF4*, *SOX2* and *OCT4*³² were modified to produce higher-titer virus by including the woodchuck post-transcriptional

responsive element of FUGW (Addgene plasmid 14883) downstream of the cDNA. VSV-g pseudotyped viruses were packaged and concentrated by the Harvard Gene Therapy Initiative at Harvard Medical School. To produce hiPS cells, 30,000 human fibroblasts were transduced at a multiplicity of infection of 10-15 with viruses containing all three genes in hES medium with 8 μg ml⁻¹ polyprene. Cells were incubated with virus for 24 h before medium was changed to standard fibroblast medium for 48 h. Cells were subsequently cultured in standard hES medium and hiPS cell colonies were manually picked on the basis of morphology within 2-4 weeks. Derived hiPS cell lines (11a, 11b, 17a, 17b and 29e) have been extensively characterized by standard assays including staining for markers of pluripotency by immunocytochemistry, cell cycle analysis, three-germ-layer differentiation potential *in vitro* and *in vivo*, and karyotype analysis³⁹. All cell cultures were maintained at 37 °C in 5% CO2. Human fibroblasts were cultured in KO-DMEM (Invitrogen), supplemented with 20% Earl's salts 199 (Gibco) and 10% hyclone (Gibco), ×1 GlutaMax, penicillin/streptomycin (Invitrogen) and 100 μM 2-mercaptoethanol, hiPS cells were maintained on gelatinized tissue culture plastic on a monolayer of irradiated CF-1 MEFs (GlobalStem), in hES media³⁸, supplemented with 20 ng ml⁻¹ of bFGF. The medium was changed every 24 h and lines were passaged by trypsinization (0.5% trypsin EDTA, Invitrogen) or dispase (Gibco, 1mg ml⁻¹ in hES media for 30 min at 37 °C). hiPS cell lines 11a, 11b, 17a, 17b, 29A and 29e were purified from MEFs by using dispase, which selectively detaches stem cells, and then were washed twice to ensure removal of any contaminating MEFs. Genomic DNA was extracted with a Qiagen DNeasy kit at the following passages: 7 (hFib17), 20 (iPS17A), 23 (iPS17B), 7 (hFib11), 24 (hFib11a), 20, (hFib11b), 8 (hFib29), 21 (hFib29e), 36 (hFib29A).

HFFXF fibroblast derivation. Primary fibroblasts were established from a foreskin biopsy of a three-year-old individual as detailed in ref. 33. Briefly, a skin sample was placed in sterile saline solution, divided into small pieces and allowed to be attached to cell culture dishes before the addition of xeno-free human foreskin fibroblast growth medium. Fibroblasts generated under xeno-free conditions (HFFxF) were reprogrammed at passage 3. DNA was isolated for sequencing from 4,000,000 HFFxF fibroblasts at passage 4 with a Qiagen DNeasy kit. FiPS3F1 and FiPS4F7 generation. For reprogramming, about 100,000 fibroblasts per six-well plate were transduced with 1 ml of retroviral supernatants encoding FLAG-tagged OCT4, SOX2, KLF4, and c-MYC(T58A) as described in ref. 34. High-titer VSV-G-pseudotyped retroviruses expressing a polycistronic vector encoding for OCT4, SOX2, KLF4 and GFP (pMXs OSKG) and containing 5 mg ml⁻¹ polybrene were produced as described in ref. 35. Infection was performed as indicated previously³³. Colonies were picked on the basis of morphology 25-35 days after the initial infection and plated onto fresh irradiated XF HFF (iXF HFF) cells. Xeno-free iPS cell lines FiPS3F1 and FiPS4F7 were maintained by mechanical dissociation in XF-hESm, which is composed of KO-DMEM (Dulbecco's modified Eagle's medium; Invitrogen) supplemented with 15% xeno-free KO-SR (Invitrogen), xeno-free KO-SR growth factor cocktail (×1), 2 mM glutamax, 50 mM 2-mercaptoethanol, penicillin/streptomycin (×0.5, all from Invitrogen), non-essential amino acids (Cambrex) and $20\,\mathrm{ng\,ml}^{-1}$ bFGF (Peprotech).

FiPS3F1 and FiPS4F7 characterization. Derived hiPS cell lines FiPS3F1 and FiPS4F7 have been extensively characterized by staining for markers of pluripotency by immunofluorescence analyses. The following antibodies were used: MAB4360 for Tra-1-60 (1:200), MAB4381 for Tra-1-81 (1:200) and AB5603 for SOX2 (1:500, all from Chemicon); MC-813-70 for SSEA-4 (1:2) and MC-631 for SSEA-3 (1:2, both from the Developmental Studies Hybridoma Bank at the University of Iowa); C-10 for OCT4 (1:100, Santa Cruz); EB06860 for NANOG (1:100, Everest Biotechnology); and Anti-FLAG (Sigma M2). Three-germ-layer differentiation potential in vitro was conducted by means of embryoid body formation, which was induced from colony fragments mechanically collected. For endoderm, embryoid bodies were cultured in KO-DMEM medium supplemented with 10% FBS, 2 mM L-glutamine, 0.1 mM 2-β-mercaptoethanol, nonessential amino acids and penicillin/streptomycin. For mesoderm differentiation, the same medium described above in the presence of ascorbic acid (0.5 mM) was used. For ectoderm induction, embryoid bodies were cultured in N2/B27 medium with the stromal cell line PA6 for two weeks. The medium for each condition was changed every other day. On day 15, cells were fixed and processed for immunofluorescence for the following antibodies: Tuj1 (1:500, Covance), α-fetoprotein (1:400), α-actinin (1:100, Sigma). Teratoma formation assay was performed by injecting about 0.5×106 XF-iPS cells into the testes of severe combined immunodeficient beige mice (Charles River Laboratories). Mice were euthanized eight weeks after cell injection, and tumours were processed and analysed following conventional immunohistochemistry protocols (Masson's trichromic stain) and immunofluorescence staining for Tuj1 (1:500, Covance), α-fetoprotein (1:400) and α-actinin (1:100, Sigma). Expression of retroviral transgenes and endogenous pluripotency-associated factors by quantitative PCR with reverse transcription

were conducted as described previously³³. hiPS cell lines FiPS3F1 and FiPS4F7 were purified from iXF HFF by mechanical dissociation and further culturing on Matrigel (BD Biosciences) for two more passages. DNA for sequencing was isolated from passage 9 for both FiPS3F1 and FiPS4F7 with a Qiagen DNeasy kit. CF-Fib, CF-RiPS1.4 and CF-RiPS1.9 derivation. CF fibroblasts (CF-Fib) were previously obtained from a skin biopsy taken from an adult with cystic fibrosis, with proper informed consent³⁶. CF-induced pluripotent stem cell lines were derived using modified mRNAs coding reprogramming factors OCT4, SOX2, KLF4, c-MYC and LIN28 (OSKML) with molar concentrations in the ratio 3:1:1:1; in an atmosphere with 5% oxygen, as previously described³⁶. Briefly, 50,000 fibroblasts were plated onto γ -irradiated human neonatal fibroblast feeders (GlobalStem) seeded at 33,00 cells cm⁻². For CF-RiPS derivations, the cationic lipid delivery system RNAiMAX was used. First, pooled RNA from the five factors OSKML (100 $\text{ng}\,\text{ml}^{-1}$) was diluted $\times 5$ and the reagent (5 μ l of RNAiMAX per microgram of RNA) was diluted ×10 in Opti-MEM basal media (Invitrogen). These components were pooled and incubated for 15 min at room temperature before being dispensed to culture media. Nutristem medium was replaced daily 4 h after transfection, and supplemented with 100 ng ml⁻¹ bFGF and 200 ng ml⁻¹ B18R (eBioscience). CF-RiPS derivation was performed in low oxygen (5%) in a NAPCO 8000 WJ incubator (Thermo Scientific). Medium was equilibrated in 5% oxygen for approximately 4 h before use and cultures were passaged with TrypLE Select recombinant protease (Invitrogen) on days five and six. The daily RNA dose applied in the RiPSC derivations was 1,200 ng per well (six-well plate format). On day 21, RiPS colonies were mechanically picked and transferred to MEF-coated 24-well plates with standard hESC medium (DMEM/F12 containing 20% KOSR (Invitrogen), 10 ng ml⁻¹ bFGF (Gembio), ×1 NEAA (Invitrogen), 0.1 mM b-ME (Sigma), 1 mM L-glutamine (Invitrogen), 50 units ml⁻¹ penicillin and 50 μg ml⁻¹ streptomycin) containing 5 mM Y27632 (BioMol). Clones were mechanically passaged once more to MEF-coated six-well plates, and then expanded via enzymatic passaging with collagenase IV (Invitrogen). Genomic DNA was extracted with a Qiagen DNeasy kit at the following passages: 9 (CF-Fib), 5 (CF-RiPS1.4), 5 (CF-RiPS1.9)

FiPS4F2 and FiPS4F-shpRb4.5 plasmid construction. pMX-Oct4, pMX-SOX2, pMX-KLF4, pMX-cMyc and pLVTHM were obtained from Addgene (plasmids 17217, 17218, 17219, 17220 and 12247, respectively). For the generation of the mammalian lentiviral plasmid encoding small hairpin RNAs against pRb-specific oligonulceotides (forwards, 5'-CGCGTGTTTCCTCTCCAAAGTAATTCAA GAGATTACTTTGGAAGAGGAAACTTTTTTTTGGAAAT-3'; reverse, 5'-CGA TTTCCAAAAAAGTTTCCTCTTCCAAAGTAATCTCTTGAATTACTTTGGA AGAGGAAACA-3'), were annealed, phosphorylated with T4 kinase and ligated into MluI/ClaI-linearized pLTVHM plasmid. The design of the small hairpin RNA was carried out using the SFOLD software (http://sfold.wadsworth.org/). All constructs generated were subjected to direct sequencing to rule out the presence of mutations.

FiPS4F2 and FiPS4F-shpRb4.5 retroviral and lentiviral production. Moloney-based retroviral vectors (pMX-) were co-transfected with packaging plasmids (pCMV-gag-pol-PA and pCMV-VSVg) in 293T cells using Lipofectamine (Invitrogen). Retroviral supernatants were collected 24 h after transfection, and passed through a 0.45 mM filter. Second-generation lentiviral vectors (pLVTHM-) were co-transfected with packaging plasmids (psPAX2 and pMD2.G, obtained from Addgene, 12260 and 12259, respectively) in 293T cells using Lipofectamine (Invitrogen). Lentiviral supernatants were collected 36 h after transfection.

FiPS4F2P9, FiPS4F2P40 and FiPS4F-shpRb4.5 derivation. Briefly, for the formation of hiPS cells IMR90 fibroblasts were infected with equal proportions of retroviruses encoding for OCT4, SOX2, KLF4 and c-MYC plus empty lentiviruses (used to generate the FiPS4F2 line) or lentiviruses encoding small hairpin RNA against pRb (used to generate the line FiPS4F-shpRb4.5) by spinfection of the cells at 1,850 r.p.m. for 1 h at room temperature in the presence of polybrene (4 μg ml $^{-1}$). After two serial infections, cells were passaged onto fresh MEFs and switched to hES cell medium (DMEM/F12 (Invitrogen) supplemented with 20% Knockout serum replacement (Invitrogen), 1 mM L-glutamine, 0.1 mM nonessential amino acids, 55 mM β-mercaptoethanol and 10 ng ml $^{-1}$ bFGF (Joint Protein Central)) four days after the first infection. For the derivation of hiPS cell lines, colonies were manually picked and maintained on fresh MEF feeder layers for five passages before the growth in Matrigel/mTesR1 (Stem Cell Technologies) conditions. DNA was extracted after nine passages for FiPS4F2P9 and FiPS4FshpRB4.5 and 40 passages for FiPS4F2P40.

FiPS4F2 and FiPS4F-shpRb4.5 characterization. Cell pellets were lysed in 10 mM Tris-HCl (pH 8), 150 mM NaCl, 1% Triton X100, 1 mM Na₃VO₄, 1 mM PMSF and the Complete protease inhibitor mixture (Roche). Total protein extracts (25 µg) were used for SDS-PAGE, transferred to nitrocellulose membranes (Amersham Biosciences) and analysed using primary antibodies against OCT4 (sc-5279, Santa Cruz), SOX2 (AB5603, Chemicom), RB1 (554136, Pharmingen)

and Tubulin (T5168, Sigma). Horseradish-peroxidase-conjugated secondary antimouse or rabbit were purchased from Cell Signaling and used at 1:5,000 dilution. Tubulin was used as a loading control. Immunoblots were visualized using SuperSignal solutions following the manufacturer's instructions (Thermo Scientific). Total RNA was isolated using TRIzol Reagent (Invitrogen), and cDNA was synthesized using the SuperScript II Reverse Transcriptase kit for RT-PCR (Invitrogen). Real-time PCR was performed using the SYBR-Green PCR Master mix (Applied Biosystems). Values of gene expression were normalized using GAPDH expression and are shown as fold change relative to the value of the sample control. All the samples were done in triplicate. Primer sequences are available upon request. The hiPS cell lines were cultured in the presence of 20 ng ml⁻¹ colcemid for 45 min. The cells were trypsinized, washed with PBS and resuspended in a hypotonic solution by drop-wise addition while vortexing at low speed. After 10 min of incubation at 37 °C, cells were fixed by drop-wise addition of 1 ml of cold Carnoy's fixative. Stained metaphases were analysed with CYTOVISION software (Applied Imaging). Teratoma analyses were performed as described in

Preparation of padlock probes. The design and preparation of padlock probes was based on published methods^{10,11,40}. Libraries of long oligonucleotides (140 nucleotides) that cover different exonic regions were synthesized from programmable microarrays (Agilent Technologies). The libraries were amplified by performing 48-96 PCR reactions (100 µl each) with 0.02 nM template oligonucleotides, 200 nM Ap1V4IU primer (G*T*AGACTGGAAGAGCAC TGTU), 200 nM Ap2V4 primer (/5Phos/TAGCCTCATGCGTATCCGAT), $\times 0.2$ SybrGreen I and 50 μ l Econo Taq PLUS master mix (Lucigen), at 94 $^{\circ}$ C for 2 min, and then 17 cycles at 94 $^{\circ}$ C for 30 s, 58 $^{\circ}$ C for 30 s, 72 $^{\circ}$ C for 30 s and 72 °C for 3 min. The amplicons were then purified by ethanol precipitation. Libraries were then digested with 40 units of Lambda Exonuclease (5 U μ l⁻¹, NEB) in ×1 Lambda Exonuclease buffer (NEB) at 37 °C for 2 h, followed by purification with four Qiagen Qiaquick PCR purification columns for every 48 wells of PCR products. Approximately 8 µg of the purified PCR amplicons were digested with ten units of DpnII (50 U μ l⁻¹) and ×1 DpnII buffer at 37 °C for 2 h, followed by the addition of four units of USER enzyme (1 U μ l⁻¹, NEB) at 37 °C for 4 h. The DNA was digested with 6% PAGE and purified into single-stranded, 102-nucleotide probes.

Multiplex capture of exonic regions. Padlock probes (600 nM total concentration), 250 ng of genomic DNA, 1 nM suppressor oligonucleotides and $\times 1$ Ampligase buffer (Epicentre) were mixed in a 15-µl reaction and denatured at 95 °C for 10 min, then gradually cooled at the rate of 0.1 °C s⁻¹ to 60 °C. The mixture was hybridized at 60 °C for 24 h. To circularize the captured targets, the reactions were then incubated at 60 °C for another 24 h after adding 2 µl of gapfilling mix (two units of AmpliTaq Stoffel (Life Technology), four units of Ampligase (Epicentre), and 500 pmol total dNTP). After circularization, 2 µl of exonuclease mix containing 10 U µl⁻¹ exonuclease II (USB) was added to digest the linear DNA, and the reactions were incubated at 37 °C for 2 h and then inactivated at 94 °C for 5 min.

Amplification of capture circles. The 15- μ l circularization products were placed in 100- μ l PCR reactions with 200 nM of each primer (NH2-CAGATGTTATCGA GGTCCGAC, NH2-GGAACGATGAGCCTCCAAC, \times 0.2 SybrGreen I and \times 1 Phusion High-Fidelity PCR Master Mix (NEB) at 98 °C for 1 min, and then 16 cycles at 98 °C for 10 s, 58 °C for 20 s, 72 °C for 20 s and 72 °C for 3 min. The amplicons of the expected size range (200 bp) were purified using Qiagen Qiaquick columns.

Shotgun sequencing library construction. Purified PCR products with the four probe sets on the same template DNA were pooled in equal molar ratio. The PCR products were transferred into Covaris microTubes with snap caps for Covaris AFA shearing using a 10% duty cycle, an intensity setting of 5 and 200 cycles per burst. The sheared DNA was concentrated to 85 µl using a vacufuge, and was then prepared for sequencing library construction using NEBNext DNA Sample Prep Master Mix Set 1 (NEB). The fragmented DNA was end-repaired at room temperature for 30 min in 100- μ l reaction consisting of $\times 1$ NEBNext End Repair Reaction Buffer and 5 µl of NEBNext End Repair Enzyme Mix. The DNA was then purified with Qiagen Qiaquick columns. Approximately 500 ng to 1 μ g of the end-repaired blunt DNA was incubated in a thermal cycler for 30 min at 37 °C along with ×1 NEBNext dA-Tailing Reaction Buffer and 3 µl of Klenow fragment. The DNA was again purified using Qiagen Qiaquick columns. The purified DNA was size-selected (125-150 nucleotides) using E-Gel SizeSelect 2% (Invitrogen) and concentrated to 36 µl using a vacufuge (Eppendorf). The dAtailed DNA was then ligated at room temperature for 15 min with ×1 Quick Ligation Reaction Buffer, 1.6 nM Illumina ligation adaptors and 2 μ l of Quick T4 DNA ligase. Ligation products were purified using Qiagen Qiaquick columns and amplified by PCR in 100-µl reactions with a 15-µl template, 200 nM Illumina PCR primers, ×0.2 SybrGreen I and ×1 Phusion High-Fidelity PCR Master Mix

(NEB) at 98 $^{\circ}$ C for 1 min, and then eight cycles at 98 $^{\circ}$ C for 10 s, 65 $^{\circ}$ C for 20 s, 72 $^{\circ}$ C for 15 s and 72 $^{\circ}$ C for 3 min. The PCR amplicons were purified with Qiaquick PCR purification columns, size-selected (200–275 nucleotides) using 6% PAGE and sequenced on an Illumina Genome Analyser IIx.

Hybridization capture with DNA or RNA baits. Liquid exome capture was performed using the commercial Roche NimbleGen SeqCap EZ Exome kit or the commercial Agilent SureSelect kit (Table 1). Experiments were performed following the manufacturers' protocols. Briefly, genomic DNA was sheared and ligated to Solexa sequencing adaptors. DNA was then hybridized with the SeqCap EZ Exome library or SureSelect RNA baits to capture exomic regions. Exome regions were captured with streptavidin beads and then PCR-amplified with Illumina sequencing adaptors. The resulting libraries were sequenced on an Illumina Genome Analyser IIx.

Consensus sequence generation and variant calling. Reads obtained from the Illumina Genome Analyser were post-processed and quality filtered using GERALD. The end of each read was then mapped to the padlock-probe capturing arm sequences using Bowtie; any reads that successfully mapped were discarded to prevent bias from capturing arms. Reads were then mapped to the whole genome using Bowtie or BWA. Any read that could not be mapped uniquely was discarded to reduce false positives due to sequence homology. The 5' and 3' ends of reads were then trimmed to reduce the effect of sequencing errors, which tend to occur near the beginnings and ends of reads on the Illumina platform. (No trimming was performed when GATK was used for variant calling.) To reduce errors introduced by pre-sequencing amplification, mapped reads that started and ended at identical locations were then removed using SAMtools or Picard to account for these clonal reads. SAMtools or GATK was then used to generate a consensus sequence for each sample by combining the results of each read that mapped to each exomic location. A minimum read depth of eight and consensus quality of 30 was required at every examined location. The consensus sequences were then compared to look for candidate novel mutations in hiPS cells. Variants that occurred at locations present in the dbSNP database (version 130) were removed from consideration to reduce the false-positive rate, as a novel mutation in the hiPS cell line is very unlikely to have been previously characterized in other cell lines and was most probably just not observed in the fibroblast line owing to stochastic sequencing bias. Because sequencing depth was relatively low in a small fraction of exomic regions, allelic imbalance can also lead to false positives, as sites in the fibroblast genome could, for example, be heterozygous but be sequenced as seven copies of the major allele and one copy of the minor allele and called as homozygous. To prevent these false positives, sites in which the fibroblast genome showed even a very small presence of minor allele were removed from consideration as candidate sites for novel mutations (as these sites are most probably truly heterozygous in both lines). Several locations were identified in which the hiPS cell sample consensus sequence showed a heterozygous call but the fibroblast sample consensus sequence showed a homozygous call; these were identified as candidate mutations, as it is expected that during mutational processes, the hiPS cell sample would most probably gain an additional allele. These candidate mutations were then validated by capillary sequencing as below.

Sanger validation of candidate mutations. Genomic DNA (6 ng) was amplified in a 50-µl PCR reaction with 100 nM specifically designed primers near the mutation site and 25 µl Taq $\times 2$ master mix (NEB) at 94 °C for 2 min, followed by 35 cycles at 94 °C for 30 s, 57 °C for 30 s and 72 °C for 30 s, and final extension at 72 °C for 3 min. The PCR products were then purified with Qiagen Qiaquick columns, and 10 ng of purified DNA was pre-mixed with 8 pmol of the sequencing primer for capillary Sanger sequencing by Genewiz.

Clonal fibroblast experiments. In an attempt to determine the mutational load present in single fibroblasts, we performed a reprogramming-like clonal colony purification strategy on fibroblasts. CV fibroblasts were thawed at passage 14 and cultured in fibroblast media (DMEM containing 15% FBS, penicillin/streptomycin, sodium pyruvate, non-essential amino acids and L-glutamine). A confluent 6-cm plate was trypsinized and cells were plated in three 96-well dishes, in the presence (two plates) or absence (one plate) of MEF feeder cells, at limiting dilutions. Another 96-well plate was plated as a reference plate. Using Poisson calculations, cells were diluted and plated such that it was extremely unlikely (<1%) for one well to contain more than one cell (leading to an expectation of eight wells per plate with one cell). These wells were cultured and progressively passaged from the 96-well dish to a 6-cm plate (96-well, 48-well, 24-well, 12-well, 6-well, 6-cm). For cells growing on MEFs, all passages from a 12-well dish to a 6-cm dish were done without MEFs to minimize contamination with mouse cells in the sequencing analysis. Only three MEF-free wells and nine MEF-containing wells successfully grew; using Poisson calculations, 24 wells should have successfully grown.

All fibroblasts grown from single cells showed heavy signs of stress. Cells grew very slowly (with passaging needed approximately every one to two weeks). MEF-free cells had a flattened morphology, whereas MEF-plated cells maintained a

normal, spindle-shaped morphology. Cells tended to senesce very soon after plating; only a few cells grew successfully. Seven clonal lines were sequenced (three grown without MEFs and four grown with MEFs). Six of the lines contained a very high number of putative mutation candidates (~100), and no mutations were found in one line grown on MEFs. We randomly selected 21 of the 600 mutation candidates for Sanger validation, and found that approximately 50% were true positives. This leads to a projection of \sim 50 protein-coding mutations in six clonal fibroblast lines, which is tenfold more than what was observed in hiPS cells and not consistent with the observations on the other clonal fibroblast line, which was completely mutation free. We proposed that the mutations in the six clonal fibroblast lines were due to the stress associated with expanding single fibroblast cells. Because fibroblast growing conditions are very different from those found in reprogramming, we cannot estimate the background somatic mutation rate in such an experiment. We therefore instead used published estimates of fibroblast mutation rate to estimate clonal fibroblast mutational load (see below).

Digital quantification of mutations. Thirty-two pairs of DigiQ-PCR primers were designed such that the forward or reverse primers are roughly 25 base pairs away from the 5' end of each mutation site. This ensured that the mutations of interest were sequenced in the part of the read length that had the highest accuracy. Primers also contained an annealing region for Illumina Solexa sequencing primers at the 5' ends. Each primer corresponding to a different mutation was amplified with a high-fidelity polymerase in three samples: the mutated hiPS cell line, the progenitor fibroblast line and a clean control. To sample DNA from 100,000 cells, 600 ng of DNA was used for each mutated hiPS cell line and fibroblast line. In cases where a separate clonal hiPS cell line not containing the mutation in question was available, this line was used as a clean control, as the chance of this line acquiring the same mutation during clonal expansion is extremely low $(\sim\!10^{-9}$ for one mutation). In other cases, a 'low-input' sample using 300 pg of DNA (~50 cells) was used, as rare mutations are unlikely to be present in such a small quantity of DNA. If any mutated DNA was sampled, it would be immediately obvious in the sequencing results and the experiment could be repeated. Firstround PCR amplification was performed with 600 ng (~100,000 cells) of DNA, 500 nM of each DigiQ-PCR primer and ×1 iProof High-Fidelity Master Mix (Bio-Rad) at 98 $^{\circ}$ C for 30 s, followed by ten cycles at 98 $^{\circ}$ C for 10 s, 59 $^{\circ}$ C for 20 s and 72 °C for 15 s, 18 cycles at 98 °C for 10 s and 72 °C for 20 s, and final extension at 72 °C for 3 min. The PCR amplicons were purified using Qiaquick columns (Qiagen). Roughly 100 ng of the first-round PCR product was used as a template for second-round PCR amplification, together with ×1 Phusion High-Fidelity PCR Master Mix (NEB) and 200 nM of each Illumina PCR primer, at 98 °C for 30 s, followed by ten cycles at 98 $^{\circ}$ C for 10 s and 64 $^{\circ}$ C for 30 s, and final extension at 72 °C for 30 s. The amplicons were purified again with Qiaquick columns (Qiagen) and size-selected (roughly 150-200 nucleotides) using an E-Gel SizeSelect 2% system (Invitrogen). PCR reactions were performed with the iProof High-Fidelity Master Mix (Bio-Rad) and Phusion High-Fidelity PCR Master Mix (NEB) to minimize amplification errors. All size-selected products were pooled together at equal ratio; these libraries were then mixed with the Illumina PhiX control library in a roughly equal ratio to balance the fluorescent signals at all four bases and improve the base-calling accuracy, and sequenced using an Illumina GA IIx. Each pair of libraries from the fibroblasts and negative controls was sequenced in two non-adjacent lanes of a same flow cell. Extreme care was taken in sample handling to ensure no cross-contamination from the positive control libraries to the other libraries. Alleles identified at each mutation position by the sequencer were counted and evaluated. The specific sample choices for each mutation (and raw allele counts) are listed in Supplementary Table 2 (for details, see Supplementary Fig. 3 and Supplementary Table 3). To verify the robustness of the DigiQ assay, the assay was repeated on CV fibroblasts. The obtained read proportions were extremely similar (Supplementary Fig. 4).

Statistical analysis—probability of mutations occurring naturally. We evaluated the likelihood that the mutations found were generated during fibroblast culturing and reprogramming (assuming a clean starting population of fibroblasts) at the normal estimated somatic mutation rate of between 10^{-6} and 10^{-7} non-synonymous coding mutations per gene per cell division, which corresponds to a rate of 6.7×10^{-10} (using the average human coding-region size of 1,500 base pairs per gene⁴¹). Assuming that mutations are independent events that occur uniformly across the genome, the number of expected mutations during fibroblast culturing and reprogramming can be estimated using a Poisson distribution with expected value $\lambda = 6.7 \times 10^{-10} ns$, where n is the number of cell divisions and s is the observed sequence. Although accurate records of the number of cell divisions experienced by each line during expansion and reprogramming are not available, we estimated that 30-35 doublings had occurred for six lines with well-documented culture histories. In these lines, a total of 206,227,380 base pairs were pairwise-sequenced (at a depth of at least eight and quality of at least 30). This

leads to a Poisson distribution with $\lambda=4.13-4.81$ for the expected number of mutations. In this case, we observed 54 coding mutations, leading to a P value of $1.29\times10^{-40}-2.72\times10^{-37}$. If this calculation is extrapolated to all 22 lines, we expect $\lambda=8.7-10.1$ coding mutations; we observed 91, leading to a P value of $4.29\times10^{-59}-1.27\times10^{-53}$. We can therefore say that these mutations did not occur by chance with more than 99% confidence for all 22 lines.

Statistical analysis—digital quantification. To quantify the frequency of each mutation in the fibroblast samples, a one-tailed binomial distribution test was used. Reads were quality-filtered; only base calls with a Phred-like quality score of 30 or greater were considered. We denote by p the probability of obtaining a sequencing read containing the minor allele. The fibroblast sample was compared with either the clean low-input sample or a clean clonal hiPS cell line. Because the two hiPS cell lines are clonally independent, they will not share any mutations. Therefore, for example, FS-low can be used as a negative control for FS and CVhiPS-B can be used as a negative control for CV-hiPS-F. Any minor allele obtained from the clonal hiPS cell or low-input fibroblast sample will be purely due to sequencing error. We denote by H0 the event that the minor allele frequency in the fibroblast sample was less than or equal to the minor allele frequency in the other clonal/low-input sample, and denote by H1 the event that the minor allele frequency in the fibroblast sample was greater. If H0 is found to be true, the mutation cannot be detected in the fibroblast, as any presence of the minor allele cannot be distinguished from sequencing error. If H1 is found to be true, the presence of the minor allele is detectable and can be quantified. We denote by n the total number of reads that called the mutated position. A critical value of a=0.01 was chosen (99% confidence). Because the number of reads for each sample was very high, both np and n(1-p) were greater than five, meaning that the minor allele presence could be approximated with a normal distribution. We can therefore set a criterion for rejection of the null hypothesis of $Z = (x - \mu)/2$ s > 2.33, where x is the minor allele count, μ is the mean of the minor allele counts of the fibroblast and low-input/clonal samples, and s is the standard deviation of the minor allele counts of the fibroblast and low-input/clonal samples. For a binomial-distribution approximation, n is the number of reads in the fibroblast sample, *p* is the minor allele frequency if the fibroblast and low-input/clonal data are merged, $\mu = np$, and s = np(1-p). If the value of Z is greater than 2.33, we are capable of distinguishing the observed fraction of minor alleles in the fibroblast sample from that observed in the clonal/low-input sample. These results are presented in Supplementary Table 3.

We can also construct a 99% confidence interval using the normal approximation for the binomial distribution. Although we observed a value for the minor allele in each fibroblast sample, due to sequencing error, this value may overestimate or underestimate the true minor allele frequency. We can counteract this

error using a normal distribution. The confidence-interval values are derived from the normal probability density function and represent the boundaries that we are 99% sure the true minor allele frequency lies within: lower bound, $\min((-2.57s+x)/n, 0)$; upper bound, $\min((2.57s+x)/n, 0)$. These estimates for the minor allele fraction in fibroblasts are shown in Supplementary Table 3. An example of calculation is shown in Supplementary Note.

Statistical analysis—NS/S **mutation ratio.** To determine whether selection pressure could have a role in reprogramming-associated mutations, we compared the mutational load associated with reprogramming with that associated with tumorigenesis. The NS/S ratio found in several previously conducted pairwise cancer sequencing analyses^{25–27} was found to be 2.4:1. The load found here out of 124 identified mutations is 2.6:1, meaning that hiPS cell lines carry a very similar mutational pattern to cancer lines.

Statistical analysis-pathway and COSMIC gene enrichment. To check for enrichment of reprogramming-associated mutated genes in cancer-related genes, the fraction of genes mutated in hiPS cells found mutated in the COSMIC18 database was identified as 50/124. As 4,471 of the 16,017 genes well targeted by our exome sequencing pipeline are considered to be commonly mutated in cancer, a γ^2 test with one degree of freedom can be used to test for equivalency of distribution. The obtained χ^2 value is 9.67, indicating that the fraction of mutated hiPS cell genes in the COSMIC set is statistically significantly greater than the normally obtained number with a P value of 0.001873. This indicates that hiPS cell mutations are enriched in COSMIC set genes at approximately 1.5-fold the normal level, of 28%, with >99% confidence. To check for commonly mutated pathways, reprogramming-associated mutated genes and mutated genes identified in three cancer sequencing papers^{25,26,27} were analysed using DAVID²⁸. No statistically significant pathway Gene Ontology terms were identified; the lowest Benjamini P value found was 0.6, which is well above the cut-off value, of 0.01, required for 99% confidence. Therefore, no common pathways seem to be mutated in hiPS cells.

- Akagi, T., Sasai, K. & Hanafusa, H. Refractory nature of normal human diploid fibroblasts with respect to oncogene-mediated transformation. *Proc. Natl Acad.* Sci. USA 100, 13567–13572 (2003).
- Cowan, C. A. et al. Derivation of embryonic stem-cell lines from human blastocysts. N. Engl. J. Med. 350, 1353–1356 (2004).
- Boulting, G. L, et al. A functionally characterized test set of human induced pluripotent stem cells. *Nature* advance online publication, doi:10.1038/nbt.1783 (3 February 2011).
- Zhang, K. et al. Digital RNA allelotyping reveals tissue-specific and allele-specific gene expression in human. Nature Methods 6, 613–618 (2009).
- 41. Meena Kishore, S., Vincent, T. K. C. & Pandjassarame, K. Distributions of exons and introns in the human genome. *In Silico Biol.* **4**, 387–393 (2004).

Hotspots of aberrant epigenomic reprogramming in human induced pluripotent stem cells

Ryan Lister^{1*}, Mattia Pelizzola^{1*}, Yasuyuki S. Kida², R. David Hawkins³, Joseph R. Nery¹, Gary Hon³, Jessica Antosiewicz–Bourget^{4,5}, Ronan O'Malley¹, Rosa Castanon¹, Sarit Klugman³, Michael Downes², Ruth Yu², Ron Stewart^{4,5}, Bing Ren^{3,6}, James A. Thomson^{4,5,7,8}, Ronald M. Evans² & Joseph R. Ecker¹

Induced pluripotent stem cells (iPSCs) offer immense potential for regenerative medicine and studies of disease and development. Somatic cell reprogramming involves epigenomic reconfiguration, conferring iPSCs with characteristics similar to embryonic stem (ES) cells. However, it remains unknown how complete the reestablishment of ES-cell-like DNA methylation patterns is throughout the genome. Here we report the first whole-genome profiles of DNA methylation at single-base resolution in five human iPSC lines, along with methylomes of ES cells, somatic cells, and differentiated iPSCs and ES cells. iPSCs show significant reprogramming variability, including somatic memory and aberrant reprogramming of DNA methylation. iPSCs share megabase-scale differentially methylated regions proximal to centromeres and telomeres that display incomplete reprogramming of non-CG methylation, and differences in CG methylation and histone modifications. Lastly, differentiation of iPSCs into trophoblast cells revealed that errors in reprogramming CG methylation are transmitted at a high frequency, providing an iPSC reprogramming signature that is maintained after differentiation.

Generation of iPSCs from somatic cells offers tremendous potential for therapeutics, the study of disease states, and elucidation of developmental processes^{1,2}. iPSC production techniques introduce active genes that are necessary for pluripotency, or their derivative RNA or protein products, into a somatic cell to induce pluripotent cellular properties that closely resemble those of ES cells^{3–8}. Indeed, iPSCs have been used to produce viable and fertile adult mice, demonstrating their pluripotent potential to form all adult somatic and germline cell types^{8,9}.

The reprogramming process by which a somatic cell acquires pluripotent potential is not a genetic transformation, but an epigenomic one. A recent study reported minimal differences in chromatin structure and gene expression between human ES cells and iPSCs, indicating that ES cells and iPSCs are nearly identical cell types¹⁰. On the other hand, there are recent reports indicating epigenomic differences between ES cells and iPSCs^{11–15} and alterations in the differentiation potential of iPSCs compared to ES cells^{13,16,17}. Together, these findings indicate that fundamental differences between ES cells and iPSCs exist, prompting the question of how complete and variable the reestablishment of ES-cell-like DNA methylation patterns are throughout the entire genome.

Presumably, optimal reprogramming of somatic cells to a pluripotent state requires complete reversion of the somatic epigenome into an ES-cell-like state, but until now a comprehensive survey of the changes in such epigenetic marks in a variety of independent iPSC lines has not been reported. Accordingly, we have performed wholegenome profiling of the DNA methylomes of multiple human ES cell, iPSC and somatic progenitor lines, encompassing reprogramming

performed in different laboratories, using different iPSC-inducing technologies and cells derived from distinct germ layers. We show that although on a global scale ES cell and iPSC methylomes are very similar, every iPSC line shows significant reprogramming variability compared to both ES cells and other iPSCs, including both somatic 'memory' and iPSC-specific differential DNA methylation. Further, all iPSC lines share numerous non-randomly distributed megabase-scale regions that are aberrantly methylated in the non-CG context, associated with alterations in CG methylation, histone modifications and gene expression. Lastly, we show that differentially methylated regions in iPSCs are transmitted to differentiated cells at a high frequency.

Globally similar ES cell and iPSC methylomes

To assess the degree to which a somatic cell DNA methylome is reprogrammed into an ES-cell-like state by induction of a pluripotent state, we generated whole-genome, single-base resolution DNA methylomes of a range of human cell types using the shotgun bisulphite-sequencing method, MethylC-Seq¹⁸. Our central focus was a high-efficiency, feederfree reprogramming system¹⁹, in which female adipose-derived stem cells (ADS) were reprogrammed into a pluripotent state by retroviral transformation with the *OCT4*, *SOX2*, *KLF4* and *MYC* genes (ADS-iPSCs), satisfying the criteria for pluripotency in human cells²⁰. Additionally, we analysed the DNA methylome of adipocytes derived from the ADS cells (ADS-adipose) through adipogenic differentiation conditions. Further, to explore the variation between independent iPSC lines potentially due to stochastic reprogramming events, progenitor somatic cell type, reprogramming technique and laboratory-specific effects, we generated full DNA methylomes for four additional iPSC

¹Genomic Analysis Laboratory, The Salk Institute for Biological Studies, La Jolla, California 92037, USA. ²Howard Hughes Medical Institute, Gene Expression laboratory, The Salk Institute for Biological Studies, La Jolla, California 92037, USA. ³Ludwig Institute for Cancer Research, 9500 Gilman Drive, La Jolla, California 92093, USA. ⁴Morgridge Institute for Research, Madison, Wisconsin 53707, USA. ⁵Genome Center of Wisconsin, Madison, Wisconsin 53706, USA. ⁶Department of Cellular and Molecular Medicine, University of California San Diego, La Jolla, California 92093, USA. ²Wisconsin National Primate Research Center, University of Wisconsin, Madison, Wisconsin 53706, USA. ⁸Department of Anatomy, University of Wisconsin—Madison, Madison, Wisconsin 53706, USA. ⁸These authors contributed equally to this work.

lines that were isolated in an independent laboratory: an iPSC line generated by lentiviral integration of the *OCT4*, *SOX2*, *NANOG* and *LIN28A* genes into IMR90 lung fibroblasts (IMR90-iPSCs)⁵, and three iPSC lines generated by reprogramming of foreskin fibroblasts (FF) by non-integrating episomal vectors (FF-iPSC 6.9, FF-iPSC 19.7, FF-iPSC 19.11), as described previously⁷. We also sequenced the DNA methylome of the somatic FF progenitor line. Lastly, to study the effects of cellular differentiation on the DNA methylomes of ES cells and iPSCs, we differentiated cells of each to trophoblast lineage cells by growth in the presence of bone morphogenic protein 4 (BMP4)²¹. High-sequence coverage of the 11 new base-resolution DNA methylomes allowed interrogation of 75.7–94.5% of the genomic cytosines (Fig. 1a and Supplementary Table 1).

The genome-wide frequency of DNA methylation at both CG and non-CG (mCH, where H = A, C or T) sites indicated that iPSCs resemble ES cells and are distinct from somatic cells. All ES cell and iPSC lines were methylated at CG dinucleotides at a higher frequency compared to the somatic cell lines (Fig. 1b), consistent with the global partially methylated state previously observed in the IMR90 fibroblast genome¹⁸. Similarly, whereas somatic cells contained negligible levels of cytosine methylation in the non-CG context, all pluripotent cells harboured significant mCH at a similar frequency (Fig. 1c), accounting for 20–30% of detected DNA methylation events in the genome. As observed in ES cells¹⁸, all iPSC genomes showed enrichment for mCH in genes (Fig. 1d). On a genome scale the DNA methylomes of ES cells and iPSCs are similar to one another and highly distinct from the primary somatic cell lines, including the adult stem cell ADS line, and this relationship agrees with clustering of cell types based on transcriptional activity (Fig. 1e and Supplementary Fig. 1a, b). Analysis of DNA methylation patterns at enhancers, transcriptionfactor-binding sites and pluripotency-related genes confirmed the previously reported methylation patterns¹⁸ (Supplementary Figs 2-6). Taken together, these data indicate that, on the genome scale and at

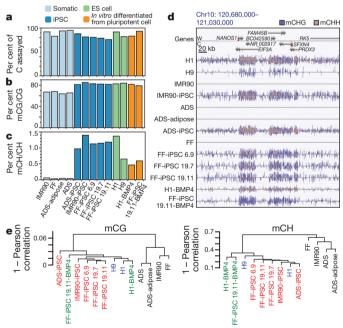


Figure 1 | Global trends of human iPSC and ES cell DNA methylomes. a, Per cent of all cytosines on each strand of the human genome assayed for each sample. b, c, The per cent of all sequencing base calls that were methylated (C, resistant to bisulphite conversion) at covered C bases in the CG (b) and CH contexts (c) (where H = A, C, or T) throughout the genome, minus the bisulphite non-conversion frequency. d, AnnoJ data browser representation of the restoration of non-CG methylation in all iPSC and ES cell lines. e, Dendrogram of the analysed cell lines based on Pearson correlation of mCG

or mCH levels in 1-kb windows throughout the genome.

these crucial genomic regions, iPSC and ES cell DNA methylomes closely resemble one another.

We discovered previously that 40% of the genome of IMR90 fibroblasts was in a partially methylated state, termed partially methylated domains (PMDs)¹⁸. The DNA methylomes of the primary somatic cell lines we have profiled here also contain PMDs in a similar proportion of the genome to IMR90 cells (Fig. 2a). As observed previously in IMR90 cells, the transcript abundance associated with genes located within PMDs was lower than the average for all other genes (Fig. 2b). Notably, these PMDs were transformed to a fully methylated state in the CG context by induction of a pluripotent state (Fig. 2a and Supplementary Fig. 7). Lastly, the reprogramming process was able to reverse the transcriptional repression associated with the PMD state (Fig. 2b).

mCG somatic memory and aberrant reprogramming

Although global patterns of DNA methylation in the CG context appeared very similar between ES cells and iPSCs (Figs 1 and 2), a comprehensive analysis of CG DNA methylation between all ES cell and iPSC lines identified 1,175 differentially methylated regions (CG-DMRs) that were differentially methylated in at least one iPSC or ES cell line (1% false discovery rate (FDR); Fig. 3a and Supplementary Table 2) and in total comprised 1.68 Mb ranging from 1–11 kb in length. Importantly, identification of CG-DMRs between the H1 and H9 ES cells with the same criteria (1% FDR) provided no results (see Supplementary Methods for details). Whereas mCG patterns within each category of cells (ES cell, iPSC, somatic) were generally consistent and distinct from the cells in each other category, individual cell lines showed some variability.

DNA methylation at CG islands proximal to gene promoters and transcriptional start sites is inhibitory to transcriptional activity²². To address whether highly methylated CG islands in differentiated cells

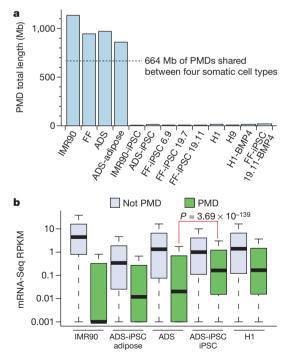


Figure 2 | Partially methylated domains become highly methylated on induction of pluripotency. a, Total length of PMDs identified in each cell line and overlap of PMDs identified in the four somatic cell types. b, mRNA-Seq RPKM (reads per kilobase of exon per million reads) values for all RefSeq genes outside PMDs, and all RefSeq genes within genomic regions defined as PMDs. For ADS-iPSC and H1 the ADS PMD genomic regions were used as PMDs. *P* value is from two-tailed Wilcoxon test between ADS PMDs and ADS-iPSC PMDs.

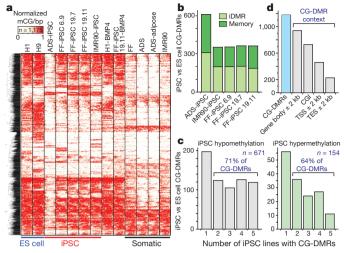


Figure 3 | CG-DMRs identified between pluripotent cells. a, Complete linkage hierarchical clustering of mCG density within CG-DMRs identified between all ES cell and iPSC DNA methylomes. Each CG-DMR was profiled over 20 equally sized bins. b, The CG-DMRs for each iPSC line with respect to H1 and H9 ES cells were categorized as having methylation patterns like the progenitor somatic cell line (memory) or iPSC-specific (iDMR). c, Number of iPSC hypomethylated and hypermethylated CG-DMRs aberrant in the indicated number of iPSC lines. d, Number of all CG-DMRs coincident with indicated genomic and genic features. CGI, CG island; TES, transcriptional end site; TSS, transcriptional start site.

can be demethylated during iPSC reprogramming, we analysed CG-DMRs between the ES cells and somatic cells (1% FDR, twofold enrichment) that overlapped with CG islands. Of 3,507 CG-DMRs coincident with CG islands (CGI-DMRs), 1,904 and 374 were hypermethylated in ES cells and somatic cells, respectively. Of the 374 CGI-DMRs hypermethylated in somatic cells, 94% were hypomethylated in the iPSCs and were similar to ES cells (Supplementary Fig. 8). Of the 1,904 CGI-DMRs hypermethylated in ES cells, 83% were hypermethylated, similar to ES cells, in the iPSCs (Supplementary Fig. 9). Together, these results indicate that CG islands in iPSCs are predominantly reprogrammed to an ES-cell-like state and, in particular, hypermethylated CG islands are not especially resistant to reprogramming.

CG-DMRs identified between iPSCs and ES cells may be categorized as either a failure to reprogram the progenitor somatic cell methylation patterns (somatic 'memory') or iPSC-specific DMRs (iDMRs) that are not observed in the progenitor somatic cells and ES cells. A recent study reported the retention of somatic cell DNA methylation patterns in early-passage (passage 4) mouse iPSCs that was sufficient to distinguish between iPSC lines derived from different progenitor cell types, and which was subsequently attenuated after further passages (10-16 in total)¹⁴. However, the iPSCs analysed here included relatively latepassage iPSC lines (15-65 passages; Supplementary Table 1), indicating that we are able to discriminate somatic DNA methylation patterns in iPSCs that are resistant to resetting to an ES-cell-like state. Comparison of iPSC lines to their respective progenitors revealed that 44-49% of CG-DMRs were aberrant with respect to ES cells (P value = 0.05) and reflected memory of the progenitor methylation state (Fig. 3b and Supplementary Fig. 10). Accordingly, 51-56% of the iPSC CG-DMRs could be classified as iDMRs, reflecting a methylation state dissimilar to the respective progenitor somatic cell and both ES cell lines (Fig. 3b and Supplementary Fig. 10).

Inspection of the concordance of methylation states in the five iPSC lines showed that 69% of the CG-DMRs were aberrant with respect to the ES cells in at least two iPSC lines, with 16% being confirmed in all five iPSC lines (Fig. 3c and Supplementary Table 3). The majority of CG-DMRs (80%) occurred at CG islands, and to a lesser extent near or within genes (62%), with 29% and 19% located within 2 kb of transcriptional

start and end sites, respectively (Fig. 3d). Analysis of biological processes attributed to genes proximal to CG-DMRs in each line or common to all iPSC lines did not identify any enrichment of specific processes, indicating that disruption of the normal regulation of these genes could affect many aspects of cellular function. Closer inspection of the CG-DMRs confirmed in all five iPSC lines revealed that the vast majority of them (119 of 130, or 92%) were hypomethylated in the iPSC lines, indicating that the general deficiency in resetting DNA methylation patterns during reprogramming is insufficient methylation. Notably, the remaining 11 CG-DMRs hypermethylated in all iPSC lines were iDMRs, as they are not differentially methylated in the progenitor cells compared to the ES cells. In addition, they were associated with transcriptional repression and the absence of the heterochromatic H3K27me3 histone modification, compared to H1 ES cells (Fig. 4a, b).

The genome sequences at the CG-DMRs present in all iPSC lines were analysed to identify motifs that could be associated with the altered DNA methylation states. Binding sites for two human transcription factors were identified in sequences conserved over the DMRs, corresponding to the reprogramming factor KLF4 and the chromatin-remodelling factor FOXL1 (Supplementary Fig. 11). Given that KLF4 has previously been found to bind to the promoter of FAM19A5 in H1 ES cells at precisely the same genomic position as one of the 11 hypermethylated iDMRs shared between all iPSC lines¹⁸, it is tempting to speculate that development of the conserved aberrant methylation states in the iPSC lines may be related to altered expression of the endogenous and/or introduced copy of *KLF4* during the reprogramming process.

By differentiation of both H1 and FF-iPSC 19.11 cells into trophoblast lineage cells with BMP4, we were able to determine the frequency at which CG-DMRs in iPSCs were transmitted through differentiation. We identified 140 hypomethylated (Fig. 4c) and 70 hypermethylated (Fig. 4d) CG-DMRs present in both FF-iPSC 19.11 cells and FF-iPSC 19.11-BMP4 trophoblasts with respect to H1 and H9 ES cells, and H1-BMP4 trophoblasts. A high proportion of the CG-DMRs in FF-iPSC 19.11 cells relative to both ES cell lines were transmitted through the differentiation process, with 88% and 46% of hypermethylated and hypomethylated CG-DMRs, respectively, still present in FF-iPSC 19.11-BMP4 trophoblasts but not in H1-BMP4 trophoblasts (Fig. 4e). These transmitted CG-DMRs were comprised of both somatic memory (Fig. 4e and Supplementary Fig. 12) and iDMR (Fig. 4e and Supplementary Fig. 13) classes. Notably, 9 of 11 hypermethylated and 57 of 119 hypomethylated CG-DMRs present in all iPSC lines were transmitted to the FF-iPSC 19.11-BMP4 trophoblast cells.

The 1,175 CG-DMRs identified between iPSCs and ES cells and the iPSC conserved CG-DMRs were profiled and confirmed in two previously reported ES cell DNA methylomes, HSF1 (ref. 23) and H9-Laurent (ref. 24) (Supplementary Fig. 14). Hierarchical clustering of the 1,175 CG-DMRs indicated that HSF1 and H9-Laurent ES cells are similar to H1 and H9. Lastly, we find that all of the iPSC hypermethylated CG-DMRs and 75% of the iPSC hypomethylated CG-DMRs are confirmed with respect to the two additional ES cell lines (*P* value < 0.05, as for H1 and H9).

Several conclusions can be made from this catalogue of CG-DMRs. First, reprogramming a somatic cell to a pluripotent state generates hundreds of aberrantly methylated loci, predominantly at CG islands and associated with genes. Second, whereas insufficient reprogramming manifested as a memory of the progenitor somatic cell methylation state is common, a high incidence of iDMRs unlike both the progenitor somatic cell and ES cells indicates that aberrant methylation patterns dissimilar to both the start and endpoints of the reprogramming process are frequently generated. Third, although there is variability in the loci that are differentially methylated between iPSC lines, a high proportion of CG-DMRs are found in multiple independent iPSC lines, indicating that these regions have a strong propensity to be insufficiently or aberrantly reprogrammed. Fourth, a core set of CG-DMRs was present in every iPSC line, representing hotspots of

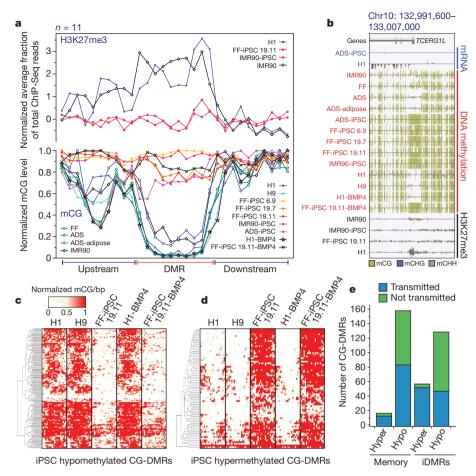


Figure 4 | Characterization of CG-DMRs in iPSCs. a, Normalized mCG levels (lower *y*-axis) and normalized H3K27me3 ChIP-Seq read density (upper *y*-axis) over CG-DMRs hypermethylated in all iPSC lines and flanking genomic regions. b, Data browser representation of mRNA, DNA methylation and H3K27me3 density for a CG-DMR identified in all iPSC lines. c, Complete linkage hierarchical clustering of mCG density within the CG-DMRs hypomethylated in both FF-iPSC 19.11 and FF-iPSC 19.11-BMP4 relative to H1, H9 and H1-BMP4 cell lines. Each CG-DMR was profiled over 20 equally

failed epigenomic reprogramming common to iPSCs. Fifth, both memory CG-DMRs and iDMRs are transmitted through differentiation of the iPSCs at a high frequency, indicating that the disrupted DNA methylation states are not simply a transient aberration during the pluripotent state. The identification of hundreds of CG-DMRs that cannot be erased by passaging and are frequently transmitted through cellular differentiation has immediate consequences for the derivation and use of iPSCs.

Megabase-scale regions of aberrant non-CG methylation

Although non-CG DNA methylation levels and distribution were very similar between ES cells and iPSCs on a whole-genome and chromosomal scale (Fig. 1), a systematic comparison of non-CG methylation levels between the H1 and the ADS-iPSC lines throughout the autosomes revealed the presence of 29 large, non-CG differentially methylated regions (FDR = 1%; Supplementary Table 4). These non-CG 'mega'-DMRs tended to be very large, with half greater than 1 Mb in length, the longest \sim 4.8 Mb, and in total all 29 made up 32.4 Mb (Fig. 5a, inset). The majority of non-CG mega-DMRs were hypomethylated in the mCH context in the ADS-iPSC line (22 of 29, total length = 29.1 Mb; Supplementary Fig. 15a, b). The H1 hypomethylated non-CG mega-DMRs contained 36 genes enriched for biological processes related to epidermal cell differentiation (54% of 36 genes; P value = 1.5×10^{-35}), and that predominantly were not expressed in H1 cells but were transcribed at a low level in ADS-iPSCs

sized bins. **d**, Same as **c** for hypermethylated CG-DMRs. **e**, FF-iPSC 19.11 CG-DMR transmission through differentiation to trophoblast cells. CG-DMRs were categorized by methylation state relative to the ES cells (hyper, hypermethylated; hypo, hypomethylated), similarity to somatic progenitor methylation (memory: like progenitor; iDMR: unlike progenitor), and whether the CG-DMR was present in FF-iPSC 19.11 differentiated into trophoblast cells with BMP4 (transmitted) or not (not transmitted).

(Supplementary Table 5). Focusing subsequent analysis on the 22 non-CG mega-DMRs hypomethylated in the ADS-iPSC line compared to the H1 line, we discovered that non-CG mega-DMR localization was strongly biased towards close proximity to centromeres and telomeres (Fig. 5a; Poisson P value = 1×10^{-12}), indicating that somatic cell reprogramming may be susceptible to DNA methylation abnormalities in these chromosomal regions. We did not find evidence that the retroviral insertions used to introduce the pluripotency factors in ADS-iPSCs was associated with the altered reprogramming of DNA methylation (Supplementary Fig. 16 and Supplementary Table 6).

Profiling non-CG DNA methylation levels throughout the 22 ADS-iPSC hypomethylated mega-DMRs for each ES cell and iPSC line, we found that depletion of non-CG methylation was a common feature of the independent iPSC lines (Fig. 5b, Supplementary Figs 1b, 17 and Supplementary Table 4). We proposed that the localized failure to restore non-CG methylation in these large regions could be mechanistically linked to the presence of particular covalent histone modifications that impart a regional chromatin conformation that is refractive to remethylation at CH sites during reprogramming. Indeed, we identified significant regional enrichment of trimethylation of histone H3 lysine 9 (H3K9me3) in two iPSC lines²⁵ that was spatially concordant with the non-CG mega-DMRs, and absent in H1 ES cells (Fig. 5c). The IMR90 genome also showed enrichment of H3K9me3 highly spatially correlated with the non-CG mega-DMRs. Additionally, we found that

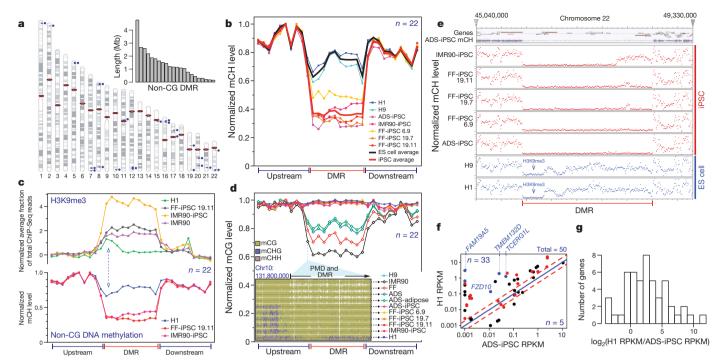


Figure 5 | Failure to restore megabase-scale regions of non-CG methylation is a hallmark of iPSC reprogramming. a, Chromosome ideograms and length distribution (inset) of the 22 ADS-iPSC non-CG mega-DMRs. Blue circles and lines indicate location of individual DMRs. Red ellipses indicate the location of centromeres. b, Normalized mCH levels over all non-CG mega-DMRs and flanking genomic regions. c, Lower *y*-axis as in b for the cell lines indicated. Upper *y*-axis shows normalized H3K9me3 ChIP-Seq read density throughout the non-CG mega-DMRs and flanking genomic regions. Dashed blue arrows indicate the inverse relationship between mCH and H3K9me3. d, Plot shows normalized mCG levels over the non-CG mega-DMRs and flanking genomic regions. Inset is a data browser representation of DNA methylation where

the non-CG mega-DMRs tend to be partially methylated in the CG context in non-pluripotent cells (99.5% of non-CG mega-DMR bases are partially methylated in ADS cells; Fig. 5d). Taken together, these data indicate that specific large regions of somatic cell genomes proximal to centromeres and telomeres that are in the partially methylated mCG state, and that bear the heterochromatin modification H3K9me3, may often be resistant to complete reprogramming of non-CG methylation to the embryonic state, remaining in a somatic configuration after induction of pluripotency (exemplified for one DMR in Fig. 5e).

To determine if the non-CG mega-DMRs affected disruption of transcriptional activity, we compared the transcript abundance between ADS-iPSCs and H1 ES cells of genes located within these regions (Fig. 5f). Of the 50 RefSeq genes within the non-CG mega-DMRs, 33 showed ≥2-fold lower transcript abundance in ADS-iPSCs compared to H1 ES cells (Supplementary Table 7). This indicates that non-CG mega-DMRs are associated with transcriptional disruption in the iPSCs (Fig. 5g). Notably, 10 of the 11 iDMRs that were consistently hypermethylated in every iPSC line (Fig. 4a, b) were located within the non-CG mega-DMRs ($P = 8.5 \times 10^{-39}$), but this was not true of any of the common hypomethylated CG-DMRs. Further, 9 of these 10 consistently hypermethylated iDMRs located in non-CG mega-DMRs were transmitted to the trophoblast cells derived from the FF-iPSC 19.11 line. Lastly, 64% of genes with lower transcript abundance in ADS-iPSCs in non-CG mega-DMRs also showed dense CG hypermethylation at the transcriptional start site (Fig. 5f, red circles), a subset of which were consistently hypermethylated at the transcriptional start site in all iPSC lines analysed and associated with aberrant loss of H3K27me3 (Fig. 5f, blue circles, Fig. 4b) providing potential molecular markers for determination of complete reprogramming in iPSC lines. Several of these suppressed genes showing

vertical bar height indicates mC level at the 5′ of a non-CG mega-DMR and PMD. e, Normalized mCH levels over a non-CG mega-DMR on chromosome 22 and flanking regions. Top panel shows gene models and ADS-iPSC mCH. f, Comparison of transcript abundance between H1 and ADS-iPSC. Each dot represents a RefSeq gene within the 22 non-CG mega-DMRs. Red dots indicate genes that have a CG-DMR within 2 kb of the transcriptional start site. Blue dots indicate genes that have a CG-DMR within 2 kb of the transcriptional start site, are hypermethylated in all iPSC lines and are associated with loss of H3K27me3. Red dashed lines represent twofold difference. g, The number of genes with a given transcript abundance ratio between H1 and ADS-iPSCs for all RefSeq genes within the non-CG mega-DMRs.

transcriptional start site CG hypermethylation encode proteins that may be pertinent to neural processes: *TMEM132D*²⁶, *FAM19A5*²⁷, *TCERG1L*²⁸ and *FZD10*. Notably, *TCERG1L* and *FAM19A5* were reported to be consistently expressed significantly higher in ES cells compared to iPSCs²⁹ (J.A.T., personal communication).

Concluding remarks

Through generation of the first unbiased, whole-genome, single-base-resolution DNA methylomes for a variety of human iPSCs and ES cells we have gained several new insights into the epigenomic reprogramming process. Reprogramming induces a remarkable reconfiguration of the DNA methylation patterns throughout the somatic cell genome, returning PMDs to a fully methylated state, reinstating non-CG methylation, and reprogramming most unmethylated and methylated CG islands to an ES-cell-like state. Overall, this process generates an iPSC methylome that, in general, is very similar to that of ES cells.

On closer inspection we identified numerous differences in DNA methylation between ES cells and iPSCs. In terms of mCG, reprogramming generated hundreds of differentially methylated regions, most associated with CG islands and genes, and seeming to represent both memory of the somatic cell DNA methylation patterns as well as iPSC-specific DNA methylation patterns. Notably, many of the CG-DMRs were shared between independent iPSC lines, indicating that these loci are inherently susceptible to aberrant methylation in the reprogramming process. Further, the presence of unique CG-DMRs in each iPSC line indicates that in addition to the aforementioned susceptible regions, there may be a stochastic element to reprogramming that results in interclone variability. Lastly, both somatic memory and iDMRs can be transmitted at high frequency through differentiation.

We also identified megabase-scale genomic regions that were repeatedly resistant to reprogramming of non-CG methylation, and were associated with altered H3K9me3 and transcriptional activity, constituting phenotypic differences at the transcriptional level that could have downstream consequences for iPSC or derived somatic cell function. The close proximity of the non-CG mega-DMRs to centromeres and telomeres indicates that there could be distinct molecular properties of these chromosomal regions—for example particular histone variants—which impede the reprogramming process. Together, the non-CG mega-DMRs, common CG-DMRs in all iPSC lines, transmitted CG-DMRs and differentially expressed genes are potentially useful as diagnostic markers for incomplete iPSC reprogramming, characterization of the efficacy of different reprogramming techniques, and potential propagation of altered methylation states into derivative differentiated cells. From these first comprehensive whole-genome, base-resolution methylome maps it seems clear that iPSCs are fundamentally distinct from ES cells, insofar as they manifest common, quantifiable epigenomic differences. Continued study of a wide variety of ES cells is needed to understand the full range of epigenomic variability, and to potentially identify factors that enable complete reprogramming to occur.

METHODS SUMMARY

Biological materials and sequencing libraries. Strand-specific mRNA-Seq libraries were produced as described previously¹⁸. MethylC-Seq libraries were generated by ligation of methylated sequencing adapters to fragmented genomic DNA followed by purification, sodium bisulphite conversion and 4–8 cycles of polymerase chain reaction (PCR) amplification as described previously¹⁸ with minor modifications (see Supplementary Materials). ChIP-Seq libraries were prepared following Illumina protocols with minor modifications (see Supplementary Materials). Sequencing was performed using the Illumina Genome Analyser IIx and HiSeq2000 instruments as per the manufacturer's instructions.

Read processing and alignment. MethylC-Seq sequencing data was processed using the Illumina analysis pipeline and FastQ format reads were aligned to the human reference genome (hg18) using the Bowtie algorithm³⁰ as described previously¹⁸ with minor modifications (see Supplementary Materials). mRNA-Seq reads were uniquely aligned to the human reference (hg18) and quantified using the TopHat³¹ and Cufflinks³² algorithms. Base calling and mapping of Chip-Seq reads was performed using the Illumina analysis pipeline.

Full Methods and any associated references are available in the online version of the paper at www.nature.com/nature.

Received 11 September 2010; accepted 11 January 2011. Published online 2 February 2011.

- Soldner, F. et al. Parkinson's disease patient-derived induced pluripotent stem cells free of viral reprogramming factors. Cell 136, 964–977 (2009).
- 2. Yamanaka, S. A fresh look at iPS cells. Cell 137, 13–17 (2009).
- Takahashi, K. & Yamanaka, S. Induction of pluripotent stem cells from mouse embryonic and adult fibroblast cultures by defined factors. Cell 126, 663–676 (2006).
- 4. Takahashi, K. et al. Induction of pluripotent stem cells from adult human fibroblasts by defined factors. *Cell* **131**, 861–872 (2007).
- Yu, J. et al. Induced pluripotent stem cell lines derived from human somatic cells. Science 318, 1917–1920 (2007).
- Park, I. et al. Reprogramming of human somatic cells to pluripotency with defined factors. Nature 451, 141–146 (2008).
- Yu, J. et al. Human induced pluripotent stem cells free of vector and transgene sequences. Science 324, 797–801 (2009).
- Zhao, X. Y. et al. iPS cells produce viable mice through tetraploid complementation. Nature 461, 86–90 (2009).
- Boland, M. J. et al. Adult mice generated from induced pluripotent stem cells. Nature 461, 91–94 (2009).
- Guenther, M. G. et al. Chromatin structure and gene expression programs of human embryonic and induced pluripotent stem cells. Cell Stem Cell 7, 249–257 (2010).
- Deng, J. et al. Targeted bisulfite sequencing reveals changes in DNA methylation associated with nuclear reprogramming. Nature Biotechnol. 27, 353–360 (2009).
- Doi, A. et al. Differential methylation of tissue- and cancer-specific CpG island shores distinguishes human induced pluripotent stem cells, embryonic stem cells and fibroblasts. Nature Genet. 41, 1350–1353 (2009).

- Kim, K. et al. Epigenetic memory in induced pluripotent stem cells. Nature 467, 285–290 (2010).
- Polo, J. M. et al. Cell type of origin influences the molecular and functional properties of mouse induced pluripotent stem cells. *Nature Biotechnol.* 28, 848–855 (2010).
- Stadtfeld, M. et al. Aberrant silencing of imprinted genes on chromosome 12qF1 in mouse induced pluripotent stem cells. Nature 465, 175–181 (2010).
- Miura, K. et al. Variation in the safety of induced pluripotent stem cell lines. Nature Biotechnol. 27, 743–745 (2009).
- Hu, B. Y. et al. Neural differentiation of human induced pluripotent stem cells follows developmental principles but with variable potency. Proc. Natl Acad. Sci. USA 107, 4335–4340 (2010).
- Lister, R. et al. Human DNA methylomes at base resolution show widespread epigenomic differences. Nature 462, 315–322 (2009).
- Sugii, S. et al. Human and mouse adipose-derived cells support feederindependent induction of pluripotent stem cells. Proc. Natl Acad. Sci. USA 108, 3558–3563 (2010).
- 20. Daley, G. et al. Broader implications of defining standards for the pluripotency of iPSCs. Cell Stem Cell 4, 200–201 (2009).
- Xu, R. H. et al. BMP4 initiates human embryonic stem cell differentiation to trophoblast. Nature Biotechnol. 20, 1261–1264 (2002).
- Cedar, H. & Bergman, Y. Linking DNA methylation and histone modification: patterns and paradigms. *Nature Rev. Genet.* 10, 295–304 (2009).
- Chodavarapu, R. K. et al. Relationship between nucleosome positioning and DNA methylation. Nature 466, 388–392 (2010).
- Laurent, L. et al. Dynamic changes in the human methylome during differentiation. Genome Res. 20, 320–331 (2010).
- Hawkins, R. D. et al. Distinct epigenomic landscapes of pluripotent and lineagecommitted human cells. Cell Stem Cell 6, 479–491 (2010).
- Erhardt, A. et al. TMEM132D, a new candidate for anxiety phenotypes: evidence from human and mouse studies. Mol. Psychiatry advance online publication, doi:10.1038/mp.2010.4 (6 April 2010).
- Yilmaz, G., Alexander, J. S., Erkuran Yilmaz, C. & Granger, D. N. Induction of neuroprotective/regenerative genes in stem cells infiltrating post-ischemic brain tissue. *Exp. Transl. Stroke Med.* 2, 11 (2010).
- Li, M. Z. et al. Molecular mapping of developing dorsal horn-enriched genes by microarray and dorsal/ventral subtractive screening. *Dev. Biol.* 292, 555–564 (2006).
- Chin, M. H. et al. Induced pluripotent stem cells and embryonic stem cells are distinguished by gene expression signatures. Cell Stem Cell 5, 111–123 (2009).
- Langmead, B., Trapnell, C., Pop, M. & Salzberg, S. L. Ultrafast and memory-efficient alignment of short DNA sequences to the human genome. *Genome Biol.* 10, R25 (2009).
- Trapnell, C., Pachter, L. & Salzberg, S. L. TopHat: discovering splice junctions with RNA-Seq. Bioinformatics 25, 1105–1111 (2009).
- 32. Trapnell, C. et al. Transcript assembly and quantification by RNA-Seq reveals unannotated transcripts and isoform switching during cell differentiation. *Nature Biotechnol.* **28**, 511–515 (2010).

Supplementary Information is linked to the online version of the paper at www.nature.com/nature.

Acknowledgements We thank L. Zhang and G. Schroth for assistance with MethylC-Seq library sequencing. R.L. is supported by a California Institute for Regenerative Medicine Training Grant. M.P. is supported by a Catharina Foundation postdoctoral fellowship. R.D.H. is supported by an American Cancer Society Postdoctoral Fellowship. Y.K. is supported by the Japan Society for the Promotion of Science. This work was supported by grants from the following: Mary K. Chapman Foundation, the National Science Foundation (NSF) (NSF 0726408), the National Institutes of Health (NIH) (U01 ES017166, U01 1U01ES017166-01, DK062434), the California Institute for Regenerative Medicine (RB2-01530), the Morgridge Institute for Research and the Howard Hughes Medical Institute. We thank the NIH Roadmap Reference Epigenome Consortium (http://www.roadmapepigenomics.org/). This study was carried out as part of the NIH Roadmap Epigenomics Program.

Author Contributions Experiments were designed by R.L., J.R.E., R.M.E., B.R., J.A.T., Y.S.K., R.Y., M.D. and R.D.H. Cells were grown by J.A.-B. and Y.S.K. MethylC-Seq and RNA-Seq experiments were conducted by R.L. and J.R.N. ChIP-Seq experiments were conducted by R.D.H. ChIP-Seq data analysis was performed by G.H., S.K. and R.D.H. Retroviral insertion site localization experiments were performed by R.O'M. and R.C. Sequencing data processing was performed by R.L. and G.H. Bioinformatic and statistical analyses were conducted by M.P., R.L. and G.H. R.S. performed data interpretation analyses. The manuscript was prepared by R.L., M.P. and J.R.E.

Author Information Analysed datasets can be browsed and downloaded from http://neomorph.salk.edu/ips_methylomes. Sequence data for MethylC-Seq, RNA-Seq and Chip-Seq experiments have been submitted to the NCBI SRA database under the accession numbers SRA023829.2 and SRP000941. Reprints and permissions information is available at www.nature.com/reprints. The authors declare no competing financial interests. Readers are welcome to comment on the online version of this article at www.nature.com/nature. Correspondence and requests for materials should be addressed to J.R.E. (ecker@salk.edu).

METHODS

Cell culture. ADS cells were obtained from Invitrogen (catalogue no. R7788110) and cultured under recommended conditions. ADS cells were grown in 10-cm² dishes (5,000 cells cm⁻²). For making iPSCs, ADS cells (3,000 cm⁻²) were plated in six-well plates. The cells were infected with the combination of human reprogramming retroviruses (MYC, KLF4, OCT4, or SOX2 in pMXs; Addgene) that had been produced in 293T cells co-transfected with gag/pol and VSV-G as described earlier. On day 5, cells were passed onto 6-cm dishes without MEFs. Cells were cultured in DMEM/F12 plus 20% knockout serum replacement (KSR) medium supplemented with β -mercaptoethanol (0.1%), non-essential amino acids (NEAA) (1 \times), Glutamax (1%), and 10 ng ml⁻¹ FGF2. Medium was changed every day. On days 18-28, individual colonies were picked and cultured feeder-free in defined mTeSR1 medium on plates coated with Matrigel (BD Biosciences). The profiled ADS-iPSC clone was assayed for pluripotency by analysis of the transcript abundance of pluripotency markers, and in vitro and in vivo (teratoma) differentiation into three germ layers, as described previously¹⁹. For differentiation from ADS cells to mature adipocytes in vitro, ADS cells $(10,000\,\mathrm{cm}^{-2})$ were plated on $10\mathrm{-cm}^2$ dishes with growth media. Differentiation was induced for 14 days using medium consisting of DMEM/F12, 10% KSR, and an adipogenic cocktail (0.5 mM IBMX, $0.25\,\mu\text{M}$ dexamethasone, $1\,\mu\text{g}\,\text{ml}^{-1}$ insulin, $0.2\,\text{mM}$ indomethacin and $1\,\mu\text{M}$ pioglitazone). For collecting mature adipocytes, the cells were detached with trypsin, then neutralized. After centrifuging detached cells, floated fat cells were transferred into new tubes. H9 cells were passage 42 including several passages in mTeSR1. IMR90-iPSCs were derived by lentiviral integration as reported previously⁵, and were passage 65, with 33 passages in mTeSR1. FF-iPSC lines were derived using nonintegrating episomal vectors as described previously⁷. FF-iPSC 19.7 (DF19-9-7) and FF-iPSC 19.11 (DF19-9-11) cells were subclones isolated from a single reprogrammed iPSC line (DF19-9), and were cultured independently for at least 20 passages. Before cell harvest aliquots of cells were assayed for OCT4 expression by flow cytometry as described previously^{33,34}. Cells were also submitted to the WiCell Cytogenetics Laboratory to confirm normal karyotype. For BMP4 differentiation, H1 or FF-iPSC 19.11 cells were grown in 10-cm² dishes (approximately 1×10^7 cells per dish) in feeder-free conditions on Matrigel using mTeSR1 media containing 50 ng ml⁻¹ BMP4 for 5 days (RND systems).

MethylC-Seq library generation. Five micrograms of genomic DNA was extracted from frozen cell pellets using the DNeasy Mini Kit (Qiagen) and spiked with 25 ng unmethylated Lambda cl857 Sam7 DNA (Promega). The DNA was fragmented with a Covaris S2 (Covaris) to 75-175 bp or 100-400 bp for single-read or paired-read libraries, respectively, followed by end repair and addition of a 3' A base. Cytosine-methylated adapters provided by Illumina were ligated to the sonicated DNA as per the manufacturer's instructions for genomic DNA library construction. For single-read libraries, adaptor-ligated DNA was isolated by two rounds of purification with AMPure XP beads (Beckman Coulter Genomics). For paired-read libraries, adaptor-ligated DNA of 275–375 bp (150–250 bp insert) was isolated by 2% agarose gel electrophoresis. Adaptor-ligated DNA (≤450 ng) was subjected to sodium bisulphite conversion using the MethylCode kit (Life Technologies) as per the manufacturer's instructions. The bisulphite-converted, adaptor-ligated DNA molecules were enriched by 4-8 cycles of PCR with the following reaction composition: 2.5 U of uracil-insensitive PfuTurboC_x Hotstart DNA polymerase (Stratagene), 5 μl 10× PfuTurbo reaction buffer, 31 μM dNTPs, 1 μl Primer 1, 1 μl Primer 2 (50 μl final). The thermocycling parameters were: 95 °C for 2 min, 98 $^{\circ}$ C for 30 s, then 4–8 cycles of 98 $^{\circ}$ C for 15 s, 60 $^{\circ}$ C for 30 s and 72 $^{\circ}$ C for 4 min, ending with one 72 $^{\circ}\text{C}$ for 10 min step. The reaction products were purified using AMPure XP beads. Up to two separate PCR reactions were performed on subsets of the adaptor-ligated, bisulphite-converted DNA, yielding up to two independent libraries from the same biological sample. Final sequence coverage was obtained by sequencing all libraries for a sample separately, thus reducing the incidence of 'clonal' reads that share the same alignment position and probably originate from the same template molecule in each PCR. The sodium bisulphite non-conversion rate was calculated as the percentage of cytosines sequenced at cytosine reference positions in the Lambda genome.

Directional RNA-Seq library generation. Total RNA was isolated from cell pellets treated with RNAlater using the RNA mini kit (Qiagen) and treated with DNaseI (Qiagen) for 30 min at room temperature (22 °C). After ethanol precipitation, biotinylated LNA oligonucleotide ribosomal RNA (rRNA) probes complementary to the 5S, 5.8S, 12S, 18S and 28S rRNAs were used to deplete the rRNA from 5 μg of total RNA by RiboMinus (Life Technologies) as per the manufacturer's instructions. Purified RNA (50 ng) was fragmented by metal hydrolysis in $1\times$ fragmentation buffer (Life Technologies) for $15\, min$ at $70\,^{\circ} \text{C}$, stopping the reaction by addition of $2\,\mu l$ fragmentation stop solution (Life Technologies). Fragmented RNA was used to generate strand-specific RNA-Seq libraries as per the Directional mRNA-Seq Library Preparation Protocol (Illumina).

Chromatin immunoprecipitation and ChIP-Seq library generation. Chromatin immunoprecipitation (ChIP) and Illumina sequencing for H3K9me2 and H3K27me3 was performed as described previously²⁵.

Mapping retroviral insertion sites. MMLV retroviral insertion sites in ADSiPSC genomic DNA were identified by an adaptor ligation-mediated method for genome-wide mapping of insertions, as described previously³⁵, except with the following modifications. Genomic DNA was fragmented by sonication with a Covaris S2, followed by ligation of modified 5' or 3' long terminal repeat (LTR)specific Illumina adapters: 5'-LTR (5'-3'): CAAGCAGAAGACGCATACGAG ATCGGTCTCGGCATTCCTGCTGAACCGCTCTTCCGATCTTCAGTGCAG CTGTTCCATCTGTTCTTGGCCC; 3'-LTR (5'-3'): CAAGCAGAAGACGG ${\tt CATACGAGATCGGTCTCGGCATTCCTGCTGAACCGCTCTTCCGATCTT}$ CAGTGGCCAGTCCTCCGATTGACTGAGTCG. A single mapping library was made for each of the 5' and 3' LTRs, and each library was sequenced on the Illumina Genome Analyser IIx. Each valid read contained the barcode sequence 'TCAGTG' prepended to the 5' of the genomic DNA read sequence. Retroviral insertion sites were identified by localized enrichment of greater than 300 reads within a 2-kb window, in both the 5' LTR and 3' LTR mapping libraries, and located on opposite genome strands between the two libraries. Cloning and Sanger sequencing of library molecules from the 3' LTR mapping library confirmed genomic DNA retroviral insertion sites for a representative fraction of the 17 insertion sites identified by high-throughput sequencing.

High-throughput sequencing. Single-read MethylC-Seq and RNA-Seq libraries were sequenced for up to 85 cycles using the Illumina Genome Analyser IIx. Paired-read MethylC-Seq libraries were sequenced for up to 75 cycles for each read using the Illumina HiSeq2000. Image analysis and base calling were performed with the standard Illumina pipeline, performing automated matrix and phasing calculations on a control library that was sequenced in a single lane of each flowcell.

Processing and alignment of MethylC-Seq data to identify methylated cytosines. All sequence alignments were performed against the NCBI36/hg18 human reference. Single-read MethylC-Seq sequences were processed and aligned as described previously¹⁸, except an additional filter was added to remove any mapped reads in which a read-C base was aligned to a reference-T base. Paired-read MethylC-Seq data was mapped and processed as described previously¹⁸ with the following modifications to accommodate the paired-read datatype. Both reads in a pair were trimmed of any low-quality sequence at their 3' ends and mapped to the reference genome with Bowtie v. 0.12.5³⁰ in paired-read mode, using the following parameters: -e 90 -l 20 -n 0 -k 10 -o 4 -I 0 -X 550 -pairtries 100 -nomaqround -solexa1.3-quals. Mapped reads in a read pair that overlapped were trimmed from their respective 3' ends until the reads no longer overlapped, leaving a 1-bp gap.

Mapped reads were filtered as follows: any read with more than three mismatches was trimmed from the 3' end to contain three mismatches, any read pair that contained a cytosine mapped to a reference sequence thymine was removed, and any read pairs that had more than three cytosines in the non-CG context within a single read was removed (possible non-conversion in bisulphite reaction). Read pairs were then collapsed to remove clonal reads potentially produced in the PCR amplification from the same template molecule, based on a common start position of read 1. The total uniquely mapped, non-clonal read number for each library, average coverage and total sequence yield are detailed in Supplementary Table 1.

For all MethylC-Seq data sets, methylated cytosines were identified from the mapped and processed read data as described previously¹⁸. The bisulphite conversion rates for all samples were over 99% (Supplementary Table 1). Correction of any DNA methylation sites incorrectly categorized as non-CG owing to SNPs in the sample versus reference genomes was performed as described previously¹⁸.

For the previously published HSF1²³ and H9-Laurent²⁴ data sets, the GEO sequence read data were mapped using the MethylC-Seq pipeline (H9-Laurent) and BS Seeker (HSF1)³⁶ (settings: $-e \le 55$, -m 3), and post-processing and methylcytosine identification was performed using MethylC-Seq pipeline as described earlier

Genome annotation. Genomic regions and CG islands were defined based on NCBI build 36/hg18 coordinates downloaded from the UCSC website. Promoters were arbitrarily defined as transcriptional start site ± 500 bp or 2,000 bp for each Ref Seq transcript (as indicated in the text). According to the UCSC annotation many Ref Seq transcripts can be associated with a given gene, and they can have the same or alternative transcriptional start site. Gene bodies are defined as the transcribed regions, from the start to the end of transcription sites for each Ref

mC and histone profiles. In Fig. 3a each CG-DMR was divided into 20 equally sized bins. The average methylation for all cytosines in the CG context within a bin in one sample was determined and normalized by the bin size. Lastly, the

whole data set was divided by its 70th percentile, and values higher then 1 were forced to 1. This was performed to produce a meaningful mapping between values and colours in the heatmap key, and to avoid extreme values masking the methylation levels of other CG-DMRs. CG-DMRs were then reorganized based on their similarity by means of complete linkage hierarchical clustering, using the heatmap.2 R function

In Fig. 4a each of the 11 CG-DMRs consistently hypermethylated in the 5 iPSC lines was profiled for both mCG and the H3K27me3 histone mark throughout the CG-DMR and equivalent upstream and downstream genomic regions divided into 30 equal-length bins. For DNA methylation, for each bin in each sample the total number of methylated/(methylated+unmethylated) reads was determined over the whole set of considered CG-DMRs. Final profiles were normalized by dividing them by their maximum value. For the H3K27me3 histone modification ChIP-Seq reads, RPKM values were determined in each CG-DMR and normalized to the average of the upstream/downstream flanking region RPKM values.

Figure 5b is as in Fig. 4a lower axis, but based on the mC in the CH sequence context profiled over the non-CG mega-DMRs and upstream/downstream flanking regions, minus the non-conversion frequency. The final profiles were normalized to their maximum level.

Figure 5c is as in Fig. 4a lower axis, but based on the mC in the CH sequence context profiled over non-CG mega-DMRs and upstream/downstream flanking regions minus the non-conversion frequency. In the upper axis the H3K9me3 histone modification ChIP-Seq reads were profiled as described for the H3K27me3 profiles in Fig. 4a.

Figure 5d is as in Fig. 4a lower axis, but based on the mC on the mCG sequence context profiled over non-CG mega-DMRs and upstream/downstream flanking regions. Profiles were normalized to their maximum levels.

Figure 5e is as in Fig. 4a lower axis for one example non-CG mega-DMR using 10-kb bins.

Clustering of mC profiles and chromosome 10 smoothed profiles. The methylation level for each C in the CG, CHG and CHH sequence context was summed in adjacent 10-kb windows over all autosomal chromosomes. Non-CG DNA methylation profiles were determined by adding mCHG and mCHH profiles. Clustering was performed based on the Pearson correlation over all 10-kb windows transformed into a distance measure (as 1- Pearson correlation) and using the hclust R function. Data for smoothing of non-CG mC on chromosome 10 were retrieved as for the clustering. In addition, smoothing with cubic splines was determined before plotting using the smooth.spline R function with spar argument set to 0.3.

Identification of DMRs. Non-CG mega-DMRs (Fig. 5) were identified by comparing H1 to ADS-iPSC mCHG and mCHH smoothed methylation profiles. The average methylation level of mC called (1% FDR) in the mCHG and mCHH sequence context was determined in 5-kb windows (sW). The genome was scanned considering groups of 10 adjacent windows sW over a distance less than 50 kb. The set of 10 smoothed values for mCHG in the H1 sample was compared to the set of set of 10 smoothed values in the ADS-iPSC sample using the Wilcoxon test. For both sets, at least 4 non-missing data points (that is, with sequence coverage) were required. Resulting P values were corrected with the Benjamini-Hochberg method. Regions with P value < 0.01 (1% FDR) and 8-fold enrichment of methylation level were identified, and regions closer than 100 bp were joined. This was repeated for the mC in the CHH sequence context. Lastly, mCHG and mCHH DMRs overlapping or closer than 100 kb were joined and the final set of regions was checked for having mCHG+mCHH fold enrichment of at least 2-fold between H1 and ADS-iPSCs. This set of 78 DMRs hypomethylated in ADS-iPSCs (Supplementary Fig. 15c-f) was further refined, considering the size and overlap with repressive histone marks. The final set of 22 regions reported in Fig. 5 includes all the DMRs larger than 1 Mb (17) and a range of smaller ones. Also, the 22 final non-CG mega-DMRs encompass ~92% of the initial set of 78 DMRs, based on size in bp.

CG-DMRs (Fig. 3) were identified similarly to non-CG mega-DMRs. Smoothed average methylation level was performed in 100-bp windows sW, and regions comprising a set of 10 adjacent windows sW over a distance less than 1,100 bp were considered. The Kruskall–Wallis test was used to score each region based on the methylation levels from the two ES cell and five iPSC lines. Regions with corrected P value < 0.01 (1% FDR) and 4-fold enrichment of methylation level (max/min over the 7 cell lines for each region) were identified, and regions closer than 100 bp were joined, resulting in a final set of 1,175 CG-DMRs. Regarding the H1 versus H9 comparison, the non parametric Wilcoxon test was applied: at 1% FDR and minimum 4-fold enrichment no CG-DMRs could be identified, while

only at 10% FDR and 4-fold enrichment could H1 versus H9 CG-DMRs be identified. This 10% FDR set has an overlap of 131 kb with the final set of 1,175 CG-DMRs. For these reasons the set of DMRs that visually appear different between H1 and H9 in the Fig. 3 heatmap are either above the 1% FDR threshold (H1 versus H9) or with insufficient sequence coverage in one of the two samples. (Regions without sequence coverage are not indicated in the heatmap, but are considered in the DMR selection. White spots in the heatmap are indicative of missing mCG; this can be due to either lack of sequence coverage or sufficient coverage and absence of mCG.) These regions are included in the list of the 1,175 CG-DRMs at the 1% FDR level based on inclusion of the iPSC data.

For the analysis of CG island reprogramming, the CG-DMRs were identified as for the Fig. 3 CG-DMRs (minimum enrichment 2-fold) but including the IMR90, ADS-adipose, ADS and FF differentiated cell lines in addition to the two ES cell and the five iPSC lines.

CG island reprogramming analysis was carried out as follows. CG-DMRs different between ES cells and differentiated cells were defined within the set of CG-DMRs identified comparing all analysed methylomes (see earlier), considering only CG-DMRs overlapping with CG islands. In particular, for each of these CG-DMR the mCG/bp levels in 20 equally sized bins was profiled in all cell types. DMRs with pooled mCG/bp levels different from differentiated and ES cell lines were identified (Wilcoxon test P value < 0.01, and P value > 0.05 between H1 and H9). Similarly, the set of reprogrammed CG-DMRs was identified by comparing pooled iPSC mCG profiles with the ES cell samples (Wilcoxon test P value > 0.05).

CG-DMR reprogramming analysis was carried out as follows. CG-DMRs aberrant in iPSCs and like or unlike parental cells were defined within the set of 1,175 CG-DMRs identified comparing all ES cell and iPSC samples. In particular, for each of these CG-DMR the mCG/bp levels in 20 equally sized bins was profiled in all cell types. CG-DMRs aberrant in each iPSC line were identified comparing their mCG/bp to both H1 and H9 ES cell lines (two-tailed Wilcoxon test P value < 0.05 for both, and P value > 0.01 between H1 and H9). Hypermethylated and hypomethylated CG-DMRs were identified in the same way but using a one-tailed test. Memory and iPSC-specific (iDMR) CG-DMRs were identified comparing the mCG/bp density between each iPSC and its parental line (Wilcoxon test P value > 0.01 and P value < 0.01, respectively).

Maintained CG-DMRs were identified in the FF 19.11 iPSC line comparing the mCG/bp density of H1+BMP4 with both H1 and H9 (one-tailed Wilcoxon test P value > 0.01 for both) and FF 19.11 BMP4 to both H1 and H9 (one-tailed Wilcoxon test P value < 0.05 for both).

Identification of PMDs. A sliding window approach was used to find regions of the genome that were partially methylated in each cell type, as described previously¹⁸. **Mapping RNA-Seq reads.** RNA-Seq read sequences produced by the Illumina analysis pipeline were aligned with the TopHat software³¹ to the NCBI build 36/hg18 reference sequence. Reads that aligned to multiple positions were discarded. Reads per kilobase of transcript per million reads (RPKM) values were calculated with the Cufflinks software³² using human RefSeq gene models.

Mapping and enrichment analysis of ChIP-Seq reads. Following sequencing cluster imaging, base calling and mapping were conducted using the Illumina pipeline. Clonal reads were removed from the total mapped tags, retaining only the non-clonal unique tags that mapped to one location in the genome, where each sequence is represented once. Regions of tag enrichment were identified as described previously²⁵.

Data visualization in the AnnoJ browser. MethylC-Seq, RNA-Seq and ChIP-Seq sequencing reads and positions of methylcytosines with respect to the NCBI build 36/hg18 reference sequence, gene models and functional genomic elements were visualized in the AnnoJ 2.0 browser, as described previously³⁷. The data mentioned above can be viewed in the AnnoJ browser at http://neomorph.salk.edu/ips_methylomes.

- Ludwig, T. et al. Feeder-independent culture of human embryonic stem cells. Nature Methods 3, 637–646 (2006).
- Ludwig, T. et al. Derivation of human embryonic stem cells in defined conditions. Nature Biotechnol. 24, 185–187 (2006).
- O'Malley, R. C., Alonso, J. M., Kim, C. J., Leisse, T. J. & Ecker, J. R. An adapter ligation-mediated PCR method for high-throughput mapping of T-DNA inserts in the Arabidopsis genome. Nature Protocols 2, 2910–2917 (2007).
- 36. Chen, P., Cokus, S. J. & Pellegrini, M. B. S. Seeker: precise mapping for bisulfite sequencing. *BMC Bioinformatics* **11**, 203 (2010).
- Lister, R. et al. Highly integrated single-base resolution maps of the epigenome in Arabidopsis. Cell 133, 523–536 (2008).

ARTICLE

HDACs link the DNA damage response, processing of double-strand breaks and autophagy

Thomas Robert¹*, Fabio Vanoli¹*, Irene Chiolo^{1,2}*, Ghadeer Shubassi¹, Kara A. Bernstein³, Rodney Rothstein³, Oronza A. Botrugno⁴, Dario Parazzoli⁵, Amanda Oldani⁵, Saverio Minucci^{4,6} & Marco Foiani^{1,6}

Protein acetylation is mediated by histone acetyltransferases (HATs) and deacetylases (HDACs), which influence chromatin dynamics, protein turnover and the DNA damage response. ATM and ATR mediate DNA damage checkpoints by sensing double-strand breaks and single-strand-DNA-RFA nucleofilaments, respectively. However, it is unclear how acetylation modulates the DNA damage response. Here we show that HDAC inhibition/ablation specifically counteracts yeast Mec1 (orthologue of human ATR) activation, double-strand-break processing and single-strand-DNA-RFA nucleofilament formation. Moreover, the recombination protein Sae2 (human CtIP) is acetylated and degraded after HDAC inhibition. Two HDACs, Hda1 and Rpd3, and one HAT, Gcn5, have key roles in these processes. We also find that HDAC inhibition triggers Sae2 degradation by promoting autophagy that affects the DNA damage sensitivity of *hda1* and *rpd3* mutants. Rapamycin, which stimulates autophagy by inhibiting Tor, also causes Sae2 degradation. We propose that Rpd3, Hda1 and Gcn5 control chromosome stability by coordinating the ATR checkpoint and double-strand-break processing with autophagy.

HATs and HDACs target histones and non-histone proteins¹⁻⁴ and regulate chromosome dynamics. They also influence the DNA damage response through acetylation of key DNA repair and checkpoint proteins². HDACs can be classified into three classes on the basis of sequence similarity⁵. HDAC inhibition is a promising therapeutic strategy against cancer⁶, and certain inhibitors—such as valproic acid (VPA)⁷—affect class I and II HDACs.

The DNA damage checkpoint response is mediated by two PI3 kinases, ATR and ATM (Mec1 and Tel1 in yeast, respectively)⁸. ATR is assisted by ATRIP (Ddc2 (also known as Lcd1) in yeast) and, in response to DNA damage, activates a signal transduction pathway that coordinates cell cycle events with DNA repair and controls apoptosis in mammals. In yeast, the Rad53 (CHK2 (also known as CHEK2) in humans) protein kinase has a pivotal role in transducing ATR signalling⁸. Double-strand breaks (DSBs) are dangerous DNA lesions that can be repaired by different recombination processes, depending on the cell cycle phase⁹. In G2, DSBs are processed into single-strand DNA (ssDNA) and engaged into homologous recombination-mediated repair pathways^{9,10}. Although several DNA repair proteins are acetylated, the functional significance of these modifications is mostly unknown.

Protein acetylation has been also implicated in promoting degradation of certain proteins through autophagy^{2,11}. Autophagy is a highly conserved process involved in protein and organelle turnover and results in their vacuolar (lysosomal in mammals) degradation. Crosstalk between ubiquitination and autophagy has been reported^{12,13}. Autophagy is triggered by a variety of stimuli, including nutrient starvation and TOR1 inhibitors, some of which are currently into clinical trials for cancer therapy^{14–16}.

Here we report a connection between the ATR pathway, DSB repair, protein acetylation and autophagy.

VPA counteracts the DNA damage response

We investigated how HDAC inhibition by VPA affects the DNA damage response in budding yeast. VPA treatment per se did not activate Rad53 (data not shown), but counteracted Rad53 phosphorylation after exposure to 4NQO (an ultraviolet-mimetic drug) in G1 and G2 cells or exposure to MMS (a DNA-alkylating agent) in S phase cells (Supplementary Fig. 1a). It is unlikely that VPA limits the accumulation of checkpoint activators, because inhibition of protein synthesis did not influence Rad53 phosphorylation (Supplementary Fig. 1b). As cycloheximide treatment did not restore checkpoint activation, it is also unlikely that VPA enhanced negative checkpoint regulators (Supplementary Fig. 1b). We then analysed the effect of VPA in cells experiencing a single and irreparable DSB at a specific chromosomal locus. We overexpressed HO, a yeast nuclease that recognizes a specific DNA sequence¹⁷ (Fig. 1a-c and Supplementary Fig. 2). Checkpoint activation after DSB formation requires Cdc28 (CDK1 in mammals) activity and DSB resection, which generates RPA-ssDNA nucleofilaments and recruitment of the Ddc2-Mec1 complex^{8,10}. Ten kilobases of ssDNA must accumulate to trigger Rad53 activation, which occurs 90 min after DSB formation¹⁷. After HO induction in G2, VPA counteracted Rad53 phosphorylation (Fig. 1a). VPA also affected Mec1-dependent Ddc2 and Srs2 phosphorylation^{8,18}. We next measured DSB resection at three loci (0.2, 1.6 and 5.7 kb from the break site) (Fig. 1b and Supplementary Fig. 2a). Resection rates were reduced compared to untreated conditions. Without VPA, resection of the 5.7-kb fragment was obvious at 120 min, whereas with VPA resection was still impaired after 300 min. Hence, VPA-treated cells failed to accumulate the 10 kb of ssDNA needed for Rad53 activation. We then measured the recruitment of Rfa1 and Ddc2 to the DSB region with or without VPA by

¹Fondazione IFOM (Istituto FIRC di Oncologia Molecolare), IFOM-IEO Campus, via Adamello 16, Milan 20139, Italy. ²LBNL, Department of Genome Biology, Berkeley, California 94710-2722, USA.

³Department of Genetics and Development, Columbia University Medical Center, New York, New York 10032-2704, USA. ⁴European Institute of Oncology, IFOM-IEO campus, Milan 20139, Italy.

⁵Cogentech, Milan 20139, Italy. ⁶DSBB-Università degli Studi di Milano, Milan 20139, Italy.

^{*}These authors contributed equally to this work.

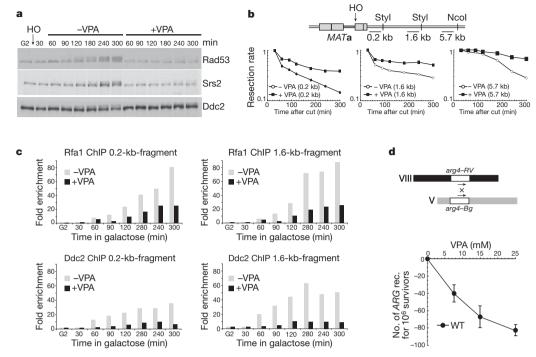


Figure 1 VPA treatment counteracts DNA double-strand-break processing. a-c, RFA1::FLAG DDC2::MYC cells were arrested in G2 and released in YP galactose to induce HO endonuclease. After 30 min, the culture was split in two: +VPA and -VPA. a, Samples were processed for western blot using anti-Rad53, Srs2 and Ddc2 antibodies. b, A schematic diagram showing

chromatin immunoprecipitation (ChIP) analysis (Fig. 1c and Supplementary Fig. 2b). VPA counteracted Rfa1 and Ddc2 recruitment at the 0.2-kb and 1.6-kb fragments, indicating that DSB processing and signalling are crippled in VPA. As DSB resection is a key step in homologous recombination, VPA should also impair recombination frequencies. Spontaneous ectopic recombination frequencies were indeed reduced by VPA treatment (Fig. 1d). Hence, VPA counteracts DSB resection and signalling, thus affecting homologous recombination and the signal transduction response mediated by Mec1.

Sae2 and Exo1 are degraded in VPA-treated cells

Next we analysed the early events mediating DSB processing (Fig. 2). Mre11 is the first factor recruited to a DSB to activate Tell²⁰. Mre11 indirectly influences DSB resection and its removal from the DSB region depends on Sae2, a CDK1 target involved in DSB processing^{20,21}. Exo1, Dna2 and Sgs1 (BLM in human cells), are also implicated in resection^{22–24}. We reasoned that VPA could limit the recruitment of Mre11 at DSBs²⁵. The timing of Mre11 loading at the 0.2-kb fragment was comparable with or without VPA, but Mre11 association persisted in VPA-treated cells (Fig. 2a and Supplementary Fig. 2c). Hence, VPA does not counteract DSB processing by preventing Mre11 recruitment.

VPA treatment affected Sae2 and Exo1 protein levels. After 180 min of HO induction in VPA, Sae2 and Exo1 were barely detectable whereas Mre11 was not affected (Fig. 2b). Hence, VPA affects Sae2 and Exo1 turnover, although with different kinetics as the decrease in Exo1 level was delayed compared to Sae2 (Fig. 2b and data not shown). These results account for the VPA-dependent accumulation of Mre11 because Sae2 is needed for Mre11 displacement at the DSB region^{15,20}, but may also explain the VPA-induced DSB resection defect as both Sae2 and Exo1 influence DSB resection.

VPA stimulates autophagy

We tested whether VPA induces autophagy in yeast as in mammals²⁶. Autophagy induction correlates with: (1) vacuolar staining of Cherry–Apel, an aminopeptidase specific for the CVT (cytoplasm to vacuole

probe locations with respect to the HO cut site. The resection rate was calculated as the rate of HO cut band disappearance. **c**, Fold enrichment of the 0.2-kb fragment was calculated after ChIP of Rfa1–Flag, Ddc2–Myc. **d**, VPA effect on ectopic recombination (rec.) in wild-type (WT) cells. Error bars represent standard deviation (s.d.) calculated from four independent experiments.

targeting) subpathway, and perivacuolar foci and vacuolar staining of GFP–Atg8, an autophagosome component²⁷; (2) increased enzymatic activity of Pho8 Δ 60, an autophagy marker²⁸; and (3) processing of GFP–Atg8²⁹.

Yeast cells grown in YPD medium (Fig. 3a) showed mostly Cherry—Ape1 foci but very little Cherry vacuolar staining. The foci may reflect

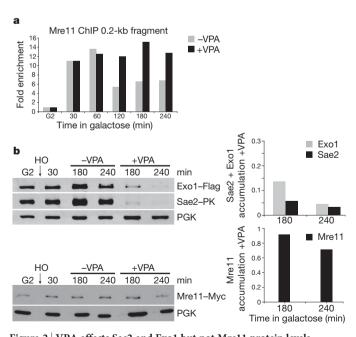


Figure 2 | VPA affects Sae2 and Exo1 but not Mre11 protein levels.
a, MRE11::MYC cells were treated as in Fig. 1a. Cell samples were processed for ChIP analysis and the fold enrichment of the 0.2-kb fragment after ChIP of Mre11–Myc without (-VPA) or with (+VPA) VPA was calculated. b, EXO1::FLAG SAE2::PK MRE11::MYC cells were grown as in a. Cell samples were taken and processed for western blot analysis using anti-Flag, PK and Myc antibodies.

Ape1 oligomer formation after synthesis²⁹. Under conditions of nitrogen starvation (SD-N medium), cells exhibiting fluorescent vacuolar staining increased, whereas the foci diminished. These results reflect starvation-induced autophagy²⁷. VPA treatment partially mimicked starvation conditions. YPD cells showed few GFP–Atg8 foci and little vacuolar staining. Conversely, starved cells expressed GFP–Atg8 foci and showed vacuolar staining. This trend was recapitulated in VPA. We then measured the Pho8 Δ 60 activity (Fig. 3b) in wild-type cells and in mutants in ATG1, encoding an essential autophagy kinase³⁰. YPD wild-type and atg1 mutants exhibited basal Pho8 Δ 60 activity. Under starvation or in VPA, Pho8 Δ 60 activity increased in wild-type cells but not in atg1 mutants. We then analysed GFP–Atg8 processing (Fig. 3c). Whereas YPD wild-type cells did not undergo GFP–Atg8 cleavage, starved and VPA cells exhibited an Atg1-dependent GFP–Atg8 processing. These results indicate that VPA induces autophagy.

VPA-induced Sae2 acetylation and degradation

Next we tested whether Sae2 and/or Exo1 were acetylated. We immunoprecipitated overexpressed HA–Sae2 in cells \pm VPA with anti-HA and subsequently \pm anti-acetyl-Lysine antibodies. Recovered Sae2

increased in VPA (Fig. 4a), indicating that Sae2 is acetylated. We failed to detect acetylated Exo1, although acetylated Exo1 has been previously described². Autophagy is the preferred pathway for the degradation of oligomeric complexes that cannot be recognized by the ubiquitin-proteasome system and form toxic aggregates 13,31. Certain proteins are specifically shunted into the autophagic pathway when they are hyperacetylated11. Hence, Sae2 might be degraded through autophagy, as its level declines in VPA, it is acetylated and forms complexes³². We tested whether Sae2 disappearance in VPA was dependent on autophagy (Fig. 4b-d). Phenylmethylsulphonyl fluoride (PMSF) inhibits serine proteases but also blocks autophagy by inhibiting vacuolar proteases³³. PMSF treatment counteracted Sae2 disappearance in VPA (Fig. 4b). We also tested whether genetic inactivation of autophagy would affect Sae2 levels. Deletion of ATG1 or ATG19 (specific for the CVT pathway)³⁰ partially compensated Sae2 destabilization in VPA (Fig. 4c). Finally, rapamycin, which induces autophagy by inhibiting Tor1³⁴, also destabilized Sae2 in an ATG1dependent manner (Fig. 4d and data not shown). Thus, in VPA, autophagy contributes to Sae2 degradation perhaps through acetylation as has been reported for the Huntingtin protein¹¹.

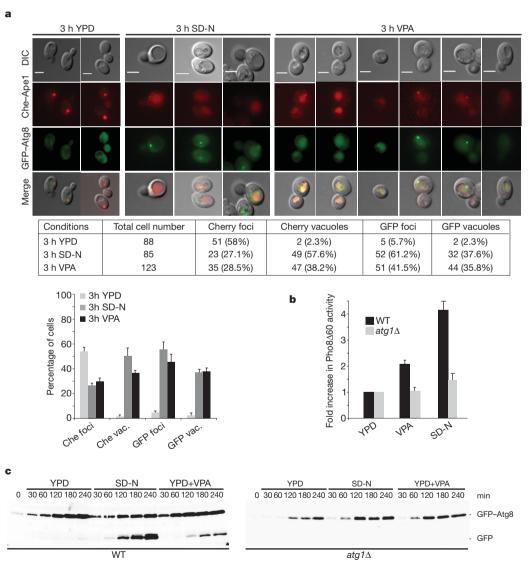


Figure 3 | GFP-Atg8 Cherry-Ape1 cellular distributions in VPA-treated cells. a, Cherry::APE1 GFP::ATG8 cells were grown and shifted to YPD, nitrogen starvation (SD-N) or YPD+VPA medium for 3 h. Samples were processed for microscopy. The table shows numbers corresponding to the experiment. Percentage of fluorescence signals is presented and error bars represent the s.d. obtained from three independent experiments. DIC,

differential interference contrast. Scale bars, 3 μ m. **b**, $pho8\Delta60$ and $pho8\Delta60$ at $g1\Delta$ cells were grown as in **a**. Pho8 $\Delta60$ activity was calculated by measuring alkaline phosphatase levels. Error bars represent s.d. calculated from five independent experiments. **c**, GFP::ATG8 and GFP::ATG8 at $g1\Delta$ cells were grown as in **a**. Cell samples were processed for western blot using anti-GFP antibody. Quantification is presented in Supplementary Fig. 3.

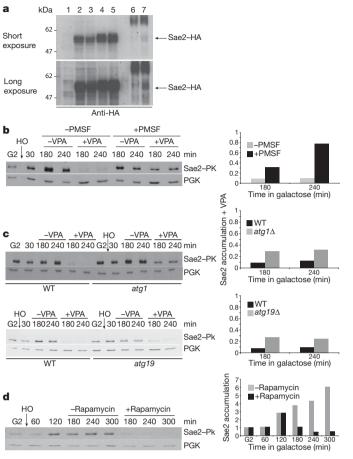


Figure 4 | **Sae2 in VPA-treated cells. a**, 4HA–Sae2 was immunoprecipitated \pm VPA with anti-HA and subsequently \pm anti-acetyl-Lysine. Eluate was analysed using anti-HA. Lane 1: input Sae2; 2: input Sae2–HA – VPA; 3: as in 2 but + VPA; 4: 3 μl elution Sae2–HA – VPA after anti-HA immunoprecipitation (IP; input AcK-IP); 5: double amount of 4; 6: IP anti-AcK elution from anti-HA IP of Sae2–HA – VPA; 7: as in 6 but + VPA. **b**, *SAE2::PK erg6*Δ cells were treated as in Fig. 2a. After 30 min induction, VPA and PMSF were added or not. Samples were processed for western blot using anti-PK. **c**, Wild-type *SAE2::PK*, *SAE2::PK atg1*Δ and *SAE2::PK atg1*9Δ cells were grown as in **b**. After 30 min induction, VPA was added or not and samples treated as in **b**. **d**, Wild-type *SAE2::PK* cells were grown as in **b**. After 120 min induction, rapamycin (200 ng ml $^{-1}$) was added or not and samples were treated as in **b**.

Gcn5, Rpd3 and Hda1 control Sae2 levels

We tested whether VPA-induced phenotypes can be recapitulated in rpd3 and hda1 mutants, altered in two class I and II HDACs, respectively³⁵. rpd3 hda1 double mutants showed hypersensitivity to 4NQO and hydroxyurea (HU; a DNA synthesis inhibitor) compared to single mutants and wild-type cells, whereas only rpd3 cells were hypersensitive to MMS (Fig. 5a). Damage-induced recombination was reduced in hda1 rpd3 mutants (data not shown). Hence, Rpd3 and Hda1 may partially substitute for each other to respond to DNA damage and to assist homologous recombination, and may be targeted by VPA. We analysed Rad53 phosphorylation in G1 or G2 arrested wild-type, hda1, rpd3 and hda1 rpd3 cells treated with 4NQO, MMS and HU and found that the double mutants failed to promote robust checkpoint activation (data not shown). Thus, both Hda1 and Rpd3 influence Rad53 activation. In response to DSB formation, rpd3 and hda1 rpd3 cells showed a severe and equivalent defect in Rad53 phosphorylation (Fig. 5b), and *rpd3* cells were resection defective although less than double mutants. Hence, Hda1 and Rpd3 influence DSB processing and signalling, although to a different extent. Sae2 failed to accumulate at wild-type levels in *hda1 rpd3* cells after HO induction in G2 (Fig. 5c). Thus, the impairment in checkpoint activation and DSB

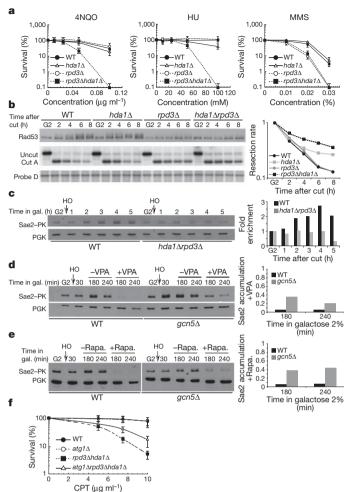


Figure 5 | Gcn5, Rpd3 and Hda1 influence Sae2 levels and cell survival in atg1 mutants in response to DNA damage. a, Survival of wild-type, $rpd3\Delta$, $hda1\Delta$ and $rpd3\Delta$ $hda1\Delta$ strains after 4NQO, MMS and HU treatment. Error bars represent s.d. calculated from seven independent experiments. b, HO was induced in G2 wild-type, $hda1\Delta$, $rpd3\Delta$ and $hda1\Delta$ $rpd3\Delta$ cells and western and Southern blot analyses were performed. c, Wild-type SAE2::PK and $hda1\Delta$ $rpd3\Delta$ SAE2::PK cells were grown as in b and western blot was performed as in Fig. 4b. d, e, Wild-type SAE2::PK and $gcn5\Delta$ SAE2::PK strains were grown as in b and after 30 min of HO induction either VPA (d) or rapamycin (e) was added or not. Western blot was performed. f, Percentage of viability of wild-type, $atg1\Delta$, $rpd3\Delta$ $hda1\Delta$ and $atg1\Delta$ $rpd3\Delta$ $hda1\Delta$ strains. Error bars represent s.d. calculated from four independent experiments.

processing and the Sae2 instability observed in VPA can be recapitulated in *rpd3 hda1* mutants. The action of Rpd3 and Hda1 is counteracted by the Gcn5 HAT (SAGA in mammals)³⁶. We found that, in the absence of Gcn5, VPA and rapamycin-mediated destabilization of Sae2 were attenuated (Fig. 5d, e).

The observations described earlier lead to the expectation that autophagy might contribute to the *hda1 rpd3* sensitivity to DNA damaging agents. *atg1* and wild-type cells exhibited comparable survival rates in response to camptothecin (CPT) treatment whereas *hda1 rpd3* cells exhibited hypersensitivity to CPT (Fig. 5f). *ATG1* ablation partially counteracted CPT-induced lethality in *hda1 rpd3* cells. Hence, in *hda1 rpd3* mutants, the Atg1-mediated autophagic response contributes to cell lethality, perhaps by destabilizing key DNA damage response factors.

Discussion

We showed that class I and II HDACs influence the DNA damage response at three levels (Supplementary Fig. 4a): checkpoint activation

throughout the cell cycle, DSB processing in G2/M and degradation of key recombination protein(s). The following considerations indicate that HDACs mediate a global DNA damage response. Firstly, besides Sae2, Cdk1, Ku, MRN, Blm² and Rfa1 (our unpublished observations) are also acetylated. Secondly, Sae2 acetylation might influence its own accumulation, thus resembling certain phenotypes of $sae2\Delta$ cells such as the inability to remove Mre11 from the DSB site³⁷. However, in contrast to sae2 mutants, checkpoint activation and DSB resection are markedly impaired by HDAC inhibition, indicating that Sae2 is not the only relevant target. Accordingly, also Exo1 is degraded in VPA, perhaps as a consequence of Sae2 destabilization. Thirdly, the DSB resection defects caused by HDAC inhibition might explain the lack of checkpoint signals (RPA filaments) in G2/M but not the checkpoint impairment in G1 and G2 cells treated with the ultravioletmimetic drug 4NQO³⁸, as 4NQO-induced checkpoint signalling does not require DSB resection. Because all the damaging agents used lead to the accumulation of RPA filaments through different mechanisms, perhaps Rfa1 acetylation also influences checkpoint signalling.

The Tip60 HAT positively influences ATM³⁹. This observation seems at odds with the findings that class I and II HDACs stimulate ATR. It is possible that HATs and HDACs have both positive and negative roles depending on the checkpoint subpathway. However, as ATR activation depends on the processing of DSBs (that represent ATM signals), it is possible that HAT-mediated ATM activation is a non-direct consequence of ATR inhibition. We note that after HDAC inhibition ATM/Tel1-mediated histone H2A phosphorylation is not affected (data not shown), probably because Mrel1 maintains Tel1 active by remaining loaded at the DSB. Moreover, the fact that Gcn5/SAGA promotes Sae2 degradation implies that this HAT indirectly negatively influences ATR signalling, perhaps by generating acetylated substrates for the autophagic pathway and/or by directly promoting autophagy.

Histone 3 lysine 9, 14, 18, 23 (converted to glycines) and histone 4 lysine 5, 8, 12, 16 (converted to arginines) mutants, altered in H3 and H4 acetylation, still activate the checkpoint (Supplementary Fig. 1c), thus indicating that H3 and H4 histone acetylation does not have a relevant role for checkpoint activation.

HDAC inhibition induces autophagy through unknown processes^{15,26} and we show that HDAC impairment destabilizes Sae2 through an autophagic pathway. However, the magnitude of autophagy induction after HDAC inhibition is not as strong as that in nitrogen-starved cells. Tor1 counteracts autophagy³⁴ and we showed that rapamycin affects Sae2 turnover. The finding that Gcn5/SAGA ablation counteracts Sae2 degradation in VPA- and rapamycin-treated cells pinpoints the HAT activity involved in this regulatory process. Intriguingly, *gcn5* mutants are sensitive to rapamycin. Moreover, *dna2* mutants are altered in DSB resection and require *TOR1* overexpression⁴⁰ for suppression. A tantalizing hypothesis is that an excess amount of Tor1 rescues *dna2* mutants by counteracting authophagy-mediated Sae2 destabilization.

We propose that (Supplementary Fig. 4b) after DSB formation, the broken chromosome arm is relocated close to the nuclear envelope⁴¹. Rpd3 and Hda1 will keep Sae2 in the deacetylated form that influences Mre11 dynamics at the DSB site³⁷. Sae2 is then released from the DSB site, perhaps as a multimeric form³² and Gcn5-mediated acetylation shunts it into autophagy-mediated degradation. This last step might be needed to counteract extensive DSB resection and/or simply to eliminate Sae2 once the first step of DSB processing has been accomplished; we note that exposure to reactive oxygen species, ultraviolet and ionizing radiation, besides damaging DNA, can cause protein damage and protein-DNA crosslinking⁴², and certain damaged repair proteins or crosslinked proteins might have to be destroyed to prevent cellular problems. Cells may use specific autophagy subpathways rather than recycle all the cellular components, including those that are not damaged. This notion is supported by the observation that Sae2 degradation depends on Atg19, a factor specific for certain types of selective autophagy. In any case, triggering unprogrammed autophagy-mediated turnover of key repair proteins, either by inhibiting HDACs and/or Tor1 would contribute to DNA damaging sensitivity. CtIP is ubiquitinated⁴³ and Sae2 levels under normal conditions increase after proteosome inhibition with MG132 (data not shown). These observations, besides indicating that Sae2 also undergoes ubiquitination, may account for the partial rescue of Sae2 levels in *atg* mutants. Crosstalk between ubiquitination and autophagy has previously been described¹². Future work will address the contribution of both pathways to DSB metabolism.

METHODS SUMMARY

Strains are listed in Supplementary Table 1. Growth conditions, synchronization and HO induction have previously been described¹⁰. VPA was used at 10 mM unless otherwise indicated. Nitrogen starvation (SD-N) medium, viability and recombination analysis have previously been described^{19,28}. Error bars represent s.d. calculated from at least three independent experiments. FACS analysis, TCA extraction and SDS-PAGE have previously been described⁴⁴. For immunodetection of Rad53 we used EL7 and F9 antibodies⁴⁵. For Myc, HA, PK, PGK1, Flag and GFP we used the 9E10, 12CA5, V5-TAG, 22C5 and M2 antibodies, respectively. Protein quantification was normalized with respect to PGK1 and accumulation was calculated as the ratio of VPA- or rapamycin-treated to untreated cells. Resection experiments were previously describe \dot{d}^{10} . Purified genomic DNA was digested with Styl (0.2-, 1.6-kb fragments) or Ncol (5.7 kb) and treated for Southern blot analysis. The density of the HO-cut band at t = 30 min (Supplementary Fig. 2a) was set to 100%. The total amount of DNA loaded in each sample was normalized by re-probing the blots with probe Control D located 170 kb from the HO site. ChIP analysis was previously described⁴⁶. The fold enrichment of fragments located 0.2 kb and 1.6 kb from the DSB was calculated as the ratio between the value of the fragment of interest and the value of the fragment used as control (ARS305). The number obtained was divided for the same ratio calculated for the whole cell extract samples of each time point. Primers for resection and ChIP experiments are the same as used previously⁴⁷. Samples for microscopic analysis were fixed in 4% formaldehyde for 5 min at room temperature (21 $^{\circ}$ C) and washed in cold 1× PBS. Images were taken with an Olympus BX51 fluorescent microscope. Oil immersion ×100 objective UPlan APO, NA 1.4 was used. We used an 800 ms exposure time for Cherry and 400 ms for GFP. Alkaline phosphatase activity was measured using the Pho8∆60 assay as described28.

Received 16 November 2009; accepted 11 January 2011.

- Bird, A. W. et al. Acetylation of histone H4 by Esa1 is required for DNA doublestrand break repair. Nature 419, 411–415 (2002).
- Choudhary, C. et al. Lysine acetylation targets protein complexes and co-regulates major cellular functions. Science 325, 834–840 (2009).
- Peterson, C. L. & Cote, J. Cellular machineries for chromosomal DNA repair. Genes Dev. 18, 602–616 (2004).
- Scott, K. L. & Plon, S. E. Loss of Sin3/Rpd3 histone deacetylase restores the DNA damage response in checkpoint-deficient strains of Saccharomyces cerevisiae. Mol. Cell. Biol. 23, 4522–4531 (2003).
- Yang, X. J. & Seto, E. The Rpd3/Hda1 family of lysine deacetylases: from bacteria and yeast to mice and men. Nature Rev. Mol. Cell Biol. 9, 206–218 (2008).
- Bolden, J. E., Peart, M. J. & Johnstone, R. W. Anticancer activities of histone deacetylase inhibitors. *Nature Rev. Drug Discov.* 5, 769–784 (2006).
- Gottlicher, M. et al. Valproic acid defines a novel class of HDAC inhibitors inducing differentiation of transformed cells. EMBO J. 20, 6969–6978 (2001).
- Harrison, J. C. & Haber, J. E. Surviving the breakup: the DNA damage checkpoint. Annu. Rev. Genet. 40, 209–235 (2006).
- Paques, F. & Haber, J. E. Multiple pathways of recombination induced by doublestrand breaks in Saccharomyces cerevisiae. Microbiol. Mol. Biol. Rev. 63, 349–404 (1999)
- İra, G. et al. DNA end resection, homologous recombination and DNA damage checkpoint activation require CDK1. Nature 431, 1011–1017 (2004).
- Jeong, H. et al. Acetylation targets mutant huntingtin to autophagosomes for degradation. Cell 137, 60–72 (2009).
- 12. Lamark, T. & Johansen, T. Autophagy: links with the proteasome. *Curr. Opin. Cell Biol.* 22, 192–198 (2009).
- Kirkin, V., McEwan, D. G., Novak, I. & Dikic, I. A role for ubiquitin in selective autophagy. Mol. Cell 34, 259–269 (2009).
- Mathew, R. et al. Autophagy suppresses tumor progression by limiting chromosomal instability. Genes Dev. 21, 1367–1381 (2007).
- Shao, Y., Gao, Z., Marks, P. A. & Jiang, X. Apoptotic and autophagic cell death induced by histone deacetylase inhibitors. *Proc. Natl Acad. Sci. USA* 101, 18030–18035 (2004).
- Degenhardt, K. et al. Autophagy promotes tumor cell survival and restricts necrosis, inflammation, and tumorigenesis. Cancer Cell 10, 51–64 (2006).

- 17. Vaze, M. B. et al. Recovery from checkpoint-mediated arrest after repair of a double-strand break requires Srs2 helicase. Mol. Cell 10, 373–385 (2002).
- Liberi, G. et al. Srs2 DNA helicase is involved in checkpoint response and its regulation requires a functional Mec1-dependent pathway and Cdk1 activity. EMBO J. 19, 5027–5038 (2000).
- 19. Robert, T., Dervins, D., Fabre, F. & Gangloff, S. Mrc1 and Srs2 are major actors in the regulation of spontaneous crossover. *EMBO J.* **25**, 2837–2846 (2006).
- Lisby, M., Barlow, J. H., Burgess, R. C. & Rothstein, R. Choreography of the DNA damage response: spatiotemporal relationships among checkpoint and repair proteins. Cell 118, 699–713 (2004).
- 21. Huertas, P., Cortes-Ledesma, F., Sartori, A. A., Aguilera, A. & Jackson, S. P. CDK targets Sae2 to control DNA-end resection and homologous recombination. *Nature* **455**, 689–692 (2008).
- Gravel, S., Chapman, J. R., Magill, C. & Jackson, S. P. DNA helicases Sgs1 and BLM promote DNA double-strand break resection. Genes Dev. 22, 2767–2772 (2008).
- Mimitou, E. P. & Symington, L. S. Sae2, Exo1 and Sgs1 collaborate in DNA doublestrand break processing. Nature 455, 770–774 (2008).
- Zhu, Z., Chung, W. H., Shim, E. Y., Lee, S. E. & Ira, G. Sgs1 helicase and two nucleases Dna2 and Exo1 resect DNA double-strand break ends. Cell 134, 981–994 (2008).
- Bernstein, K. A. & Rothstein, R. At loose ends: resecting a double-strand break. Cell 137, 807–810 (2009).
- Fu, J., Shao, C. J., Chen, F. R., Ng, H. K. & Chen, Z. P. Autophagy induced by valproic acid is associated with oxidative stress in glioma cell lines. *Neuro Oncol.* 12, 328–340 (2010).
- Shintani, T. & Reggiori, F. Fluorescence microscopy-based assays for monitoring yeast Atg protein trafficking. Methods Enzymol. 451, 43–56 (2008).
- Noda, T. & Klionsky, D. J. The quantitative Pho8∆60 assay of nonspecific autophagy. Methods Enzymol. 451, 33–42 (2008).
- 29. Cheong, H. & Klionsky, D. J. Biochemical methods to monitor autophagy-related processes in yeast. *Methods Enzymol.* **451**, 1–26 (2008).
- Nakatogawa, H., Suzuki, K., Kamada, Y. & Ohsumi, Y. Dynamics and diversity in autophagy mechanisms: lessons from yeast. *Nature Rev. Mol. Cell Biol.* 10, 458–467 (2009).
- 31. Xie, Z. & Klionsky, D. J. Autophagosome formation: core machinery and adaptations. *Nature Cell Biol.* **9**, 1102–1109 (2007).
- Kim, H. S. et al. Functional interactions between Sae2 and the Mre11 complex. Genetics 178, 711–723 (2008).
- Lee, D. H. & Goldberg, A. L. Selective inhibitors of the proteasome-dependent and vacuolar pathways of protein degradation in *Saccharomyces cerevisiae*. *J. Biol. Chem.* 271, 27280–27284 (1996).
- 34. Kamada, Y., Sekito, T. & Ohsumi, Y. Autophagy in yeast: a TOR-mediated response to nutrient starvation. *Curr. Top. Microbiol. Immunol.* **279**, 73–84 (2004).
- Robyr, D. et al. Microarray deacetylation maps determine genome-wide functions for yeast histone deacetylases. Cell 109, 437–446 (2002).
- Grant, P. A. et al. Yeast Gcn5 functions in two multisubunit complexes to acetylate nucleosomal histones: characterization of an Ada complex and the SAGA (Spt/ Ada) complex. Genes Dev. 11, 1640–1650 (1997).
- Clerici, M., Mantiero, D., Lucchini, G. & Longhese, M. P. The Saccharomyces cerevisiae Sae2 protein negatively regulates DNA damage checkpoint signalling. EMBO Rep. 7, 212–218 (2006).

- Neecke, H., Lucchini, G. & Longhese, M. P. Cell cycle progression in the presence of irreparable DNA damage is controlled by a Mec1- and Rad53-dependent checkpoint in budding yeast. EMBO J. 18, 4485–4497 (1999).
- Sun, Y., Jiang, X., Chen, S., Fernandes, N. & Price, B. D. A role for the Tip60 histone acetyltransferase in the acetylation and activation of ATM. *Proc. Natl Acad. Sci. USA* 102, 13182–13187 (2005).
- Fiorentino, D. F. & Crabtree, G. R. Characterization of Saccharomyces cerevisiae dna2 mutants suggests a role for the helicase late in S phase. Mol. Biol. Cell 8, 2519–2537 (1997).
- 41. Nagai, S. et al. Functional targeting of DNA damage to a nuclear pore-associated SUMO-dependent ubiquitin ligase. *Science* **322**, 597–602 (2008).
- Branzei, D. & Foiani, M. The checkpoint response to replication stress. DNA Repair 8. 1038–1046 (2009).
- 43. Yu, X., Fu, S., Lai, M., Baer, R. & Chen, J. BRCA1 ubiquitinates its phosphorylation-dependent binding partner CtIP. Genes Dev. 20, 1721–1726 (2006).
- Pellicioli, A. et al. Activation of Rad53 kinase in response to DNA damage and its
 effect in modulating phosphorylation of the lagging strand DNA polymerase.
 EMBO J. 18, 6561–6572 (1999).
- Fiorani, S., Mimun, G., Caleca, L., Piccini, D. & Pellicioli, A. Characterization of the activation domain of the Rad53 checkpoint kinase. Cell Cycle 7, 493–499 (2008).
- Lucca, C. et al. Checkpoint-mediated control of replisome-fork association and signalling in response to replication pausing. Oncogene 23, 1206–1213 (2004).
- Wang, X. & Haber, J. E. Role of Saccharomyces single-stranded DNA-binding protein RPA in the strand invasion step of double-strand break repair. PLoS Biol. 2, 104–112 (2004).

Supplementary Information is linked to the online version of the paper at www.nature.com/nature.

Acknowledgements We thank S. Piatti, M. P. Longhese, M. Grunstein, J. K. Tyler, A. Pellicioli, M. Costanzo, R. Brost, M. Vogelauer, D. Klionsky, T. Roberts and C. Bertoli for reagents and technical suggestions, J. Barlow for DNA damage foci analysis, A. Sartori and S. Ferrari for communicating unpublished results, C. Lucca, D. Branzei, R. Bermejo and the members of our laboratories for comments. Work in M.F. laboratory was supported by grants from the Italian Association for Cancer Research and partially from Telethon, European Community (GENICA) and the Italian Ministry of Health. T.R. was supported by fellowships from FRM and EMBO and I.C. was supported by a short fellowship from HFSP and from FIRC. This work was also supported by GM50237 (to R.R.), GM67055 (to R.R.) and GM088413 (to K.B.).

Author Contributions T.R. and F.V. performed the experiments in Figs 1, 2, 4 and 5, T.R. performed those in Fig. 3 and Supplementary Fig. 3, F.V. and I.C. those in Supplementary Figs 1 and 2. I.C. contributed to Fig. 1, G.S. to Fig. 5, O.A.B. to Fig. 4. K.A.B., A.O. and D.P. provided advice and technical support for imaging. T.R., F.V., I.C. and M.F. conceived the experiments. T.R., F.V., G.S., R.R., S.M. and M.F. analysed the results. T.R., F.V., G.S. and M.F. wrote the paper, S.M. and M.F. conceived the project.

Author Information Reprints and permissions information is available at www.nature.com/reprints. The authors declare no competing financial interests. Readers are welcome to comment on the online version of this article at www.nature.com/nature. Correspondence and requests for materials should be addressed to to M.F. (marco.foiani@ifom-ieo-campus.it) or S.M. (saverio.minucci@ifom-ieo-campus.it).



The unusual minimum of sunspot cycle 23 caused by meridional plasma flow variations

Dibyendu Nandy¹, Andrés Muñoz-Jaramillo^{2,3} & Petrus C. H. Martens^{2,3}

Direct observations over the past four centuries1 show that the number of sunspots observed on the Sun's surface varies periodically, going through successive maxima and minima. Following sunspot cycle 23, the Sun went into a prolonged minimum characterized by a very weak polar magnetic field^{2,3} and an unusually large number of days without sunspots⁴. Sunspots are strongly magnetized regions⁵ generated by a dynamo mechanism⁶ that recreates the solar polar field mediated through plasma flows⁷. Here we report results from kinematic dynamo simulations which demonstrate that a fast meridional flow in the first half of a cycle, followed by a slower flow in the second half, reproduces both characteristics of the minimum of sunspot cycle 23. Our model predicts that, in general, very deep minima are associated with weak polar fields. Sunspots govern the solar radiative energy^{8,9} and radio flux, and, in conjunction with the polar field, modulate the solar wind, the heliospheric open flux and, consequently, the cosmic ray flux at Earth^{3,10,11}

The creation and emergence of tilted, bipolar sunspot pairs and their subsequent decay and dispersal through flux transport processes determine the properties of the solar magnetic cycle^{6,12-17}. The average tilt angle of the sunspots of cycle 23 did not differ significantly from earlier cycles². However, the axisymmetric meridional circulation of plasma¹⁸ which is observationally constrained only in the upper 10% of the Sun, where it has an average poleward speed of 20 m s⁻¹—is known to have significant intra- and intercycle variation^{19–22}. The equatorward counterflow of this circulation in the solar interior is believed to have a crucial role; it governs the equatorward migration and spatiotemporal distribution of sunspots and determines the solar cycle period^{6,22,23}. We perform kinematic solar dynamo simulations to investigate whether internal meridional flow variations can produce deep minima between cycles in general, and, in particular, explain the observed characteristics of the minimum of cycle 23 (Supplementary Information)—a comparatively weak dipolar field strength and an unusually long period without sunspots.

We use a recently developed axisymmetric, kinematic solar dynamo model²⁴ to solve the evolution equations for the toroidal and poloidal components of the magnetic field. This model has been further refined using a buoyancy algorithm that incorporates a realistic representation of bipolar sunspot eruptions following the double-ring formalism^{25,26} and qualitatively captures the surface flux transport dynamics leading to solar polar field reversal⁷ (including the observed evolution of the radial component of the Sun's dipolar field). To explore the effect of changing meridional flows on the nature of solar minima, it is necessary to introduce fluctuations in the meridional flow. The large-scale meridional circulation in the solar interior is believed to be driven by Reynolds stresses and small temperature differences between the solar equator and poles; variations in the flows may be induced by changes in the driving forces or through the feedback of magnetic fields²⁷. The feedback is expected to be highest at the solar maximum (polar field minimum), when the toroidal magnetic field in the solar interior is the strongest. We therefore perform dynamo simulations by randomly varying the meridional flow speed between 15 and $30\,\mathrm{m\,s}^{-1}$ (with the same amplitude in both the hemispheres) at the solar cycle maximum, and study its effect on the nature of solar cycle minima. Details of the dynamo model are described in Supplementary Information.

Our simulations extend over 210 sunspot cycles corresponding to 1,860 solar years; for each of these simulated cycles, we record the meridional circulation speed, the cycle overlap (which includes the information on the number of days with no sunspots) and the strength of the polar radial field at cycle minimum. Figure 1 shows the sunspot butterfly diagram and surface radial field evolution over a selected 40-yr slice of the simulation. Here cycle to cycle variations (mediated by varying meridional flows) in the strength of the polar field at minimum and the structure of the sunspot butterfly diagram are apparent, hinting that the number of spotless days during a minimum is governed by the overlap (or lack thereof) of successive cycles.

We designate the minimum in activity following a given sunspot cycle, say n, as the minimum of n (because the sunspot eruptions from cycle n contribute to the nature of this minimum). We denote the amplitude of the meridional flow speed after the random change at

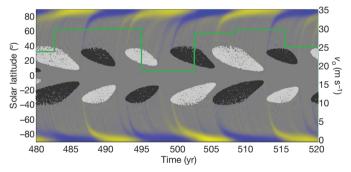


Figure 1 | Simulated sunspot butterfly diagram with a variable meridional flow. Starting with the pioneering telescopic observations of Galileo Galilei and Christopher Scheiner in the early seventeenth century, sunspots have been observed more or less continuously up to the present. Except for the period AD 1645-1715, known as the Maunder minimum, when hardly any sunspots were observed, the sunspot time series shows a cyclic variation going through successive epochs of maximum and minimum activity. This cyclic temporal variation in the latitude of sunspot emergence gives rise to the 'butterfly' diagram. In this simulated butterfly diagram, the green line shows the meridional flow speed, v_0 , which is made to vary randomly between 15 and 30 m s⁻¹ at sunspot maxima and to remain constant between maxima. The varying meridional flow induces cycle-to-cycle variations in both the amplitude as well as the distribution of the toroidal field in the solar interior from which bipolar sunspot pairs buoyantly erupt. This variation is reflected in the spatiotemporal distribution of sunspots, shown here as shaded regions (the lighter shade represents sunspots that have erupted from positive toroidal field and the darker shade represents those that have erupted from negative toroidal field). The sunspot butterfly diagram shows a varying degree of cycle overlap (of the 'wings' of successive cycles) at cycle minimum. The polar radial field strength (yellow, positive; blue, negative) is strongest at sunspot cycle minimum and varies significantly from one cycle minimum to another.

¹Department of Physical Sciences, Indian Institute of Science Education and Research, Kolkata, Mohanpur 741252, West Bengal, India. ²Department of Physics, Montana State University, Bozeman, Montana 59717, USA. ³Harvard-Smithsonian Center for Astrophysics, Cambridge, Massachusetts 02138, USA.

the maximum of cycle n by v_n , which remains constant through the minimum of cycle n and changes again at the maximum of cycle n+1. According to this convention, the speed during the first (rising) half of cycle n would be v_{n-1} . To explore the relationship between the varying meridional flow, the polar field strength and cycle overlap, we generate statistical correlations between these quantities separately for the northern and southern solar hemispheres from our simulations over 210 sunspot cycles. We note that slight hemispheric asymmetries arise in the simulations owing to the stochastic nature of the active-region emergence process.

Unexpectedly, we find that there is no correlation between the flow speed at a given minimum (say v_n) and cycle overlap (or the number of spotless days) during that minimum, and the polar field strength at that minimum, B_n is only moderately correlated with v_n (Fig. 2a, b). Because transport of magnetic flux by the meridional flow involves a finite time, it is likely that the characteristics of a given minimum could depend on the flow speed at an earlier time. We find that this is indeed the case (Fig. 2c, d), with cycle overlap (or the number of spotless days) and the

polar field strength at a given minimum, n, being strongly correlated with the flow speed v_{n-1} (that is, meridional flow during the early, rising, part of cycle n). We also find that the cycle overlap is moderately correlated and that the polar field strength is strongly correlated with the change in flow speed between the first and second halves of the cycle (Fig. 2e, f). Taken together, these results show that a fast flow during the early part of the cycle, followed by a relatively slower flow during the later, declining, part of the cycle, results in a deep solar minimum.

The main characteristics of the minimum of solar cycle 23 are a large number of spotless days and a relatively weak polar field strength. In Fig. 3, we plot the polar field versus cycle overlap and find that very deep minima are in fact associated with relatively weak polar field strengths. Thus, the qualitative characteristics of the unusual minimum of sunspot cycle 23 are self-consistently explained in our simulations driven by changes in the Sun's meridional plasma flow. Our model predicts that, in general, extremely deep solar minima—with a large number of spotless days—would also be characterized by relatively weak solar polar field strengths.

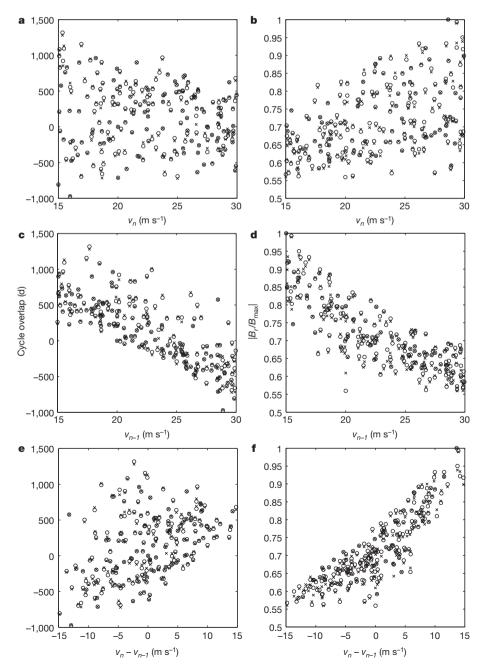


Figure 2 | Cycle overlap and polar field strength at solar minimum in response to variable **meridional flows.** Here v_n denotes flow speed during the minimum of sunspot cycle n, v_{n-1} denotes the speed during the early, rising, part of cycle n and $v_n - v_{n-1}$ denotes the change in flow speed between the declining and rising parts of the cycle. Cycle overlap is measured in days. Positive overlap denotes the number of days on which simulated sunspots from successive cycles erupted together, whereas negative overlap denotes the number of spotless days during a solar minimum; large negative overlap implies a deep (that is, long) minimum. The polar field ($|B_r/B_{max}|$) is represented by the peak radial field attained during a solar minimum normalized with respect to the maximum radial field attained during the complete model run (here $B_{\text{max}} = 16.66 \times 10^3 \,\text{G}$; see Supplementary Information for a discussion of polar field amplitudes). The relationship between the above parameters is determined by the Spearman's rank correlation coefficient (210 data points for each solar hemisphere, with northernand southern-hemisphere data depicted as crosses and circles, respectively). **a**, Cycle overlap versus v_n ; correlation coefficient: r = -0.13 (northern hemisphere), -0.13 (southern hemisphere); confidence level: P = 93.42% (northern hemisphere), 94.53% (southern hemisphere). **b**, Polar field strength versus v_n ; r = 0.45, 0.45; P = 99.99%, 99.99%. **c**, Cycle overlap versus v_{n-1} ; r = -0.81, -0.80; P = 99.99%, 99.99%. **d**, Polar field strength versus v_{n-1} ; r = -0.83, -0.83; P = 99.99%, 99.99%. **e**, Cycle overlap versus $v_n - v_{n-1}$; r = 0.45, 0.45; P = 99.99%, 99.99%**f**, Polar field strength versus $v_n - v_{n-1}$; r = 0.87, 0.87; P = 99.99%, 99.99%. Evidently, a change from fast to slow internal meridional flow results in deep solar minima.

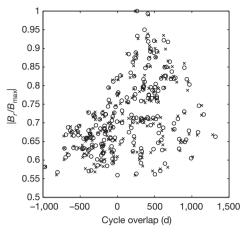


Figure 3 | Polar field strength versus cycle overlap at solar minimum. Simulated normalized polar field strength is plotted versus cycle overlap at sunspot cycle minimum. Spearman's rank correlation estimate: r = 0.46, 0.47 and P = 99.99%, 99.99% for data from the northern (crosses) and southern (circles) hemispheres, respectively. The results show that a deep solar minimum with a large number of spotless days is typically associated with a relatively weak polar field—as observed during the minimum of sunspot cycle 23.

We find that our model results are robust with respect to reasonable changes in the driving parameters. Simulations with continuous flow variations (as opposed to discrete changes), relatively higher magnetic diffusivity and a different threshold for buoyant active-region eruption all yield qualitatively similar relationships between the nature of solar minima and flow speed variations (Supplementary Information).

Valuable insights into our simulation results may be gained by invoking the physics of meridional-flow-mediated magnetic flux transport. A faster flow (v_{n-1}) before and during the first half of cycle *n* would sweep the poloidal field of the previous cycle quickly through the region of differential rotation responsible for toroidal field induction; this would allow less time for toroidal field amplification and would hence result in a sunspot cycle (n) which is not too strong. The fast flow, followed by a slower flow during the second half of cycle *n* and persisting to the early part of the next cycle, would also distance the two successive cycles (that is, successive wings in the sunspot butterfly diagram), contributing to a higher number of spotless days during the intervening minimum. Moreover, a strong flow during the early half of cycle n would sweep both the positive and the negative polarity sunspots of cycle n (erupting at mid to high latitudes) to the polar regions; therefore, lower net flux would be available for cancelling the polar field of the old cycle and building the field of the new cycle resulting in a relatively weak polar field strength at the minimum of cycle n. We believe that a combination of these effects contributes to the occurrence of deep minima such as that of solar cycle 23.

Independent efforts using surface flux transport simulations show that surface meridional flow variations alone (observed during solar cycle 23; see also Supplementary Information) are inadequate for reproducing the weak polar field of cycle 23 (ref. 28). Dynamo simulations—which encompass the entire solar convection zone—are therefore invaluable for probing the internal processes that govern the dynamics of the solar magnetic cycle, including the origin of deep minima such as that of cycle 23. We anticipate that NASA's recently launched Solar Dynamics Observatory will provide more precise constraints on the structure of the plasma flows deep in the solar interior, which could be useful for complementing these simulations.

Received 23 April 2010; accepted 5 January 2011.

 Hoyt, D. V. & Schatten, K. H. Group sunspot numbers: a new solar activity reconstruction. Sol. Phys. 179, 189–219 (1998).

- Schrijver, C. J. & Liu, Y. The global solar magnetic field through a full sunspot cycle: observations and model results. Sol. Phys. 252, 19–31 (2008).
- Wang, Y.-M., Robbrecht, E. & Sheeley, N. R. Jr. On the weakening of the polar magnetic fields during solar cycle 23. Astrophys. J. 707, 1372–1386 (2009).
- Solar Influences Data Analysis Center. Daily sunspot number (http://sidc.oma.be/sunspot-data/dailyssn.php) (2011).
- 5. Solanki, S. K. Sunspots: an overview. Astron. Astrophys. Rev. 11, 153-286 (2003).
- Charbonneau, P. Dynamo models of the solar cycle. Living Rev. Solar Phys. 7, 3 (http://solarphysics.livingreviews.org/Articles/Irsp-2010-3/) (2010).
- Muñoz-Jaramillo, A., Nandy, D., Martens, P. C. H. & Yeates, A. R. A double-ring algorithm for modeling solar active regions: unifying kinematic dynamo models and surface flux-transport simulations. *Astrophys. J.* 720, L20–L25 (2010).
- Krivova, N. A., Balmaceda, L. & Solanki, S. K. Reconstruction of the solar total irradiance since 1700 from the surface magnetic flux. Astron. Astrophys. 467, 335–346 (2007).
- Lean, J. The Sun's variable radiation and its relevance for Earth. Annu. Rev. Astron. Astrophys. 35, 33–67 (1997).
- Solanki, S. K., Schüssler, M. & Fligge, M. Evolution of the Sun's large-scale magnetic field since the Maunder minimum. *Nature* 408, 445–447 (2000).
- Lara, A. et al. Coronal mass ejections and galactic cosmic-ray modulation. Astrophys. J. 625, 441–450 (2005).
- Babcock, H. W. The topology of the Sun's magnetic field and the 22-year cycle. Astrophys. J. 133, 572–587 (1961).
- Leighton, R. B. A magneto-kinematic model of the solar cycle. Astrophys. J. 156, 1–26 (1969).
- 14. Choudhuri, A. R., Schussler, M. & Dikpati, M. The solar dynamo with meridional circulation. *Astron. Astrophys.* **303**, L29–L32 (1995).
- Dikpati, M., de Toma, G. & Gilman, P. A. Predicting the strength of solar cycle 24 using a flux-transport dynamo-based tool. Geophys. Res. Lett. 33, L05102 (2006).
- Choudhuri, A. R., Chatterjee, P. & Jiang, J. Predicting solar cycle 24 with a solar dynamo model. *Phys. Rev. Lett.* 98, 131103 (2007).
- Yeates, A. R., Nandy, D. & Mackay, D. H. Exploring the physical basis of solar cycle predictions: flux transport dynamics and persistence of memory in advectionversus diffusion-dominated solar convection zones. *Astrophys. J.* 673, 544–556 (2008).
- Giles, P. M., Duvall, T. L., Scherrer, P. H. & Bogart, R. S. A subsurface flow of material from the Sun's equator to its poles. *Nature* 390, 52–54 (1997).
- Zhao, J. & Kosovichev, A. G. Torsional oscillation, meridional flows, and vorticity inferred in the upper convection zone of the Sun by time-distance helioseismology. Astrophys. J. 603, 776–784 (2004).
- González Hernández, I. et al. Meridional circulation variability from large-aperture ring-diagram analysis of global oscillation network group and Michelson Doppler imager data. Astrophys. J. 638, 576–583 (2006).
- Švanda, M., Kosovichev, A. G. & Zhao, J. Speed of meridional flows and magnetic flux transport on the Sun. Astrophys. J. 670, L69–L72 (2007).
- Hathaway, D. H., Nandy, D., Wilson, R. M. & Reichmann, E. J. Evidence that a deep meridional flow sets the sunspot cycle period. Astrophys. J. 589, 665–670 (2003).
- Nandy, D. & Choudhuri, A. R. Explaining the latitudinal distribution of sunspots with deep meridional flow. Science 296, 1671–1673 (2002).
- Muñoz-Jaramillo, A., Nandy, D. & Martens, P. C. H. Helioseismic data inclusion in solar dynamo models. Astrophys. J. 698, 461–478 (2009).
- Durney, B. R. On a Babcock-Leighton solar dynamo model with a deep-seated generating layer for the toroidal magnetic field. IV. Astrophys. J. 486, 1065–1077 (1997).
- Nandy, D. & Choudhuri, A. R. Toward a mean field formulation of the Babcock-Leighton type solar dynamo. I. α-coefficient versus Durney's double-ring approach. Astrophys. J. 551, 576–585 (2001).
- 27. Rempel, M. Origin of solar torsional oscillations. *Astrophys. J.* **655**, 651–659
- Jiang, J., Işik, E., Cameron, R. H., Schmitt, D. & Schüssler, M. The effect of activityrelated meridional flow modulation on the strength of the solar polar magnetic field. Astrophys. J. 717, 597–602 (2010).

Supplementary Information is linked to the online version of the paper at www.nature.com/nature.

Acknowledgements This work was supported through the Ramanujan Fellowship of the Government of India at the Indian Institute of Science Education and Research, Kolkata, and by a NASA Living With a Star grant to the Smithsonian Astrophysical Observatory and Montana State University. We are grateful to D. Hathaway for providing the observational data on days without sunspots; the analysis of these data is reported in Supplementary Fig. 1.

Author Contributions D.N. conceived the principal idea and, in conjunction with P.C.H.M. and A.M.-J., planned the simulations, which were performed by A.M.J. under the guidance of D.N. and P.C.H.M. D.N. led the interpretation of the results and all authors contributed to writing the paper.

Author Information Reprints and permissions information is available at www.nature.com/reprints. The authors declare no competing financial interests. Readers are welcome to comment on the online version of this article at www.nature.com/nature. Correspondence and requests for materials should be addressed to D.N. (dnandi@iiserkol.ac.in).



Spin-orbit-coupled Bose-Einstein condensates

Y.-J. Lin¹, K. Jiménez-García^{1,2} & I. B. Spielman¹

Spin-orbit (SO) coupling—the interaction between a quantum particle's spin and its momentum—is ubiquitous in physical systems. In condensed matter systems, SO coupling is crucial for the spin-Hall effect^{1,2} and topological insulators³⁻⁵; it contributes to the electronic properties of materials such as GaAs, and is important for spintronic devices6. Quantum many-body systems of ultracold atoms can be precisely controlled experimentally, and would therefore seem to provide an ideal platform on which to study SO coupling. Although an atom's intrinsic SO coupling affects its electronic structure, it does not lead to coupling between the spin and the centre-of-mass motion of the atom. Here, we engineer SO coupling (with equal Rashba⁷ and Dresselhaus⁸ strengths) in a neutral atomic Bose-Einstein condensate by dressing two atomic spin states with a pair of lasers9. Such coupling has not been realized previously for ultracold atomic gases, or indeed any bosonic system. Furthermore, in the presence of the laser coupling, the interactions between the two dressed atomic spin states are modified, driving a quantum phase transition from a spatially spinmixed state (lasers off) to a phase-separated state (above a critical laser intensity). We develop a many-body theory that provides quantitative agreement with the observed location of the transition. The engineered SO coupling—equally applicable for bosons and fermions—sets the stage for the realization of topological insulators in fermionic neutral atom systems.

Quantum particles have an internal 'spin' angular momentum; this can be intrinsic for fundamental particles like electrons, or a combination of intrinsic (from nucleons and electrons) and orbital for composite particles like atoms. SO coupling links a particle's spin to its motion, and generally occurs for particles moving in static electric fields, such as the nuclear field of an atom or the crystal field in a material. The coupling results from the Zeeman interaction $-\mu \cdot B$ between a particle's magnetic moment μ , parallel to the spin σ , and a magnetic field B present in the frame moving with the particle. For example, Maxwell's equations dictate that a static electric field $\mathbf{E} = E_0 \hat{z}$ in the laboratory frame (at rest) gives a magnetic field $\mathbf{B}_{SO} = E_0(\hbar/mc^2)(-k_y,k_x,0)$ in the frame of an object moving with momentum $\hbar \mathbf{k} = \hbar(k_x, k_y, k_z)$, where *c* is the speed of light in vacuum and *m* is the particle's mass. The resulting momentumdependent Zeeman interaction $-\mathbf{\mu} \cdot \mathbf{B}_{SO}(\mathbf{k}) \propto \sigma_x k_y - \sigma_y k_x$ is known as the Rashba⁷ SO coupling. In combination with the Dresselhaus⁸ coupling $\propto -\sigma_x k_y - \sigma_y k_x$, these describe two-dimensional SO coupling in solids

In materials, the SO coupling strengths are generally intrinsic properties, which are largely determined by the specific material and the details of its growth, and are thus only slightly adjustable in the laboratory. We demonstrate SO coupling in an ^{87}Rb Bose–Einstein condensate (BEC) where a pair of Raman lasers create a momentum-sensitive coupling between two internal atomic states. This SO coupling is equivalent to that of an electronic system with equal contributions of Rashba and Dresselhaus 9 couplings, and with a uniform magnetic field B in the $\hat{y}-\hat{z}$ plane, which is described by the single-particle Hamiltonian:

$$\hat{H} = \frac{\hbar^2 \hat{\mathbf{k}}^2}{2m} \check{\mathbf{1}} - \left[\mathbf{B} + \mathbf{B}_{SO} \left(\hat{\mathbf{k}} \right) \right] \cdot \mathbf{\mu} = \frac{\hbar^2 \hat{\mathbf{k}}^2}{2m} \check{\mathbf{1}} + \frac{\Omega}{2} \check{\sigma}_z + \frac{\delta}{2} \check{\sigma}_y + 2\alpha \hat{k}_x \check{\sigma}_y \quad (1)$$

 α parametrizes the SO-coupling strength; $\Omega = -g\mu_{\rm B}B_z$ and $\delta = -g\mu_{\rm B}B_y$ result from the Zeeman fields along \hat{z} and \hat{y} , respectively; and $\check{\sigma}_{x,y,z}$ are the 2×2 Pauli matrices. Without SO coupling, electrons have group velocity $v_x = \hbar k_x/m$, independent of their spin. With SO coupling, their velocity becomes spin-dependent, $v_x = \hbar (k_x \pm 2\alpha m/\hbar^2)/m$ for spin $|\uparrow\rangle$ and $|\downarrow\rangle$ electrons (quantized along \hat{y}). In two recent experiments, this form of SO coupling was engineered in GaAs heterostructures where confinement into two-dimensional planes linearized the native cubic SO coupling of GaAs to produce a Dresselhaus term, and asymmetries in the confining potential gave rise to Rashba coupling. In one experiment a persistent spin helix was found⁶, and in another the SO coupling was only revealed by adding a Zeeman field¹⁰.

SO coupling for neutral atoms enables a range of exciting experiments, and importantly, it is essential in the realization of neutral atom topological insulators. Topological insulators are novel fermionic band insulators including integer quantum Hall states and now spin quantum Hall states that insulate in the bulk, but conduct in topologically protected quantized edge channels. The first-known topological insulators—integer quantum Hall states11—require large magnetic fields that explicitly break time-reversal symmetry. In a seminal paper³, Kane and Mele showed that in some cases SO coupling leads to zero-magnetic-field topological insulators that preserve timereversal symmetry. In the absence of the bulk conductance that plagues current materials, cold atoms can potentially realize such an insulator in its most pristine form, perhaps revealing its quantized edge (in two dimensions) or surface (in three dimensions) states. To go beyond the form of SO coupling we created, almost any SO coupling, including that needed for topological insulators, is possible with additional lasers12-14.

To create SO coupling, we select two internal 'spin' states from within the ⁸⁷Rb 5S_{1/2}, F=1 ground electronic manifold, and label them pseudo-spin-up and pseudo-spin-down in analogy with an electron's two spin states: $|\uparrow\rangle = |F=1$, $m_F=0\rangle$ and $|\downarrow\rangle = |F=1$, $m_F=-1\rangle$. A pair of $\lambda=804.1$ nm Raman lasers, intersecting at $\theta=90^\circ$ and detuned by δ from Raman resonance (Fig. 1a), couple these states with strength Ω ; here $\hbar k_L=\sqrt{2}\pi\hbar/\lambda$ and $E_L=\hbar^2k_L^2/2m$ are the natural units of momentum and energy. In this configuration, the atomic Hamiltonian is given by equation (1), with k_x replaced by a quasimomentum q and an overall E_L energy offset. Ω and δ give rise to effective Zeeman fields along \hat{z} and \hat{y} , respectively. The SO-coupling term $2E_Lq\check{\sigma}_y/k_L$ results from the laser geometry, and $\alpha=E_L/k_L$ is set by λ and θ , independent of Ω (see Methods). In contrast with the electronic case, the atomic Hamiltonian couples bare atomic states $|\uparrow, \hat{k}_x=q+k_L\rangle$ and $|\downarrow, \hat{k}_x=q-k_L\rangle$ with different velocities, $\hbar k_x/m=\hbar(q\pm k_L)/m$.

The spectrum, a new energy–quasimomentum dispersion of the SO-coupled Hamiltonian, is displayed in Fig. 1b at $\delta=0$ and for a range of couplings Ω . The dispersion is divided into upper and lower branches $E_{\pm}(q)$, and we focus on $E_{-}(q)$. For $\Omega < 4E_{\rm L}$ and small δ (see Fig. 2a), $E_{-}(q)$ consists of a double well in quasi-momentum 15, where the group velocity $\partial E_{-}(q)/\partial\hbar q$ is zero. States near the two minima are dressed spin states, labelled as $|\uparrow'\rangle$ and $|\downarrow'\rangle$. As Ω increases, the two dressed spin states merge into a single minimum and the simple picture of two dressed spins is inapplicable. Instead, that strong coupling limit

¹Joint Quantum Institute, National Institute of Standards and Technology, and University of Maryland, Gaithersburg, Maryland, 20899, USA. ²Departamento de Física, Centro de Investigación y Estudios Avanzados del Instituto Politécnico Nacional, México DF, 07360, México.

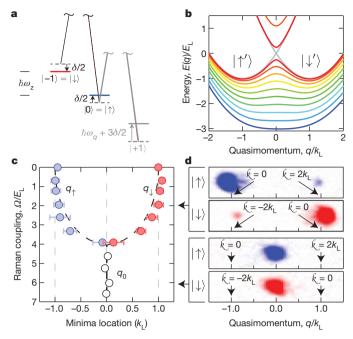


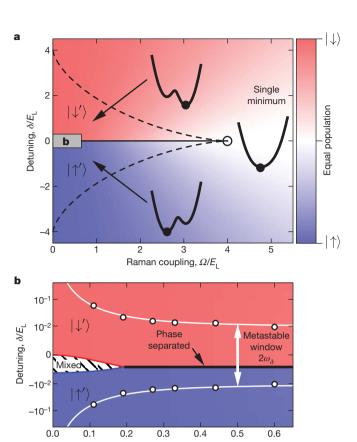
Figure 1 | Scheme for creating SO coupling. a, Level diagram. Two $\lambda=804.1$ nm lasers (thick lines) coupled states $|F=1,m_F=0\rangle=|\uparrow\rangle$ and $|F=1,m_F=-1\rangle=|\downarrow\rangle$, differing in energy by a $\hbar\omega_Z$ Zeeman shift. The lasers, with frequency difference $\Delta\omega_L/2\pi=(\omega_Z+\delta/\hbar)/2\pi$, were detuned δ from the Raman resonance. $|m_F=0\rangle$ and $|m_F=+1\rangle$ had a $\hbar(\omega_Z-\omega_q)$ energy difference; because $\hbar\omega_q=3.8E_L$ is large, $|m_F=+1\rangle$ can be neglected. b, Computed dispersion. Eigenenergies at $\delta=0$ for $\Omega=0$ (grey) to $5E_L$. When $\Omega<4E_L$ the two minima correspond to the dressed spin states $|\uparrow'\rangle$ and $|\downarrow'\rangle$. c, Measured minima. Quasimomentum $q_{\uparrow,\downarrow}$ of $|\uparrow',\downarrow'\rangle$ versus Ω at $\delta=0$, corresponding to the minima of $E_-(q)$. Each point is averaged over about ten experiments; the uncertainties are their standard deviation. d, Spin–momentum decomposition. Data for sudden laser turn-off: $\delta\approx0$, $\Omega=2E_L$ (top image pair), and $\Omega=6E_L$ (bottom image pair). For $\Omega=2E_L$, $|\uparrow'\rangle$ consists of $|\uparrow, \pounds_x\approx0\rangle$ and $|\downarrow, \pounds_x\approx-2k_L\rangle$, and $|\downarrow'\rangle$ consists of $|\uparrow, \pounds_x\approx2k_L\rangle$ and $|\downarrow, \pounds_x\approx0\rangle$

effectively describes spinless bosons with a tunable dispersion relation with which we engineered synthetic electric and magnetic fields for neutral atoms.

In the absence of Raman coupling, atoms with spins $|\uparrow\rangle$ and $|\downarrow\rangle$ spatially mixed perfectly in a BEC. By increasing Ω we observed an abrupt quantum phase transition to a new state where the two dressed spins spatially separated, resulting from a modified effective interaction between the dressed spins.

We studied SO coupling in oblate ⁸⁷Rb BECs with about 1.8×10^5 atoms in a $\lambda=1,064$ -nm crossed dipole trap with frequencies $(f_x,f_y,f_z)\approx (50,50,140)$ Hz. The bias magnetic field $B_0\hat{y}$ generated a $\omega_Z/2\pi\approx 4.81$ MHz Zeeman shift between $|\uparrow\rangle$ and $|\downarrow\rangle$. The Raman beams propagated along $\hat{y}\pm\hat{x}$ and had a constant frequency difference $\Delta\omega_L/2\pi\approx 4.81$ MHz. The small detuning from the Raman resonance $\delta=\hbar(\Delta\omega_L-\omega_Z)$ was set by B_0 , and the state $|m_F=+1\rangle$ was decoupled owing to the quadratic Zeeman effect (see Methods).

We prepared BECs with an equal population of $|\uparrow\rangle$ and $|\downarrow\rangle$ at Ω , $\delta=0$, then we adiabatically increased Ω to a final value up to $7E_{\rm L}$ in 70 ms, and finally we allowed the system to equilibrate for a holding time $t_{\rm h}=70$ ms. We abruptly ($t_{\rm off}<1$ µs) turned off the Raman lasers and the dipole trap—thus projecting the dressed states onto their constituent bare spin and momentum states—and absorption-imaged them after a 30.1-ms time of flight (TOF). For $\Omega>4E_{\rm L}$ (Fig. 1d), the BEC was located at the single minimum q_0 of $E_-(q)$ with a single momentum component in each spin state corresponding to the pair $\{|\uparrow,q_0+k_{\rm L}\rangle,\ |\downarrow,q_0-k_{\rm L}\rangle\}$. However, for $\Omega<4E_{\rm L}$ we observed two momentum components in each spin state, corresponding to the two minima of $E_-(q)$ at q_{\uparrow} and q_{\downarrow} . The agreement between the data (symbols), and the expected minima locations (curves), demonstrates



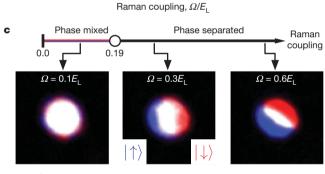


Figure 2 | Phases of a SO-coupled BEC. a, b, Mean field phase diagrams for infinite homogeneous SO-coupled 87 Rb BECs (1.5-kHz chemical potential). The background colours indicate atom fraction in $|\uparrow\rangle$ and $|\downarrow\rangle$. Between the dashed lines there are two dressed spin states, $|\uparrow'\rangle$ and $|\downarrow'\rangle$. a, Single-particle phase diagram in the $\Omega-\delta$ plane. b, Phase diagram (enlargement of the grey rectangle in a), as modified by interactions. The dots represent a metastable region where the fraction of atoms $f_{\uparrow',\downarrow'}$ remains largely unchanged for $t_h=3$ s. c, Miscible-to-immiscible transition. Phase line for mixtures of dressed spins and images after TOF (with populations $N_{\uparrow}\approx N_{\downarrow}$), mapped from $|\uparrow'\rangle$ and $|\downarrow'\rangle$ showing the transition from phase-mixed to phase-separated within the 'metastable window' of detuning.

the existence of the SO coupling associated with the Raman dressing. We kept $\delta \approx 0$ when turning on Ω by maintaining equal populations in bare spins $|\uparrow\rangle$, $|\downarrow\rangle$ (see Fig. 1d).

We experimentally studied the low-temperature phases of these interacting SO-coupled bosons as a function of Ω and δ . The zero-temperature mean-field phase diagram (Fig. 2a, b) includes phases composed of a single dressed spin state, a spatial mixture of both dressed spin states, and coexisting but spatially phase-separated dressed spins.

This phase diagram can largely be understood as the result of non-interacting bosons condensing into the lowest-energy single particle state, and can be divided into three regimes (Fig. 2a). In the region of positive detuning marked $|\downarrow'\rangle$, there are double minima at $q=q_\uparrow,q_\downarrow$ in $E_-(q)$ with $E_-(q_\downarrow) < E_-(q_\uparrow)$ and the bosons condense at q_\downarrow . In the

region marked $|\uparrow'\rangle$ the reverse holds. The energy difference between the two minima is $\Delta(\Omega,\delta)=E_-(q_\uparrow)-E_-(q_\downarrow)\approx\delta$ for small δ (see Methods). In the third 'single minimum' regime, the atoms condense at the single minimum q_0 . These dressed spins act as free particles with group velocity $\hbar K_x/m$ (with an effective mass $m^*\approx m$, for small Ω), where $K_x=q-q_{\uparrow\downarrow,0}$ for the different minima.

We investigated the phase diagram using BECs with initially equal spin populations prepared as described previously, but with $\delta \neq 0$ and $t_{\rm h}$ up to 3 s. We probed the atoms after abruptly removing the dipole trap, and then ramping $\Omega \to 0$ in 1.5 ms. This approximately mapped $|\uparrow'\rangle$ and $|\downarrow'\rangle$ back to their undressed counterparts $|\uparrow\rangle$ and $|\downarrow\rangle$ (see Methods). We absorption-imaged the atoms after a 30-ms TOF, during the last 20 ms of which a Stern–Gerlach magnetic field gradient along \hat{y} separated the spin components.

Figure 3a shows the condensate fraction $f_{\downarrow'} = N_{\downarrow'}/(N_{\downarrow'} + N_{\uparrow'})$ in $|\downarrow'\rangle$ at $\Omega = 0.6E_{\rm L}$ as a function of δ , at $t_{\rm h} = 0.1$ s, 1 s and 3 s, where $N_{\uparrow'}$ and $N_{\downarrow'}$ denote the number of condensed atoms in $|\uparrow'\rangle$ and $|\downarrow'\rangle$, respectively. The BEC is all $|\uparrow'\rangle$ for $\delta \lesssim 0$ and all $|\downarrow'\rangle$ for $\delta \gtrsim 0$, but both dressed spin populations substantially coexisted for detunings within $\pm w_{\delta}$ (obtained by fitting $f_{\downarrow'}$ to the error function where $\delta = \pm w_{\delta}$ corresponds to $f_{\downarrow'} = 0.50 \pm 0.16$). Figure 3b shows w_{δ} versus Ω for hold times $t_{\rm h}$. w_{δ} decreases with $t_{\rm h}$; even by our longest $t_{\rm h}$ of 3 s it has not reached equilibrium.

Conventional F = 1 spinor BECs have been studied in ²³Na and ⁸⁷Rb without Raman coupling ^{19–21}. For our $|\uparrow\rangle$ and $|\downarrow\rangle$ states, the interaction energy depends on the local density in each spin state, and is described by:

$$\hat{H}_{\rm I} = \frac{1}{2} \int d^3r \left[\left(c_0 + \frac{c_2}{2} \right) \left(\hat{\rho}_{\uparrow} + \hat{\rho}_{\downarrow} \right)^2 + \frac{c_2}{2} \left(\hat{\rho}_{\downarrow}^2 - \hat{\rho}_{\uparrow}^2 \right) + \left(c_2 + c'_{\uparrow\downarrow} \right) \hat{\rho}_{\uparrow} \hat{\rho}_{\downarrow} \right]$$

where $\hat{\rho}_{\uparrow}$ and $\hat{\rho}_{\downarrow}$ are density operators for $|\uparrow\rangle$ and $|\downarrow\rangle$, and normal ordering is implied. In the $^{87}\text{Rb}\ F=1$ manifold, the spin-independent interaction is $c_0=7.79\times10^{-12}\ \text{Hz}\ \text{cm}^3$, the spin-dependent interaction 22 is $c_2=-3.61\times10^{-14}\ \text{Hz}\ \text{cm}^3$, and $c'_{\uparrow\downarrow}=0$. Because $|c_0|\!\gg\!|c_2|$, the interaction is almost spin-independent, but $c_2<0$, so the two-component mixture of $|\uparrow\rangle$ and $|\downarrow\rangle$ has a spatially mixed ground state (is miscible). When $\hat{H}_{\rm I}$ is re-expressed in terms of the dressed spin states, $c'_{\uparrow\downarrow}\!\approx\!c_0\Omega^2\big/\big(8E_L^2\big)$ is non-zero and corresponds to an effective interaction between $|\uparrow'\rangle$ and $|\downarrow'\rangle$. This modifies the ground state of our SO-coupled BEC (mixtures of $|\uparrow'\rangle$ and $|\downarrow'\rangle$) from phase-mixed to phase-separated above a critical Raman coupling strength Ω_c . This transition lies outside the common single-mode approximation 20 .

The effective interaction between $|\uparrow'\rangle$ and $|\downarrow'\rangle$ is an exchange energy resulting from the non-orthogonal spin part of $|\uparrow'\rangle$ and $|\downarrow'\rangle$ (see Methods): a spatial mixture produces total density modulations¹⁵ with wavevector $2k_{\rm L}$, in analogy with the spin-textures of the electronic case⁶. These increase the state-independent interaction energy in $\hat{H}_{\rm I}$ wherever the two dressed spins spatially overlap, contributing to the $c'\uparrow_{\downarrow}$ term. (Such a term does not appear for radio-frequency-dressed

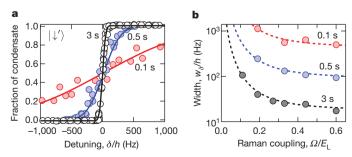


Figure 3 | **Population relaxation. a**, Condensate fraction $f_{\downarrow'}$ in $|\downarrow'\rangle$ at $\Omega = 0.6E_{\rm L}$ versus detuning δ at $t_{\rm h} = 0.1$, 0.5 and 3 s showing w_{δ} decrease with increasing $t_{\rm h}$. The solid curves are fits to the error function from which we obtained the width w_{δ} . **b**, Metastable detuning width. Width w_{δ} versus Ω at $t_{\rm h} = 0.1$, 0.5 and 3 s; the data fits well to $a[b + (\Omega/E_{\rm I})^{-2}]$ (dashed curves).

states, which are always spin-orthogonal.) Because $c'_{\uparrow\downarrow}$ and c_2 have opposite sign here, the dressed BEC can go from miscible to immiscible at the miscibility threshold¹⁹ for a two-component BEC $c_0+c_2+c'_{\uparrow\downarrow}/2=\sqrt{c_0(c_0+c_2)}$, when $\Omega=\Omega_c$ (this result is in agreement with an independent theory presented in ref. 23).

Figure 2b depicts the mean field phase diagram including interactions, computed by minimizing the interaction energy H_1 plus the single particle detuning $\Delta(\Omega,\delta)\approx\delta$. This phase diagram adds two new phases, mixed (hashed) and phase-separated (bold line), to those present in the non-interacting case. The $c_2\left(\hat{\rho}_{\downarrow}^2-\hat{\rho}_{\uparrow}^2\right)/2$ term in \hat{H}_1 implies that the energy difference between a $|\uparrow\rangle$ BEC and a $|\downarrow\rangle$ BEC is proportional to N^2c_2 . The detuning required to compensate for this difference slightly displaces the symmetry point of the phase diagram downwards. As evidenced by the width of the metastable window $2w_{\delta}$ in Fig. 2b, for $|\delta| < w_{\delta}$ the spin-population does not have time to relax to equilibrium. The miscibility condition does not depend on atom number, so the phase line in Fig. 2c shows the system's phases for $|\delta| < w_{\delta}$: phase-mixed for $\Omega < \Omega_c$ and phase-separated for $\Omega > \Omega_c$ where $\Omega_c \approx \sqrt{-8c_2/c_0}E_L \approx 0.19E_L$.

We measured the miscibility of the dressed spin components from their spatial profiles after TOF, for $\Omega=0$ to $2E_{\rm L}$ and $\delta\approx 0$ such that $N_{{\rm T}\uparrow'}\approx N_{{\rm T}\downarrow'}$, where $N_{{\rm T}\uparrow',\downarrow'}$ is the total atom number including both the condensed and thermal components in $|\uparrow'\rangle,|\downarrow'\rangle$. For each TOF image, we numerically re-centred the Stern–Gerlach-separated spin distributions (Fig. 2c, and see Methods), giving condensate densities $n_{\uparrow'}(x,y)$ and $n_{\downarrow'}(x,y)$. Given that the self-similar expansion of BECs released from harmonic traps essentially magnifies the *in situ* spatial spin distribution, these reflect the *in situ* densities 24 .

A dimensionless metric $s = 1 - \langle n_{\uparrow}, n_{\downarrow} \rangle / (\langle n_{\uparrow}^2 \rangle \langle n_{\downarrow}^2 \rangle)^{\frac{1}{2}}$ quantifies

the degree of phase separation (where $\langle ... \rangle$ is the spatial average over a single image). s=0 for any perfect mixture $n_{\uparrow'}(x,y) \propto n_{\downarrow'}(x,y)$, and s=1 for complete phase separation. Figure 4 displays s versus Raman coupling Ω with a hold time $t_{\rm h}=3$ s, showing that $s\approx 0$ for small Ω (as expected given our miscible bare spins) and s abruptly increases above a critical $\Omega_{\rm c}$. The inset to Fig. 4 plots s as a function of time, showing that s reaches steady state in 0.14(3) s, which is much less than $t_{\rm h}$. To obtain $\Omega_{\rm c}$, we fitted the data in Fig. 4 to a slowly increasing function below $\Omega_{\rm c}$ and the power-law $1-(\Omega/\Omega_{\rm c})^{-a}$ above $\Omega_{\rm c}$. The resulting $\Omega_{\rm c}=0.20(2)E_{\rm L}$ is in agreement with the mean field prediction

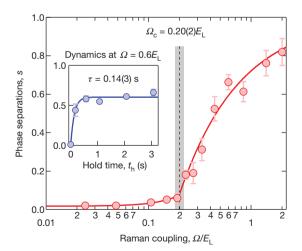


Figure 4 | **Miscible to immiscible phase transition.** Phase separation s versus Ω with $t_h=3$ s; the solid curve is a fit to the function described in the text. The power-law component of the fit has an exponent $a=0.75\pm0.07$; this is not a critical exponent, but instead results from the decreasing size of the domain wall between the regions of $|\uparrow'\rangle$ and $|\downarrow'\rangle$ as Ω increases. Each point represents an average over 15 to 50 realizations and the uncertainties are the standard deviation. Inset, phase separation s versus t_h with $\Omega=0.6E_L$ fitted to an exponential showing the rapid 0.14(3)-s timescale for phase separation.

RESEARCH LETTER

 $\Omega_{\rm c}=0.19E_{\rm L}.$ This demonstrates a quantum phase transition for a two-component SO-coupled BEC, from miscible when $\varOmega<\Omega_{\rm c}$ to immiscible when $\varOmega>\Omega_{\rm c}.$

Even below Ω_c , s slowly increased with increasing Ω . To understand this effect, we numerically solved the two-dimensional spinor Gross–Pitaevskii equation in the presence of a trapping potential. This demonstrated that the differential interaction term $c_2\left(\hat{\rho}_{\downarrow}^2-\hat{\rho}_{\uparrow}^2\right)/2$ in \hat{H}_I favours slightly different density profiles for each spin component, while the $(c_2+c'_{\uparrow\downarrow})\hat{\rho}_{\uparrow}\hat{\rho}_{\downarrow}$ term favours matched profiles. Thus, as $c_2+c'_{\uparrow\downarrow}$ approached zero from below this balancing effect decreased, causing s to increase.

An infinite system should fully phase separate (s=1) for all $\Omega > \Omega_c$. In our finite system, the boundary between the phase-separated spins, set by the spin-healing length $(\xi_s = \sqrt{\hbar^2/2m|c_2 + c'_{\uparrow\downarrow}|n}$, where n is the local density), can be comparable to the system size. We interpret the increase of s above Ω_c as resulting from the decrease of ξ_s with increasing Ω .

We realized SO coupling in an ⁸⁷Rb BEC, and observed a quantum phase transition from spatially mixed to spatially separated. By operating at lower magnetic field (with a smaller quadratic Zeeman shift), our method extends to the full F=1 or F=2 manifold of ⁸⁷Rb or ²³Na, enabling a new kind of tuning for spinor BECs, without the losses associated with Feshbach tuning²⁵. Such modifications may allow access to the expected non-abelian vortices in some F=2 condensates²⁶. Because our SO coupling is in the small Ω limit, this technique is practical for fermionic ⁴⁰K, with its smaller fine-structure splitting and thus larger spontaneous emission rate²⁷. When the Fermi energy lies in the gap between the lower and upper bands (for example, Fig. 1b) there will be a single Fermi surface; this situation can induce p-wave coupling between fermions²⁸ and more recent work anticipates the appearance of Majorana fermions²⁹.

METHODS SUMMARY

System preparation. Our experiments began with nearly pure ⁸⁷Rb BECs of approximately 1.8×10^5 atoms in the $|F=1, m_F=-1\rangle$ state³⁰ confined in a crossed optical dipole trap. The trap consisted of a pair of 1,064-nm laser beams propagating along $\hat{x} - \hat{y}$ ($1/e^2$ radii of $w_{\hat{x}+\hat{y}} \approx 120$ µm and $w_{\hat{z}} \approx 50$ µm) and $-\hat{x} - \hat{y}$ ($1/e^2$ radii of $w_{\hat{x}-\hat{y}} \approx w_{\hat{z}} \approx 65$ µm).

We prepared equal mixtures of $|F=1,m_F=-1\rangle$ and $|1,0\rangle$ using an initially off-resonant radio-frequency magnetic field $B_{\rm rf}(t)\hat{x}$. We adiabatically ramped δ to $\delta\approx 0$ in 15 ms, decreased the radio-frequency coupling strength $\Omega_{\rm rf}$ to about 150 Hz, which is much less than $\hbar\omega_q$, in 6 ms, and suddenly turned off $\Omega_{\rm rf}$ projecting the BEC into an equal superposition of $|m_F=-1\rangle$ and $|m_F=0\rangle$. We subsequently ramped δ to its desired value in 6 ms and then linearly increased the intensity of the Raman lasers from zero to the final coupling Ω in 70 ms.

Magnetic fields. Three pairs of Helmholtz coils, orthogonally aligned along $\hat{x} + \hat{y}$, $\hat{x} - \hat{y}$ and \hat{z} , provided bias fields $(B_{x+y}, B_{x-y}, and B_z)$. By monitoring the $|F = 1, m_F = -1\rangle$ and $|1,0\rangle$ populations in a nominally resonant radio-frequency dressed state, prepared as above, we observed a short-time (less than about 10 min) rootmean-square field stability $g\mu_B B_{\rm RMS}/h \lesssim 80$ Hz. The field drifted slowly on longer timescales (but changed abruptly when unwary colleagues entered through our laboratory's ferromagnetic doors). We compensated for the drift by tracking the radio-frequency and Raman resonance conditions.

The small energy scales involved in the experiment meant that it was crucial to minimize magnetic field gradients. We detected stray gradients by monitoring the spatial distribution of $|m_F=-1\rangle-|m_F=0\rangle$ spin mixtures after TOF. Small magnetic field gradients caused this otherwise miscible mixture to phase-separate along the direction of the gradient. We cancelled the gradients in the $\hat{x}-\hat{y}$ plane with two pairs of anti-Helmholtz coils, aligned along $\hat{x}+\hat{y}$ and $\hat{x}-\hat{y}$, to $g\mu_B B'/h \lesssim 0.7 \, \mathrm{Hz} \, \mathrm{\mu m}^{-1}$.

Full Methods and any associated references are available in the online version of the paper at www.nature.com/nature.

Received 27 November 2010; accepted 27 January 2011.

 Kato, Y. K., Myers, R. C., Gossard, A. C. & Awschalom, D. D. Observation of the spin Hall effect in semiconductors. Science 306, 1910–1913 (2004).

- Konig, M. et al. Quantum spin Hall insulator state in HgTe quantum wells. Science 318, 766–770 (2007).
- Kane, C. L. & Mele, E. J. Z₂ topological order and the quantum spin Hall effect. Phys. Rev. Lett. 95, 146802 (2005).
- Bernevig, B. A., Hughes, T. L. & Zhang, S.-C. Quantum spin Hall effect and topological phase transition in HgTe quantum wells. Science 314, 1757–1761 (2006)
- Hsieh, D. et al. A topological Dirac insulator in a quantum spin Hall phase. Nature 452, 970–974 (2008).
- Koralek, J. D. et al. Emergence of the persistent spin helix in semiconductor quantum wells. Nature 458, 610–613 (2009).
- Bychkov, Y. A. & Rashba, E. I. Oscillatory effects and the magnetic susceptibility of carriers in inversion layers. J. Phys. C 17, 6039 (1984).
- Dresselhaus, G. Spin-orbit coupling effects in zinc blende structures. Phys. Rev. 100. 580–586 (1955).
- Liu, X.-J., Borunda, M. F., Liu, X. & Sinova, J. Effect of induced spin-orbit coupling for atoms via laser fields. *Phys. Rev. Lett.* **102**, 046402 (2009).
- Quay, C. H. L. et al. Observation of a one-dimensional spin-orbit gap in a quantum wire. Nature Phys. 6, 336–339 (2010).
- von Klitzing, K., Dorda, G. & Pepper, M. New method for high-accuracy determination of the fine-structure constant based on quantized Hall resistance. *Phys. Rev. Lett.* 45, 494–497 (1980).
- Ruseckas, J., Juzeliūnas, G., Öhberg, P. & Fleischhauer, M. Non-abelian gauge potentials for ultracold atoms with degenerate dark states. *Phys. Rev. Lett.* 95, 010404 (2005).
- Stanescu, T. D., Zhang, C. & Galitski, V. Nonequilibrium spin dynamics in a trapped Fermi gas with effective spin-orbit interactions. *Phys. Rev. Lett.* 99, 110403 (2007).
- Dalibard, J., Gerbier, F., Juzeliūnas, G. & Öhberg, P. Artificial gauge potentials for neutral atoms. Preprint at (http://arxiv.org/abs/1008.5378) (2010).
- Higbie, J. & Stamper-Kurn, D. M. Generating macroscopic quantum-superposition states in momentum and internal-state space from Bose-Einstein condensates with repulsive interactions. *Phys. Rev. A* 69, 053605 (2004).
- Lin, Y.-J. et al. Bose-Einstein condensate in a uniform light-induced vector potential. Phys. Rev. Lett. 102, 130401 (2009).
- 17. Lin, Y.-J. et al. A synthetic electric force acting on neutral atoms. Nature Phys. (in the press); preprint at (http://arxiv.org/abs/1008.4864) (2010).
- Lin, Y. J., Compton, R. L., Jimenez-Garcia, K., Porto, J. V. & Spielman, I. B. Synthetic magnetic fields for ultracold neutral atoms. *Nature* 462, 628–632 (2009).
- Stenger, J. et al. Spin domains in ground-state Bose–Einstein condensates. Nature 396, 345–348 (1998).
- Chang, M.-S. et al. Observation of spinor dynamics in optically trapped ⁸⁷Rb Bose-Einstein condensates. Phys. Rev. Lett. 92, 140403 (2004).
- 21. Ho, T.-L. Spinor Bose condensates in optical traps. *Phys. Rev. Lett.* **81**, 742–745 (198)
- Widera, A. et al. Precision measurement of spin-dependent interaction strengths for spin-1 and spin-2 ⁸⁷Rb atoms. N. J. Phys. 8, 152 (2006).
- Ho, T.-L. & Zhang, S. Bose–Einstein condensates in non-abelian gauge fields. Preprint at (http://arxiv.org/abs/1007.0650) (2010).
- Hall, D. S., Matthews, M. R., Ensher, J. R., Wieman, C. É. & Cornell, E. A. Dynamics of component separation in a binary mixture of Bose-Einstein condensates. *Phys. Rev. Lett.* 81, 1539–1542 (1998).
- Erhard, M., Schmaljohann, H., Kronjäger, J., Bongs, K. & Sengstock, K. Measurement of a mixed-spin-channel Feshbach resonance in ⁸⁷Rb. *Phys. Rev. A* 69, 032705 (2004).
- Kobayashi, M., Kawaguchi, Y., Nitta, M. & Ueda, M. Collision dynamics and rung formation of non-abelian vortices. *Phys. Rev. Lett.* 103, 115301 (2009).
- Goldman, N. et al. Realistic time-reversal invariant topological insulators with neutral atoms. Phys. Rev. Lett. 105, 255302 (2010).
- 28. Zhang, C., Tewari, S., Lutchyn, R. M. & Das Sarma, S. $\rho_x + i \rho_y$ superfluid from s-wave interactions of fermionic cold atoms. *Phys. Rev. Lett.* **101**, 160401 (2008).
- Sau, J. D., Tewari, S., Lutchyn, R. M., Stanescu, T. D. & Das Sarma, S. Non-Abelian quantum order in spin-orbit-coupled semiconductors: search for topological Majorana particles in solid-state systems. *Phys. Rev. B* 82, 214509 (2010).
- Lin, Y.-J., Perry, A. R., Compton, R. L., Spielman, I. B. & Porto, J. V. Rapid production of ⁸⁷Rb Bose-Einstein condensates in a combined magnetic and optical potential. *Phys. Rev. A* 79, 063631 (2009).

Acknowledgements We thank E. Demler, T.-L. Ho and H. Zhai for conceptual input; and we appreciate conversations with J. V. Porto and W. D. Phillips. This work was partially supported by ONR, ARO with funds from the DARPA OLE programme, and the NSF through the Physics Frontier Center at the Joint Quantum Institute. K.J.-G. acknowledges CONACYT.

Author Contributions All authors contributed to writing of the manuscript. Y.-J. L. led the data-taking effort in which K.J.-G. participated. I.B.S. conceived the experiment; performed numerical and analytic calculations; and supervised this work.

Author Information Reprints and permissions information is available at www.nature.com/reprints. The authors declare no competing financial interests. Readers are welcome to comment on the online version of this article at www.nature.com/nature. Correspondence and requests for materials should be addressed to I.B.S. (ian.spielman@nist.gov).

METHODS

System preparation. Our experiments began with nearly pure 87 Rb BECs of approximately 1.8×10^5 atoms in the $|F=1, m_F=-1\rangle$ state³⁰ confined in a crossed optical dipole trap. The trap consisted of a pair of 1,064-nm laser beams propagating along $\hat{x}-\hat{y}$ ($1/e^2$ radii of $w_{\hat{x}+\hat{y}}\approx 120~\mu \text{m}$ and $w_{\hat{z}}\approx 50~\mu \text{m}$) and $-\hat{x}-\hat{y}$ ($1/e^2$ radii of $w_{\hat{x}-\hat{y}}\approx w_{\hat{z}}\approx 65~\mu \text{m}$).

We prepared equal mixtures of $|F=1,m_F=-1\rangle$ and $|1,0\rangle$ using an initially off-resonant radio-frequency magnetic field $B_{\rm rf}(t)\hat{x}$. We adiabatically ramped δ to $\delta\approx 0$ in 15 ms, decreased the radio-frequency coupling strength $\Omega_{\rm rf}$ to about 150 Hz, which is much less than $\hbar\omega_q$, in 6 ms, and suddenly turned off $\Omega_{\rm rb}$ projecting the BEC into an equal superposition of $|m_F=-1\rangle$ and $|m_F=0\rangle$. We subsequently ramped δ to its desired value in 6 ms and then linearly increased the intensity of the Raman lasers from zero to the final coupling Ω in 70 ms.

Magnetic fields. Three pairs of Helmholtz coils, orthogonally aligned along $\hat{x} + \hat{y}$, $\hat{x} - \hat{y}$ and \hat{z} , provided bias fields $(B_{x+y}, B_{x-y}, and B_z)$. By monitoring the $|F=1, m_F=-1\rangle$ and $|1,0\rangle$ populations in a nominally resonant radio-frequency dressed state, prepared as above, we observed a short-time (less than about 10 min) rootmean-square field stability $g\mu_B B_{RMS}/h \lesssim 80$ Hz. The field drifted slowly on longer timescales (but changed abruptly when unwary colleagues entered through our laboratory's ferromagnetic doors). We compensated for the drift by tracking the radio-frequency and Raman resonance conditions.

The small energy scales involved in the experiment meant that it was crucial to minimize magnetic field gradients. We detected stray gradients by monitoring the spatial distribution of $|m_F=-1\rangle-|m_F=0\rangle$ spin mixtures after TOF. Small magnetic field gradients caused this otherwise miscible mixture to phase-separate along the direction of the gradient. We cancelled the gradients in the $\hat{x}-\hat{y}$ plane with two pairs of anti-Helmholtz coils, aligned along $\hat{x}+\hat{y}$ and $\hat{x}-\hat{y}$, to $g\mu_{\rm B}B'/h\lesssim 0.7~{\rm Hz~\mu m}^{-1}$.

SO-coupled Hamiltonian. Our system³⁰ consisted of a F=1 BEC with a bias magnetic field along \hat{y} at the intersection of two Raman laser beams propagating along $\hat{x}+\hat{y}$ and $-\hat{x}+\hat{y}$ with angular frequencies $\omega_{\rm L}$ and $\omega_{\rm L}+\Delta\omega_{\rm L}$, respectively. The rank-1 tensor light shift of these beams produced an effective Zeeman magnetic field along the z direction with Hamiltonian $\hat{H}_{\rm R}=\Omega_{\rm R}\check{\sigma}_{3,z}\cos(2k_{\rm L}\hat{x}+\Delta\omega_{\rm L}t)$, where $\check{\sigma}_{3,x,y,z}$ are the 3×3 Pauli matrices and we define $\check{\rm I}_3$ as the 3×3 identity matrix. If we take \hat{y} as the natural quantization axis (by expressing the Pauli matrices in a rotated basis $\check{\sigma}_{3,y}\to\check{\sigma}_{3,z}$, $\check{\sigma}_{3,x}\to\check{\sigma}_{3,y}$ and $\check{\sigma}_{3,z}\to\check{\sigma}_{3,x}$) and make the rotating wave approximation, the Hamiltonian for spin states $\{|m_F=+1\rangle, |0\rangle, |-1\}\}$ in the frame rotating at $\Delta\omega_{\rm L}$ is:

$$\hat{H}_{3} = \frac{\hbar^{2} \hat{\mathbf{k}}^{2}}{2m} \check{\mathbf{I}}_{3} + \begin{pmatrix} 3\delta/2 + \hbar \omega_{q} & 0 & 0\\ 0 & \delta/2 & 0\\ 0 & 0 & -\delta/2 \end{pmatrix} + \frac{\Omega_{R}}{2} \check{\sigma}_{3,x} \cos(2k_{L}\hat{x}) - \frac{\Omega_{R}}{2} \check{\sigma}_{3,y} \sin(2k_{L}\hat{x})$$
(2)

As we justify below, $|m_F=+1\rangle$ can be neglected for large enough $\hbar\omega_q$, which gives the effective two-level Hamiltonian:

$$\hat{H}_2 = \frac{\hbar^2 \hat{\mathbf{k}}^2}{2m} \check{\mathbf{1}} \, + \frac{\delta}{2} \, \check{\sigma}_z + \frac{\Omega}{2} \, \check{\sigma}_x \mathrm{cos}(2k_{\mathrm{L}} \hat{x}) - \frac{\Omega}{2} \, \check{\sigma}_y \mathrm{sin}(2k_{\mathrm{L}} \hat{x})$$

for the pseudo-spins $|\uparrow\rangle = |m_F = 0\rangle$ and $|\downarrow\rangle = |-1\rangle$ where $\Omega = \Omega_{\rm R}/\sqrt{2}$. After a local pseudo-spin rotation by $\theta(\hat{x}) = 2k_{\rm L}\hat{x}$ about the pseudo-spin \hat{z} axis followed by a global pseudo-spin rotation $\check{\sigma}_z \rightarrow \check{\sigma}_y$, $\check{\sigma}_y \rightarrow \check{\sigma}_x$ and $\check{\sigma}_x \rightarrow \check{\sigma}_z$, the 2×2 Hamiltonian takes the SO-coupled form:

$$\hat{H}_2 = \frac{\hbar^2 \hat{\mathbf{k}}^2}{2m} \check{\mathbf{1}} + \frac{\Omega}{2} \check{\sigma}_z + \frac{\delta}{2} \check{\sigma}_y + 2 \frac{\hbar^2 k_L \hat{k}_x}{2m} \check{\sigma}_y + E_L \check{\mathbf{1}}$$

The SO term linear in k_x results from the non-commutation of the spatially dependent rotation about the pseudo-spin z axis and the kinetic energy.

Effective two-level system. For atoms in $|m_F=-1\rangle$ and $|m_F=0\rangle$ with velocities $\hbar \xi_{,x}/m{\approx}0$ and Raman-coupled near resonance, $\delta\approx 0$, the $|m_F=+1\rangle$ state is detuned from resonance owing to the $\hbar\omega_q=3.8E_{\rm L}$ quadratic Zeeman shift. For $\delta/4E_{\rm L}{\ll}1$ and $\Omega<4E_{\rm L}$, we have $\Delta(\Omega,\delta)\approx\delta[1-(\Omega/4E_{\rm L})^2]^{1/2}$.

Effect of the neglected state. In our experiment, we focused on the two-level system formed by the $|m_F=-1\rangle$ and $|m_F=0\rangle$ states. We verified the validity of this assumption by adiabatically eliminating the $|m_F=+1\rangle$ state from the full three-level problem. To second-order in Ω , this procedure modifies the detuning δ and SO-coupling strength α in equation (1) by:

$$\delta^{(2)} = \left(\frac{\Omega}{2}\right)^2 \frac{1}{4E_{\rm L} + \hbar\omega_a} \approx \frac{1}{32} \frac{\Omega^2}{E_{\rm L}}$$

$$\alpha^{(2)} = \left(\frac{\Omega}{2}\right)^2 \frac{\alpha}{\left(4E_{\rm L} + \hbar\omega_q\right)^2} \approx \frac{\alpha}{256} \left(\frac{\Omega}{E_{\rm L}}\right)^2$$

In these expressions, we have retained only the largest term in a $1/\omega_q$ expansion. In our experiment, where $\hbar\omega_q=3.8E_{\rm L}$, δ is substantially changed at our largest coupling $\Omega=7E_{\rm L}$. To maintain the desired detuning δ in the simple two-level model (that is, $\Delta\approx\delta+\delta^{(2)}=0$ in Fig. 1c), we changed $g\mu_{\rm B}B_0$ by as much as $3E_{\rm L}$ to compensate for $\delta^{(2)}$. We did not correct for the change to α , which was always small.

Although both terms are small at the $\Omega=0.2E_{\rm L}$ transition from miscible to immiscible, slow drifts in B_0 prompted us to locate $\varDelta=0$ empirically from the equal-population condition, $N_{{\rm T}\uparrow^\prime}=N_{{\rm T}\downarrow^\prime}$. As a result, δ in equation (1) implicitly includes the perturbative correction $\delta^{(2)}$.

Origin of the effective interaction term. The additional $c'_{\uparrow\downarrow}$ term in the interaction Hamiltonian for dressed spins directly results from transforming into the basis of dressed spins, which are:

$$|\uparrow', K_x\rangle \approx |\uparrow, k_x = K_x + q_\uparrow + k_L\rangle - \varepsilon|\downarrow, k_x = K_x + q_\uparrow - k_L\rangle$$

and

$$|\downarrow', K_x\rangle \approx |\downarrow, k_x = K_x + q_{\perp} - k_{\perp}\rangle - \varepsilon |\uparrow, k_x = K_x + q_{\perp} + k_{\perp}\rangle \tag{3}$$

where $\hbar K_x/m$ is the group velocity, $K_x = q - q_{\uparrow}$ for $|\uparrow'\rangle$ and $K_x = q - q_{\downarrow}$ for $|\downarrow'\rangle$, and $\varepsilon = \Omega/8E_L \ll 1$. Thus, in second quantized notation, the dressed field operators transform according to:

$$\hat{\psi}_{\uparrow}(r) = \hat{\psi}_{\uparrow'}(r) + \varepsilon e^{2ik_{\rm L}x} \hat{\psi}_{\downarrow'}(r)$$

and

$$\hat{\psi}_{\perp}(r) = \hat{\psi}_{\perp'}(r) + \varepsilon e^{-2ik_{\rm L}x} \hat{\psi}_{\uparrow'}(r)$$

where $q_1 \approx -\sqrt{1-4\varepsilon^2}k_{\rm L} \approx -k_{\rm L}$ and $q_1 \approx \sqrt{1-4\varepsilon^2}k_{\rm L} \approx k_{\rm L}$. Inserting the transformed operators into:

$$\hat{H}_{\rm I} = \frac{1}{2} \int d^3r \left[\left(c_0 + \frac{c_2}{2} \right) \left(\hat{\rho}_{\downarrow} + \hat{\rho}_{\uparrow} \right)^2 + \frac{c_2}{2} \left(\hat{\rho}_{\downarrow}^2 - \hat{\rho}_{\uparrow}^2 \right) + c_2 \hat{\rho}_{\downarrow} \hat{\rho}_{\uparrow} \right]$$

gives the interaction Hamiltonian (with normal ordering implied) for dressed spins which can be understood order-by-order (both c_2/c_0 and ε are treated as small parameters). In this analysis, the terms proportional to c_2 are unchanged to the order of c_2/c_0 , and we only need to evaluate the transformation of the spin-independent term (proportional to c_0). At $O(\varepsilon)$ and $O(\varepsilon^3)$ all the terms in the expansion include the high-spatial-frequency prefactors $e^{\pm 2ik_Lx}$ or $e^{\pm 4ik_Lx}$. For density distributions that vary slowly on the $\lambda/2$ length scale these average to zero. The $O(\varepsilon^2)$ term, however, has terms without these modulations, and is:

$$\hat{H}_{\rm I}^{(\varepsilon^2)} = \frac{1}{2} \int \mathrm{d}^3 r \left(8c_0 \varepsilon^2 \hat{\psi}_{\downarrow^{\prime}}^{\dagger} \hat{\psi}_{\uparrow^{\prime}}^{\dagger} \hat{\psi}_{\downarrow^{\prime}} \hat{\psi}_{\uparrow^{\prime}} \right)$$

giving rise to $c'_{\uparrow\downarrow} = c_0 \Omega^2 / (8E_L^2)$.

Mean field phase diagram. We compute the mean-field phase diagram for a ground-state BEC composed of a mixture of dressed spins in an infinite homogeneous system. This applies to our atoms in a harmonic trap in the limit of $R\gg\xi_s$, where *R* is the system size, $\xi_s = \sqrt{\hbar^2/2m|c_2 + c'_{\uparrow\downarrow}|n}$ is the spin healing length and *n* is the density. We first minimize the interaction energy \hat{H}_I at fixed $N_{\uparrow',\downarrow'}$, with an effective interaction $c'_{\uparrow\downarrow}$ as a function of Ω . The two dressed spins are either phasemixed, both fully occupying the system's volume V, or phase-separated with a fixed total volume constraint $V=V_{\uparrow'}+V_{\downarrow'}.$ For the phase-separated case, minimizing the free energy gives the volumes $V_{\uparrow'}$ and $V_{\downarrow'}$, determined by $N_{\uparrow',\downarrow'}$ and V. The interaction energy of a phase-mixed state is smaller than that of a phaseseparated state for the miscibility condition $c_0 + c_2 + c'_{\uparrow\downarrow}/2 < \sqrt{c_0(c_0 + c_2)}$, corresponding to $\Omega < \Omega_c$. This condition is independent of $N_{\uparrow',\downarrow'}$: for any $N_{\uparrow',\downarrow'}$ the system is miscible at $\Omega < \Omega_c$. Then, at a given Ω , we minimize the sum of the interaction energy and the single-particle energy from the Raman detuning, $(N_{\uparrow'}-N_{\downarrow'})\delta/2$, allowing $N_{\uparrow',\downarrow'}$ to vary. For the miscible case ($\Omega < \Omega_{\rm c}$), the BEC is a mixture with fraction $N_{\downarrow'}/(N_{\uparrow'}+N_{\downarrow'}) \in (0,1)$ only in the range of detuning $\delta \in (\delta_0 - W_\delta, \delta_0 + W_\delta), \quad \text{where} \quad \delta_0 = c_2 n/2, \quad W_\delta = |\delta_0| (1 - \Omega/\Omega_c)^{1/2}$ $n = (N_{\uparrow'} + N_{\downarrow'})/V$. For the immiscible case $(\Omega > \Omega_c)$, $W_{\delta} = (c_2/8c_0)c_2n$ is negligibly small compared to c_2n .

Figure 2b shows the mean field phase diagram as a function of (Ω, δ) , where δ/E_L is displayed with a quasi-logarithmic scaling, using the sign function $\mathrm{sgn}(\delta/E_L)[\log_{10}(|\delta/E_L|+|\delta_{\min}/E_L|)-\log_{10}|\delta_{\min}/E_L|]$, in order to display δ within the range of interest. This scaling function smoothly evolves from logarithmic, that



is, approximately $\mathrm{sgn}(\delta/E_{\mathrm{L}})\mathrm{log_{10}}|\delta/E_{\mathrm{L}}|$ for $|\delta| \gg \delta_{\mathrm{min}}$, to linear, that is, approximately δ for $|\delta| \ll \delta_{\mathrm{min}}$, where $\delta_{\mathrm{min}}/E_{\mathrm{L}} = 0.001E_{\mathrm{L}} = 1.5$ Hz.

In our measurement of the dressed spin fraction $f_{\downarrow^{\prime}}$ (see Fig. 3a), $\delta=0$ is determined from the $N_{\mathrm{T}\uparrow^{\prime}}=N_{\mathrm{T}\downarrow^{\prime}}$ condition. We identify this condition as $\delta=\delta_0$ and apply it for all hold times t_h . Because $|\delta_0|\approx 3\,\mathrm{Hz}$ is below our approximately 80-Hz root-mean-square field noise, we are unable to distinguish δ_0 from 0.

Recombining TOF images of dressed spins. To probe the dressed spin states (equation (3)), each of which is a spin and momentum superposition, we adiabatically mapped them into bare spins, $|\uparrow, k_{\downarrow x} = q_{\uparrow} + k_{L}\rangle$ and $|\downarrow, k_{\downarrow x} = q_{\downarrow} - k_{L}\rangle$, respectively. Then, in each image outside an ~90-µm radius disk containing the condensate for each spin distribution, we fitted $n_{T\uparrow',T\downarrow'}(x,y)$ to a gaussian modelling the thermal background and subtracted that fit from $n_{T\uparrow',T\downarrow'}(x,y)$ to obtain the condensate two-dimensional density $n_{\uparrow',\downarrow'}(x,y)$. Thus, for each dressed spin we readily obtained the temperature, total number $N_{T\uparrow',T\downarrow'}$, and condensate densities $n_{\uparrow',\downarrow'}(x,y)$.

To analyse the miscibility from the TOF images where a Stern–Gerlach gradient separated individual spin states, we re-centred the distributions to obtain $n_{\uparrow^{\prime}}(x,y)$ and $n_{\downarrow^{\prime}}(x,y)$. This took into account the displacement due to the Stern–Gerlach gradient and the non-zero velocities $\hbar k_{x}/m$ of each spin state (after the adiabatic mapping). The two origins were determined in the following way: we loaded the dressed states at a desired coupling Ω but with detuning δ chosen to put all atoms in either $|\downarrow^{\prime}\rangle$ or $|\uparrow^{\prime}\rangle$. Because $q_{\uparrow,\downarrow}=\mp\left(1-\Omega^{2}/32E_{\rm L}^{2}\right)k_{\rm L}$ (see Fig. 1c), these velocities $\hbar k_{x}/m=\hbar\left(q_{\uparrow}+k_{\rm L}\right)/m$, $\hbar\left(q_{\downarrow}-k_{\rm L}\right)/m$ depend slightly on Ω , and our technique to determine the origin of the distributions accounts for this effect.

Calibration of Raman coupling. Both Raman lasers were derived from the same Ti:sapphire laser at $\lambda \approx 804.1$ nm, and were offset from each other by a pair of acousto-optic modulators driven by two phase-locked frequency synthesizers near 80 MHz. We calibrated the Raman coupling strength Ω by fitting the three-level Rabi oscillations between the $m_F=-1$, 0 and + 1 states driven by the Raman coupling to the expected behaviour.



Quantum Metropolis sampling

K. Temme¹, T. J. Osborne², K. G. Vollbrecht³, D. Poulin⁴ & F. Verstraete¹

The original motivation to build a quantum computer came from Feynman¹, who imagined a machine capable of simulating generic quantum mechanical systems—a task that is believed to be intractable for classical computers. Such a machine could have farreaching applications in the simulation of many-body quantum physics in condensed-matter, chemical and high-energy systems. Part of Feynman's challenge was met by Lloyd2, who showed how to approximately decompose the time evolution operator of interacting quantum particles into a short sequence of elementary gates, suitable for operation on a quantum computer. However, this left open the problem of how to simulate the equilibrium and static properties of quantum systems. This requires the preparation of ground and Gibbs states on a quantum computer. For classical systems, this problem is solved by the ubiquitous Metropolis algorithm³, a method that has basically acquired a monopoly on the simulation of interacting particles. Here we demonstrate how to implement a quantum version of the Metropolis algorithm. This algorithm permits sampling directly from the eigenstates of the Hamiltonian, and thus evades the sign problem present in classical simulations. A small-scale implementation of this algorithm should be achievable with today's technology.

Since the early days of quantum mechanics, it has been clear that there is a fundamental difficulty in studying many-body quantum systems: the configuration space, or Hilbert space, of a collection of particles grows exponentially with the number of particles. Many of the important breakthroughs in quantum physics during the twentieth century resulted from efforts to address this problem, leading to fundamental theoretical and numerical methods to approximate solutions of the many-body Schrödinger equation. However, most of these methods are limited to weakly interacting particles; unfortunately, it is precisely when the interactions are strong that the most interesting physics arises. Notable examples include high-transition-temperature superconductors, electronic structure in large molecules and quark confinement in quantum chromodynamics.

This problem with configuration space is not unique to quantum mechanics: the task of simulating interacting classical particles is challenging for the same reason. It was only with the advent of computers in the 1950s that a systematic way of simulating classical many-body systems was made possible. In their seminal paper³, Metropolis *et al.* devised a general method to calculate the properties of any substance comprising individual molecules with classical statistics. This paper is a cornerstone in the simulation of interacting systems and has had a huge influence on a wide variety of fields (see, for example, refs 4–6). The Metropolis method can also be used to simulate certain quantum systems by means of a 'quantum-to-classical map'⁷. Unfortunately, this quantum Monte Carlo method is only scalable when the mapping conserves the positivity of the statistical weights, and fails in the case of fermionic systems as a result of the infamous sign problem⁷.

As the reality of quantum computers comes closer, it is crucial to revisit the original motivation of Feynman for building a quantum simulator and to develop a general method, suitable for quantum computing machines, to calculate the properties of any substance comprising interacting quantum molecules. Such an algorithm would

have a multitude of applications. In quantum chemistry, it could be used to compute the electronic binding energy as a function of the coordinates of the nuclei, thus solving the central problem of interest. In condensed-matter physics, it could be used to characterize the phase diagram of the Hubbard model as a function of filling factor, interaction strength and temperature. Finally, it could conceivably be used to predict the mass of elementary particles, solving a central problem in high-energy physics.

The seminal work of Lloyd² demonstrated that a quantum computer can reproduce the dynamical evolution of any quantum many-body system. It did not address, however, the crucial problem of initial conditions: how to prepare the quantum computer efficiently in a state of physical interest such as a thermal (Gibbs) or ground state. Ground states could in principle be prepared using the quantum phase estimation algorithm^{8,9}, but this method is in general not scalable, because it requires a variational state with a large overlap with the ground state. Methods are known for systems with frustration-free interactions¹⁰ and systems that are adiabatically connected to trivial Hamiltonians¹¹, but such conditions are not generically satisfied. Suggestions have been made of how a quantum computer could sample from the thermal state of a system. One¹² is related to the Metropolis rule but left open the problem of how to overcome the no-cloning result and construct local updates that can be rejected. This shortcoming immediately leads to an exponential running time of the algorithm¹². A second¹² approach to preparing thermal states is by simulating the system's interaction with a heat bath. However, this procedure seems to produce large errors when run on a quantum computer with finite resources, and a precise framework to describe these errors seems to be out of reach. Moreover, certain systems such as polymers¹³, binary mixtures¹⁴ and critical spin chains^{15,16} experience extremely slow relaxation when put into interaction with a heat bath. The Metropolis dynamics solves this problem by allowing transformations that are not physically achievable, speeding up relaxation by many orders of magnitude and bridging the microscopic and relaxation timescales; this freedom is to a large extent responsible for the tremendous empirical success of the Metropolis method.

In this Letter, we propose a direct quantum generalization of the classical Metropolis algorithm and show how one iteration of the algorithm can be implemented in polynomial time on a quantum computer. Our quantum algorithm is not affected by the sign problem and can be used to prepare ground and thermal states of generic quantum many-body systems, bosonic and fermionic. Like the classical Metropolis algorithm, the quantum Metropolis algorithm is not expected to reach the ground state of an arbitrary Hamiltonian in polynomial time. The ability to prepare the ground state of a general Hamiltonian in polynomial time would allow the solution of quantum Merlin Arthur (QMA)-complete problems^{17,18}, which is highly unlikely. However, for realistic physical systems, the convergence rate of the classical Metropolis algorithm is often very good, and it is conceivable that the same is also true for the quantum Metropolis algorithm. It also inherits all the flexibility and versatility of the classical method, leading, for instance, to a quantum generalization of simulated annealing6.

¹Vienna Center for Quantum Science & Technology, Fakultät für Physik, Universität Wien, 1090 Wien, Austria. ²Institute of Theoretical Physics, Gottfried Wilhelm Leibniz Universität Hannover, 30167 Hannover, Germany. ³Max Planck Institut für Quantenoptik, 85748 Garching, Germany. ⁴Département de Physique, Université de Sherbrooke, Sherbrooke, Québec J1K 2R1, Canada.

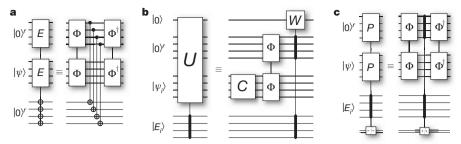


Figure 1 | **Building blocks for the quantum algorithm.** a, The first step of the quantum circuit: the input is an arbitrary state, $|\psi\rangle$, and two r-qubit registers initialized to $|0\rangle^r$. Quantum phase estimation, Φ , is applied to the state and the second register. The energy value in this register is then copied to the first register by a sequence of Controlled NOT gates. An inverse quantum phase estimation (Φ^{\dagger}) is then applied to the state and the second register. b, The elementary step in the quantum circuit: the input is the eigenstate $|\psi_i\rangle$ with energy register $|E_i\rangle$ and two registers initialized to $|0\rangle^r$ and $|0\rangle$, respectively. The unitary transformation C is then applied, followed by a quantum phase estimation step and the coherent Metropolis gate W. The state evolves as

follows: $|\psi_i\rangle|E_i\rangle|0\rangle|0\rangle \to C|\psi_i\rangle|E_i\rangle|0\rangle|0\rangle = \sum_k x_k^i|\psi_k\rangle|E_i\rangle|0\rangle|0\rangle \to \sum_k x_k^i|\psi_k\rangle|E_i\rangle|E_k\rangle|0\rangle \to \sum_k x_k^i\sqrt{f_k^i}|\psi_k\rangle|E_i\rangle|E_k\rangle|1\rangle + \sum_k x_k^i\sqrt{1-f_k^i}|\psi_k\rangle|E_i\rangle|E_k\rangle|0\rangle$ with $f_k^i=\min(1,\exp(-\beta(E_k-E_i)))$. c, The binary measurement checks whether the energy of the state $|\psi\rangle$ is the same as the energy of the original one, $|\psi_i\rangle$. This is done by using an extra register containing phase estimation ancillas, a step that checks whether or not the energy is equal to E_i , and finally an undoing of the phase estimation step that preserves coherence.

To set the stage for the quantum Metropolis algorithm, let us first recall the classical version. We can assume for definiteness that the system is composed of n two-level particles, that is, Ising spins. A lattice of 100 spins has 2^{100} different configurations, so it is inconceivable to average them all. The key insight of Metropolis $et\ al.^3$ was to set up a rapidly mixing Markov chain obeying detailed balance that samples from the configurations with the most significant probabilities. This can be achieved by randomly transforming an initial configuration to a new one (for example by flipping a randomly selected spin): if the energy of the new configuration, $E_{\rm new}$, is lower than the original, $E_{\rm old}$ we retain the move, but if the energy is larger we retain the move only with probability $\exp(\beta(E_{\rm old}-E_{\rm new}))$, where β is the inverse temperature.

The challenge we address is to set up a similar process in the quantum case, that is, to initiate an ergodic random walk on the eigenstates of a given quantum Hamiltonian with the appropriate Boltzmann weights. In analogy to a spin flip, the random walk can be realized by a random local unitary transformation, and the 'move' should be accepted or rejected following the Metropolis rule. There are, however, three obvious complications. First, we do not know what the eigenvectors of the Hamiltonian are (this is one of the problems that we want to solve). Second, certain operations, such as energy measurements, are fundamentally irreversible in quantum mechanics, but the Metropolis method requires rejecting, and hence undoing, certain transformations. Third, it is necessary to devise a criterion which proves that the fixed point of the quantum random walk is the Gibbs state.

To address the first obstacle, we assume for simplicity that the Hamiltonian has non-degenerate eigenvalues, E_i , and denote the corresponding eigenvectors $|\psi_i\rangle$. In the Supplementary Information, we show that those conditions are unnecessary. We can use the phase estimation algorithm^{8,19,20} to prepare a random energy eigenstate and measure the energy of a given eigenstate. Then each quantum Metropolis step (Fig. 1) takes as input an energy eigenstate $|\psi_i\rangle$ with known energy E_i and applies a random local unitary transformation C, creating the superposition $C|\psi_i\rangle=\sum_k x_k^i|\psi_k\rangle$. The transformation C could be a bit flip at a random location, as in the classical setting, or some other simple transformation. The phase estimation algorithm is then used in a coherent way, producing $\sum_k x_k^i|\psi_k\rangle|E_k\rangle$, where $|E_k\rangle$ is an extra register encoding the energy in binary format. At this point, we could measure the second register to read out the energy E_k and accept or reject the move following the Metropolis prescription. However, such an energy measurement would involve an irreversible collapse of the wave function, making it impossible to return to the original configuration in the case of a reject step.

Classically, we overcome this second obstacle by keeping a copy of the original configuration in the computer's memory, allowing a rejected move to be easily undone. Unfortunately, this solution is ruled out in the quantum setting by the no-cloning theorem²¹. The key to the solution is to engineer a measurement that reveals as little information as possible about the new state, and therefore only slightly disturbs it. This can be achieved by a measurement that only reveals one bit of information—accept or reject the move—rather than a full energy

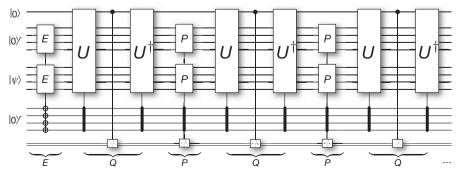


Figure 2 | **Quantum Metropolis stochastic map.** The circuit corresponds to a single application of the map \mathcal{E} . The first step, E, prepares an eigenstate of the Hamiltonian. The second step, Q, measures whether we want to accept or reject the proposed update. In the case of rejection, the complete quantum circuit comprises a sequence of measurements of the Hermitian projectors Q_i and P_i .

The recursion is aborted whenever the outcome P_1 is obtained, which indicates that we have returned to a state with the same energy as the input. Because each iteration has a constant success probability, the overall probability of obtaining the outcome P_1 approaches one exponentially as the number of iterations increases.

Figure 3 | Decision tree for unwinding the measurement. Given an input state, $|\psi\rangle$, we first perform phase estimation to collapse to an eigenstate with known energy, E. This graph represents the plan of action conditioned on the different measurement outcomes of the binary P_i and Q_i measurements. Each

node in the graph corresponds to an intermediate state in the algorithm. One iteration of the map is completed when we reach one of the final leaves labelled either 'Accept' or 'Reject'. The sequence $E \rightarrow Q_1 \rightarrow L$ corresponds to accepting the update; all other leaves correspond to a rejection.

measurement. The circuit that generates this binary measurement is shown at Fig. 1b. It transforms the initial state $|\psi_i\rangle$ into

$$\underbrace{\sum_{k} x_{k}^{i} \sqrt{f_{k}^{i}} |\psi_{k}\rangle |E_{i}\rangle |E_{k}\rangle |1\rangle}_{+ \underbrace{\sum_{k} x_{k}^{i} \sqrt{1 - f_{k}^{i}} |\psi_{k}\rangle |E_{i}\rangle |E_{k}\rangle |0\rangle}_{|\psi_{i}^{-}\rangle}$$

where $f_k^i = \min(1, \exp(-\beta(E_k - E_i)))$. The state can be seen as a coherent superposition of accepting the update or rejecting it. The amplitudes $x_k^i \sqrt{f_k^i}$ correspond exactly to the transition probabilities, $|x_k^i|^2 f_k^i$, of the classical Metropolis rule. The measurement is completed by measuring the last qubit in the computational basis. The outcome $|1\rangle$ will project the other registers in the state $|\psi_i^+\rangle$. On obtaining this outcome, we can measure the second register to learn the new energy, E_k , and use the resulting energy eigenstate as input to the next Metropolis step.

A measurement outcome $|0\rangle$ signals that the move must be rejected, so we must return to the input state, $|\psi_i\rangle$. As $|\psi_i^+\rangle$ is orthogonal to $|\psi_i^-\rangle$, we actually work in a simple two-dimensional subspace, that is, a qubit. In such a case, it is possible to go back to the initial state by an iterative scheme similar to one previously used in the context of QMA amplification²². The circuit implementing this process is shown in Fig. 2. In essence, it repeatedly implements two binary measurements. The first is the one described in the previous paragraph. The second, after a basis change, determines whether or not the computer is in the eigenstate $|\psi_i\rangle$. A positive outcome to the latter measurement implies that we have returned to the input state, completing the rejection; in the case of a negative outcome, we repeat both measurements. Every sequence of these two measurements has a constant probability of achieving the rejection, so recursive repetition yields a success probability exponentially close to one (Fig. 3).

The quantum Metropolis algorithm can be used to generate a sequence of m states, $|\phi_j\rangle$, j=1,...,m, that reproduce the statistical averages of the thermal state $\rho_{\rm G} \propto {\rm e}^{-\beta H}$ for any observable X:

$$\frac{1}{m} \sum_{j=1}^{m} \left\langle \phi_j | X | \phi_j \right\rangle = \text{Tr} X \rho + \mathcal{O} \left(1 / \sqrt{m} \right)$$

To show that the fixed point of the quantum random walk is the Gibbs state, we made use of the theoretical framework of 'quantum detailed balance' (Supplementary Information). Let $\{|\psi_i\rangle\}$ be a complete basis of the physical Hilbert space and let $\{p_i\}$ be a probability distribution on this basis. Assume that a completely positive map, \mathcal{E} , obeys the condition

$$\sqrt{p_n p_m} \langle \psi_i | \mathcal{E}(|\psi_n\rangle \langle \psi_m|) | \psi_i \rangle = \sqrt{p_i p_j} \langle \psi_m | \mathcal{E}(|\psi_j\rangle \langle \psi_i|) | \psi_n \rangle$$

Then $\sigma = \sum_i p_i |\psi_i\rangle\langle\psi_i|$ is a fixed point of \mathcal{E} . The quantum detailed balance condition only ensures that the thermal state ρ_G is a possible fixed point of the quantum Metropolis algorithm. The uniqueness of

this fixed point and the rate at which the algorithm converges to it depend on the choice of the set of random unitary transformations $\{C\}$. If the set of moves is chosen such that the map \mathcal{E} is ergodic, the uniqueness of the fixed point is ensured. The Metropolis step obeys the quantum detailed balance condition if the probability of applying a specific transformation C is equal to the probability of applying its conjugate, C^{\dagger} . This can be seen as the quantum analogue of the classical symmetry condition for the update probability. In some cases, it even suffices to apply the same local unitary transformation at every step of the algorithm (Fig. 4). In this case, the single unitary transformation has to be Hermitian. The local unitary transformation can be seen to induce 'non-local' transitions between the eigenstates because it is followed by a phase estimation procedure.

In conclusion, even though an implementation of this algorithm for full-scale quantum many-body problems may be out of reach with today's technological means, the algorithm is scalable to system sizes that are interesting for actual physical simulations. In Supplementary Information, we describe a small-scale implementation of the algorithm that can be achieved with present-day technology. Moreover, a discussion is included that sketches the basic steps necessary for the simulation of some notoriously hard quantum many-body problems. Like in the classical setting, the convergence rate and, hence, the run-time of the algorithm are dictated by the spectral gap of the stochastic map. The scaling of the gap depends on the Hamiltonian in the problem and the choice of updates, {C}. Just as for the classical Metropolis algorithm, efficient thermalization is not expected for an arbitrary Hamiltonian. This would allow the solution of QMA-complete problems in polynomial time²³⁻²⁵. It is, however, expected that the algorithm will thermalize for realistic physical systems. The inverse gap of the quantum Metropolis map for the XX chain in a transverse magnetic field at zero temperature with a simple, single spin-flip update is shown in Fig. 4. This plot indicates that the gap scales like O(1/N), where N is the number of spins, even at criticality. To prove a polynomial scaling of

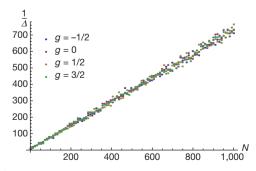


Figure 4 | Inverse spectral gap of the completely positive map for the quantum Ising model. Inverse gap, $1/\Delta$, of the quantum Metropolis map at zero temperature as a function of the number of spins, N, in a chain with Hamiltonian $H = \sum_k X_k X_{k+1} + Y_k Y_{k+1} + g Z_k$. The update rule is a single spin flip, X_1 . The observed linear scaling indicates that, at least in the case of one-dimensional spin chains with nearest-neighbour Hamiltonians, the quantum Metropolis algorithm seems to converge in polynomial time. Proving this remains an interesting open problem.



the gap for more complex Hamiltonians remains a challenging open problem. Also, it is well known that the choice of updates, {*C*}, can have a drastic impact on the convergence rate of the Markov chain in the classical setting. Finding good updates in the quantum setting is a very interesting open question, although the above example suggests that the problem might be simpler in the quantum case than in the classical case. The algorithm can be seen as a classical random walk on the eigenstates of the Hamiltonian. All samples are thus computed with respect to the actual eigenstates. This is why our method is suitable for the simulation of fermionic systems by exploiting the Jordan-Wigner transformation²⁶, as discussed in ref. 27. The fermionic sign problem is therefore not an issue for the quantum Metropolis algorithm. It is worth noting that an additional quadratic speed-up might be achievable using the methods of refs 28-30.

Received 29 September; accepted 21 December 2010.

- Feynman, R. Simulating physics with computers. Int. J. Theor. Phys. 21, 467-488 (1982).
- Lloyd, S. Universal quantum simulators. Science 273, 1073-1078 (1996).
- Metropolis, N., Rosenbluth, A. W., Rosenbluth, M. N., Teller, A. H. & Teller, E. Equation of state calculation by fast computing machines. J. Chem. Phys. 21, 1087 (1953)
- Durr, S. et al. Ab initio determination of light hadron masses. Science 322, 1224–1227 (2008).
- Geman, S. & Geman, D. Stochastic relaxation, Gibbs distributions, and the Bayesian restoration of images. IEEE Trans. Pattern Anal. Mach. Intell. 6, 721-741 (1984).
- Kirkpatrick, S., Gelatt, C. D. & Vecchi, M. P. Optimization by simulated annealing. Science 220, 671-680 (1983).
- Suzuki, M. (ed.) Quantum Monte Carlo Methods in Equilibrium and Nonequilibrium Systems (Springer Ser. Solid-State Sci. 74, Springer, 1987).
- Abrams, D.S. & Lloyd, S. Quantum algorithm providing exponential speed increase for finding eigenvalues and eigenvectors. Phys. Rev. Lett. 83, 5162-5165 (1999).
- Aspuru-Guzik, A., Dutoi, A. D., Love, P. J. & Head-Gordon, M. Simulated quantum computation of molecular energies. Science 309, 1704-1707 (2005)
- Verstraete, F., Wolf, M. M. & Cirac, J. I. Quantum computation and quantum-state engineering driven by dissipation. Nature Phys. 5, 633-636 (2009).
- 11. Farhi, E. et al. A quantum adiabatic evolution algorithm applied to random instances of an NP-complete problem. Science 292, 472-475 (2001).
- 12. Terhal, B. M. & DiVincenzo, D. P. Problem of equilibration and the computation of correlation functions on a quantum computer. Phys. Rev. A 61, 022301 (2000).
- 13. Binder, K. Monte Carlo and Molecular Dynamics Simulations in Polymer Science
- (Oxford Univ. Press, 1995). Liu, J. & Luijten, E. Rejection-free geometric cluster algorithm for complex fluids. Phys. Rev. Lett. **92**, 035504 (2004).
- Swendsen, R. H. & Wang, J.-S. Nonuniversal critical dynamics in Monte Carlo simulations. Phys. Rev. Lett. 58, 86-88 (1987).

- 16. Evertz, H. G. The loop algorithm. Adv. Phys. 52, 1-66 (2003).
- Kitaev, A. Y., Shen, A. H. & Vyalyi, M. N. Classical and Quantum Computation (American Mathematical Society, 2002).
- Aharonov, D. & Naveh, T. Quantum NP a survey. Preprint at (http://arxiv.org/abs/ quant-ph/0210077) (2002).
- Kitaev, A. Y. Quantum computations: algorithms and error correction. Russ. Math. Surv. 52, 1191-1249 (1997).
- Cleve, R., Ekert, A., Macchiavello, C. & Mosca, M. Quantum algorithms revisited. Proc. R. Soc. Lond. A 454, 339-354 (1998)
- 21. Wootters, W. K. & Zurek, W. H. A single quantum cannot be cloned. Nature 299, 802-803 (1982)
- 22. Marriott, C. & Watrous, J. Quantum Arthur-Merlin games. Comput. Complex. 14, 122-152 (2005).
- Oliveira, R. & Terhal, B. M. The complexity of quantum spin systems on a twodimensional square lattice. Quant. Inf. Comp. 8, 900-924 (2008).
- Aharonov, D., Gottesman, D., Irani, D. & Kempe, J. The power of quantum systems on a line. Commun. Math. Phys. 287, 41-65 (2009).
- Schuch, N. & Verstraete, F. Computational complexity of interacting electrons and fundamental limitations of density functional theory. Nature Phys. 5, 732-735
- Jordan, P. & Wigner, E. Über das Paulische Äquivalenzverbot. Zeit. Phys. A 47, 631-651 (1928).
- Abrams, D. S. & Lloyd, S. Simulation of many-body Fermi systems on a universal quantum computer. Phys. Rev. Lett. 79, 2586-2589 (1997)
- Szegedy, M. in Proc. Annu. IEEE Symp. Found. Comput. Sci. 32-41 (IEEE, 2004).
- Somma, R. D., Boixo, S., Barnum, H. & Knill, E. Quantum simulations of classical annealing processes. Phys. Rev. Lett. 101, 130504 (2008).
- Poulin, D. & Wocjan, P. Sampling from the thermal quantum Gibbs state and evaluating partition functions with a quantum computer. Phys. Rev. Lett. 103, 220502 (2009).

Supplementary Information is linked to the online version of the paper at www.nature.com/nature.

Acknowledgements We would like to thank S. Bravyi, C. Dellago, J. Kempe and H. Verschelde for discussions. Part of this work was done during a workshop at the Erwin Schrödinger Institute for Mathematical Physics. K.T. was supported by the FWF programme CoQuS. T.J.O. was supported, in part, by EPSRC. K.G.V. is supported by DFG FG 635. D.P. is partly funded by NSERC, MITACS and FQRNT. F.V. is supported by the FWF grants FoQuS and ViCoM, by the European grant QUEVADIS and by the ERC grant OUERG.

Author Contributions This project was started by T.J.O. and F.V. five years ago and rejuvenated by an inspiring visit of K.G.V. with K.T. and F.V. in 2009. The connection to the QMA amplification scheme of Marriott and Watrous was made by D.P. at the Erwin Schrödinger Institute, and the project was finalized by K.T. and F.V. by proving quantum detailed balance.

Author Information Reprints and permissions information is available at www.nature.com/reprints. The authors declare no competing financial interests. Readers are welcome to comment on the online version of this article at www.nature.com/nature. Correspondence and requests for materials should be addressed to F.V. (fverstraete@gmail.com).



Synchronicity of Antarctic temperatures and local solar insolation on orbital timescales

Thomas Laepple¹, Martin Werner¹ & Gerrit Lohmann¹

The Milankovitch theory states that global climate variability on orbital timescales from tens to hundreds of thousands of years is dominated by the summer insolation at high northern latitudes^{1,2}. The supporting evidence includes reconstructed air temperatures in Antarctica that are nearly in phase with boreal summer insolation and out of phase with local summer insolation³⁻⁵. Antarctic climate is therefore thought to be driven by northern summer insolation⁵. A clear mechanism that links the two hemispheres on orbital timescales is, however, missing. We propose that key Antarctic temperature records derived from ice cores are biased towards austral winter because of a seasonal cycle in snow accumulation. Using present-day estimates of this bias in the 'recorder' system, here we show that the local insolation can explain the orbital component of the temperature record without having to invoke a link to the Northern Hemisphere. Therefore, the Antarctic ice-core-derived temperature record, one of the best-dated records of the late Pleistocene temperature evolution, cannot be used to support or contradict the Milankovitch hypothesis that global climate changes are driven by Northern Hemisphere summer insolation variations.

Reconstructions of Antarctic local temperature based on the measured ratio of stable water isotopes within deep ice cores show a strong signature of orbital insolation variability³⁻⁶. Recently, a new absolute dating technique^{5,7} enabled the phasing between the Antarctic temperature and the insolation to be determined and hence inferences could be made about the Milankovitch theory¹. Because the tilt of the Earth, corresponding to the obliquity parameter, influences the high latitudes on both hemispheres in an identical way, the strong obliquity component found in the temperature reconstructions³⁻⁶ does not help to distinguish between a local or a remote insolation forcing. However, the precession component, which is out of phase between the Northern Hemisphere and the Southern Hemisphere, was found to be coherent and nearly in phase with the Northern Hemisphere summer insolation intensity (21 June insolation at 65° N)^{5,7}. This nearly in-phase relationship therefore puts the Antarctic climate response into the early group of responses according to the SPECMAP classifications² and would support the Milankovitch theory¹ that the global climate is driven by insolation changes at high northern latitudes⁵. However, these findings pose the question of how the Northern Hemisphere solar forcing is transferred to the Southern Hemisphere, and why Southern Hemisphere local insolation changes have no imprint on the Antarctic temperature record. Variations in greenhouse gas concentrations are too weak to explain the interhemispheric link8; there exists no evidence that atmospheric dynamics can directly transfer the orbital signal to the Southern Hemisphere⁹, and changes in the thermohaline circulation are thought to favour an asymmetric pattern¹⁰.

To explain the observed phasing of the precession signal in the Antarctic temperature records, different possible mechanisms have been proposed: (1) When the summer solstice in one hemisphere occurs in perihelion (the Earth's closest point to the Sun), the summer solstice on the other hemisphere occurs in aphelion (the Earth's furthest point from the Sun). A comparison of the summer insolation of both

hemispheres with the temperature record leads to the hypothesis that the Antarctic climate on orbital timescales is paced by northern summer insolation⁵. (2) The summer insolation intensity and summer duration are out of phase in the precessional band because by Kepler's law a closer pass to the Sun (higher summer intensity) must be faster (shorter summer). It was recently proposed that Antarctic temperatures respond sensitively to changes of the local summer duration¹¹. However, this nonlinear response on insolation cannot be fully confirmed by present-day observations (Supplementary Note 7). (3) Changes of Southern Ocean sea-ice coverage by variations in winter or spring insolation could affect the Antarctic temperature by modifying the heat transport from the Southern Ocean to the ice sheet and would be in phase with the isotopic record^{12,13} depending on the definition of the season¹⁴. In first climate-model simulation experiments this sea-ice effect on the annual mean temperature in Antarctica is minor¹³.

Here we propose an alternative mechanism, related to the interplay of a seasonal cycle in the accumulation of Antarctic snow (that is, the 'recording system') with the seasonal variations of the precession component of the incoming solar insolation. It is based on the idea that the snow accumulation on the Antarctic Plateau has a minimum in austral summer, and therefore the recorded temperature signal is biased towards the remaining seasons.

The measured temporal variations of the isotopic composition within Antarctic ice cores on glacial-interglacial timescales can be safely interpreted as accumulation-weighted temperature changes¹⁵. Numerous authors have drawn attention to the possible influence of a change in the seasonal precipitation distribution during glacialinterglacial cycles on the isotopic record^{15,16}, and it has been shown that this effect significantly biases the Greenland temperature records but probably has only a minor effect on Antarctica¹⁷. There are other biasing effects of the interplay of temperature and precipitation, namely the intermittent precipitation behaviour, which increases the interannual variability in the isotopic record¹⁸, and the link of precipitation to specific weather patterns that are not representative for the mean temperature¹⁹. However, not only changes in the seasonality of the precipitation, but also the complementary effect, that is, changes of the seasonal cycle of temperature together with a stable seasonality in precipitation, could influence the record²⁰.

For present-day climate, the surface temperature on the East-Antarctic Plateau is largely determined by the local insolation²¹. This is supported by the seasonal cycle in temperature, which strongly follows the incoming radiation (Fig. 1). When we introduce a small time lag of 7–9 days (caused by the thermal capacity), the daily insolation explains 96–99% of the variance of the surface air-temperature cycle measured by the Automatic Weather Stations at Dome C²², Dome Fuji²² and Vostok (Fig. 1). We can therefore approximate the local temperature by the insolation. Following this argument, the accumulation-weighted insolation is used in this study as proxy for the isotopically derived temperature record.

Owing to low local precipitation and strong wind-drift, a direct measurement of seasonal accumulation on the Antarctic Plateau is difficult²³. However, several different accumulation estimates for the

¹Alfred Wegener Institute for Polar and Marine Research, Bremerhaven, Germany.

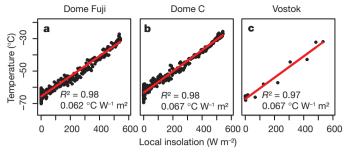


Figure 1 | **Relationship of daily local insolation and surface air temperature. a**, Dome Fuji, Automatic Weather Station data²² (February 1995 to November 2006). **b**, Dome C, Automatic Weather Station data²² (January 1984 to December 1994).**c**, Vostok, monthly data from the Arctic and Antarctic Research Institute (AARI) (1958–2007). We removed the time lag between insolation and temperature (9 days in **a**, 7 days in **b**, no time lag in **c** because monthly data are used). We could not detect any systematic deviations from a linear relationship (especially no higher sensitivity to lower temperatures as proposed in a recent study¹¹, see Supplementary Note 7). This supports the concept of using the insolation as an approximation for the surface air temperature.

East Antarctic Plateau (Methods Summary) show a strong similarity, with a minimum in accumulation in summer (Fig. 2a). It has been argued that the winter maxima in accumulation on the East Antarctic Plateau are caused by the gentle terrain slopes, which leave radiative cooling as the primary mechanism to maintain saturation and cause clear-sky precipitation, as well as by the increased moisture transport caused by the weather systems in the local winter^{23,24}. Furthermore, summer ablation reduces the summer accumulation²⁴.

For glacial climates, at present, no direct measurements of the seasonality of accumulation on the East Antarctic Plateau exist. However, it seems safe to assume that the seasonality of precipitation has been rather stable over time because the present-day temperatures on the plateau are far below the freezing point and therefore any effect of the additional glacial cooling on precipitation and sublimation is probably limited. Furthermore, Antarctic boundary conditions, such as the circular symmetry and the topography, are only weakly affected by glacial-interglacial changes. For the remainder of this study we use the mean over the different data sets as a best guess for the seasonal cycle of the accumulation on the East Antarctic Plateau. However, the following results are also obtained if using any of the single time series (Supplementary Note 1). Folding the mean seasonal accumulation cycle with the insolation anomaly between the precession phases leads to a positive net anomaly of the accumulation-weighted insolation forcing (Fig. 2b, Methods Summary). This weighted insolation signal has the opposite phase to the precession component of the local summer anomaly and is in phase with Northern Hemisphere summer intensity.

To quantitatively analyse this effect, we focus on the Dome Fuji temperature reconstruction (T_{site} , Fig. 3a) because this record is based on a absolute chronology⁵. The results are not sensitive to this choice and also apply for the other long temperature reconstructions on the East Antarctic plateau, Vostok and Dome C (Supplementary Note 5). We weight the daily insolation at the position of the core (77° S) (ref. 25) with the mean local accumulation displayed in Fig. 2. This accumulation-weighted insolation shows very similar temporal variations compared to the local temperature reconstruction from Dome Fuji in the orbital bands (Fig. 3b) (R = 0.70, T_{site} bandpass-filtered between 1/15,000 years and 1/50,000 years). The main deviations from the data are during deglaciations, where our model cannot capture the strong amplitude of the $T_{\rm site}$ variations. Furthermore, the local weighted insolation is nearly indistinguishable from the Northern Hemisphere summer insolation, which shows a similar relationship to the Dome Fuji temperature reconstruction (Fig. 3c, R = 0.70). In contrast to these two hypotheses, the local maximum summer insolation (Fig. 3d) cannot explain the data because the precession has the inverse phase to the observation (R = -0.37), and the local

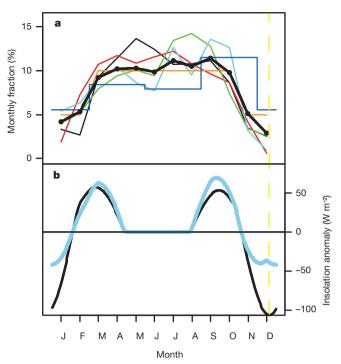


Figure 2 | Seasonal cycle of accumulation and insolation anomaly. a, Monthly accumulation fractions are shown as coloured lines. Thin black line, Vostok precipitation from corrected gauge measurements (AARI) (1958-2007), Cvan line, Vostok snow-stake-based accumulation (1970-1995), Red line, *P* minus *E* reanalysis moisture budget from the European Centre for Medium-Range Weather Forecasts (ECMWF) for altitudes exceeding 2,500 m. Green line, precipitation estimate at Mizuho station (70.6° S, 44.3° E) (1980). Blue line, *P* minus *E* rawinsonde-based moisture budget for the area $0-55^{\circ}$ E, 69.3-76.8° S. Orange line, constant precipitation plus 50% sublimation in NDJF (that is, November to February), following observations at Dome Fuji. The thick black line joining points is the average of all estimates. References to these data sets can be found in Supplementary Note 1. b, Unweighted (black) and accumulation-weighted (blue) difference in local diurnal insolation between the two extreme states of the precession (austral summer solstice at aphelion minus austral summer solstice at perihelion, for a fixed eccentricity value of 0.05). The annual mean insolation anomaly is zero, but folding the anomaly with the accumulation estimates leads to a positive net response. The austral summer solstice (21 December) is marked as a vertical yellow dashed line.

unweighted annual mean insolation (Fig. 3e) does not contain a precession component and therefore does not describe the proxy data very well (R = 0.34) either.

A more detailed analysis of the temporal temperature and insolation changes reveals that the local temperature data slightly lags behind the weighted insolation (precession 26.8°, obliquity 52.7°). However, our time lag is approximately the same as the lag of local temperature to the northern summer insolation (precession 27.3°, obliquity 53.0°). The latter was found to be insignificant if the uncertainty of the chronology as well as the sampling uncertainty is taken into account 11 .

Assuming the seasonal temperature sensitivity observed in the present-day seasonal cycle of temperature (Fig. 1, 0.067 °C W ⁻¹ m²), we can also compare the strength of isotope-based temperature changes with the ones obtained from our model. The modelled insolation-based temperature amplitude (around 0.7 °C peak-to-peak) is too low compared to the reconstructed temperature change in the orbital bands (3 °C peak-to-peak). However, the equilibrium temperature sensitivity is considerably higher than the seasonal temperature sensitivity²⁶. This will affect the temperature response on long-term insolation anomalies caused by changes in the Earth's axial tilt. Our model is based completely on modern observations, so other mechanisms not captured by our approach might increase the amplitude further. One example is the dependence of the seasonal accumulation on the summer insolation intensity, caused by the temperature dependence of the snow

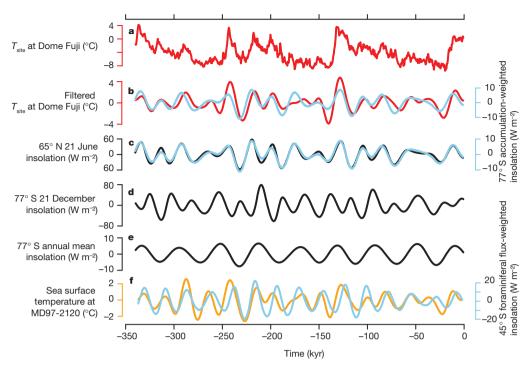


Figure 3 Comparison of the temperature reconstruction with the accumulation-weighted insolation. a, $T_{\rm site}$ at Dome Fuji⁵. b, $T_{\rm site}$ filtered in the orbital band (bandpass-filtered between 1/15,000 years and 1/50,000 years, 101,000-year window, Finite Response Filter) (red trace) compared with the accumulation-weighted insolation at 77° S (blue trace). c, Northern boreal summer insolation at 65° N (black trace) compared with the accumulation-weighted local insolation at 77° S (blue trace). d, Local unweighted austral summer insolation. e, Local annual mean insolation. f, MgCa-derived sea

surface temperature of sediment core MD97-2120 (ref. 27), filtered in the orbital band (orange trace), compared with the local insolation weighted by the seasonal cycle of local foraminiferal flux²⁹ (blue trace). See also Supplementary Note 6. The local accumulation-weighted insolation, which is a proxy for the isotopic record, is coherent and nearly in phase with $T_{\rm site}$ (b) and very similar to the Northern Hemisphere summer intensity (c). Therefore $T_{\rm site}$ cannot be used to support the remote forcing hypothesis.

ablation. Sensitivity studies show that this additional effect could explain the full precession amplitude (Supplementary Note 3). Furthermore, the linearity between insolation and temperature within our conceptual model implies that the temperature of the polar winter remains constant during all precession phases. However, enhanced summer insolation intensity is accompanied by longer Antarctic winters, and by reduced winter insolation intensity in the Southern Hemisphere, in regions north of the Antarctic Circle. These effects might decrease Antarctic winter temperatures and thus lead to reduction of the accumulation-weighted annual temperature signal. This would amplify the precession signal that is in phase with Northern Hemisphere summer insolation (Supplementary Note 4).

Given the results of our model, we propose that the orbital variations in Antarctic local temperature are a response to the local insolation if the seasonal pattern of accumulation is correctly taken into account. This implies that the interhemispheric symmetry in polar climate change might not be due to a causal relationship between the hemispheres, but is simply an artefact of the recording system.

Do these findings contradict the orbital period variability observed in sub-Antarctic marine records²⁷? Local climate feedbacks can lead to a winter-to-spring sensitivity of the annual temperature and therefore to local precession signals in phase with Northern Hemisphere summer insolation²⁸; one example is the spring sensitivity of sea ice¹³. Furthermore, modern sediment-trap data indicate highly seasonal patterns of foraminifera fluxes at Chatham rise, one of the key locations for sub-Antarctic marine records. Here, the foraminifera species used for the palaeotemperature estimates mainly peak in the austral spring^{27,29}. This seasonal recording leads to a precession signal resembling Northern Hemisphere summer insolation (Fig. 3f, Supplementary Note 6). Additionally, some parts of the marine sediment chronology are not independently dated but are based on Antarctic ice-core chronologies. Thus, it seems likely that the precession signal of the south polar regions is a combination of different mechanisms,

and our findings demand a careful re-evaluation of these Southern Hemisphere climate records and recorder systems.

The local interpretation of the precession and obliquity signal also provides insight into the stronger quasi-100,000-year cycle by decoupling the orbital variability in both hemispheres. In contrast to the viewpoint that Antarctic temperature is driven by Northern Hemispheric summer insolation, the hypothesis presented is consistent with terminations triggered by either the Northern or the Southern Hemisphere¹², or as a combination of both³⁰. In such a scenario, the insolation-sensitive sub-Antarctic sea ica¹³, the Southern Ocean as a potential driver for CO_2 (ref. 31) and the insolation-sensitive icesheet of the Northern Hemisphere¹ might act together. A Southern Hemisphere influence could also explain the phasing of the circulation response relative to insolation forcing that contradicts the SPECMAP hypothesis³².

METHODS SUMMARY

Studies of seasonal accumulation on the East Antarctic Plateau are sparse and we therefore also considered the three accumulation-related quantities precipitation P, net precipitation (P minus evaporation E) and sublimation for our analysis. The analysed records that include gauge measurements of precipitation, accumulation estimates from stake networks, and moisture flux calculations are described in Supplementary Note 1.

To derive the weighted annual mean insolation, in 100-year steps, the daily insolation is weighted with the accumulation estimate, linearly interpolated to daily values:

$$W_{\text{weight}} = \frac{\int_{T} W(t)A(t)d(t)}{\int_{A(t)d(t)}}$$

 W_{weight} is the annual weighted insolation, t is the day of the year, W(t) is the daily insolation, A(t) is the daily accumulation estimate, and T corresponds to one year.

To define a past calendar, a reference date must be arbitrarily chosen in which a certain day is aligned to a position of the Earth on the ellipse around the Sun^{14,25}. A



common solution is to fix 21 March to the vernal equinox for any period of the past. But because we are studying the local Antarctic insolation, we use a different calendar approach and choose to fix the austral solstice to 21 December. Our results are insensitive to this choice. Furthermore, using a method completely independent of any calendar definitions gives similar results (Supplementary Note 2).

Received 4 June 2010; accepted 10 January 2011.

- Milankovitch, M. Kanon der Erdbestrahlung und seine Anwendung auf das Eiszeitproblem. Akad. R. Serbe 133, 1-633 (1941).
- Imbrie, J. et al. On the structure and origin of major glaciation cycles. 1. Linear responses to Milankovitch forcing. Paleoceanography 7, 701-738 (1992).
- Petit, J. R. et al. Climate and atmospheric history of the past 420,000 years from the Vostok ice core, Antarctica. *Nature* **399**, 429–436 (1999).
- Lorius, C. et al. A 150,000-year climatic record from Antarctic ice. Nature 316, 591-596 (1985).
- Kawamura, K. et al. Northern Hemisphere forcing of climatic cycles in Antarctica 5 over the past 360,000 years. Nature **448**, 912–916 (2007).
- Jouzel, J. et al. Orbital and millennial Antarctic climate variability over the past 800,000 years. Science **317**, 793–796 (2007).
- Suwa, M. & Bender, M. L. Chronology of the Vostok ice core constrained by O₂/N₂ ratios of occluded air, and its implication for the Vostok climate records. Quat. Sci. Rev. 27, 1093-1106 (2008).
- Lorius, C., Jouzel, J., Raynaud, D., Hansen, J. & Le Treut, H. The ice-core record: climate sensitivity and future greenhouse warming. Nature 347, 139-145 (1990).
- Manabe, S. & Broccoli, A. The influence of continental ice sheets on the climate of an ice age. J. Geophys. Res. 90, 2167-2190 (1985).
- Stocker, T. F. Climate change—the seesaw effect. Science 282, 61-62 (1998).
- 11. Huybers, P. & Denton, G. Antarctic temperature at orbital timescales controlled by local summer duration. Nature Geosci. 1, 787–792 (2008).
- 12. Stott, L., Timmermann, A. & Thunell, R. Southern hemisphere and deep-sea warming led deglacial atmospheric CO₂ rise and tropical warming. Science 318, 435-438 (2007)
- Timmermann, A., Timm, O., Stott, L. & Menviel, L. The roles of CO2 and orbital forcing in driving southern hemispheric temperature variations during the last 21 000 yr. *J. Clim.* **22,** 1626–1640 (2009).
- Joussaume, S. & Braconnot, P. Sensitivity of paleoclimate simulation results to season definitions. *J. Geophys. Res.* 102, 1943–1956 (1997).
 Steig, E. J., Grootes, P. M. & Stuiver, M. Seasonal precipitation timing and ice core
- records. Science **266**, 1885–1886 (1994).
- Werner, M., Mikolajewicz, U., Heimann, M. & Hoffmann, G. Borehole versus isotope temperatures on Greenland: seasonality does matter. Geophys. Res. Lett. 27, 723-726 (2000).
- 17. Jouzel, J. et al. Magnitude of isotope/temperature scaling for interpretation of central Antarctic ice cores. J. Geophys. Res. 108, 4361 (2003).
- 18. McConnell, J. R., Bales, R. C. & Davis, D. R. Recent intra-annual snow accumulation at South Pole: implications for ice core interpretation. J. Geophys. Res. 102, 21947-21954 (1997).

- 19. Noone, D., Turner, J. & Mulvaney, R. Atmospheric signals and characteristics of accumulation in Dronning Maud Land, Antarctica. J. Geophys. Res. 104, 19191-19211 (1999).
- Gildor, H. & Ghil, M. Phase relations between climate proxy records: potential effect of seasonal precipitation changes. Geophys. Res. Lett. 29, 1024 (2002).
- Schwerdtfeger, W. Weather and Climate of the Antarctic (Elsevier, 1984).
- Keller, L. Antarctic Automatic Weather Station Data for the Calendar Year 2001 (University of Wisconsin, Space Science and Engineering Center, 2007).
- Bromwich, D. H. Snowfall in high southern latitudes. Rev. Geophys. 26, 149-168 (1988)
- 24. Ekaykin, A., Petit, J. & Arapov, P. Meteorological regime of central Antarctica and its role in the formation of isotope composition of snow thickness. PhD thesis, Univ. Joseph Fourier (2003).
- Berger, A. & Loutre, M. Insolation values for the climate of the last 10 million years. Quat. Sci. Rev. 10, 297–317 (1991).
- Hansen, J. et al. Climate response times: dependence on climate sensitivity and ocean mixing. Science 229, 857-859 (1985).
- Pahnke, K., Zahn, R., Elderfield, H. & Schulz, M. 340,000-year centennial-scale marine record of Southern Hemisphere climatic oscillation. Science 301, 948-952 (2003)
- Laepple, T. & Lohmann, G. The seasonal cycle as template for climate variability on astronomical time scales. Paleoceanography 24, PA4201 (2009).
- King, A. & Howard, W. Seasonality of foraminiferal flux in sediment traps at Chatham Rise, SW Pacific: implications for paleotemperature estimates. Deep-Sea Res. I 48, 1687-1708 (2001).
- Schulz, K. G. & Zeebe, R. E. Pleistocene glacial terminations triggered by synchronous changes in Southern and Northern Hemisphere insolation: the insolation canon hypothesis. Earth Planet. Sci. Lett. 249, 326–336 (2006).
- 31. Sigman, D. M., Hain, M. P. & Haug, G. H. The polar ocean and glacial cycles in atmospheric CO₂ concentration. Nature 466, 47-55 (2010).
- Lisiecki, L., Raymo, M. & Curry, W. Atlantic overturning responses to Late Pleistocene climate forcings. Nature 456, 85-88 (2008).

Supplementary Information is linked to the online version of the paper at www.nature.com/nature.

Acknowledgements We thank K. Fujita for providing the original data of δ^{18} O measurements from precipitation samples and the Arctic and Antarctic Research Institute (AARI) for providing meteorological data sets of Vostok station. The work benefited from discussions with S. Kipfstuhl, O. Eisen and V. Masson-Delmotte, as well as from comments by P. Huybers and K. Kawamura.

Author Contributions T.L. designed the study, performed the statistical analysis, and wrote the paper. Both M.W. and G.L. contributed significantly to the discussion of results and manuscript refinement.

Author Information Reprints and permissions information is available at www.nature.com/reprints. The authors declare no competing financial interests. Readers are welcome to comment on the online version of this article at www.nature.com/nature. Correspondence and requests for materials should be addressed to T.L. (thomas.laepple@awi.de).



Phylogenomic analyses unravel annelid evolution

Torsten H. Struck¹, Christiane Paul², Natascha Hill³, Stefanie Hartmann³, Christoph Hösel¹, Michael Kube⁴, Bernhard Lieb⁵, Achim Meyer⁵, Ralph Tiedemann², Günter Purschke¹ & Christoph Bleidorn^{2,6}

Annelida, the ringed worms, is a highly diverse animal phylum that includes more than 15,000 described species and constitutes the dominant benthic macrofauna from the intertidal zone down to the deep sea. A robust annelid phylogeny would shape our understanding of animal body-plan evolution and shed light on the bilaterian ground pattern. Traditionally, Annelida has been split into two major groups: Clitellata (earthworms and leeches) and polychaetes (bristle worms), but recent evidence suggests that other taxa that were once considered to be separate phyla (Sipuncula, Echiura and Siboglinidae (also known as Pogonophora)) should be included in Annelida¹⁻⁴. However, the deep-level evolutionary relationships of Annelida are still poorly understood, and a robust reconstruction of annelid evolutionary history is needed. Here we show that phylogenomic analyses of 34 annelid taxa, using 47,953 amino acid positions, recovered a well-supported phylogeny with strong support for major splits. Our results recover chaetopterids, myzostomids and sipunculids in the basal part of the tree, although the position of Myzostomida remains uncertain owing to its long branch. The remaining taxa are split into two clades: Errantia (which includes the model annelid Platynereis), and Sedentaria (which includes Clitellata). Ancestral character trait reconstructions indicate that these clades show adaptation to either an errant or a sedentary lifestyle, with alteration of accompanying morphological traits such as peristaltic movement, parapodia and sensory perception. Finally, life history characters in Annelida seem to be phylogenetically informative.

Annelids are found throughout the world's terrestrial, aquatic and marine habitats. They represent one of three major animal groups with segmentation, so understanding annelid body-plan evolution is crucial for elucidating aspects of the evolution of Bilateria^{5–7}. Several annelid taxa have recently emerged as model organisms in various biological disciplines⁸. Surprisingly, the evolution of Annelida is still poorly understood, and it is uncertain how well these model organisms represent the ancestral character traits in Annelida. To rectify this situation, multigene data sets are needed to evaluate the diversity and the relationships of major annelid clades.

Annelida traditionally included Polychaeta and Clitellata. Morphological and molecular data corroborate clitellate monophyly and provide robust phylogenetic hypotheses within this taxon⁹. Polychaetes are classified into approximately 80 family-level taxa that are generally supported as monophyletic; however, arrangement of these taxa into well-supported, more-inclusive nodes is problematic^{2,10}. Historically, polychaetes were classified as either Sedentaria or Errantia on the basis of their morphology and mode of life^{11–13}. This systematization was dismissed in the 1970s as being arbitrary groupings useful only for practical purposes¹⁴. About 15 years ago, on the basis of morphological cladistic analyses, a monophyletic Polychaeta consisting of two major clades, Scolecida and Palpata, was proposed, with the latter clade divided into Canalipalpata and Aciculata¹⁵. There is increasing molecular evidence, however, that places Clitellata, as well as the non-segmented taxa Echiura and Sipuncula, within polychaetes and thus

renders Polychaeta paraphyletic¹⁻⁴. So far, molecular work based on only a few genes has not supported the proposed monophyly¹⁵ of most major polychaete clades. Yet, support for basal nodes in these studies is less than 50 or 0.50 for bootstrap support (BS) or posterior probability (PP), respectively, resulting in a lack of support for alternative hypotheses^{2,3}.

To address these major outstanding issues of annelid phylogeny, we used a phylogenomic approach, generating expressed sequence tag (EST) libraries for 17 annelid taxa, which are in addition to the publicly available EST or genomic data from annelids. We reconstructed relationships of major annelid taxa using 47,953 amino acid positions derived from 231 gene fragments that span 20 traditional polychaete 'families', Siboglinidae, Myzostomida, Echiura, Clitellata, Sipuncula and five outgroup taxa. This is the largest phylogenomic data set explored so far in annelid phylogeny and has a mean data coverage of 41.7% per taxon.

Sensitivity analyses of our data (Supplementary Tables 4 and 6) showed that increasing the number of positions and mean leaf stability had a positive impact on BS, whereas increasing the data coverage by removing either genes or taxa with low coverage had no such impact (Supplementary Fig. 1). Therefore, the largest data set (47,953 positions), with either all taxa (denoted ALL) or excluding the five annelid taxa that showed leaf stabilities below 0.925 (denoted EX) was used in maximum likelihood and Bayesian inference analyses. These analyses retrieved a clade (called clade 1) comprising all annelids with the exception of Chaetopteridae, Sipuncula and Myzostomida. This clade received significant branch support: ALL, PP = 0.98 (Bayesian inference), BS = 88 (maximum likelihood); EX, PP = 0.99 (Bayesian inference), BS = 100 (maximum likelihood) (Fig. 1 and Supplementary Figs 2, 3, 6 and 8). Reconstructing ancestral morphological traits for clade 1 and Annelida revealed that they were similar, except for some larval characters (Fig. 2a and Supplementary Table 5).

On the basis of this reconstruction, the ancestral annelid had a pair of anterior appendages (that is, grooved palps), which functioned in food gathering and sensory perception. Other head or pygidial appendages were absent. Eyes and nuchal organs were present as sensory organs. Of the different chaetal types, only internalized supporting chaetae and simple chaetae were part of the ancestral pattern. Reconstructions of most other parapodial characters were uncertain, except for the possession of prominent notopodial lobes. Although the fossil record of early annelids from the Cambrian period is sparse, it nonetheless reveals that, congruent with our reconstructions, the early annelids had palps, simple chaetae and internalized supporting chaetae but did not have other chaetae or appendages such as tentacular, parapodial or pygidial cirri^{16,17}.

In agreement with previous molecular studies^{1–3,18}, Chaetopteridae, which have three distinct body regions, are found in the basal part of the annelid tree. Thus, the evolution of segmentation—with predominantly homonomous segmentation in clade 1 and Myzostomida, heteronomous segmentation in Chaetopteridae and complete reduction in Sipuncula—is already highly variable at basal nodes in the

¹University of Osnabrück, FB05 Biology/Chemistry, AG Zoology, Barbarastrasse 11, 49069 Osnabrück, Germany. ²University of Potsdam, Institute of Biochemistry and Biology, Unit of Evolutionary Biology/ Systematic Zoology, Karl-Liebknecht-Strasse 24-25, Haus 26, 14476 Potsdam, Germany. ³University of Potsdam, Institute of Biochemistry and Biology, Unit of Bioinformatics, Karl-Liebknecht-Strasse 24-25, Haus 14, 14476 Potsdam, Germany. ⁴Max Planck Institute for Molecular Genetics, Ihnestrasse 63–73, 14195 Berlin, Germany. ⁵Johannes Gutenberg University, Institute of Zoology, Müllerweg 6, 55099 Mainz, Germany. ⁶University of Leipzig, Institute for Biology II, Molecular Evolution and Systematics of Animals, Talstrasse 33, 04103 Leipzig, Germany.

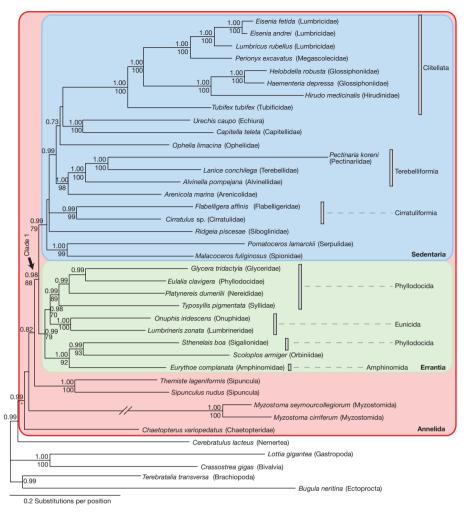


Figure 1 | Reconstruction of the Annelida phylogenetic tree. Majority rule consensus trees of the Bayesian inference analysis using the site-heterogeneous CAT model of the data set with 39 taxa and 47,953 amino acid positions. Only PP (top of branch or alone) and BS (bottom) values \geq 0.70 or 70, respectively,

are shown. The branch leading to Myzostomida is reduced by 75%. Annelida are highlighted in red, with Sedentaria in blue and Errantia in green. Grey bars indicate additional annelid groups. *, BS value for the monophyly of Annelida without Myzostomida in the maximum likelihood analysis is 99.

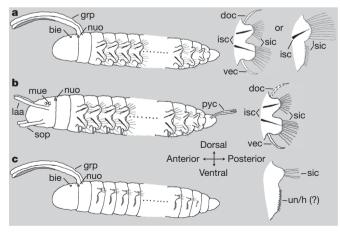


Figure 2 | Ancestral reconstructions of body and parapodial characters.
a, Annelida and clade 1. b, Errantia. c, Sedentaria. Body characters (left) and parapodial characters (right) are depicted. The state of several parapodial characters in Annelida and clade 1 is uncertain, so we depict the two most extreme possibilities. Dashed lines or question marks indicate that the state of the character is uncertain. bie, bicellular eyes; doc, dorsal cirrus; grp, grooved palps; isc, internalized supporting chaetae; laa, lateral antenna; mue, multicellular eyes; nuo, nuchal organ; pyc, pygidial cirrus; sic, simple chaetae; sop, solid palps; un/h, uncini/hooks; vec, ventral cirrus.

annelid phylogeny¹. Moreover, we acknowledge that, in addition to Chaetopteridae, Myzostomida and Sipuncula, other taxa such as Oweniidae, Dinophilidae or Protodrilida, which were not covered here because of a lack of data, might also be placed in the basal part of the annelid tree².

The major difference between the maximum likelihood and Bayesian inference analyses is the placement of Myzostomida. Myzostomids are either ectocommensals or endoparasites of echinoderms, and the systematic placement of this aberrant taxon has proved to be problematic^{19,20}. Bayesian inference analysis places Myzostomida within Annelida (PP = 0.99 for both data sets (ALL and EX); Fig. 1 and Supplementary Fig. 6). By contrast, by maximum likelihood analyses, long-branched Myzostomida are grouped with Ectoprocta, the outgroup taxon with the longest branch (Supplementary Figs 2 and 3). There is conclusive support from mitochondrial gene order and morphological data that Myzostomida are part of the annelid radiation 19,20, and it has been shown that their derived sequences can be affected by long-branch attraction (LBA)¹⁸. The CAT model of Bayesian inference analyses is known to be less affected by LBA than other models, and this model proved to be better suited for our data set than was the LG model of maximum likelihood analyses (Supplementary Information). Notwithstanding the different position of Myzostomida (possibly owing to LBA), both maximum likelihood analyses support the monophyly of Annelida: ALL, BS = 99; EX, BS = 100 (Supplementary Figs 2 and 3). Moreover, the exclusion of Myzostomida did not substantially

alter the phylogenetic reconstruction of annelid ingroup relationships and BS values (Supplementary Fig. 7). Finally, the different placement of Myzostomida in the Bayesian inference and maximum likelihood analyses did not affect the reconstructions of ancestral morphological traits (Supplementary Table 5).

Clade 1 split into two well-supported clades: Errantia, which comprised Phyllodocida, Eunicida, Amphinomida and Orbiniidae; and Sedentaria, which comprised Clitellata and Echiura, as well as most other Scolecida (Capitellidae, Opheliidae and Arenicolidae) and Canalipalpata (Terebelliformia, Cirratuliformia, Siboglinidae, Serpulidae and Spionidae). Both clades were significantly supported: ALL, PP = 0.99 (Bayesian inference), BS = 79 (maximum likelihood); EX, PP = 0.99 (Bayesian inference), BS = 100 (maximum likelihood) (Fig. 1 and Supplementary Figs 2, 3, 6 and 8). The placement of Clitellata indicated a closer relationship to Terebelliformia/Arenicolidae, Opheliidae and Capitellidae/Echiura. Moreover, analyses of branch attachment frequencies based on the data set comprising all taxa showed that each of the five removed annelid taxa is nested in either Sedentaria (*Ridgeia*, *Ophelia*, *Pomatoceros* and *Malacoceros*) or Errantia (*Eurythoe*), and none is moving between clades (Supplementary Figs 4 and 5).

In an influential publication in the 1990s, the two main competing hypotheses of annelid evolution were discussed²¹: one, starting with a ground pattern that resembles an errant, epibenthic organism; and, the other, starting with an infaunal burrowing form. Interestingly, we found both trends to be realized within annelids. The ground pattern of Errantia reveals some important changes with respect to sensory perception and motility. On the basis of our reconstructions, the last common ancestor of Errantia had lateral antennae, palps (which are solid and restricted to sensory perception), a pair of pygidial cirri, nuchal commissures and two pairs of multicellular eyes facing in different directions²² (Fig. 2b and Supplementary Table 5). The parapodia had prominent notopodial and neuropodial lobes supported by internalized chaetae, as well as ventral cirri. Overall, this pattern can be regarded as adaptations to a more active and mobile lifestyle, which requires increased perception of the environment, as well as motility by undulation. Prominent parapodial lobes are advantageous for rapid movements based on undulation, which is mainly achieved by the well-developed longitudinal musculature arranged in at least four separate bundles. For example, in sexually mature (that is, epigamous) nereidids, adopting a temporary pelagic reproductive stage, parapodial lobes are even further enlarged and paddle-like than in immature stages¹⁷. Most taxa of Phyllodocida, Eunicida and Amphinomida show such an errant, often predatory, mode of life and hence were traditionally named Errantia¹¹. The position of Orbiniidae, which were previously grouped with Scolecida¹⁵, might be surprising; however, placing them within or close to the errant forms had previously been debated on the basis of morphological and molecular evidence^{2,3,12}. Therefore, we named this clade Errantia, as it is characterized by adaptation to a more errant life.

The evolution of parapodia in Sedentaria shows the opposite trend. Neuropodial and notopodial lobes are generally smaller than in Errantia and lack internalized supporting chaetae (Fig. 2c). In general, chaetae are in close proximity to the stiff body wall, an arrangement that facilitates a better anchorage in tubes and burrows. Moreover, antennae are absent, and palps have been lost independently in several taxa. The taxa of this clade are commonly characterized by a sedentary life, as more or less sessile organisms that live below stones, tube builders, or burrowers by means of peristals is such as earthworms $^{\!\scriptscriptstyle 17}\!.$ Sedentaria are generally microphagous. Taxa without appendages such as those formerly grouped as Scolecida¹⁵ are deposit feeders, often ingesting sediment. By contrast, taxa with sometimes elaborate head appendages such as terebellids or serpulids are surface deposit feeders or filter feeders, respectively²³. The deposit feeding lifestyle also generally applies to most Clitellata. Therefore, we named this clade Sedentaria¹² (now including Clitellata), and it is characterized by adaptations to a more sedentary lifestyle by, for example, the reduction of parapodia and loss of internalized supporting chaetae. A key feature is that the chaetae are in closer proximity to the stiff body wall, rather than being embedded in parapodial lobes (which are more flexible) as is typical for errant annelids. Interestingly, errant polychaetes with sedentary life strategies such as Lumbrineridae or Onuphidae have adapted to such a lifestyle by using different solutions¹⁷.

Hence, within Annelida, there are two major clades, Errantia and Sedentaria, whose evolution was driven by the adaptation to two different modes of life. Errantia show a more mobile and active life strategy than Sedentaria, and this is correlated to increased sensory perception and motility. Sedentaria are more sessile, with accompanying reductions of head and body appendages and the position of the chaetae being in closer proximity to the body wall than in Errantia. Annelids have been successfully established as models in evolutionary developmental studies to deduce the characteristics of the last common bilaterian ancestor²⁴. Of the recent model organisms, *Platynereis*, with its well-developed head and parapodial appendages, is a good representative of Errantia. By contrast, *Capitella* (as a burrower with reduced appendages), *Helobdella* (as a clitellate) and *Hydroides* (as a filter feeder using its radiolar crown) represent different microphagous feeder types in Sedentaria.

METHODS SUMMARY

EST libraries of 1,370 clones, on average, were prepared for 17 annelid species (Supplementary Table 1). All original sequence data have been deposited in the NCBI Expressed Sequence Tag database (dbEST). EST or genomic data from 17 additional annelid species and 5 outgroup species were obtained from public archives (Supplementary Table 1). These raw EST data were further processed as described previously²⁵. Sets of orthologous genes were determined using the program HaMStR in combination with the InParanoid database (without ribosomal proteins)²⁶, and were translated into amino acid sequences using the program ESTwise²⁷. In parallel, we retrieved all ribosomal proteins from databases as described previously²⁵ (Supplementary Table 2). Each orthologous gene set was aligned using MAFFT software²⁸ and masked using the program REAP²⁹. Only genes that had taxon coverage of at least 33.3% were included in the final super-matrix.

Phylogenetic trees were inferred from this data set of 39 taxa by using a Bayesian inference approach (using the site-heterogeneous CAT model) and a maximum likelihood approach (using the LG model). Stabilities of taxa were assessed using the leaf stability index as calculated by Phyutility software³⁰ (Supplementary Table 3). The five annelid taxa with an index below 0.925 were removed in the second data set, and the Bayesian inference analysis was repeated. Branch attachment frequencies of these unstable annelid taxa were assessed using the lineage movement option in Phyutility³⁰ based on the data set with all taxa.

Full Methods and any associated references are available in the online version of the paper at www.nature.com/nature.

Received 2 September 2010; accepted 18 January 2011.

- Dordel, J., Fisse, F., Purschke, G. & Struck, T. H. Phylogenetic position of Sipuncula derived from multi-gene and phylogenomic data and its implication for the evolution of segmentation. J. Zool. Syst. Evol. Res. 48, 197–207 (2010).
- Struck, T. H., Nesnidal, M. P., Purschke, G. & Halanych, K. M. Detecting possibly saturated positions in 18S and 28S sequences and their influence on phylogenetic reconstruction of Annelida (Lophotrochozoa). *Mol. Phylogenet. Evol.* 48, 628–645 (2008).
- Struck, T. H. et al. Annelida phylogeny and the status of Sipuncula and Echiura. BMC Evol. Biol. 7, 57 (2007).
- McHugh, D. Molecular evidence that echiurans and pogonophorans are derived annelids. Proc. Natl Acad. Sci. USA 94, 8006–8009 (1997).
- Raible, F. et al. Vertebrate-type intron-rich genes in the marine annelid Platynereis dumerilii. Science 310, 1325–1326 (2005).
- Tessmar-Raible, K. & Arendt, D. Emerging systems: between vertebrates and arthropods, the Lophotrochozoa. Curr. Opin. Genet. Dev. 13, 331–340 (2003).
- Rivera, A. & Weisblat, D. And Lophotrochozoa makes three: Notch/Hes signaling in annelid segmentation. Dev. Genes Evol. 219, 37–43 (2009).
- 8. Shain, D. H. Annelids in Modern Biology (Wiley, 2009).
- Erséus, C. Phylogeny of oligochaetous Clitellata. Hydrobiologia 535–536, 357–372 (2005).
- McHugh, D. Molecular systematics of polychaetes (Annelida). Hydrobiologia 535– 536, 309–318 (2005).
- 11. Fauvel, P. Polychètes errantes. Faune de France 5, 1-488 (1923).
- 12. Fauvel, P. Polychètes sédentaires. Faune de France 16, 1-494 (1927).
- de Quatrefages, A. M. Histoire Naturelle des Annelides, Marine et d'Eau Douce. Annelides et Gephyriens Vol. 1 (Librairie Encyclopédique de Roret, 1866).



- 14. Day, J. H. A Monograph on the Polychaeta of Southern Africa. Part 1. Errantia (British Museum (Natural History), 1967).
- Rouse, G. W. & Fauchald, K. Cladistics and polychaetes. Zool. Scr. 26, 139-204
- Eibye-Jacobsen, D. A reevaluation of Wiwaxia and the polychaetes of the Burgess Shale. Lethaia 37, 317–335 (2004).

 17. Rouse, G. W. & Pleijel, F. Polychaetes (Oxford Univ. Press, 2001).
- Bleidorn, C. et al. On the phylogenetic position of Myzostomida: can 77 genes get it wrong? BMC Evol. Biol. 9, 150 (2009).
- Bleidorn, C. et al. Mitochondrial genome and nuclear sequence data support Myzostomida as part of the annelid radiation. Mol. Biol. Evol. 24, 1690-1701 (2007)
- 20. Eeckhaut, I., Fievez, L. & Müller, M. C. M. Larval development of Myzostoma cirriferum (Myzostomida). J. Morphol. 258, 269–283 (2003).
- Westheide, W. The direction of evolution within the Polychaeta. J. Nat. Hist. 31, 1-15(1997)
- 22. Suschenko, D. & Purschke, G. Ultrastructure of pigmented adult eyes in errant polychaetes (Annelida): implications for annelid evolution. Zoomorphology 128, 75-96 (2009).
- 23. Fauchald, K. & Jumars, P. A. The diet of worms: a study of polychaete feedings guilds. Oceanogr. Mar. Biol. Annu. Rev. 17, 193-284 (1979).
- Christodoulou, F. et al. Ancient animal microRNAs and the evolution of tissue identity. Nature 463, 1084-1088 (2010).
- 25. Hausdorf, B. et al. Spiralian phylogenomics supports the resurrection of Bryozoa comprising Ectoprocta and Entoprocta. Mol. Biol. Evol. 24, 2723–2729 (2007).
- 26. Ebersberger, I., Strauss, S. & von Haeseler, A. HaMStR: profile Hidden Markov Model based search for orthologs in ESTs. BMC Evol. Biol. 9, 157 (2009)
- 27. Birney, E., Clamp, M. & Durbin, R. GeneWise and Genomewise. Genome Res. 14, 988-995 (2004).
- 28. Katoh, K., Kuma, K.-i., Toh, H. & Miyata, T. MAFFT version 5: improvement in accuracy of multiple sequence alignment. Nucleic Acids Res. 33, 511-518 (2005).
- Hartmann, S. & Vision, T. Using ESTs for phylogenomics: can one accurately infer a phylogenetic tree from a gappy alignment? BMC Evol. Biol. 8, 95 (2008).

30. Smith, S. A. & Dunn, C. W. Phyutility: a phyloinformatics tool for trees, alignments and molecular data. Bioinformatics 24, 715-716 (2008).

Supplementary Information is linked to the online version of the paper at www.nature.com/nature.

Acknowledgements We are grateful to I. Ebersberger, S. Strauss and A. von Haeseler for the processing of our raw EST libraries. We also thank M. Aguado for species identification of Typosyllis pigmentata, as well as K. M. Halanych and P. A. Ramey-Balci for suggestions. T.H.S. and C.B. acknowledge support from the marine biological stations in Bamfield, Helgoland, List and Roscoff for collection of annelids. This work was funded by the priority programme 'Deep Metazoan Phylogeny' of the Deutsche Forschungsgemeinschaft by grants DFG-STR 683/5-2 (T.H.S.), DFG-Pu-84/5-1 (G.P. and T.H.S.), DFG-TI-349/4-1 (R.T.), DFG Li 998/3-1 (B.L.), DFG-HA 5744/1-1 (S.H.) and DFG-BL-787/2-1 (C.B.).

Author Contributions T.H.S., G.P., R.T. and C.B. conceived this study. T.H.S. took the lead on data collection of sedentary polychaetes, and writing. T.H.S. and S.H. performed phylogenomic analyses. C.H. aided in the data collection of Sedentaria. C.B. and C.P. took the lead on data collection of errant polychaetes, and C.B., S.H. and N.H. on compilation of the data sets from the EST libraries. A.M. and B.L. generated the EST library of Sipunculus nudus, and M.K. was responsible for the sequencing of the EST libraries. T.H.S., G.P., R.T. and C.B. were the main contributors to the writing of the manuscript.

Author Information Sequence data have been deposited in the NCBI Expressed Sequence Tag database (dbEST) under accession numbers FN424437-FN428571, FR754554-FR771822, HQ729923-HQ729975. The largest aligned data set has been deposited at http://www.treebase.org. Reprints and permissions information is available at www.nature.com/reprints. The authors declare no competing financial interests. Readers are welcome to comment on the online version of this article at www.nature.com/nature. Correspondence and requests for materials should be addressed to T.H.S. (struck@biologie.uni-osnabrueck.de) or C.B. (bleidorn@uni-leipzig.de).

METHODS

General outline. EST libraries were prepared for 17 annelid species, and they were used in combination with EST or genomic data from 17 additional annelid species and 5 outgroup species from public archives, and further processed as described previously²⁵. Sets of orthologous genes were determined using the program HaMStR in combination with the InParanoid database (without ribosomal proteins)²⁶, and were translated into amino acid sequences using the program ESTwise²⁷. In parallel, we retrieved all ribosomal proteins from databases as described previously²⁵. Each orthologous gene set was aligned using MAFFT software²⁸ and masked using the program REAP²⁹. Phylogenetic trees were constructed by using a Bayesian inference approach and a maximum likelihood approach. Stabilities of taxa were assessed using the leaf stability index as calculated by Phyutility software³⁰. The five annelid taxa with an index below 0.925 were removed, and the Bayesian inference analysis was repeated. Branch attachment frequencies of these unstable annelid taxa were assessed using the lineage movement option in Phyutility³⁰.

Data assembly. Supplementary Table 1 lists taxa (34 annelids and 5 outgroup taxa) used in this study. On collection, samples were frozen at $-80\,^{\circ}$ C. Total RNA was isolated using an RNeasy Plant Mini Kit (Qiagen) and then reverse transcribed to double-stranded cDNA with the Mint- Universal cDNA synthesis kit (Evrogen) to produce amplified cDNA libraries. The cDNA was size fractioned using CHROMA SPIN-1000 (Clontech). SfiI-digested cDNA allowed directional cloning into pDNR-lib. On average, 1,370 clones—ranging from 368 in *Ophelia limacina* to 4,135 in *Myzostoma cirriferum*—were successfully 5'-end sequenced from recombinant plasmids (at the htpt group of R. Reinhardt) by using Sanger-based sequencing technology. For *Glycera tridactyla*, sequences were generated with 454 technology by LGC Genomics. All original sequence data have been deposited in NCBI dbEST³¹.

Recent studies successfully used ribosomal proteins obtained from EST databases to resolve deep metazoan phylogeny^{1,25,32,33}. Therefore, ribosomal protein sequences were extracted from these EST data (Supplementary Table 2) using the human ribosomal proteome (retrieved from the Ribosomal Protein Gene Database³⁴) as a search template during local BLAST searches (tblastn algorithm and an e-value $\leq e^{-10}$ as a match criterion). To substantially increase the amount of data, we also determined sets of orthologous genes using the program HaMStR²⁶, which derives a set of primer taxa from the InParanoid database³⁵, generating a set of core orthologous genes to build, train and calibrate a profile Hidden Markov Model. This model is then used to search for orthologues in the EST data. Further confirmation of the orthology of determined EST sequences was achieved in a final step of a reciprocal BLAST search against the proteome of one of the primer taxa, ideally the closest relative of the primer taxa to the query taxon. Orthology was accepted only if the same gene was retrieved as the best hit as in the set of core orthologous genes. We used the following set of primer taxa: Capitella teleta, Helobdella robusta, Lottia gigantea, Schistosoma mansoni, Daphnia pulex, Apis mellifera and Caenorhabditis elegans. The nucleotide sequence was translated into amino acids using ESTwise²⁷, and each set of orthologous genes was individually aligned using MAFFT²⁸ with default settings. Questionably aligned positions were eliminated with the alignment masker REAP²⁹ for each individual partition using default parameters.

For the sensitivity analyses, we generated three super-matrices based on taxon coverage per gene. The first matrix consisted of genes that were present in at least one-third of the taxa. In the second, the genes were present in at least one-half of the taxa, and in the third, the genes were present in at least two-thirds of the taxa. Thus, matrix coverage increased from the first to the third super-matrix, but the number of positions decreased. Custom Perl scripts were written for all of these steps. The data set consisting of genes that were present in at least one-third of the taxa was deposited at http://www.treebase.org and can be accessed at http://purl. org/phylo/treebase/phylows/study/TB2:S10986. Together with the information provided in Supplementary Table 6 and the Supplementary Information, all data sets used in the course of our analyses can be generated from this data set.

Phylogenetic analyses. The most appropriate substitution model for these three matrices was $LG + I + \Gamma$ as determined based on the Akaike information criterion using ProtTest³⁶. Before the time-consuming Bayesian inference analyses, we conducted a series of maximum likelihood analyses to assess the influence of the number of positions, the percentage of missing data and leaf stability on BS. Therefore, taxa that had less than 15%, 17.5% or 20% of the total positions in the largest super-matrix were excluded (Supplementary Table 2). Similarly, taxa with a leaf stability index of less than 0.875, 0.900 or 0.925 were excluded from the three super-matrices (Supplementary Table 3). We did not exclude annelid taxa with an index less than 0.950 because this was above the mean leaf stability of 0.943. Moreover, we also prepared one data set excluding only Myzostomida from the largest data set with 47,953 positions. Finally, we partitioned this data set based on our two strategies to assemble the data set. The first data set comprised only the ribosomal proteins; the second, the genes that were identified by HaMStR, without any ribosomal proteins; and the third, all HaMStR-identified genes, including the

ribosomal genes (which were also detected by HaMStR). Thus, we had a total of 25 data sets (Supplementary Table 4). Maximum likelihood analyses were conducted with RAxML version 2.7.6 (ref. 37), using 100 replicate searches starting from randomized maximum parsimony trees. Confidence values for the edges of the maximum likelihood trees were determined based on bootstrap replicates. We used the automatic bootstopping option³⁸ (-# autoMRE) in RAxML to a maximum of 1,000 replicates (Supplementary Table 4). Leaf stability indices, as well as lineage movements of the unstable taxa, were determined using Phyutility³⁰ and the bootstrap trees of the analyses comprising all taxa.

On the basis of the results of the sensitivity analyses, we conducted two Bayesian inference analyses using PhyloBayes v3.2d39 and the site-heterogeneous CAT model (which is not available for RAxML), as it has been shown that this model is more robust against LBA artefacts and thus less prone to systematic errors in phylogenetic data sets⁴⁰. One data set comprised all 39 taxa and 47,953 positions, and in the other all annelids showing a leaf stability index below 0.925 were excluded (34 taxa, 47,953 positions). Each analysis ran eight chains in parallel for 29,525 cycles on average (ranging from 28,894 to 29,808) for the data set with 39 taxa and for 34,693 on average (ranging from 33,560 to 34,944) for the one with 34 taxa. To conduct these analyses, we used Mac OS X v10.6.4 with 2×2.93 GHz Quad-core Intel Xeon processors and 16 GB, 1,066 MHz DDR3 RAM. Using all eight processors in parallel, the two PhyloBayes analyses ran for 37 days, which is equivalent to nearly 10,000 h of CPU time. Stable convergence of likelihood values, alpha parameter and tree length of the eight chains was assessed using Tracer v1.4.1 (ref. 41), and if we had sampled nearly two times more trees than would be discarded as burn-in, this was taken as a stopping point. The first 10,000 cycles (trees) of each chain were discarded as burn-in, and the majority rule consensus tree containing the PPs was calculated from the remaining trees of the eight chains of each Bayesian inference analysis, sampling each second tree. Thus, the consensus trees are based on a total of 78,099 or 98,771 trees, respectively. We also tested a posteriori whether the CAT model was superior to the LG model in the PhyloBayes analyses using the cross-validation test⁴² implemented in PhyloBayes. On the basis of the data set comprising 39 taxa and 47,953 positions, this test was conducted using ten replicates with a tenfold cross-validation. This means that the learning alignment consisted of 90% of the positions of the original alignment, and the test alignment consisted of the remaining 10%. The tests were run using the tree shown in Fig. 1 as a fixed topology, as suggested by the manual, and 1,100 cycles with a burn-in of 100.

Ancestral state reconstruction. For the ancestral reconstructions, we used a morphological data matrix reported previously⁴³, which is largely based on previously published data matrices^{15,44}. We slightly modified this matrix (Supplementary Information) by updating/changing the coding of characters related to "shape of parapodia", "pygidial cirri", "uncini", "hooks" and "presence of eyes" according to the literature^{17,22,43,45–47}. Instead of the character "aciculae", we coded the presence of internalized supporting chaetae¹⁷.

Ancestral reconstructions were done for the last common ancestor of Annelida, clade 1, Sedentaria and Errantia based on the Bayesian inference as well as the maximum likelihood tree of the 39-taxa data set with 47,953 positions, using Mesquite v2.72 (ref. 48). We used the parsimony reconstruction option, and all characters were regarded as unordered. Sipuncula and Echiura have lost nearly all of their morphological annelid characters. However, it is well known that severe secondary losses of characters can strongly hamper reconstructions based on morphological data because they cannot easily be differentiated from primary absence 49-55. Therefore, we did not consider these two taxa in the ancestral reconstructions.

To visualize the results of the ancestral reconstructions (Supplementary Table 5), we drew graphical depictions of body and parapodial characters using a basic schematic approach (Fig. 2). We refrained from using a representative approach for two reasons. First, no family of recent polychaetes shows only all of the characters of any of the four ancestral reconstructions. Second, a representative approach using, for example a recent polychaete family, has the potential to mislead in that this family might be taken to fully represent basal Annelida, Sedentaria or Errantia. However, each recent taxon is a patchwork of plesiomorphic and apomorphic characters and is as closely or distantly related to an ancestor in evolutionary times as any other recent descendant of that ancestor is.

For each of the four clades, we used a schematic representation of a homonomously segmented worm with parapodia. For Annelida and clade 1, this worm also had grooved palps, nuchal organs and bicellular eyes (Fig. 2a). The reconstruction of parapodial features was uncertain except for the composition of chaetae, because the last common ancestors of both clades had only simple chaetae and internalized supporting chaetae. Therefore, we depicted the two extreme possibilities: we included either all features that were eventually present in the ground pattern (such as large dorsal notopodial and ventral neuropodial lobes and dorsal and ventral cirri (sensory parapodial appendages)) or only those features that, on the basis of the reconstruction, were definitely present (such as a large

notopodial and a small neuropodial lobe). For Sedentaria, the parapodia were reduced, with a small neuropodial lobe and the absence of internalized supporting chaetae. The uncertain presence of uncini/hooks in the ground pattern of Sedentaria is indicated by a question mark (Fig. 2c). For Errantia, we also inferred one pair of antennae and pygidial cirri (sensory appendages at the body end), multicellular eyes (instead of bicellular eyes) and solid, sensory palps, which moved from a dorsal to a ventral position as is typical for such palps (Fig. 2b). The parapodia consisted of large notopodial and neuropodial lobes and ventral cirri. The presence of dorsal cirri in the ground pattern of Errantia was uncertain, so we have shown them with dashed lines only.

- NCBI dbEST (Expressed Sequence Tags Database) (http://www.ncbi.nlm.nih.gov/projects/dbEST/) (2010).
- Helmkampf, M., Bruchhaus, I. & Hausdorf, B. Phylogenomic analyses of lophophorates (brachiopods, phoronids and bryozoans) confirm the Lophotrochozoa concept. Proc. R. Soc. Lond. B 275, 1927–1933 (2008).
- 33. Struck, T. H. & Fisse, F. Phylogenetic position of Nemertea derived from phylogenomic data. *Mol. Biol. Evol.* **25**, 728–736 (2008).
- 34. Ribosomal Protein Gene Database (http://ribosome.med.miyazaki-u.ac.jp) (2010).
- 35. InParanoid: Eukaryotic Ortholog Groups (100 organisms: 1687023 sequences) (http://inparanoid.sbc.su.se/cgi-bin/index.cgi) (2010).
- Abascal, F., Zardoya, R. & Posada, D. ProtTest: selection of best-fit models of protein evolution. *Bioinformatics* 21, 2104–2105 (2005).
- Stamatakis, A. RAxML-VI-HPC: maximum likelihood-based phylogenetic analyses with thousands of taxa and mixed models. *Bioinformatics* 22, 2688–2690 (2006).
- Pattengale, N. D., Alipour, M., Bininda-Emonds, O. R. P., Moret, B. M. E. & Stamatakis, A. in *RECOMB 2009, LNCS 5541* (ed. Batzoglou, S.) 184–200 (Springer, 2009).
- Lartillot, N. & Philippe, H. A Bayesian mixture model for across-site heterogeneities in the amino-acid replacement process. *Mol. Biol. Evol.* 21, 1095–1109 (2004).
- Lartillot, N., Brinkmann, H. & Philippe, H. Suppression of long-branch attraction artefacts in the animal phylogeny using a site-heterogeneous model. *BMC Evol. Biol.* 7, S4 (2007).

- 41. Rambaut, A. & Drummond, A. J. *Tracer v1. 4* (http://beast.bio.ed.ac.uk/Tracer) (2007).
- 42. Žhou, Y., Rodrigue, N., Lartillot, N. & Philippe, H. Evaluation of the models handling heterotachy in phylogenetic inference. *BMC Evol. Biol.* **7**, 206 (2007).
- Zrzavý, J., Riha, P., Pialek, L. & Janouskovec, J. Phylogeny of Annelida (Lophotrochozoa): total-evidence analysis of morphology and six genes. *BMC Evol. Biol.* 9, 189 (2009).
- 44. Rouse, G. W. Trochophore concepts: ciliary bands and the evolution of larvae in spiralian Metazoa. *Biol. J. Linn. Soc.* **66**, 411–464 (1999).
- 45. Hartmann-Schröder, G. Teil 58. Annelida, Borstenwürmer, Polychaeta 2nd edn (Gustav Fischer, 1996).
- Westheide, W. & Rieger, R. M. Spezielle Zoologie. Erster Teil: Einzeller und Wirbellose Tiere (Gustav Fischer, 1996).
- Purschke, G., Arendt, D., Hausen, H. & Müller, M. C. M. Photoreceptor cells and eyes in Annelida. Arthropod Struct. Dev. 35, 211–230 (2006).
- Maddison, W. P. & Maddison, D. R. Mesquite: a modular system for evolutionary analysis. Version 2.71. Mesquite Project (http://mesquiteproject.org) (2009).
- Purschke, G., Hessling, R. & Westheide, W. The phylogenetic position of the Clitellata and the Echiura — on the problematic assessment of absent characters. J. Zool. Syst. Evol. Res. 38, 165–173 (2000).
- Wiens, J. J. Does adding characters with missing data increase or decrease phylogenetic accuracy? Syst. Biol. 47, 625–640 (1998).
- Wiens, J. J., Bonett, R. M. & Chippindale, P. T. Ontogeny discombobulates phylogeny: paedomorphosis and higher-level salamander relationships. Syst. Biol. 54, 91–110 (2005).
- Bleidorn, C. The role of character loss in phylogenetic reconstruction as exemplified for the Annelida. J. Zool. Syst. Evol. Res. 45, 299–307 (2007).
- Bleidorn, C., Hill, N., Erséus, C. & Tiedemann, R. On the role of character loss in orbiniid phylogeny (Annelida): molecules vs. morphology. *Mol. Phylogenet. Evol.* 52, 57–69 (2009).
- Struck, T. H. Progenetic species in polychaetes (Annelida) and problems assessing their phylogenetic affiliation. *Integr. Comp. Biol.* 46, 558–568 (2006).
- Struck, T. H. Data congruence, paedomorphosis and salamanders. Front. Zool. 4, 22 (2007).



A tension-induced mechanotransduction pathway promotes epithelial morphogenesis

Huimin Zhang¹, Frédéric Landmann¹†*, Hala Zahreddine¹*, David Rodriguez¹, Marc Koch² & Michel Labouesse¹

Mechanotransduction refers to the transformation of physical forces into chemical signals. It generally involves stretch-sensitive channels or conformational change of cytoskeleton-associated proteins1. Mechanotransduction is crucial for the physiology of several organs and for cell migration^{2,3}. The extent to which mechanical inputs contribute to development, and how they do this, remains poorly defined. Here we show that a mechanotransduction pathway operates between the body-wall muscles of Caenorhabditis elegans and the epidermis. This pathway involves, in addition to a Rac GTPase, three signalling proteins found at the hemidesmosome: p21-activated kinase (PAK-1), the adaptor GIT-1 and its partner PIX-1. The phosphorylation of intermediate filaments is one output of this pathway. Tension exerted by adjacent muscles or externally exerted mechanical pressure maintains GIT-1 at hemidesmosomes and stimulates PAK-1 activity through PIX-1 and Rac. This pathway promotes the maturation of a hemidesmosome into a junction that can resist mechanical stress and contributes to coordinating the morphogenesis of epidermal and muscle tissues. Our findings suggest that the C. elegans hemidesmosome is not only an attachment structure, but also a mechanosensor that responds to tension by triggering signalling processes. We suggest that similar pathways could promote epithelial morphogenesis or wound healing in other organisms in which epithelial cells adhere to tension-generating contractile cells.

Most organs and complex tissues contain several cell types, all of which can contribute to define organ or tissue shape. The way in which different cell types communicate during morphogenesis is poorly understood. In C. elegans, the epidermis and muscles both guide embryonic elongation⁴. The role of epidermal cells in elongation is well defined⁴. By contrast, our understanding of how muscles affect elongation and interact with the epidermis remains vague. Mutants with defective muscles arrest midway through elongation at a stage known as two-fold, and this phenotype is called Pat (paralysed at twofold)⁵. Communication between muscles and the epidermis could be channelled through junctions that attach the epidermis to the extracellular matrix at the muscle-epidermis interface. These junctions fasten muscles to the exoskeleton and are essential for elongation⁶ (Fig. 1a). Each junction includes two hemidesmosome-like units at the apical and basal epidermis plasma membranes, with intermediate filaments in between⁶ (Supplementary Fig. 1a). Hereafter, we refer to hemidesmosome-like junctions as CeHDs (C. elegans hemidesmosomes). The physiological role of CeHDs led us to consider whether muscles could signal to the epidermis through a mechanical input. We thus examined whether muscle contractions mechanically modify the epidermis, and we searched for CeHD proteins that respond to this mechanical change.

If muscles deform the epidermis, their contractions should modify the relative positions of two points within the epidermis. We tested this possibility using the actin bundles anchored to the plasma membrane⁷ as spatial landmarks, measuring the distance between bundles when muscles become active (Fig. 1b-d). Kymographs show that muscle contractions reduced this distance by about 50%, because the reduction in distance was abolished in muscle-defective embryos (Fig. 1c, d and Supplementary Movies 1 and 2). Thus, muscle contractions laterally stretch and squeeze the epidermis, a process comparable to the stretching of cultured cells grown on elastic membranes^{8,9}. Disruption of the CeHD core component, VAB-10A10 (a plectin and BPAG1e homologue), also strongly compromised this process (Fig. 1c, d and Supplementary Movie 3), outlining the crucial role of CeHDs in transmitting muscle tension. Moreover, consistent with earlier findings suggesting that muscles help the patterning of CeHDs^{5,11}, muscles promoted the maturation of CeHDs from an initial punctate distribution (Fig. 1e, f) to short parallel circumferential stripes (Fig. 1g, h), co-localizing with epidermal actin bundles (Supplementary Fig. 1d). CeHD structure was initially normal in embryos with defective myofilaments, but the reorganization of CeHDs was abnormal in the absence of muscle tension (Supplementary Fig. 1b, c).

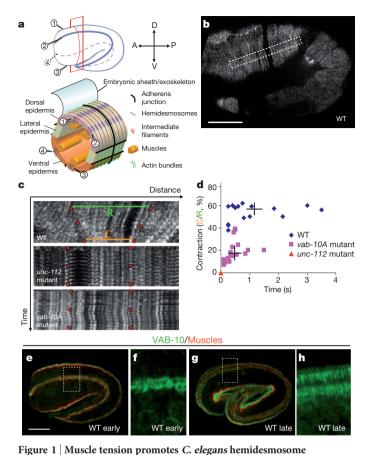
To identify epidermal proteins that are activated by tension, we relied on a recent genetic screen that identified 14 genes whose knockdown—combined with a weak mutation in *vab-10*, called *vab-10a(e698)* (Fig. 2a)—affects CeHD biogenesis¹². Among these genes, we focused on the signalling molecule PAK-1 (Fig. 2b), because its mammalian homologues control the cytoskeleton and can relay changes in arterial pressure to activate downstream signalling^{13,14}. We found that PAK-1 distribution coincides with intermediate-filament proteins at all stages of development, reorganizing into short parallel stripes typical of CeHDs (Fig. 2c–e and Supplementary Fig. 2a–c). PAK-1 was enriched at basal CeHDs marked by LET-805 (also known as myotactin), although it was also present at apical CeHDs (Supplementary Fig. 2d–g). Lack of PAK-1 function affected embryonic elongation, reducing body length by 19% (Supplementary Fig. 2h, i, l).

Consistent with PAK-1 presence at CeHDs, the kinase-domain deletion mutant *pak-1(ok448)* (Fig. 2b), combined with the weak viable mutation *vab-10A(e698)*, affected CeHD integrity. In these *vab-10A(e698)*; *pak-1(ok448)* double mutants, staining for VAB-10A showed a failure to form stripes in many areas (arrow in Fig. 2n) or less staining where muscles had detached from the body wall (arrowhead in Fig. 2n). As a result, more than 60% of these double mutants showed muscle detachment, which was associated with elongation arrest (Fig. 2k and Supplementary Table 1), and this was not seen in either single mutant (Fig. 2f, g, i, j and Supplementary Table 1). VAB-10A distribution became abnormal in *vab-10A(e698)*; *pak-1(ok448)* double mutants after the 1.7-fold stage (Fig. 2h), when muscles start to contract, suggesting that CeHDs cannot maintain their integrity when exposed to muscle-induced tension. Taken together, these findings indicate that PAK-1 functions with VAB-10A to strengthen CeHD stability.

Next, we investigated how PAK-1 helps the assembly of CeHDs. *In vitro* studies established that vertebrate PAK1 phosphorylates the

¹Development and Stem Cells Program, IGBMC, CNRS (UMR7104), INSERM (U964), Université de Strasbourg, 1 rue Laurent Fries, BP10142, 67400 Illkirch, France. ²Imaging Centre, IGBMC, CNRS (UMR7104), INSERM (U964), Université de Strasbourg, 1 rue Laurent Fries, BP10142, 67400 Illkirch, France. †Present address: MCBD Department, University of California, Santa Cruz, California 95064, USA

^{*}These authors contributed equally to this work.



maturation. a, Schemes showing a C. elegans embryo (top) and a cross-section of the embryo (at the level of red lines; bottom) and its hemidesmosomes (CeHDs), numbered 1-4. Three epidermal cell types are found around the circumference: dorsal and ventral (which uniquely express elt-3); and lateral. A, anterior; D, dorsal; P, posterior; V, ventral. b, Actin bundles (white) in WT embryo imaged by following an actin-binding domain labelled with GFP²⁰. The dashed box shows the region selected for the kymograph in c. Scale bar, 10 μ m. c, Kymographs showing the distance change between actin bundles (white) in WT embryos, *unc-112*(RNAi) mutant embryos (which are muscle deficient) and vab-10A(RNAi) embryos (which are CeHD deficient) (see also Supplementary Movies 1-3). Red circles indicate actin-anchoring points displaced by muscle contractions. C, contracted distance (orange); R, relaxed distance (green). d, Quantification of tension changes in terms of distance (contracted divided by relaxed) and time span per contraction. Individual data points (n = 15) and mean \pm s.e.m. (black crosses) are shown. e-h, Immunostaining of WT embryos at the 1.5-2-fold stage of development (early; **e**, **f**) or the 3–4-fold stage (late; **g**, **h**): muscles (red) and VAB-10A (green). Dashed boxes in e and g demarcate the regions shown in f and

intermediate-filament protein vimentin¹⁵. Hence, *C. elegans* PAK-1 might also phosphorylate epidermal intermediate filaments (Supplementary Fig. 1a). We directly tested this hypothesis in two ways. First, we used two-dimensional gel analysis of embryonic extracts followed by immunoblotting with MH4 monoclonal antibody, which recognizes the CeHD proteins IFA-2 (also known as MUA-6) and IFA-3, as well as the non-epidermal protein IFA-1 (ref. 16). This revealed the presence of two major intermediate-filament isoelectric spots, which were not present after phosphatase treatment of extracts (Fig. 3a, arrows) or in *pak-1(ok448)* extracts (Fig. 3b, arrows). Second, tagging IFA-3, the major intermediate-filament protein in the embryonic epidermis, with Myc showed that PAK-1 specifically affects phosphorylation of IFA-3 (Supplementary Fig. 3c). We therefore conclude that PAK-1 indeed affects the phosphorylation of an epidermal intermediate-filament protein.

We next assessed the effect of phosphorylation on intermediate-filament organization. Staining *vab-10A(e698)*; *pak-1(ok448)* double

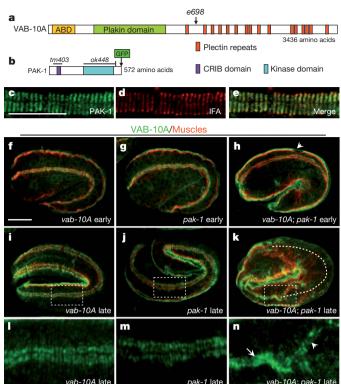


Figure 2 | PAK-1 function is required for CeHD maturation.
a, b, Conserved domains of VAB-10A and PAK-1 proteins. The missense mutation *e698* maps to the region predicted to bind to intermediate filaments¹⁰. The deletions *tm403* and *ok448* remove the PAK-1 CRIB domain and kinase domain, respectively. ABD, actin-binding domain. c-e, Co-localization of PAK-1 with IFA-2 and IFA-3 in a WT larva, as determined by immunofluorescence: PAK-1 (green) and IFA (red). Scale bar, 10 μm. f-n, Immunostaining for muscle (red) and VAB-10A (green) of *vab-10A(e698)* (f, i, l), *pak-1(ok448)* (g, j, m) and *vab-10A(e698)*; *pak-1(ok448)* (h, k, n) mutant embryos at early or late stages of development. Dashed boxes indicate area shown in panel below. Dashed line in k shows where muscles should be. Arrow in n shows area with muscles still attached. Arrowheads in h and n show areas with muscles detached. Scale bar, 10 μm.

mutants with the MH4 monoclonal antibody revealed that abnormal, ectopic, intermediate-filament bundles were present outside CeHDs (Fig. 3g, arrow). We also observed this phenotype in combination with the CRIB domain deletion allele pak-1(tm403) (that is, in vab-10A(e698); pak-1(tm403) double mutants) but not in vab-10A(e698), pak-1(ok448) or pak-1(tm403) single mutants (Fig. 3d-f and Supplementary Fig. 4a, b). The ectopic intermediate-filament bundles seem to result from defective anchoring of intermediate filaments to the mutant VAB-10A in CeHDs, because tagging the IFA-2/3 heterodimer partner IFB-1 with green fluorescent protein (GFP) resulted in the same ectopic intermediate-filament stripes and muscle detachment phenotypes as observed in vab-10A(e698); pak-1(ok448) mutants (Supplementary Fig. 5a-d and Supplementary Table 1). Furthermore, we identified the S470 residue of IFA-3 as an important regulatory site. Changing this serine residue to an alanine abolished IFA-3 phosphorylation and disrupted the localization of IFA-3 to CeHDs in the vab-10A(e698) background (Supplementary Fig. 5e-k). Together, these data suggest that lack of IFA-3 phosphorylation reduces the recruitment of this protein to CeHDs and alters CeHD strength in vab-10A(e698) mutants.

Having established PAK-1 as a functionally important CeHD kinase, we next showed that muscle contractility triggers PAK-1 activity. We used intermediate-filament phosphorylation and organization as readouts. We examined two classes of muscle-defective embryo: one lacking EGL-19, a Ca^{2^+} -activated channel that is required for muscle

h, respectively.

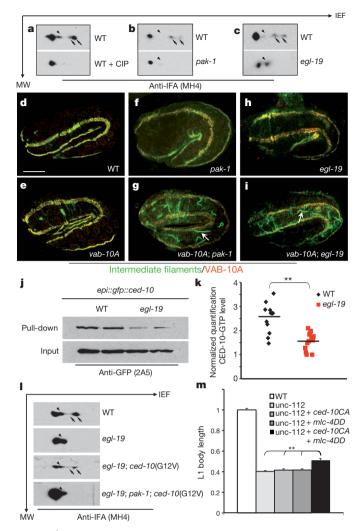


Figure 3 PAK-1-induced intermediate-filament phosphorylation depends on muscle tension. a-c, Two-dimensional immunoblotting analysis showing spots that indicate IFA proteins and their phosphorylated forms. Arrows point to phosphorylated proteins that are present in WT embryos but not phosphatase-treated WT embryos, pak-1 mutants or egl-19 mutants. Arrowheads point to isoelectric species, which are always visible in this type of analysis. CIP, calf intestinal phosphatase; IEF, isoelectric focusing; MW, molecular weight. d-i, Immunostaining of WT and mutant embryos for IFA proteins (green) and VAB-10A (red). Arrows point to ectopic intermediatefilament bundles (\mathbf{g} , \mathbf{i}). Scale bar, 10 μ m. \mathbf{j} , Pull-down assay for two independent samples showing levels of GTP-bound CED-10 in WT embryos and a muscle mutant (egl-19), both expressing GFP-tagged CED-10 under an epidermal promoter (epi::gfp::ced-10). k, CED-10-GTP level, as determined by pull-down experiment in j, was normalized to total CED-10 levels after densitometry analysis (n = 13; mean, black bar). **, P = 0.0006 (Mann–Whitney U test). l, Two-dimensional immunoblotting analysis showing phosphorylated IFA (arrows) restored in egl-19 mutants by CED-10(G12V) in a PAK-1-dependent manner. Arrowheads point to isoelectric species. m, Body length of unc-112(RNAi) L1 larvae expressing constitutively active CED-10, MLC-4 or both (n > 26; y axis, arbitrary units). Data are presented as mean \pm s.e.m. **, $P < 3 \times 10^{-8}$ (Student's *t*-test).

contraction¹⁷; and the other lacking UNC-112, a kindlin homologue that is essential for myofilament assembly¹⁸. As is the case in *pak-1* mutants, two-dimensional immunoblotting revealed that both classes of muscle-defective embryo (Fig. 3c and Supplementary Fig. 3d, arrows), as well as embryos lacking LET-805 or VAB-10A (Supplementary Fig. 3d), lacked two phospho-specific IFA spots. Moreover, antibody staining showed ectopic intermediate-filament bundles in *vab-10A*(*e698*); *egl-19*(*n2368*cs) double mutants and in *vab-10A*(*e698*); *unc-112*(RNAi) embryos (where *unc-112*(RNAi) denotes mutants that

lack UNC-112 owing to RNA interference (RNAi)) (Fig. 3i and Supplementary Fig. 4c, d; compare with single mutants in Fig. 3e, h and *vab-10A(e698)*; *pak-1(ok448)* double mutants in Fig. 3g and Supplementary Fig. 4j). Abolishing PAK-1 function did not cause an intermediate-filament organization defect in *egl-19(n2368cs)* embryos (Supplementary Fig. 4e, j) and did not make the defect worse in *vab-10A(e698)*; *egl-19(n2368cs)* mutants (Supplementary Fig. 4f, j and Supplementary Table 1). We therefore suggest that PAK-1 acts in the pathway defined by muscle tension and that this pathway requires VAB-10A function. Together, these data strongly suggest that epidermal PAK-1 responds to mechanical stimulation by modifying intermediate-filament phosphorylation.

We extended our study to identify the missing links between PAK-1 activity and muscle tension. Consistent with the GTPases Rac and CDC42 being the most common PAK activators¹³, we found that PAK-1 activation by tension requires the GTPase Rac. First, we measured the levels of GTP-bound CED-10 (the C. elegans homologue of Rac) and CDC-42 in the epidermis by pull-down assays. We observed a significant reduction (38%) in the CED-10-GTP level when muscle tension was lost (Fig. 3j, k). In comparison, the CDC-42 GTP level was reduced by only 12%, with a lower level of confidence (Supplementary Fig. 6b). In vivo, reducing the function of CED-10 in vab-10A(e698) embryos caused similar ectopic intermediate-filament bundling phenotypes (Supplementary Figs 4j and 6f; compare with Fig. 3g). Conversely, epidermal expression of CED-10(G12V)¹⁹, an amino acid substitution mutant that is constitutively active, rescued intermediate-filament phosphorylation and bundling defects caused by tension loss (Fig. 3l and Supplementary Fig. 6c, d) in a PAK-1dependent manner (Fig. 3l). Yet CED-10(G12V) failed to rescue the elongation arrest of muscle-defective embryos (Fig. 3m).

One possibility is that muscle tension promotes epidermal processes in addition to intermediate-filament phosphorylation. Specifically, because CeHDs co-localize with actin bundles, muscle tension could activate non-muscle myosin II, a key molecule that drives cell shape changes in elongation^{20,21}. We tested this possibility and found that the combined expression of a constitutively active CED-10 (CED-10(G12V)) and a constitutively active version of the myosin regulatory light chain MLC-4 (MLC-4DD)²⁰ significantly rescued the elongation of unc-112-defective embryos (Fig. 3m). Rescue was partial, and we presume that this is either because CED-10(G12V) and MLC-4DD cannot fully recapitulate the on-off pattern of muscle tension or because tension stimulates additional pathways. We have not tried to unravel the pathway leading to MLC-4 activation in normal embryos, but we conclude that muscle tension has more than one output in the epidermis. Together, we suggest that CED-10 responds to muscle tension, inducing the kinase activity of PAK-1 and strengthening CeHDs with VAB-10A.

The involvement of CED-10 in relaying muscle tension prompted us to look for the Rac guanine-nucleotide exchange factor (RacGEF) that acts in the pathway. We examined the potential involvement of four GEF proteins that are commonly found to act with PAK in vertebrates¹³, and we identified PAK-interacting exchange factor (PIX-1) as being involved in C. elegans (Fig. 4c and Supplementary Fig. 4g-i). Previous studies have defined a highly conserved signalling complex containing PAK, PIX and G-protein-coupled receptor kinase interactor (GIT) that interacts with Rac/CDC42 GTPases^{22,23}. Strikingly, both C. elegans PIX-1 and GIT-1, visualized by functional translational GFP constructs²⁴, localized to CeHDs (Fig. 4a, b and Supplementary Fig. 7a-g), suggesting that they could act together with PAK-1. Lack of either PIX-1 or GIT-1 function affected normal elongation (Supplementary Fig. 2h-l), and when combined with vab-10A(e698) resulted in CeHD defects (Fig. 4c-f and Supplementary Table 1). Moreover, two-dimensional immunoblotting showed that pix-1- and pak-1-null mutants have identical intermediate-filament phosphorylation profiles (Supplementary Fig. 7h and Fig. 3b). We conclude that PIX-1, GIT-1 and PAK-1 together regulate intermediate-filament phosphorylation and CeHD biogenesis.

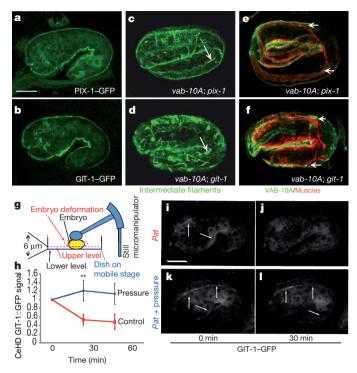


Figure 4 | GIT-1 maintenance at CeHDs in a tension-dependent manner and PIX-1 promote PAK-1 activation. a, b, Localization of translational PIX-1-GFP (a) and GIT-1-GFP (b) in WT embryos. c, d, Immunostaining for IFA proteins (green) in vab-10A(e698); pix-1(gk416) and vab-10A(e698); git-1(tm1962) double mutants in early-stage embryos. Arrows point to ectopic intermediate-filament bundles. e, f, Immunostaining for VAB-10A (green) and muscle (red) in late-stage embryos of listed mutants, showing muscle detachment (arrows). g, Diagram showing the set-up of force stimulation. h, Quantification of CeHD-localized GIT-1-GFP level compared with time zero (n = 12). Data are presented as mean \pm s.e.m. **, P = 0.009 (Mann-Whitney U test). i-1, Representative images showing GIT-1-GFP localization (arrows) in unc-112(RNAi) embryos (denoted pat) with (k, l) or without (i, j) external force stimulation. a-f, i-l, Scale bars, 10 μ m.

Previous reports defined a Rac-independent PIX-1–GIT-1–PAK-1 signalling pathway driving distal-tip cell migration in *C. elegans*²⁴. However, PIX-1 seems to act through Rac during CeHD maturation, because CED-10–GTP levels were 25% lower in *pix-1*-null embryos than in wild-type embryos (Supplementary Fig. 7i, j). We interpret the differences in CED-10–GTP levels in *pix-1*-null and muscle-deficient mutants (25% reduction versus 38% reduction) as an indication that muscles activate CED-10 outside CeHDs, whereas PIX-1 is mainly found at CeHDs (Fig. 4a).

The identification of PIX-1 and GIT-1 as crucial factors in CeHD biogenesis posits them as early effectors of muscle tension. To define how they become activated, we examined their distribution in muscledeficient embryos. Whereas PAK-1 and PIX-1 still localized to CeHDs in the absence of muscle tension (Supplementary Fig. 8a-h and Supplementary Movies 4 and 5), GIT-1 progressively disappeared from CeHDs as embryos stopped elongation (Fig. 4i, j, Supplementary Fig. 8i-l and Supplementary Movies 6 and 7). This finding suggests that muscle tension is required for maintaining GIT-1 protein at CeHDs. If correct, this model predicts that external mechanical pressure should substitute for muscle tension. We tested this prediction by submitting UNC-112-defective embryos to repeated mechanical pressure (Fig. 4g and Supplementary Fig. 9). Compared with untreated embryos, this regimen considerably retarded the diffusion of GIT-1 away from CeHDs in UNC-112-depleted embryos (Fig. 4h-l). We conclude that CeHDs are indeed mechanosensitive and are under the direct influence of physical forces.

Studies relying on cell stretching *in vitro* have outlined the role of integrin receptors in relaying tensile stretch^{1,25}. Likewise, in *C. elegans*,

we propose that the extracellular matrix receptor LET-805 or its interacting partners relays muscle tension. This could in turn trigger a conformational change of a CeHD protein (for example, VAB-10A) able to maintain GIT-1 at CeHDs, as has been observed for talin in focal adhesions²⁶. The identity of the protein(s) that transmits muscle tension and anchors GIT-1 to CeHDs remains to be uncovered. Furthermore, we suggest that GIT-1 maintains a functional link between tension and PIX-1–CED-10–PAK-1, possibly by keeping PIX-1 in a conformational state in which it is able to activate CED-10 (Supplementary Fig. 10).

In conclusion, the identification of the GIT-1–PIX-1–PAK-1 signal-ling module implies that CeHDs, and presumably vertebrate hemides-mosomes, not only are structural entities, but also are endowed with signalling potential. Since the discovery of the Pat mutant phenotype⁵, the reason why muscle contraction is required for embryonic elongation has remained elusive. Our demonstration that muscle tension activates PAK-1–PIX-1–GIT-1 signalling and non-muscle myosin II clearly supports a hypothesis based on a mechanotransduction process during elongation. Our results raise the possibility that contractile cells could locally influence the behaviour of adjacent epithelial cells in other developmental settings, particularly in organs in which epithelial cells are lined with smooth muscle cells or in pathological situations such as wound healing and cancer. Contractile forces seem to act like yin and yang in development: too much force will tear a tissue apart, but moderate and sustained force will promote differentiation.

METHODS SUMMARY

Pull-down assays to analyse GTPase activity were performed using the Rac/Cdc42 activation assay Biochem Kit (Cytoskeleton). To apply external forces to embryos, a needle with a 40- μ m blunt end was positioned above embryos that had been immobilized on a glass-based culture dish (IWAKI) coated with poly-lysine and placed on a inverted TCS SP2 confocal microscope (Leica). The microscope was then programmed for a time-lapse sequence in xyzt dimension with a 6- μ m z distance, at a 1.6-s periodicity to mimic the pulse of muscle contraction. A full description, including strain details, construct descriptions, other microscopy experiments and immunoblotting approaches, can be found in the Methods.

Full Methods and any associated references are available in the online version of the paper at www.nature.com/nature.

Received 12 March; accepted 20 December 2010.

- Orr, A. W., Helmke, B. P., Blackman, B. R. & Schwartz, M. A. Mechanisms of mechanotransduction. *Dev. Cell* 10, 11–20 (2006).
- Jaalouk, D. E. & Lammerding, J. Mechanotransduction gone awry. Nature Rev. Mol. Cell Biol. 10, 63–73 (2009).
- 3. Wozniak, M. A. & Chen, C. S. Mechanotransduction in development: a growing role for contractility. *Nature Rev. Mol. Cell Biol.* **10**, 34–43 (2009).
- Chisholm, A. D. & Hardin, J. Epidermal morphogenesis. in WormBook (ed. The C. elegans Research Community) doi:10.1895/wormbook.1.7.1 (2005).
- Williams, B. D. & Waterston, R. H. Genes critical for muscle development and function in *Caenorhabditis elegans* identified through lethal mutations. *J. Cell Biol.* 124, 475–490 (1994).
- Zhang, H. & Labouesse, M. The making of hemidesmosome structures in vivo. Dev. Dyn. 239, 1465–1476 (2010).
- Costa, M., Draper, B. W. & Priess, J. R. The role of actin filaments in patterning the Caenorhabditis elegans cuticle. Dev. Biol. 184, 373–384 (1997).
- Katsumi, A. et al. Effects of cell tension on the small GTPase Rac. J. Cell Biol. 158, 153–164 (2002).
- Sawada, Y. & Sheetz, M. P. Force transduction by triton cytoskeletons. J. Cell Biol. 156, 609–615 (2002).
- Bosher, J. M. et al. The Caenorhabditis elegans vab-10 spectraplakin isoforms protect the epidermis against internal and external forces. J. Cell Biol. 161, 757–768 (2003).
- Hresko, M. C., Schriefer, L. A., Shrimankar, P. & Waterston, R. H. Myotactin, a novel hypodermal protein involved in muscle-cell adhesion in *Caenorhabditis elegans. J. Cell Biol.* 146, 659–672 (1999).
- Zahreddine, H., Zhang, H., Diogon, M., Nagamatsu, Y. & Labouesse, M. CRT-1/ Calreticulin and the E3 Ligase EEL-1/HUWE1 control hemidesmosome maturation in C. elegans development. Curr. Biol. 20, 322–327 (2010).
- Bokoch, G. M. Biology of the p21-activated kinases. *Annu. Rev. Biochem.* 72, 743–781 (2003).
- Orr, A. W., Hahn, C., Blackman, B. R. & Schwartz, M. A. p21-activated kinase signaling regulates oxidant-dependent NF-κB activation by flow. Circ. Res. 103, 671–679 (2008).



- 15. Goto, H. et al. Phosphorylation and reorganization of vimentin by p21-activated kinase (PAK). Genes Cells 7, 91–97 (2002).
- Woo, W. M., Goncharov, A., Jin, Y. & Chisholm, A. D. Intermediate filaments are required for C. elegans epidermal elongation. Dev. Biol. 267, 216–229 (2004).
- Lee, R. Y., Lobel, L., Hengartner, M., Horvitz, H. R. & Avery, L. Mutations in the α1 subunit of an L-type voltage-activated Ca²⁺ channel cause myotonia in Caenorhabditis elegans. EMBO J. 16, 6066–6076 (1997).
- Rogalski, T. M., Mullen, G. P., Gilbert, M. M., Williams, B. D. & Moerman, D. G. The unc-112 gene in Caenorhabditis elegans encodes a novel component of cell-matrix adhesion structures required for integrin localization in the muscle cell membrane. J. Cell Biol. 150, 253–264 (2000).
- Bourne, H. R., Sanders, D. A. & McCormick, F. The GTPase superfamily: conserved structure and molecular mechanism. *Nature* 349, 117–127 (1991).
- Gally, C. et al. Myosin II regulation during C. elegans embryonic elongation: LET-502/ROCK, MRCK-1 and PAK-1, three kinases with different roles. Development 136, 3109–3119 (2009).
- 21. Lecuit, T. & Lenne, P. F. Cell surface mechanics and the control of cell shape, tissue patterns and morphogenesis. *Nature Rev. Mol. Cell Biol.* **8**, 633–644 (2007).
- Zhao, Z. S., Manser, E., Loo, T. H. & Lim, L. Coupling of PAK-interacting exchange factor PIX to GIT1 promotes focal complex disassembly. *Mol. Cell. Biol.* 20, 6354–6363 (2000).
- 23. Zhang, H., Webb, D. J., Asmussen, H., Niu, S. & Horwitz, A. F. A GIT1/PIX/Rac/PAK signaling module regulates spine morphogenesis and synapse formation through MLC. J. Neurosci. 25, 3379–3388 (2005).
- 24. Lucanic, M. & Cheng, H. J. A RAC/CDC-42-independent GIT/PIX/PAK signaling pathway mediates cell migration in *C. elegans. PLoS Genet.* **4**, e1000269 (2008).

- Giannone, G. & Sheetz, M. P. Substrate rigidity and force define form through tyrosine phosphatase and kinase pathways. Trends Cell Biol. 16, 213–223 (2006).
- del Rio, A. et al. Stretching single talin rod molecules activates vinculin binding. Science 323, 638–641 (2009).

Supplementary Information is linked to the online version of the paper at www.nature.com/nature.

Acknowledgements We are grateful to H.-J. Cheng, the CGC and NBP-Japan, L. Lim, J. Nance, C. Gally and L. Broday for reagents, as well as M. Argentini for technical advice. We thank J. Ahringer for a discussion, and O. Pourquié, J.-L. Bessereau, S. Jarriault and members of the Labouesse laboratory (C. Gally, I. Kolotueva, N. Osmani and S. Quintin) for critical reading of the manuscript. This work was supported by grants from the ANR, ARC and EU (STREP-FP6 programme) (M.L.) and by institutional funds from the CNRS and INSFRM

Author Contributions H. Zhang and M.L. designed the study, analysed the data and wrote the paper. H. Zhang conducted most of the experiments. F.L. and H. Zahreddine made some initial observations (tension-change modification of the epidermis, and PAK-1 distribution and mutant phenotype) that proved to be essential for designing the study. D.R. provided technical help. M.K. helped to design and analyse the pressing experiment.

Author Information Reprints and permissions information is available at www.nature.com/reprints. The authors declare no competing financial interests. Readers are welcome to comment on the online version of this article at www.nature.com/nature. Correspondence and requests for materials should be addressed to M.L. (Imichel@igbmc.fr).

METHODS

Strains and genetic methods. Control N2 (Bristol) and other strains of *C. elegans* were propagated as described previously²⁷ at 20 °C. Mothers were shifted to 15 °C or 12 °C before egg-laying, when indicated. Alleles used in this study are vab-10A(e698), pak-1(ok448), pak-1(tm403), egl-19(n2368cs), ced-10(n3246), pix-1(gk416) and git-1(tm1962). The actin-binding-domain-GFP construct mcIs51[lin-26p::ABD_{vab-10}::GFP, myo-2p::GFP] is driven by an epidermal promoter and reveals only actin filaments present in the epidermis²⁰. *egl-19* encodes the α -subunit of the voltage-gated Ca²⁺ channel; it is expressed in muscles and neurons but not in the epidermis¹⁷. The missense allele egl-19(n2368cs) leads to mild muscle defects at 20 °C and to a Pat phenotype at 12 °C5. The allele pak-1(ok448) encodes a protein with a deleted kinase domain; pak-1(tm403) encodes a protein with a deleted CRIB domain^{20,24}. vab-10A(e698) is a viable mutation causing animals to have a bent head 10,28 . The null allele *pix-1*(*gk416*) encodes a protein with the entire SH3 domain deleted, causing a premature frameshift²⁴. The strong loss-of-function allele git-1(tm1962) encodes a protein that lacks the second GIT domain, which is presumably required for binding to PIX-1 (ref. 24). The loss-offunction allele ced-10(n3246) is a G-to-A missense mutation resulting in a G60R substitution²⁹. The tvIs41[ifb-1::GFP, rol-6(su1006)] integrated strain was provided by L. Broday30.

RNAi. RNAi was induced either by bacterial feeding using specific clones from the MRC feeding RNAi library, after verifying the sequence identity of the corresponding insert^{12,31}, or by microinjecting double-stranded RNA corresponding to the relevant gene. Bacterial feeding RNAi was used for all experiments involving *unc-112* and for additional biochemical tests involving *let-805* and *vab-10A* knockdown. Mothers were fed with double-stranded RNA corresponding to those genes from the L3 stage, generating 80–100% of embryos arrested at about the two-fold stage. RNAi by microinjection was used to test whether *pix-1*, *vav-1*, *unc-73* or *sos-1* induced an intermediate-filament bundling phenotype in the *vab-10A*(*e698*) background. The following primers were used for generating double-stranded RNA: *pix-1*, 5′-taatacgactcactatagggatttgtgtgaaacccttcg, 3′-taatacgactcactataggcatgaaaa cactcacttcttcg; and *sos-1*, 5′-taatacgactcactatagggaaaaacggaaagatttgtct, 3′- taatacgactcactatagggacccattgattgatgacac. Double-stranded RNA for *vav-1* and *unc-73* were generated using plasmids from the MRC RNAi library as templates³¹.

Molecular biology and transgenesis. The translational PAK-1-GFP fusion was generated by PCR cloning of the pak-1 coding sequence upstream of the GFP coding sequence in the vector pPD95.75, using a primer located 4 kilobases (kb) upstream of the pak-1 start codon. Translational PIX-1-GFP and GIT-1-GFP fusion constructs were provided by H.-J. Cheng. To drive gfp::ced-10 and gfp::cdc-42 in the epidermis, wild-type ced-10 and cdc-42 cDNAs were PCR amplified from total embryonic RNA and cloned in-frame downstream of the GFP coding sequence under the control of a 432-base-pair dpy-7 promoter fragment³² (pPD95.75 backbone). Sequence of the constitutively active CED-10(G12V) construct (provided by J. Nance) was extracted by PCR from the plasmid pDA80 (ref. 33) and inserted into a pPD95.75 derivative lacking the GFP coding sequence; the same dpy-7 promoter piece was added. The constitutively active MLC-4(T17DS18D) form was generated from the plasmid Pmlc-4::gfp::mlc-4(T17DS18D)20; the mlc-4 promoter was replaced by the elt-3 promoter, which is active only in dorsal and ventral epidermal cells in contact with muscles³⁴. Pelt-3::gfp::mlc-4(T17DS18D) is referred to in the text as MLC-4DD. The ifa-3::myc fusion construct was generated by using 6-kb ifa-3 genomic sequence, including 3-kb upstream promoter, with the tag inserted just before the ifa-3 stop codon. Mutagenesis was carried out using a mutagenesis kit (Stratagene). Transgenes were injected at a concentration of 10 ng μ l⁻¹ for *Ppak*-1::pak-1::gfp, Ppix-1::pix-1::gfp, Pgit-1::git-1::gfp, Pdpy-7::gfp::ced-10 and Pdpy-7::gfp::cdc-42; $\ln g \mu l^{-1}$ for Pdpy-7::ced-10(G12V) and ifa-3::myc; and $2 ng \mu l^{-1}$ for Pelt-3::mlc-4(T17DS18D). For each transgene, two lines were selected for further

Elongation/body-length measurement. To measure the elongation defects of pak-1, pix-1 and git-1 mutants, wild-type and mutant mothers were bleached, and eggs were left to hatch without bacteria at 20 °C for 20 h. DIC images of newly hatched L1 larvae were taken under ×10 magnification, and the body length of each larva was measured using ImageJ software (http://rsb.info.nih.gov/ij/). To test whether expression of the constitutively active proteins CED-10(G12V) and MLC-4DD rescues the elongation of muscle-defective (Pat) embryos, strains carrying Pdpy-7::ced-10(G12V), Pelt-3::mlc-4DD or both transgenes were fed on bacteria containing unc-112(RNAi) for 48 h. Paralysed larvae were obtained by 3-h egg laying followed by 24-h incubation at 20 $^{\circ}\text{C}.$ DIC images and fluorescent images (for visualizing the presence of the transgene by co-injection markers) of newly hatched L1 larvae were taken under ×20 magnification, and the body length of each larva was measured using ImageJ. Comparisons were made between transgene-negative and transgene-positive larvae produced from the same mothers. Statistical analysis was carried out by using Student's t-test, and significance was accepted at P < 0.01.

Immunostaining and fluorescence microscopy. Embryos were fixed and stained by indirect immunofluorescence as described elsewhere¹⁰. Dilution factors for primary antibodies were anti-VAB-10A (4F2)¹⁰, 1/1000; anti-PAK-1 (provided by L. Lim)³⁵, 1/200; anti-intermediate filament (MH4)³⁶ and anti-LET-805 (MH46)¹¹, 1/500; uncharacterized muscle antigen³⁷ (NE8/4C6, MRC), 1/50; anti-GFP (2A3, IGBMC antibody lab), 1/500; and anti-Myc (M6, IGBMC antibody lab), 1/1000. MH monoclonal antibodies were purchased from the DSHB (Iowa University). The MH4 monoclonal antibody recognizes three IFA intermediate filaments, IFA-1, IFA-2 and IFA-3, all of which can form heterodimers with IFB-1 (refs 16, 33, 38, 39). IFA-1 is present in the pharynx, vulva and several neurons; IFA-2 and IFA-3 function results in embryonic elongation and CeHD phenotypes comparable to those observed when IFB-1, VAB-10A or LET-805 are missing^{10,11,16}. By contrast, IFA-2 acts during larval development^{16,38,40}.

For still images of immunostained embryos and translational GFP-fusion embryos, stacks of images were captured every 0.3 μ m using a TCS SP5 confocal microscope (Leica); generally, 20 confocal sections were projected with maximum intensity and processed using ImageJ. Translational GFP-fusion strains carrying the cryosensitive *egl-19*(*n2368*cs) allele were grown and kept at 12 °C before imaging.

Time-lapse movies were taken using a DMI6000 spinning-disk set-up (Andor Revolution/Leica). Images of the actin-binding–GFP line²0 were captured every 125 ms, using five stacks of images with 0.2-µm spacing. Kymograph analysis was performed using MetaMorph software (Universal Imaging). Movies of PAK-1–GFP and GIT-1–GFP in elongating or paralysed embryos were recorded every 5 min, using ten stacks of images with 0.3-µm spacing for about 1 h.

To quantify ectopic intermediate-filament stripes, images of 7–15 MH4-immunostained embryos were taken for each genotype. Images were then shuffled and genotype blinded. An investigator who was not previously involved in the study counted the number of ectopic intermediate-filament stripes for each embryo. Results are shown as the mean number of ectopic intermediate-filament stripes present in each embryo for each genotype.

Two-dimensional gel electrophoresis and immunoblotting. Two-dimensional gel electrophoresis was carried out using 11-cm ReadyStrip IPG strips pH 5–8 (for MH4 antibody) or pH 3–6 (for anti-Myc antibody) in a PROTEAN IEF cell (Bio-Rad) according to the manufacturer's protocol. *C. elegans* embryos at 1.5/3-fold stage were obtained by 2-h egg laying followed by growth for 6 h at 20 °C or 16 h at 12 °C. Embryonic protein extracts were prepared by homogenization in a rehydration buffer containing 8 M urea, 3% CHAPS, 50 mM dithiothreitol and 0.2% Bio-Lyte Ampholyte. Proteins were transferred and immunoblotted with MH4 (anti-intermediate filament) antibody or anti-Myc (M6) monoclonal antibody using standard protocols. The major spots in each sample were positioned at the same distance from the anode.

GTPase pull-down assay. The pull-down assay to analyse CED-10 and CDC-42 activity was performed using a Rac/Cdc42 activation assay Biochem Kit (Cytoskeleton) according to the manufacturer's protocol. To ensure that we would measure only the amount of GTP-bound and GDP-bound Rac/CDC-42 present in the epidermis, extracts were prepared from animals carrying a GFP-tagged GTPase transgene under the control of the epidermis-specific promoter dpy-7 (ref. 32) (see above). Embryonic protein extracts were prepared by homogenizing 1.5/3-fold stage C. elegans embryos (see previous section) in cell-lysis buffer (CLB01, Cytoskeleton) at 4 °C. Two to three pairs of samples were processed together each time to ensure quick processing. The compatibility of the Rac/ Cdc42 activation assay kit with the C. elegans system was tested and confirmed by GTP- γ -loaded or GDP-loaded CED-10 or CDC-42 in embryo lysates before the analysis, as recommended by the manufacturer's protocol. After pull-down, the amount of GTP-bound GTPase was analysed by immunoblotting against the GFP tag. Densitometry analysis was performed using ImageJ. For all quantification experiments, statistical analysis was carried out by using the non-parametric Mann–Whitney *U* test, and significance was accepted for P < 0.01.

External mechanical stimulation of *C. elegans* embryos. To apply external forces to embryos lacking internal muscle tension, microfilament needles were produced from glass capillaries using a DMZ universal puller. The needle tip was melted using a heater scope to create a blunt end of about 40 μ m in diameter. The blunt-ended needle was installed onto an NK2 micromanipulator (Eppendorf) next to a TCS SP2 confocal microscope (Leica). Pat embryos carrying a GIT-1– GFP translational reporter were obtained by unc-112(RNAi) feeding. Embryos were placed on a 12-mm glass-based culture dish (IWAKI) coated with polylysine. The culture dish was filled with M9 buffer at 1/2 dilution. After mounting the culture dish containing embryos onto the microscope, the glass needle tip was carefully placed on top of the embryo so that it just touched the eggshell. The confocal microscope was programmed for a time-lapse sequence in xyzt dimension, with a z distance of 6 μ m, such that each upward movement of the stage



towards the needle tip squeezed the embryo in between. Pressing was done every 1.6 s, at a rhythm that approximately mimicked the pulse of muscle contractions. Confocal images were taken before pressing at about the 1.4-fold stage, 30 min and 60 min after pressing. Individual stacks acquired with the confocal microscope were processed using ImageJ and a three-dimensional median filter followed by a maximum intensity projection 1. The GIT-1-GFP levels at CeHDs were determined by subtracting the background levels immediately adjacent to the CeHDs (Supplementary Fig. 7c, d). All final values were presented as the ratio against time zero. Statistical analysis was carried out with the non-parametric Mann–Whitney U test, and significance was accepted for P < 0.01.

- 27. Brenner, S. The genetics of Caenorhabditis elegans. Genetics 77, 71-94 (1974).
- Hodgkin, J. Male phenotypes and mating efficiency in *Caenorhabditis elegans*. Genetics 103, 43–64 (1983).
- Reddien, P. W. & Horvitz, H. R. CED-2/Crkll and CED-10/Rac control phagocytosis and cell migration in Caenorhabditis elegans. Nature Cell Biol. 2, 131–136 (2000).
- Kaminsky, R. et al. SUMO regulates the assembly and function of a cytoplasmic intermediate filament protein in C. elegans. Dev. Cell 17, 724–735 (2009).
- 31. Kamath, R. S. et al. Systematic functional analysis of the Caenorhabditis elegans genome using RNAi. Nature **421**, 231–237 (2003).
- 32. Gilleard, J. S., Barry, J. D. & Johnstone, I. L. cis regulatory requirements for hypodermal cell-specific expression of the *Caenorhabditis elegans* cuticle collagen gene *dpy-7*. *Mol. Cell. Biol.* **17**, 2301–2311 (1997).

- Anderson, D. C., Gill, J. S., Cinalli, R. M. & Nance, J. Polarization of the *C. elegans* embryo by RhoGAP-mediated exclusion of PAR-6 from cell contacts. *Science* 320, 1771–1774 (2008).
- 34. Gilleard, J. S., Shafi, Y., Barry, J. D. & McGhee, J. D. ELT-3: a *Caenorhabditis elegans* GATA factor expressed in the embryonic epidermis during morphogenesis. *Dev. Biol.* **208**, 265–280 (1999).
- Chen, W., Chen, S., Yap, S. F. & Lim, L. The Caenorhabditis elegans p21-activated kinase (CePAK) colocalizes with CeRac1 and CDC42Ce at hypodermal cell boundaries during embryo elongation. J. Biol. Chem. 271, 26362–26368 (1996).
- Francis, R. & Waterston, R. H. Muscle cell attachment in Caenorhabditis elegans. J. Cell Biol. 114, 465–479 (1991).
- Schnabel, R. Duels without obvious sense: counteracting inductions involved in body wall muscle development in the Caenorhabditis elegans embryo. Development 121, 2219–2232 (1995).
- Karabinos, A., Schmidt, H., Harborth, J., Schnabel, R. & Weber, K. Essential roles for four cytoplasmic intermediate filament proteins in *Caenorhabditis elegans* development. *Proc. Natl Acad. Sci. USA* 98, 7863–7868 (2001).
- Karabinos, A., Schulze, E., Schunemann, J., Parry, D. A. & Weber, K. In vivo and in vitro evidence that the four essential intermediate filament (IF) proteins A1, A2, A3 and B1 of the nematode Caenorhabditis elegans form an obligate heteropolymeric IF system. J. Mol. Biol. 333, 307–319 (2003).
- Hapiak, V. et al. mua-6, a gene required for tissue integrity in Caenorhabditis elegans, encodes a cytoplasmic intermediate filament. Dev. Biol. 263, 330–342 (2003).
- Iannuccelli, E. et al. NEMO: a tool for analyzing gene and chromosome territory distributions from 3D-FISH experiments. Bioinformatics 26, 696–697 (2010).



SCF^{FBW7} regulates cellular apoptosis by targeting MCL1 for ubiquitylation and destruction

Hiroyuki Inuzuka¹, Shavali Shaik¹*, Ichiro Onoyama²*, Daming Gao¹, Alan Tseng¹, Richard S. Maser^{3,4}, Bo Zhai⁵, Lixin Wan¹, Alejandro Gutierrez⁶, Alan W. Lau¹, Yonghong Xiao³, Amanda L. Christie^{6,7}, Jon Aster⁸, Jeffrey Settleman⁹, Steven P. Gygi⁵, Andrew L. Kung^{6,7}, Thomas Look⁶, Keiichi I. Nakayama², Ronald A. DePinho³ & Wenyi Wei¹

The effective use of targeted therapy is highly dependent on the identification of responder patient populations. Loss of FBW7, which encodes a tumour-suppressor protein, is frequently found in various types of human cancer, including breast cancer, colon cancer¹ and T-cell acute lymphoblastic leukaemia (T-ALL)². In line with these genomic data, engineered deletion of Fbw7 in mouse T cells results in T-ALL3-5, validating FBW7 as a T-ALL tumour suppressor. Determining the precise molecular mechanisms by which FBW7 exerts antitumour activity is an area of intensive investigation. These mechanisms are thought to relate in part to FBW7-mediated destruction of key proteins relevant to cancer, including Jun⁶, Myc⁷, cyclin E⁸ and notch 1 (ref. 9), all of which have oncoprotein activity and are overexpressed in various human cancers, including leukaemia. In addition to accelerating cell growth¹⁰, overexpression of Jun, Myc or notch 1 can also induce programmed cell death¹¹. Thus, considerable uncertainty surrounds how FBW7-deficient cells evade cell death in the setting of upregulated Jun, Myc and/or notch 1. Here we show that the E3 ubiquitin ligase SCF^{FBW7} (a SKP1-cullin-1-F-box complex that contains FBW7 as the F-box protein) governs cellular apoptosis by targeting MCL1, a pro-survival BCL2 family member, for ubiquitylation and destruction in a manner that depends on phosphorylation by glycogen synthase kinase 3. Human T-ALL cell lines showed a close relationship between FBW7 loss and MCL1 overexpression. Correspondingly, T-ALL cell lines with defective FBW7 are particularly sensitive to the multi-kinase inhibitor sorafenib but resistant to the BCL2 antagonist ABT-737. On the genetic level, FBW7 reconstitution or MCL1 depletion restores sensitivity to ABT-737, establishing MCL1 as a therapeutically relevant bypass survival mechanism that enables FBW7-deficient cells to evade apoptosis. Therefore, our work provides insight into the molecular mechanism of direct tumour suppression by FBW7 and has implications for the targeted treatment of patients with FBW7-deficient T-ALL.

MCL1 is frequently overexpressed in various leukaemias through mechanisms that are not fully understood¹². MCL1 is distinct from other BCL2 family members in its extremely unstable nature¹³, which provides a mechanism for cells to switch to either survival or apoptotic mode in response to various stresses¹⁴. Phosphorylation of MCL1 by glycogen synthase kinase 3 (GSK3) regulates the stability of MCL1 (ref. 13), but little is known about the identity of the E3 ubiquitin ligase that targets phosphorylated MCL1 for destruction. On examination of the GSK3-mediated phosphorylation sites in MCL1, we surmised that they resemble a degron sequence that can be recognized by FBW7 (also known as FBXW7) (Fig. 1a), prompting us to test the possibility that

GSK3-mediated phosphorylation of MCL1 triggers the degradation of MCL1 by FBW7. Depletion of FBW7 (Fig. 1b) or the SCF components cullin 1 (CUL1), RBX1 and SKP1 (Fig. 1c), but not other F-box proteins that we examined (Fig. 1b), resulted in a significant increase in the amount of MCL1 protein. T-cell-lineage-specific depletion of FBW7 in *Fbw7* conditional knockout (Lck-Cre/*Fbw7*^{fl/fl})mice³ resulted in increased MCL1 levels in the thymuses of these mice (Fig. 1d), as well as thymic lymphoma (Supplementary Fig. 1a) and the presence of acute leukaemia cells in the thymuses (Supplementary Fig. 1b). Consistent with a recent study¹⁵, $FBW7^{-/-}$ human DLD1 cells (Fig. 1e) and HeLa cells treated with short interfering RNA (siRNA) directed against FBW7 (Supplementary Fig. 1c) have elevated MCL1 expression mainly in the mitosis (M) and early G1 phases of the cell cycle.

The clinical relevance of this finding is further demonstrated by the finding that human T-ALL cell lines harbouring *FBW7* mutations and/ or deletions have a significant increase in MCL1 (Fig. 1f). Additionally, depletion of FBW7 in DND41 cells or Loucy cells (both of which have wild-type *FBW7*) leads to increased MCL1 expression (Fig. 1g), whereas reintroduction of wild-type *FBW7* dramatically reduced MCL1 expression in FBW7-deficient T-ALL cells (Fig. 1h), supporting a causal relationship between loss of FBW7 activity and elevated MCL1 expression in the T-ALL cells examined. More importantly, elevated MCL1 expression is also observed in both primary human and mouse T-ALL samples with deficient FBW7 activity²⁻⁴ (Fig. 1i, j and Supplementary Fig. 1a, b), and depletion of MCL1 impaired T-ALL disease progression *in vivo* (Fig. 1k–m).

Consistent with a post-translational mode of regulation, no changes in MCL1 mRNA levels were observed after depletion of FBW7 in DLD1 cells (Supplementary Fig. 2d), and no positive relationship was observed between MCL1 mRNA levels and loss of FBW7 in T-ALL cells (Supplementary Fig. 2e). The half-life of MCL1 was significantly extended in the thymuses of $Fbw7^{-/-}$ mice and FBW7-deficient human T-ALL cells (Supplementary Fig. 3a–c), and experimental manipulation of FBW7 levels changed MCL1 stability accordingly (Supplementary Fig. 3d, e). Together, these results suggest that MCL1 is a downstream ubiquitylation target of SCF^{FBW7}.

As the proper substrate phosphorylation events are required for FBW7 to recognize and target its substrates for ubiquitylation ¹⁶, we next investigated which phosphorylation events trigger MCL1 destruction by FBW7. Mass spectrometry analysis showed that MCL1 is phosphorylated at multiple sites *in vivo* (Fig. 2a and Supplementary Fig. 5a–c). In addition to serine at position 159 (S159) and threonine at position 163 (T163)^{13,17}, S64 and S121 were also phosphorylated *in vivo*. Consistent with previous reports^{13,17}, MCL1 destruction is promoted by GSK3 (Fig. 2b) but not by the protein kinases ERK1 (also

¹Department of Pathology, Beth Israel Deaconess Medical Center, Harvard Medical School, 330 Brookline Avenue, Boston, Massachusetts 02215, USA. ²Department of Molecular and Cellular Biology, Medical Institute of Bioregulation, Kyushu University, Fukuoka, Fukuoka 812-8582, Japan. ³Belfer Institute for Applied Cancer Science, Department of Medical Oncology, Dana-Farber Cancer Institute, Harvard Medical School, Boston, Massachusetts 02115, USA. ⁴The Jackson Laboratory, Bar Harbor, Maine 04609, USA. ⁵Department of Cell Biology, Harvard Medical School, Boston, Massachusetts 02115, USA. ⁷Lurie Family Imaging Center, Dana-Farber Cancer Institute, Boston, Massachusetts 02115, USA. ⁸Department of Pathology, Brigham and Women's Hospital, Harvard Medical School, Boston, Massachusetts 02115, USA. ⁹Department of Medicine, Massachusetts General Hospital Cancer Center, Harvard Medical School, Charlestown, Massachusetts 02129, USA. ^{*}These authors contributed equally to this work.

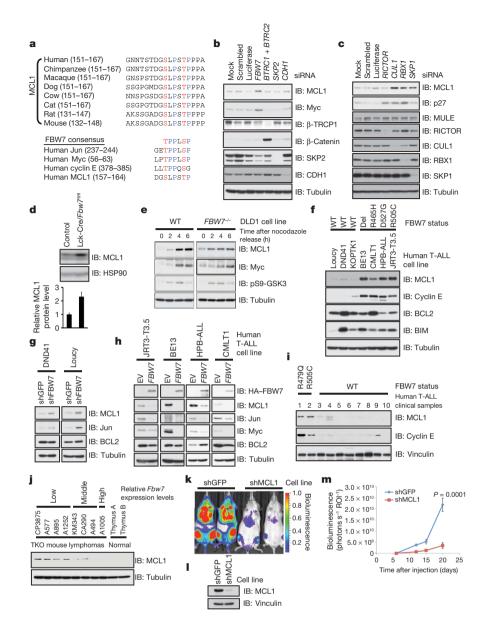


Figure 1 | MCL1 stability is controlled by FBW7. a, Sequence alignment of MCL1 with the phosphodegron sequences recognized by FBW7 in Jun, Myc and cyclin E. The putative FBW7 phosphodegron sequence present in MCL1 is conserved across different species. Conserved serine and threonine residues within the degron sequences are shown in red, and conserved proline residues are shown in blue. b, c, Immunoblotting (IB) analysis, with antibodies specific for the indicated proteins (right), of HeLa cells transfected with siRNA oligonucleotides directed against the indicated genes (top). d, IB analysis of thymocytes derived from control (Lck-Cre/Fbw7^{+/fl}) mice or Fbw7 conditional knockout (Lck-Cre/Fbw7^{fl/fl}) mice (whose thymocytes lack Fbw7). For the histogram, MCL1 band intensity was normalized to HSP90 and then normalized to the control lane. Data are shown as mean \pm s.e.m. for three independent experiments. e, IB analysis of wild-type (WT) and FBW7 DLD1 cells after synchronization of the cell cycles with nocodazole and release from mitotic arrest at the indicated time points. pS9-GSK3, GSK3 that is phosphorylated at the S9 residue. f, IB analysis of the indicated human T-ALL cell lines, which have either WT FBW7 or mutant FBW7 (a deletion (Del) or an amino acid substitution). g, The human T-ALL cell lines DND41 and Loucy cells, which contain wild-type FBW7, were infected with the indicated lentiviral shRNA constructs and selected with $1\,\mu\text{g}\,\text{ml}^{-1}$ puromycin to eliminate the non-infected cells. Cell lysates were collected for IB analysis. shFBW7, shRNA

known as MAPK3) and/or ERK2 (also known as MAPK1) (Supplementary Fig. 5d-f). To investigate further the significance of each individual phosphorylation site, we created a panel of MCL1 mutants

specific for FBW7; shGFP, shRNA specific for the gene encoding green fluorescent protein (GFP). h, Human T-ALL cell lines deficient in FBW7 were infected with an FBW7-expressing retroviral construct (with empty vector (EV) as a negative control) and selected with $1 \mu g \, ml^{-1}$ puromycin to eliminate the non-infected cells. Cell lysates were collected for IB analysis. HA, haemagglutinin tag. i, IB analysis of the indicated primary human T-ALL clinical samples. j, IB analysis of the indicated mouse T-ALL cell lines derived from $Terc^{-/-}Atm^{-/-}Tp53^{-/-}$ (TKO) mice. **k-m**, *In vivo* effects of MCL1 depletion in FBW7-deficient T-ALL cells. An in vivo model of FBW7-deficient T-ALL was created by orthotopic engraftment of luciferase-expressing CMLT1 cells in immunodeficient (NOD SCID Il2rg-null) mice. Mice were injected with 1×10^7 cells (n = 7 per group) through the lateral tail vein. Before engraftment, cells were infected with retroviral constructs expressing the indicated shRNAs. k, Representative images of luciferase expression (photonic flux, in number of photons s⁻¹ cm⁻² sr⁻¹ \times 10⁶) detected in live mice, which had received CMLT1-shGFP (left) or CMLT1-shMCL1 (right). I, IB analysis of the engineered CMLT1 cell lines, showing the efficient depletion of MCL1. m, Tumour burden was determined by quantification of total body luminescence and is expressed as photons s⁻¹ ROI⁻¹. Data are presented as mean \pm s.e.m., with statistical significance determined by Student's *t*-test.

(Fig. 2c). Using *in vitro* kinase assays, we identified S159 and T163 as the major GSK3-mediated phosphorylation sites¹⁷ and S121 as a minor GSK3-mediated phosphorylation site (Fig. 2d, e and Supplementary

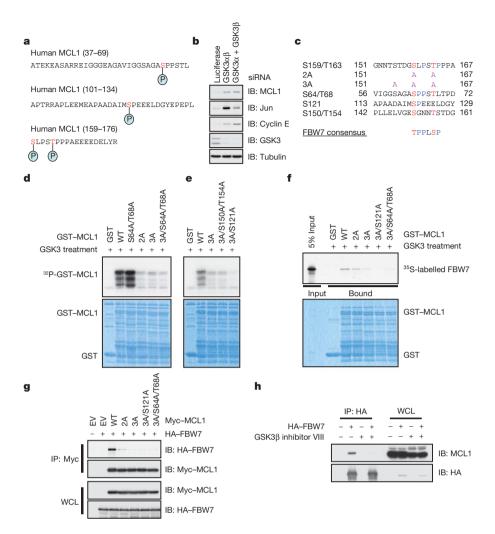


Figure 2 | Phosphorylation of MCL1 by GSK3 triggers the interaction of MCL1 with FBW7. a, *In vivo* MCL1 phosphorylation sites detected by mass spectrometry analysis. Phosphorylated residues are shown in red, with phosphate in blue. b, IB analysis, with antibodies specific for the indicated proteins (right), of HeLa cells transfected with siRNA oligonucleotides directed against the indicated genes (top) (where GSK3 α B indicates depletion of *GSK3A* and *GSK3B* with a single siRNA and GSK3 α + GSK3 β indicates depletion with siRNAs targeting each gene separately). c, Illustration of the various MCL1 mutants generated for this study. Conserved serine and threonine residues within the degron sequence are shown in red, and conserved proline residues are shown in blue. 2A, MCL1 S159A/T163A; 3A, MCL1 S155A/S159A/T163A. d, e, GSK3 phosphorylates MCL1 *in vitro* at multiple sites. Purified GSK3 protein was incubated with 5 µg of the indicated glutathione *S*-transferase (GST)–MCL1 fusion proteins (top, WT and mutant as in c) in the presence of γ - 32 P]ATP. The protein kinase reaction products were resolved by SDS–

Fig. 5g). Inactivation of these GSK3-mediated phosphorylation sites impairs the interaction between MCL1 and FBW7 both *in vitro* (Fig. 2f and Supplementary Fig. 5h) and *in vivo* (Fig. 2g and Supplementary Fig. 5i). Furthermore, pharmacological inhibition of GSK3 activity blocked the interaction between HA-tagged FBW7 and endogenous MCL1 (Fig. 2h) and inhibited the localization of FBW7 to the mitochondria, where MCL1 resides (Supplementary Fig. 5j, k). These results indicate that GSK3-dependent phosphorylation of MCL1 is necessary for the interaction of MCL1 with FBW7. Consistent with this FBW7–MCL1 regulatory axis, MCL1 specifically interacts with FBW7 (Supplementary Fig. 6a, b, j–l) and CUL1 (Supplementary Fig. 6c, d), and depletion of endogenous CUL1 increases MCL1 abundance (Supplementary Fig. 11a).

We next explored the mechanism by which FBW7 alters MCL1 stability. Overexpression of FBW7 and GSK3 significantly decreased

PAGE, and phosphorylation was detected by autoradiography. **f**, Phosphorylation of MCL1 at multiple sites by GSK3 triggers the interaction of MCL1 with FBW7 *in vitro*. Autoradiograms show recovery of ^{35}S -labelled FBW7 protein bound to the indicated GST–MCL1 fusion proteins (with GST protein as a negative control) incubated with GSK3 before the pull-down assays. **g**, IB analysis of whole-cell lysates (WCL) and immunoprecipitates (IP) derived from 293T cells transfected with HA–FBW7 together with the indicated Myc–MCL1 constructs (top). Thirty hours after transfection, cells were pretreated with 10 μ M MG132 for 10 h to block the proteasome pathway before cell collection. **h**, IB analysis of WCL and IP derived from 293T cells transfected with HA–FBW7. Thirty hours after transfection, cells were pretreated with 20 μ M MG132 for 8 h to block the proteasome pathway before cell collection. Where indicated, 25 μ M GSK3 β inhibitor VIII (with dimethylsulphoxide (DMSO) as a negative control) was added for 8 h before cell collection.

MCL1 abundance (Fig. 3a and Supplementary Fig. 6h), whereas inactivation of the major GSK3-dependent phosphorylation sites on MCL1 impaired FBW7-mediated destruction (Fig. 3b and Supplementary Fig. 6e–g). All FBW7 isoforms (particularly the α -isoform and the γ -isoform) participate in MCL1 stability control, and FBW7 dimerization is not required for the degradation of MCL1 (Supplementary Fig. 7a–e). Mutant FBW7 constructs derived from patients with T-ALL showed a reduced ability to interact with MCL1 (Supplementary Fig. 6i) and were therefore unable to degrade MCL1 (Fig. 3c). Moreover, the FBW7- and GSK3-mediated destruction of MCL1 was blocked by the proteasome inhibitor MG132, indicating the involvement of the ubiquitin–proteasome pathway in this process (Fig. 3a). In support of this idea, co-expression of GSK3 and FBW7 resulted in a marked reduction in the half-life of wild-type MCL1, but not of the 2A or 3A MCL1 mutants (Fig. 3d), with reduced interaction with FBW7

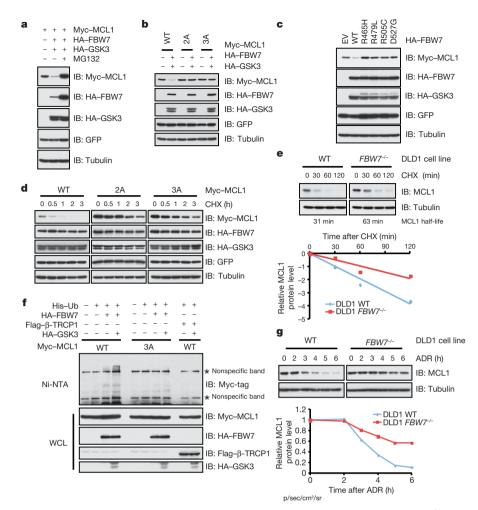


Figure 3 | FBW7 promotes MCL1 ubiquitylation and destruction in a GSK3-mediated phosphorylation-dependent manner. a–c, GSK3-mediated phosphorylation-dependent degradation of MCL1 by FBW7. IB analysis of 293T cells transfected with plasmids expressing the indicated Myc–MCL1 and HA–FBW7 proteins in the presence or absence of HA–GSK3 (top), with antibodies specific for the Myc tag, HA tag, GFP or tubulin (right). A plasmid encoding GFP was used as a negative control for transfection efficiency. Where indicated, the proteasome inhibitor MG132 was added. d, 293T cells were transfected with the indicated Myc–MCL1 constructs together with the HA–FBW7- and HA–GSK3-expressing plasmids. Twenty hours after transfection, cells were split into 60-mm dishes. After another 20 h, cells were treated with 20 μg ml $^{-1}$ cycloheximide (CHX). At the indicated time points, WCL were prepared, and IB analysis was carried out with antibodies specific for the

(Fig. 2g). Furthermore, loss of FBW7 extends the half-life of endogenous MCL1 (Fig. 3e), and FBW7 promotes the ubiquitylation of MCL1 in a GSK3-dependent manner (Fig. 3f and Supplementary Fig. 8a, b, e). The decrease of MCL1 expression is also impaired in response to various DNA-damaging agents¹⁸ in $FBW7^{-/-}$ DLD1 cells (Fig. 3g and Supplementary Fig. 8f). Together, these data suggest a physiological role for FBW7 in promoting MCL1 destruction *in vivo* in a GSK3-mediated phosphorylation-dependent manner.

Next, we explored how FBW7 affects the cellular apoptotic response by modulating MCL1 abundance. As predicted, $Fbw7^{-/-}$ mouse thymocytes and FBW7-deficient human T-ALL cells with increased MCL1 levels were less sensitive to apoptotic stimuli (Supplementary Fig. 9a–f). More interestingly, compared with T-ALL cell lines that had wild-type FBW7, FBW7-deficient T-ALL cells with elevated MCL1 expression (Fig. 1f and Supplementary Fig. 9h) were more sensitive to the multi-kinase inhibitor sorafenib, which can effectively reduce MCL1 expression^{19,20} (Fig. 4a and Supplementary Fig. 9g–i). Although the ability of sorafenib to repress MCL1 has been attributed to the

indicated proteins. **e**, Top, WT or $FBW7^{-/-}$ DLD1 cells were treated with $20\,\mu\mathrm{g\,m\,m^{-1}}$ CHX. At the indicated time points, WCL were prepared, and IB analysis was carried out with antibodies specific for the indicated proteins. Bottom, MCL1 band intensity was normalized to tubulin and then normalized to the t=0 controls. **f**, IB of WCL and His tag pull-down of HeLa cells transfected with plasmids expressing the indicated proteins. Twenty hours after transfection, cells were treated with the proteasome inhibitor MG132 for 12 h before cell collection. His tag pull-down was performed in the presence of 8 M urea to eliminate any possible contamination from MCL1-associated proteins. Ni-NTA, nickel-nitrilotriacetic acid; Ub, ubiquitin. **g**, Top, IB analysis of WT and $FBW7^{-/-}$ DLD1 cells treated with $10\,\mu\mathrm{M}$ adriamycin (ADR) for the indicated time durations. Bottom, MCL1 band intensity was normalized to tubulin and then normalized to the t=0 controls.

inactivation of the RAF-ERK pathway and/or the activation of GSK3 activity¹⁹, the exact mechanism remains unclear. Nonetheless, these data suggest that FBW7-deficient T-ALL cell lines might require elevated levels of MCL1 to evade apoptosis, a phenotype known as 'oncogene addiction'21. By contrast, FBW7-deficient T-ALL cell lines were more resistant to ABT-737 (Fig. 4a and Supplementary Fig. 9g, j). ABT-737 is a BH3 domain mimetic and a pan inhibitor of the BCL2 family of anti-apoptotic proteins, and it is reported to kill leukaemia cells effectively²². However, leukaemia cells with elevated MCL1 levels are refractory to treatment with ABT-737 (refs 23, 24), primarily because ABT-737 fails to inactivate MCL1 (ref. 22). Experimental evidence from both double staining with 7-amino-actinomycin D (7-AAD) and annexin V (Supplementary Fig. 9j) and immunoblotting specific for apoptotic biomarkers (Fig. 4b) suggests that ABT-737induced apoptosis is impaired in FBW7-deficient T-ALL cells. Moreover, specific depletion of MCL1 in multiple FBW7-deficient T-ALL cell lines restored the sensitivity of these cells to ABT-737 (Fig. 4c, d), supporting the idea that increased MCL1 expression is

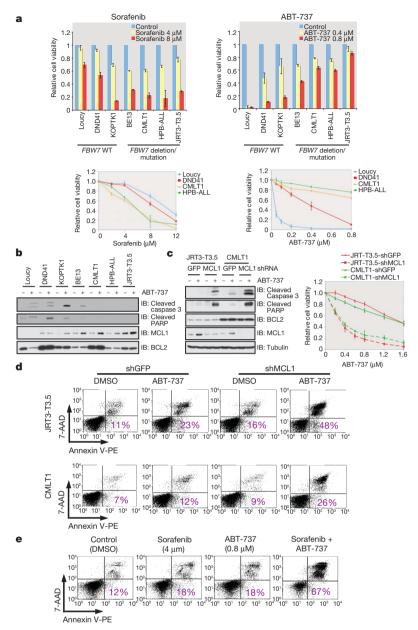


Figure 4 | Elevated MCL1 expression protects FBW7-deficient T-ALL cell lines from ABT-737-induced apoptosis. a, Cell viability assays showing that FBW7-deficient human T-ALL cell lines were more sensitive to sorafenib but were relatively resistant to ABT-737 treatment. T-ALL cells were cultured in 10% FBS-containing medium with the indicated concentrations of sorafenib or ABT-737 for 48 h before cell viability assays were performed. Data are shown as mean \pm s.d. for three independent experiments. **b**, IB analysis of the indicated human T-ALL cell lines with or without ABT-737 (0.8 μM) treatment. PARP, poly(ADP-ribose) polymerase. c, Specific depletion of endogenous MCL1 expression restored sensitivity to ABT-737 in the indicated FBW7-deficient human T-ALL cell lines. Various T-ALL cell lines were infected with lentiviral shGFP- or shMCL1-encoding vectors and selected in 0.5 μg ml⁻¹ puromycin to eliminate non-infected cells. The generated cell lines were cultured in 10% FBScontaining medium with the indicated concentrations of ABT-737 for 48 h before cell viability assays were performed (right) or with or without ABT-737 $(0.8\,\mu\text{M})$ treatment for 24 h before WCL were collected for IB analysis with the primary cause of desensitization to ABT-737 in vivo^{23,24}. It also suggests that patients with FBW7-deficient T-ALL will not respond well to treatment with ABT-737. We further demonstrated that manipulation of FBW7 activity or ectopic expression of a non-degradable form of MCL1 in human T-ALL cells affects their sensitivity to ABT-737 (Supplementary Fig. 10a, b) and responses to other apoptotic

antibodies specific for the indicated proteins (left). For cell viability assays, data are shown as mean \pm s.d. for three independent experiments. **d**, Double staining with 7-AAD and annexin-V-PE (annexin V conjugated to phycoerythrin), followed by flow cytometry analysis to detect the percentage of apoptotic cells (axes indicate intensity of fluorochrome). In the indicated FBW7-deficient human T-ALL cell lines, endogenous MCL1 was depleted by infection with lentiviral vectors encoding shRNA (lentiviral shGFP was used as a negative control). Cell lines were cultured in 10% FBS-containing medium with or without ABT-737 (0.8 µM) treatment, with DMSO as a negative control, for 48 h before the flow cytometry analysis. Purple numbers indicate the percentage of apoptotic cells. e, Staining and flow cytometry analysis as in d, demonstrating that sorafenib treatment restores ABT-737 sensitivity to FBW7-deficient HPB-ALL cells. HPB-ALL cells were cultured in 10% FBScontaining medium with the indicated concentrations of sorafenib and/or ABT-737 for 48 h before analysis. Coloured numbers indicate the percentage of apoptotic cells.

Our results indicate that inhibition of MCL1 could be used to restore sensitivity to ABT-737 in FBW7-deficient T-ALL cells. Given that the clinical application of siRNA- or short hairpin RNA (shRNA)-mediated target extinction is not yet feasible owing to delivery challenges, we instead exploited small molecule strategies to reduce MCL1 expression, specifically with the use of sorafenib (Supplementary Fig. 9h). The combined use of sorafenib and ABT-737 produced a dose-dependent

stimuli (Supplementary Fig. 10c-f).

increase in the sensitivity of HPB-ALL cells, a human T-ALL cell line, to ABT-737 (Supplementary Fig. 10g), and this decrease correlated with a significant increase in the induction of apoptosis (Fig. 4e). Similar results were obtained for other FBW7-deficient T-ALL cell lines (Supplementary Fig. 10h).

Our studies provide experimental evidence of a role for FBW7 in governing the apoptotic pathway by controlling MCL1 destruction. MCL1 has a key role in regulating the apoptosis of T cells¹⁴ but not of cells from other tissue types, such as liver cells. Therefore, our studies also provide a possible mechanistic explanation for why loss of FBW7 is frequently seen in patients with T-ALL. Although other E3 ubiquitin ligases, including MULE²⁵ and β-transducin-repeat-containing protein (β-TRCP)¹⁷, have been implicated in controlling MCL1 stability, MULE activity was not implicated in the GSK3-dependent regulation of MCL1 (refs 17, 25) (Supplementary Fig. 11a-e). Additionally, no correlation was found between MULE and MCL1 expression in various T-ALL cells (Supplementary Fig. 11f), thereby excluding a physiological role for MULE in regulating MCL1 abundance in T-ALL cells. We further found that depletion of FBW7, but not β-TRCP, leads to a significant induction of MCL1 expression (Fig. 1b and Supplementary Fig. 11a-c). Array comparative genomic hybridization analysis demonstrated a high frequency of FBW7 loss2 but not simultaneous loss of BTRC1 and BTRC2, which encode β-TRCPs, in T-ALL cells (data not shown). Together, these data support the hypothesis that $\mathrm{SCF}^{\mathrm{FBW7}}$ is a physiological E3 ubiquitin ligase for MCL1, with USP9X being the nominated deubiquitylase²⁶, and that loss of FBW7 contributes to T-ALL development through the upregulation of MCL1 expression. More importantly, our studies suggest that there is a correlation between FBW7 genetic status and sensitivity to ABT-737, and they provide insight into the use of MCL1 inhibitors as a practical method for specifically killing FBW7-deficient T-ALL cells. This work provides a basis for the rational treatment of patients with T-ALL and provides motivation for the development of specific MCL1 antagonists, or agents that significantly reduce MCL1 expression, for the improved management of patients with T-ALL.

METHODS SUMMARY

Expression plasmid constructs, proteins, antibodies and cell lines are described in the Methods. The sequences of various siRNA oligonucleotides used in this study are also listed in the Methods. *In vivo* phosphorylation of MCL1 was detected by mass spectrometry analysis, and the major GSK3-dependent phosphorylation sites that were identified were subsequently examined by *in vitro* kinase assays. All mutants were generated using PCR, and the sequences were verified. FBW7-mediated MCL1 ubiquitylation and destruction were examined by cell-based ubiquitylation and degradation assays. Cell viability assays were used to detect the response of various T-ALL cell lines to sorafenib and ABT-737. Double staining with annexin V and 7-AAD was used to detect the percentage of apoptotic

Full Methods and any associated references are available in the online version of the paper at www.nature.com/nature.

Received 12 October 2009; accepted 29 November 2010.

- Wood, L. D. et al. The genomic landscapes of human breast and colorectal cancers. Science 318, 1108–1113 (2007).
- Maser, R. S. et al. Chromosomally unstable mouse tumours have genomic alterations similar to diverse human cancers. Nature 447, 966–971 (2007).
- Onoyama, I. et al. Conditional inactivation of Fbxw7 impairs cell-cycle exit during T cell differentiation and results in lymphomatogenesis. J. Exp. Med. 204, 2875–2888 (2007).
- Matsuoka, S. et al. Fbxw7 acts as a critical fail-safe against premature loss of hematopoietic stem cells and development of T-ALL. Genes Dev. 22, 986–991 (2008).
- Thompson, B. J. et al. The SCF^{FBW7} ubiquitin ligase complex as a tumor suppressor in T cell leukemia. *J. Exp. Med.* 204, 1825–1835 (2007).

- Wei, W., Jin, J., Schlisio, S., Harper, J. W. & Kaelin, W. G. Jr. The v-Jun point mutation allows c-Jun to escape GSK3-dependent recognition and destruction by the Fbw7 ubiquitin ligase. Cancer Cell 8, 25–33 (2005).
- Welcker, M. et al. The Fbw7 tumor suppressor regulates glycogen synthase kinase 3 phosphorylation-dependent c-Myc protein degradation. Proc. Natl Acad. Sci. USA 101, 9085–9090 (2004).
- Koepp, D. M. et al. Phosphorylation-dependent ubiquitination of cyclin E by the SCF^{Fbw7} ubiquitin ligase. *Science* 294, 173–177 (2001).
- Gupta-Rossi, N. et al. Functional interaction between SEL-10, an F-box protein, and the nuclear form of activated Notch1 receptor. J. Biol. Chem. 276, 34371–34378 (2001).
- Shaulian, E. & Karin, M. AP-1 as a regulator of cell life and death. Nature Cell Biol. 4, E131–E136 (2002).
- 11. Sanchez, I. & Yuan, J. A convoluted way to die. Neuron 29, 563-566 (2001).
- Akgul, C. McI-1 is a potential therapeutic target in multiple types of cancer. Cell. Mol. Life Sci. 66, 1326–1336 (2009).
- Maurer, U., Charvet, C., Wagman, A. S., Dejardin, E. & Green, D. R. Glycogen synthase kinase-3 regulates mitochondrial outer membrane permeabilization and apoptosis by destabilization of MCL-1. Mol. Cell 21, 749–760 (2006).
- Opferman, J. T. et al. Development and maintenance of B and T lymphocytes requires antiapoptotic MCL-1. Nature 426, 671–676 (2003).
- Wertz, I. E. et al. Sensitivity to antitubulin chemotherapeutics is regulated by MCL1 and FBW7. Nature doi:10.1038/nature09779 (this issue).
- Welcker, M. & Clurman, B. E. FBW7 ubiquitin ligase: a tumour suppressor at the crossroads of cell division, growth and differentiation. *Nature Rev. Cancer* 8, 83–93 (2008).
- Ding, Q. et al. Degradation of Mcl-1 by β-TrCP mediates glycogen synthase kinase 3-induced tumor suppression and chemosensitization. Mol. Cell. Biol. 27, 4006–4017 (2007).
- 18. Nijhawan, D. et al. Élimination of Mcl-1 is required for the initiation of apoptosis following ultraviolet irradiation. *Genes Dev.* **17**, 1475–1486 (2003).
- Panka, D. J., Cho, D. C., Atkins, M. B. & Mier, J. W. GSK-3β inhibition enhances sorafenib-induced apoptosis in melanoma cell lines. J. Biol. Chem. 283, 726–732 (2008).
- Yu, C. et al. The role of Mcl-1 downregulation in the proapoptotic activity of the multikinase inhibitor BAY 43-9006. Oncogene 24, 6861–6869 (2005).
- Sharma, S. V. & Settleman, J. Oncogene addiction: setting the stage for molecularly targeted cancer therapy. Genes Dev. 21, 3214–3231 (2007).
- Cragg, M. S., Harris, C., Strasser, A. & Scott, C. L. Unleashing the power of inhibitors of oncogenic kinases through BH3 mimetics. *Nature Rev. Cancer* 9, 321–326 (2009)
- Konopleva, M. et al. Mechanisms of antileukemic activity of the novel Bcl-2 homology domain-3 mimetic GX15-070 (obatoclax). Cancer Res. 68, 3413–3420 (2008).
- van Delft, M. F. et al. The BH3 mimetic ABT-737 targets selective Bcl-2 proteins and efficiently induces apoptosis via Bak/Bax if Mcl-1 is neutralized. Cancer Cell 10, 389–399 (2006).
- Zhong, Q., Gao, W., Du, F. & Wang, X. Mule/ARF-BP1, a BH3-only E3 ubiquitin ligase, catalyzes the polyubiquitination of Mcl-1 and regulates apoptosis. Cell 121, 1085–1095 (2005).
- Schwickart, M. et al. Deubiquitinase USP9X stabilizes MCL1 and promotes tumour cell survival. Nature 463, 103–107 (2010).

Supplementary Information is linked to the online version of the paper at www.nature.com/nature.

Acknowledgements We thank J. Lawler, C. Schorl, Q. Zhang and S. Glueck for critical reading of the manuscript, J. DeCaprio, M.-C. Hung, M. A. Kelliher, W. Harper and W. Hahn for providing reagents, L. Cantley and A. Toker for suggestions, I. Wertz and V. Dixit for sharing unpublished data, and members of the Wei and DePinho labs for useful discussions. W.W. is a Kimmel Scholar and V Scholar. This work was supported in part by the Emerald Foundation New Investigator award (W.W.), the Leukemia and Lymphoma Society Special Fellow award (W.W.) and a grant from the National Institutes of Health (W.W.; GM089763). R.A.D. is an American Cancer Society Research Professor and is supported by the Robert A. and Renée E. Belfer Foundation Institute for Applied Cancer Science.

Author Contributions H.I. performed most of the experiments with critical assistance from S.S. and D.G. A.T., L.W. and A.W.L. also helped perform a portion of the experiments. I.O. performed the *Fbw7* conditional knockout mouse experiments, and A.L.C. performed the orthotopic engraftment mouse experiments. B.Z. performed the mass spectrometry analysis, and Y.X. and R.S.M. helped to perform the experiments with tumours derived from the TKO mice. A.G. helped to perform the experiments with the human T-ALL clinical samples. W.W., R.A.D. and K.I.N. designed the experiments with assistance from J.A., J. S., A.L.K., H.I., S.P.G. and T.L. W.W. supervised the study. W.W. wrote the manuscript with help from H.I. and S.S. All authors commented on the

Author Information Reprints and permissions information is available at www.nature.com/reprints. The authors declare no competing financial interests. Readers are welcome to comment on the online version of this article at www.nature.com/nature. Correspondence and requests for materials should be addressed to W.W. (wwei2@bidmc.harvard.edu).

METHODS

Plasmids. HA-FBW7 and HA-GSK3 constructs were described previously6. Human FBW7 cDNA was subcloned using Pfu polymerase (Stratagene) into the pBabe-Puro-HA retrovirus vector. Myc-MCL1 WT, Myc-MCL1 3A, and GST-MCL1 WT constructs were gifts from M.-C. Hung. FBW7 and MCL1 mutants were generated with the QuikChange XL Site-Directed Mutagenesis Kit (Stratagene) according to the manufacturer's instructions. HA-ERK1, shERK1 and shERK2 constructs were gifts from J. Blenis. Flag-β-TRCP1, Flag-Ub, shTRCP1 and shTRCP1+2 retroviral constructs were gifts from W. Harper. The shFBW7 retroviral vector (Addgene) was validated and described previously²⁷. To generate the lentiviral shFBW7 and shMULE vectors, DNA oligonucleotides encoding shRNA directed against FBW7 and MULE were annealed and subcloned into AgeI and EcoRI sites of the pLKO lentiviral plasmid. The following are DNA oligonucleotide sequences for the FBW7-directed shRNA (sense, 5'-CCGGAACCTTCTCTGGAGAGAAACTCGAGTTTCTCTCCAGAGAAGGTTTTTTG-3'; antisense, 5'-AATTCAAAAAAACCTTCTCTGGAGAG AGAAACTCGAGTTTCTCTCTCCAGAGAAGGTT-3'), and for MULE-directed shRNA (sense, 5'-CCGGAATTGCTATGTCTCTGGGACACTCGAGTGTCCCA GAGACATAGCAATTTTTTTG-3'; antisense, 5'-AATTCAAAAAAATTGCTA TGTCTCTGGGACACTCGAGTGTCCCAGAGACATAGCAATT-3'). Lentiviral shRNA constructs against GFP and MCL1 were obtained from W. Hahn. WT MCL1 and 3A MCL1 cDNAs were amplified with PCR and subcloned into the BamHI and SalI sites of the pLenti-GFP-Puro construct (Addgene, catalogue number 658-5).

Antibodies and reagents. Anti-Myc antibody (catalogue number sc-40), polyclonal anti-HA antibody (SC-805), anti-cyclin A antibody (SC-751), anti-PLK1 antibody (SC-17783), anti-CUL1 antibody (sc-70895), anti-RICTOR antibody (sc-81538), anti-p27 antibody (sc-528), anti-SKP1 antibody (sc-7163), anti-MCL1 antibody (sc-819) and anti-cyclin E antibody (SC-247) were purchased from Santa Cruz Biotechnology. Anti-tubulin antibody (T-5168), polyclonal anti-Flag antibody (F2425), monoclonal anti-Flag antibody (F-3165), anti-βcatenin antibody (C7207), anti-vinculin antibody (V9131), peroxidase-conjugated anti-mouse secondary antibody (A4416) and peroxidase-conjugated anti-rabbit secondary antibody (A4914) were purchased from Sigma. Anti-MCL1 antibody (4572), anti-BCL2 antibody (2872), anti-COX IV antibody (4850), anti-cleaved caspase 3 (Asp175) antibody (9661), anti-cleaved PARP (Asp214) antibody (9541), anti-ERK1/2 antibody (4695), anti-Jun antibody (9162), anti-phospho-GSK3ß (Ser9) antibody (9336) and anti-BIM antibody (4582) were purchased from Cell Signaling Technology. Anti-MULE antibody (A300-486A) was purchased from Bethyl. Monoclonal anti-HA antibody (MMS-101P) was purchased from Covance. Anti-RBX1 antibody (RB-069P1) was purchased from NeoMarker. Another anti-MCL1 antibody (559027) was purchased from BD Pharmingen. Anti-GFP antibody (632380) and another anti-CUL1 antibody (32-2400) were purchased from Invitrogen. Anti-CDH1 antibody (CC43) was purchased from Oncogene. Oligofectamine, Lipofectamine and Plus reagents were purchased from Invitrogen. GSK3β inhibitor VIII was purchased from Calbiochem.

siRNAs. Human siRNA oligonucleotides directed against FBW7, SKP2, CDH1 and CUL1 have been described previously^{6,28,29}. A human siRNA oligonucleotide that can deplete both β-TRCP1 and β-TRCP2 (sense, 5'-AAGUGGAAUUUGU GGAACAUC-3') was purchased from Dharmacon. Human siRNA oligonucleotides directed against MULE (MULE-A: sense, 5'-CAUGCCGCAAUCCAGACA UAU-3')25 and (MULE-B: sense, 5'-AAUUGCUAUGUCUCUGGGACA-3')30 have been validated previously and were purchased from Dharmacon. Luciferase GL2 siRNA oligonucleotide was purchased from Dharmacon. siRNA oligonucleotides to deplete endogenous RBX1 (sense, 5'-AACUGUGCCAUCUGCAGGA ACAA-3'), CUL1 (sense, 5'-GGUCGCUUCAUAAACAACAUU-3') and RICTOR (sense, 5'-AAACUUGUGAAGAAUCGUAUCUU-3') were synthesized by Dharmacon. Cocktailed siRNAs targeting SKP1 were purchased from Invitrogen (1299003). A GSK3α-depleting siRNA oligonucleotide (6312) and a GSK3α/βdepleting siRNA oligonucleotide (6301) were purchased from Cell Signaling Technology. The GSK3β-depleting siRNA oligonucleotide (51012) was purchased from Ambion. As described previously, siRNA oligonucleotides were transfected into subconfluent cells with Oligofectamine or Lipofectamine 2000 (Invitrogen) according to the manufacturer's instructions⁶.

Cell culture. Cell culture including synchronization and transfection has been described previously 6,28 . Wild-type and $FBW7^{-/-}$ DLD1 cell lines were gifts from B. Vogelstein. Mouse T-ALL cell lines derived from Tal1-transgenic mice were gifts from M. A. Kelliher. Human T-ALL cell lines were previously described. Loucy and CMLT1 T-ALL cell lines were obtained from J. Aster. For various assays described below, as indicated in the figure legends, T-ALL cells were cultured in either 0.5% FBS or 10% FBS-containing medium for sorafenib (ALEXIS Biochemicals) or ABT-737 (Symansis) treatment. In the case of combined treatment with both sorafenib and ABT-737, T-ALL cells were maintained in 10% FBS-containing medium.

Lentiviral shRNA virus packaging, retrovirus packaging and subsequent infections were performed as described previously²⁸. For cell viability assays, cells were plated at 10,000 per well in 96-well plates, and incubated with the appropriate medium containing sorafenib, ABT-737 or DMSO for 48 h. Assays were performed with CellTiter-Glo Luminescent Cell Viability Assay kit (Promega) according to the manufacturer's instructions. For detection of apoptosis, cells treated with various drugs were stained with propidium iodide (Roche) or co-stained with annexin-V-PE and 7-AAD (Annexin V-PE Apoptosis Detection Kit I, BD Bioscience) according to the manufacturer's instructions. Stained cells were sorted with a Dako-Cytomation MoFlo sorter (Dako) at the Dana-Farber Cancer Institute FACS core facility.

Immunoblotting and immunoprecipitation. Cells were lysed in EBC buffer (50 mM Tris, pH 8.0, 120 mM NaCl and 0.5% NP-40) supplemented with protease inhibitors (Complete Mini, Roche) and phosphatase inhibitors (phosphatase inhibitor cocktail set I and II, Calbiochem). The protein concentrations of the lysates were measured using the Bradford Protein Assay reagent (Bio-Rad) on a DU 800 spectrophotometer (Beckman Coulter). The lysates were then resolved by SDS-PAGE and immunoblotted with the indicated antibodies. For immunoprecipitation, 800 µg lysates were incubated with the appropriate antibody (1–2 µg) for 3–4 h at 4 $^{\circ}$ C followed by 1 h incubation with protein-A sepharose beads (GE Healthcare). Immuno-complexes were washed five times with NETN buffer (20 mM Tris, pH 8.0, 100 mM NaCl, 1 mM EDTA and 0.5% NP-40) before being resolved by SDS-PAGE and immunoblotted with the indicated antibodies. Quantification of the immunoblot band intensity was performed with ImageJ software.

Detection of MCL1 phosphorylation sites in vivo. To map MCL1 phosphorylation status in vivo, 293T cells were transfected with HA-MCL1 using the calcium phosphate method. Thirty hours after transfection, 293T cells were treated with 10 µM MG132 for 16 h to block the 26S proteasome pathway before collecting whole-cell lysates for HA-immunoprecipitation. After extensive washing with NETN buffer, the HA-immunoprecipitates were separated by SDS-PAGE and visualized with colloidal Coomassie blue. The band containing MCL1 was excised and treated with dithiothreitol (DTT) to reduce disulphide bonds and iodoacetamide to derivatize cysteine residues. In-gel digestion of the protein was done using trypsin or chymotrypsin. The resultant peptides were extracted from the gel and analysed by nanoscale-microcapillary reversed phase liquid chromatography tandem mass spectrometry (LC-MS/MS). Peptides were separated across a 37-min gradient ranging from 4% to 27% (v/v) acetonitrile in 0.1% (v/v) formic acid in a microcapillary $(125\,\mu\text{m}\times18\,\text{cm})$ column packed with C_{18} reversed-phase material (Magic C18AQ, 5 µm particles, 200 Å pore size, Michrom Bioresources) and online analysed on the LTQ Orbitrap XL hybrid FTMS (Thermo Scientific). For each cycle, one full MS scan acquired on the Orbitrap at high mass resolution was followed by ten MS/ MS spectra on the linear ion trap XL from the ten most abundant ions. MS/MS spectra were searched using the SEQUEST algorithm against a database that was created based on a protein sequence database containing the sequence for MCL1. They were searched for common contaminants, such as human keratin protein with static modification of cysteine carboxymethylation, dynamic modification of methionine oxidation and serine, threonine and tyrosine phosphorylation. All peptide matches were filtered based on mass deviation, tryptic state, XCorr and dCn and confirmed by manual validation. The reliability of site localization of phosphorylation events was evaluated using the Ascore algorithm.

Real-time RT-PCR analysis. RNA was extracted using the RNeasy mini kit (Qiagen), and the reverse transcription (RT) reaction was performed using TaqMan Reverse Transcription Reagents (ABI, N808-0234). After mixing the resultant template with *MCL1* (Hs00172036_m1) or *GAPDH* (Hs99999905_m1) primers and TaqMan Fast Universal PCR Master Mix (ABI, 4352042), the real-time RT-PCR was performed with the 7500 Fast Real-time PCR system (ABI). *FBW7* (Hs00217794_m1), *SKP2* (Hs00180634_m1), *BTRC1* (Hs00182707_m1), *MCL1* (Hs00172036_m1) and *GAPDH* (Hs99999905_m1) primers were purchased from ABI.

Protein degradation analysis. Cells were transfected with Myc–MCL1 along with HA–FBW7 or Flag– β -TRCP1, and GFP as a negative control, in the presence or absence of HA–GSK3 and/or HA–ERK1. For half-life studies, cycloheximide (20 $\mu g\,ml^{-1}$; Sigma) was added to the media 40 h after transfection. At various time points thereafter, cells were lysed, and protein abundances were measured by immunoblotting analysis.

In vivo ubiquitylation assay. Cells were transfected with a plasmid encoding Flag–Ub along with Myc–MCL1 and HA–FBW7 in the presence or absence of HA–GSK3. Thirty-six hours after transfection, cells were treated with the proteasome inhibitor MG132 (30 μ M; Calbiochem) for 6 h and then collected. Anti-Myc immunoprecipitates were recovered and immunoblotted with anti-Flag antibody. Alternatively, cells were transfected with His–Ub along with Myc–MCL1 and HA–FBW7 in the presence or absence of HA–GSK3. Thirty-six hours after transfection,

cells were collected, and the lysates were incubated with Ni-NTA matrices (Qiagen) at 4 $^{\circ}$ C for 12 h in the presence of 8 M urea, pH 7.5. Immobilized proteins were washed five times with 8 M urea, pH 6.3, before being resolved by SDS–PAGE and immunoblotted with anti-Myc antibody.

In vitro ubiquitylation assay. The *in vitro* ubiquitylation assays were performed as described previously. To purify the SCFFBW7 E3 ligase complex, 293T cells were transfected with vectors encoding GST–FBW7, HA–CUL1, Myc–SKP1 and Flag–RBX1. The SCFFBW7 E3 complexes were purified from the whole-cell lysates using GST–agarose beads. Purified, recombinant GST–MCL1 proteins were incubated with purified SCFFBW7 complexes in the presence of purified, recombinant active E1, E2 (UBCH5A and UBCH3), ATP and ubiquitin. The reactions were stopped by the addition of $2\times$ SDS–PAGE sample buffer, and the reaction products were resolved by SDS–PAGE gel and probed with the indicated antibodies.

In vitro kinase assay. GSK3 was purchased from New England Biolabs. The *in vitro* kinase reaction was performed according to the manufacturer's instructions. Briefly, 5 μg indicated GST fusion proteins were incubated with purified active GSK3 in the presence of 5 $\mu Ci \ [\gamma^{-3^2}P]ATP$ and 200 μM cold ATP in the kinase reaction buffer for 20 min. The reaction was stopped by the addition of SDS-containing lysis buffer, the proteins resolved by SDS-PAGE and phosphorylation detected by autoradiography.

MCL1-binding assays. Binding to immobilized GST proteins was performed as described previously²⁸. Where indicated, the GST–MCL1 proteins were incubated with GSK3 in the presence of ATP for 1 h before the binding assays.

Subcellular fractionation. Mitochondrial and cytosolic (S100) fractions were prepared by resuspending HeLa cells in 0.8 ml ice-cold buffer A (250 mM sucrose, 20 mM HEPES, pH 7.4, 10 mM KCl, 1.5 mM MgCl₂, 1 mM EDTA, 1 mM EGTA, 1 mM DTT, 17 μ g ml⁻¹ phenylmethylsulphonyl fluoride, 8 μ g ml⁻¹ aprotinin, 2 μ g ml⁻¹ leupeptin). Cells were then passed through an ice-cold cylinder cell homogenizer. Unlysed cells and nuclei were pelleted by a 10 min, 750 g spin.

The recovered supernatant was spun at $10,000\,g$ for 25 min. This pellet was resuspended in buffer A and represents the mitochondrial fraction. The supernatant was spun at $100,000\,g$ for 1 h. The supernatant from this final centrifugation represents the S100 (cytosolic) fraction.

Mice. Generation of conditional Fbw7 knockout mice (Lck-Cre/ $Fbw7^{fl/fl}$) and Mx1-Cre/ $Fbw7^{fl/fl}$) was described previously^{3,4}.

In vivo imaging. CMLT1 cells were infected with lentiviral vectors encoding a shRNA directed against MCL1 (shMCL1) or an irrelevant control (shGFP). After selection in $1\,\mu g\,ml^{-1}$ puromycin, cells were engineered for in vivo imaging by transduction with a retrovirus encoding a fusion of firefly luciferase fused to neomycin phosphotransferase and were then selected with 0.5 mg ml $^{-1}$ G418. After selection, the luciferase activity of each engineered cell line was measured and found to have a similar reading. Subsequently, equal numbers of viable cells $(0.5\text{--}1\times10^7$ cells) were injected into NOD SCID Il2rg-null mice through the lateral tail vein. Tumour burden was determined using bioluminescence imaging (IVIS Spectrum, Caliper Life Sciences) after intraperitoneal injection of 75 mg kg $^{-1}$ D-luciferin. Total body luminescence was quantified using the Living Image software package (Caliper Life Sciences) and is expressed as photons per second per standardized region of interest (photons s $^{-1}$ ROI $^{-1}$), encompassing the entire mouse. Data are presented as mean \pm s.e.m. with statistical significance determined by Student's t-test.

- Popov, N. et al. The ubiquitin-specific protease USP28 is required for MYC stability. Nature Cell Biol. 9, 765–774 (2007).
- Gao, D. et al. Phosphorylation by Akt1 promotes cytoplasmic localization of Skp2 and impairs APCCdh1-mediated Skp2 destruction. Nature Cell Biol. 11, 397–408 (2009).
- Benmaamar, R. & Pagano, M. Involvement of the SCF complex in the control of Cdh1 degradation in S-phase. Cell Cycle 4, 1230–1232 (2005).
- Chen, D. et al. ARF-BP1/Mule is a critical mediator of the ARF tumor suppressor. Cell 121, 1071–1083 (2005).



Sensitivity to antitubulin chemotherapeutics is regulated by MCL1 and FBW7

Ingrid E. Wertz¹, Saritha Kusam¹, Cynthia Lam¹*, Toru Okamoto²*, Wendy Sandoval³, Daniel J. Anderson⁴, Elizabeth Helgason¹, James A. Ernst^{1,3}, Mike Eby⁴, Jinfeng Liu⁵, Lisa D. Belmont⁴, Josh S. Kaminker⁵, Karen M. O'Rourke⁶, Kanan Pujara⁷, Pawan Bir Kohli⁸, Adam R. Johnson⁸, Mark L. Chiu⁹, Jennie R. Lill³, Peter K. Jackson⁴, Wayne J. Fairbrother¹, Somasekar Seshagiri⁷, Mary J. C. Ludlam⁴, Kevin G. Leong⁴, Erin C. Dueber¹, Heather Maecker⁴, David C. S. Huang^{2,10} & Vishva M. Dixit⁶

Microtubules have pivotal roles in fundamental cellular processes and are targets of antitubulin chemotherapeutics1. Microtubuletargeted agents such as Taxol and vincristine are prescribed widely for various malignancies, including ovarian and breast adenocarcinomas, non-small-cell lung cancer, leukaemias and lymphomas¹. These agents arrest cells in mitosis and subsequently induce cell death through poorly defined mechanisms². The strategies that resistant tumour cells use to evade death induced by antitubulin agents are also unclear². Here we show that the pro-survival protein MCL1 (ref. 3) is a crucial regulator of apoptosis triggered by antitubulin chemotherapeutics. During mitotic arrest, MCL1 protein levels decline markedly, through a post-translational mechanism, potentiating cell death. Phosphorylation of MCL1 directs its interaction with the tumour-suppressor protein FBW7, which is the substratebinding component of a ubiquitin ligase complex. The polyubiquitylation of MCL1 then targets it for proteasomal degradation. The degradation of MCL1 was blocked in patient-derived tumour cells that lacked FBW7 or had loss-of-function mutations in FBW7, conferring resistance to antitubulin agents and promoting chemotherapeutic-induced polyploidy. Additionally, primary tumour samples were enriched for FBW7 inactivation and elevated MCL1 levels, underscoring the prominent roles of these proteins in oncogenesis. Our findings suggest that profiling the FBW7 and MCL1 status of tumours, in terms of protein levels, messenger RNA levels and genetic status, could be useful to predict the response of patients to antitubulin chemotherapeutics.

BCL2 family proteins are key regulators of cell survival and can either promote or inhibit cell death³. Pro-survival members, including BCL- X_L and MCL1, inhibit apoptosis by blocking the cell death mediators BAX and BAK (also known as BAK1). When uninhibited, BAX and BAK permeabilize the outer mitochondrial membranes, which releases pro-apoptotic factors that activate caspases, the proteases that catalyse cellular demise. This intrinsic, or mitochondrial, pathway is initiated by the damage-sensing BH3-only proteins, including BIM (encoded by BCL2L11) and NOXA (also known as PMAIP1), which neutralize the pro-survival family members when cells are irreparably damaged⁴.

Because aberrant expression of pro-survival BCL2 family proteins promotes tumorigenesis and resistance to chemotherapeutics³, we evaluated whether these proteins regulate the cell death induced by antitubulin agents. Multiple lineages of $Bax^{-/-}Bak^{-/-}$ mouse embryonic fibroblasts (MEFs) were resistant to killing by Taxol or nocodazole, whereas wild-type (WT) MEFs were significantly more sensitive to such killing (Fig. 1a and Supplementary Fig. 2a–e). These results were confirmed in myeloid cells (Fig. 1b). As inhibitor of apoptosis

(IAP) proteins⁵ do not have a significant role in the cellular response to antitubulin agents (Supplementary Fig. 3), we conclude that BCL2 family proteins are key regulators of antitubulin-agent-induced cell death in diverse cell types.

Next we determined the sensitivity of MEFs lacking individual BCL2 family members to killing by Taxol or vincristine, two mechanistically distinct antitubulin chemotherapeutics. $Bclx^{-/-}$ cells were more sensitive to Taxol than were WT cells, and $Mcl1^{-/-}$ cells showed greater sensitivity than WT cells to Taxol or vincristine (Fig. 1c, d). Because the ratio of pro-survival to pro-apoptotic BCL2 family proteins dictates cell fate³, we monitored the levels of these proteins during mitotic arrest, as indicated by phosphorylation of the anaphase-promoting complex subunit CDC27 (ref. 6). MCL1 protein levels declined markedly in synchronized cells released into nocodazole or Taxol (Fig. 1e and Supplementary Fig. 4). The decrease in NOXA protein levels is probably an indirect consequence of MCL1-regulated stability (D.C.S.H., unpublished observations). MCL1 protein levels also declined in unsynchronized cells that were arrested in mitosis (Supplementary Figs 5 and 34).

MCL1 transcription was not significantly decreased during mitotic arrest in human cell lines (Fig. 2a). This implicated a role for the ubiquitin–proteasome system, the primary conduit for regulated protein degradation in eukaryotic cells⁷, in the reduction of MCL1 protein levels. Indeed, the proteasome inhibitor MG132 blocked MCL1 degradation (Fig. 2b and Supplementary Fig. 6), and endogenous MCL1 was ubiquitylated during mitotic arrest (Supplementary Fig. 7).

MCL1 contains potential degron motifs for association with the F-box proteins β-transducin-repeat-containing protein (β-TRCP; also known as FBXW1 or FWD1)8 and FBW7 (also known as FBXW7, AGO, CDC4 or SEL10)9 (Supplementary Fig. 8). F-box proteins are substrate receptors for SKP1-CUL1-F-box (SCF)-type ubiquitin ligase complexes, which mediate degradative polyubiquitylation^{9,10}. Consistent with a role for CUL1-based ubiquitin ligases in MCL1 turnover, ectopic expression of a dominant-negative CUL1 protein blocked MCL1 degradation during mitotic arrest (Supplementary Fig. 9). These data indicate that CUL1-containing ubiquitin-ligase complexes have a more prominent role in regulating MCL1 turnover during mitotic arrest than MULE, a ligase that ubiquitylates MCL1 (ref. 11), an idea corroborated by knocking down MULE expression in Taxoltreated cells by using RNA interference (RNAi) (Supplementary Fig. 10a-c). RNAi-mediated knockdown of FBW7 expression, but not β-TRCP expression, attenuated MCL1 degradation in tumour cells (Fig. 2c and Supplementary Figs 11 and 12) and untransformed cells (Supplementary Fig. 13a, b). MCL1 degradation (Fig. 2d) and turnover (Supplementary Fig. 14) was protracted in FBW7-null cells relative to

Department of Early Discovery Biochemistry, Genentech, South San Francisco, California 94080, USA. The Walter and Eliza Hall Institute of Medical Research, Parkville, Victoria 3052, Australia.

Department of Protein Chemistry, Genentech, South San Francisco, California 94080, USA. Department of Research Oncology, Genentech, South San Francisco, California 94080, USA. Department of Bioinformatics, Genentech, South San Francisco, California 94080, USA. Department of Physiological Chemistry, Genentech, South San Francisco, California 94080, USA. Department of Molecular Biology, Genentech, South San Francisco, California 94080, USA. Department of Biochemical Pharmacology, Genentech, South San Francisco, California 94080, USA. Department of Structural Biology, Willinois 60064, USA. Department of Medical Biology, University of Melbourne, Parkville, Victoria 3010, Australia.

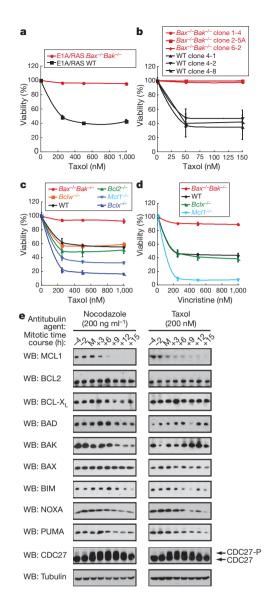


Figure 1 | BCL2 family proteins regulate cell death induced by antitubulin chemotherapeutic agents. a–d, Viability of cell lines treated for 48 h with the indicated agents. Data are presented as the mean \pm s.e.m.; n=3. E1A/RAS-transformed $Bax^{-/-}Bak^{-/-}$ MEFs (a) and factor-dependent myeloid (FDM) cells (b) are resistant to Taxol-induced cell death. c, Genetic deletion of Mcl1 or Bclx enhances sensitivity to Taxol. d, Genetic deletion of Mcl1, but not of Bclx, enhances sensitivity to vincristine. e, Assessment of BCL2 family protein levels, by western blotting (WB), during mitotic arrest. The mitotic time course indicates when synchronized cells were collected relative to the onset of mitotic arrest: that is, -2 denotes 2 h before mitosis (M), and +3 denotes 3 h after cells entered mitosis. CDC27 and tubulin are indicators of mitotic arrest and equal loading, respectively. CDC27-P, phosphorylated CDC27.

WT cells, and complementation with FBW7 isoforms restored MCL1 degradation (Fig. 2d and Supplementary Fig. 15). Endogenous MCL1 was recruited to cellular SCF complex subunits in FBW7-WT but not FBW7-null cells during mitotic arrest (Fig. 2e). Recombinant MCL1 was ubiquitylated *in vitro* by the reconstituted FBW7-containing SCF complex (SCF^{FBW7}) when the complete ligase complex was assembled (Fig. 2f). Collectively, these results demonstrate that SCF^{FBW7} promotes MCL1 degradation during mitotic arrest.

Because substrate phosphorylation promotes recruitment to FBW7 (ref. 9), the phosphorylation status of candidate FBW7-binding degrons on MCL1 was evaluated in cells arrested in mitosis (Fig. 3a). Mass spectrometry identified phosphorylation of residues S64, S121, S159 and T163 (Fig. 3a and Supplementary Fig. 16a–d). Myc-tagged MCL1

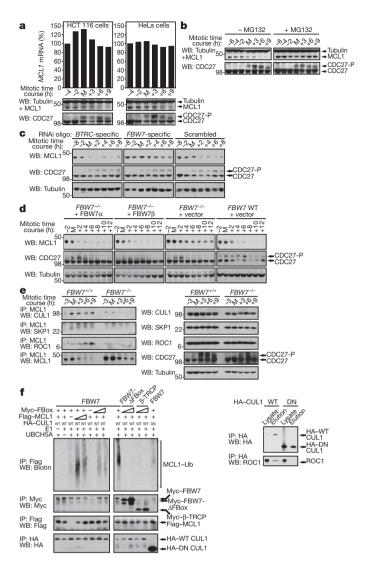


Figure 2 | SCF^{FBW7} targets MCL1 for proteasomal degradation during mitotic arrest. a-e, Human carcinoma cell lines were synchronized and collected throughout the mitotic time course as in Fig. 1a. During mitotic arrest, MCL1 mRNA levels are not significantly decreased relative to MCL1 protein, as determined by WB (numbers indicate molecular mass in kDa). MCL1 expression was monitored by real-time PCR, and the percentage mRNA is indicated relative to the -4-h time point. **b**, MG132 stabilizes MCL1 degradation during mitotic arrest in Heta cells. c, RNAi oligonucleotides targeting FBW7, but not control scrambled RNAi or RNAi oligonucleotides targeting BTRC (which encodes β-TRCP), attenuate MCL1 degradation during mitotic arrest in HCT 116 cells. d, MCL1 degradation is attenuated in $FBW7^{-/-}$ HCT 116 cells during mitotic arrest. Complementation with the α-isoform or β-isoform of FBW7 restores MCL1 degradation. e, FBW7 recruits MCL1 to the SCF ubiquitin ligase complex core, the components of which are CUL1, SKP1 and ROC1, in HCT 116 cells in mitotic arrest. IP, immunoprecipitation. f, Left, reconstitution of the SCF^{FBW7} ubiquitin ligase complex promotes MCL1 ubiquitylation in vitro. Ubiquitylation reactions containing the indicated components were reacted in vitro with biotinylated ubiquitin. Reacted components were denatured, and Flag-MCL1 was immunoprecipitated (IP) and blotted (WB) for biotin to reveal in vitroubiquitylated MCL1 (MCL1-Ub). Myc-tagged F-box proteins (including F-box-deleted FBW7 (FBW7-ΔFBox)), Flag-MCL1 and HA-tagged CUL1 variants were also immunoprecipitated and analysed as indicated by WB analysis to reveal the respective input levels. Wedges indicate an increasing amount of the indicated reaction component. Right, endogenous ROC1 does not associate with dominant-negative (DN) HA-tagged CUL1. E1, ubiquitinactivating enzyme; UBCH5A, E2 ubiquitin-conjugating enzyme.

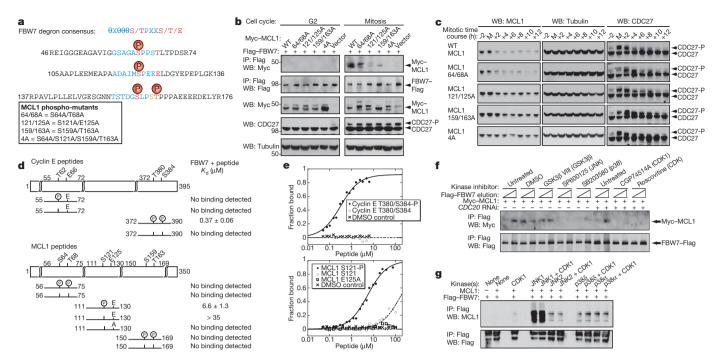


Figure 3 | Identification of MCL1 degron motifs and protein kinases that direct recruitment to FBW7 during mitotic arrest. a, The FBW7 degron consensus sequence (top, with potential phosphorylation sites or phosphomimic residues in red), corresponding MCL1 residues (coloured, centre) and confirmed phosphorylation sites (P) during mitosis are indicated for three MCL1-derived peptide sequences. Phosphorylation at S159 (red) rather than S162 (orange) was confirmed by co-elution with a synthetic peptide (see Supplementary Fig. 16). θ, hydrophobic amino acid; X, any amino acid. The MCL1 phospho-mutant nomenclature used is indicated. b, Association of Flag-FBW7 with Myc-MCL1 mutants S121A/E125A, S159A/T163A, and 4A is attenuated in mitotic arrest. The indicated constructs were expressed in HeLa cells that were synchronized, released into Taxol, and processed as indicated. c, MCL1 phospho-mutants S121A/E125A, S159A/T163A and 4A have attenuated degradation during mitotic arrest. HCT 116 cells were synchronized and collected throughout the mitotic time course as in Fig. 1a. d, Schematic representation of MCL1- or cyclin-E-derived peptides and their calculated dissociation constants (K_d), averaged from duplicate experiments

was efficiently recruited to Flag-tagged FBW7 during mitotic arrest (Supplementary Fig. 17), and MCL1 residues 1–170 directed binding to FBW7 (Supplementary Fig. 18), thus mutant MCL1 constructs were tested to identify the degrons that confer FBW7 association (Fig. 3a). The MCL1 mutants S121A/E125A (in which the serine residue at position 121 and the glutamic acid residue at position 125 are both replaced by alanine residues) and S159A/T163A bound to FBW7 less efficiently than WT FBW7 (Fig. 3b), and their degradation during mitotic arrest was attenuated (Fig. 3c). Assessment of the relative affinities of the phosphorylated WT MCL1 degrons for FBW7 showed that the S121/E125 site is a higher affinity degron than the S159/T163 site (Fig. 3d, e). Thus, similar to other FBW7 substrates such as cyclin E9, MCL1 contains high-affinity and low-affinity FBW7 degrons, both of which are required for efficient recruitment to (Fig. 3b) and subsequent degradation by (Fig. 3c) SCF^{FBW7} in the context of full-length MCL1.

To investigate the protein kinase or kinases that direct MCL1 recruitment to FBW7 in response to antitubulin chemotherapeutics, we focused on kinases that contain MCL1 degron consensus sites and demonstrate activity in mitotic arrest. This includes CDK1, casein kinase II (CKII), ERK isoforms (also known as MAPK1 and MAPK2), GSK3β, JNK isoforms (also known as MAPK8, MAPK9 and MAPK10) and p38 isoforms (also known as MAPK11, MAPK12, MAPK13 and MAPK14) (Supplementary Figs 19 and 24c). Studies using protein kinase inhibitors (Supplementary Figs 20a, 21, 22a, b and 24a, b) or RNAi (Supplementary Figs 20b, 23a–c

(mean \pm s.d.), for FBW7 binding as determined by ELISA. **e**, The MCL1derived peptide containing the phosphorylated S121/E125 degron (MCL1 S121-P) preferentially binds to FBW7 in vitro. Graphical representation of the fraction of FBW7-bound cyclin E or MCL1 peptides as a function of peptide concentration is shown. DMSO, dimethylsulphoxide. f, Pharmacological inhibition of JNK, p38 or CDK1 (with inhibitor (and targeted kinase) indicated, top) attenuates recruitment of Myc-MCL1 to Flag-FBW7 during mitotic arrest. The indicated constructs were expressed in HeLa cells with or without CDC20 RNAi oligonucleotides or control scrambled RNAi oligonucleotides, and cells were then synchronized and released into Taxol. When cells entered mitotic arrest, the indicated agents were added for 1 h followed by a 3-h incubation with 25 µM MG132 before collection and processing as indicated (see Supplementary Fig. 25). g, In vitro phosphorylation of recombinant MCL1 drives FBW7 binding. Full-length MCL1 was subjected to in vitro phosphorylation with the indicated kinases and subsequently incubated with recombinant Flag-FBW7. Anti-Flag immunoprecipitates were resolved by SDS-PAGE and probed with antibodies specific for the indicated proteins.

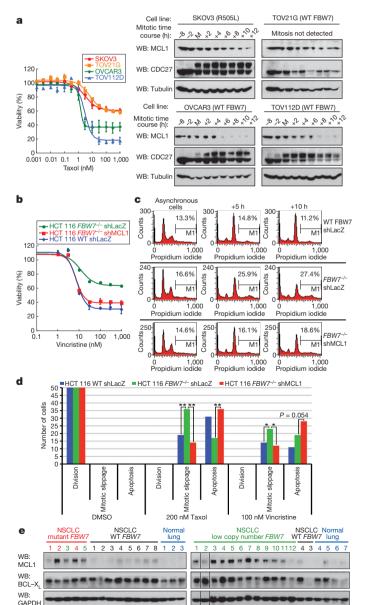
and 24a–c) indicated that the activities of JNK, p38, CKII and CDK1 regulate MCL1 degradation during mitotic arrest. Because CDK1 inhibition drives cells out of mitosis¹² (Supplementary Figs 21 and 22a, b), non-degradable cyclin B1 was expressed, or *CDC20* expression was knocked down, to maintain cells in mitotic arrest¹³ (Supplementary Fig. 24a, b). Inhibition of JNK, p38 or CDK1 also attenuated MCL1 recruitment to FBW7 (Fig. 3f and Supplementary Figs 25 and 26). JNK, p38 and CKII, but not CDK1, directly phosphorylated MCL1 degrons (Supplementary Table 1a–c). JNK and p38 directly promoted MCL1–FBW7 binding, whereas the contribution by CDK1 was negligible (Fig. 3g), suggesting that CDK1 indirectly enhances MCL1 phosphorylation to promote binding to FBW7 in the cellular context. Indeed, CDK1 phosphorylates T92 (Supplementary Table 1d), a residue that is phosphorylated (Supplementary Fig. 16e) and regulates MCL1 turnover (Supplementary Fig. 27a) during mitotic arrest.

Because the phosphatase inhibitor okadaic acid regulates MCL1 phosphorylation in a manner similar to Taxol¹⁴, we evaluated whether CDK1-directed phosphorylation of T92 blocked the association of the okadaic-acid-sensitive phosphatase PP2A with MCL1 during mitotic arrest. PP2A more readily dissociated from WT MCL1 than the T92A mutant, concomitant with increasing CDK1 activity (Supplementary Fig. 27b). MCL1-associated PP2A protein levels and phosphatase activity are low in mitotic arrest when CDK1 activity is high, but they are restored after exit from mitosis, when CDK1 is inactivated (Supplementary Fig. 27c). Thus, the phosphorylation of MCL1 degron

residues by JNK, p38 and CKII during mitotic arrest is probably initially opposed by phosphatases such as PP2A. Maximal activation of CDK1 in prolonged mitotic arrest promotes T92 phosphorylation and PP2A dissociation, allowing sufficient phosphorylation of MCL1 degron residues to drive FBW7-mediated degradation (Supplementary Fig. 1). These effects are revealed when microtubule-targeted agents are washed out of cells that are in mitotic arrest: the activities of JNK, p38 and CDK1 decline, and MCL1 protein levels are restored (Supplementary Fig. 28). Sufficient loss of MCL1 activates BAK and BAX (Supplementary Fig. 29) to promote apoptosis.

FBW7 is a haploinsufficient tumour suppressor that targets proto-oncoproteins—including Myc, Jun, NOTCH and cyclin E—for degradation⁹. *FBW7* mutations that were identified in patient-derived cell lines disrupted the association of FBW7 with MCL1 during mitotic arrest (Supplementary Fig. 30). Thus, failure of inactivated FBW7 to promote MCL1 degradation could confer resistance to antitubulin chemotherapeutics. Indeed, *FBW7*-null cell lines showed attenuated MCL1 degradation and were more resistant to Taxol- or vincristine-induced cell death than were WT cells (Supplementary Figs 31 and 32). BCL-X_L remained stable regardless of *FBW7* status (Supplementary Fig. 31).

Similar trends were seen in patient-derived ovarian (Fig. 4a) and colon (Supplementary Fig. 33) cancer cell lines harbouring naturally



occurring FBW7 mutations. Although the response to antitubulin agents is heterogeneous within a cell population¹⁵, mitotic arrest was similarly activated by Taxol treatment in synchronized and asynchronous ovarian cancer cell lines (Fig. 4a and Supplementary Fig. 34). Moreover, MCL1 degradation profiles were similar in synchronized and asynchronous cells: MCL1 was efficiently degraded in FBW7-WT cells that are effectively arrested in mitosis, yet MCL1 persisted in TOV21G cells that undergo only transient mitotic arrest and in FBW7-mutant SKOV3 cells (Fig. 4a and Supplementary Fig. 34). Thus, the inappropriate survival of cells that are arrested in mitosis positively correlates with attenuated MCL1 degradation, which is, in turn, regulated by FBW7.

FBW7 with an R505L mutation was expressed in FBW7-WT TOV112D-X1 cells to mimic cells harbouring one mutated FBW7 allele⁹ and to assess the *in vivo* effects. Tumours expressing mutant FBW7 were more resistant to Taxol (Supplementary Fig. 35a) and had higher levels of MCL1 than FBW7-WT parental tumours (Supplementary Fig. 35b, c). BCL-X_L protein levels were unaffected by FBW7 status (Supplementary Fig. 35b, d). Reducing the amount of MCL1 protein in FBW7-null cells restored their sensitivity to Taxol- and vincristine-induced death (Fig. 4b and Supplementary Fig. 36), demonstrating that MCL1 is a crucial pro-survival factor that is responsible for resistance to antitubulin agents in FBW7-deficient cells.

Previous studies have shown that blocking apoptosis during mitotic arrest allows cells to exit mitosis and evade cell death¹⁵ and that FBW7null cells more frequently exit mitosis and undergo endoreduplication to render cells polyploid¹⁶. Our work identifying MCL1 as an FBW7 substrate therefore suggests a molecular link to explain antitubulin agent resistance and chemotherapy-induced polyploidy. Indeed, FBW7-null cells exit Taxol- or vincristine-induced mitotic arrest more readily (Fig. 4d and Supplementary Figs 37 and 38) and show more pronounced polyploidy (Fig. 4c) than do FBW7-WT cells. Reducing the MCL1 protein levels in the FBW7-null cells with short hairpin RNA (shRNA) decreased mitotic slippage, enhanced Taxol- or vincristineinduced apoptosis (Fig. 4d and Supplementary Figs 37 and 38) and reduced chemotherapeutic-induced polyploidy (Fig. 4c) compared with FBW7-null cells treated with control shRNA. Thus, MCL1 promotes resistance to death induced by antitubulin chemotherapeutics and facilitates genomic instability when FBW7 is inactivated.

The hostile tumour micro-environment, like chemotherapeutic insults, exerts selective pressures on malignant cells; therefore, tumour

Figure 4 | FBW7 inactivation and increased MCL1 levels promote antitubulin agent resistance and tumorigenesis in human cancers. a, FBW7-WT ovarian cancer cell lines that undergo mitotic arrest are sensitive to Taxol (left) and rapidly degrade MCL1 relative to FBW7-mutant and Taxol-resistant cells (right). FBW7 status is specified in parentheses. ${\bf b}$, Sensitivity to vincristineinduced cell death is restored in FBW7^{-/-} cells on MCL1 ablation (red). WT or FBW7^{-/-} HCT 116 cells were transduced with the indicated doxycyclineinducible shRNA constructs, cultured in the presence of doxycycline, and treated with various concentrations of vincristine for 48 h before cell viability assessment. shLacZ, control shRNA (green and blue). Data are presented as mean \pm s.e.m.; n = 3. c, MCL1 expression modulates polyploidy in FBW7deficient HCT 116 cells. WT or FBW7^{-/-} HCT 116 cells were transduced with the indicated doxycycline-inducible shRNA constructs, cultured in the presence of doxycycline, synchronized and released into vincristine. They were then collected at 5 h (+5 h) or 10 h (+10 h) after mitotic arrest and fixed, stained with propidium iodide and analysed by FACS (x axis, fluorescence units; y axis, number of cells). M1, percentage of cells with >2N DNA content. **d**, MCL1 expression increases mitotic slippage and attenuates apoptosis in FBW7-deficient cells. WT or $FBW7^{-/-}$ HCT 116 cells were transduced with the indicated doxycycline-inducible shRNA constructs, cultured in the presence of doxycycline, transduced with an H2B-GFP-expressing baculovirus synchronized, treated with the indicated antitubulin agents and imaged live. Three images were acquired every 10 min for 43 h, and 50 cells were analysed for each condition. *, P < 0.05; **, P < 0.001 (one-tailed Fisher's exact test). e, MCL1 levels are elevated in non-small-cell lung cancer (NSCLC) samples with mutant FBW7 or low FBW7 copy number relative to FBW7-WT tumours and normal lung samples (see also Supplementary Table 2). NSCLC FBW7-mutant samples 3 and 5 (green) also have low FBW7 copy number.

RESEARCH LETTER

cells harbouring alterations in FBW7 and MCL1 should be selected for and enriched in primary patient tumour samples. To this end, copy number analysis of FBW7 and MCL1 was performed in ovarian tumour samples (Supplementary Fig. 39). The co-occurrence of MCL1 gain and FBW7 loss was more frequent than expected, a finding that is consistent with selection for both genetic alterations (Supplementary Fig. 39). Data from non-small-cell lung cancer samples showed similar trends but were not statistically significant owing to insufficient sample size (data not shown). Immunoblotting of patient samples revealed that most tumours in which FBW7 was inactivated had increased MCL1 protein levels relative to FBW7-WT tumours and normal lung samples (Fig. 4e and Supplementary Table 2). By contrast, BCL-X_T protein levels were not correlated with FBW7 status (Fig. 4e). Thus, functional FBW7 is required to downregulate MCL1 expression in primary patient samples, a particularly significant finding given that antitubulin agents are therapeutic mainstays for non-small-cell lung cancers and ovarian cancers.

The signalling pathways that activate cell death induced by antitubulin chemotherapeutics are of crucial interest, and we provide genetic evidence that both MCL1 and BCLX are important regulators of this therapeutic response. Whereas BCL-X_L is functionally inactivated by phosphorylation¹⁷ and is unaffected by FBW7 status, MCL1 inactivation is coordinated by the concerted activities of phosphatases, stress-activated and mitotic kinases, and the SCF^{FBW7} ubiquitin ligase. As such, we define a unique molecular mechanism for regulation of MCL1 and initiation of apoptosis during mitotic arrest (Supplementary Fig. 1). By identifying SCF^{FBW7} as a crucial ubiquitin ligase that directs MCL1 degradation during mitotic arrest, we also elucidate a mechanism for resistance to antitubulin chemotherapeutics. Analysis of patient samples suggests that drug-efflux pumps¹⁸ or tubulin alterations¹⁹ do not always account for resistance to antitubulin agents, thus evasion of apoptosis owing to inappropriately increased levels of MCL1 is probably a crucial strategy. We also show that the elevated MCL1 protein levels in FBW7-deficient cells favours increased mitotic slippage, endoreduplication and subsequent polyploidy in response to antitubulin therapeutics. The role of MCL1 in FBW7-deficient cells therefore extends beyond the simple inhibition of apoptosis; it also facilitates genomic aberrations, thus fuelling the transformed state.

METHODS SUMMARY

The viability of cancer cell lines, and MEFs in which genes encoding IAPs had been knocked out, was analysed by using the CellTiter-Glo Luminescent Cell Viability Assay (Promega). Cells were treated in triplicate with antitubulin agents for the indicated times, using dimethylsulphoxide treatment as a control. The viability of BCL2-family-member-null MEFs was analysed by propidium iodide staining, as described previously 20 , after treatment with antitubulin agents for 48 h. Cell synchronization was achieved by culture either in serum-free medium for 12–16 h or in medium containing 2 mM thymidine for 18–24 h, release from the thymidine block with three washes in PBS, followed by culture for 8–12 h in complete growth media (compositions are described in the Supplementary Information). Cells then underwent a second thymidine block for 16–20 h, three further washes in PBS and release into complete medium containing the indicated reagents. To block MCL1 degradation, 25 μ M MG132 was added as cells entered mitotic arrest, as assessed by visual inspection. See Supplementary Information for full methods.

Received 13 October 2009; accepted 21 December 2010.

- Jackson, J. R., Patrick, D. R., Dar, M. M. & Huang, P. S. Targeted anti-mitotic therapies: can we improve on tubulin agents? *Nature Rev. Cancer* 7, 107–117 (2007).
- Rieder, C. L. & Maiato, H. Stuck in division or passing through: what happens when cells cannot satisfy the spindle assembly checkpoint. Dev. Cell 7, 637–651 (2004).
- 3. Youle, R. J. & Strasser, A. The BCL-2 protein family: opposing activities that mediate cell death. *Nature Rev. Mol. Cell Biol.* **9**, 47–59 (2008).

- Willis, S. N. et al. Apoptosis initiated when BH3 ligands engage multiple Bcl-2 homologs, not Bax or Bak. Science 315, 856–859 (2007).
- Varfolomeev, E. & Vucic, D. (Un)expected roles of c-IAPs in apoptotic and NFκB signaling pathways. Cell Cycle 7, 1511–1521 (2008).
- King, R. W. et al. A 20S complex containing CDC27 and CDC16 catalyzes the mitosis-specific conjugation of ubiquitin to cyclin B. Cell 81, 279–288 (1995)
- Finley, D. Recognition and processing of ubiquitin-protein conjugates by the proteasome. *Annu. Rev. Biochem.* 78, 477–513 (2009).
- Frescas, D. & Pagano, M. Deregulated proteolysis by the F-box proteins SKP2 and β-TrCP: tipping the scales of cancer. *Nature Rev. Cancer* 8, 438–449 (2008).
- Welcker, M. & Clurman, B. E. FBW7 ubiquitin ligase: a tumour suppressor at the crossroads of cell division, growth and differentiation. *Nature Rev. Cancer* 8, 83–93 (2008).
- Deshaies, R. J. & Joazeiro, C. A. RING domain E3 ubiquitin ligases. Annu. Rev. Biochem. 78, 399–434 (2009).
- Zhong, Q., Gao, W., Du, F. & Wang, X. Mule/ARF-BP1, a BH3-only E3 ubiquitin ligase, catalyzes the polyubiquitination of Mcl-1 and regulates apoptosis. *Cell* 121, 1085–1095 (2005).
- Potapova, T. Á. et al. The reversibility of mitotic exit in vertebrate cells. Nature 440, 954–958 (2006).
- Huang, H. C., Shi, J., Orth, J. D. & Mitchison, T. J. Evidence that mitotic exit is a better cancer therapeutic target than spindle assembly. Cancer Cell 16, 347–358 (2009).
- Domina, A. M., Vrana, J. A., Gregory, M. A., Hann, S. R. & Craig, R. W. MCL1 is phosphorylated in the PEST region and stabilized upon ERK activation in viable cells, and at additional sites with cytotoxic okadaic acid or Taxol. *Oncogene* 23, 5301–5315 (2004).
- Gascoigne, K. E. & Taylor, S. S. Cancer cells display profound intra- and interline variation following prolonged exposure to antimitotic drugs. Cancer Cell 14, 111–122 (2008).
- Finkin, S., Aylon, Y., Anzi, S., Oren, M. & Shaulian, E. Fbw7 regulates the activity of endoreduplication mediators and the p53 pathway to prevent drug-induced polyploidy. *Oncogene* 27, 4411–4421 (2008).
- Terrano, D. T., Upreti, M. & Chambers, T. C. Cyclin-dependent kinase 1-mediated Bcl-x_L/Bcl-2 phosphorylation acts as a functional link coupling mitotic arrest and apoptosis. *Mol. Cell. Biol.* 30, 640–656 (2010).
- Ozalp, S. S., Yalcin, O. T., Tanir, M., Kabukcuoglu, S. & Etiz, E. Multidrug resistance gene-1 (*Pgp*) expression in epithelial ovarian malignancies. *Eur. J. Gynaecol. Oncol.* 23, 337–340 (2002).
- Mesquita, B. et al. No significant role for β tubulin mutations and mismatch repair defects in ovarian cancer resistance to paclitaxel/cisplatin. BMC Cancer 5, 101 (2005).
- Chen, L. et al. Differential targeting of prosurvival Bcl-2 proteins by their BH3-only ligands allows complementary apoptotic function. Mol. Cell 17, 393–403 (2005).

Supplementary Information is linked to the online version of the paper at www.nature.com/nature

Acknowledgements We thank P. Ekert for FDM cell lines, J. Stinson for sequencing assistance, S. Johnson and C. Santos for assistance with obtaining patient samples, P. Haverty for bioinformatics analysis, C. Grimaldi for cloning assistance, J. Dynek for TagMan advice, D. French for tumour analysis, C. Quan and J. Tom for peptide synthesis, I. Zilberleyb and the Baculovirus Expression Group for cloning and protein production, S. Charuvu for generating MCL1 point mutants, A. Bruce for graphics assistance, the Genentech Cancer Genome Project Team, Z. Modrusan, R. Soriano and the microarray lab for ovarian tumour data sets, K. Newton for editorial assistance, W. Wei for sharing unpublished results, and A. Eldridge, D. Kirkpatrick, D. Vucic, E. Varfolomeev, T. Goncharov, A. Cochran, O. Huang, A. Huang, Y. Pereg, A. Loktev, D. Phillips, J. Wu, M. van Delft, D. Eaton, E. Shaulian, T. Hunter, S. Cory, J. Adams, A. Strasser, R. Deshaies and G. Evan for discussions. Work in the Huang laboratory is supported by the National Health and Medical Research Council (program grant #461221, IRIISS grant #361646 and a fellowship to D.C.S.H.), the Leukemia and Lymphoma Society (SCOR 7413), the National Institutes of Health (grants CA043540 and CA80188), the Australian Cancer Research Foundation, and an Australian Research Council Australian Postdoctoral fellowship to T.O. We apologize to our colleagues whose primary work could not be cited owing to space constraints.

Author Contributions I.E.W., S.K., T.O., J.A.E., P.B.K., A.R.J., C.L., E.C.D., E.H., H.M. and K.G.L. designed and performed *in vitro*, cell-based and *in vivo* experiments. D.J.A. and M.J.C.L. designed and performed microscopy experiments. S.K., C.L., K.M.O., M.L.C. and M.E. made constructs. J.L. and J.K. performed bioinformatics analysis, K.P. and S.S. provided sequencing analysis. W.S. and J.R.L. designed and performed mass spectrometry experiments. I.E.W., S.K., C.L., T.O., W.S., D.J.A., M.J.C.L., K.G.L., E.C.D., H.M. and V.M.D. prepared the manuscript and figures. W.S., L.D.B., P.K.J., W.J.F., D.J.A., P.B.K., A.R.J., M.J.C.L., H.M., D.C.S.H. and I.E.W. contributed to the study design and data analysis.

Author Information Reprints and permissions information is available at www.nature.com/reprints. The authors declare no competing financial interests. Readers are welcome to comment on the online version of this article at www.nature.com/nature. Correspondence and requests for materials should be addressed to I.E.W. (ingrid@gene.com).



X chromosome dosage compensation via enhanced transcriptional elongation in *Drosophila*

Erica Larschan^{1,2,3}*, Eric P. Bishop^{4,5}*, Peter V. Kharchenko⁴, Leighton J. Core⁶, John T. Lis⁶, Peter J. Park⁴ & Mitzi I. Kuroda^{1,2}

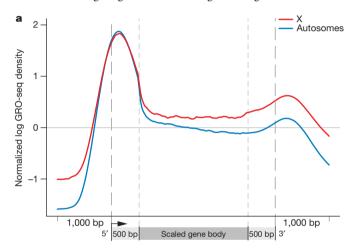
The evolution of sex chromosomes has resulted in numerous species in which females inherit two X chromosomes but males have a single X, thus requiring dosage compensation. MSL (Male-specific lethal) complex increases transcription on the single X chromosome of Drosophila males to equalize expression of X-linked genes between the sexes¹. The biochemical mechanisms used for dosage compensation must function over a wide dynamic range of transcription levels and differential expression patterns. It has been proposed² that the MSL complex regulates transcriptional elongation to control dosage compensation, a model subsequently supported by mapping of the MSL complex and MSL-dependent histone 4 lysine 16 acetylation to the bodies of X-linked genes in males, with a bias towards 3' ends³⁻⁷. However, experimental analysis of MSL function at the mechanistic level has been challenging owing to the small magnitude of the chromosome-wide effect and the lack of an in vitro system for biochemical analysis. Here we use global run-on sequencing (GRO-seq)8 to examine the specific effect of the MSL complex on RNA Polymerase II (RNAP II) on a genome-wide level. Results indicate that the MSL complex enhances transcription by facilitating the progression of RNAP II across the bodies of active X-linked genes. Improving transcriptional output downstream of typical gene-specific controls may explain how dosage compensation can be imposed on the diverse set of genes along an entire chromosome.

To investigate how the MSL complex specifically increases transcription of X-linked genes, we performed GRO-seq in SL2 cells, a male Drosophila cell line that has been extensively characterized for MSL function^{4,9}. To show the average enrichment across genes, a 3-kb 'metagene' profile was plotted in which the internal regions were rescaled so that all genes appear to have the same length (Fig. 1). Analysis was restricted to expressed genes that were sufficiently large (>2.5 kb) so that gene-body effects could be clearly assessed (822 X-linked genes, 3,420 autosomal genes), and all gene profiles were normalized by their copy number as determined by analysis of SL2 DNA content¹⁰. High correlation coefficients were observed between replicate libraries (Pearson correlation coefficient, ≥ 0.98; Supplementary Fig. 1). The metagene profiles revealed a prominent 5' peak of paused RNAP II consistent with previous chromatin immunoprecipitation (ChIP) and analysis of short 5' RNAs11,12 (RNA-seq). In addition, a peak of RNAP II density downstream of the metagene 3' processing site is evident, possibly due to slow release in regions of transcription termination8. The 3' peak is present even when the influence of neighbouring gene transcription is eliminated (Supplementary Fig. 2).

The central question with regard to dosage compensation is how genes on the X chromosome differ on average from genes on autosomes. Overall, we found that RNAP II density on active X-linked genes was higher than on autosomal genes, specifically over gene bodies (Fig. 1a). The increase in tag density over the bodies of X-linked genes compared to autosomal genes was approximately

1.4-fold, consistent with previous estimates of MSL-dependent dosage compensation^{9,10,13}. We also performed RNAP II ChIP in SL2 cells, confirming higher occupancy on X-linked genes compared to autosomes but with lower resolution and reduced sensitivity (Supplementary Fig. 3). Therefore, we proceeded with GRO-seq to analyse X and autosomal differences.

To measure how X and autosomes differed on average in the distribution of elongating RNAP II, we segmented genes into their 5'



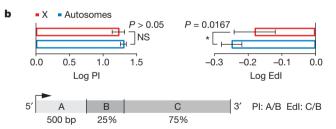


Figure 1 | The male X chromosome has higher levels of engaged RNAP II over gene bodies relative to autosomes. a, Average GRO-seq profiles of expressed genes are shown for X (red) and autosomes (blue). Read counts on all chromosomes were normalized to genomic read coverage to control for copy number variation, mappability and other potential biases. To construct a metagene profile, genes are scaled as follows: (1) the 5' end (1 kb upstream of the transcription start site (TSS) to 500 bp downstream) and the 3' end (500 bp upstream of the transcript termination site (TTS) to 1 kb downstream) were unscaled; (2) the remainder of the gene is scaled to 2 kb (see Supplementary Methods). b, PI values do not differ between X (red bar) and autosomal genes (blue bar). EdI values are significantly different between X (red bar) and autosomal genes (blue bar). Error bars represent a 95% confidence interval for the mean PI or EdI (1.96 × s.e.m.: n = 1,344 (X genes); n = 6,090 (autosomal genes)). The definitions of PI and EdI are shown in the schematic. The PI and EdI are calculated with unscaled GRO-seq tag counts. NS, not significant.

¹Division of Genetics, Department of Medicine, Brigham and Women's Hospital, Boston, Massachusetts 02115, USA. ²Department of Genetics, Harvard Medical School, Boston, Massachusetts 02115, USA. ³Department of Molecular Biology, Cell Biology, and Biochemistry, Brown University, Providence, Rhode Island 02912, USA. ⁴Center for Biomedical Informatics, Harvard Medical School & Informatics Program, Children's Hospital, Boston, Massachusetts 02115, USA. ⁵Bioinformatics Program, Boston University, Boston, Massachusetts 02215, USA. ⁶Department of Molecular Biology and Genetics, Cornell University, Ithaca, New York, 14850, USA.

^{*}These authors contributed equally to this work.

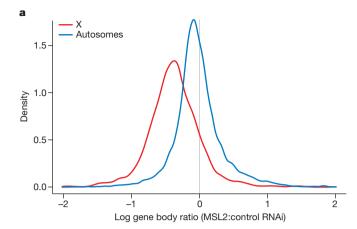
500 bp and the remainder of the coding region. We subdivided further the remainder of the coding region into 5' and 3' segments (25% and 75%, respectively). Using this segmentation, we quantified RNAP II pausing and elongation separately on the basis of the unscaled GRO-seq signal (Fig. 1b). The pausing index (PI) was previously defined as the ratio of the GRO-seq signal at the 5' peak to the average signal over gene bodies⁸. Here, we calculated the PI for X and autosomal genes as the ratio of the 5' peak (segment A) to the first 25% of the remaining gene body (segment B), and found no statistically significant difference when the two groups were compared (Fig. 1b).

To examine separately transcription elongation across gene bodies, we defined the elongation density index (EdI) as the ratio of tag density in the 3' region of each gene (segment C) compared to its 5' region after the first 500 bp (segment B). In contrast to our analysis of 5' pausing, we found statistically significant differences in EdI (P value < 0.0162) between X and autosomes (Fig. 1b). This conclusion was robust to how the 5' and 3' regions of genes were divided (Supplementary Table 1). As defined, the average PI (log scale) is a positive number because RNAP II is generally enriched at 5' ends compared to gene bodies; the average EdI (log scale) is a negative number, as the relative density of RNAP II typically decreases from the beginning to the end of gene bodies. We conclude that X-linked genes, on average, show a significantly smaller decrease in RNAP II density along their gene bodies when compared to autosomal genes.

To measure the specific contribution of the MSL complex to the increase in RNAP II within X-linked gene bodies, we used MSL2 RNA interference (RNAi) to reduce complex levels in male SL2 cells as described previously9. Excellent correlations between replicate data sets were observed (Supplementary Fig. 1). To confirm the X-specific effect of MSL2 RNAi, we computed the distributions of the GRO-seq signal (averaged over the bodies of genes excluding the 5' peak) for all genes before and after RNAi. When comparing X versus autosomes, we found a preferential decrease on the X chromosome, with an average control:MSL RNAi ratio of 1.4 (Fig. 2a). MSL-dependent changes in average GRO-seq density showed a weak but statistically significant correlation with changes in steady-state messenger RNA levels assayed by expression array⁹ (Pearson correlation = 0.22, P value $< 1 \times 10^{-15}$) or mRNA-Seq¹⁰ (Pearson correlation = 0.30, P value $< 1 \times 10^{-15}$). These results confirm that MSL-dependent changes in steadystate RNA levels reflect differences in active transcription on the X chromosome.

In addition to assessing the average decrease of X-linked RNAP II density after MSL2 RNAi, we asked whether any genes showed strong MSL-dependence, a hallmark of the *roX* genes that encode RNA components of the complex^{14,15}. We found that *roX2* showed a strong loss in GRO-seq density (ninefold) after MSL2 RNAi, as predicted (Fig. 2b and Supplementary Fig. 4). Interestingly, in the untreated or control RNAi samples, there is a prominent GRO-seq peak downstream of the major *roX2* 3′ end, coincident with an MSL recruitment site (see discussion later). *roX1* expression is low in this isolate of SL2 cells, and no other expressed genes on X or autosomes showed strong MSL dependence in our assays (>6-fold). Examples of additional individual gene profiles are shown in Supplementary Figs 5 and 6.

Next we compared the average RNAP II density along X and autosomal metagene profiles after control and MSL2 RNAi. Unlike our initial analysis of X and autosomes, where different gene populations were compared (Fig. 1), here we could examine the same genes in the presence and absence of the MSL complex (Fig. 3). We found that after MSL2 RNAi, the density of elongating RNAP II over the bodies of X-linked genes decreased, approaching the level on autosomes (Fig. 3 and Supplementary Fig. 7). The presence of the MSL complex affected RNAP II density starting just downstream of the 5' peak and continuing through the bodies of X-linked genes (Fig. 3 and Supplementary Fig. 7). Thus, GRO-seq functional data correlate with physical association of the MSL complex, which is biased towards the 3' ends of active genes on the male X chromosome^{4,5}.



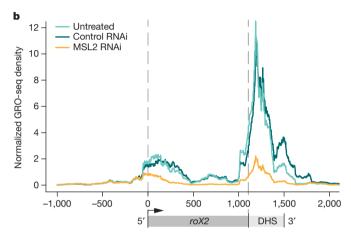


Figure 2 | The MSL complex increases engaged RNAP II density on the male X chromosome. a, The log ratio of sense-strand reads in the MSL2 RNAi sample to the control RNAi sample was computed within the body of each gene. Here, the distributions of these ratios are plotted for all genes on X and autosomes. b, GRO-seq sense-strand read densities within the *roX2* gene (*x*-axis denotes base pairs from the *roX2* transcription start site) for the untreated, control RNAi and MSL2 RNAi samples. Schematic below GRO-seq profiles indicates the location of the DHS site, which contains sequences that can recruit the MSL complex to the X chromosome.

To quantify the differences in density of engaged RNAP II in the presence and absence of the MSL complex, we calculated the PI and EdI for each gene, followed by the PI and EdI ratios comparing MSL2 and control RNAi treatment. We found that both X and autosomes increased PI and decreased EdI after MSL2 RNAi treatment (Supplementary Fig. 8). However, in each case the change was larger on X than on autosomes, and the most profound difference was an MSL-dependent change in EdI on X compared with autosomes $(P < 1 \times 10^{-15})$; Fig. 3b). EdI was computed, as before, by defining the 5' and 3' regions as 25% and 75%, respectively, of the gene body after removing the 5' peak, but the difference was statistically significant for all other values until the 3' end was reached (Supplementary Table 1). When these analyses were performed separately for two independently prepared sets of GRO-seq libraries (Supplementary Fig. 9), the results were also statistically significant (P value $< 7.6 \times 10^{-14}$, P value $< 1.1 \times 10^{-4}$ for each of two replicates). We conclude that the MSL complex causes the transcriptional elongation profiles of X-linked genes to differ from those of autosomal genes.

To visualize the location along gene bodies at which the MSL complex functions, we calculated control:MSL2 RNAi GRO-seq ratios and generated a metagene profile (Fig. 4a). Here, values above zero represent higher relative amounts of engaged RNAP II in the presence of the MSL complex compared to after RNAi treatment. In contrast, values below

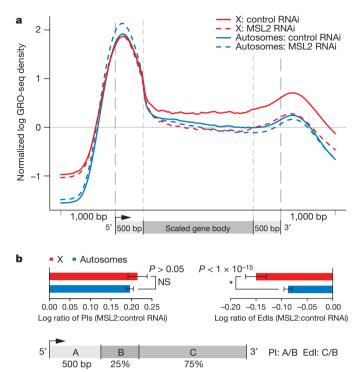
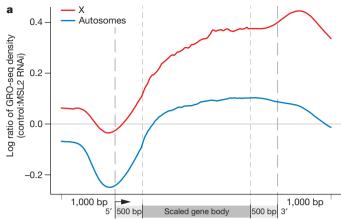


Figure 3 | The MSL complex facilitates the progression of engaged RNAP II across transcription units. a, Metagene profiles of expressed X chromosome genes and autosomal genes in control RNAi and MSL2 RNAi samples. Higher RNAP II density can be seen within the bodies of genes on the X chromosome (solid red) compared to those on autosomes (solid blue) in the control RNAi sample. After MSL2 RNAi, average RNAP II density on X decreases over gene bodies (dashed red) becoming similar to autosomal gene bodies (dashed blue). b, Ratios of PI between control and MSL2 RNAi treated cells are not significantly different for genes on the X chromosome (red bar) compared to those on autosomes (blue bar). In contrast, ratios of EdI between the control and MSL2 RNAi sample decreased significantly for genes on the X (red bar) compared to those on the autosomes (blue bar). PI and EdI were calculated as described for Fig. 1. Error bars represent a 95% confidence interval for the mean PI or EdI ratios $(1.96 \times \text{s.e.m.}: n = 1,358 \text{ (X genes)}; n = 6,135 \text{ (autosomal genes)}).$

zero represent a relative increase in engaged RNAP II after MSL2 RNAi. In the absence of the MSL complex, there is a relative increase in the amount of RNAP II localized to the 5' ends of both autosomal and X-linked genes, perhaps due to relocalization of RNAP II from the bodies of X-linked genes (Fig. 4a). A limitation of the GRO-seq assay is that we cannot currently distinguish between initiating and 5' paused polymerase, so we cannot assign a definitive role for this 5' increase in RNAP II after MSL2 RNAi treatment. However, relative RNAP II levels over autosomal gene bodies do not increase, indicating that any relocalized enzyme in this experiment is likely to remain paused rather than progressing across transcription units. This is consistent with a model in which the functional outcome of MSL2 RNAi is to shift RNAP II density away from productive transcription through X-linked gene bodies

We plotted the local effect of the MSL complex in Fig. 4a to compare it to the status of histone 4 lysine 16 (H4K16) acetylation (Fig. 4b) catalysed by the MOF component of the MSL complex^{3,16}. H4K16 acetylation typically is enriched at the 5' ends of most active genes in mammals and flies^{6,17}; in contrast, a 3' bias of this mark is a distinctive characteristic of the dosage compensated male X chromosome in *Drosophila*^{3,6,7}. Interestingly, there is an overall coincidence across gene bodies between the MSL-complex-dependent GRO-seq signal and the presence of H4K16 acetylation⁷ (Fig. 4a). How might H4K16 acetylation biased towards the 3' end of genes generate the improved transcriptional elongation indicated by our GRO-seq results? During transcription elongation, nucleosomes are thought to comprise a barrier to the progress of



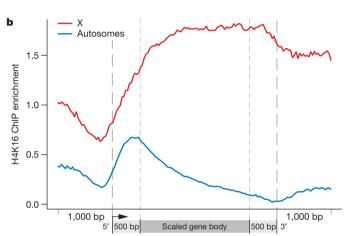


Figure 4 | MSL function correlates with the presence of H4K16 acetylation. a, The MSL2-dependent effect on RNAP II density as shown by metagene profiles of control: MSL2 RNAi GRO-seq sense-strand reads shown on log scale (base 2). The black line (y=0) indicates no change after MSL2 RNAi treatment. The cumulative effect of MSL2 RNAi treatment peaks towards the 3' ends of X-linked genes (red) while having less effect on autosomal genes (blue). b, Similar to the effect of the MSL complex on engaged RNAP II, H4K16 acetylation on the male X chromosome localizes to the bodies of active genes with a 3' bias (red). On autosomes, H4K16 acetylation is present at 5' ends (blue) as described previously.

RNAP II 18-20 and several well-studied elongation factors, including Spt6 and the FACT complex, are proposed to function by removing nucleosomes that block RNAP II progression and replacing them in the wake of transcription 18,21. Interestingly, H4K16 acetylation of nucleosomes has been observed to act in opposition to the formation of higher-order chromatin structure *in vitro* 22,23. Thus, H4K16 acetylation is likely to reduce further the steric hindrance to RNAP II progression through chromatin. Improving the entry of RNAP II into the bodies of genes may allow 5′, gene-specific events to proceed at an increased but still regulated rate. Furthermore, reduction in the repressive effect of nucleosomes could increase mRNA output by improving the processivity of RNAP II on each template. Available methodologies cannot distinguish between these mechanisms *in vivo*, and therefore future approaches will be required to assess their relative contributions to dosage compensation.

In addition to increasing the transcription of X-linked genes for dosage compensation, the MSL complex also positively regulates the *roX* noncoding RNA components of the complex, to promote their male specificity^{14,15}. *roX1* expression is low in our SL2 cell line, but our GRO-seq data indicate that active transcription of *roX2* is highly dependent on MSL2 as predicted (Fig. 2b and Supplementary Fig. 4). Interestingly, there is a strong GRO-seq peak at the 3' *roX2* DHS (DNaseI hypersensitive site), which contains sequences important for



targeting the MSL complex to the X chromosome. Sites of roX gene transcription are thought to be critical for MSL complex assembly ^{24,25}. Therefore, it is possible that paused RNAP II at the roX2 DHS could promote an open chromatin structure that facilitates MSL complex targeting or incorporation of noncoding *roX2* RNA into the complex.

In summary, we propose that the MSL complex functions on the male X chromosome to promote progression and processivity of RNAP II through the nucleosomal template, as foreseen by Lucchesi². Improving transcriptional output downstream of typical gene-specific regulation makes biological sense when compensating the diverse set of genes found along an entire chromosome.

METHODS SUMMARY

To measure the density of engaged RNAP II, GRO-Seq experiments were conducted on DRSC SL2 cells grown in Schneider's medium with 10% FBS8. To determine how the MSL complex contributes to dosage compensation, MSL2 and control (GFP) RNAi treatments were conducted using a bathing protocol9. Nuclei were subjected to GRO-seq analysis after RNAi treatment. Two biological replicates were performed for the untreated, control RNAi and MSL2 RNAi experiments.

Full Methods and any associated references are available in the online version of the paper at www.nature.com/nature.

Received 1 July; accepted 14 December 2010.

- Gelbart, M. E. & Kuroda, M. I. Drosophila dosage compensation: a complex voyage 1. to the X chromosome. Development 136, 1399-1410 (2009).
- Lucchesi, J. C. Dosage compensation in flies and worms: the ups and downs of X-chromosome regulation. Curr. Opin. Genet. Dev. 8, 179–184 (1998).
- Smith, E. R., Allis, C. D. & Lucchesi, J. C. Linking global histone acetylation to the transcription enhancement of X-chromosomal genes in Drosophila males. J. Biol. Chem. 276, 31483-31486 (2001).
- Alekseyenko, A. A., Larschan, E., Lai, W. R., Park, P. J. & Kuroda, M. I. High-resolution ChIP-chip analysis reveals that the Drosophila MSL complex selectively identifies active genes on the male X chromosome. Genes Dev. 20, 848-857 (2006).
- Gilfillan, G. D. et al. Chromosome-wide gene-specific targeting of the Drosophila dosage compensation complex. Genes Dev. 20, 858-870 (2006).
- Kind, J. et al. Genome-wide analysis reveals MOF as a key regulator of dosage
- compensation and gene expression in *Drosophila*. *Cell* **133**, 813–828 (2008). Gelbart, M. E., Larschan, E., Peng, S., Park, P. J. & Kuroda, M. I. *Drosophila* MSL complex globally acetylates H4K16 on the male X chromosome for dosage compensation. *Nature Struct. Mol. Biol.* **16**, 825–832 (2009).
- Core, L. J., Waterfall, J. J. & Lis, J. T. Nascent RNA sequencing reveals widespread pausing and divergent initiation at human promoters. Science 322, 1845-1848
- Hamada, F. N., Park, P. J., Gordadze, P. R. & Kuroda, M. I. Global regulation of X chromosomal genes by the MSL complex in Drosophila melanogaster. Genes Dev. **19,** 2289–2294 (2005)
- Zhang, Y. et al. Expression in an euploid Drosophila S2 cells. PLoS Biol. 8, e1000320

- 11. Muse, G. W. et al. RNA polymerase is poised for activation across the genome. Nature Genet. 39, 1507-1511 (2007).
- Zeitlinger, J. et al. RNA polymerase stalling at developmental control genes in the Drosophila melanogaster embryo. Nature Genet. 39, 1512-1516 (2007).
- 13. Belote, J. M. & Lucchesi, J. C. Male-specific lethal mutations of Drosophila melanogaster. Genetics 96, 165-186 (1980).
- 14. Bai, X., Alekseyenko, A. A. & Kuroda, M. I. Sequence-specific targeting of MSL complex regulates transcription of the roX RNA genes. EMBO J. 23, 2853-2861 (2004).
- 15. Meller, V. H. & Rattner, B. P. The *roX* genes encode redundant male-specific lethal transcripts required for targeting of the MSL complex. EMBO J. 21, 1084–1091 (2002).
- Hilfiker, A., Hilfiker-Kleiner, D., Pannuti, A. & Lucchesi, J. C. mof, a putative acetyl 16. transferase gene related to the Tip60 and MOZ human genes and to the SAS genes of yeast, is required for dosage compensation in Drosophila. EMBO J. 16, 2054-2060 (1997).
- Wang, Z. et al. Combinatorial patterns of histone acetylations and methylations in the human genome. Nature Genet. 40, 897-903 (2008).
- Kaplan, C. D., Laprade, L. & Winston, F. Transcription elongation factors repress transcription initiation from cryptic sites. Science 301, 1096-1099 (2003).
- Mavrich, T. N. et al. Nucleosome organization in the Drosophila genome. Nature **453**, 358–362 (2008).
- 20. Mavrich, T. N. et al. A barrier nucleosome model for statistical positioning of nucleosomes throughout the yeast genome. Genome Res. 18, 1073–1083 (2008).
- Belotserkovskaya, R. et al. FACT facilitates transcription-dependent nucleosome alteration. Science 301, 1090-1093 (2003).
- 22. Robinson, P. J. et al. 30 nm chromatin fibre decompaction requires both H4-K16 acetylation and linker histone eviction. J. Mol. Biol. 381, 816-825 (2008).
- Shogren-Knaak, M. et al. Histone H4-K16 acetylation controls chromatin structure and protein interactions. Science 311, 844-847 (2006).
- 24. Park, Y., Kelley, R. L., Oh, H., Kuroda, M. I. & Meller, V. H. Extent of chromatin spreading determined by roX RNA recruitment of MSL proteins. Science 298, 1620-1623 (2002).
- Oh, H., Park, Y. & Kuroda, M. I. Local spreading of MSL complexes from *roX* genes on the Drosophila X chromosome. Genes Dev. 17, 1334-1339 (2003).

Supplementary Information is linked to the online version of the paper at www.nature.com/nature.

Acknowledgements We thank F. M. Winston, S. Buratowski, A. Alekseyenko, M. Gelbart, C. Wang and A. Gortchakov for comments on the manuscript, and are grateful to N. Gehlenborg for graphic design expertise. This work was supported by the following NIH grants: GM45744 (M.I.K.), GM082798 (P.J.P.) and HG4845 (J.T.L.). E.L. was supported by a Charles A. King Trust fellowship from the Medical Foundation.

Author Contributions E.L. performed the experiments and E.P.B. and P.V.K. performed the computational analyses. P.J.P. advised on the computational analyses and the manuscript preparation. L.J.C., J.T.L. and M.I.K. advised on experimental protocols and/ or design. E.L. and M.I.K. prepared the manuscript.

Author Information Data are deposited in NCBI's Gene Expression Omnibus and are accessible through GEO Series accession numbers GSE25321 and GSE25887. Reprints and permissions information is available at www.nature.com/reprints. The authors declare no competing financial interests. Readers are welcome to comment on the online version of this article at www.nature.com/nature. Correspondence and requests for materials should be addressed to M.I.K. (mkuroda@genetics.med.harvard.edu) or P.J.P. (peter_park@harvard.edu).

METHODS

RNAi and cell culture methods. Control and MSL2 RNAi were performed in SL2-DRSC cells as described previously⁷. The control RNAi construct targeted the eGFP gene that is not present in SL2 cells, and the experimental RNAi construct targeted the MSL2 gene (http://www.flyrnai.org: DRSC 00829). Primer sequences for generation of the eGFP double-stranded RNA (dsRNA) template by PCR from pEGFP-N1(Clontech) were: forward, 5'-TAATACGACTCACTATAGGGAGA GGTGAGCA-AGGGCGA-GGAGCT-3'; and reverse, 5'-TAATACGACTCACT ATAGGGAGATCT-TGAAGTTCACCTTGATGC-CG-3'. The primers used for amplifying the MSL2 gene from *Drosophila* genomic DNA were: 5'-TAATACGACTCACTATAGGGAGAGTTGGCTGTG-CTGGCTG-3'; and reverse, 5'-TAATACGACTCACTATAGGGAGAGTTGGCTGTC-CTGGCTG-3'.

dsRNA was synthesized from PCR products containing T7 promoters using the Ambion MEGAscript kit, and 225 µg of dsRNA was added to 2×10^7 cells in a T225 flask. RNAi treatment was performed for 6 days after which mRNA was prepared and transcriptionally active nuclear extracts were generated as described later. mRNA preparation, complementary DNA synthesis and qPCR analysis of roX2 and msl2 RNA compared with the PKA normalization control were performed as described previously⁷. A 12.3-fold average decrease of msl2 mRNA was observed after MSL2 RNAi treatment when compared with the control treatment. Preparation of GRO-seq libraries for next-generation sequencing. Preparation of transcriptionally active nuclei from Drosophila SL2-DRSC cells after RNAi treatment was conducted as follows: SL2 cells grown in a T225 tissue culture flask were scraped and 1×10^8 cells were pelleted at 500g for 3 min at 4 °C. Then, cells were washed in 10 ml of cold PBS and spun at 500g for 3 min at 4 °C. Cells were swelled by resuspending gently in 10 ml ice-cold swelling buffer (10 mM Tris (pH = 7.5), 2 mM MgCl₂, 3 mM CaCl₂) and placed on ice for 5 min. Next, cells were pelleted at 600g for 10 min at 4 $^{\circ}$ C. Pelleted cells were resuspended in 1 ml lysis buffer (10 mM Tris (pH = 7.5), 2 mM MgCl₂, 3 mM CaCl₂, 10% glycerol, 0.5% NP40, 2 U ml⁻¹ SUPERaseIN (Invitrogen)) and pipetted 20 times with a P1000 tip with the end cut off. Nine millilitres of lysis buffer was added and nuclei were pelleted at 600g for 5 min. Nuclei were washed in 1 ml lysis buffer and then 9 ml was added followed by pelleting for 5 min at 600g at 4 °C. A small aliquot was taken for Trypan blue staining to check that lysis occurred and nuclei were still intact. Next, nuclei were resuspended in 1 ml freezing buffer (50 mM Tris-Cl (pH = 8.3), 40% glycerol, 5 mM MgCl₂, 0.1 mM EDTA) using a P1000 tip with the end cut off. Nuclei were pelleted for 1 min and resuspended in 500 µl of freezing buffer and aliquoted into 100 µl aliquots and frozen in liquid nitrogen. All solutions were prepared with DEPC-treated water.

GRO-seq libraries were prepared as described previously⁸ with the following changes: glycoblue (3 μ l: 15 mg ml $^{-1}$; Ambion) was used in all of the ethanol precipitations to assure the release of the nascent RNAs from the interior surface of Eppendorf tubes; and wash buffers for BrU immunoprecipitation differ from those described in ref. 8 as follows. Firstly, high salt wash buffer for anti-BrdU (0.25 \times SSPE, 1 mM EDTA, 0.05% Tween, 137.5 mM NaCl; secondly, binding buffer for anti-BrdU (0.25 \times SSPE, 1 mM EDTA, 0.05% Tween, 37.5 mM NaCl); thirdly, elution buffer (20 mM DTT, 300 mM NaCl, 50 mM Tris-Cl pH 7.5, 1 mM EDTA, 0.1% SDS); lastly, all immunoprecipitation wash buffers contain superRNAsin (1 μ l per 5 ml buffer) (Invitrogen) to block degradation that can occur during the immunoprecipitation process.

Overview of computational analysis of GRO-seq data. For data generation and quality assessment, sequencing was performed on an Illumina Genome Analyser IIx. Two independent biological replicates were generated for each of the three experiments (untreated, control RNAi and MSL2 RNAi). Data are available from GEO under accession numbers GSE25321 and GSE25887. Reads were aligned to the D. melanogaster genome (dm3) using the Bowtie alignment software²⁶. Only uniquely mapping reads with no more than one mismatch were retained. We obtained 10.6 million aligned reads from the untreated samples (7.1 M from replicate I; 3.5 M from replicate II), 25.2 million aligned reads from the control RNAi samples (20.5 M from replicate I, 4.7 M from replicate II), and 28.4 million from the MSL2 RNAi samples (22.4 M from replicate I, 6.0 M from replicate II). To assess the agreement between replicates, a correlation coefficient was computed between sense-strand read densities across genes in the two replicates for each of the three treatments. The agreement between replicates is excellent, with the following correlation coefficients: (1) untreated: Spearman, 0.97; Pearson, 0.98; (2) control RNAi: Spearman, 0.99; Pearson, 0.98; and (3) MSL2 RNAi: Spearman, 0.99; Pearson, 0.98 (Supplementary Fig. 1). For most of the analysis, the two replicates were combined and processed together to increase statistical power. Key results were also confirmed in each replicate separately.

Generating average profiles. To examine the difference between RNAi and control as well as between X and autosomes, it was important to derive accurate 'metagene' profiles. To improve existing TSS annotations, previously published small (<100 bp), capped nuclear RNA-seq data²⁷ were used. This data set contains

RNA isolated from 5' ends of transcripts. Starting with FlyBase build 5.23, start sites for each annotated transcript were adjusted by up to 150 bp from the original location. The position within the 301 bp window centred on the existing TSS annotation with the highest number of reads from this capped nuclear RNA-seq data set was annotated as the new TSS for that transcript. In the event that two positions within the search space had the same number of reads, the most 5' position was designated the TSS. Finally, transcripts with identical start sites were filtered out, ensuring each annotation is unique.

To derive the metagene profile, we first computed the profile for each gene before computing the average. For each gene, the GRO-seq read profile on each strand was normalized to total sequencing depth and was smoothed using Gaussian smoothing with a bandwidth of 200 bp. To adjust for copy number variations, alignability and sequencing biases, the GRO-seq read density was further normalized by the analogous density of genomic sequencing reads. Specifically, each gene was divided into 200 bins and the log ratio (base 2) between GRO-seq and genomic sequencing read densities were computed for each bin. To avoid ratios becoming infinity when the denominator is zero, we applied the common technique of adding a pseudocount (1 in this case) to both numerator and denominator. To average the log ratios across genes for the metagene profile, the 5′ end (1 kb upstream of the TSS to 500 bp downstream) and the 3′ end (500 bp upstream of the transcript termination site (TTS) to 1 kb downstream) were unscaled. The region within the gene body extending from 500 bp downstream of the TSS and 500 bp upstream of the TTS was scaled to 2 kb (see Fig. 1a).

Only genes longer than 2.5 kb were considered to avoid short genes in which the 5′ peak is difficult to distinguish from the body of the gene. In addition, genes with less than one RPKM (reads per kilobase per million)/gene copy in the untreated GRO-seq sample were considered unexpressed and thus excluded. In a number of genes, the read distribution downstream of the 5′ peak contained high peaks, possibly due to unannotated internal TSS that distorted the average profiles. To mitigate the effect of these outliers, we removed 5% of the genes in which the highest density peak was downstream of the first 500 bp. These genes were not removed when computing *P* values or for other analyses.

The ChIP-chip metagene profiles (Supplementary Fig. 3) were computed from array data by the same scaling method used for the GRO-seq metagene profiles. There was no need for further normalization in these profiles because we also normalized to array input, thereby controlling for copy number.

Individual gene profiles (Fig. 2b and Supplementary Figs 4–6) were computed in a similar manner to the metagene profiles, only no scaling was performed and a 100-bp sliding window was used to smooth the reads instead of Gaussian smoothing. As before, read density was normalized to total sequencing depth and for copy number using genomic sequencing reads as in the GRO-seq metagene profile calculations.

The control/MSL2 RNAi log ratio metagene plot (Fig. 4a) was produced by taking the log ratio of the Gaussian-smoothed read densities in MSL2 RNAi and control samples across the body of each gene. The log ratios (base 2) were computed for each gene before scaling (with pseudocount of 1) and then averaged across genes (thus, this ratio is not simply the ratio of the profiles in Fig. 3a). Overall, higher values in Fig. 4a represent a greater drop in the GRO-seq signal after MSL2 RNAi treatment.

Computing the PI and EdI. To compare the level of RNAP II at the 5' ends of genes compared with that progressing into gene bodies, we defined a 'pausing index' (PI) as the ratio of 5' GRO-seq read density within the first 500 bp downstream of the TSS to the read density within the next 25% of the gene body. The 5' read density is calculated as the number of sense-strand reads in the 5' region divided by the number of uniquely mappable positions (as determined using PeakSeq²⁸) in this same region. A position is 'mappable' if, given only the 36 bp sequence at that position, the position in the genome can be uniquely identified. Correcting for mappablity in this manner prevents regions that have no reads because they are unmappable from biasing the analysis. A similar calculation is performed to determine the density in the next 25% of the gene. A high PI indicates that RNAP II is biased towards the 5' end.

To analyse the distribution of active RNAP II within a given gene, we calculated an 'elongation density index' (EdI) by taking the ratio of the 3' read density to the 5' read density. The first 500 bp of the gene is excluded from this calculation to eliminate the effect of the large 5' peak frequently associated with paused polymerase. The remainder of the gene is then split into two portions, the 5' region and the 3' region. We state the main results with the 5' region containing the first 25% of the gene (after the first 500 bp) and the 3' region the remaining 75%, but multiple points of division were tested (Supplementary Table 1). The 3' density is calculated as it was done above. A low EdI indicates that RNAP II is biased towards the 5' end, whereas a larger value indicates greater RNAP II towards the 3' end.



The gene set considered in the analysis of EdIs is similar to that used to produce the profile plots, except that no outliers were removed and only short genes less than 500 bp (instead of 2.5 kb) were excluded. These criteria were relaxed to make our analysis more conservative. To avoid outlier ratios that can result from a small number of reads, genes with fewer than 3 reads in the first 500 bp of the gene, the 5' region or in the 3' region were removed. A one-sided Wilcoxon test was used to test whether EdIs on the X chromosome are significantly greater than on autosomes in the untreated sample. To compare the elongation density indices for the MSL2 RNAi with the control RNAi, the same procedure was followed, except that only genes with an EdI defined in both samples were considered.

To determine whether removing outliers (as defined previously for the metagene profiles) alters our results, we compared EdI ratios (MSL2/control RNAi) with and without outlier removal. When outliers were removed, the shift in the distribution of EdI ratios on X relative to autosomes remained significant (P value $< 1 \times 10^{-15}$). Likewise, the difference between the EdI distribution on X relative to autosomes in the untreated sample remains significant after outlier removal (P value < 0.017 before removal, P value < 0.020 after outlier removal). Overall, outlier removal has little effect on the statistical significance of our EdI comparisons.

Comparing GRO-seq data with mRNA-seq. To compare our data with previous experiments⁹ that measured the effect of MSL2 RNAi on expression levels, we examined GRO-seq read densities before and after treatment with MSL2 RNAi.

Ratios of gene expression levels before and after MSL2 RNAi obtained by RNA-Seq experiments of were compared to analogous GRO-seq ratios. GRO-seq ratios were computed only from reads mapping to the gene bodies. The region extending from the TSS to 500 bp downstream was excluded from these calculations so that the 5′ peak around the TSS would not bias the results. Read densities for each gene with at least 10 reads in both the MSL2 RNAi data set and the control RNAi data set were normalized to data-set size, and then a ratio was computed. The Pearson correlation coefficient between GRO-seq ratios and those derived from RNA-seq is highly significant (P value $< 1 \times 10^{-15}$), but with relatively low absolute magnitude (R = 0.30). If only X-linked genes are considered, the Pearson correlation remains unchanged (R = 0.30) and is still highly significant (P value $< 1 \times 10^{-15}$). When a similar comparison was performed between GRO-seq ratios and expression array data, a significant Pearson correlation of R = 0.22 was observed (P value $< 1 \times 10^{-15}$).

- 26. Langmead, B., Trapnell, C., Pop, M. & Salzberg, S. L. Ultrafast and memory-efficient alignment of short DNA sequences to the human genome. *Genome Biol.* **10**, R25 (2009)
- Nechaev, S. et al. Global analysis of short RNAs reveals widespread promoterproximal stalling and arrest of Pol II in *Drosophila*. Science 327, 335–338 (2010).
- Rozowsky, J. et al. PeakSeq enables systematic scoring of ChIP-seq experiments relative to controls. Nature Biotechnol. 27, 66–75 (2009).



The RAG2 C terminus suppresses genomic instability and lymphomagenesis

Ludovic Deriano¹, Julie Chaumeil¹, Marc Coussens¹, Asha Multani², YiFan Chou¹, Alexander V. Alekseyenko³, Sandy Chang⁴, Jane A. Skok^{1,5} & David B. Roth¹

Misrepair of DNA double-strand breaks produced by the V(D)I recombinase (the RAG1/RAG2 proteins) at immunoglobulin (Ig) and T cell receptor (Tcr) loci has been implicated in pathogenesis of lymphoid malignancies in humans¹ and in mice²⁻⁷. Defects in DNA damage response factors such as ataxia telangiectasia mutated (ATM) protein and combined deficiencies in classical non-homologous end joining and p53 predispose to RAG-initiated genomic rearrangements and lymphomagenesis²⁻¹¹. Although we showed previously that RAG1/RAG2 shepherd the broken DNA ends to classical nonhomologous end joining for proper repair^{12,13}, roles for the RAG proteins in preserving genomic stability remain poorly defined. Here we show that the RAG2 carboxy (C) terminus, although dispensable for recombination^{14,15}, is critical for maintaining genomic stability. Thymocytes from 'core' Rag2 homozygotes (Rag2^{c/c} mice) show dramatic disruption of $Tcr\alpha/\delta$ locus integrity. Furthermore, all $Rag2^{c/c} p53^{-/-}$ mice, unlike $Rag1^{c/c} p53^{-/-}$ and $p53^{-/-}$ animals, rapidly develop thymic lymphomas bearing complex chromosomal translocations, amplifications and deletions involving the $Tcr\alpha/\delta$ and Igh loci. We also find these features in lymphomas from Atm^{-/-} mice. We show that, like ATM-deficiency³, core RAG2 severely destabilizes the RAG post-cleavage complex. These results reveal a novel genome guardian role for RAG2 and suggest that similar 'end release/ end persistence' mechanisms underlie genomic instability and lymphomagenesis in $Rag2^{c/c} p53^{-/-}$ and $Atm^{-/-}$ mice.

RAG mutations can cause specific defects in the joining stage of V(D)J recombination 12,13,16 . The 'dispensable' RAG2 C terminus (murine amino acids 1-383) is of particular interest: loss of the RAG2 C terminus impairs joining of substrates 17 , increases levels of double-strand breaks 17 that persist through the cell cycle 18 , and increases accessibility of the broken DNA ends to alternative non-homologous end joining 12,19 . Despite these defects, $Rag2^{c/c}$ mice are not lymphoma-prone. We reasoned that $Rag2^{c/c}$ $p53^{-/-}$ double-mutant mice might dis-

play genomic instability and lymphomagenesis, even in the context of intact classical non-homologous end joining. Consistent with previous reports¹⁵, our Rag2^{c/c} mice displayed partial developmental blocks in B and T lymphopoiesis because of a selective V-to-DJ rearrangement defect (Supplementary Fig. 1). Rag2^{c/c} animals, observed for up to 1 year, showed no obvious signs of tumorigenesis (Fig. 1a and data not shown). As expected²⁰, approximately two-thirds of $p53^{-/-}$ mice developed thymic lymphoma at an average age of approximately 23 weeks (mean survival = 22.8 weeks) (Fig. 1a, b). Similar findings in RAG/p53-deficient mice²¹ demonstrate that RAG-initiated doublestrand breaks are not critical initiators of lymphomagenesis in p53deficient mice. In sharp contrast, 100% (n = 25) of our $Rag2^{c/c}$ $p53^{-/-}$ mice died within 16 weeks (mean survival = 12.1 weeks) with aggressive thymic lymphomas (Fig. 1a-c). Tumour cells were highly proliferative and expressed cell surface CD4 and CD8 (Supplementary Fig. 2), with little or no surface TCR (CD3ε or TCRβ) (data not shown), indicating that these tumours originate from immature thymocytes.

Tumours with highly proliferating lymphoblasts were detected in 4- to 6-week-old $Rag2^{c/c}$ $p53^{-/-}$ thymi, but not in other organs (data not shown), confirming their thymic origin. $Rag2^{c/c}$ $p53^{-/-}$ tumours generally displayed one or a few predominant D β 1–J β 1 or D β 2–J β 2 rearrangements, indicating a clonal or oligoclonal origin (Supplementary Fig. 3).

We next examined genomic stability in lymphomas from $Rag2^{c/c}$ $p53^{-/-}$ mice, first by analysis of Giemsa-stained metaphase spreads prepared from 12 $Rag2^{c/c}$ $p53^{-/-}$ and two $p53^{-/-}$ thymic lymphomas (Supplementary Table 1). Wild-type thymocytes showed almost no abnormal metaphases (0–3%) (Supplementary Table 1). In contrast, $p53^{-/-}$ and $Rag2^{c/c}$ $p53^{-/-}$ tumours harboured a variety of cytogenetic aberrations (aberrant metaphases: 8–94%), including aneuploidy, chromosome breaks and chromosome fusions (Supplementary Table 1). We

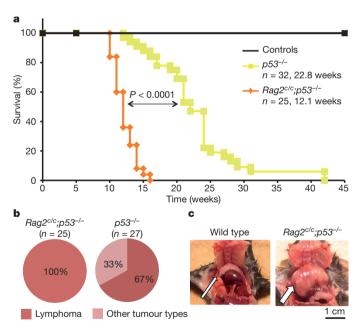


Figure 1 | The C terminus of RAG2 is a tumour suppressor in developing thymocytes. a, Kaplan–Meier tumour-free survival analysis for cohorts of control (wild type, n=12; $Rag2^{c/c}$, n=19), $p53^{-/-}$ (n=32) and $Rag2^{c/c}$ $p53^{-/-}$ (n=25) mice. Animals were monitored for 50 weeks. The average age of death in weeks is shown for $p53^{-/-}$ (22.8 weeks) and $Rag2^{c/c}$ $p53^{-/-}$ (12.1 weeks) genotypes with the P value determined by a Wilcoxon rank sum test. b, Tumour spectrum observed for $Rag2^{c/c}$ $p53^{-/-}$ (n=25) and $p53^{-/-}$ mice (n=27). All $Rag2^{c/c}$ $p53^{-/-}$ animals (n=25) showed enlarged thymus. $p53^{-/-}$ animals showed either enlarged thymus and/or spleen (n=18) or other non-lymphoid tumour mass (n=9). c, Physical appearance of normal thymus (wild type) and thymic lymphoma ($Rag2^{c/c}$ $p53^{-/-}$, arrow) of 3-month-old animals.

¹Department of Pathology, New York University School of Medicine, New York, NY 10016, USA. ²Department of Genetics, The M.D. Anderson Cancer Center, Houston, TX 77030, USA. ³Department of Medicine, Division of Clinical Pharmacology, Center for Health Informatics and Bioinformatics, New York University School of Medicine, NY 10016, USA. ⁴Department of Laboratory Medicine, Yale University School of Medicine, New Haven, CT 06520, USA. ⁵Department of Immunology and Molecular Pathology, Division of Infection and Immunity, University College London, London W1T 4JF, UK.

analysed three $Rag2^{c/c}$ $p53^{-/-}$ thymic lymphomas using spectral (1790T and 1745T) and G-band (1779T) karyotyping (Fig. 2). We observed recurrent translocations involving chromosomes that harbour Tcr (chromosomes 14 and 6) and Ig (chromosomes 12, 6 and 16) loci, suggesting that these might have been initiated by RAG-generated breaks. Moreover, all three lymphomas harboured translocations of the Igh locus-containing chromosome 12 and/or the $Tcr\alpha/\delta$ locus-containing chromosome 14, loci that rearrange in thymocytes²². Analysis of lymphoma 1779T revealed a C12;14 translocation (Fig. 2). These results suggest that $Rag2^{c/c}$ $p53^{-/-}$ T cell tumours harbour clonal translocations involving the $Tcr\alpha/\delta$ and Igh loci, as seen in T-cell lymphomas from patients with ataxia–telangiectasia and $Atm^{-/-}$ mice $^{7.8,10,11}$, rearrangements not observed in $p53^{-/-}$ lymphomas 21,23 .

To confirm the involvement of the $Tcr\alpha/\delta$ locus in chromosome translocations, we performed DNA fluorescence in situ hybridization (DNA FISH) analyses on metaphases from $Rag2^{c/c}$ $p53^{-/-}$ thymic lymphomas (2489T and 2805T) using probes centromeric ($Tcr\alpha/\delta$ V) and telomeric ($Tcr\alpha/\delta$ C) to the $Tcr\alpha/\delta$ locus plus a paint for chromosome 14 (Fig. 3a). In both tumours, breakpoints within the $Tcr\alpha/\delta$ locus of one of the two chromosomes 14 resulted in amplification of the $Tcr\alpha/\delta$ V region (Fig. 3a). The telomeric fragment (including $Tcr\alpha/\delta$ V) was either translocated (2489T), or lost (2805T) (Fig. 3a). DNA FISH analysis of tumours 1790T and 1779T (from Fig. 2) using $Tcr\alpha/\delta$ V and V probes also confirmed translocation of chromosome 14 with breakpoints within the $Tcr\alpha/\delta$ locus, although without obvious amplification (Supplementary Fig. 4).

We next performed DNA FISH on $Rag2^{c/c}$ $p53^{-/-}$ thymic lymphomas 2489T and 2805T using probes centromeric ($Igh\ C$) and telomeric ($Igh\ V$) to the Igh locus along with a chromosome 12 paint (Fig. 3b). In both lymphomas, one chromosome 12 showed translocation with another chromosome, with accompanying loss of both $Igh\ C$ and V signals (Fig. 3b). This could result from RAG-induced breaks with loss of the telomeric end of the chromosome (including $Igh\ V$) and loss of the $Igh\ C$ region by end degradation before fusion to the partner chromosome, as previously reported in $Atm^{-/-}$ mouse T cells⁸.

Moreover, dual chromosome 12 and 14 paint analysis showed a C12;14 translocation in lymphoma 2489T (Fig. 3b). In contrast to $Rag2^{c/c}$ $p53^{-/-}$ lymphomas, DNA FISH on metaphases from one $p53^{-/-}$ thymic lymphoma (6960T) indicated that both $Tcr\alpha/\delta$ and Igh loci were intact (Supplementary Fig. 5), consistent with previous work²¹.

We next performed array-based comparative genomic hybridization (a-CGH) analysis on genomic DNA from five Rag2^{c/c} p53^{-/} thymic lymphomas (2489T, 2805T, 1348T, 1779T, 1780T). We observed loss or gain of a region within the $Tcr\alpha/\delta$ and Igh loci, reflecting V(D)J recombination (Supplementary Fig. 6). All five Rag2^{c/c} p53^{-/-} lymphomas examined showed substantial amplification of a common region on chromosome 14, centromeric of the $Tcr\alpha/\delta$ locus (Supplementary Fig. 6a), in agreement with our FISH analyses (Fig. 3a). We also observed loss of a common region on chromosome 12, telomeric of the *Igh* locus in all five $Rag2^{c/c}p53^{-/-}$ thymic lymphomas analysed (Supplementary Fig. 6b). Tumours 1779T, 2489T and 2805 also showed loss of a large region centromeric of the Igh locus, probably reflecting DNA-end degradation before fusion to the partner chromosome (Figs 2 and 3a, b and Supplementary Fig. 6b). In contrast, aCGH analysis of p53^{-/-} thymic lymphoma 6960T failed to reveal amplification centromeric to the $Tcr\alpha/\delta$ locus or deletion telomeric to the Igh locus (Supplementary Fig. 7a, b), in agreement with our FISH analysis (Supplementary Fig. 5) and previous data²³.

Blocking lymphocyte development in early stages can lead to persistent RAG activity, which, in the absence of p53, can provoke lymphomagenesis²³. To investigate whether the partial developmental block in $Rag2^{c/c}$ thymocytes¹⁵ is sufficient to produce genomic instability and lymphomagenesis, we crossed *core Rag1* knock-in animals, which display diminished recombination and a strong block in B- and T-cell development^{14,24} (Supplementary Fig. 1), into a p53-deficient background. $Rag1^{c/c}$ $p53^{-/-}$ mice survived at an average age of 18.7 weeks (Supplementary Fig. 8a), barely distinguishable from $p53^{-/-}$ mice. Also like $p53^{-/-}$ mice, only two-thirds of $Rag1^{c/c}$ $p53^{-/-}$ mice developed thymic lymphomas (Supplementary Fig. 8b).

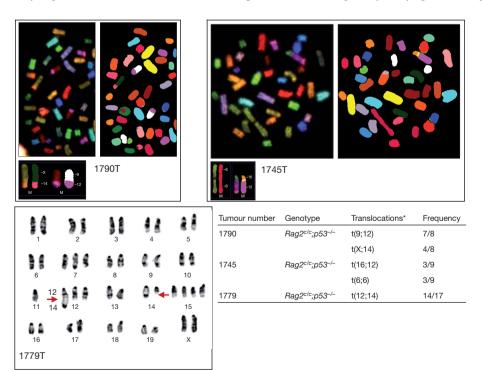


Figure 2 | $Rag2^{c/c}$ $p53^{-/-}$ thymic lymphomas display recurrent translocations involving chromosomes that harbour antigen-receptor loci. Representative images of spectral karyotyping (1790T and 1745T) and G-band karyotyping (1779T) analysis of three $Rag2^{c/c}$ $p53^{-/-}$ T cell lymphomas.

Metaphase number analysed and translocations for each tumour sample are listed in the table. All three tumours harbour clonal translocations involving chromosomes that carry Tcr (chromosome 14, $Tcr\alpha/\delta$; chromosome 6, $Tcr\beta$) and/or Ig (chromosome 12, Igh; chromosome 6, $Ig\kappa$; chromosome 16, $Ig\lambda$) loci.

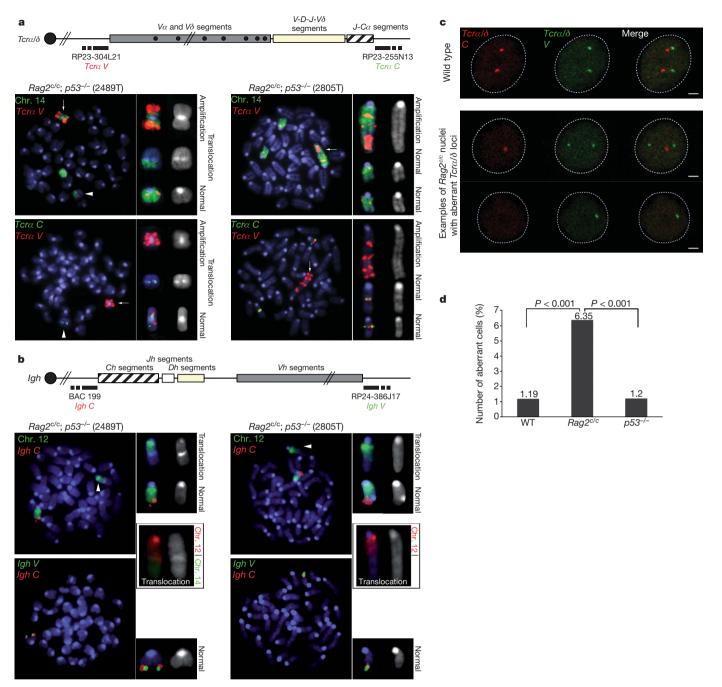


Figure 3 | $Rag2^{c/c} p53^{-/-}$ thymocytes display $Tcr\alpha/\delta$ - and Igh-associated genomic instability. a, Top panel: schematic of the $Tcr\alpha/\delta$ locus, with positions of the BACs used for generation of DNA FISH probes indicated. Bottom panels: representative metaphases from two $Rag2^{c/c} p53^{-/-}$ thymic lymphomas using the $Tcr\alpha/\delta$ V BAC probe (red signal) combined with chromosome 14 paint (green signal, top row) or with the $Tcr\alpha/\delta$ C BAC probe (green signal, bottom row). Arrows point to the amplification of the $Tcr\alpha/\delta$ V region, arrowheads point to the translocated chromosome 14. b, Top panel: schematic of the Igh locus, with positions of the BACs used for generation of DNA FISH probes indicated. Bottom panels: representative metaphases from the same two $Rag2^{c/c}$ $p53^{-/-}$ thymic lymphomas using the Igh C BAC probe

Furthermore, metaphase DNA FISH analyses on two $Rag1^{c/c}$ $p53^{-/-}$ thymic lymphomas (8383T and 8411T) (Supplementary Fig. 9) and aCGH analysis on genomic DNA from four $Rag1^{c/c}$ $p53^{-/-}$ thymic lymphomas (8315T, 8333T, 8383T, 8411T) (Supplementary Fig. 10) showed no evidence of recurrent translocations, genomic amplification or genomic deletion at chromosome 14 and chromosome 12. The genomic instability observed in $Rag2^{c/c}$ $p53^{-/-}$ thymic lymphomas is

(red signal) combined with chromosome 12 paint (green signal, top row) or with the *Igh V* BAC probe (green signal, bottom row). Combination of chromosome 12 (red) and chromosome 14 (green) paints is shown for both tumours in black boxes. Arrowheads point to the translocated chromosome 12. **c**, Examples of confocal sections of three-dimensional $Tcr\alpha/\delta$ DNA FISH on freshly isolated wild-type (top row) or $Ragz^{c/c}$ (bottom rows) double-positive thymocytes. $Tcr\alpha/\delta$ V (green) and C (red) BAC probes were used. Scale bar, 1 μ m. **d**, Representative experiment showing the frequency at which $Tcr\alpha/\delta$ V and/or $Tcr\alpha/\delta$ C signals are lost in wild-type (WT), $p53^{-/-}$ and $Ragz^{c/c}$ thymocytes (n > 200; see Supplementary Fig. 11 for additional experiments and statistical analysis).

therefore associated specifically with loss of the RAG2 C terminus, and does not result from the developmental block in *core RAG2* homozygotes.

We next asked whether core RAG2 promotes genomic instability in the presence of p53 by using three-dimensional interphase DNA FISH to examine the integrity of $Tcr\alpha/\delta$ locus (Fig. 3c) in $Rag2^{c/c}$ double-positive thymocytes. The two alleles appeared as two pairs of signals $(Tcr\alpha/\delta\ V\ and\ Tcr\alpha/\delta\ C$, mapping the two ends of the locus) in most

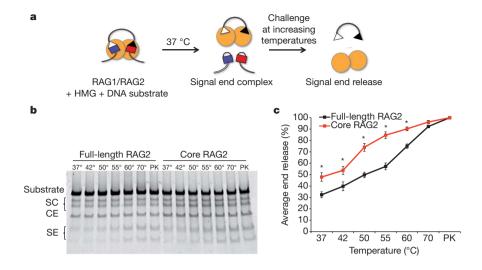


Figure 4 | The C terminus of RAG2 stabilizes the RAG post-cleavage complex. a, Biochemical end-release assay. Purified glutathione S-transferase (GST)-tagged core RAG1 and non-tagged RAG2 (full length or core) proteins (yellow circles) cleave a 500 base pair (bp) DNA substrate at 37 °C. Post-cleavage signal end complexes are thermally challenged at increasing temperatures to force the release of signal ends, which are detected after electrophoresis and gel staining. b, Representative gel for end-release assays.

Numbers above each lane indicate the temperatures (in degrees Celsius) the reactions were heated to before electrophoresis. CE, coding ends; SC, single cleavages; PK, samples treated with proteinase K and SDS. c, Quantification of signal end release, measured as the combined amount of signal ends divided by the signal from the total amount of DNA in the lane, from six experiments using two different protein preparations (*P < 0.05, Student's t-test).

(>98%) wild-type and $p53^{-/-}$ double-positive thymocytes (Fig. 3d and Supplementary Fig. 11), indicating that p53 deficiency alone does not disrupt the integrity of the $Tcr\alpha/\delta$ locus, as expected²⁵. In contrast, $Rag2^{c/c}$ double-positive thymocytes displayed a three- to fivefold increase in the number of cells showing loss of at least one signal (Fig. 3c, d and Supplementary Fig. 11). These results suggest that core RAG2 promotes genomic instability at the $Tcr\alpha/\delta$ locus, a phenotype similar to that previously reported in $Atm^{-/-}$ and $53bp1^{-/-}$ animals^{9,25}.

We noted that both $Rag2^{c/c}p53^{-/-}$ and $Atm^{-/-}$ mice feature RAGdependent genomic instability at the $Tcr\alpha/\delta$ and Igh loci, with development of pro-T cell lymphomas bearing clonal translocations, including 12/14 translocations^{2,3,7-11}. To determine whether $Atm^{-/-}$ lymphomas also harbour amplification close to the $Tcr\alpha/\delta$ locus, we performed DNA FISH analysis for $Tcr\alpha/\delta$ and chromosome 14 on metaphases from one $Atm^{-/-}$ thymic lymphoma (10375T) (Supplementary Fig. 12a). Both chromosomes 14 showed translocations with breakpoints within the $Tcr\alpha/\delta$ locus, and amplification of the $Tcr\alpha/\delta V$ region on one allele (Supplementary Fig. 12a), results that were confirmed by aCGH analysis (Supplementary Fig. 12b). We also observed loss of DNA at a distal region of chromosome 12, near the Igh locus (Supplementary Fig. 12b), as in Rag2^{c/c} p53^{-/-} lymphomas (Fig. 3 a, b and Supplementary Fig. 6). These data agree with recent analysis of thymic lymphomas from ATM-deficient mice7. Thymic lymphomas that arise in other mutant backgrounds such as p53, core RAG1/p53 (Supplementary Figs 8-10), Eβ/p53 or H2AX/p53 lack recurrent amplifications of chromosome 14 regions and/or recurrent chromosome 12/14 translocations, and thus appear to arise from distinct mechanisms.

Our data reveal a novel *in vivo* function for the RAG2 C terminus in promoting genomic stability. How does core RAG2 allow genomic instability? We hypothesized that core RAG2, like the absence of ATM³, destabilizes the post-cleavage complex. To investigate this, we generated RAG-signal end complexes by *in vitro* cleavage and challenged them at increasing temperatures, followed by gel electrophoresis (Fig. 4). Complexes containing full-length RAG2 did not release 50% of signal ends until 55 °C (Fig. 4b, c), as expected^{13,26}. In contrast, core RAG2-containing complexes displayed statistically significant instability at lower temperatures, with 50% end release at 37 °C (Fig. 4b, c). To examine the post-cleavage complex *in vivo*, we analysed

inversional recombination, which requires coordination of all four DNA ends. Decreased inversional recombination and increased formation of hybrid joints (generated by joining of a coding end to a signal end, in this case revealing defects in formation of four-ended inversion products) has been reported in ATM- and MRE11 complex-deficient cells^{3,27,28}. As expected^{3,28}, we observed increased hybrid joint formation at the $Ig\kappa$ locus ($V\kappa6-23$ to $J\kappa1$) in $Atm^{-/-}$ and $Nbs^{AB/AB}$ splenocytes (Supplementary Fig. 13). Importantly, we observed increased $V\kappa6-23$ -to- $J\kappa1$ hybrid joints in $Rag2^{e/c}$ splenocytes, compared with their wild-type and $Rag2^{e/c}$ counterparts (Supplementary Fig. 13). These results are supported by the observation that $Rag2^{e/c}$ lymphocytes exhibit defects in inversional recombination¹⁵. Together, these data support our hypothesis that core RAG2 impairs the stability of the RAG post-cleavage complex *in vitro* and *in vivo*.

Our data support a common model for genomic instability in $Rag2^{c/c} p53^{-/-}$ and $Atm^{-/-}$ mice: premature release of RAG-generated double-strand breaks from the RAG post-cleavage complex allows ends to escape the normal joining mechanisms, to persist and to be potentially joined by alternative non-homologous end joining, a pathway permissive for chromosome translocations and amplification 4.29. Both end release and end persistence are promoted by ATM deficiency 2.3, probably because ATM both stabilizes the RAG post-cleavage complex and activates p53-dependent checkpoints/apoptosis. In $Rag2^{c/c}$ $p53^{-/-}$ mice, end persistence might be augmented by ongoing RAG activity through the cell cycle resulting from impaired degradation of core RAG2, which lacks the cell-cycle-regulated degradation motif^{18,30}.

The complete penetrance, rapid development of lymphoma and extraordinary degree of RAG-mediated genomic instability make $Rag2^{c/c}p53^{-/-}$ mice an attractive model for investigating the spectrum of somatic genome rearrangements underlying lymphomagenesis.

METHODS SUMMARY

Mice. Mice were bred in the New York University Specific Pathogen Free facility; animal care was approved by the NYU SoM Animal Care and Use Committee (protocol number 090308-2).

Analysis of tumour cells. Lymphoid tumours were analysed by flow cytometry with antibodies against surface B- and T-cell markers. Metaphases were prepared and analysed as described in Methods.

FISH and image analysis. DNA FISH was performed using BAC probes as described in Methods. Interphase FISH was performed on double-positive



thymocytes isolated by cell sorting according to protocols described in Methods. Images were obtained by confocal microscopy on a Leica SP5 AOBS system, with optical sections separated by $0.3 \, \mu m$. Images were analysed using Image J software. Metaphase spreads were imaged by fluorescent microscopy on a Zeiss Imager Z2 Metasystems METAFER 3.8 system and analysed using ISIS software. Statistical analysis of image parameters used a two-tailed Fisher's exact test.

Biochemical end-release assay. The stability of RAG-signal end complexes was measured as described in Methods. Briefly, RAG cleavage reactions were divided into aliquots in microfuge tubes and incubated at the indicated temperatures for 30 min, followed by polyacrylamide gel electrophoresis. DNA was stained using SYBR Safe DNA Gel Stain (Invitrogen) and quantified with Quantity One software (Biorad). Student's t-test assuming equal variance was used to calculate statistical significance.

aCGH analysis. For CGH, genomic DNA from mouse thymic lymphomas was profiled against matched thymic DNA from wild-type mice. aCGH experiments were performed on two-colour Agilent 244A Mouse Genome Microarrays. Data analysis was performed as described in Methods.

Full Methods and any associated references are available in the online version of the paper at www.nature.com/nature.

Received 6 May; accepted 15 December 2010.

- Kuppers, R. & Dalla-Favera, R. Mechanisms of chromosomal translocations in B cell lymphomas. Oncogene 20, 5580-5594 (2001).
- Callen, E. et al. ATM prevents the persistence and propagation of chromosome breaks in lymphocytes. Cell 130, 63-75 (2007).
- Bredemeyer, A. L. et al. ATM stabilizes DNA double-strand-break complexes during V(D)J recombination. Nature 442, 466-470 (2006).
- Zhu, C. et al. Unrepaired DNA breaks in p53-deficient cells lead to oncogenic gene amplification subsequent to translocations. Cell 109, 811-821 (2002)
- Gao, Y. et al. Interplay of p53 and DNA-repair protein XRCC4 in tumorigenesis, genomic stability and development. Nature 404, 897-900 (2000).
- Difilippantonio, M. J. et al. DNA repair protein Ku80 suppresses chromosomal aberrations and malignant transformation. Nature 404, 510-514 (2000).
- 7. Zha, S. et al. ATM-deficient thymic lymphoma is associated with aberrant tcrd rearrangement and gene amplification. J. Exp. Med. 207, 1369–1380 (2010).
- Callen, E. et al. Chimeric IgH-TCR α / δ translocations in T lymphocytes mediated by RAG. Cell Cycle **8**, 2408–2412 (2009). 8.
- 9. Matei, I. R. et al. ATM deficiency disrupts Tcra locus integrity and the maturation of CD4+CD8+ thymocytes. Blood 109, 1887-1896 (2007).
- Liyanage, M. et al. Abnormal rearrangement within the α/δ T-cell receptor locus in lymphomas from Atm-deficient mice. Blood 96, 1940-1946 (2000).
- Barlow, C. et al. Atm-deficient mice: a paradigm of ataxia telangiectasia. Cell 86, 159-171 (1996).
- Corneo, B. et al. Rag mutations reveal robust alternative end joining. Nature 449, 483-486 (2007).
- Lee, G. S., Neiditch, M. B., Salus, S. S. & Roth, D. B. RAG proteins shepherd doublestrand breaks to a specific pathway, suppressing error-prone repair, but RAG nicking initiates homologous recombination. Cell 117, 171-184 (2004).
- Jones, J. M. & Simkus, C. The roles of the RAG1 and RAG2 "non-core" regions in V(D)J recombination and lymphocyte development. Arch. Immunol. Ther. Exp. (Warsz.) **57**, 105–116 (2009). Liang, H. E. *et al.* The "dispensable" portion of RAG2 is necessary for efficient V-to-
- DJ rearrangement during B and T cell development. Immunity 17, 639–651 (2002).
- Qiu, J. X., Kale, S. B., Yarnell Schultz, H. & Roth, D. B. Separation-of-function mutants reveal critical roles for RAG2 in both the cleavage and joining steps of V(D)J recombination. Mol. Cell 7, 77-87 (2001).

- 17. Steen, S. B., Han, J.-O., Mundy, C., Oettinger, M. A. & Roth, D. B. Roles of the "dispensable" portions of RAG-1 and RAG-2 in V(D)J recombination. Mol. Cell. Biol. 19, 3010-3017 (1999).
- 18. Curry, J. D. & Schlissel, M. S. RAG2's non-core domain contributes to the ordered regulation of V(D)J recombination, Nucleic Acids Res. 36, 5750-5762 (2008).
- Talukder, S. R., Dudley, D. D., Alt, F. W., Takahama, Y. & Akamatsu, Y. Increased frequency of aberrant V(D)J recombination products in core RAG-expressing mice. Nucleic Acids Res. 32, 4539-4549 (2004).
- 20. Jacks, T. et al. Tumor spectrum analysis in p53-mutant mice. Curr. Biol. 4, 1-7 (1994).
- 21. Liao, M. J. et al. No requirement for V(D)J recombination in p53-deficient thymic lymphoma. Mol. Cell. Biol. 18, 3495-3501 (1998).
- Forster, A., Hobart, M., Hengartner, H. & Rabbitts, T. H. An immunoglobulin heavychain gene is altered in two T-cell clones. Nature 286, 897-899 (1980).
- Haines, B. B. et al. Block of T cell development in P53-deficient mice accelerates development of lymphomas with characteristic RAG-dependent cytogenetic alterations. Cancer Cell 9, 109-120 (2006).
- 24. Dudley, D. D. et al. Impaired V(D)J recombination and lymphocyte development in core RAG1-expressing mice. J. Exp. Med. 198, 1439-1450 (2003).
- 25. Difilippantonio, S. et al. 53BP1 facilitates long-range DNA end-joining during V(D)J recombination. Nature 456, 529-533 (2008).
- 26. Arnal, S. M., Holub, A. J., Salus, S. S. & Roth, D. B. Non-consensus heptamer sequences destabilize the RAG post-cleavage complex, making ends available to alternative DNA repair pathways. Nucleic Acids Res. 38, 2944-2954 (2010).
- 27. Helmink, B. A. et al. MRN complex function in the repair of chromosomal Ragmediated DNA double-strand breaks. J. Exp. Med. 206, 669-679 (2009)
- 28. Deriano, L., Stracker, T. H., Baker, A., Petrini, J. H. & Roth, D. B. Roles for NBS1 in alternative nonhomologous end-joining of V(D)J recombination intermediates. Mol. Cell 34, 13-25 (2009).
- 29. Simsek, D. & Jasin, M. Alternative end-joining is suppressed by the canonical NHEJ component Xrcc4-ligase IV during chromosomal translocation formation. Nature Struct. Mol. Biol. 17, 410-416 (2010).
- Li, Z., Dordai, D. I., Lee, J. & Desiderio, S. A conserved degradation signal regulates RAG-2 accumulation during cell division and links V(D)J recombination to the cell cycle. Immunity 5, 575-589 (1996).

Supplementary Information is linked to the online version of the paper at www.nature.com/nature.

Acknowledgements We thank M. Schlissel for the gift of core Rag2 mice, F. Alt for the gift of core Rag1 mice and S. Hewitt for the Igh BAC probes. D.B.R. was supported by National Institutes of Health Roadmap Initiative in Nanomedicine through a Nanomedicine Development Center award (1PN2EY018244), a National Institutes of Health grant CA104588 and the Irene Diamond Fund. L.D. is a Fellow of The Leukemia and Lymphoma Society. A.V.A. was supported in part by grant 1UL1RR029893 from the National Center for Research Resources, National Institutes of Health. J.A.S. was supported by a National Institutes of Health grant R01GM086852, a National Institutes of Health Challenge grant NCI R01CA145746-01, a Leukemia and Lymphoma Scholar Award and a Wellcome trust project grant 085096.

Author Contributions L.D. and D.B.R. conceived the study and co-wrote the manuscript. L.D. designed the experiments. L.D., J.C., M.C. and A.M. performed the experiments. Y.C. provided assistance with the mouse colonies. A.V.A. performed the aCGH data analysis. J.A.S. and S.C. provided technical and conceptual support. J.C. and J.A.S revised the manuscript. All the authors read and approved the manuscript.

Author Information Reprints and permissions information is available at www.nature.com/reprints. The authors declare no competing financial interests. Readers are welcome to comment on the online version of this article at www.nature.com/nature. Correspondence and requests for materials should be addressed to D.B.R. (david.roth@nyumc.org).



METHODS

Mice. We obtained wild type (Taconic), $Rag2^{c/c15}$, $Rag1^{c/c24}$, $p53^{-/-}$ (Jackson laboratory²⁰) and $Atm^{-/-}$ (Jackson laboratory¹¹) mice for this study. $Rag2^{c/c}$ or $Rag1^{c/c}$ mice were bred with p53-deficient mice to generate doubly deficient mice. Genotyping of these mutants was performed by PCR of tail DNA as described in the relevant references^{11,15,20,24}.

Characterization of tumour cells and metaphase preparation. Lymphoid tumours were analysed by flow cytometry with antibodies against surface B-cell (CD43, B220, IgM) and T-cell (CD4, CD8, CD3, TCR- β) markers. FACS analysis used a BD LSRII flow cytometer (BD Biosciences) equipped with FacsDiVa and FlowJo. For metaphase preparation, tumour cells were prepared as previously described^{31,32}. Briefly, primary tumour cells were grown in complete RPMI media for 4h and exposed to colcemid (0.04 μ g ml $^{-1}$, GIBCO, KaryoMAX Colcemid Solution) for 2 hours at 37 °C. Then, cells were incubated in KCl 75 mM for 15 min at 37 °C, fixed in fixative solution (75% methanol/25% acetic acid) and washed three times in the fixative. Cell suspension was dropped onto pre-chilled glass slides and air-dried for further analysis.

G-banding and spectral karyotyping. Optimally aged slides were treated for the induction of G-banding following the routine procedure³³. Spectral karyotyping was performed using the mouse chromosome SKY probe Applied Spectral Imaging according to the manufacturer's instructions to determine chromosomal rearrangements in the tumour samples. The slides were analysed using a Nikon Eclipse 80i microscope. G-banding as well as SKY images were captured and karyotyped using an Applied Spectral Imaging system.

DNA FISH probes. BAC probes for the Igh and $Tcr\alpha/\delta$ loci were labelled by nick-translation and prepared as previously described^{34,35}. For the Igh locus, BAC 199 (Igh C) and BAC RP24-386J17 (Igh V) were labelled in Alexa Fluor 594 and 488 respectively (Molecular Probes). For the $Tcr\alpha/\delta$ locus, BAC RP23-304L21 ($Tcr\alpha/\delta$ V) and RP-23 255N13 ($Tcr\alpha/\delta$ C) were labelled in Alexa Fluor 488 or 594. StarFISH-concentrated mouse FITC or Cy3 chromosome 12 or 14 paints were prepared following supplier's instructions (Cambio). BAC probes were re-suspended in hybridization buffer (10% dextran sulphate, 5× Denharts solution, 50% formamide) or in paint hyb buffer, denatured for 5 min at 95 °C and pre-annealed for 45 min at 37 °C before hybridization on cells.

DNA FISH on metaphase spreads. Slides were dehydrated in ethanol series, denatured in 70% formamide / $2\times$ SSC (pH 7–7.4) for 1 min 30 s at 75 °C, dehydrated again in cold ethanol series, and hybridized with probes o/n at 37 °C in a humid chamber. Slides were then washed twice in 50% formamide / $2\times$ SSC and twice in $2\times$ SSC for 5 min at 37 °C each. Finally, cells were mounted in ProLong Gold (Invitrogen) containing 4′,6-diamidino-2-phenylindole (DAPI) to counterstain total DNA.

DNA FISH on interphase nuclei. Double-positive thymocytes were isolated from total thymi on a Beckman-Coulter MoFlo cell sorter as $Thy1.2^+CD4^+CD8^+$ cells using the following antibodies: PE-Cy7-coupled anti-CD90.2 (Thy1.2; 53-2.1), APC-coupled anti-CD4 (L3T4) and FITC-coupled anti-CD8 (53-6.7). Cells were washed two times in $1\times PBS$ and dropped onto poly-L-lysine-coated coverslips.

For three-dimensional DNA FISH analyses, we used a protocol for immunofluorescence / DNA FISH previously described 34,35 , with protein detection step omitted. Briefly, cells were fixed in 2% paraformaldehyde / 1× PBS for 10 min at room temperature, permeabilized in 0.4% Triton / 1× PBS for 5 min on ice, incubated with 0.01 mg ml $^{-1}$ Rnase A for 1 h at 37 $^{\circ}$ C and permeabilized again in 0.7% Triton / 0.1M HCl for 10 min on ice. Cells were then denatured in 1.9 M HCl for 30 min at room temperature, rinsed in cold 1× PBS and hybridized overnight with probes at 37 $^{\circ}$ C in a humid chamber. Cells were then rinsed in 2× SSC at 37 $^{\circ}$ C, 2× SCC at room temperature and 1× SSC at RT, 30 min each. Finally, cells were mounted in ProLong Gold (Invitrogen) containing DAPI to counterstain total DNA.

Biochemical end-release assay. End-release assay to measure the stability of the signal-end complexes was performed as previously described²⁶. For RAG-mediated cleavage, 100 ng of recombination substrate (PCR product from pJH289) was incubated for 3 h at 37 °C with 200 ng purified RAG protein and 200 ng of purified recombinant HMGB1 in a buffer containing 50 mM HEPES (pH 8.0), 25 mM KCl, 4 mM NaCl, 1 mM DTT, 0.1 mg BSA, 5 mM CaCl₂ and 5 mM MgCl₂. Reactions were then divided into aliquots in microfuge tubes and incubated at different temperatures, or treated with stop buffer (10 mM Tris (pH 8.0), 10 mM EDTA, 0.2% SDS, 0.35 mg ml⁻¹ proteinase K (Sigma Aldrich)) for 30 min and then run out on 4–20% acrylamide tris-borate-EDTA (TBE) gels (Invitrogen).

aCGH analysis. aCGH experiments were performed on two-colour Agilent 244A Mouse Genome Microarray. After internal Agilent quality control, the collected data were background subtracted and normalized using the Loess method³⁶. We used circular binary segmentation method to define regions of copy number alteration compared with the control³⁷ and applied the cghMCR method for extraction of altered minimum common regions between the samples³⁸. The analyses and visualizations were performed using the R statistical program³⁹.

- 31. Theunissen, J. W. & Petrini, J. H. Methods for studying the cellular response to DNA damage: influence of the Mre11 complex on chromosome metabolism. *Methods Enzymol.* **409**, 251–284 (2006).
- 32. Multani, A. S. et al. Caspase-dependent apoptosis induced by telomere cleavage and TRF2 loss. *Neoplasia* **2**, 339–345 (2000).
- 33. Pathak, S. Chromosome banding techniques. J. Reprod. Med. 17, 25-28 (1976).
- Hewitt, S. L. et al. RAG-1 and ATM coordinate monoallelic recombination and nuclear positioning of immunoglobulin loci. Nature Immunol. 10, 655–664 (2009).
- 35. Skok, J. A. et al. Reversible contraction by looping of the Tcra and Tcrb loci in rearranging thymocytes. *Nature Immunol.* **8**, 378–387 (2007).
- Yang, Y. H. et al. Normalization for cDNA microarray data: a robust composite method addressing single and multiple slide systematic variation. *Nucleic Acids Res.* 30, e15 (2002).
- Olshen, A. B., Venkatraman, E. S., Lucito, R. & Wigler, M. Circular binary segmentation for the analysis of array-based DNA copy number data. *Biostatistics* 5, 557–572 (2004).
- 38. Aguirre, A. J. et al. High-resolution characterization of the pancreatic
- adenocarcinoma genome. Proc. Natl Acad. Sci. USA 101, 9067–9072 (2004).
 R. development Core Team. R: A Language and Environment for Statistical Computing. Vienna: R Foundation for Statistical Computing (2006).

CORRECTIONS & AMENDMENTS

CORRIGENDUM

doi:10.1038/nature09804

Growth of graphene from solid carbon sources

Zhengzong Sun, Zheng Yan, Jun Yao, Elvira Beitler, Yu Zhu & James M. Tour

Nature 468, 549-552 (2010)

In this Letter, the assigned values for melamine XPS signals of 284.5 eV (C 1s) and 395.8 eV (N 1s) were incorrect (Supplementary Fig. 7). Repeating the melamine spectrum with a graphite additive standard (C 1s = 284.5 eV) showed that the assignments for melamine should be 286.8 eV (C1s) with N 1s in the ring at 397.8 eV and N 1s external to the ring at 398.7 eV. Therefore, the monolayer N-doped graphene on SiO₂ substrates having signals of 284.5 eV (C1s) and 399.8 eV (N 1s) remains clearly distinguished from the melamine starting material. Furthermore, the Li et al.1 (ref. 29 in this Letter) assignment for quaternary N was misquoted. Although high-temperature (1,000 °C) growth favours quaternary N in the N-doped graphene film (this is supported by ref. 1), our assignment of 399.8 eV (N 1s) for monolayer N-doped graphene is different from the Li et al.1 assignment, because their assignment of 401 eV (N 1s) is for thick N-doped graphene films. In our experiments, when we used poly(ethylene imine) as a growth source, multilayer N-doped graphene was attained and similarly gave 401.2 eV (N 1s) as the assignment. Therefore, either there is a difference between the thick film assignments of Li et al.1 and our assignment of monolayer N-doped graphene on SiO2 substrates, or the N signals in our material are more pyridinic and/or pyrrolic in content². We thank T. Susi for bringing this to our attention.

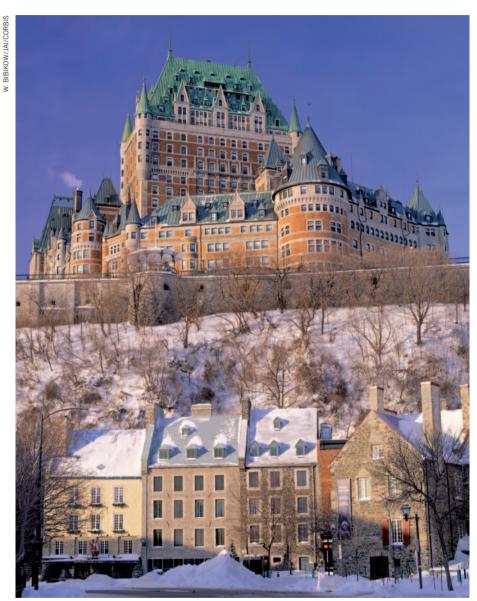
- Li, X. et al. Simultaneous nitrogen doping and reduction of graphene oxide. J. Am. Chem. Soc. 131, 15939–15944 (2009).
- Pels, J. R., Kapteijn, F., Moulijn, J. A., Zhu, Q. & Thomas, K. M. Evolution of nitrogen functionalities in carbonaceous materials during pyrolysis. *Carbon* 33, 1641–1653 (1995).

CAREERS

TURNING POINT An interest in mycology leads to a focus on bioenergy **p.127**

EUROPE Universities seek the right to pursue new income sources **p.127**

NATUREJOBS For the latest career listings and advice www.naturejobs.com



The Frontenac Hotel in Quebec City. The city hosts part of Quebec's optics and photonics research cluster.

DECIONS

Quebec's research ambitions

Some science fields in Canada's second most-populous province are booming; others are stagnating.

BY HANNAH HOAG

The Pavilion of Optics and Photonics at Laval University in Quebec City, Canada, resembles other university construction projects of recent years: grey, boxy and modernist. Yet, despite its sober design, the facility is one of the main reasons that physicist Younès Messaddeq moved to the area from Brazil last year. The 5,000-square-metre building, which opened in 2006, is devoted to the development and testing of lenses, optical coatings and fibre optics made of silica and exotic glasses. The building's design minimizes dust contamination, isolates the laboratories from vibration and controls temperature and humidity. Messaddeq says that the facility's participation in Quebec province's multi-institutional Centre for Optics, Photonics and Lasers (COPL) — the largest optics and photonics university research centre in Canada — as well as its modern equipment and laboratories, the depth and breadth of technical expertise among its employees and its close ties with the local photonics industry will allow him to develop complex optical devices quickly. "I've worked around the world and I've never seen a facility like this," he says.

Messaddeq took up his position as a professor of physics and optics at Laval after unemployment in Quebec peaked at 9.1% in late summer 2009. In another field, the timing might have been unfortunate, with industry partners hurting. But Quebec's photonics sector has fared well throughout the economic downturn, and still offers career opportunities in both industry and academia. By contrast, biomedicine in the province has partially withered, with parts of the biopharmaceutical sector shrinking and laying off workers, but bright spots remaining in areas such as genomics, proteomics and medical imaging. Even so, tax incentives, targeted research funding, infrastructure investments and a solid industry presence make Quebec a destination for many young scientists, including foreigners — especially those willing to embrace a new culture and possibly a new language.

PHOTONICS LEGACY

For decades, academic and industrial institutions in Quebec have excelled in optics and photonics, specializing in defence and telecommunication and expanding into remote-sensing and biophotonics. According to a 2009 survey by the Canadian Photonics Consortium, 104 photonics companies and 4,750 employees generated Can\$600 million (US\$609 million) in revenue. It's the

second-largest research and development photonics cluster in Canada — beaten only by Ontario, which has 117 companies, 10,200 employees and Can\$3 billion in revenue, notes Michel Têtu, chief executive of the Quebec Photonic Network in Montreal.

Large and small companies in the Quebec City region are all actively looking for research scientists with graduate degrees in laser photonics, chemistry or material sciences. Fernand Sylvain, co-founder and vice-president of operations at CorActive, a Quebec company that manufactures speciality fibres, says that his firm has grown by about 10% a year, even during the recession, generally hiring a scientist and two technicians each year. He hopes to have hired five more employees by the end of 2011. André Fougères, director of programme management at the National Optics Institute (INO), a design and development company, says that it employs 240 people and plans to double in size by 2016. Fougères says that the INO is looking for scientists with backgrounds in microfabrication and biophotonics. "But we're really looking for people who are application driven," he says. "They have to be willing to take risks, to jump on a project without all the details. They have to be entrepreneurial."

The high concentration of companies makes Quebec a good place for technology transfer, says Messaddeq. The Pavilion of Optics and Photonics is the administrative centre for the Canadian Institute for Photonics Innovations, a network of centres of excellence that brings together university, government and industry researchers. Messaddeq, whose research focuses on laser technologies, hopes to launch spin-off companies and technologies in the next five years, based on either university research or collaborations with the INO.

Messaddeq came to Laval through the first round of the Canada Excellence Research Chairs (CERC) programme. An initiative of Canada's three major federal funding agencies, the programme grants universities Can\$1.4 million a year for seven years for each chair that it supports. Of the 19 CERCs awarded in 2010, three went to universities in Quebec. The next competition will be announced in 2015.

Federally funded programmes such as the CERC and the Canada Research Chairs programme, which the government started in 2000 and which grants Can\$300 million a year, aim to attract and retain "the world's most accomplished and promising minds", and have been key to bringing early- and mid-career scientists to Quebec. Of the 1,845 CRCs awarded by November 2010, 30% went to academics recruited from outside Canada, including expatriates, and 20% were awarded to health, natural-science and engineering researchers at Quebec universities. Postdoctoral fellows have several possible sources of income, including federal and provincial funding agencies and the prestigious Banting Postdoctoral Fellowships, worth Can\$70,000 a year for two years, for Canadian and international researchers. "It would be harder to recruit top-notch researchers to Quebec without these programmes," says Paul Fortier, vice-rector of research and innovation at Laval

BIOTECH STUMBLING BLOCKS

The biopharmaceutical industry has long been a staple of Quebec's science community, but it hasn't fared as well as optics and photonics. Clusters of pharmaceutical and biotechnology companies, including spin-offs and multinationals, have assembled around Montreal. As of 2010, Quebec hosts 150 pharmaceutical, contract research and biotechnology companies, and about 18,600 people are employed in the field. Many companies set up in the province because of competitive tax incentives for companies and tax holidays for foreign researchers — a five-year tax break on 75% of their personal income while they participate in research and development activities at a corporation.

But in the past decade the industry has sagged. In 2001, Quebec had 110 health biotech research and development companies. By 2008, the latest date for which statistics are available, that number had dropped by almost half. Ven-



"You can have a curiositydriven career here, make a good living and do it all." David Colman

ture capital, which fuels such start-ups, has been drying up around the world, and Quebec is no exception. In Montreal, the most conspicuous loss was the closure of the Merck Frosst Centre for Therapeutic Research, a research lab for the pharmaceutical giant Merck. When the drug-maker closed the facility in July 2010, it laid off most of its nearly 200 employees.

These setbacks have come despite a decade in which Quebec

has developed a genomics research niche. Montreal's McGill University and Génome Québec Innovation Centre, a high-throughput research facility, opened in 2002, and has contributed to, among other things, the Hap-Map project, a study of genetic diversity. Last month, McGill repatriated Mark Lathrop, a biostatistician from the Center for the Study of Human Polymorphisms in Paris, to lead the centre. His appointment includes a Can\$5million budget that can be used to help recruit more scientists.

EARLY-CAREER OPPORTUNITIES

Despite niche opportunities, recruiting and retaining early-career scientists from non-Francophone countries remains a challenge. Only three of Quebec's universities teach mainly in English. Those who don't speak French can still find a spot at a French-speaking university, but may have to forgo a year or two of teaching until their language skills catch up. When Huixiang Xie, a marine chemist, was hired by the Institute of Marine Sciences in Rimouski soon after he finished his postdoc at the Woods Hole Oceanographic Institution in Massachusetts and the US Environmental Protection Agency, he didn't know any French. "Frankly, I wasn't worried about it. I'd learned English in China, and I thought learning French would be similar," he says. Even with a tutor, he struggled, but his colleagues and neighbours have helped him improve to the point where he can teach in French.

Concordia University in Montreal prepares graduate students and postdocs for work in Quebec by offering French-language training as part of a suite of professional-development workshops. "It provides highly qualified personnel with job-ready skills that allow them to move into the academic, private or public sector workforce," says Graham Carr, dean of graduate studies at Concordia. Further workshops are being planned in entrepreneurship, communication skills and research ethics.

A move to Quebec can also present a cultural adjustment. "My first night, I told myself, 'I can't do this. It's a different culture and a different country," recalls neuroscientist David Colman, recruited in 2002 to head the Montreal Neurological Institute and Hospital, known as the Neuro. "But by the third day, after I'd met with the researchers, I realized there were a lot of things I could do here that I couldn't do in New York," he says. Colman was lured from the Mount Sinai School of Medicine with the promise of launching a multimillion-dollar neuroengineering research programme and making a neuroscience IMAX movie for pre-teens.

Since Colman's arrival, the Neuro has hired 16 faculty members, mostly at the assistant and associate professor level, recalling Canadians from abroad and attracting many international scientists. The CRCs and the Canada Foundation for Innovation, an independent corporation in Ottawa, Ontario, created by the government to fund research infrastructure and recruit scientists, helped the Neuro to get the scientists it wanted, says Colman. It has also hired radiochemists, pathologists and positron emission tomography (PET) physicists, and will soon recruit a magnetoencephalographist to round out the expansion of the McConnell Brain Imaging Centre, which is doubling its size to 4,600 square metres and adding two magnetic resonance imaging scanners, a PET scanner and a magnetoencephalography system.

"The US funding environment and the falling success rates have made it easier for us to recruit from the United States," says Bruce Pike, the centre's director.

Colman recommends taking a chance on Quebec. "You can have a curiosity-driven career here, make a good living and do it all." ■

Hannah Hoag is a freelance writer in Montreal, Canada.

TURNING POINT Louise Glass

In January, Louise Glass, a microbiologist specializing in fungi at the University of California, Berkeley, was awarded a fellowship from the Adolph C. and Mary Sprague Miller Institute for Basic Research in Science, which offers opportunities for Berkeley faculty members and students to explore creative research projects.

Why did fungi captivate you?

They are weird and eclectic, with almost other-worldly life cycles that we simply don't understand very well. As a result, they are interesting organisms through which to explore fundamental biology.

Which fungal species do you work on?

Neurospora crassa, a filamentous fungus associated with a long history of biochemical and genetic laboratory techniques. It was the perfect organism for me to study because it married my interests in fungi with my aptitude for genetics. For 20 years, I've used it as a model system to understand cell signalling and communication.

Have you always aspired to be an academic scientist?

No. I studied mycology as an undergraduate at Colorado State University in Fort Collins. After college, I worked as a mycologist at the American Type Culture Collection, a non-profit biological resource centre in Manassas, Virginia. There, I had direct interactions with PhD scientists who encouraged me to continue my schooling. I didn't have any female role models as scientists, but, with continued encouragement from mentors, I ended up pursuing a PhD in plant pathology at the University of California, Davis.

How did you get interested in bioenergy?

It was an unexpected series of events. After my PhD I kept track of plant-degradation research. The Energy Biosciences Institute (EBI), a joint venture between the University of California, Berkeley, and energy company BP, formed on campus in 2007 and established a focus on Miscanthus, a tall perennial grass that is related to sugar cane — the crop in which most Neurospora isolates come from. Although little was known about Neurospora's ability to degrade plant cell walls, the EBI funded a proposal to genetically profile this fungus growing on Miscanthus. It has worked out well. We discovered several genes previously not known to be associated with cellwall degradation, and have helped industry



leaders to engineer a cheaper fermentation process yielding higher ethanol production.

What does the Miller award allow you to do?

It is difficult to take a sabbatical at Berkeley at present because our department will typically not fund a replacement lecturer for courses. The Miller award pays your salary to the department so that they can hire someone to teach your courses. I feel like I'm due a sabbatical, so this is a perfect time for a new project. I'm looking forward to the luxury of being able to give my undivided attention to this topic when my fellowship starts in 2012.

Do you consider the bioenergy research to be a career turning point?

Yes. I am now able to explore applications of my interests in the basic biology of filamentous fungi. Interestingly, a synergy is developing between the bioenergy work and other research in the lab. For example, we want to understand the cell-signalling pathways that allow *Neurospora* to regulate the secretions of enzymes that degrade plant cell walls.

What has been the biggest change in science during your career?

The pace. When I was a graduate student, a postdoc across the hall from me sequenced one kilobyte of DNA. We have just finished sequencing the 40-megabyte genome of 100 wild *Neurospora* isolates. In this day and age, it is so easy to get data. The advantage is being able to ask very elegant questions because you are not limited by data. But it is also easy to lose sight of the biological problem you are trying to address. That is the danger.

INTERVIEW BY VIRGINIA GEWIN

BIOINFORMATICS

UK data-project hiring

A pan-European biomolecular-data storage and access system based in Britain is to hire up to 100 bioinformaticians, biocurators and software developers from 2012. The European Life Science Infrastructure for Biological Information (ELIXIR) will standardize and boost the quality and quantity of genomics and systems-biology data. Funds will come from the UK Large Facilities Capital Fund, but ELIXIR's business plan must be approved by the UK Treasury, says Cath Brooksbank, head of outreach and training at the European Bioinformatics Institute (EBI) in Hinxton, UK, which coordinates ELIXIR. The EBI is seeking funding from the European Commission for recruitment and operation.

UNIVERSITIES

Academia feels crunch

US university presidents and executives had a median pay rise of 1.4% in 2010, less than the inflation rate of 1.6%, says a survey published on 21 February. The College and University Professional Association for Human Resources (CUPA-HR) in Knoxville, Tennessee, polled 1,256 institutions for its 'Administrative Compensation Survey Report'. Some 14% of heads of single-campus universities got a bonus in 2010. Respondents foresaw restricted hiring for 2011, with fewer than 1% expecting to fill "significantly more" posts than last year. Andy Brantley, head of CUPA-HR, says that private institutions are planning hires according to conservative predictions of enrolments and revenue, and public ones are struggling because of state governments' economic woes.

EUROPE

Rules restrict income

European governments must ease rules to let universities seek extra income, says a report released on 22 February. According to the European University Association (EUA) in Brussels, institutions face financial uncertainty as public funding shrinks. The group surveyed more than 150 universities across 27 nations; 61% said that regulations bar them from industry partnerships, spin-out opportunities and participation in European research programmes. Thomas Estermann, EUA head of governance, autonomy and funding, says that as universities find new revenue, early-career researchers must aggressively seek external funding.

GREEN FUTURE

But is it art?

BY DEBORAH WALKER

ev, Mrs M." Miriam ignores the boy. She pushes her way through the tangled undergrowth of Trafalgar Square, past the stone lions with their impassive eyes virtually obscured by their liana manes. She must remember to bring a pair of shears tomorrow.

"Hold on. Hold on." The boy skips through the waist-high vegetation. He'll catch her soon enough. He's a kid from the Bloomsbury favela, born and bred to London's jungle. His name is Crich, and he's been bothering Miriam for a couple of months. Rather than let him overtake her, Miriam

waits for him. Crich runs up. His smile gleams in his greenflecked face. Miriam's face is clean; she washes herself properly, every morning.

"Hey, Mrs M. What are you doing? You cleaning, again?"

"Yes, Crich. I'm cleaning, again. Somebody's got to do it."

Miriam has always been a cleaner. A long time ago, she'd worked in an office. Now, she has a more important cleaning job.

"You sure like cleaning."

"I do."

"Mama says that you should come home and live with us."

"Does she, indeed?"

Mama isn't his real mother. The favelas have developed their own customs. Mama is the head of Crich's tribe.

"Can I come with you, Mrs M?"

"Can I stop you?"

He grins. They cross the square and climb the steps of the National Gallery. Crich chats about the comings and goings of his tribe: a girl he likes; a cache of food tins the scouts had found squirrelled in a forgotten basement; a trade agreement with the Islington favela. Miriam thinks about which picture she should restore. She flicks through the catalogue of her mind and decides upon the Venus. When they reach the top of the stairs, Miriam pauses, to catch her breath.

"You alright, Mrs M?" asks Crich.

"I'm not as young as I used to be," says Miriam with a wry smile. She sighs and rubs her hip. "No rest for the wicked," she mutters. "Come on, young man, let's get going." She collects her cleaning equipment, which she keeps hidden behind the customer informa-

"Which picture, today?" asks Crich.

"Velázquez's Venus, it's on the ground

"I know the way," says Crich. He steps quickly though the gallery. Miriam follows him. She walks carefully, trying to minimize the pain in her hip. Miriam sighs when sees the family of green-black rats, chattering in the corner of the room. "Go on. Clear out of here." She snaps a tea-towel at the nest, and the rats scurry out of the gallery.

"There's good eating on those things," remarks Crich. Miriam ignores him. She places the folding table close to the Venus, and sets out the tray. She pours a quantity

of bleach solution into the tray and wets her cotton rag. Slowly, she applies the weakwater bleach to the old master and wipes away the film of algae. Slowly, the pink flesh of the reclining Venus is revealed.

"She sure is fat," says Crich.

"She is."

"But she's pretty."

"She's clean now." Miriam steps back to admire her work.

"Clean, but not for long," says Crich.

Miriam's work is done for the day. She will return home, and think about things. Think about things past.

"I want to show you something," says Crich. He takes a sheet of paper from his bag and hands it to Miriam.

Miriam stares at the green-brown image, an oval-shape of algae colonies, clustered onto the paper. It was a face, a

◇ NATURE.COM Follow Futures on Facebook at: go.nature.com/mtoodm smudge of red-bloom for a mouth, weaving tendrils for the hair.

"It's a picture of Mama," explains Crich.

"Did you make this, Crich?"

"Sure did. Everyone's making them. Mine's not so good, really. You should see some of the others." Miriam stares at the picture. Art out of algae.

"Mama doesn't like you out here, living by yourself," says Crich. "She says you should be with your family."

"I need to be close to the gallery."

"The thing about my picture, Mrs M, is that it grows. It changes. New colonies of air-borne algae adhere to the surface. That golden web of tendrils across her cheek wasn't there yesterday."

> Miriam hands the picture back to Crich. "I'm sure it's very nice, but I've never really cared for modern art." Miriam packs up her cleaning tools.

"You'll come home with me today," says Crich. It's a statement, not a question.

"But I've got to clean the paintings. Somebody's got to

"No, Mrs M. We've got our own art, now. You'll come home with us." He looks at her and grins. "And we sure could do with someone who likes to clean up."

"Somebody's got to clean the pictures."

"No more old pictures," says Crich. There's insistence in his voice. Miriam realizes that Crich is older than she thought. When did he get so old? And when did she get so old?

"Let me have another look at that picture of yours." Crich passes her the portrait.

"Will you come home with me? Please,

"Maybe I will come — just for a short visit," she says. Miriam looks at the reclining Venus. She was so beautiful, but was it time to leave her behind? Perhaps there were other things to see in this hot, green

"Let's go home, Mrs M." Crich picks up Miriam's cleaning equipment. He gently takes her arm, and he leads her, slowly, out of the National Gallery.

Deborah Walker lives in London. Find her in the British Museum, nicking ideas from ancient cultures.